

20th Symposium on Application of Plasma Processes



COST TD1208 Workshop on Application of Gaseous Plasma with Liquids

Book of Contributed Papers

Tatranská Lomnica, Slovakia
17-22 January, 2015

Edited by P. Papp, J. Országh, L. Moravský, A. Ribar, Š. Matejčík

Book of Contributed Papers: 20th Symposium on Application of Plasma Processes and COST TD1208 Workshop on Application of Gaseous Plasma with Liquids, Tatranská Lomnica, Slovakia, 17-22 January 2015

Symposium organised by Department of Experimental Physics, Faculty of Mathematics, Physics and Informatics, Comenius University in Bratislava; Society for Plasma Research and Applications, in hotel Slovan, Tatranská Lomnica, Slovakia, 17-22 January 2015

Editors: P. Papp, J. Országh, L. Moravský, A. Ribar, Š. Matejčík

Publisher: Department of Experimental Physics, Faculty of Mathematics, Physics and Informatics, Comenius University in Bratislava (Slovakia); Society for Plasma Research and Applications in cooperation with Library and Publishing Centre CU, Bratislava, Slovakia

Issued: January 2015, Bratislava, first issue

Number of pages: 341

URL: <http://neon.dpp.fmph.uniba.sk/sapp>

ISBN: 978-80-8147-027-1

EAN: 9788081470271

International Scientific Committee

Miroslav Černák	Masaryk University, Brno	Czech Republic
Zoltán Donkó	Hungarian Academy of Sciences, Budapest	Hungary
Tom Field	Queen's University, Belfast	United Kingdom
František Krčma	Brno University of Technology, Brno	Czech Republic
Nigel J. Mason	Open University, Milton Keynes	United Kingdom
Tilmann D. Märk	Leopold-Franzens University, Innsbruck	Austria
Jerzy Mizeraczyk	Polish Academy of Sciences, Gdansk	Poland

Local Organizing Committee

Štefan Matejčík	Chairman, Comenius University, Bratislava	Slovakia
František Krčma	Brno University of Technology, Brno	Czech Republic
Peter Papp	Comenius University, Bratislava	Slovakia
Juraj Országh	Comenius University, Bratislava	Slovakia
Ladislav Moravský	Comenius University, Bratislava	Slovakia
Anita Ribar	Comenius University, Bratislava	Slovakia
Zuzana Lichvanová	Comenius University, Bratislava	Slovakia

Reading Committee

Štefan Matejčík	Comenius University, Bratislava	Slovakia
Peter Papp	Comenius University, Bratislava	Slovakia
Juraj Országh	Empa, Thun	Switzerland
Nigel J. Mason	Open University, Milton Keynes	United Kingdom
František Krčma	Brno University of Technology, Brno	Czech Republic

Jan D. Skalný's Prize Awarding Committee

Štefan Matejčík	Comenius University, Bratislava	Slovakia
František Krčma	Brno University of Technology	Czech Republic
Wiesława Barszczewska	Siedlce University, Siedlce	Poland
Zoltán Donkó	Hungarian Academy of Sciences, Budapest	Hungary
Tom Field	Queen's University, Belfast	United Kingdom
Ivo Utke	Empa, Thun	Switzerland
Satoshi Hamaguchi	Osaka University, Osaka	Japan

Organizers

Department of Experimental Physics, Comenius University, Bratislava, Slovakia
Society for Plasma Research and Applications, Bratislava, Slovakia

Conference Topics

1. Electrical discharges and other plasma sources
2. Elementary processes and plasma chemical reactions
3. Plasma-surface interactions
4. Plasma treatment of polymer and biological material
5. Nanometer-scaled plasma technologies
6. Ion mobility spectrometry
7. COST TD1208 Workshop

Invited Speakers

Jan Benedikt	Ruhr-University, Bochum	Germany
Mário Janda	Comenius University, Bratislava	Slovakia
Ivo Utke	Empa, Thun	Switzerland
Andreas Walte	Airsense Analytics GmbH, Schwerin	Germany
Philipp Sulzer	IONICON Analytik GmbH, Innsbruck	Austria
Satoshi Hamaguchi	Osaka University, Osaka	Japan
Rony Brandenburg	INP, Greifswald	Germany
Petr Vašina	Masaryk University, Brno	Czech Republic
Jean-Paul Booth	Ecole Polytechnique, Palaiseau	France
Denis Kalupin	EUROfusion PMU, Garching	Germany

COST TD1208 Workshop on Application of Gaseous Plasma with Liquids

Malte Hammer	INP, Greifswald	Germany
Zdenko Machala	Comenius University, Bratislava	Slovakia
Eva Doležalová	Institute of Plasma Physics, Prague	Czech Republic
Fernando Brandi	INO and IIT, Pisa	Italy

Contents

COST TD1208 Workshop on Application of Gaseous Plasma with Liquids	11
IL-01 INFLUENCE OF PLASMA-TREATED LIQUIDS ON STRUCTURE AND FUNCTION OF LIPID MEMBRANES	
<u>M. U. Hammer</u> , S. Kupsch, E. Forbrig, H. Jablonowski, K. Masur, K.-D. Weltmann, A. Beerlink, T. Gutschmann, S. Reuter	12
IL-02 WATER ELECTROSPRAY THROUGH AIR CORONA AND SPARK DISCHARGES AND INDUCED WATER CHEMISTRY	
B. Pongráč, V. Martišovits, M. Janda, B. Tarabová, K. Hensel, <u>Z. Machala</u>	13
IL-03 ACTIVE BUT NONCULTURABLE STATE OF ESCHERICHIA COLI INDUCED BY PLASMA GENERATED IN GAS AND LIQUID PHASE	
<u>E. Dolezalova</u> , V. Prukner, P. Lukes, M. Simek	17
IL-04 NANOPARTICLE GENERATION BY PULSED LASER ABLATION IN LIQUID	
<u>F. Brandi</u>	22
HT-01 ELEMENTARY PROCESSES IN ARGON COVERED CLUSTERS - THE WAY TO NOVEL PLASMA CHEMISTRY?	
<u>J. Kocisek</u> , J. Lengyel, P. Slavicek, M. Farnik	23
HT-02 DETECTION OF ROS/RNS IN WATER ACTIVATED BY AIR TRANSIENT SPARK DISCHARGE	
<u>B. Tarabová</u> , P. Lukeš, K. Tarabová, K. Hensel, L. Šikurová, Z. Machala	27
HT-03 DEGRADATION OF AMOXICILLIN IN WATER TREATED WITH DBD PLASMA	
<u>T. Izdebski</u> , E. Ceriani, E. Marotta, C. Paradisi, M. Dors	32
20 th Symposium on Application of Plasma Processes	38
HT-04 ELECTRON AFFINITY EVALUATION FROM NEGATIVE ION MASS SPECTROMETRY DATA	
<u>N. Asfandiarov</u> , S. Pshenichnyuk, A. Vorob'ev, E. Nafikova, Y. Elkin, A. Modelli	39
HT-05 ANION CHEMISTRY ON TITAN: A POSSIBLE ROUTE TO LARGE HYDROCARBONS	
<u>J. Žabka</u> , M. Polášek, C. Romanzin, C. Alcaraz	43
IL-05 STUDY OF PLASMA-CHEMISTRY PROCESSES IN ATMOSPHERIC PRESSURE PLASMAS: ABSOLUTE DENSITY MEASUREMENTS OF RADICALS, VUV SPECTROSCOPY AND SIMULATIONS	
<u>J. Benedikt</u> , K. Rügner, S. Schneider, S. Große-Kreul, V. Layes, G. Willems, M. Hefny, S. Hübner, A. von Keudell	44
IL-06 SPATIOTEMPORAL IMAGING OF SELF-PULSING NANOSECOND DISCHARGES	
<u>M. Janda</u> , K. Hensel, A. Buček, V. Martišovits, Z. Machala	50
HT-06 FAST NEUTRALS AND ENERGY-DEPENDENT SECONDARY ELECTRON EMISSION COEFFICIENTS IN PIC/MCC SIMULATIONS OF CAPACITIVELY COUPLED PLASMAS	
<u>A. Derzsi</u> , I. Korolov, E. Schüngel, Z. Donkó, J. Schulze	56

IL-07	WRITING NOVEL NANOSCALE MATERIALS WITH FOCUSED ELECTRON BEAMS AND VOLATILE METAL-CONTAINING COMPOUNDS	
	<u>I. Utke</u>	61
HT-07	SYNTHESIS OF GRAPHENE-LIKE NANOMATERIALS BY CARBON ARC DISCHARGE	
	O. Łabędź, H. Lange, M. Bystrzejewski, <u>A. Huczko</u>	63
HT-08	BREAKDOWN VOLATGE CURVES AND VOLT-AMPERE CHARACTERISTICS OF WATER VAPOR IN MICROGAPS	
	<u>M. Radmilović-Radjenović</u> , Š. Matejčik, M. Klas, B. Radjenović.....	68
IL-08	ION MOBILITY SPECTROMETRY FOR THE DETECTION OF TOXIC GASES– OVERVIEW OF THE TECHNOLOGY AND IMPROVEMENTS	
	<u>A. Walte</u> , B. Ungethüm, W. Münchmeyer.....	74
IL-09	SELECTIVE-REAGENT-IONIZATION MASS SPECTROMETRY (SRI-MS): ADVANCEMENTS IN INSTRUMENTATION AND NOVEL APPLICATIONS	
	M. Lanza, W. Joe Acton, K. Breiev, S. Jürschik, R. Gutmann, A. Jordan, E. Hartungen, G. Hanel, J. Herbig, L. Märk, C. A. Mayhew, T. D. Märk, <u>P. Sulzer</u>	84
HT-09	IONIZATION CHARACTERISTICS OF AMINO ACIDS IN DIRECT ANALYSIS IN REAL TIME MASS SPECTROMETRY USING ATMOSPHERIC PRESSURE HELIUM PLASMA	
	<u>K. Sekimoto</u> , M. Takayama.....	96
HT-10	DIRECT LIQUID SAMPLING FOR CORONA DISCHARGE ION MOBILITY SPECTROMETRY	
	<u>M. Sabo</u> , M. Malásková, O. Harmathová, J. Hradsky, M. Masár, Š. Matejčik.....	101
HT-11	MICROCHIP ELECTROPHORESIS IN THE ANALYSIS OF BIOLOGICAL AND ENVIRONMENTAL SAMPLES	
	<u>M. Masár</u> , J. Hradski, M. Sabo, Š. Matejčik.....	105
HT-12	ION MOBILITY SPECTROMETRY APPARATUS WITH RADIOACTIVE IONIZATION SOURCE	
	<u>B. Michalczuk</u> , K. Wnorowski, A. Jówko, W. Barszczewska.....	108
IL-10	REACTION AND TRANSPORT OF PLASMA-GENERATED REACTIVE SPECIES IN LIQUID	
	K. Ikuse, <u>S. Hamaguchi</u>	111
IL-11	NOVEL INSIGHTS IN THE DEVELOPMENT OF DIELECTRIC BARRIER DISCHARGES	
	<u>R. Brandenburg</u>	118
HT-13	RAPE TREATMENT BY THE LOW PRESSURE MICROWAVE PLASMA DISCHARGE AND GLIDING ARC PLASMA	
	<u>P. Olšan</u> , P. Kříž, Z. Havelka, A. Bohatá, M. Strejčková, P. Bartoš, P. Špatenka.....	119
IL-12	UNDERSTANDING OF HYBRID PVD-PECVD PROCESS WITH AIM TO CONTROL GROW OF NANOSTRUCTURED COMPOSITE COATINGS	
	<u>P. Vasina</u> , T. Schmidtova, P. Soucek, R. Zemlicka, P. Vogl, M. Jilek.....	125
HT-14	INVESTIGATION OF METAL COATED HIGHLY ORDERED PYROLITIC GRAPHITE	

	<u>S. Ralser</u> , S. Raggl, M. Harnisch, P. Scheier	130
HT-15	ELECTRICAL CHARACTERIZATION OF HYDROGEN MICRODISCHARGES FROM DIRECT CURRENT UP TO 13,56 MHZ	
	<u>M. Klas</u> , L. Moravský, Š. Matejčík	132
HT-16	CHARACTERIZATION OF A NON-EQUILIBRIUM ATMOSPHERIC PRESSURE PLASMA JET DRIVEN BY NANOSECOND VOLTAGE PULSES	
	M. Boselli, V. Colombo, <u>M. Gherardi</u> , R. Laurita, A. Liguori, P. Sanibondi, E. Simoncelli, A. Stancampiano.....	135
HT-17	GLIDING ARC SUBJECTED TO HYPERGRAVITY	
	L. Potočňáková, J. Šperka, P. Zikán, J. J.W.A. van Loon, J. Beckers, <u>V. Kudrle</u>	140
HT-18	INTERACTION OF FREE ELECTRONS WITH NANO-SOLVATED BIOMOLECULES	
	<u>M. Neustetter</u> , J. Aysina, P. Scheier, S. Denifl.....	145
IL-13	QUANTITATIVE DIAGNOSTICS OF INDUCTIVE PLASMAS IN Cl₂, O₂ AND Cl₂/O₂ MIXTURES	
	<u>J.-P. Booth</u> , M. Foucher, D. Marinov, P. Chabert.....	147
IL-14	INTEGRATED MODELLING ACTIVITIES FOR TOKAMAKS	
	<u>D. Kalupin</u> , S. Matejčík, F. Zaitsev	152
HT-19	ATMOSPHERIC PRESSURE PLASMA CO POLYMERIZATION OF MALEIC ANHYDRIDE AND ACETYLENE IN DIELECTRIC BARRIER DISCHARGE	
	<u>L. Zajíčková</u> , A. Manakhov, M. Eliáš, M. Michlíček, A. Obrusník, P. Jelínek, J. Polčák	153
Posters - COST TD1208		159
P-01	HIGH FREQUENCY DISCHARGE BETWEEN SOLID AND LIQUID ELECTRODES	
	<u>Al. F. Gaisin</u> , R. Sh. Sadriev, I. Sh. Abdullin, V. S. Zheltuhin.....	160
P-02	LOW TEMPERATURE PLASMA OF ELECTRIC DISCHARGES WITH LIQUID ELECTROLYTE ELECTRODES IN THE SURFACE TREATMENT PROCESS	
	<u>F.M. Gaisin</u> , Al. F. Gaisin, F. Shakirova, G. T. Samitova	164
P-03	PLASMA TREATMENT OF HOLLOW OBJECTS USING SURFACE DBD WITH LIQUID ELECTRODES	
	D. Pavliňák, O. Galmiz, A. Brablec, <u>V. Kudrle</u> , M. Černák.....	166
P-04	THE EFFECT OF THE PLASMA NEEDLE ON THE WOUND HEALING PROCESS	
	I. Korolov, B. Fazekas, M. Széll, L. Kemény, <u>K. Kutasi</u>	169
P-05	PLASMA GUN DECONTAMINATION OF BACTERIA IN LIQUID SUSPENSIONS	
	M. Boselli, F. Cavrini, V. Colombo, M. Gherardi, R. Laurita, A. Liguori, <u>E. Simoncelli</u> , A. Stancampiano, L. Viola.....	173

Posters – SAPP XX.....	178
P-06 COMPARISON OF RESULTS FROM ELECTRON INDUCED FLUORESCENCE STUDY OF DEUTERIUM AND HYDROGEN MOLECULE	
<u>M. Danko</u> , A. Ribar, J. Országh, Š. Matejčík	179
P-07 DISSOCIATIVE ELECTRON ATTACHMENT TO CARBON AND NITROGEN RICH MOLECULES: DEVELOPMENTS FROM QUEEN'S UNIVERSITY BELFAST	
<u>T. Gilmore</u> , T. Field	184
P-08 ION INDUCED WATER RELEASE FROM ACETURIC ACID	
J. Kopyra, <u>J. Kocisek</u> , R. Delaunay, B. A. Huber, P. Rousseau, A. Domaracka	185
P-09 STUDY OF OZONE THERMAL DECOMPOSITION ON METAL SURFACES	
Z. Kozáková, <u>F. Krčma</u> , M. Procházka, R. Veverková, E. Krejsková	190
P-10 ELECTRON INDUCED DISSOCIATION ON DICYCLOHEXYL PHTHALATE	
<u>M. Lacko</u> , P. Papp, Š. Matejčík.....	195
P-11 DETERMINATION OF THE NITROGEN ATOM WALL RECOMBINATION PROBABILITY IN LATE AFTERGLOW	
<u>V. Mazánková</u> , D. Trunec, F. Krčma	200
P-12 REACTION OF BENZYNE RADICAL ANIONS WITH ACETYLENE. A STEP TOWARDS THE FORMATION OF PAHS IN EXTRATERRESTRIAL ENVIRONMENTS?	
<u>M. Obluková</u> , M. Polášek, J. Žabka	204
P-13 LUMINESCENCE OF PHOSPHORS INDUCED BY ELECTRON IMPACT	
<u>J. Országh</u> , I. Utke, Š. Matejčík.....	205
P-14 A COMPLEX STUDY OF ELECTRON IMPACT IONISATION AND DISSOCIATION OF METHYL-, DIMETHYL- AND TRIMETHYLPHENYLSILANE	
M. Lacko, <u>P. Papp</u> , A. Al Mahmoud Alsheikh, J. Žídek, F. Krčma, Š. Matejčík.....	210
P-15 ELECTRON IMPACT DISSOCIATIVE IONIZATION OF TETRAETHYL ORTHOSILICATE	
J. Maljković, <u>P. Papp</u> , M. Lacko, M. Stano, A. Milosavljević, Š. Matejčík.....	214
P-16 DIFFERENCES BETWEEN FLUORESCENCE SPECTRA OF VARIOUS HYDROCARBONS WITH EMPHASIS ON NITROMETHANE	
<u>A. Ribar</u> , M. Danko, J. Országh and Š. Matejčík.....	217
P-17 ROTATIONAL TEMPERATURES IN HYDROGEN AND HYDROGEN-ARGON DC DISCHARGE	
<u>M. Suchoňová</u> , J. Krištof, M. Anguš, P. Veis	222
P-18 KINETICS OF LOW ENERGY ELECTRON ATTACHMENT TO SOME CHLORINATED ALCOHOLS IN THE GAS PHASE	
<u>K. Wnorowski</u> , J. Wnorowska, B. Michalczyk, W. Barszczewska	228
P-19 STUDY OF THE CH₃⁺ + O₂ REACTION AT TEMPERATURES RELEVANT TO THE ATMOSPHERE OF TITAN	

	<u>I. Zymak</u> , J. Žabka, M. Polášek	232
P-20	ELECTROHYDRAULIC LEACHING OF ALKALI METALS FROM ZINNWALDITE MICA	
	M. Faltus, V. Babický, J. Botula, N. Hong Vu, <u>M. Člupek</u>	234
P-21	LOW PRESSURE PLASMA CHEMICAL TREATMENT FOR METAL ARTEFACTS - CONSERVATION APPROACH	
	<u>H. Grossmannová</u> , F. Krčma	240
P-22	PLASMA NEEDLE DECOLOURISATION OF DIRECT RED (DR 28) DIAZO DYE	
	T. Mitrović, N. Božović, N. Tomić, Z. Dohčević-Mitrović, D. Maletić, <u>S. Lazović</u> , G. Malović, U. Cvelbar, Z.Lj. Petrović	245
P-23	DECOMPOSITION AND ANALYSIS OF HARD AND MODERATELY DUCTILE MOBC COATINGS BY PULSED DC SPUTTERING	
	<u>V. Peřina</u> , P. Souček, P. Vašina, V. Buršíková, V. Havránek	248
P-24	ATMOSPHERIC PRESSURE PLASMA JET SURFACE CLEANING, SURFACE MODIFICATION AND NANO-COATING	
	<u>P. Urbán</u>	253
P-25	EXPERIMENTAL AND MODELING STUDIES OF LOW-PRESSURE CAPACITIVE OXYGEN PLASMAS EXCITED BY TAILORED VOLTAGE WAVEFORMS	
	A. Derzsi, T. Lafleur, I. Korolov, J. P. Booth, <u>Z. Donkó</u>	256
P-26	RADIOFREQUENCY AND DIRECT CURRENT BREAKDOWN IN HYDROGEN: EXPERIMENT AND KINETIC SIMULATIONS	
	<u>I. Korolov</u> , Z. Donkó	262
P-27	FORCE BALANCE OF DUST PARTICLES IN RF+DC DISCHARGES	
	N. Kh. Bastykova, <u>A. Zs. Kovács</u> , S. K. Kodanova, T. S. Ramazanov, I. Korolov, P. Hartmann, Z. Donkó	268
P-28	A PHOTOELECTRIC FRANK-HERTZ EXPERIMENT AND ITS KINETIC SIMULATION	
	<u>P. Magyar</u> , I. Korolov, Z. Donkó	273
P-29	STUDY OF MICRODISCHARGES IN HYDROGEN	
	<u>L. Moravský</u> , M. Klas and Š. Matejčík	279
P-30	HIGH SPEED CAMERA IMAGING OF MINI GLIDARC DISCHARGE	
	P. Terebun, M. Kwiatkowski, P. Krupski, <u>J. Pawlat</u> , J. Diatczyk, M. Janda, K. Hensel, Z. Machala	283
P-31	NON-RADIOACTIVE SOURCE OF ELECTRONS AT ATMOSPHERIC PRESSURE	
	<u>M. Sámel</u> , M. Stano, Š. Matejčík	288
P-32	UPGRADE OF THE 5-CHANNEL NEUTRAL PARTICLE ANALYSER FOR THE COMPASS TOKAMAK	
	<u>M. Stano</u> , A. Seman, Š. Matejčík, J. Stöckel	291

P-33	PLASMA-ASSISTED ENCAPSULATION OF POLLEN FOR QUANTITATIVE ANALYSIS USING LASER INDUCED BREAKDOWN SPECTROSCOPY	
	<u>M. Suchoňová</u> , C. Foissac, M. Horňáčková, B. Mutel, A. Anušová, P. Veis, P. Supiot	295
P-34	LIPID MODIFICATIONS BY COLD ATMOSPHERIC PLASMA TREATMENTS AND THE INFLUENCE OF CHOLESTEROL	
	<u>M. U. Hammer</u> , S. Kupsch, E. Forbrig, H. Jablonowski, K. Masur, K.-D. Weltmann, A. Beerlink, T. Gutschmann, S. Reuter	300
P-35	DC TRANSIENT SPARK DISCHARGE IN WATER: EFFECTS ON CELLS, DNA, PROTEINS AND ENZYMES	
	<u>K. Hensel</u> , K. Tarabová, K. Sano, B. Tarabová, M. Janda, Z. Machala, R. Jijie, C.T. Mihai, L. Gorgan, V. Pohoata, I. Topala	302
P-36	IMPROVEMENT OF POLYMER SURFACE CYTOTOXICITY BY PLASMA TREATMENT AND SUBSEQUENT GRAFTING OF VICINAL COMPOUNDS	
	<u>Z. Kolská</u> , S. Lupínková, K. Výborný, N. Kasálková Slepíčková, A. Řezníčková, M. Nagyová, V. Švorčík.....	306
P-37	SURFACE TREATMENT OF HIGH-IMPACT POLYSTYRENE USING RF-APPJ	
	<u>J. Pawlat</u> , P. Terebun, M. Kwiatkowski, P. Krupski, J. Diatczyk, T. Murakami.....	310
P-38	GRAFTING OF PROTEINS ON PLASMA TREATED POLYMERS FOR TISSUE ENGINEERING	
	<u>V. Švorčík</u> , N. Kasálková Slepíčková, Z. Kolská, Š. Kučková, P. Slepíčka.....	314
P-39	USING DIRECT LIQUID SAMPLING FOR AMINO ACID MEASUREMENTS BY CORONA DISCHARGE ION MOBILITY SPECTROMETRY (CD-IMS)	
	<u>O. Harmathová</u> , M. Sabo, Š. Matejčík.....	318
P-40	POSSIBILITIES OF COUPLING ION MOBILITY SPECTROMETRY TO MINIATURIZED SEPARATION TECHNIQUES	
	<u>J. Hradski</u> , M. Sabo, Š. Matejčík, M. Masár	323
P-41	THE RESEARCH OF EXPLOSIVE 2,4,6- TRINITROTOLUENE BY CORONA DISCHARGE-ION MOBILITY-MASS SPECTROMETRY	
	<u>Z. Lichvanová</u> , M. Sabo, B. Michalczuk, Š. Matejčík.....	326
P-42	LASER DESORPTION OF EXPLOSIVES USING ION MOBILITY SPECTROMETRY	
	<u>M. Malásková</u> , M. Sabo, Š. Matejčík	331
P-43	DETECTION OF 2,4,6-TRINITROTOLUENE USING CORONA DISCHARGE-ION MOBILITY SPECTROMETRY WITH AN ORTHOGONAL ACCELERATED TIME OF FLIGHT	
	<u>B. Michalczuk</u> , M. Sabo, Z. Lichvanova, W. Barszczewska.....	335
P-44	USING ION MOBILITY SPECTROMETRY FOR DIRECT DETECTION OF 2,4,6-TRICHLOROANIZOL FROM CORK STOPPER	
	<u>M. Sabo</u> , M. Malásková, Š. Matejčík.....	339

COST TD1208
Workshop on Application of Gaseous Plasma with Liquids

Oral Presentations

INFLUENCE OF PLASMA-TREATED LIQUIDS ON STRUCTURE AND FUNCTION OF LIPID MEMBRANES

M. U. Hammer¹, S. Kupsch¹, E. Forbrig¹, H. Jablonowski¹, K. Masur¹, K.-D. Weltmann², A. Beerlink⁴, T. Gutsmann³, S. Reuter¹

¹*Centre for Innovation Competence (ZIK) plasmatis at the INP Greifswald, Felix-Hausdorff-Str. 2, 17489 Greifswald, Germany*

²*Leibniz Institute for Plasma Science and Technology (INP Greifswald e.V.), Felix-Hausdorff-Straße 2, 17489, Greifswald, Germany*

³*Divisions of Biophysics, Leibniz Centre for Medicine and Biosciences, Research Centre Borstel, 23845 Borstel, Germany*

⁴*Deutsches Elektronen-Synchrotron (DESY), Notkestraße 85, 22607 Hamburg, Germany*
E-mail: Malte.Hammer@INP-Greifswald.de

In plasma medicine, cells and bacteria are treated with cold atmospheric plasma that create reactive species both in the gas and in the liquid phase. A dogma of membrane biophysics is, that any externally applied substance has to interact or overcome the most outward interface of a cell to its environment -the membrane- before a cellular reaction takes place. Therefore the membrane is the first cellular target of reactive species during plasma treatment of eu- and prokaryotes. We used model systems composed out of lipids to investigate the effect of plasma treatments on cellular membranes. We studied the modification of important biophysical parameters of the membrane by plasma treatment. The observed effects on a membrane model representing eukaryotes were significantly reduced compared to the effects on a model representing prokaryotes. The findings help to understand the observed lower susceptibility of eukaryotes compared to prokaryotes against plasma treatment.

WATER ELECTROSPRAY THROUGH AIR CORONA AND SPARK DISCHARGES AND INDUCED WATER CHEMISTRY

B. Pongráč, V. Martišovits, M. Janda, B. Tarabová, K. Hensel, and Z. Machala

Faculty of Mathematics, Physics and Informatics, Comenius University, Bratislava, Slovakia

E-mail: machala@fmph.uniba.sk

Decontamination of water polluted with organic and microbial pollutants, and biomedical effects on cells mediated through aqueous solutions can be efficiently achieved by using various non-thermal plasma discharges. These effects can be further enhanced when air discharges are combined with water electro spray. The presence of the electrical discharge generating non-thermal plasma in the spraying area allows for very efficient mass transfer of plasma-generated species into the water [1, 2].

We investigated the effect of the electro spraying of water in combination with positive DC corona discharge. Our key finding is that the discharge has a significant effect on the electro spray behavior and vice versa [3-6]. Such water electro spray-air discharge system was demonstrated to be very efficient in inducing bactericidal and various chemical effects in treated water [1, 7].

1. Imaging of corona generation during the intermittent electro spray

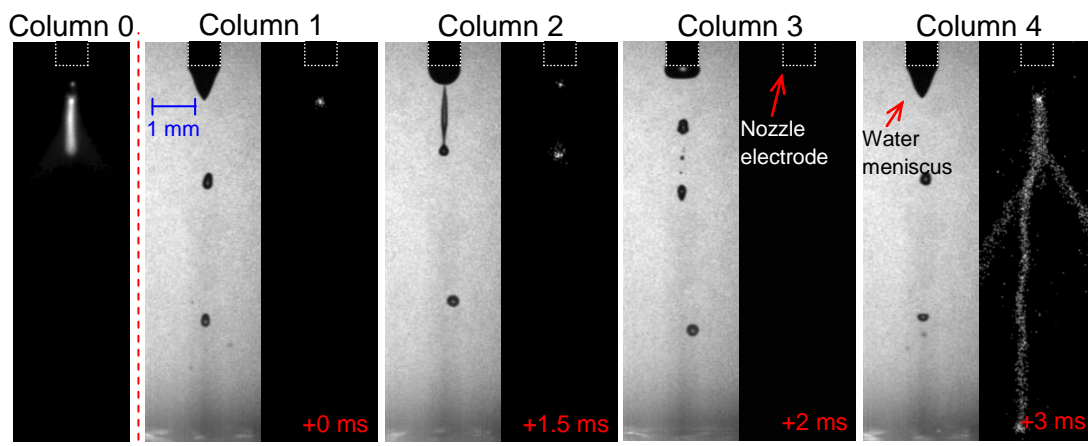


Fig. 1. iCCD time sequence images of electro spraying of water (illuminated, columns 1-4 with exposure time $10 \mu\text{s}$) with corona discharge (dark, columns 1-4 with exposure time $100 \mu\text{s}$) in spindle mode for water conductivity $500 \mu\text{S/cm}$, $+6 \text{ kV}$, gap 1 cm , nozzle 0.8 mm o.d. and 0.6 mm i.d. iCCD dark image in column 0 with exposure time 5 s represent an integrated emission over the long period with many droplet formation cycles. [5]

The experimental setups, materials and methodology have been described in great detail in our previous papers. [1-2, 5-7]

We investigated the corona discharge generation during the electro spray of water. Fig. 1 shows different stages of the electro spraying event and the discharge propagation from 0 to 3 ms.

The glow corona is first visible at the tip of the water cone (column 1). As the water cone gradually elongates and creates the filament which propagates axially towards the grounded electrode, the bright spot of the glow corona remains present at the tip of this filament and propagates with it (column 2). After the detachment of the elongated water fragment, and the contraction of the water meniscus back towards the nozzle, the glow corona disappears (column 3). Finally, after a few ms, a new cone is formed, and the filamentary discharge occurs from the cone tip (column 4).

The dark image in column represent an integrated emission over the long period (5s) with many cycles of droplet formation and corona discharge on the water cone tip during this intermittent

electrospraying mode, and its movement with elongating water filament. The image also represents the visual appearance of the discharge during the electrospray.

We showed that the appearance of the corona on the water filament tip is primarily the electric field effect due to the various curvatures of this water filament tip [5].

2. Measurements of the electrosprayed droplet size and time of flight

The fast camera image sequences also enabled us to estimate the average time of flight (time between the water filament disintegration and the droplet fall on the grounded electrode) in 1 cm gap and the sizes of the sprayed water droplets between the electrodes. For instance, in the case of low conductivity water ($2 \mu\text{S}/\text{cm}$) this average time of flight is $\sim 100 \mu\text{s}$ for the first incoming droplets from the head of the filament, and $\sim 2.5 \text{ ms}$ for the last one. The characteristic size of the water droplet (approximating to a spherical shape) vary approximately from $<10 \mu\text{m}$ to $\sim 250 \mu\text{m}$ in diameter. The droplet size becomes larger with higher liquid conductivities (from $\sim 190 \mu\text{m}$ to $\sim 280 \mu\text{m}$ for $400 \mu\text{S}/\text{cm}$). The same applies to the time of flight which becomes longer (from $\sim 2.7 \text{ ms}$ to $\sim 6.3 \text{ ms}$ for $400 \mu\text{S}/\text{cm}$). Since the droplets are formed by disintegration of the thin water filament, the sizes of droplets are determined by this filament thickness. The time of flight is related with the velocity of filament propagation and its length before disintegration. Both of these parameters (filament size and filament velocity) depend on the water conductivity, as also described elsewhere [6].

Knowing the typical droplet size and time of flight is important in water decontamination applications when considering the mass transfer of plasma generated active species into the water droplets while they are sprayed through the discharge. Our results on bio-decontamination of water in streamer corona or transient spark showed that even such short times of flight enable efficient mass transfer of air plasma generated reactive oxygen and nitrogen species in the sprayed water to induce significant bactericidal effects [1,7]. In addition, water activated by the electrospray with very low flow rates ($\sim 0.05 \text{ ml}/\text{min}$) demonstrated enhanced bactericidal effects when sprayed on the surfaces [2]. The key is probably in very high surface to volume ratio of the droplets.

3. Influence of the water conductivity on the corona properties

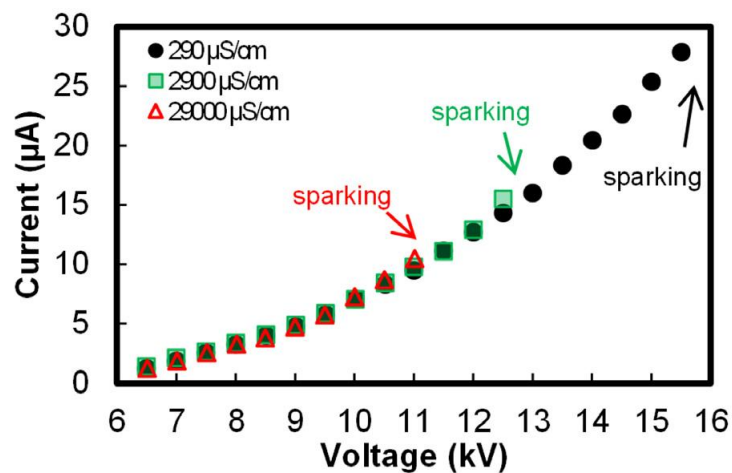


Fig. 2. I-V characteristics of the electrospray with corona discharge. Different breakdown voltages for corona-to-spark transition are due to different conductivity effect.

Depending on the conductivity, various spray properties were observed: pointy, prolonged, and fast spreading water filaments for lower conductivity; in contrast to rounder, broader, and shorter quickly disintegrating filaments for higher conductivity. When the conductivity increases, the breakdown voltage for corona-to-spark transition decreases (Fig. 2).

Since the highly conductive liquid acts as a good conductor, the electric field is stronger on the highly conductive water meniscus. The discharge is thus permitted to occur at the liquid surface and the

discharge activity on the water filament tip is then enhanced as the filament proceeds toward the ground electrode.

For poorly conductive liquids, the liquid acts more as an insulator and the electrical resistance of the growing water filament suppresses the corona activity on its surface. So the discharge is forced to occur on the metal electrode. Subsequently, the spark does not occur until the higher voltage [6].

4. Chemistry induced in water electrosprayed through air discharges

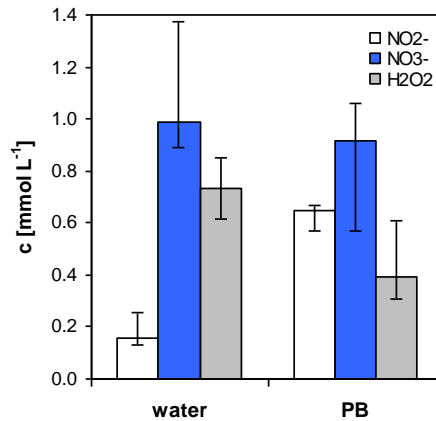


Fig. 3. Nitrite (NO₂⁻), nitrate (NO₃⁻) and hydrogen peroxide (H₂O₂) concentrations measured in modeled tap water (acidification occurs) and *phosphate buffer* (no acidification occurs) solutions air transient spark plasma treatment via electro-spray. [1]

Chemical and bactericidal effects induced by plasma in water upon electro-spraying through DC-driven positive transient spark discharge in air were investigated. Inactivation of *E. coli* bacteria in water was determined in dependence on pH (controlled by buffers) and correlated with chemical changes induced in water, namely generation of reactive oxygen and nitrogen species (RONS) that play significant roles in cell physiology and many medical therapies [8]. The discharges in humid air (or air with water microdroplets) produce OH radicals, nitrogen oxides and in some cases ozone, resulting in the formation of hydrogen peroxide, nitrites, nitrates, peroxyxynitrites and pH changes in the sprayed water. The degree of inactivation and oxidative damage of bacteria increased with the increasing acidity of the solution. Acidified nitrites interacting with hydrogen peroxide were determined as the most important bactericidal ROS/RNS agents in plasma-treated water leading to peroxyxynitrites (peroxyxynitrous acid) [1, 9].

In the specific case of low power corona discharge with water electro-spray, the bactericidal effect of ozone dissolved in water may play an important role. Since the diffusive solubility of ozone in water is relatively low, the interaction of non-thermal plasma with the micrometric droplets of water in the spraying area allows for very efficient mass transfer of ozone into the water.

5. Acknowledgement

This work was supported by Slovak Research and Development Agency APVV-0134-12 and APVV SK-RO-0024-12, and Slovak grant agency VEGA 1/0998/12 and COST Action TD1208 – Electrical Discharges with Liquids for Future Applications. We thank our partners and collaborators H.-H. Kim (*AIST Tsukuba, Japan*), P. Lukeš (*Institute of Plasma Physics AS CR, Prague, Czech Republic*), and D.B. Graves (*University of California, Berkeley, USA*) for stimulating discussions and sharing their advanced imaging, analytical, and biochemical instrumentation and expertise.

6. References

- [1] Machala Z, Tarabová B, Hensel K, Špetlíková E, Šikurová L, and Lukeš P 2013 *Plasma Process. Polym.* **10** 649.

- [2] Kovařová Z, Tarabová K, Hensel K and Machala Z 2013 *Eur. Phys. J. Appl. Phys.* **61** 24306.
- [3] Borra J P, Ehouarn P and Boulaud D 2004 *J. Aerosol Sci.* **35** 1313.
- [4] S. Kuroda S and Horiuchi T 1984 *Jpn J. Appl. Phys.* **23** 1598.
- [5] Pongráč B, Kim H H, Janda M, Martišovits V, Machala Z 2014 *J. Phys. D: Appl. Phys.* **43** 315202.
- [6] Pongráč B, Kim H H, Negishi N and Machala Z 2014 *Eur. Phys. J. D* **68** 224.
- [7] Machala Z, Chládeková L and Pelach M 2010 *J. Phys. D: Appl. Phys.* **43** 222001
- [8] Graves D B 2012 *J. Phys. D: Appl. Phys.* **45** 263001.
- [9] Lukeš P, Doležalová E, Sisrová I and Člupek M 2014 *Plasma Sources Science Technol.* **23** 015019.

ACTIVE BUT NONCULTURABLE STATE OF *ESCHERICHIA COLI* INDUCED BY PLASMA GENERATED IN GAS AND LIQUID PHASE

Eva Dolezalova, Vaclav Prukner, Petr Lukes, Milan Simek

¹*Department of Pulse Plasma Systems, Institute of Plasma Physics AS CR, v.v.i., Za Slovankou 3, 18200 Prague, Czech Republic*

E-mail: dolezalova@ipp.cas.cz

Non-thermal atmospheric pressure plasma is extensively applied as an efficient decontamination medium; however, the decontamination is usually evaluated by the simplest classical cultivation method. We investigated the plasma induced inactivation by the conventional cultivation and fluorescent LIVE/DEAD BacLight™ Bacterial Viability techniques. The decontamination effect was studied on a culture of *Escherichia coli* deposited either on a solid surface or dispersed in a saline solution. We observed that the bacterial counts decreased with increasing treatment time of atmospheric pressure plasma jet and coplanar surface dielectric barrier discharge. We assume that interaction of plasma with bacteria induces a stress which does not lead to the death of bacteria, but to the loss of their ability to be cultivated, thus viable but nonculturable state (VBNC) occurs.

1. Introduction

The application of non-thermal atmospheric pressure plasma appears to be promising in a field of medicine and biology. Plasma decontamination related research has been carried out recently. Plasma produces synergistic reactions through physical and chemical processes which are able to kill microorganisms. The processes potentially involved in plasma-induced bio-decontamination are heat, UV radiation, electric field, various reactive species and charged particles [1]. Recently, it has been suggested that significant pathway of dry gas plasma inactivation is erosion of the bacteria by primary reactive species. However, plasma generated in humid environment changes significantly the bio-inactivation mechanisms due to numerous plasma-chemical reactions which produce secondary reactive species interacting with living cells [2]. Major part of reactive species is generated in a very thin plasma layer close to the surface of the electrode system in the case of coplanar surface dielectric barrier discharge (CSDBD) [3]. In the case of atmospheric pressure plasma jet (APPJ) driven inactivation, it was reported that the contribution of reactive oxygen species and reactive nitrogen species is significant [4]. Generally, reactive species interact with cells causing oxidative damages to microorganisms on cell envelope, proteins, DNA or other cellular components.

The production of plasma generated reactive species and the plasma treatment itself induces bacterial cell stress, which may not cause cellular death. The most frequently used technique to evaluate bacterial inactivation is growing cells in a suitable medium using the classical colony counting cultivation [5]. Generally, variations in the surrounding environment, such as lack of nutrients or oxidation stress, can lead to higher bacterial inactivation assayed by cultivation, even though they still possess cellular activity. Remaining cellular activity of nonculturable bacteria suggests that bacteria entered a VBNC state [6, 7]. The VBNC state relates to an inhibition of bacterial growth assayed using the conventional cultivation technique under conditions in which they would normally grow and develop colonies. It was reported that VBNC bacteria possess measurable cellular activity and can be resuscitated in proper conditions; therefore, they are able to be cultivated again [8]. In this case, evaluation of bacterial inactivation using exclusively colony-counting methodology would be inaccurate [9]. However, critical point in the VBNC definition is the resuscitation. Many published studies did not reveal whether resuscitation of bacteria was caused by the regrowth of a small number of persisting culturable cells, or by recovery of the VBNC. Kell *et al.* suggested the term active but not culturable (ABNC) for cells exhibiting measurable activity but failing to grow to a detectable level. The ABNC state is related to the cells possessing activity independently on the recovery [10]. The activity of VBNC/ABNC bacteria can be determined using various techniques that evaluate intracellular metabolic pathways or the intactness of the cellular membrane [11]. Generally, the VBNC/ABNC state of bacteria represents potential threat to public health [12].

In this work, we investigated the plasma-induced bacterial inactivation and VBNC/ABNC state of bacteria after treatment induced by plasmas generated by the APPJ and CSDBD discharge devices. Cultures of *Escherichia coli* were used as a model organism in both cases. We assayed the bacterial counts with both conventional cultivation on agar plates and fluorescent method using the LIVE/DEAD® BacLight™ Bacterial Viability kit.

2. Materials and methods

We used the non-thermal APPJ (kINPen® 09, Greifswald, Germany) placed in contact with the water surface (*E. coli* dispersed in liquid phase) and the CSDBD single microdischarge generator [3] placed at a fixed distance from the target holder (*E. coli* deposited on the surface of the solid target).

2.1 Single streamer CSDBD

The CSDBD was produced on the surface of a diameter 25.4 mm disc (5 mm thick) made from MACOR® machinable glass-ceramic sealed in a polyamide holder (Fig. 1). The filamentary streamer micro-discharges were initiated by an electric field formed by the high-voltage waveforms imposed between 2 silver electrodes embedded approximately 0.4 mm below the disc's surface with a minimum distance of 1 mm between them [13]. The CSDBD was powered by an AC high voltage power supply composed of the TG1010A Function Generator (TTi), Powertron Model 250A RF Amplifier, and a high-voltage step-up transformer. The surfaces (diameter 25 mm) contaminated with bacterial suspensions of *E. coli* were exposed to single micro-discharges at a fixed distance of 2 mm. The discharge was fed humid synthetic air with a fixed flow rate 0.1 l/min.

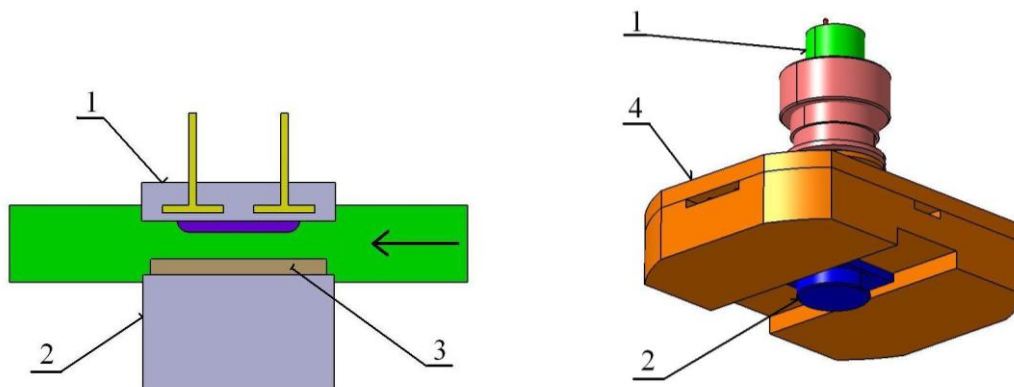


Fig. 1. Scheme of the single micro-discharge CSDBD reactor: (1) electrode system, (2) sample holder, (3) filter with bacteria, (4) body of the reactor with observation windows [13].

2.2 The atmospheric pressure plasma jet

The APPJ (kINPen® 09, Greiswald, Germany) was generated in contact with the water surface (Fig. 2) [14]. The argon plasma jet consisted of a quartz capillary with a 1.6 mm inner diameter. A pin-type electrode (1 mm diameter) was attached to the centre of the capillary. Argon flowed through the capillary, and we used a fixed argon flow rate of 4.9 l/min. A radio frequency voltage (1-5 kV, 1.5 MHz) was connected to the pin-type electrode, and a grounded ring electrode was placed near a nozzle. The plasma was generated on the top of the pin-type electrode and expanded from the nozzle to a sterile Petri dish (diameter 6 cm) containing 6 ml *E. coli* suspension. The suspension was shaken to equally disperse the effect of the plasma. The distance of the nozzle from the water surface was 6 mm.

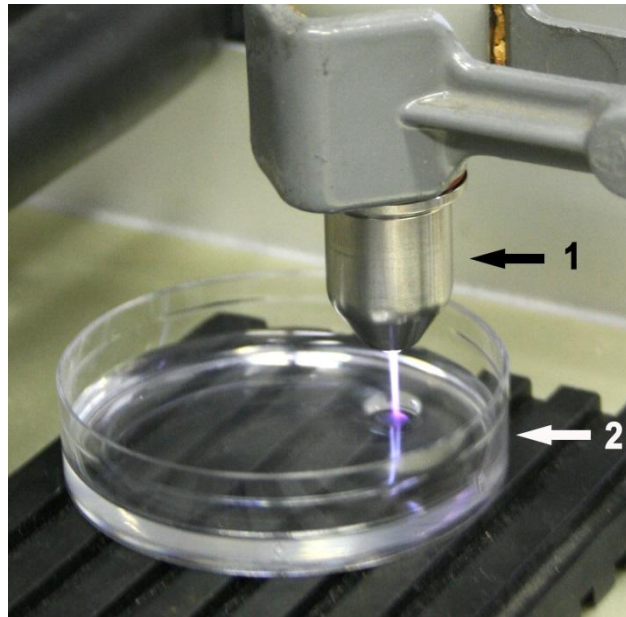


Fig. 2. Experimental procedure for bacterial decontamination by plasma jet kINPen[®] 09 (1) in a 60 mm diameter Petri dish (2) [4].

2.3 Bacterial cultures and procedures

Bacterial suspensions of *E. coli* (ATCC 25922) were prepared by dissolving bacteria in gelatine discs in a physiological solution (8.5 g NaCl in 1 l distilled water). For CSDBD treatment, 10 ml of initial bacterial suspension (10^6 CFU in 1 ml) was filtered through nylon filter (diameter 25 mm, porosity 0.45 μm) and placed at the sample holder. After the treatment, the sample was transferred to sterile dilution bottle with 10 ml of physiological solution with 3 balottini beads and shook for 45 seconds in order to disperse all bacteria from filter to solution. Direct inoculation method of 1 ml of the bacterial suspension to Petri dishes (9 cm) was used after both treatments. *E. coli* was cultivated on selective nutrient medium plates (M-FC agar base and supplement Rosolic acid, HiMedia, Mumbai, India) at temperature 37 °C for one day.

LIVE/DEAD staining (Molecular Probes Inc., Leiden, The Netherlands) was used as the fluorescent staining for determining live or dead bacteria. Staining solution was prepared by adding 6 μl of SYTO 9 dye and 6 μl of PI to 2 ml of sterile deionised water. 100 μl of staining solution was added to 100 μl of a cell suspension. Each sample was prepared in a microtiter plate and measured by a microplate reader. We incubated mixture at room temperature for 15 minutes at dark and measured with excitation wavelength centred at 485 nm and the fluorescence intensity emission at 530 and 630 nm.

3. Results and discussion

3.1 ABNC/VBNC state after plasma treatment

The number of surviving organisms in liquid and surface culture treated by CSDBD and APPJ was assayed by conventional cultivation techniques and fluorescent LIVE/DEAD kit assay (Fig. 3). The survival number decreased with time of treatment with both plasma sources; however, the survival number assayed with LIVE/DEAD kit assay was always higher than the number assayed by conventional cultivation. These results indicate that (1) plasma treatment does not necessary lead to the death of bacteria and (2) bacteria may have entered in the VBNC/ABNC state due to plasma-induced stress. This stress may have been caused by the plasma treatment itself or by consequences of the plasma generated reactive species [15].

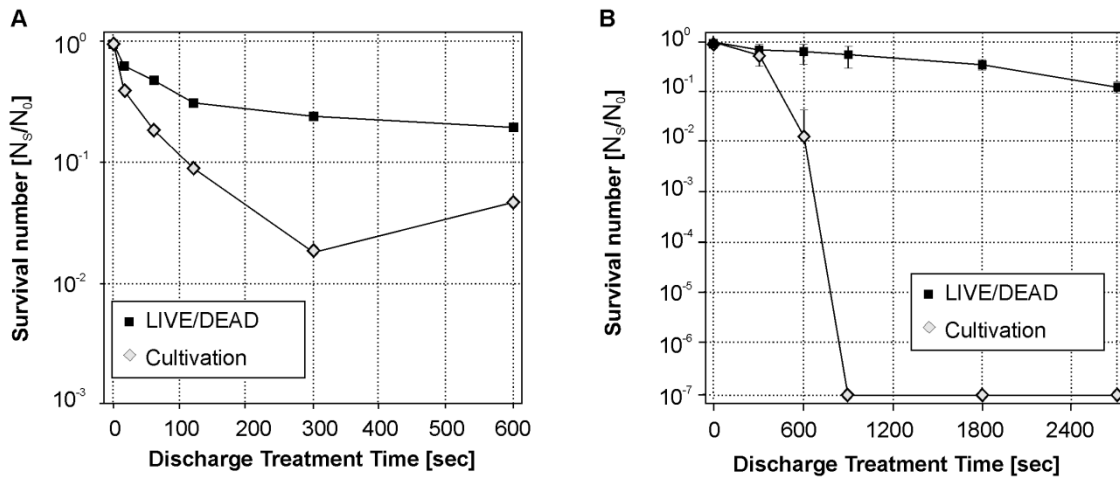


Fig. 3. Inactivation effect of plasma treatment A) bacteria on surface treated by CSDBD, B) bacteria in liquid treated by APPJ. The bacteria were assayed by the conventional colony counting methodology and using the LIVE/DEAD[®] BacLight[™].

Furthermore, we observed the VBNC/ABNC bacteria after the APPJ treatment and we examined their ability to recover and grow again in a suitable medium. Resuscitation of nonculturable bacteria is the key to the VBNC hypothesis; however, many authors argue that such resuscitation occurs because of survival of culturable cells [10, 16]. We observed that nonculturable bacteria did not grow in Petri dishes up to 6 months of resuscitation after plasma treatment. Therefore, because we did not observe cell recovery, we believe that bacteria were rather in the ABNC state. We assume that the bacteria did not grow because of unsuitable resuscitation or inhibition of the replication process by the plasma treatment. The integrity of bacterial membranes retained up to 3 months after the plasma treatment; therefore, we assume that cells still possess the ability to be virulent. Several studies observed persisting bacterial pathogenicity when bacteria were no longer able to grow and form colonies [8, 12].

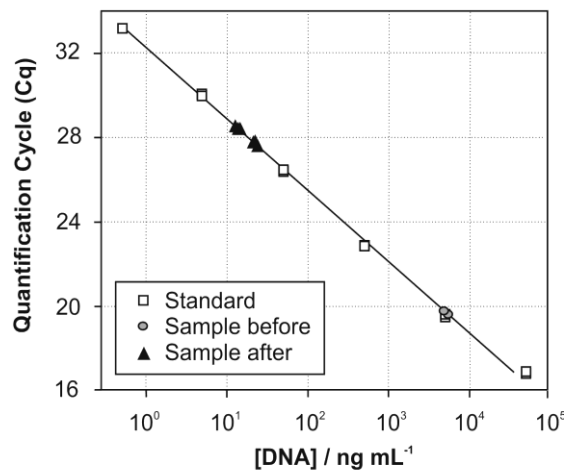


Fig. 4. Amplification of *E. coli* DNA [4].

The resuscitation of plasma-treated nonculturable bacteria did not occur; therefore, we performed a preliminary experiment to determine whether the plasma causes damages of the DNA strand. We treated solution of the isolated DNA by plasma and subsequently observed the approximate concentration of target gene on DNA strand (C_q). We measured the concentration of DNA by comparing the C_q values of known copy number and the plasma-treated/untreated DNA solution

(Fig. 4). A higher concentration of DNA was detected in the initial solution than in the plasma-treated solution. We assume that it was caused because plasma induced DNA strand damage, and thus, inhibited the polymerase progression. Sikorsky *et al.* showed that the polymerase stop assays could be used to determine whether a single DNA damage can block the polymerase progression. The presence even of a single 8-oxo-7,8-dihydro-20-deoxyadenosine (8-oxodA), an apurinic/aprimidinic site or a thymine dimer in DNA can dramatically reduce amplification [17].

4. Conclusions

We studied the ability of plasma treated *Escherichia coli* to enter the VBNC/ABNC state under different conditions of plasma-inactivation experiments. *E. coli* was treated by the APPJ in liquid culture and by the CSDBD on the surface of solid target. Bacterial samples were evaluated both by conventional cultivation and fluorescent LIVE/DEAD assay. We conclude that the treatment of the bacteria appears effective when assayed by conventional cultivation; however, only a slight reduction was observed when assayed by fluorescent staining. These results confirm that the bacteria may have entered the ABNC state during the plasma-induced treatment performed both in the liquid and on the solid surface. We did not observe resuscitation of the nonculturable cells in liquid culture after APPJ treatment; therefore, we propose that bacteria were rather in the ABNC state. We assume that the regrowth of bacteria did not occur because of unsuitable technique of resuscitation or inhibition of the replication process by transformation of DNA strands by the plasma treatment. Experiment with the plasma-treated DNA indicated that the APPJ treatment inhibited replication by transformation of DNA strand.

Acknowledgement

This work was supported by the Academy of Sciences of the Czech Republic (projects M100431203), the Ministry of education, Youth and Sports of the Czech Republic project LD 14080 (COST Action TD 1208) and the MEYS under project LD13010, VES13 COST CZ (COST Action MP 1101).

References

- [1] von Woedke T, Reuter S Masur K and Weltmann K D 2013 *Phys. Rep.* **530** 291-320.
- [2] Lukes P, Brisset J L, Locke B R 2012 In: *Plasma Chemistry and Catalysis in Gases and Liquids*, Parvulescu V. I., Magureanu M., Lukes P. Eds. Wiley VCH, Weinheim.
- [3] Šimek M, Prukner V, Schmidt J 2011 *Plasma Sources Sci. Technol.*, **20** 025009.
- [4] Dolezalova E, Lukes P 2014 *Bioelectrochemistry* in press.
- [5] Greenberg A E, Clesceri L S, Eaton A D 1992 American Public Health Association, American Water Works Association, Water Environment Federation. Washington.
- [6] Asakura H, Igimi S, Kawamoto K, Yamamoto S, Makino S 2005 *FEMS Microbiol. Lett.* **253** 243-249.
- [7] Troussellier M, Bonnefont J L, Courties C, Derrien A, Dupray E, Gauthier M, Gourmelon M, Joux F, Lebaron P, Martin Y, Pommepuy M 1998 *Oceanol. Acta* **21** 965-981.
- [8] Colwell R R, Brayton P, Herrington D, Tall B, Huq A, Levine M M 1996 *World J. Microbiol. Biotechnol.* **12** 28-31.
- [9] Hoefel D, Grooby W L, Monis P T, Andrews S, Saint C P 2003 *J. Microbiol. Methods* **55** 585-597.
- [10] Kell D B, Kaprelyants A S, Weichart D H, Harwood C R, Barer M R 1998 *Anton. Leeuw. Int.* **73** 169-187.
- [11] Oliver J D, 2005 *J. Microbiol.* **43** 93-100.
- [12] Rahman I, Shahamat M, Kirchman P A, Russekcohen E, Colwell R R 1994 *Appl. Environ. Microbiol.* **60** 3573-3578.
- [13] Prukner V, Doležalová E, Šimek M 2013 *31st International Conference on Phenomena in Ionized Gases*.
- [14] Neoplas tools, 2009, Neoplas tools GmbH.
- [15] Cooper M, Fridman G, Fridman, Joshi S G, 2010 *J Appl. Microbiol.* **109** 2039-2048.
- [16] Bogosian G, Bourneuf E V 2001 *EMBO Rep.* **2** 770-774.
- [17] Sikorsky J A, Primerano D A, Fenger T W, Denvir J, 2004 *Biochem. Biophys. Res. Commun.* **323** 823-830.

NANOPARTICLE GENERATION BY PULSED LASER ABLATION IN LIQUID

Fernando Brandi^{1,2}

¹ *Istituto Nazionale di Ottica, CNR, Via G. Moruzzi 1, 56124 Pisa, Italy*

² *Istituto Italiano di Tecnologia, Nanophysics Department, Via Morego 30, 16163 Genova, Italy*
E-mail: fernando.brandi@ino.it

Pulsed Laser Ablation in Liquid (PLAL) has significantly emerged in the past years as a versatile and efficient method for the production of nanoparticles, and it is nowadays an established approach for the synthesis and commercialization of stable colloidal solutions of pure nanoparticles. In this seminar PLAL technique is presented and several examples are discussed.

In PLAL a solid target is ablated by pulsed laser irradiation in liquid creating a plasma plume that expands, cools down and collapses due to the pressure of the surrounding liquid environment. Inside this *micro-reactor* the constituents of the plume, i.e., atoms and ions, nucleate during the cooling down process to form nanoparticles. The process depends on many factors like laser parameters (i.e., pulse time duration, fluence on the target, wavelength, and repetition rate) and liquid properties (optical transparency and chemical composition).

Two PLAL examples will be discussed in details, i.e., PLAL of semiconductors (silicon) and of metals (silver and gold).

Luminescent silicon nanoparticles (Si-NPs) are very good candidates for various applications ranging from optoelectronics to nano-labels for imaging. The size control, the optical properties of the silicon nanoparticles produced by PLAL with femtosecond laser, their *in-situ* bioconjugation, and application as light emitting nano-labels for imaging are presented [1-4]. In the perspective to achieve high production yield of NPs by PLAL, the use of picosecond laser is more attractive due to recent advancements of such lasers towards high average power. PLAL of silicon with picosecond laser pulses is investigated [5,6] and it is found that 40 nm and 3 nm silicon nanoparticles are produced with the fundamental beam and the UV third-harmonic beam respectively due to photo-fragmentation. An ablation/photo-fragmentation model is developed to describe the productivity of silicon nanoparticles, and an outlook is given towards the gram scale synthesis of Si-NPs by ps-PLAL. The phenomenological model has a general validity and it can be applied to investigate and optimize PLAL also with other materials.

Metallic nanoparticles are useful for plasmonic and catalytic applications. In both cases ligand free nanoparticles, i.e., without the presence of stabilizers on their surface, are more efficient. Such colloidal solutions are efficiently produced via PLAL of metals and a method for the production of bi-metallic nanoparticles with tunable plasmonic resonance is discussed [7].

References

- [1] Intartaglia R, Bagga K, Brandi F, Das G, Genovese A, Di Fabrizio E and Diaspro A 2011 *J. Phys. Chem. C* **115** 5102.
- [2] Intartaglia R, Bagga K, Scotto M, Diaspro A and Brandi F 2012 *Opt. Mater. Express* **5** 510.
- [3] Intartaglia R, Barchanski A, Bagga K, Genovese A, Das G, Wagener P, Di Fabrizio E, Diaspro A, Brandi F and Barcikowski S 2012 *Nanoscale* **4** 1271.
- [4] Bagga K, Barchanski A, Intartaglia R, Dante S, Marotta R, Diaspro A, Sajti C L and Brandi F 2013 *Laser Phys. Lett.* **10** 065603.
- [5] Intartaglia R, Bagga K, Genovese A, Athanassiou A, Cingolani R, Diaspro A and Brandi F 2012 *Phys. Chem. Chem. Phys.* **14** 15406.
- [6] Intartaglia R, Bagga K and Brandi F 2014 *Opt. Express* **22** 3117.
- [7] Intartaglia R, Das G, Bagga K, Gopalakrishnan A, Genovese A, Povia M, Di Fabrizio E, Cingolani R, Diaspro A and Brandi F 2013 *Phys. Chem. Chem. Phys.* **15** 3075.

ELEMENTARY PROCESSES IN ARGON COVERED CLUSTERS - THE WAY TO NOVEL PLASMA CHEMISTRY?

Jaroslav Kocisek^{1,2}, Jozef Lengyel^{2,3}, Petr Slavicek^{2,3} and Michal Farnik²

¹*CIMAP, UMR 6252, Bd. Henri Becquerel, BP 5133, 14070 Caen Cedex 5, France*

²*J. Heyrovský Institute of Physical Chemistry v.v.i., Academy of Sciences of the Czech Republic, Dolejškova 3, 18223 Prague, Czech Republic*

³*Department of Physical Chemistry, Institute of Chemical Technology, Technická 5, 16628 Prague 6, Czech Republic*

E-mail: kocisek@ganil.fr

We present a short review of our recent studies of electron interaction with pure, mixed and argon covered clusters. Fundamental electron induced reactions in argon – water and argon – acetylene systems are discussed with emphasis on the differences between the gas phase chemistry and the cluster chemistry. Such differences could have novel applications in plasmas as well as plasma generated chemistries.

1. Introduction

Argon is the most frequently used rare gas in low temperature plasmas. Ar is used to stabilize plasmas in variety of applications ranging from micro discharges [1] through industrial equipment [2] up to large scale facilities [3]. In the contribution we will explore how the Ar buffer gas can change the electron induced chemistry of water and acetylene clusters. Both species are well known for plasma physicists.

The water as an important gas impurity accompanies the low temperature plasma physics since its foundations [4]. Protonated water cluster ions are then typical mark of this impurity in the low temperature plasmas [5]. The interest in water aerosol plasmachemistry is on the rise due to novel applications [6][7] as well as the water cluster occurrence in variety of atmospheric pressure ionization sources used in analytical chemistry [8,9,10].

Acetylene clusters in plasmas has been studied as a dusty plasma precursor [11]. They have been reported also in the technical applications such as plasma polymerization or deposition [12, 13].

Electron ionization is a primary ion formation channel in low temperature plasmas. We will show how the structure of cluster influences the electron ionization reaction. We will focus on the reactions which are of particular interest for low temperature plasmas.

2. Experiment

Experiments have been carried out by the means of the cluster beam (CLUB) experimental setup at the J. Heyrovsky Institute of Chemical Physics in Prague. The setup is described in the publication [14].

Clusters were prepared by the expansion of studied molecules through a conical nozzle into vacuum. This way molecular beam was formed which allowed us to study individual cluster particles by vacuum restricted methods. The clusters were ionized ~ 1m downstream the nozzle by electrons produced in the pulsed electron source. The energy of electrons has been changed in the 5eV – 70eV range and the formed ions were analyzed by the reflectron TOF mass spectrometer. Three dimensional mass over charge - electron energy - intensity spectra were obtained. The electron energy resolution during the studies was ~ 0.7 eV and the mass resolution was $\Delta M/M \sim 4000$. The ionization thresholds were obtained by the fitting of the electron energy dependent ion yields by the method of Matejcek [15]. The detail information about the expansion conditions used for the preparation of particular species could be found in the corresponding publication [16] for acetylene expansions and [17] for water expansions.

3. Ionization of pure clusters

The electron ionization of pure water clusters is dominated by the formation of well known $(\text{H}_2\text{O})_n\text{H}_3\text{O}^+$ species. Similar to the bulk, these ions are formed by the water ionization and subsequent dissociation of the water dimer ion in the reaction:



The ultrafast reaction results into formation of energetic OH radical with ~ 1 eV of kinetic energy that is enough to leave the cluster [18]. The diffusion path of such OH radical in water has several nanometers and one can expect the stabilization of $\text{OH}(\text{H}_2\text{O})_n\text{H}_3\text{O}^+$ above this cluster size. However, two facts act against the OH stabilization within the cluster. First, the OH is generated near the cluster surface, since the electron predominantly interacts with surface layer of the cluster. Second, we are dealing with weakly bound isolated system and the energy deposited in the system by stopping of the radical produced in reaction (1) significantly violates its equilibrium. Similar to plasma instabilities the result is a rapid cluster fragmentation. After the electron ionization, the fragmentation is extremely efficient even at electron energies near the ionization threshold, as we have shown recently [19]. It is interesting to note that contrary to this result photon induced ionization near threshold is much softer [20].

Ionization of pure acetylene clusters is dominated by the formation of $(\text{C}_2\text{H}_2)_n^+$ cluster ions. That species are accompanied by $[(\text{C}_2\text{H}_2)_n - k \times \text{H}]^+$, type cluster ions up to the size of $n=7$. The dehydrogenation can be explained by the formation of the covalently bound ionic species. [16] This phenomenon was observed previously. By the way of example, significant efforts have been done to assign the C_6H_6^+ structure to the benzene cation [21]. Small acetylene clusters could be therefore good polymerization precursors. At higher energies above 21 eV acetylene can dissociate and $(\text{C}_2\text{H}_2)_n\text{CH}^+$ species are observed. Similar to $(\text{C}_2\text{H}_2)_n$ species these are followed by dehydrogenated ions.

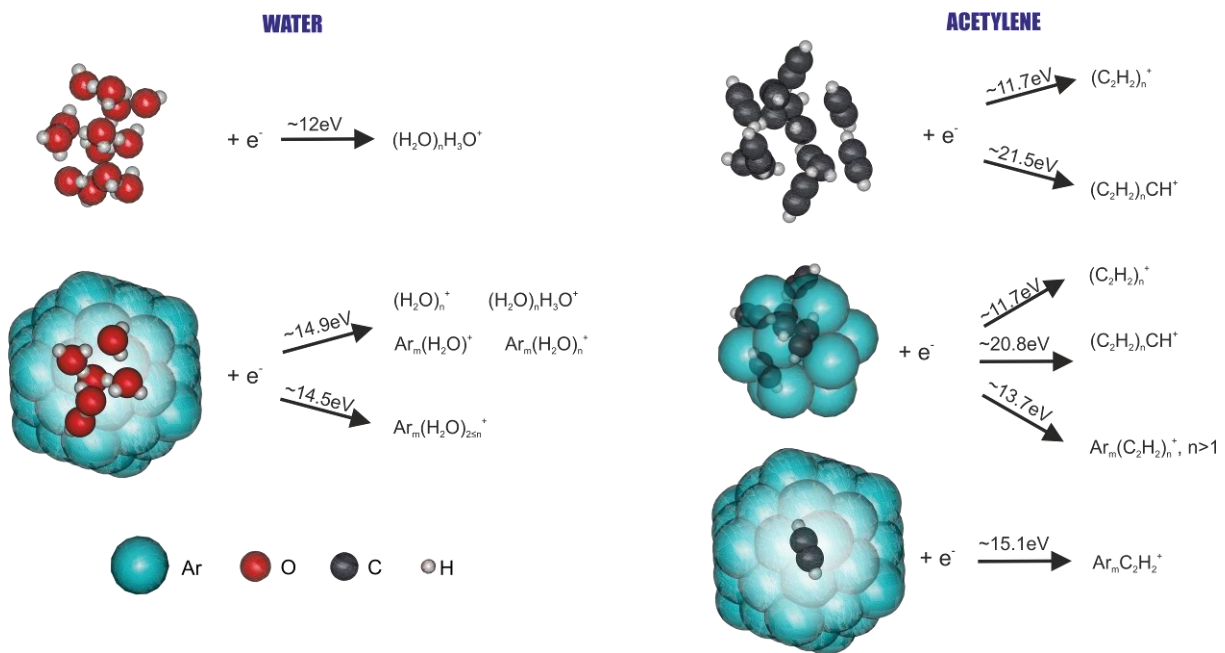


Fig. 1: The schematic cluster structures discussed in present contribution with the indication of ionization thresholds for particular ionization channels. More details can be found in the works [17] and [19] concerning water clusters and in the work [16] concerning the acetylene clusters.

4. Ionization of mixed clusters

Ionization of mixed argon – water and argon – acetylene clusters by the near threshold energy electrons results in the formation of the $(\text{H}_2\text{O})_n \text{H}_3\text{O}^+$; $(\text{C}_2\text{H}_2)_n^+$ and $(\text{C}_2\text{H}_2)_n\text{CH}^+$ ions similar to the pure water and acetylene clusters. Additionally, mixed cluster ions are formed containing Ar atoms. The typical electron energy dependent ion yield for pure clusters also changes upon the mixing. The yield changes at energies above the argon ionization threshold (in clusters $\sim 14.5\text{eV}$) due to the contribution of the Ar excitation and ionization.

The main change of the acetylene chemistry in co-expansion with argon is in suppression of the dehydrogenated $[(\text{C}_2\text{H}_2)_n - k \times \text{H}]^+$ and $[(\text{C}_2\text{H}_2)_n\text{CH} - k \times \text{H}]^+$ cluster ion yield and therefore less polymerization. The suppression of the yield can be caused by two facts. First, the cluster formed in Ar co-expansion can be significantly colder. Both collisional and evaporative cooling are more intense in the case of Ar co-expansion. By the way of example, evaporative cooling in the expansion is limited by the binding energy of the cluster constituents. The binding energy of acetylene is $\sim 120\text{meV}$ [22] and the binding energy of argon can be as low as 12meV [23]. The suppression of polymerization reactions is then caused by low energy carried by the cluster which is not enough to overpass the energy barriers in the polymerization process. Second, the ion can be stabilized by evaporative cooling after the ionization. Instead of the hydrogen release the ions are stabilized by the evaporation of Ar atoms. The polymerization reaction is therefore suppressed due to competition with another stabilization mechanism – collision with Ar atom. We believe that the second process is dominant in observed systems similar to the behavior known for RF plasmas in rare gas – acetylene mixtures [24]

5. Ionization of argon covered clusters

The characterization of cluster structure is not trivial task. In the particular case of studied molecules we exploit the simple fact that the electron ionization threshold of Ar is significantly different of that of acetylene or water. By careful change in the molecular beam parameters we found the conditions at which the appearance potential of all the observed ionic species shifts up to the value for argon (in clusters in between $(14.5-15.5)\text{eV}$). This is unambiguous evidence of the shielding of the interaction between the incoming electron and the cluster by the Ar solvent. We are speaking about the argon covered cluster.

We will focus here on the water cluster case since we explore this in the more details [17]. The shielding effect is not restricted to the low energies and the energy dependent ion yield changes in the whole studied range up to 70eV . In the comparison to mixed clusters the change is more pronounced and the energy dependent ion yield copies the curve of argon. The shape of the ion yield can be used to identify the nature of different ion formation channels. E.g. in the studied energy range $\text{Ar}_n(\text{H}_2\text{O})_m^+$, $\text{Ar}_n(\text{H}_3\text{O})_m^+$ and $(\text{H}_2\text{O})_n^+$ clusters are formed exclusively in the interaction of embedded water clusters with the ground state Argon ions. On the other hand, Ar_nH^+ type ions are formed exclusively at higher energies, where the excited Ar^+ ions are observed and $(\text{H}_2\text{O})_n\text{H}_3\text{O}^+$ ions are then formed in both processes.

It is interesting to compare the near threshold ionization of mixed clusters to the ion molecule reactions in the gas phase. By the way of example the $\text{Ar}^+\text{H}_2\text{O}$ reaction in gas phase results into the formation of unstable $(\text{ArH}_2\text{O})^+$ complex with at least $\sim 0.6\text{eV}$ excess energy [25]. In clusters, the complex can be stabilized after the reaction by Ar evaporation and we can observe the mixed cluster species. The nature of ionization process can be also different in clusters, where the neutral precursor of the reaction is under the influence of neighboring molecules. We believe that such collective influence can better explain the observed behavior. The neutral cluster is stabilized and the polarization of the solvent causes significant lowering of the ionization potential of the Ar. According to our observation the ionization threshold is 14.9eV that is $\sim 0.6\text{eV}$ below the Ar ionization threshold in the gas phase. The difference is exactly the difference between the $(\text{ArH}_2\text{O})^+$ ground state and unstable $\text{Ar}^+\text{H}_2\text{O}$ reaction product.

Summing up the entire part, the electron interaction with molecular cluster can be shielded by Ar. The electron ionization is then changed to Ar^+ ion reaction with molecular cluster. However, the character of ion molecule reaction is different in clusters due to the the “solvated” nature of the Ar^+ ion.

6. Conclusions

We used the simple plasma relevant molecules as an example to demonstrate the main solvent induced effects in electron induced chemistry. These are:

cooling of precursors and products of the electron interaction → suppression of the polymerization process.

caging of electron interaction products and preventing the dissociation → initialization of the polymerization process.

covering of clusters by Ar solvent and shielding the interaction of the embedded molecule with incoming electron → shift in the ionization potential.

catalysis of the electron ionization reaction to the ion induced reaction → suppression of one type of reaction products at the expense of second one.

We believe that introduction of molecular clusters into plasmas can help to identify different processes in plasmas by controlling the plasma chemistry, e.g. by suppression of particular electron induced reaction or cluster ion polymerization. The cluster ion polymerization can also result into the formation of novel materials and reactive species in the plasmas as well as in the plasma deposits.

7. References

- [1] Klas M et al 2011 *Physica Scripta* **83(4)** 045503.
- [3] Hlina M 2014 *Waste Management* 2014 **34** 63
- [4] Crookes W. On Radiant matter, lecture to the British Association for the Advancement of Science, Sheffield 1879
- [5] Sakata S and Okada T 1994 *J. Aerosol Sci.* **25(5)** 879
- [6] Locke BR and Shih K-Y 2011 *Plasma Sources Sci. Technol.* **20** 034006
- [7] Yi-Wei Yang 2014 *Plasma Processes and Polymers* **11(11)** 1102
- [8] Ellis AM and Mayhew ChA *Proton Transfer Reaction Mass Spectrometry: Principles and Applications*, John Wiley & Sons 2014
- [9] Sabo M et al. 2011 *The European Physical Journal Applied Physics* **55(1)** 13808
- [10] Laughlin BC, Mulligan CC and Cooks RG 2005 *Anal. Chem.* **77** 2928
- [11] Kovačević E et al. 2005 *Astrophysical Journal* **623** 242
- [12] Benedikt J 2010 *J. Phys. D: Appl. Phys.* **43** 043001
- [13] De Bleecker K Bogaerts A Goedheer W 2006 *Appl. Phys. Lett.* **88** 151501
- [14] Fárník M *Molecular Dynamics in Free Clusters and Nanoparticles Studied in Molecular Beams*, ICT Prague Press, Prague 2011
- [15] Wnorowski K 2012 *Rapid Commun. Mass Spectrom.* **26** 2093
- [16] Kocisek J 2013 *J. Chem. Phys.* **138** 124306
- [17] Kocisek J 2013 *J. Chem. Phys.* **139** 214308
- [18] Svoboda O et al. 2013 *Phys Chem Chem Phys* **15(27)** 11531
- [19] Lengyel J 2014 *Chemical Physics Letters* **612** 256
- [20] Litman JH 2013 *Phys. Chem. Chem. Phys.* **15** 940
- [21] Momoh PO 2006 *J. Am. Chem. Soc.* **128(38)** 12409
- [22] Shuler K and Dykstra CE 2000 *J. Phys. Chem. A* **104(49)** 11522
- [23] Malakhovskii AV and Ben-Zion M 2001 *Chem. Phys.* **264** 135
- [24] Vasile MJ and Smolinsky G 1977 *Int. J. of Mass Spec. and Ion Phys.* **24** 11
- [25] Glosik J et al 1981 *Chemical Physics* **60** 369

DETECTION OF ROS/RNS IN WATER ACTIVATED BY AIR TRANSIENT SPARK DISCHARGE

Barbora Tarabová¹, Petr Lukeš², Katarína Tarabová¹, Karol Hensel¹, Libuša Šikurová¹, Zdenko Machala¹

¹*Faculty of Mathematics, Physics and Informatics, Comenius University, Mlynská dolina, 84248 Bratislava, Slovakia*

²*Institute of Plasma Physics, AS CR, v.v.i., Za Slovankou 3, 18200 Prague 8, Czech Republic*
E-mail: tarabova@fmph.uniba.sk

Chemical effects in aqueous solutions induced by DC transient spark discharge generated in atmospheric pressure air were investigated. Changes of pH, conductivity and formation of reactive oxygen (ROS) and nitrogen (RNS) species were observed in water or PB solutions after treatment by water electro-spray system or water electrode system. The concentrations of hydrogen peroxide, nitrites and nitrates were measured. By addition of the enzyme catalase we showed that hydrogen peroxide does not have any influence on the Griess reagent colorimetric method for nitrites detection. We found out that the indigo blue method for measuring ozone in water is not selective in plasma treated solutions. It seems that hydroxyl radical is responsible for the false positive reaction of the indigo method.

1. Introduction

Bio-decontamination by cold atmospheric plasmas under wet conditions is very important. Plasmas generated in air and in contact with liquids generate a number of primary reactive species in the gas phase, which induce formation of secondary reactive species in the liquid phase through the gas-liquid interface. Reactive oxygen and nitrogen species such as hydrogen peroxide H_2O_2 , hydroxyl radical $\cdot\text{OH}$, nitrites NO_2^- , nitrates NO_3^- , hypochlorite OCl^- and peroxynitrites ONOO^- induce chemical changes in water solutions and various biocidal effects on microorganisms or therapeutic effects for biomedical applications [1, 2]. It was shown that the acidic environment with plasma agents (especially hydrogen peroxide, nitrites, nitrates) lead to the strong bacterial inactivation [3,4]. However, it is not clear enough yet, which ROS/RNS play dominant role in bio-decontamination and biomedical applications of cold plasma. According to some papers, the key species responsible for bio-decontamination in plasma treated water solutions or tissue and cell injuries *in vivo* may be peroxynitrites [4,5,6].

In this work we focused on the formation of reactive oxygen and nitrogen species (ROS/RNS) induced by plasma gas-liquid chemistry in treated aqueous solutions. We measured formation of hydrogen peroxide, nitrites, nitrates, and dissolved ozone in water treated by DC-driven positive transient spark discharge generated in ambient air. We compared the accuracy of the Griess reagent method for nitrites detection with the (high precision) ion chromatography (IC) method. We also attempted to increase the detection limit of Griess assay by addition of the catalase to decompose hydrogen peroxide thus avoid its potential effect on the nitrite detection. The chemistry was also investigated in synthetically prepared aqueous solution that should simulate the plasma activated water (PAW).

2. Experimental set-up and methods

Aqueous solutions with different initial pH and electrolytic conductivities σ were used for plasma treatment. The solutions were prepared by the dissolution of different salts in deionized water:

- **water** = NaH_2PO_4 solution (pH 5-5.5 and $\sigma = 0.6$ mS/cm) mimics the conductivity of tap water and has similar chemical composition with the phosphate buffer but no buffering capacity,
- **PB** = $\text{Na}_2\text{HPO}_4/\text{KH}_2\text{PO}_4$ buffer (pH 6.9 and $\sigma = 0.56$ mS/cm),
- **solution of 1 mM H_2O_2 + 1 mM NaNO_2** (at pH 3.3 (in H_3PO_4) or 6.8 (in PB)) = simulates the chemistry of the plasma treated water without plasma.

The transient spark discharge was generated in ambient air in two systems: the **water spray** [4] and the **water electrode** system. Their set-ups are depicted in Figure 1. The main difference between these

systems was that in the water spray (WS) system, the solution was electro-sprayed through the active zone of the discharge and in the water electrode (WE) system the solution was repetitively circulated by peristaltic pump. DC transient spark discharge was generated in ambient air in point-to-plane geometry with hypodermic hollow needle used as the high voltage (HV) electrode. In the WE system the treated solution circulated repetitively 28 times through the discharge zone, while in the WS system solution passed the inter-electrode gap once and then was collected under the metallic mesh in contrary to the WE system, where the water circulated for 28 times during the treatment. In both systems we tried to keep the similar conditions: voltage 10-13 kV, spark pulse frequency ~ 1 kHz, inter-electrode gap 10 mm, treatment time 10 min and treated volume of water solution 5 mL. A positive DC HV was applied through the ballast resistor R (10 M Ω). The voltage signal was measured by the HV probe *Tektronix P6015A* and the current signal was measured on 1 Ω resistor or by Rogowski current monitor *Pearson 2877*. These signals were processed by a digitizing 200 MHz oscilloscope *Tektronix TDS 2024*

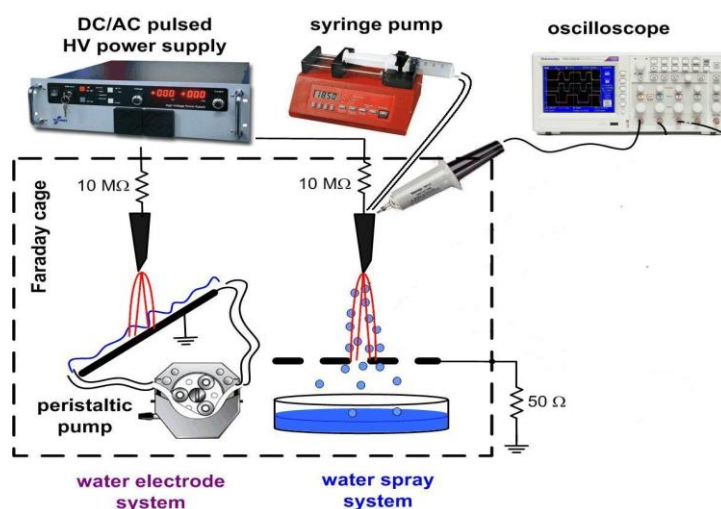


Fig.1 The experimental set-up of the water electrode and water spray systems.

ROS and RNS in plasma treated water (plasma activated water PAW) were detected mostly by colorimetric methods (UV/VIS absorption spectrometer UV-1700 SHIMADZU), but also additional comparative methods were used:

1. Analysis of H_2O_2 : Titanium ions Ti^{4+} react with H_2O_2 in the presence of NaN_3 and create pertitanic acid with the absorption maximum at 407 nm [4].
2. Analysis of NO_2^- : Nitrites NO_2^- react with Griess reagents and create azo-dye with the absorption maximum at 540 nm. We used two different Griess reagents: Griess 1 [7] and Griess 2 (Nitrate/Nitrite Colorimetric Assay Kit, Cayman Chemical). Furthermore, to verify the accuracy of the Griess reagents while keeping in mind the possible interaction of NO_2^- and H_2O_2 at acidic pH [6], we also measured the concentration of NO_2^- and NO_3^- by ion chromatography (IC) using the HPLC system Shimadzu LC-A1p with UV (210 nm) and suppressed conductivity detection. Treated samples for ion chromatography were fixed by buffer to stop the acidic decomposition of nitrites. We also used the Griess reagents in combination with the enzyme catalase (Catalase from Bovine Liver, Sigma-Aldrich) due to the possibility that NO_2^- could be consumed by the reaction with hydrogen peroxide during the peroxy-nitrites chemistry in PAW. Catalase is the enzyme which catalyzes the decomposition of hydrogen peroxide to hydrogen and oxygen. The working solution of catalase with the activity ~ 10.6 units/mL was prepared in 50 mM K_2HPO_4 solution.
3. Analysis of O_3 : Indigo dye with the absorption maximum at 600 nm is supposed to react with O_3 and the colorless product isatin is created by the bleaching process [8]. The presence of dissolved ozone was also verified by other indirect analytical method: phenol was used as a chemical probe to characterize the reactive pathways of the ROS and RNS, especially of the dissolved ozone in solutions produced by air plasmas. The specific chemical products of these pathways were

detected after direct air plasma treatment by HPLC system Shimadzu LC-Avp with UV and fluorescence detection.

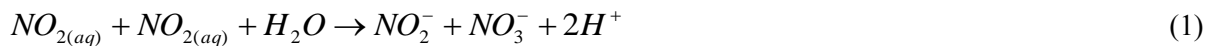
3. Results and discussions

3.1 Transient spark discharge

Transient spark discharge was operated in atmospheric air in electro-spray or water electrode systems in contact with water. Electric parameters and emission spectra of TS were documented in detail in our previous works [4,9,10]. In the WS system, water was sprayed through the HV hollow needle with the water flow rate 0.5 mL/min and in the WE systems water was circulated with the flow rate 14 mL/min, which increases the number of the discharge contacts with the treated water [12].

3.2 PAW chemistry with focus on the nitrite detection

The transient spark discharge was generated in ambient air at atmospheric pressure in the direct contact with treated liquid samples. It was shown that the bactericidal effects of plasma treatment of bacterial suspensions are accompanied with the decrease of pH and the chemical changes (formation of ROS and RNS: H₂O, NO₂⁻, NO₃⁻, O₃, ONOO⁻). Figure 2a shows concentration of H₂O₂ (colorimetric method), NO₃⁻ and NO₂⁻ (HPIC) determined in water and PB solutions after treatment by the water spray system. Dissolution of NO_x along with the formation of NO₂⁻, NO₃⁻ was responsible for the acidification of the plasma treated solution:



Nitrites decompose under acidic conditions via NO[•] and NO₂[•] cytotoxic intermediates to nitrate ions or react with H₂O₂ to peroxyxynitrites, which are also very reactive through their decay products OH and NO₂ radicals. Therefore, so called *acidified nitrites* possess strong bactericidal properties [1,11].

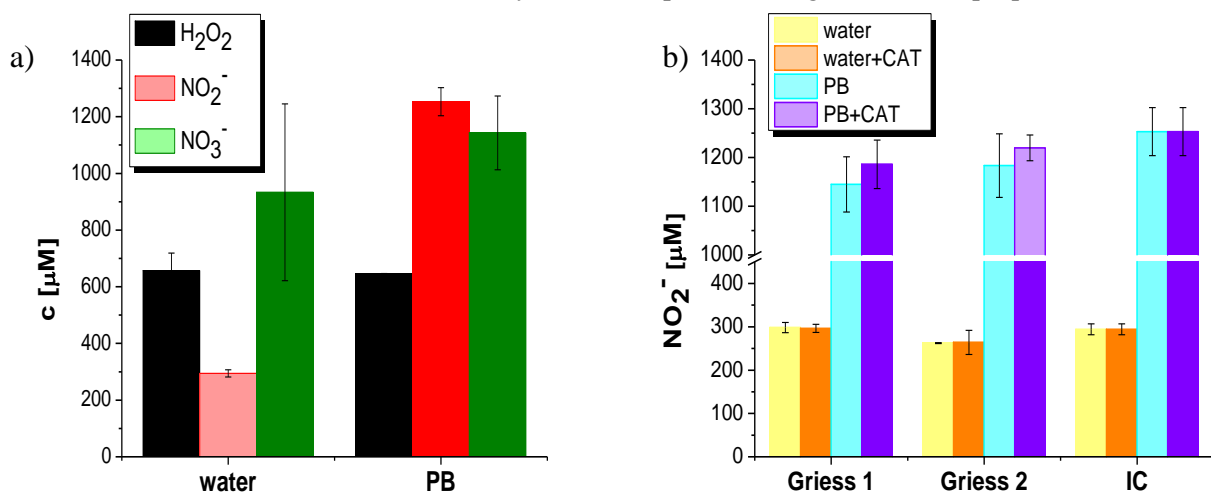


Fig.2 a) H₂O₂, NO₂⁻, NO₃⁻ (average +/- SD) in water and PB treated by the WS system.

b) NO₂⁻ (average +/- SD) measured by Griess 1, 2 (with or without added catalase) compared to IC measurements in water and PB treated by the WS system.

In this work we focused on the nitrite detection in PAW. We used the colorimetric method based on the Griess assay using two different Griess reagents: Griess 1 [7] and Griess 2 (Cayman Chemical) and as a comparative method we used the high precision ion chromatography. To avoid possible interference of hydrogen peroxide on Griess assay, we used the catalase (CAT) as a H₂O₂ scavenger. In PAW H₂O₂ react with NO₂⁻ in time by forming peroxyxynitrites and so the concentration of NO₂⁻ is decreasing (very fast at acidic pH). The water and PB solution was treated by the WS system and each sample was divided for nitrite analysis by IC, Griess 1 and 2 (with or without catalase) and the results are shown in Figure 2b. The results of the Griess assay showed no significant difference between the samples with or without added catalase. It seems that the reaction of Griess reagents with NO₂⁻ is faster than the reaction of hydrogen peroxide with NO₂⁻. Also due to the dilution of the treated

samples for Griess assay, the concentration of hydrogen peroxide in the analyzed sample was 10 to 40 times lower and perhaps this decreased concentration does not affect the reaction of Griess reagents with nitrites. The comparison of the measured nitrites concentration by Griess reagents (Griess 1 and Griess 2) and by ion chromatography showed no significant difference in the nitrite concentration.

3.3 The dissolved ozone detection

The water solution of 1 mM H₂O₂ + 1 mM NaNO₂ (at pH 3.3 or 6.8) was used to mimic the plasma treated water (or PB). We measured the time developments of H₂O₂ and NO₂⁻, as shown in Figure 3. At pH 6.8 (Fig. 3b), the concentrations of H₂O₂ and NO₂⁻ were time-stable, unlike at pH 3.3 (Fig. 3a), where we observed the decrease of these species. The reason for this decrease was the reaction between H₂O₂ and NO₂⁻ via formation of peroxyntrites occurring under acidic conditions [6]:

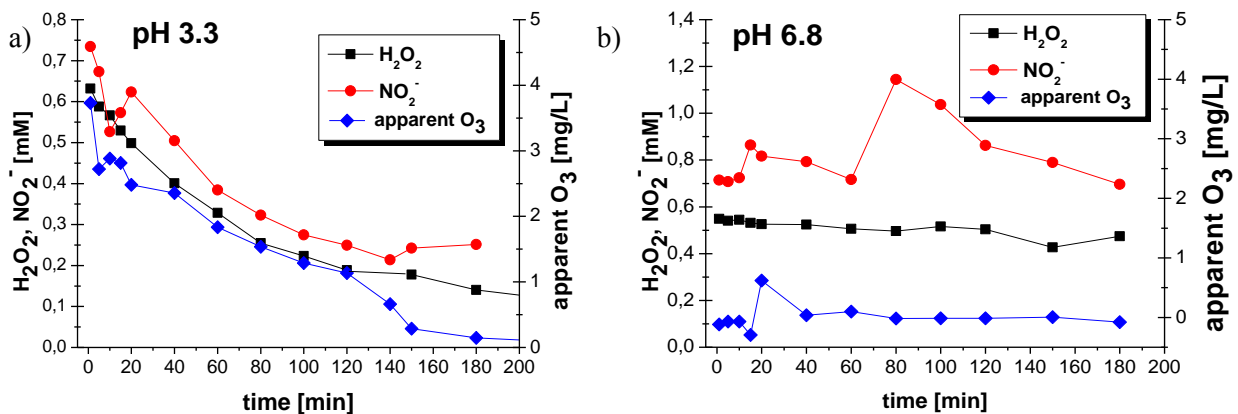


Fig.3 Time developments of important reactive species in the simulated plasma treated water at pH 3.3 (a) and pH 6.8 (b). Apparent ozone means bleaching of the indigo dye.

We previously observed the dissolved ozone in the PAW by the indigo method and detected the concentrations 0.6-0.8 mg/L of dissolved ozone in the plasma treated deionized water by the WS and WE systems [12]. Because TS discharge treatment bleached the indigo more than pure ozone bubbled through the deionized water in much higher concentrations, we had to check the selectivity of the indigo method in the simulated plasma treated water solution with similar chemical composition and pH as our plasma activated water but with no presence of ozone (Fig. 3). Interestingly, we detected “ozone” even in this simulated solution without plasma treatment where no ozone could have been present. The degradation of the indigo dye in the solution without ozone was caused most likely by the formation of hydroxyl radical ·OH created as a decay product of peroxyntrites. This was probably also the reason for false positive response of indigo dye method on the presence of ozone in PAW [6,11] in our previous experiments [12]:



Furthermore, 500 μM phenol solution was used a chemical probe to characterize the specific primary products of the degradation of the phenol by the reactive species during the plasma treatment [6]. In water and PB solutions treated by the water spray system were detected the hydroxylated degradation products (catechol, hydroquinone, 1,4-benzoquinone, hydroxyl-1,4-benzoquinone) and nitrated by-products (4-nitrocatechol, 2-nitrohydroquinone, 4-nitrophenol, 2-nitrophenol). The most important product we focused at was the *cis, cis*-muconic acid (and its *cis, trans*-isomer) as a specific product of the reaction of ozone with phenol [6]. Contrary to seemingly detected ozone by indigo method, the results from the phenol degradation product analyses (Tab. 1.a, b) showed no muconic acid. This result support the fact that the indigo method is not selective to ozone in PAW and more examination is needed to truly measure ozone and determine reasons for indigo bleaching. It seems that the ozone reacts with nitrite in PAW [13]:



Table 1. Summary of the degradation products of phenol (hydroxylated, nitrated and specific ozone products) in air spark treated water and PB solutions (average +/- SD).

c [μM]	water	PB
catechol	15.4+/-4.6	9.5+/-3.2
benzoquinone	1.6+/-0.4	2.9+/-0.9
hydroquinone	6.4+/-1.7	6.1+/-1.7
hydroxybenzoquinone	3.1+/-0.9	2.6+/-0.7
4-nitrocatechol	4.7+/-1.4	1.1+/-0.0
2-nitrohydroquinone	3.4+/-1.0	0.2+/-0.1
4-nitrophenol	1.8+/-0.6	0.5+/-0.0
2-nitrophenol	1.0+/-0.2	0.1+/-0.0
<i>cis,cis</i> -muconic acid	0.0+/-0.0	0.0+/-0.0
<i>cis, trans</i> -muconic acid	0.0+/-0.0	0.0+/-0.0

Acknowledgement

This work was supported by Slovak Research and Development Agency APVV-0134-12, Comenius University Grant UK/403/2014, the Ministry of Education and Sports of the Czech Republic (project LD 14080) and COST Action TD1208 – Electrical Discharges with Liquids for Future Applications.

- [1] Graves D B 2012 *J. Phys. D: Appl. Phys.* **45** (263001)
- [2] Fridman G, Friedman G, Gutsol G, Shekhter A B, Vasilets V N and Fridman A 2008 *Plasma Process. Polym.*, **5** (6): 503-533
- [3] Oehmingen K, Winter J, Hahnel M, Wilke C, Branderburg R, Weltmann K D and von Woedtke T 2011 *Plasma Process. Polym.*, **8** (10): 904-913
- [4] Machala Z, Tarabova B, Hensel K, Spetlikova E, Sikurova L and Lukes P 2013 *Plasma Process. Polym.* **10** (7): 649-659
- [5] Brisset J L and Hnatiuc E 2012 *Plasma Chem. Plasma Process.* **32** (4): 655-674
- [6] Lukeš P, Doležalová E, Sisrová I and Člupek M 2014 *Plasma Sourc. Sci. Technol.* **23** (015019)
- [7] Rice E W, Baird R B, Eaton A D and Clesceri L S eds 1998 Method 4500-NO₂⁻ B. Colorimetric Method, In: *Standard Methods for the Examination of Water and Wastewater, 20th Edition*, American Public Health Association (APHA), American Water Works Association (AWWA), Water Environment Federation (WEF), p. 4-112 – 4-114
- [8] Rice E W, Baird R B, Eaton A D and Clesceri L S eds 1998 Method 4500-O₃ B. Indigo Colorimetric Method, In: *Standard Methods for the Examination of Water and Wastewater*, American Public Health Association (APHA), American Water Works Association (AWWA), Water Environment Federation (WEF), p. 4-137 – 4-139
- [9] Janda M, Martišovitéš V and Machala Z 2011 *Plasma Sources Sci. Technol.* **20** (035015)
- [10] Machala Z, Janda M, Hensel K, Jedlovský I, Leštinská L, Foltin V, Martišovitéš V and Morvová M 2007 *J. Mol. Spec.* **243** (2): 194-201
- [11] Traylor M J, Pavlovich M J, Karim S, Hait P, Sakiyama Y, Clark D S and Graves D B 2011 *J. Phys. D: Appl. Phys.* **44** (472001)
- [11] Lukeš P, Doležalová E, Člupek M, Tresp H, Reuter S and von Woedtke T 2014 Kinetic analysis of peroxyxynitrite formation in liquids treated by air plasma, In *Book of Contributions, HAKONE XIV*, Zinnowitz (Germany), September 21-26
- [12] Tarabová B, Tarabová K, Hensel K, Šikurová L and Machala Z 2014 Chemical and bactericidal effects induced in water treated by air transient spark, In *Book of Contributions, HAKONE XIV*, Zinnowitz (Germany), September 21-26
- [13] Lukeš P, Locke B R and Brisset J L 2012 Aqueous-phase chemistry of electrical discharge plasma in water and in gas-liquid environments *Plasma Chemistry and Catalysis in Gases and Liquids* ed V I Parvulescu et al (Weinheim: Wiley-VCH) pp 241-307

DEGRADATION OF AMOXICILLIN IN WATER TREATED WITH DBD PLASMA

Tomasz Izdebski¹, Elisa Ceriani², Ester Marotta²,

Cristina Paradisi², Mirosław Dors¹

¹*Center for Plasma and Laser Engineering, The Szewalski Institute of Fluid-Flow Machinery Polish Academy of Sciences, Fiszera 14 st. Gdańsk 80-231, Poland*

²*Dipartimento di Scienze Chimiche, Università di Padova, Via Marzolo 1, 35131 Padova, Italy*

E-mail: tizdebski@imp.gda.pl

In this paper, an investigation of the degradation of the antibiotic amoxicillin in a DBD reactor is reported. It was found that amoxicillin can be degraded with 100% conversion using DBD discharge and that the reaction rate depends on the drug initial concentration. Moreover, at low concentration, the drug can be oxidized exhaustively to CO₂. By means of HPLC/MS analysis, a few organic intermediates in the oxidation of amoxicillin (A) have also been detected: from their mass spectra they are identified as two isomeric monooxygenated (A + O) and one dioxygenated (A + 2 O) products.

1. Introduction

With the introduction of modern day pharmaceuticals and in particular antibiotics in the treatment and therapy of humans and animals there is much concern about the possible accumulation of the pharmaceuticals and their degradation products and metabolites in surface waters and the environment. That's why there is growing interest in the development of antibiotics degradation processes [1-4]. Due to the complex structure of antibiotics their diagnostics in water matrix can only be done using high performance liquid chromatography and mass spectrometry to analyze, identify and quantify the antibiotics and products of their degradation.

The investigated antibiotic is amoxicillin 6-[[amino(4-hydroxyphenyl)acetyl]amino]-3,3-dimethyl-7-oxo-4-thial-1-azabicyclo[3.2.0]heptanes-2-carboxylic acid, which belongs to β -lactam antibiotics of penicillin group. It is widely used all over the world and there is evidence of its presence in surface waters. Worldwide investigations of this potential risk have led to the detection of pharmaceuticals, particularly antibiotics in wastewater, surface water, groundwater, fish ponds, hospital effluents and even seawater. We report in this paper the results of a study on the non-thermal plasma induced degradation of amoxicillin carried out at the University of Padova using a DBD reactor which was described and characterized in previous publications [5-7].

2. Experimental setup

Chemicals and compounds used in the experiment:

Amoxicillin trihydrate (98.7%) analytical standard was purchased from Fluka Analytical. For eluent and sample preparation, high purity MilliQ water was used of pH 5.5 and conductivity ~5 μ S.

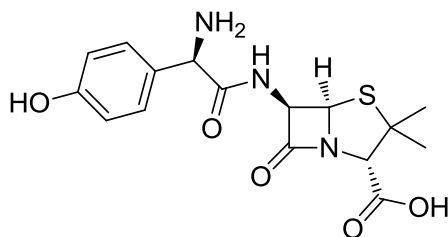


Fig. 1. Chemical structure of amoxicillin.

HPLC analyses were performed using the chromatograph by Thermo Separation Products comprising a pump system P2000 Spectra System and a diode array detector UV6000LP. Two types of column were used: Gemini C18 150 x 4.6 and Zorbax SB C18 150 x 4.6 mm, 3.5 μm . The first set of eluents used were acetonitrile plus 0.1% formic acid and H_2O plus 0.1% formic acid, but under these conditions amoxicillin, which is very polar, comes out of the column too fast. So we changed the eluents for better peak separation in HPLC to 99:1 H_2O plus phosphate buffer (20 mM) with pH of 2.2 and acetonitrile (1%).

HPLC/MS analysis was performed using an Agilent Technologies mass spectrometer with ion trap MSD Trap SL model G2245D and ESI and HPLC series 1100 with binary pump model G1312A. The MS parameters were as follows: positive polarity, N_2 dry gas temperature 350°C, N_2 flow 10 L/min, N_2 nebulizer pressure 60 psi, capillary voltage 4 kV, mass acquired from m/z 50 to 500. The eluents were: H_2O + 0.1% HCOOH (A) and CH_3CN + 0.1% HCOOH (B). The gradient was: 5% B to 100% B in 20 min.

The decomposition process induced by the discharge was also followed by FTIR analysis of the air flowing out of the reactor in order to observe the CO_2 emission from the solution. A Nicolet 5700 spectrometer was used with a 10 cm cell with CaF_2 windows 38 mm in diameter. The absorption band of CO_2 centered at 2340 cm^{-1} was used for quantitative determinations: the area of the peaks was integrated and converted in a concentration value with a calibration curve. The final carbon mass emitted from the solution was calculated via integration of the concentration of CO_2 over total volume of air passed through the reactor and converted for the carbon mass according to calculated carbon mass of the initial amoxicillin solution.

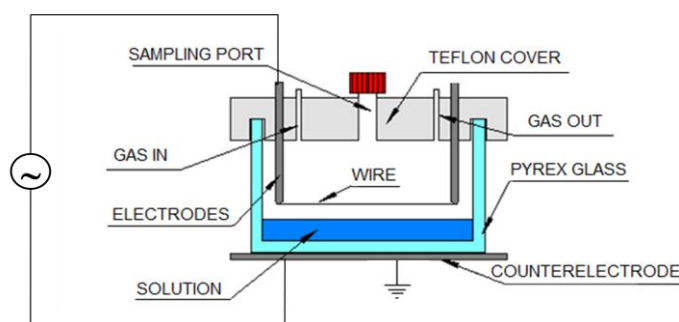


Fig. 2. Schematics of non-thermal plasma reactor.

The reactor is a glass vessel (internal dimensions 95 x 75 mm and 60 mm height) closed by a PTFE cover with four passing electrodes of stainless steel which support two parallel stainless steel wires (0.15 mm diameter x 75 mm length) fixed upon their tips (Fig. 2). The wires are set 38 mm apart and about 15 mm above the solution to be treated. Volume of the solution was 70 mL. The outside surface of the reactor base is covered with a film of silver and connected to a grounded plate. Humidified air is swept through the reactor above the solution at a flow rate of 30 $\text{mL}\cdot\text{min}^{-1}$. The reactor is

powered with an AC high-voltage transformer with 18 kV and a frequency of 50 Hz to produce discharge in the gas phase above the liquid surface. During the experiments the voltage was maintained constant. Current and voltage profiles were monitored with a digital oscilloscope (TDS5032B, bandwidth 350 MHz, sample rate 5 Gs/s) to assure the reproducibility of the electrical conditions.

3. Results and discussion

Experiments were performed with amoxicillin in two initial concentration values: $3 \cdot 10^{-4}$ M and $1 \cdot 10^{-5}$ M. Amoxicillin degradation rate constants for the two plasma discharge experiments were extrapolated from the plots in Fig. 3. These plots were made using data from HPLC analysis of samples taken during the treatment.

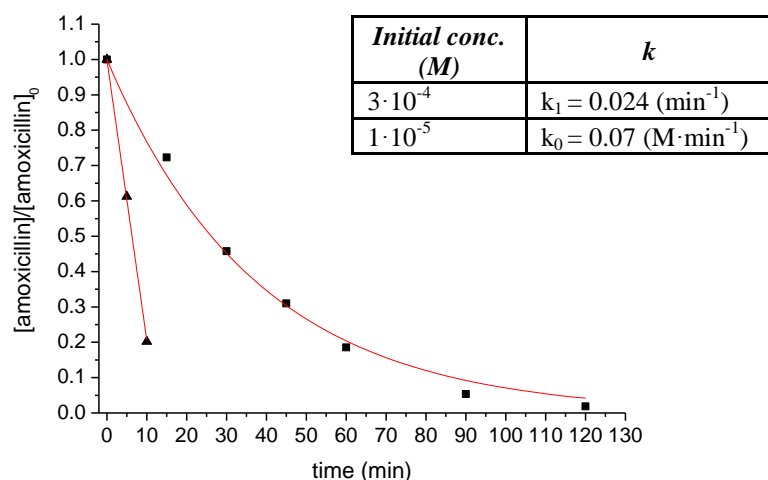


Fig. 3 Degradation of amoxicillin performed with two different initial concentrations: $3 \cdot 10^{-4}$ M (■) and $1 \cdot 10^{-5}$ M (▲).

The rate constant of amoxicillin degradation was higher when the initial concentration was lower. It also seems that the kinetic order of the reaction changes from first (at high initial concentration) to zero order (at low initial concentration). This means that the advanced oxidation processes are influenced by the concentration of the pollutant in the treated solution [6].

The HPLC chromatograms are shown in Fig. 4. It is seen that there is a 100% degradation of amoxicillin after 180 min of discharge time, but we still have large amounts of degradation intermediates in the solution. This chromatogram is for amoxicillin initial concentration of $3 \cdot 10^{-4}$ M. Nitric acid is also formed, as reported in the literature, due to the production of NO by the discharge in air [5].

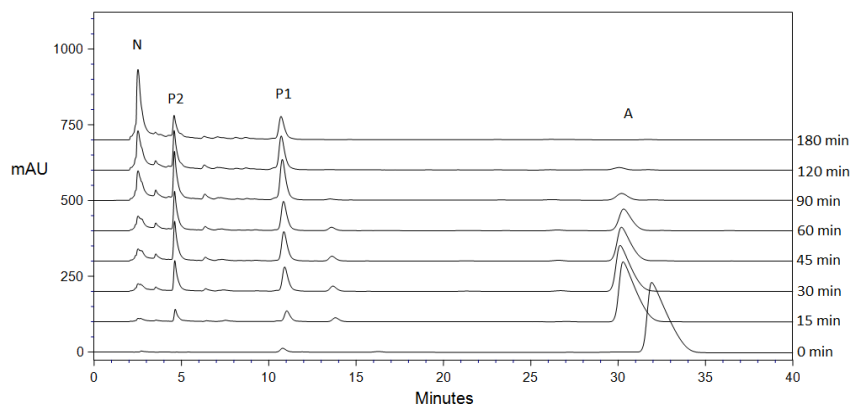


Fig. 4. HPLC chromatogram of samples taken at different times during discharge induced amoxicillin degradation. A – Amoxicillin, P1 – Degradation product 1; P2 – Degradation product 2; N – Nitric acid.

The emission of CO_2 during the discharge with amoxicillin at an initial concentration of $3 \cdot 10^{-4}$ M is shown in Fig 5. It is seen that after a treatment time of 180 min (which corresponds to 5.4 L of air passed through the reactor), there is still CO_2 emission from the solution. Since amoxicillin is largely consumed in a much shorter time (less than 120 min - see Fig. 3), this CO_2 emission is attributed to the oxidation of some organic intermediates which are formed in the complex process leading from amoxicillin to CO_2 . Indeed, the total carbon mass emitted as CO_2 from the solution in 180 min discharge treatment time was only 5% of the total initial carbon mass in the solution.

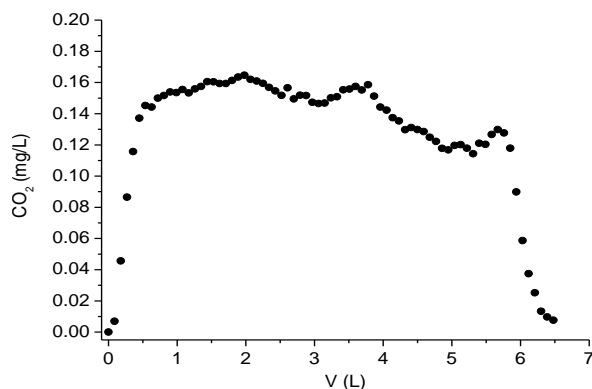


Fig. 5. CO_2 emission during discharge as a function of the volume of air passed through the reactor. The flow rate was $30 \text{ mL} \cdot \text{min}^{-1}$.

However, when the amoxicillin initial concentration was $1 \cdot 10^{-5}$ M the total carbon mass emitted as CO_2 in 6 hours of discharge time was 100%. So it is concluded that low initial concentrations of the organic pollutant lead not only to a faster process (Fig. 3) but also to better conversion into CO_2 . These are very interesting results in view of possible applications of DBD for the treatment of amoxicillin contaminated waters, since in the environment amoxicillin is present at very low concentrations.

Further insight on the amoxicillin degradation pathway was obtained by means of HPLC/MS analysis. Results are summarized in Table 1.

Table. 1. Results of HPLC/MS analysis

#	Retention time (min)	[M+H] ⁺ (m/z)	Other signals (m/z) and attribution	Attributions
1	1.7	382	365, [MH - NH ₃] ⁺	P1
2	2.2	398	381, [MH - NH ₃] ⁺	P2
3	2.5	382	365, [MH - NH ₃] ⁺	P3
4	4.3	366	349, [MH - NH ₃] ⁺	Amoxicillin (A)

These results allow us to identify the elementary composition of intermediates P1-P3. The mass spectra are presented in Figs. 6-8.

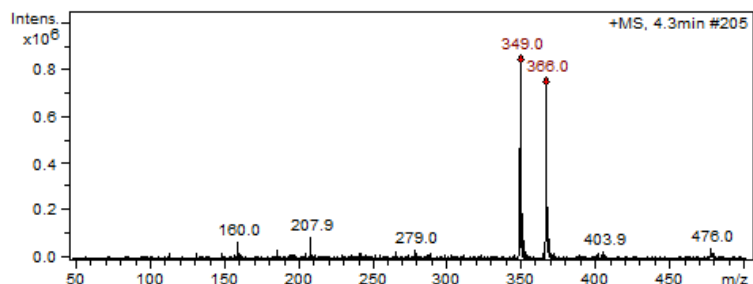


Fig. 6. Mass spectrum of amoxicillin.

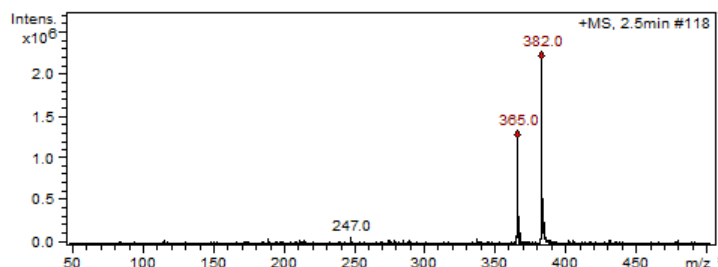
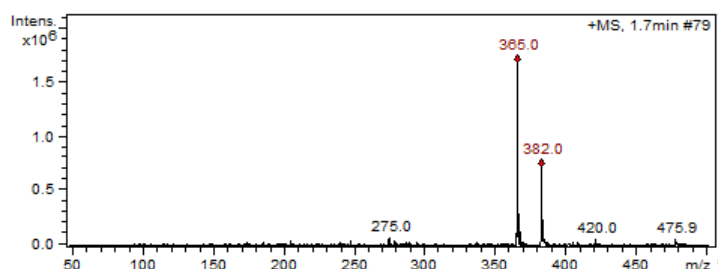


Fig. 7. Mass spectra of the degradation intermediates P1 and P3 eluted with retention times of 1.7 and 2.5 min, respectively.

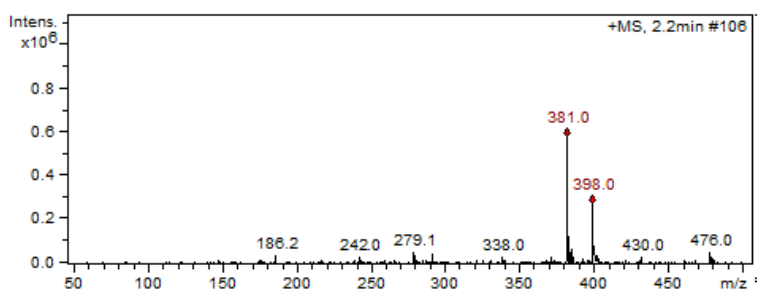


Fig. 8. Mass spectrum of the degradation intermediate P2 eluted with retention time of 2.2 min.

As shown in Fig. 9, P1-P3 are oxidized intermediates of amoxicillin, which differ in mass from their precursor by +16 (P1 and P3) and +32 uma (P2) and thus contain one (A + O)

or two atoms of oxygen ($A + 2O$) more than amoxicillin, respectively. These can be products of hydroxylation or of sulphur oxidation [8].

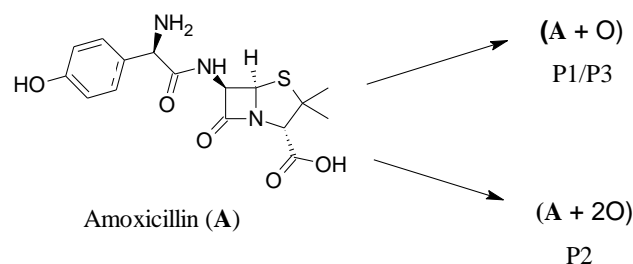


Fig. 9. Degradation intermediates of amoxicillin under DBD plasma discharge above water.

Work is in progress to further characterize these intermediates and their reactions.

Acknowledgment

TI gratefully acknowledges support by COST Action TD1208 for a short term scientific mission.

4. References

- [1] M. Magureanu, D. Piroi, N. B. Mandache, V. David, A. Medvedovici, C. Bradu, V. I. Parvulescu, Degradation of antibiotics in water by non-thermal plasma treatment, *Water Res.* 45 (2011) 3407-3416.
- [2] N. Bhakta, Y. Munekage, Degradation of antibiotics (trimethoprim and sulphamethoxazole) pollutants using UV and TiO_2 in aqueous medium, *Modern Appl. Sci.* 3 (2009) 3-13.
- [3] F. Yuan, C. Hu, X. Hu, D. Wei, Y. Chen, J. Qu, Photodegradation and toxicity changes of antibiotics in UV and UV/ H_2O_2 process, *J. Hazard. Mater.* 185 (2011) 1256-1263.
- [4] R. Andreozzi, M. Canterino, R. Marotta, N. Paxeus, Antibiotic removal from wastewaters: the ozonation of amoxicillin, *J. Hazard. Mater.* 122 (2005) 243-250.
- [5] E. Marotta, M. Schiorlin, X. Ren, M. Rea, C. Paradisi, Advanced oxidation process for degradation of aqueous phenol in a dielectric barrier discharge reactor, *Plasma Process. Polym.* 8 (2011) 867-875.
- [6] E. Marotta, E. Ceriani, V. Shapoval, M. Schiorlin, C. Ceretta, M. Rea, C. Paradisi, Characterization of plasma induced phenol advanced oxidation process in a DBD reactor, *Eur. Phys. J. Appl. Phys.* 55 (2011) 13811.
- [7] E. Marotta, E. Ceriani, M. Schiorlin, C. Ceretta, C. Paradisi, Comparison of the rates of phenol advanced oxidation in deionized and tap water within a dielectric barrier discharge reactor, *Water Res.* 46 (2012) 6239-6246.
- [8] I. Gozlan, A. Rotstein, D. Avisar, Investigation of an amoxicillin oxidative degradation product formed under controlled environmental conditions. *Environ. Chem.* 7 (2010) 435-442.

20th Symposium on Application of Plasma Processes

Oral Presentations

ELECTRON AFFINITY EVALUATION FROM NEGATIVE ION MASS SPECTROMETRY DATA

Nail Asfandiarov^{1,2}, Stanislav Pshenichnyuk¹, Alexander Vorob'ev¹, Ekaterina Nafikova¹, Yurii Elkin³, Alberto Modelli^{4,5}

¹ *Institute of Molecule and Crystal Physics, Ufa Research Centre, Russian Academy of Sciences, Prospect Oktyabrya 151, 450075 Ufa, Russia*

² *Bashkir State Pedagogical University, Oktyabrskoy Revolutsii st., 3a, 450000, Ufa, Russia*

³ *Pacific Institute of Bioorganic Chemistry, Far Eastern Branch of Russian Academy of Sciences. Prospect 100 Let Vladivostoku, 159, Vladivostok, 690022, Russia*

⁴ *Dipartimento di Chimica "G. Ciamician", Università di Bologna, via Selmi 2, 40126 Bologna, Italy*

⁵ *Centro Interdipartimentale di Ricerca in Scienze Ambientali (CIRSA), Università di Bologna, via S. Alberto 163, 48123 Ravenna, Italy*

E-mail: nail@anrb.ru

Naphthoquinone (NQ), eleven of its hydroxyl-derivatives, pyromellitic diimide (PMDI), anthraquinone (AQ), azobenzene (AB) and phthalimide (PTI) were investigated by means of Negative Ion Mass Spectrometry (NIMS). All molecules under investigation, except PTI, form long-lived ($\tau_a > 10 \mu\text{s}$) molecular anions in the 0-2 eV energy range. NI lifetime measurements by means of a modified NIMS instrumentation can provide quantitative data of Electron Affinity (EA). A simple Arrhenius approximation seems to be adequate to describe the process of electron detachment from molecular anions.

1. Introduction

The energies of the frontier molecular orbitals (MOs), namely, the lowest unoccupied MO (LUMO) and the highest occupied MO (HOMO), define the so-called energy gap which is often used as a descriptor to correlate the molecular electronic structure with chemical reactivity^[1] and biological properties^[2,3] in quantitative structure–activity relationship (QSAR) studies. The energy of the LUMO and the electron affinity (EA) of a neutral molecule play an important role in the properties of the corresponding molecular negative ion (NI), defining its stability relative to electron detachment (mean autodetachment lifetime, τ_a).^[4,5] Therefore, quantitative evaluations of the EAs and the characterization of empty-level structures constitute a highly topical question. One of the most widespread methods for measuring EAs in the gas phase is the electron transfer reaction (ETR) method,^[6] which supplies adiabatic EA (EA_a) data. EA values can be measured with various experimental methods, although their availability is still relatively limited. We have recently applied the NIMS technique to a series of compounds which form long-lived molecular anion.^[7-10]

2. Results and discussion

The negative ion mass spectrometer features and method of experiment were described in detail earlier.^[7] The signals associated with formation of long-lived molecular NIs by electron attachment to six naphthoquinone derivatives, as a function of incident electron energy, are shown in Fig. 1, and summarized in Table 1 for all compounds under investigation. In all cases, these molecular anion signals are more intense than those associated with negative fragments produced by dissociative electron attachment (DEA). The temperature of the collision chamber for the various DEA spectra is reported in Table 1. It is easy to see that the mean detachment time τ_a is a function of molecular structure, collision chamber temperature and also the number and nature of substituents.

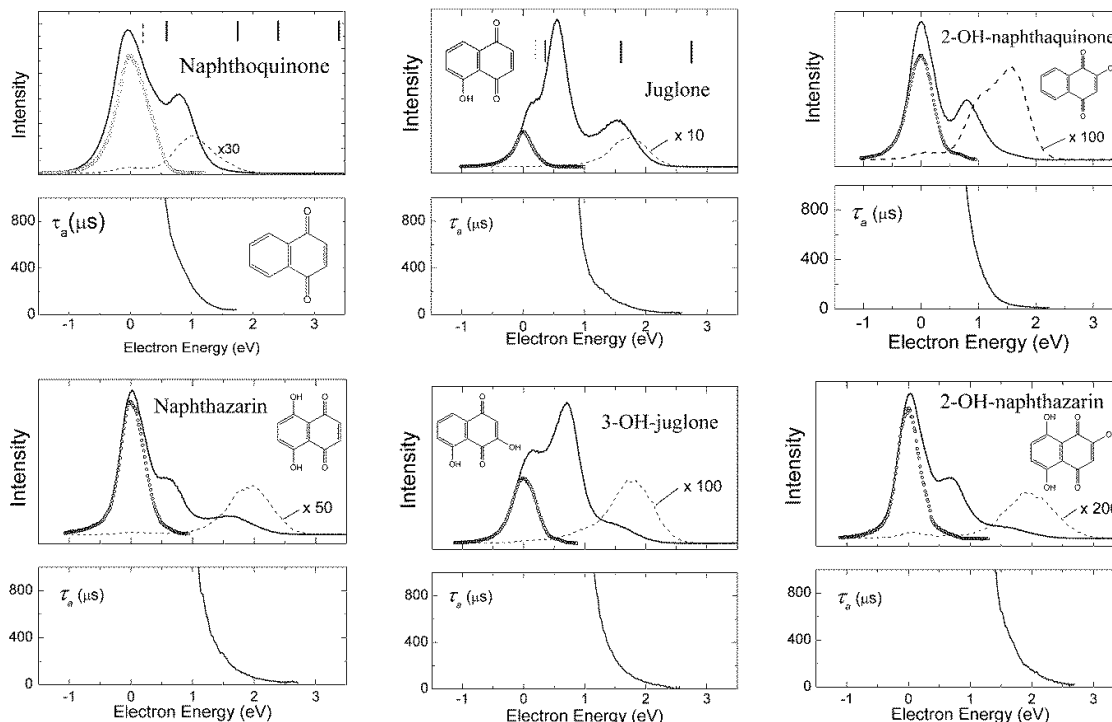


Fig. 1. *Upper panels*: Currents of mass-selected molecular negative ions (solid lines), signals from the corresponding neutral molecules (dashed lines) and SF_6^- currents (open circles) as a function of incident electron energy; *Lower panels*: Electron detachment time (τ_a) from the molecular negative ions as a function of incident electron energy. The collision cell temperature was 70 °C. Vertical lines indicate the VAEs measured in the ET spectra of NQ and Juglone.

The spectra of all sixteen compounds display an M^- peak at zero energy (see Fig. 1) because of the formation of vibrationally excited ground anion states. The occurrence of these long-lived molecular NIs is thus ascribed to formation of nuclear excited Feshbach resonances (NEFRs).^[4,5] In the cases of juglone, and 3-OH-juglone the zero energy signal looks like a shoulder on the low-energy side of the next (more intense) signal (see Fig. 1).

Measurements of electron autodetachment lifetime are based on detection of a beam of neutral species formed in the free drift region between the mass analyzer and the secondary electron multiplier. NI lifetime measurements include two stages. Firstly we measure the sum of the ions and neutrals (which are formed in the second free drift region, see supporting information) currents. Secondly we deflect the negative ions from the input slit of the secondary electron multiplier using special deflection plates, and measure the neutrals current only. The NI lifetime τ_a , assuming an exponential NI decay, can be evaluated according to the formula:

$$\tau_a = -\frac{t_0}{\ln\left(1 - \frac{I_n}{I}\right)}, \quad (1)$$

where t_0 is the anion drift time from the magnet mass analyzer and secondary electron multiplier, I_n is the neutral species current, and I is the total current of the neutral and charged components of the beam.^[7] This method was used for the first time in a time-of-flight experiment,^[11] and later implemented by Khvostenko and colleagues using a magnetic mass analyser.^[5]

The excess energy of anions formed through higher-lying resonances includes the energy (ε) of the incident electron beam^[8,10]:

$$E^- = EA_a + E_m + \varepsilon, \quad (2)$$

where E_m is the vibration energy storage of the target molecule.

Tab. 1. Parameters of the molecular negative ions. ε is the electron energy corresponding to a lifetime (τ_a) of $10^3 \mu\text{s}$, N the number of internal degrees of freedom, T the temperature of the ionization chamber. The column LUMO^{sc} reports the scaled LUMO energies (see text). The EA_a values were

obtained with equation (4), ΔE with DTF B3LYP/6-31G+(d) calculations, as the energy difference between the optimized neutral and anion states. All energy values in eV.

#	Compound	ε	N	T, K	LUMO ^{sc}	EA_a	ΔE
1	NQ	0.56	48	343	1.64	1.78*	1.99
2	Juglone	0.91	51	343	1.78	1.95	2.22
3	Lowsone	0.79	51	343	1.65	1.85	2.05
4	Naphthazarine	1.10	54	343	1.86	1.97	2.34
5	3-OH-Juglone	1.16	54	343	1.76	2.01	2.24
6	Naphthopurpurin	1.42	57	343	1.84	2.07	2.35
7	Spinochrome B	1.30	60	433	1.74	2.16	2.29
8	Spinochrome C	2.80	78	413	1.94	2.30	2.62
9	Spinochrome D	1.45	63	423	1.78	2.11	2.36
10	Spinochrome E	1.57	66	433	1.75	2.12	2.35
11	Echinochrome A	2.40	81	393	1.71	2.01	2.23
12	Spinochrome A	2.40	75	383	2.00	2.12	2.67
13	PMDI	0.85	54	350	2.08	2.07	2.31
14	Anthraquinone	0.44	66	353	1.37	1.61**	1.75
15	Azobenzene	0.85	66	363	0.83	1.25	1.19
16	PTI	0.0	42	363	0.86	1.23	1.11

* The EA_a obtained with the ETR method is 1.81 eV.^[6]

** The EA_a obtained with the ETR method is 1.59 eV.^[6]

The simplest relationship between the detachment time of the anion state and other parameters of the system is an Arrhenius approximation:

$$k_a = \frac{\omega_0}{2\pi} \cdot \exp\left[-\frac{EA_a}{kT^-}\right], \quad (3)$$

where $k_a = \tau_0^{-1}$ is the autodetachment rate constant, ω_0 is the typical anion vibrational frequency (τ_0 is the vibration relaxation time^[13]), k is the Boltzmann constant, T^- is the anion effective temperature.^[14] Therefore, accurate measurements of anion lifetimes should allow us to evaluate the EA_a of the target molecule. Although an accurate calculation of the anion lifetime from EA_a , vibrational frequencies and temperature is not a simple routine task,^[7,9] we can try to solve the inverse problem of EA_a evaluation from NI lifetime data through the simple use of equation (3). In a rough approximation, $kT^- = (EA_a + E_m + \varepsilon)/N$, where $N = 3n - 6$ is the number of internal degrees of freedom.^[15] In the same way we can evaluate $E_m = NkT$, where T is the temperature of the target molecule (ionization chamber temperature). Assuming that the pre-exponent factor $\omega_0/2\pi$ is equal to the inverse of the intramolecular vibrational energy redistribution (IVR) time (τ_0) of the anion^[13], then eq. (3) may be written as:

$$\tau_a \approx \tau_0 \cdot \exp\left[\frac{EA_a}{kT}\right] = \tau_0 \cdot \exp\left[\frac{N \cdot EA_a}{EA_a + E_m + \varepsilon}\right] = \tau_0 \cdot \exp\left[\frac{N \cdot EA_a}{EA_a + NkT + \varepsilon}\right]. \quad (4)$$

The results of adiabatic EA evaluation using eq. (4) are shown in Fig. 2. The EA_a values obtained with eq. (4) display a trend quite similar to those of the calculated EAs, lying between the EA_v s predicted by the scaling procedure $EA_v = -0.8065E_{LUMO} - 0.9194$ (DFT B3LYP/6-31G(d))^[16] and the EA_a s calculated at the B3LYP/6-31G+(d) level as the neutral/anion energy difference. The only experimental EA values available for the compounds under investigation are those of NQ ($EA_a = 1.81$ eV) and AQ ($EA_a = 1.59$ eV).^[6] The present results are satisfactory, and demonstrate that NI lifetime measurements can supply reliable EA_a evaluations.

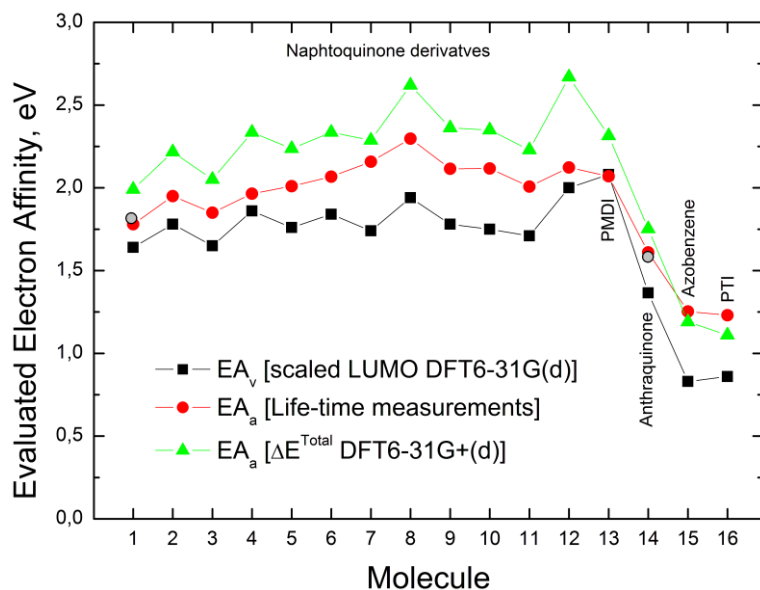


Fig. 2. Comparison of the EA_a s calculated from eq. (4) (circles) with the EA_v s supplied by the scaled LUMO energies (squares) and the ΔE s obtained with B3LYP/6-31G+(d) calculations (triangles).

NI lifetime measurements by means of a modified DEAS instrumentation can provide quantitative data of EA. A simple Arrhenius approximation seems to be adequate to describe the process of electron detachment from molecular anions.

3. References

- [1] Woodward RB and Hoffmann R 1965 *J.A.C.S.* **87** 395.
- [2] Ferreira MMC 2001 *Chemosphere* **44** 125.
- [3] Burrow PD and Modelli A 2013 *SAR QSAR Environ. Res.* **24** 647.
- [4] Illenberger E and Momigny J 1992 *Gaseous Molecular Ions. An Introduction to Elementary Processes Induced by Ionization*, Steinkopff Verlag Darmstadt, Springer-Verlag, New York.
- [5] Khvostenko VI 1980 *Negative Ion Mass Spectrometry in Organic Chemistry*, Nauka, Moscow.
- [6] Kebarle P and Chowdhury S 1987 *Chem. Rev.* **7** 513.
- [7] Pshenichnyuk SA, Vorob'ev AS and Modelli A 2011 *J. Chem. Phys.* **135** 184301.
- [8] Asfandiarov NL, Pshenichnyuk SA, Vorob'ev AS, Nafikova EP, Elkin YN, Pelageev DN, Koltsova EA, Modelli A 2014 *Rapid Commun. Mass Spectrom.* **28** 1580.
- [9] Vorob'ev AS, Pshenichnyuk SA, Asfandiarov NL, Nafikova EP 2014 *Technical Physics (Rus.)* **59** 1277.
- [10] Pshenichnyuk SA, Vorob'ev AS, Asfandiarov NL, Modelli A 2010 *J. Chem. Phys.* **132** 244313.
- [11] Edelson D, Griffiths JE and McAfee KB Jr. 1962 *J. Chem. Phys.* **37** 917.
- [12] Illenberger E and Smirnov BM 1998 *Physics-Uspekhi (Rus.)* **41** 651.
- [13] Makarov AA, Malinovsky AL and Ryabov EA 2012 *Physics-Uspekhi (Rus.)* **55** 977.
- [14] Klots CE 1967 *J. Chem. Phys.* **46** 1197.
- [15] Matejčík Š, Märk TD, Španěl P, Smith D, Jaffke T and Illenberger E 1995 *J. Chem. Phys.* **102** 2516.
- [16] Scheer M and Burrow PD 2006 *J. Phys. Chem. B* **110** 17751.

ANION CHEMISTRY ON TITAN: A POSSIBLE ROUTE TO LARGE HYDROCARBONS

J. Žabka¹, M. Polášek¹, C. Romanzin², and C. Alcaraz²

¹ *J. Heyrovský Institute of Physical Chemistry of the ASCR, v. v. i., Dolejškova 2155/3, Prague 8, 182 23, Czech Republic*

² *Laboratoire de Chimie Physique, Bât 350, Centre Universitaire Paris-Sud, 91405 Orsay, France*

Cassini CAPS-ELS spectrometer revealed the presence of large negative ions in the ionosphere of Titan [1]. Recently, a mechanism has been proposed for the possible formation of these ions, in which the cyanoacetylene, HC₃N, played a key role [2]. Chemical ionization technique (NCI and APCI-) were used successfully to prepare model complex (HC₃N)_x.C_yN⁻ anions in the gas phase. The reaction itself and CID experiments was studied using a Waters Quattro Premier TM tandem quadrupole mass spectrometer operating in negative ion mode and VG ZAB2-SEQ mass spectrometer. CID mass spectra of these anions, as well as their ion molecule reactions with HC₃N support the previously proposed reaction scheme [2]. Quantum chemistry calculations revealed details of the ion structures, energetics and reaction mechanisms. High-energy CID spectra of (HC₃N)_x.C_yN⁻ anions showed a complexity of ionic and neutral products that can be expected to be formed by the high-energy ion precipitation observed at Titan [3].

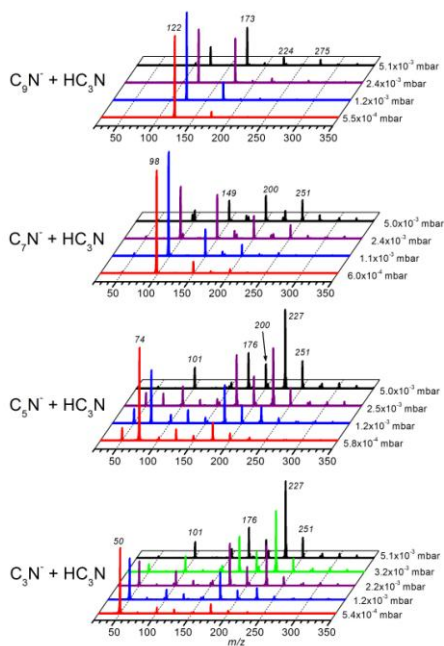


Fig.1. Pressure dependent mass spectra of reactions C_xN⁻ anions (x =3,5,7,9) with HC₃N

Presented experiments shows that in spite of its low abundance in Titan atmosphere [4], the cyanoacetylene is probably one of the most important species in the ionospheric chemistry of Titan.

References

- [1] A.J. Coates, F.J. Crary, G.R. Lewis, D.T. Young, J.H. Waite, E.C. Sittler, "Discovery of heavy negative ions in Titan's ionosphere", *Geophys. Res. Lett.* **34** L22103 (2007)
- [2] J. Žabka, M. Polášek, C. Romanzin, C. Alcaraz, "Anion Chemistry: A possible route to large hydrocarbons in Titan ionosphere", *Icarus*, **219**, 161, (2012)
- [3] T.E. Cravens, I.P. Robertson, S.A. Ledvina, D. Mitchell, S.M. Krimigis, J.H. Waite Jr., "Negative ions at Titan and Enceladus: recent results", *Geophys. Res. Lett.*, **35**, L03103 (2008)
- [4] V. Vuitton, P. Lavvas, R.V. Yelle, M. Galand, A. Wellbrock, G.R. Lewis, A.J. Coates, J.E. Wahlund, "Negative ion chemistry in Titan's upper atmosphere", *Planet. Space Sci.* **57**(13), 1558-72 (2009).

STUDY OF PLASMA-CHEMISTRY PROCESSES IN ATMOSPHERIC PRESSURE PLASMAS: ABSOLUTE DENSITY MEASUREMENTS OF RADICALS, VUV SPECTROSCOPY AND SIMULATIONS

Jan Benedikt, Katja Rügner, Simon Schneider, Simon Große-Kreul, Vincent Laves, Gert Willems, Mohamed Hefny, Simon Hübner, Achim von Keudell

*Research Department Plasma with Complex interactions,
Ruhr-University Bochum, Germany
E-mail: jan.benedikt@rub.de*

Atmospheric pressure non-equilibrium plasmas (APPs) are effective source of large densities of reactive radicals, metastables and ions and also high fluxes of photons with wavelengths down to the 60 nm in the vacuum UV range. The resulting high reactivity of these APPs can be used in many surface treatment applications such as activation of polymer surfaces, treatment of living tissues (decontamination, acceleration of wound healing) or in deposition of thin films or nanostructured materials. However, the complexity of plasma-chemical processes in the discharge requires combined experimental and theoretical approach in plasma analysis, where quantitative and qualitative plasma diagnostics are compared with theoretical plasma simulations. In this contribution, the mass spectrometry for detection of neutral and ionized species and the windowless VUV spectroscopy will be introduced and discussed in details. The mass spectrometry of neutral species measures the plasma composition directly at the surface and is not limited by existence of accessible optical transitions. When properly designed and carefully calibrated mass spectrometry provides absolute densities of the measured species. It can even provide information about vibrational excitation of the detected species. The ion mass spectrometry can provide information about the formation of positive and negative ions (and ion clusters) in the effluent and provides supporting information about the influence of variety of species (including impurities) on plasma chemistry. The windowless VUV spectroscopy allows detection of VUV photons from excited states into the ground states and provides hence additional qualitative information about processes occurring in plasma. These experimental results serve for validation of plasma-chemistry models and rate-equation calculations, which can provide deep insight into the whole plasma process.

1. Mass spectrometry

The plasma chemistry of cold atmospheric pressure plasmas is rich in neutral and charged species as for example demonstrated by recent simulations [1,2]. Mass spectrometry (MS) can provide absolute densities and ion fluxes to validate these models and to provide more insight into plasma chemistry processes. The general principles of quadrupole MS of reactive plasmas has been provided recently [3], here we will focus on the investigation of atmospheric pressure discharges.

The one of the most critical issues is the proper gas sampling into the mass spectrometer. The gas mixture is usually sampled through a very small orifice (diameter from 20 to 100 μm diameter) into differentially pumped system with typically three pumping stages. By aligning the sampling orifice with orifices connecting the pumping stages, the molecular beam (MB) is formed and the gas mixture including ions and very reactive species can be transported into the ionizer or ion optics of the mass spectrometer [3]. The challenge by sampling from the atmospheric pressure is the fact that it is collisional and that the gas is accelerated to the supersonic velocities. An example of the fluid simulation of the expansion of Argon gas into the 100 Pa background pressure vacuum chamber through a 100 μm diameter and 250 μm long sampling orifice, using compressible Navier-Stokes equations, is shown in Fig. 1. The pressure 100 Pa is still high enough that the mean free path in the low pressure region ($\sim 100 \mu\text{m}$ at 100 Pa) is still large enough to justify the fluid simulation approach.

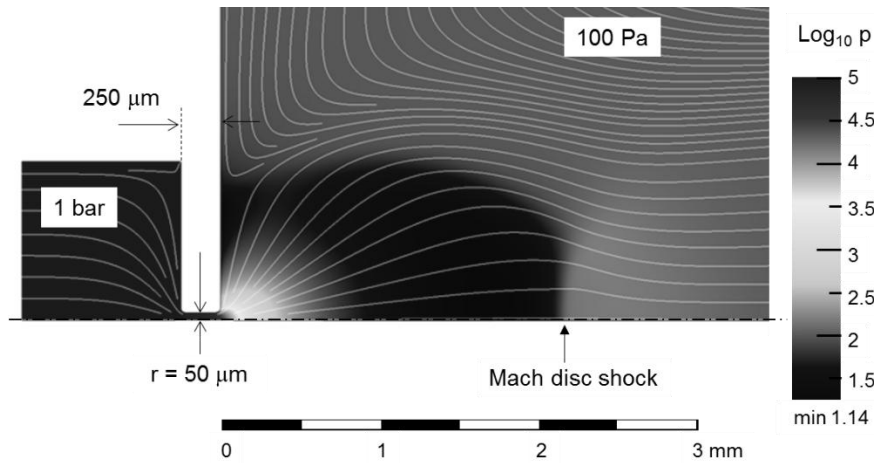


Fig. 1. Fluid simulation of the expansion of argon gas into the 100 Pa background pressure of the first pumping stage of the mass spectrometer. The \log_{10} of the pressure (colour scheme) and the gas streamlines are shown. The steep pressure drop behind the orifice, the zone of silence (region with supersonic gas velocities visible as a dark area with the pressure lower than the background pressure) and the Mach disc shock are visible.

The background pressure of 100 Pa is often reported in the literature as a pressure in the first pumping stage, but as the simulation shows, the species undergo a shock equilibration with the background gas, which can result into a loss of reactive species and formation of new ones, especially in the case of ions. This leads to composition distortion in the MB. Therefore, the sampling system with much lower background pressure in the stage behind the sampling orifice should be used. Our approach for realising this low pressure is the use of a beam chopper with a rotating skimmer (see Fig. 2 and [4]). The MB is formed only for 1% of the period and the background pressure is reduced in the remaining 99% resulting in the effective background pressure of 10^{-2} Pa.

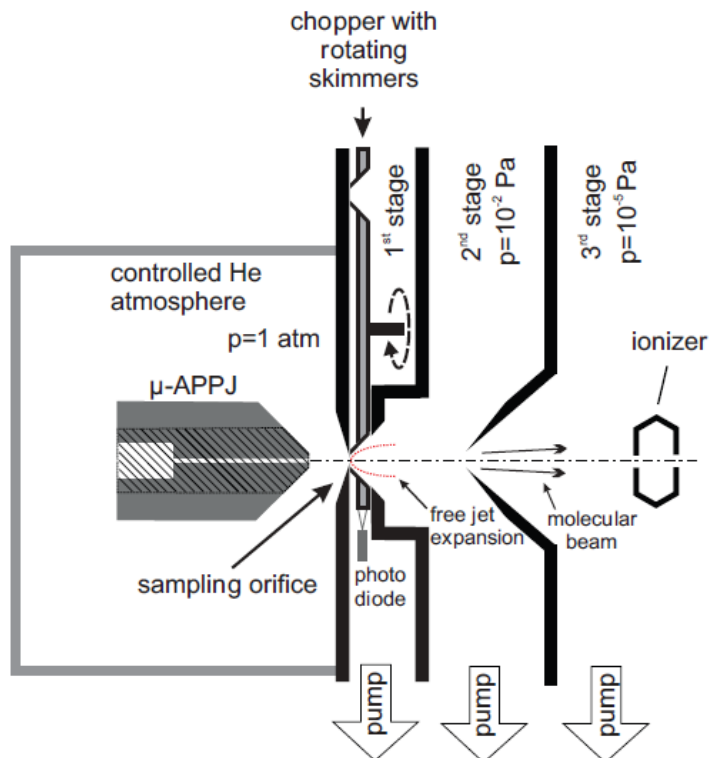


Fig. 2. Differentially pumped sampling system with rotating chopper with imbedded skimmer.

This approach avoids composition distortion during the sampling and have been used in the past for measuring effectively reactive species in cold APPs [5-8].

Fig. 3 shows as an example the electron energy scan of a He/0.3%N₂ gas mixture measured at the nozzle of a microscale atmospheric pressure plasma jet (μ -APPJ). This source uses radiofrequency voltage to ignite a homogeneous discharge between electrodes 1 mm apart from each other (see [5,6,9]).

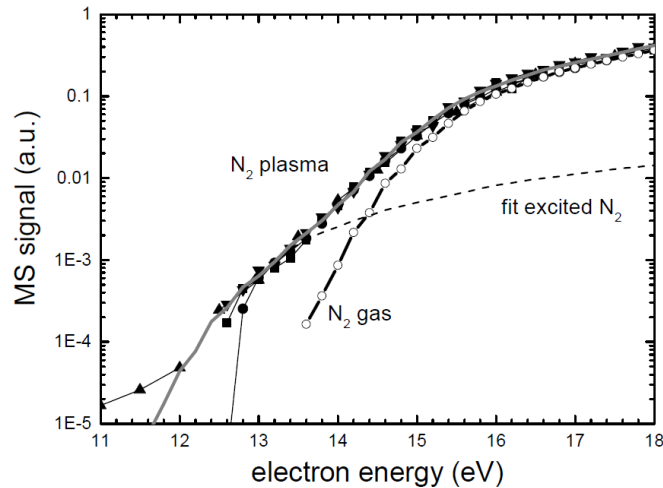


Fig. 3 Two scans of the electron energy of the electrons in the ionizer of the mass spectrometer performed at mass 28 amu (N₂) for the cases of plasma off and plasma on. The curve for the case with plasma running (full symbols) could be fitted by combining the curve measured for plasma off case (open circles) with the same curved, which was scaled and shifted 2.2 eV on the energy scale (dashed line). This fit (solid grey line) reproduces the measured data very well.

By scanning the electron energy in the ionizer of the mass spectrometer, the species can be identified based on their ionisation energy. The scans at mass 28 amu (mass of N₂) taken without and with plasma running clearly shows that some N₂ molecules can be ionized at lower electron energies. The additional signal can be fitted by rescaling and shifting the curve for N₂ ionization by 2.2 eV, which corresponds to the vibrational excitation of N₂ molecules into the 7th vibrational level. Fig. 4 compares the measured absolute atomic nitrogen densities and the relative signal of the vibrationally excited N₂ molecules as measured by MS. This comparison shows that more energy goes to the vibrational excitation of the N₂ compare to its dissociation at higher N₂ concentrations, an expected behaviour for a plasma with increasing fraction of a molecular gas.

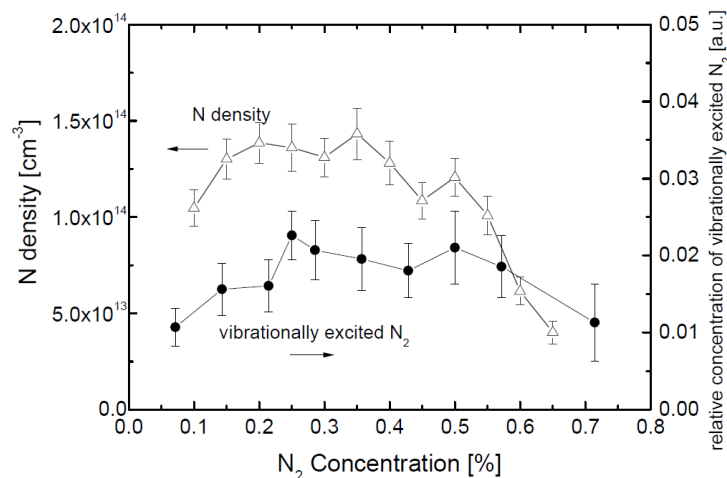


Fig. 4. Comparison of the N density (taken from [8]) with the relative presence of vibrationally excited N₂ molecules.

2. Windowless VUV Spectroscopy

The APPs are also emitting photons in the vacuum ultraviolet (VUV) range below 200 nm. This photons cannot propagate through air, but since many of the APP sources are operated in argon or helium, they can propagate through the gas channel formed by the noble gas and can therefore reach the surface even at the distance of several tens of mm from the jet. It is, therefore, important to investigate at least quantitatively the VUV spectra of APPs. A windowless VUV spectrometer has been designed for this measurements and is schematically shown in Fig. 5.

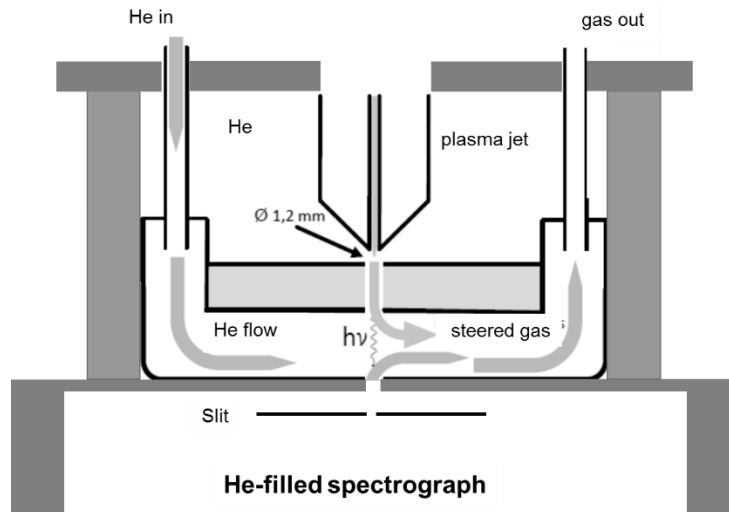


Fig. 5 Windowless VUV spectrograph: principle of coupling the plasma emitted VUV and UV photons into the He-filled VUV spectrograph without necessity of having any window between the plasma and the spectrograph. All the potentially absorbing species in the plasma (such as molecules introduced into the plasma) are steered by the additional helium flow into the side and cannot enter the spectrograph. Additionally, controlled atmosphere around the jet is used to prevent air to diffuse into the light path.

Fig. 6 shows the measured spectrum of the μ -APPJ operated with helium gas in the 50 to 140 nm wavelength range. Next to the few atomic oxygen lines, resulting from the excitation of the gas impurities, the clear emission of the 1st and 2nd helium excimer continuum is visible.

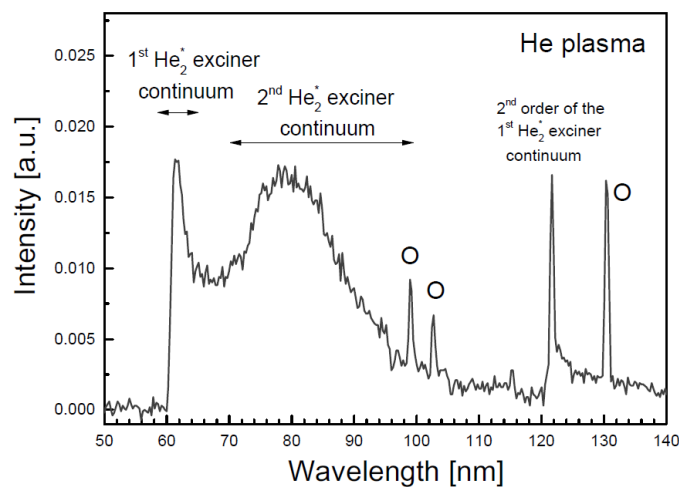


Fig. 6. VUV spectrum of the μ -APPJ operated in the 5.0 grade helium gas.

These photons can propagate through the helium gas without being absorbed, since the first photon absorption by ground state helium is possible to the (1s)(2p) level corresponding to the wavelength of 58.44 nm only. The spectrum in Fig. 6 is very similar to the spectrum reported for a micro-hollow cathode discharge in helium [10].

The windowless VUV spectrograph have been used to analyse emission spectra of several gases admixed at concentrations below 1% into the helium in the μ -APPJ. Three examples of the plasma with O₂, N₂ and Ar are compared to the spectrum of helium gas only from Fig. 6 in Fig. 7.

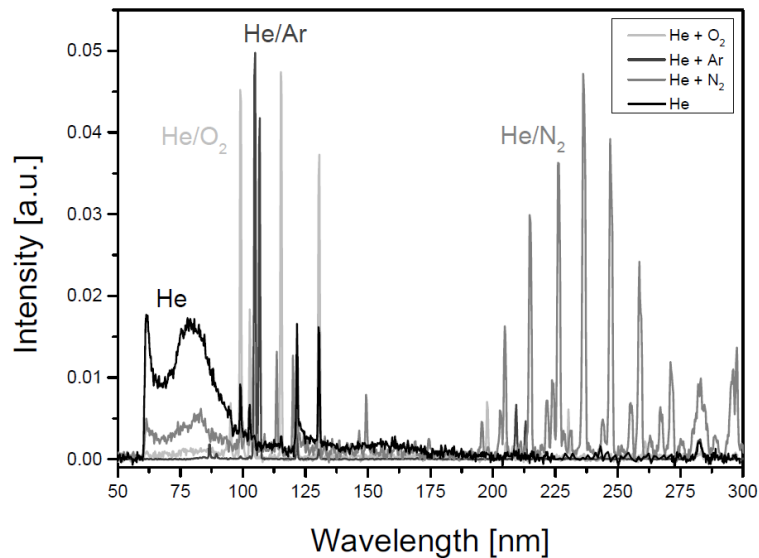


Fig. 7. Exemplary VUV and UV spectra of μ -APPJ with He, He/O₂, He/N₂ and He/Ar.

The VUV spectra, and their dependence on the variety of plasma parameters, can be used as an additional information for the analysis of the plasma-chemical processes in APPs. Special feature of this high energy VUV photons is that they can photoionize species at larger distances from the jet, which should be considered for example in the treatment of the biological materials. We have reported the possible effect of protonated water cluster ions, which formation was initialized through photoionization, on bacteria recently [11].

3. Summary

Some examples of application of advanced APPs diagnostics, namely molecular beam mass spectrometry and windowless vacuum UV optical emission spectroscopy, to atmospheric pressure plasmas have been demonstrated and discussed above. The obtained data provide information about plasma-chemical processes in the plasma and its effluent and can be used for calculation/estimation of fluxes of detected species to the treated surface or for benchmarking of the simulation results.

4. Acknowledgments

This work has been funded by the German Research Foundation (DFG), project package PAK 728 „PlasmaDecon“ and research unit FOR 1123 „Physics of Microplasmas“, and by 7FP Marie Curie Initial Training Network RAPID „Reactive Atmospheric Plasma Processing–Education Network“.

5. References

- [1] van Gaens W, Bogaerts A 2013 J. Phys. D: Appl. Phys. **46** 275201
- [2] Murakami T, Niemi K, Gans T, O'Connell D, Graham W G, 2013 Plasma Sources Sci. Technol. **22** 015003
- [3] Benedikt J, Hecimovic A, Ellerweg D, von Keudell A 2012 J. Phys. D: Appl. Phys. **45** 403001
- [4] Benedikt J, Ellerweg D, von Keudell A 2009 Rev. Sci. Instrum. **80** 055107
- [5] Ellerweg D, von Keudell A and Benedikt J 2012 Plasma Sources Sci. Technol. **21** 034019
- [6] Ellerweg D, Benedikt J, Knake N, Schulz-von der Gathen V and von Keudell A 2010 New J. Phys. **12** 013021
- [7] Benedikt J, Ellerweg D, Schneider S, Rügner K, Reuter R, Kersten H, Benter T 2013 J. Phys. D: Appl. Phys. **46** 464017
- [8] Schneider S, Dünnbier M, Hübner S, Reuter S, Benedikt J 2014 J. Phys. D: Appl. Phys. **47** 505203
- [9] Knake N, Schulz-von der Gathen V 2010 Eur. Phys. J. D **60** 645
- [10] Kurunczi P, Lopez J, Shah H, Becker K 2001 Int. J. Mass Spectr. **205** 277
- [11] Schneider S, Lackmann J-W, Ellerweg D, Denis B, Narberhaus F, Bandow J E, Benedikt J 2012 Plasma Process. Polym. **9** 561

SPATIOTEMPORAL IMAGING OF SELF-PULSING NANOSECOND DISCHARGES

Mário Janda¹, Karol Hensel¹, Andrej Buček¹, Viktor Martišovič¹, Zdenko Machala¹

¹*Faculty of Mathematics, Physics and Informatics, Comenius University, Mlynská dolina, 84248 Bratislava, Slovakia*
E-mail: janda@fmph.uniba.sk

A streamer-to-spark transition in a self-pulsing transient spark (TS) discharge of positive polarity was investigated using a fast iCCD camera. The entire temporal evolution of the TS, including the primary streamer, the secondary streamer, and the transition to spark was recorded with 2 ns time resolution. Additionally, a streak camera like images were obtained using spatiotemporal reconstruction of the discharge emission detected by a photomultiplier tube with light collection system placed on a micrometric translation stage. With increasing TS repetition frequency f (from ~1 to 6 kHz), the increase of the propagation velocity of both the primary and the secondary streamer was observed. Accelerating propagation of the secondary streamer crossing the entire gap could explain short streamer-to-spark transition times τ (~100 ns) at f above ~3 kHz. Acceleration of the primary and secondary streamers and shortening of τ with increasing f was attributed to the memory effect composed of pre-heating, pre-ionization, or gas composition changes induced by the previous TS pulses.

1. Introduction

Streamer-to-spark transition leading to the gas breakdown is a critical issue when working with various atmospheric pressure electrical discharges, as well as in the design of high voltage (HV) devices and switches. The most typical approach preventing the spark breakdown is to maintain the low temperature plasma character and to prevent excessive discharge currents. On the other hand, periodic streamer-to-spark transition with restricted spark phase can bring multiple benefits in various applications of non-thermal plasmas, such as local and transient elevation of the gas temperature, formation of hydrodynamic expansion, producing high concentrations of reactive species, etc. [1-5]. A relatively simple discharge operating with periodic streamer-to-spark transition and controlled spark phase is the transient spark (TS) discharge [5-7].

The TS is typically generated in atmospheric pressure air or other gases between metal electrodes in point-to-plane configuration with distance $d = 4-10$ mm, by a DC HV power supply connected to the electrodes via a series resistor $R = 5-10$ M Ω (Figure 1). Both polarities are possible, but here we present a study of positive polarity TS discharge with anode as the HV point electrode. The TS is initiated by a primary streamer creating a relatively conductive plasma bridge between the electrodes. It enables partial discharging of the internal capacity C of the electric circuit, and a local gas heating inside the plasma channel [7]. When the gas temperature T inside the plasma channel reaches ~1000 K, a very short (~10-100 ns) high current (>1 A) spark current pulse appears (Figure 2).

During the spark phase lasting only a few tens of nanoseconds, the internal circuit capacity C discharges completely and the potential V on the HV electrode drops to almost zero. Transition to steady-state arc after the spark is restricted by the ballast resistor R , and the discharge starts to decay after the V drop. Eventually, the potential V starts to gradually increase as the capacity C recharges.

A new TS pulse, initiated by a new primary streamer, occurs when V reaches the breakdown voltage again. The TS is thus characteristic of the repetitive primary streamer formation transiting to the spark, with the frequency f in the kHz range. The increase of f , achieved by increasing the generator voltage [6], is accompanied by changes of several TS characteristics (decrease of the breakdown voltage, smaller and broader spark current pulses). It also influences the breakdown mechanism via shortening of the streamer-to-spark transition time (τ) [7]. These frequency-dependent phenomena occur due to the various 'memory' effects (especially pre-heating, pre-ionization and gas composition changes by previous TS pulses) in the gap. The objective of this paper is to explore the changes of the breakdown mechanism in the TS discharge due to the memory effects in greater detail.

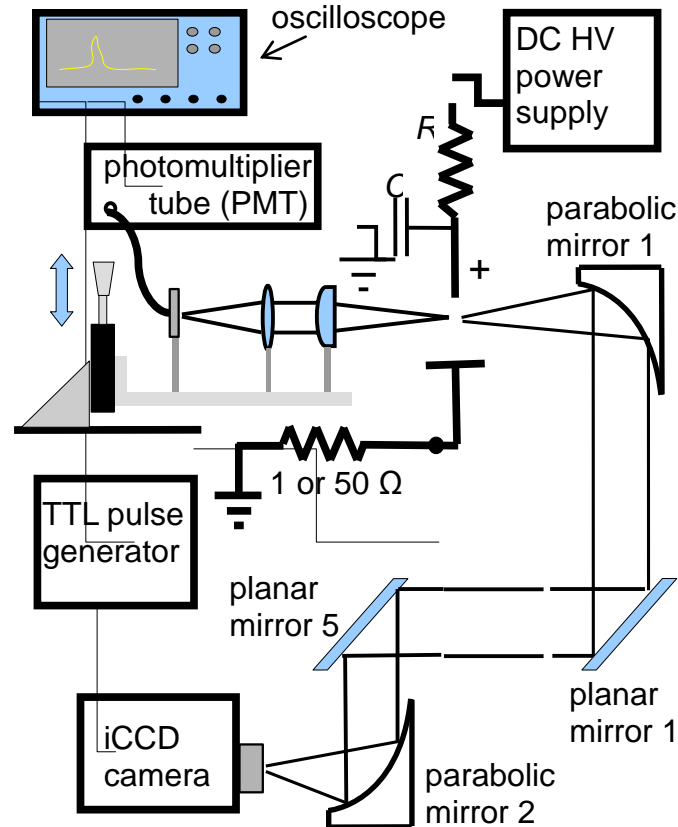


Fig. 1. Schematic of the experimental setup.

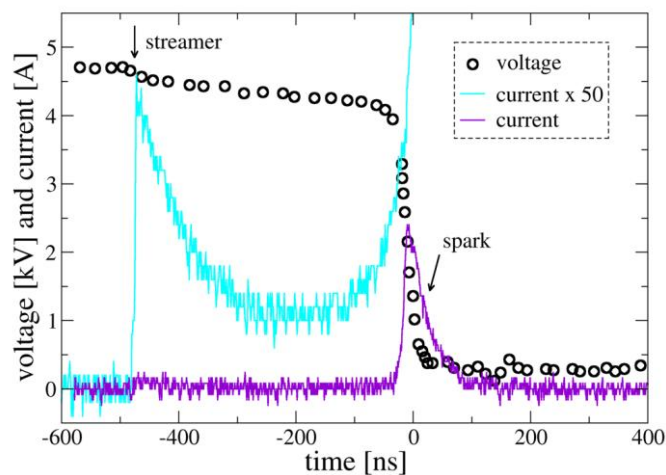


Fig. 2. Typical waveforms of transient spark discharge.

2. Experimental setup

Besides electrical measurements, various non-invasive optical spectroscopic methods are commonly used to investigate the plasma characteristics. Due to fast changes of plasma properties in short pulsed discharges such as TS, time-resolved techniques with ~ 1 ns time resolution must be used. This can be accomplished by using intensified high speed CCD cameras [3, 7-9]. In order to achieve high spatial resolution, iCCD microscopy technique can be employed [10]. Fast streak cameras and cross-

correlation spectroscopy also provide valuable information about the evolution of transient discharge events [11, 12]. We performed time resolved imaging of the TS using a fast iCCD camera Andor iStar. Since the TS is a self-pulsing discharge, the synchronization between TS current pulses and the iCCD camera cannot be provided by an external trigger generator. Instead, the current signal of the TS itself was used to trigger the acquisition of the optical signal. The discharge current signal, linked to the 200 MHz digitizing oscilloscope Tektronix TDS2024, was measured on a 50 Ω or 1 Ω resistor shunts. The measurement of the discharge current on these shunts enabled us to synchronize the acquisition of the emission either with the beginning of the primary streamer (50 Ω shunt), or with the beginning of the spark (1 Ω shunt). As the current pulse reached a specified value, a TTL generator sent a voltage pulse to the iCCD camera to initiate the light acquisition. However, the initial ~ 45 ns of the emission were impossible to acquire due to a delay caused by the trigger generator, the transmission time of the signal by BNC cables, and the camera insertion delay. For this reason we built an optical system consisting of two parabolic and five planar mirrors so that the light emitted by the discharge travels ~ 16 m before it reaches the iCCD camera (Figure 1). The disadvantage of this approach was a complicated alignment of the optical system and weak signal. However, resulting delay of the optical signal enabled us to visualize the entire evolution of the streamer-to-spark transition in the TS.

Additionally to the iCCD temporal imaging, the spatiotemporal evolution of the discharges was analyzed by a photomultiplier tube (PMT). The light collection system was set on a micrometric translation stage to enable mapping of the light emission along the electrode's axis (2 points/mm). A cylindrical lens was used in the optical system to collect all the light in the plane perpendicular to the electrode's axis to avoid missing any discharge channel. The waveforms of the discharge current and PMT signal averaged over 128 individual discharges were recorded by the oscilloscope and subsequently processed and visualized. Processing of the PMT signals in the gap space and in time (2 ns resolution) enabled us to reconstruct the propagation of the streamer, secondary streamer and spark, with the visual output equivalent to a streak camera.

3. Results and Discussion

When the iCCD camera was synchronized with the beginning of the primary streamer current pulse, the propagation of the light from the anode to the cathode was observed. Figure 3 shows a sequence of the iCCD images obtained for the TS with $f \approx 4$ kHz, gate width 2 ns, ~ 250 accumulations, $d = 5$ mm. The light propagation from the needle anode across the gap to the cathode in the time interval from 2 to 12 ns was appointed to the primary streamer. This streamer created a relatively conductive plasma bridge that after a certain delay enables transition to the spark. The spark itself is preceded by another light wave starting from the anode (time interval 16-36 ns), appointed to the so called secondary streamer. This name was given by Loeb who suggested it was a new ionization wave [13], but it is governed by the attachment processes [14]. The distribution of the attachment rate along the plasma filament generated by the primary streamer results in the reduced electric field E/N increase near the anode [14-17]. A decrease in the gas density N leads to the extension of this region with the increased E/N , i.e. the secondary streamer propagation, as was shown in the model of Bastien and Marode [14].

After the secondary streamer reaches the cathode, the spark may be launched. It takes a few tens of ns more before the actual spark appears (Figure 3). The earliest sparks appeared ~ 70 ns after the beginning of the streamer, the highest probability of the spark onset was around 90 ns. The delay between the onset of spark and the moment when the secondary streamer reaches the cathode is probably because an additional heating of the plasma channel up to observed ~ 1000 K is needed. This suggests that the final step in the breakdown is governed by the mechanism suggested by Marode [18]: the increase of T in the channel leads to an increase of the pressure, which is followed by a hydrodynamic channel expansion that empties the core of the channel and decreases the gas density N . For this reason, a reduced electric field strength E/N in the plasma channel increases and accelerates the electron-impact ionization. When the iCCD camera was synchronized with the beginning of the spark pulse, the emitted light appeared simultaneously in the entire plasma channel: no propagation of the light from the anode to the cathode was observed. We suppose that the E/N was high enough so that the ionization processes dominate along the entire discharge channel.

Fig. 3. Time resolved iCCD images of the TS discharge, $f \approx 4$ kHz, $d = 5$ mm, camera gate width 2 ns, accumulated over ~ 250 pulses. The time delay with respect to the streamer initiation is indicated on individual frames. The brightness of images is shown relative (normalized) in each frame, the actual light emission of the secondary streamer is stronger than of the streamer, and that of the spark is much more intense than both streamer and secondary streamer.

The average streamer propagation velocity estimated from Fig. 3 was $\sim 5 \times 10^7$ cm/s, the secondary streamer was only ~ 2 times slower. More precise determination of these velocities, including their evolution along the gap was possible from the spatiotemporal reconstruction of PMT measurements (Figures 4 and 5). While the primary streamer accelerates as it approaches the anode, the secondary streamer slows down. The velocities of both primary and secondary streamers increase with f (Figure 6). According to the model of Bastien and Marode [14], the propagation of the secondary streamer can be explained by the increase of N . From faster propagation of the secondary streamers at higher TS frequencies we could thus deduce faster decrease of N . Assuming that decrease of N is caused by the heating of the gas inside the plasma channel, the heating should be faster at higher TS frequencies. This agrees with our previous experimental findings [7].

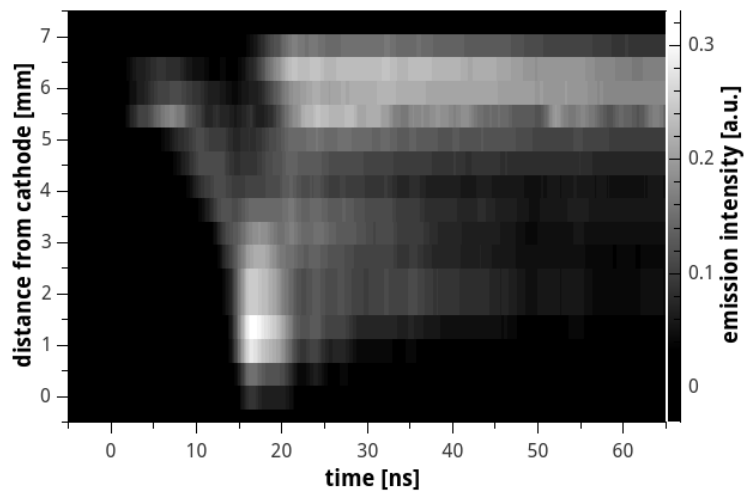


Fig. 4. Visualization of the streamer and secondary streamer from spatiotemporal reconstruction of the PMT signals (i.e. streak camera-like image), TS, $f \approx 2.2$ kHz, $d = 7$ mm.

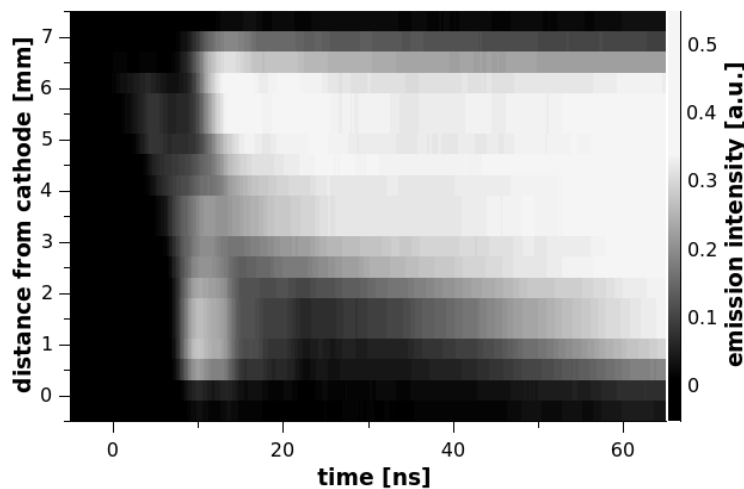


Fig. 5. Visualization of the streamer and secondary streamer from spatiotemporal reconstruction of the PMT signals (i.e. streak camera-like image), TS, $f \approx 6$ kHz, $d = 7$ mm.

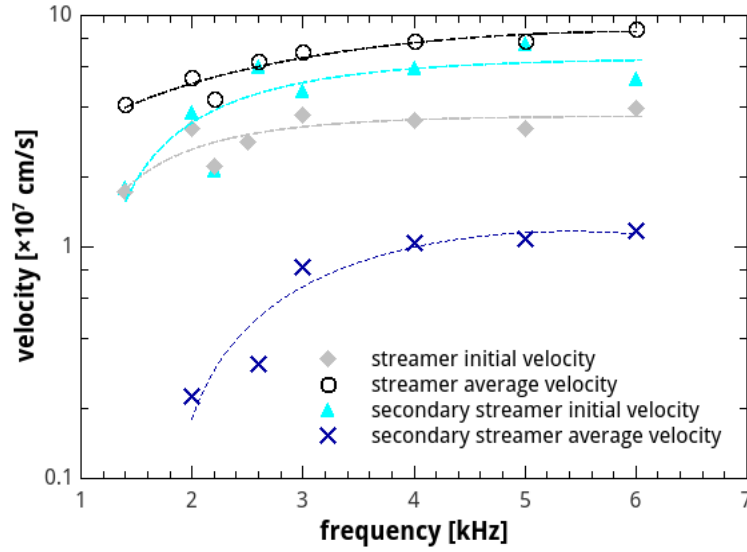


Fig. 6. Primary and secondary streamer propagation velocities as functions of TS repetition frequency.

The fast propagation of the secondary streamer through the whole gap could explain short streamer-to-spark transition times in TS at repetition frequencies above 3 kHz. At lower TS repetition frequencies, the initial velocity of the secondary streamer is also relatively high, but it does not propagate through the whole gap (Figure 4). These implies that the role of the secondary streamer on the breakdown increases with the increasing f . We suppose that this change in the streamer-to-spark transition mechanism is due to the memory effects induced by the previous TS pulses. The secondary streamer is governed by the attachment controlled processes, and the pre-heating can decrease the attachment rate due to decrease of N or by the acceleration of thermal detachment reactions. Accumulation of species such as atomic oxygen could increase the collisional detachment rate.

4. Conclusions

We investigated the breakdown mechanism in the Transient Spark (TS) discharge in atmospheric pressure air, using time resolved imaging techniques. The TS is a self-pulsing discharge initiated by a streamer, with the subsequent short spark current pulse. The TS repetition frequency (1-10 kHz) can be controlled by the applied voltage. Despite this repetition frequency is not absolutely regular, we succeeded to observe the emission from the complete TS event. The iCCD camera was triggered by the rising slope of the streamer current pulse and the light was delayed by the system of mirrors. The disadvantage of this approach is complicated alignment of the optical system. Less effort was needed to obtain streak camera like pictures from set of optical emission intensity profiles measured by the PMT module. The signal from the PMT module was also synchronized by the rising slope of the streamer current pulse.

Based on the obtained images we suppose that the role of the so called attachment control processes [14] and secondary streamer on the breakdown mechanism increases with the increasing TS repetition frequency. The fast propagation of the secondary streamer through the whole gap at TS repetition frequencies above 3 kHz can explain the significant shortening of the streamer-to-spark transition time. The increasing propagation velocities of streamers and secondary streamers with increasing TS repetition frequency is probably due to a memory effect (pre-heating, pre-ionization, or gas composition changes) induced by previous TS pulses. Further research is required, including kinetic modeling, to verify this hypothesis and distinguish the respective contributors to the memory effect.

Acknowledgement

Effort sponsored by the Slovak Research and Development Agency APVV-0134-12, and Slovak grant agency VEGA 1/0998/12.

5. References

- [1] Larsson A 1998 *J. Phys. D: Appl. Phys.* **31** 1100.
- [2] Naidis G V 2009 *Eur. Phys. J. Appl. Phys.* **47** 22803.
- [3] Pai D Z, Lacoste D A and Laux C O 2010 *Plasma Sources Sci. Technol.* **19** 065015.
- [4] Pai D Z, Lacoste D A and Laux C O 2010 *J. Appl. Phys.* **107** 093303.
- [5] Gerling T et al. 2013 *J. Phys. D: Appl. Phys.* **46** 145205.
- [6] Janda M, Martišovič V and Machala Z 2011 *Plasma Sources Sci. Technol.* **20** 035015.
- [7] Janda M, Machala Z, Niklová A and Martišovič V 2012 *Plasma Sources Sci. Technol.* **21** 045006.
- [8] Pai D Z, Stancu G D, Lacoste D A and Laux C O 2009 *Plasma Sources Sci. Technol.* **18** 045030.
- [9] Mihaila I, Ursu C, Gegiuc A and Popa G 2010 *J. Phys. Conf. Ser.* **207** 012005.
- [10] Šimek M, Ambrico P F and Prukner V 2011 *Plasma Sources Sci. Technol.* **20** 025010.
- [11] Marode E 1975 *J. Appl. Phys.* **46** 2005.
- [12] Brandenburg R, Grosch H, Hoder T and Weltmann K-D 2011 *Eur. Phys. J.- Appl. Phys.* **55** 13813.
- [13] Loeb L B 1965 *Electrical Coronas* (Univ. of California Press, Berkeley, California).
- [14] Bastien F and Marode E 1985 *J. Phys. D: Appl. Phys.* **18** 377.
- [15] Sigmond S R 1984 *J. Appl. Phys.* **56** 1355.
- [16] Marode E et al. 2009 *Plasma Phys. Control. Fusion* **51** 124002.
- [17] Ono R and Oda T 2007 *J. Phys. D: Appl. Phys.* **40** 176.
- [18] Marode E, Bastien F and Bakker M 1979 *J. Appl. Phys.* **50** 141.

FAST NEUTRALS AND ENERGY-DEPENDENT SECONDARY ELECTRON EMISSION COEFFICIENTS IN PIC/MCC SIMULATIONS OF CAPACITIVELY COUPLED PLASMAS

A. Derzsi¹, I. Korolov¹, E. Schüngel², Z. Donkó¹, J. Schulze²

¹*Institute for Solid State Physics and Optics, Wigner Research Centre for Physics, Hungarian Academy of Sciences, 1121 Budapest, Konkoly Thege Miklós str. 29-33, Hungary*

²*Department of Physics, West Virginia University, Morgantown, WV 26506, USA*
E-mail: derzsi.aranka@wigner.mta.hu

We study the effects of including fast neutrals and using energy-dependent secondary electron emission coefficients for heavy particles in PIC/MCC simulations of capacitively coupled plasmas (CCP) operated in argon at 13.56 MHz. We find that the plasma density and the ion flux to the electrodes increase, if fast neutrals are traced in the model. The plasma parameters are significantly affected also by implementing a realistic description of the secondary electron emission induced by ions and fast neutrals at the electrodes. The simulation results indicate that fast neutrals and energy-dependent secondary electron emission coefficients have to be included in simulations of CCPs in order to obtain more realistic discharge characteristics.

1. Introduction

Capacitively coupled plasmas (CCP) are widely used in plasma processing applications such as plasma-enhanced chemical vapor deposition and plasma etching in the semiconductor industry, as well as in medicine for surface treatment [1]. In these applications, the separate control of the particle fluxes and energies at the electrodes is of key importance. The self-consistent kinetic description of low-pressure CCPs is mainly realized by using the Particle-in-Cell simulation method combined with Monte Carlo type treatment of collision processes, known as the PIC/MCC numerical technique [2]. By tracing “superparticles”, representing a large number of real plasma particles, this method makes it possible to follow the spatio-temporal evolution of discharge characteristics and to obtain information about various plasma parameters in a very efficient way.

In most PIC/MCC studies of CCPs, several simplifications are common: (i) the plasma species that are included in the model are the electrons and the ions of the background gas; other plasma species, such as metastables and fast neutrals, are usually not traced, (ii) excitation and ionization induced by heavy particles are neglected, (iii) secondary electron emission from boundary surfaces due to neutral particle impact is not taken into account, and (iv) a constant value for the secondary electron yield, γ , is assumed, that is independent of the incident particle energy and the surface conditions. However, besides ions, the fast neutrals, metastables and VUV photons can also contribute to secondary electron emission, depending on the surface conditions and the energy of the incident particle [3]. Their effect can be considered in the simulations by defining an „effective” secondary electron emission coefficient, γ^* , as the ratio of the secondary electron flux to the ion flux at the electrode [3,4].

The importance of including fast neutrals and realistic secondary electron yields in the calculations have been pointed out in several previous studies for specific geometries and discharge conditions, e.g. in low-pressure DC and RF analytical glow discharges in argon [5], in a low-frequency CCP [6], in single-frequency and dual-frequency CCPs [7], in capacitive hydrogen discharges [8]. Secondary electrons have a great effect on the realization of the separate control of the ion flux and the mean ion energy at the electrodes in dual-frequency CCPs [9]. A different electron emission property of the two electrodes in a CCP can induce an asymmetry effect [10], which significantly influences the independent tuning of the ion properties in electrically asymmetric discharges [11]. These studies indicate that it is very important to carefully select the plasma species included in models of CCPs and to describe precisely the processes that are implemented in the model.

Here we report a study of the effects of fast neutrals and realistic energy-dependent secondary electron emission coefficients on the calculated discharge characteristics resulting from PIC/MCC simulations of single-frequency CCPs in argon, under conditions relevant for plasma processing applications. Simulations are performed by switching on and off the tracing of fast neutrals in the model and including different implementations of the secondary electron emission from the electrodes due to heavy particle impact. The simulation method is described in section 2. The results obtained for the different simulation settings are presented and compared to each other in section 3.

2. PIC/MCC simulation

The calculations are based on an electrostatic Particle-in-Cell code complemented with Monte Carlo treatment of collision processes (PIC/MCC) [12]. The code is one-dimensional in space and three-dimensional in velocity space. The plane, parallel, and infinite electrodes are separated by a distance of 2.5 cm. The discharges investigated are geometrically symmetric. The electrodes are assumed to be made of the same material with identical surface conditions, hence characterized by the same electron emission and particle reflection properties. At the electrodes, 20% of the electrons are reflected [13]. The discharge gas is argon with a constant temperature set to 350 K. One of the electrodes is grounded, the other one is driven by the following voltage waveform:

$$V(t) = V_0 \cos(2\pi ft). \quad (1)$$

The discharges are operated at $f=13.56$ MHz.

Tracing of fast atoms (neutrals with energy above 23 eV) can be switched on/off. For the description of the secondary electron emission due to heavy particle impact, using a constant secondary electron emission coefficient or using a secondary electron yield dependent on the energy of the incident particle can be set in the simulations. The energy-dependent secondary yields for ions and fast atoms, γ_i and γ_a , respectively, are calculated based on the formulae given in [3,14] for “dirty” electrode surfaces (typical for laboratory conditions). The effective secondary yield is determined as in [4]:

$$\gamma^* = \frac{\sum_{k=1}^{N_i} \gamma_i(\varepsilon_k) + \sum_{k=1}^{N_a} \gamma_a(\varepsilon_k)}{N_i}, \quad (2)$$

where N_i and N_a are the total number of ions and fast atoms reaching a given electrode during a RF period, and ε_k is the energy of the ion or fast atom noted by k .

As elementary processes, the collisions of electrons, ions, and fast atoms with thermal neutrals (elastic scattering, ionization, excitations) are implemented. The cross sections for these processes are taken from [15].

In order to clarify the effect of fast neutrals on the calculated discharge characteristics, simulation results obtained by (i) tracing only ions as heavy particles and (ii) tracing both ions and fast atoms are compared, while the secondary electron emission is neglected ($\gamma = 0$). To study the effect of considering energy-dependent secondary yields in the model, simulation results are compared for the following conditions: (i) only ions are traced and a constant secondary electron emission coefficient, $\gamma = 0.1$, is used – this corresponds to conditions often found in PIC/MCC simulations of CCPs; (ii) only ions are traced as heavy particle species and the energy-dependence of the secondary electron yield is taken into account; (iii) both ions and fast neutrals are traced and energy-dependent secondary yields for these species are used.

3. Results

Here, PIC/MCC simulation results obtained for 20 Pa neutral gas pressure are presented. In Figure 1, the ion density in the discharge center, the ion flux, Γ_i , and the mean energy of ions, $\langle E_i \rangle$, at the electrodes are shown as a function of the driving voltage amplitude for conditions when (i) tracing of fast atoms is switched off in the model and (ii) both ions and fast neutrals are traced. It is assumed that no secondary electron emission is induced by the heavy particles hitting the electrodes, i.e. $\gamma = 0$ for all cases.

Tracing fast atoms in the model influences the calculated discharge characteristics at high voltage amplitudes: at 1000 V, an increase of the plasma density by a factor of about 1.3 is obtained compared to the case when only ions are included in the model [Figure 1(a)]. The higher plasma densities can be explained by the ionization caused by fast atoms in the sheath and the effective multiplication of these electrons in the sheath, which finally leads to higher ion fluxes at the electrodes [Figure 1(b)].

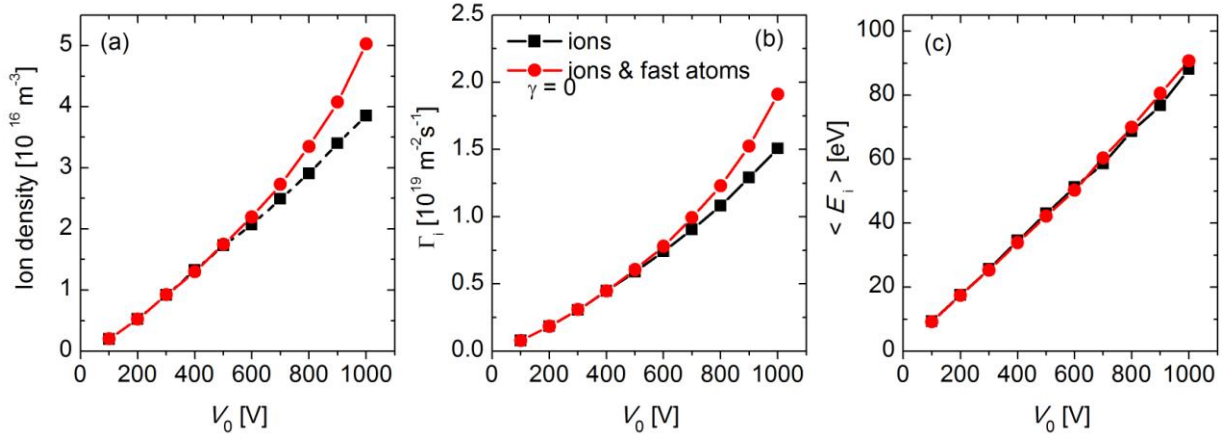


Fig. 1. Ion density in the center of the discharge (a), ion flux (b), and mean ion energy (c) at the electrodes as a function of the driving voltage amplitude, obtained by tracing only ions (line with squares) and both ions and fast neutrals (line with circles) in the PIC/MCC simulation. Discharge conditions: 20 Pa, 13.56 MHz, 2.5 cm electrode gap, $\gamma = 0$.

Tracing fast atoms in the model results in slightly higher mean ion energies at the electrodes for high voltage amplitudes compared to the scenario of tracing only ions [Figure 1(c)]. This is due to the influence of fast atoms on the length of the sheath: as it can be seen in Figure 2 for 1000 V driving voltage amplitude, when fast atoms are traced, higher plasma densities and shorter sheath lengths are obtained. The decrease of the sheath length leads to less collisions involving ions in the sheath. Therefore, ions reach the electrodes with higher energies.

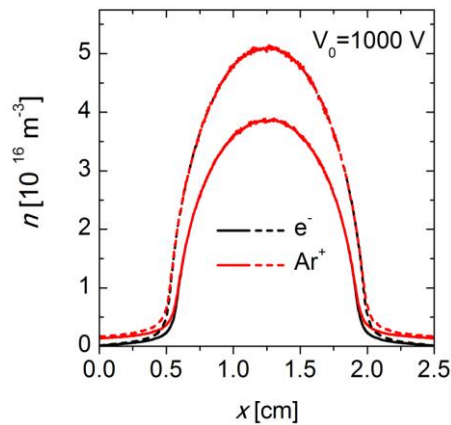


Fig. 2. Time averaged charged particle density distributions for $V_0 = 1000$ V voltage amplitude, obtained by tracing only ions (continuous lines) and both ions and fast neutrals (dashed lines) in the PIC/MCC simulations. Discharge conditions: 20 Pa, 13.56 MHz, 2.5 cm electrode gap, $\gamma = 0$.

Figure 3 shows the central ion density, ion flux, and the mean ion energy at the electrodes as a function of the driving voltage waveform for conditions when (i) only ions are traced as heavy particle species and $\gamma = 0.1$ is used – this corresponds to the conditions typical in PIC/MCC simulations of CCPs, (ii) only ions are traced as heavy particles and an energy-dependent secondary electron yield is

implemented, and (iii) ions and fast atoms are traced and energy-dependent γ -coefficients for both heavy particle species are used.

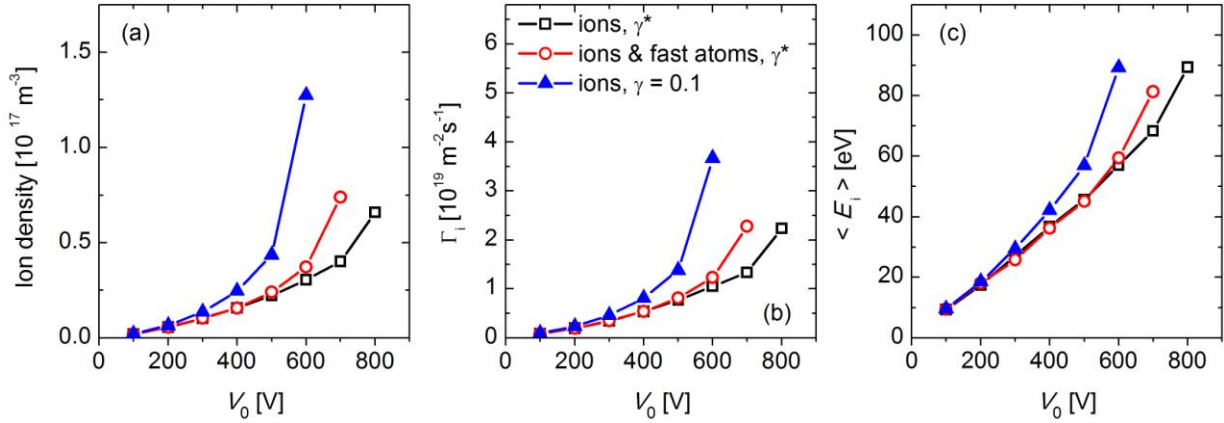


Fig. 3. Ion density in the center of the discharge (a), ion flux (b), and mean ion energy (c) at the electrodes as a function of the driving voltage amplitude, obtained from PIC/MCC simulations using an effective secondary electron emission coefficient, γ^* , and tracing only ions (line with squares) and both ions and fast neutrals (line with circles). Simulation results obtained by using a constant secondary electron emission coefficient, $\gamma = 0.1$, and tracing only ions in the model are also shown (line with triangles). Discharge conditions: 20 Pa, 13.56 MHz, 2.5 cm electrode gap.

Tracing only ions as heavy particles in the simulation and using energy-dependent γ -coefficient results in lower ion density, flux, and mean ion energy compared to the case of tracing fast neutrals in addition to ions and using realistic energy-dependent γ -coefficients. This can be explained by the influence of fast neutrals on the ionization dynamics and the generation of secondary electrons at the electrodes by fast neutral impact. These effects lead to the divergence of the simulations for driving voltage amplitudes above 700 V, if energy-dependent γ -coefficients are included and fast neutrals are traced in the model.

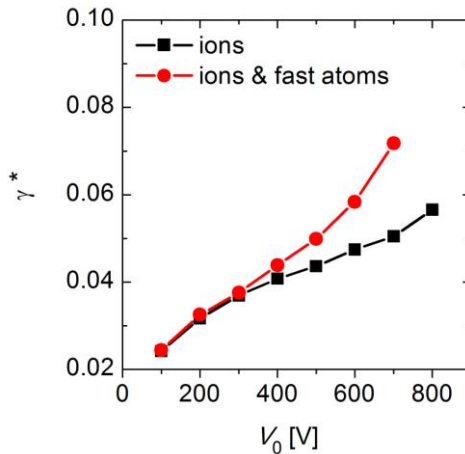


Fig. 4. Effective electron emission coefficient, γ^* , as a function of the driving voltage amplitude obtained from PIC/MCC simulations using energy-dependent secondary electron emission coefficients and tracing only ions (line with squares) and both ions and fast neutrals (line with circles) in the model. Discharge conditions: 20 Pa, 13.56 MHz, 2.5 cm electrode gap.

Tracing only ions and using $\gamma = 0.1$ in the simulations (typical PIC/MCC simulation settings) results in the highest central ion density, flux, and mean ion energy, because the calculated γ^* is lower than 0.1 for all voltage amplitudes (Figure 4).

In conclusion, our results show that tracing fast neutrals and including realistic energy-dependent γ -coefficients in PIC/MCC simulations of CCPs has a considerable effect on the calculated discharge characteristics at high driving voltage amplitudes. In particular, our results demonstrate that the plasma density as well as the ion fluxes and energies at the electrodes strongly depend on the treatment of the heavy particles and of their surface reaction. In order to obtain more realistic results from the simulations, fast neutrals and energy-dependent surface coefficients have to be included in PIC/MCC simulations of CCPs.

This work was supported by the Hungarian Scientific Research Fund through the grant OTKA-K-105476.

4. References

- [1] Lieberman M A and Lichtenberg A J 2005 *Principles of Plasma Discharges and Materials Processing* 2nd edn. (New York: Wiley-Interscience); Makabe T and Petrovic Z Lj 2006 *Plasma Electronics: Applications in Microelectronic Device Fabrication* (London: Taylor & Francis).
- [2] Birdsall C K 1991 *IEEE Trans. Plasma Sci.* **19** 65
- [3] Phelps A V and Petrovic Z Lj 1999 *Plasma Sources Sci. Technol.* **8** R21
- [4] Donkó Z 2000 *J. Appl. Phys.* **88** 2226; Donkó Z 2001 *Phys. Rev. E* **64** 026401; Maric D, Hartmann P, Malovic G, Donkó Z, and Petrovic Z Lj 2003 *J. Phys. D* **36** 2639
- [5] Bogaerts A, and Gijbels R 1995 *J. Appl. Phys.* **78** 6429; Bogaerts A, Gijbels R, and Goedheer W J 1996 *Anal. Chem.* **68** 2296; Bogaerts A, and Gijbels R 2002 *Plasma Sources Sci. Technol.* **11** 27; Bogaerts A, Jan M, and Gijbels R 1999 *J. Appl. Phys.* **86** 2990; Bogaerts A, and Gijbels R 1999 *IEEE Trans. Plasma Sci.* **27** 1406
- [6] Braginsky O, Kovalev A, Lopaev D, Proshina O, Rakhimova T, Vasilieva A, Voloshin D and Zyryanov S 2012 *J. Phys. D.* **45** 015201
- [7] Bojarov A, Radmilovic-Radjenovic M, and Petrovic Z Lj 2010 *Proc. 20th ESCAMPIG* (13-17 July 2010, Novi Sad, Serbia) P2.38, Bojarov A, Radmilovic-Radjenovic M, and Petrovic Z Lj 2010, *Publ. Astron. Obs. Belgrade* No. **89** 131; Bojarov A, Radmilovic-Radjenovic M, and Petrovic Z Lj 2012 *Proc. 65th Annual Gaseous Electronics Conference* (22-26 October 2012, Austin, Texas); Bojarov A, Radmilovic-Radjenovic M, and Petrovic Z Lj 2014 *Proc. 27th Summer School and International Symposium on the Physics of Ionized Gases* (26-29 August 2014, Belgrade, Serbia)
- [8] Panarese A, Diomede P and Longo S 2013 *Plasma Sources Sci. Technol.* **22** 045017 <http://dx.doi.org/10.1088/0963-0252/22/4/045017>
- [9] Donkó Z, Schulze J, Hartmann P, Korolov I, Czarnetzki U, and Schüngel E 2010 *Appl. Phys. Lett.* **97** 081501; Schulze J, Donkó Z, Schüngel E, and Czarnetzki U 2011 *Plasma Sourc. Sci. Technol.* **20** 045007
- [10] Lafleur T, Chabert P, and Booth J P 2013 *J. Phys. D: Appl. Phys.* **46** 135201
- [11] Korolov I, Derzsi A, Donkó Z, Schulze J 2013 *Appl. Phys. Lett.* **103** 064102; Czarnetzki U, Heil B G, Schulze J, Donkó Z, Mussenbrock T, and Brinkmann R P 2009 *J. Phys. Conf. Ser.* **162** 012010
- [12] Donkó Z *Plasma Sources Sci. Technol.* **20** 024001; Donkó Z, Schulze J, U Czarnetzki, Derzsi A, Hartmann P, Korolov I, and Schüngel E 2012 *Plasma Phys. Control. Fusion* **54** 124003
- [13] Kollath R 1956 *Encyclopedia of Physics* Vol. XXI, ed. Flügge S (Berlin, Springer) p 264
- [14] Phelps A V, Pitchford L C, Pédoussat C, and Donkó Z 1999 *Plasma Sources Sci. Technol.* **8** B1-B2
- [15] Phelps A V http://jilawww.colorado.edu/~avp/collision_data/ unpublished; Phelps A V 1991 *J. Phys. Chem. Ref. Data* **20** 557; Phelps A V 1994 *J. Appl. Phys.* **76** 747

WRITING NOVEL NANOSCALE MATERIALS WITH FOCUSED ELECTRON BEAMS AND VOLATILE METAL- CONTAINING COMPOUNDS

Ivo Utke

Empa

*Swiss Federal Laboratories for Materials Science and Technology
Feuerwerkerstrasse 39, 3602 Thun, Switzerland*

E-mail: ivo.utke@empa.ch

The control of products from electron triggered adsorbate dissociation reactions takes the pole position in the wish list of further development in focused electron beam induced processing (FEBIP) [1,2], presently tackled in a the European CELINA (Chemistry for electron-induced nanofabrication, <http://celina.uni-bremen.de/celina/>) COST Action. FEBIP relies on local surface reactions of physisorbed molecules with energetic electrons, see figure 1.

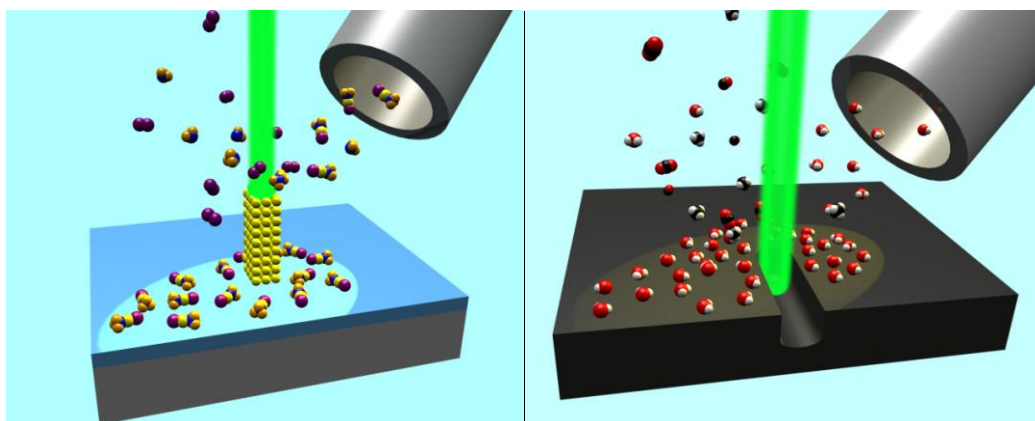


Fig. 1. Focused electron beam induced deposition and focused electron beam induced etching. Note that the process conditions are chosen such that writing is naturally localized to the vicinity of the focused electron beam and does not proceed spontaneously. This is due to the fact that electrons trigger the dissociation reactions with surface physisorbed molecules in contrast to thermal dissociation or surface chemisorption prevailing in thin film CVD and ALD deposition methods.

These electron triggered dissociation reactions have been recognized to be often distinctly different to thermal dissociation or dissociative chemisorption mechanisms prevailing for volatile molecules designed for chemical vapour deposition (CVD) or atomic layer deposition (ALD) techniques. Figure 2 schematically illustrates a few possible dissociation pathways: complete dissociation (2a) would be the most desired pathway which removes all the ligands and leaves only the central atom as deposit. Incomplete dissociation (2b) [3] or ligand codeposition (2c) are the more frequently observed pathways for organometallic compounds, leaving the central atom together with a matrix of ligand elements. The addition of gases (2d) allows a greater control of deposit composition and can be used to remove part of the co-deposited ligand elements [4].

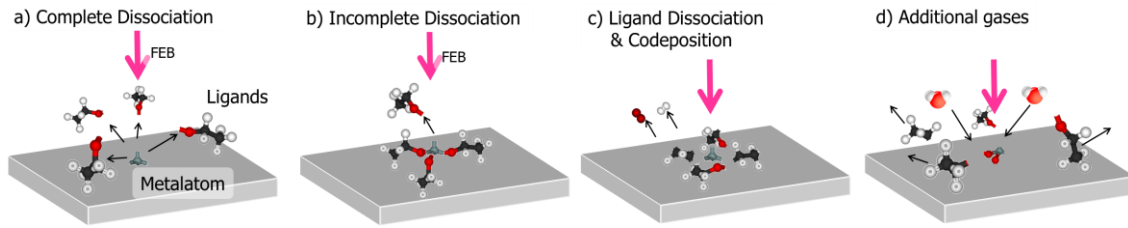


Fig. 2. Schemes of electron triggered dissociation reactions leading to different products and deposit composition. a) to c) is for one adsorbate species while d) involves an additional gas, like H₂O becoming reactive when irradiated with electrons.

We will review the use of molecules in FEBIP and their dissociation products and discuss which classic and novel materials can be synthesized and used in sensor applications [5-7].

- [1] I. Utke and A. Götzhäuser, Highlight Article: Small, Minimally Invasive, Direct: Electrons Induce Local Reactions of Adsorbed Functional Molecules on the Nanoscale. *Angewandte Chemie-International Edition* 49 (2010) 9328 – 9330.
- [2] L. Bernau, M. Gabureac, R. Erni, I. Utke, Tunable Nanosynthesis of Composite Materials by Electron-Impact Reaction. *Angewandte Chemie-International Edition*. 49 (2010) 8880 – 8884.
- [3] J.D. Wnuk, W.F. Van Dorp, C.W. Hagen, D.H. Fairbrother et al., *Surface Science* 605 (2010) 257-266.
- [4] I. Utke, P. Hoffmann and J. Melngailis, Review: Gas-assisted focused electron beam and ion beam processing and fabrication. *Journal of Vacuum Science & Technology B* 26 (2008) 1198-1276.
- [5] Gabureac, M., L. Bernau, I. Utke et al., Granular Co-C nano-Hall sensors by focused-beam-induced deposition. *Nanotechnology* 21(11) (2010).
- [6] F. Kolb, H. Plank et al., Variable tunneling barriers in FEBID based PtC metal-matrix nanocomposites as a transducing element for humidity sensing, *Nanotechnology* 24(30) (2013) 305501.
- [7] Ch. Schwalb, M. Huth et al., A Tunable Strain Sensor Using Nanogranular Metals, *SENSORS* 10 (11) (2010) 9847-9856.

SYNTHESIS OF GRAPHENE-LIKE NANOMATERIALS BY CARBON ARC DISCHARGE

Olga Łabędź, Hubert Lange, Michał Bystrzejewski, Andrzej Huczko

*Laboratory of Nanomaterials Physics and Chemistry, Faculty of Chemistry, Warsaw University,
1 Pasteur str., 02-093 Warsaw, Poland*

E-mail: olabedz@chem.uw.edu.pl

Fluorographite polymer, CF_x , was efficiently exfoliated using carbon arc plasma into few layered graphene, FLG. The product was characterized using the SEM and TEM electron microscopy, XRD diffraction, and Raman spectroscopy. These results show that carbon arc discharge exfoliation technique is a good approach for the preparation of FLG.

1. Introduction

Graphene, a single-atom-thick sheet of hexagonally arrayed sp^2 bonded carbon atoms, is considered to be the most attractive and ground-breaking material for scientific community, because of its exceptional, mostly electronic and mechanical properties [1]. Since the first isolation of single graphene sheet by Scotch tape method [2], there have been many efforts to develop efficient routes for bulk synthesis of graphene [3]. There are dozens of possible methods of producing graphene currently being researched [4]. Each known approach for graphene synthesis possesses, however, its own advantages and disadvantages. Regarding prosperous electronic applications, the chemical vapor deposition (CVD) is one of the mastered techniques to directly grow large surface graphene on metal (mostly Cu and Ni) foils [5] to be later transferred to any desired substrate [6], even in a continuous mode of operation, but its cost is high. High quality graphene sheets for electronics can be also produced via epitaxial growth on SiC [7]. This is, again, a very costly approach due to the specific process environment [8]. Physicochemical exfoliation of graphite has been commonly used for the synthesis of bulk graphene [9] mostly for composites [10]. It is, however, a very tedious, time-consuming wet-chemistry approach which involves highly hazardous chemicals (strong oxidants and reducers) thus creating severe environmental problems. In the first step, the graphite is oxidized (by wet chemistry) into graphite (or graphene) oxide GO which is followed by subsequent reduction into graphene or reduced graphene oxide (rGO). Such drastic chemical treatment also introduces different defects in graphene morphology. A thermal exfoliation of GO was also proposed [11], but the product suffered from high oxygen-containing defects and structural defects. The arc discharge has been extensively used for the production of different nanocarbons for many years [12, 13, 14]. Recently, Wu et al. [15] synthesized graphite sheets by hydrogen arc discharge exfoliation from graphite oxide, but the process yield was low (10 mg). We propose here a rapid and reactive heating of CF_x by carbon arc discharge in a mixed buffer gas to produce few layered graphite, FLG.

2. Experimental

Fluorographite polymer, CF_x ($x=0,72$) was used as obtained (abcr, Germany). The plasma splitting of the starting material was carried out (batch mode of operation) in carbon arc plasma reactor (Fig. 1) described in details elsewhere [16]. During the arcing a composed graphite anode was consumed and the fluorine eliminated from the polymer while the vapors condensed forming the desired exfoliated graphite. Required amounts of fluorinated graphite CF_x and graphite powder (below $50\mu m$) was mixed properly and a homogeneous, composite anode (dia. 8mm) was manufactured following the procedure presented elsewhere [17]. Drilled and filled heterogeneous anodes were also arced in reference runs. The powders from the reactor walls were characterized using the SEM (Zeiss Merlin) and TEM (Zeiss Libra 120) electron microscopy, XRD diffraction (Powder Diffractometer, Bruker D8 Discover, Cu $K\alpha$ radiation), and Raman spectroscopy (Jobin Yvon T-64 000). Table I presents the operational parameters of all runs.

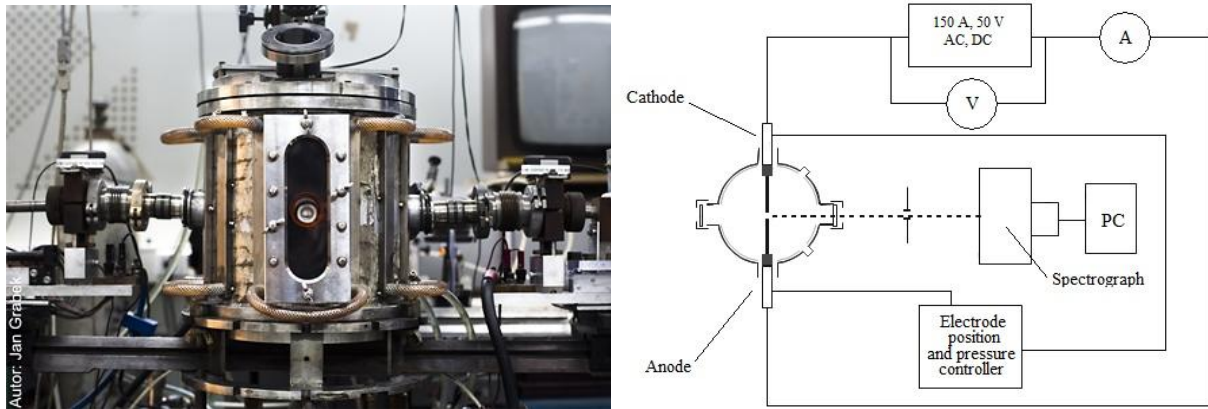


Fig. 1. Carbon arc reactor and the scheme of experimental set-up

Tab. 1. Operational parameters of carbon arc exfoliation of fluorinated graphite

Run #	Anode composition	Plasma gas	Pressure, mbar	Arc current, A	Product
1	Drilled anode, 50 wt% CF_x /50 wt% graphite	Ar	600	10-70	Soot-like, ca 50 mg
2	Drilled anode, 50 wt% CF_x /50 wt% graphite	He/ H_2 (1:1)	600	10-70	Soot-like, ca 100 mg
3	Homogeneous anode, 20 wt% CF_x	Ar/ H_2 (1:1)	600	40-60	Soot-like, few mg
4	Homogeneous anode, 60 wt% CF_x	Ar/ H_2 (1:1)	600	40-60	Soot-like, few mg
5	Homogeneous anode, 20 wt% CF_x	He	600	40-60	Soot-like, several hundreds mg
6	Homogeneous anode, 40 wt% CF_x	He	600	40-60	Soot-like, several hundreds mg

3. Results and discussion

Following the procedure presented elsewhere and taking into account the self-absorption phenomenon [18], the C_2 emission spectra from the interelectrode gap (2mm distance) were collected and the plasma temperatures were estimated (Fig. 2). It is evident from the results obtained the arc plasma temperatures are high enough to sublime the carbon anode material.

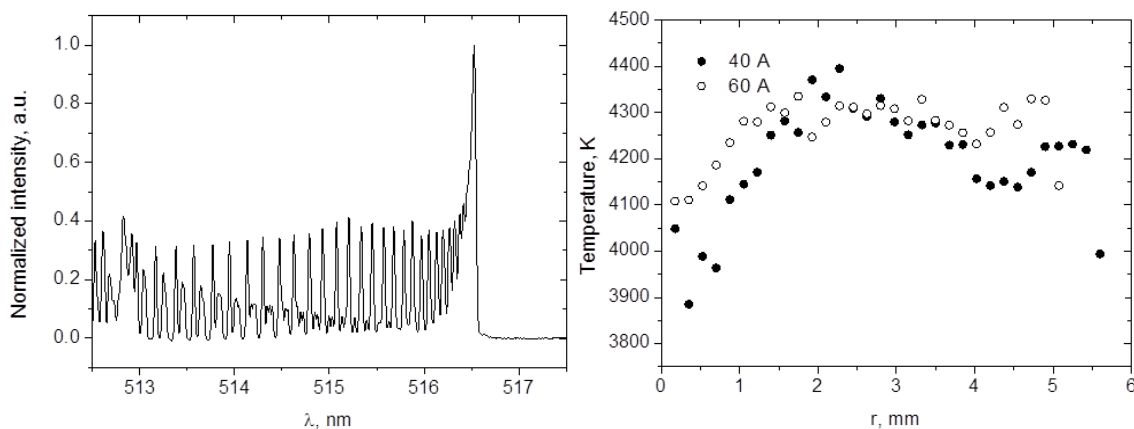


Fig. 2. Left: C_2 emission spectrum, homogeneous anode (40 wt% CF_x), Ar/ H_2 (1:1) plasma gas, arc current 40 A, Right: Interelectrode gap temperature distribution estimated from C_2 emission spectrum, homogeneous anode (40 wt% CF_x), Ar/ H_2 (1:1) plasma gas, arc current 40 A and 60 A

Fig. 3 presents the results of SEM observations of products.

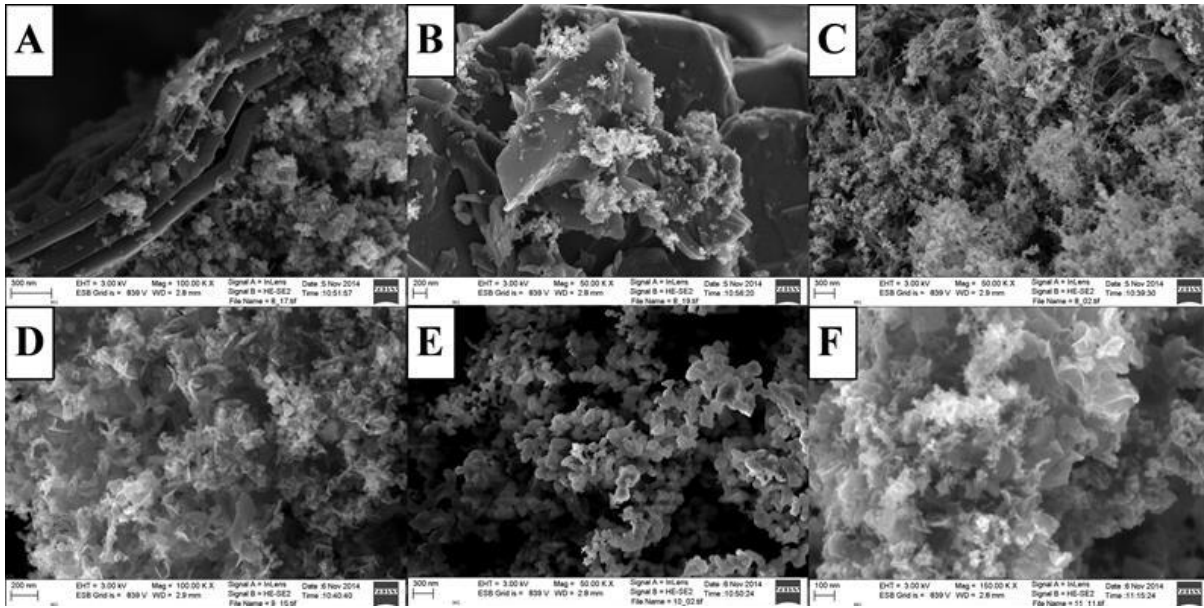


Fig. 3. SEM images of arc discharge-exfoliated and reduced FLG: A, B, C – run #1; D – run #2; E – run #6; F – run #4

The product morphology depends upon the process operating parameters. It has a loose, accordion-like structure (A). Most of CF_x were efficiently defluorinated into FLG to form separate ultrathin platelets (B) or petal-like (D, F) nanostructures (specifically under hydrogen atmosphere). Evidently, however, the individual sheets in the FLG were agglomerated and overlapped. Therefore, the following sonication is required to obtain single-layer graphene. Surprisingly, carbon nanotubes can also be spotted in the raw product (C). In case of He atmosphere (e), only soot-like product was obtained. TEM was used to further characterize the structure of as-prepared FLG (Fig. 4).

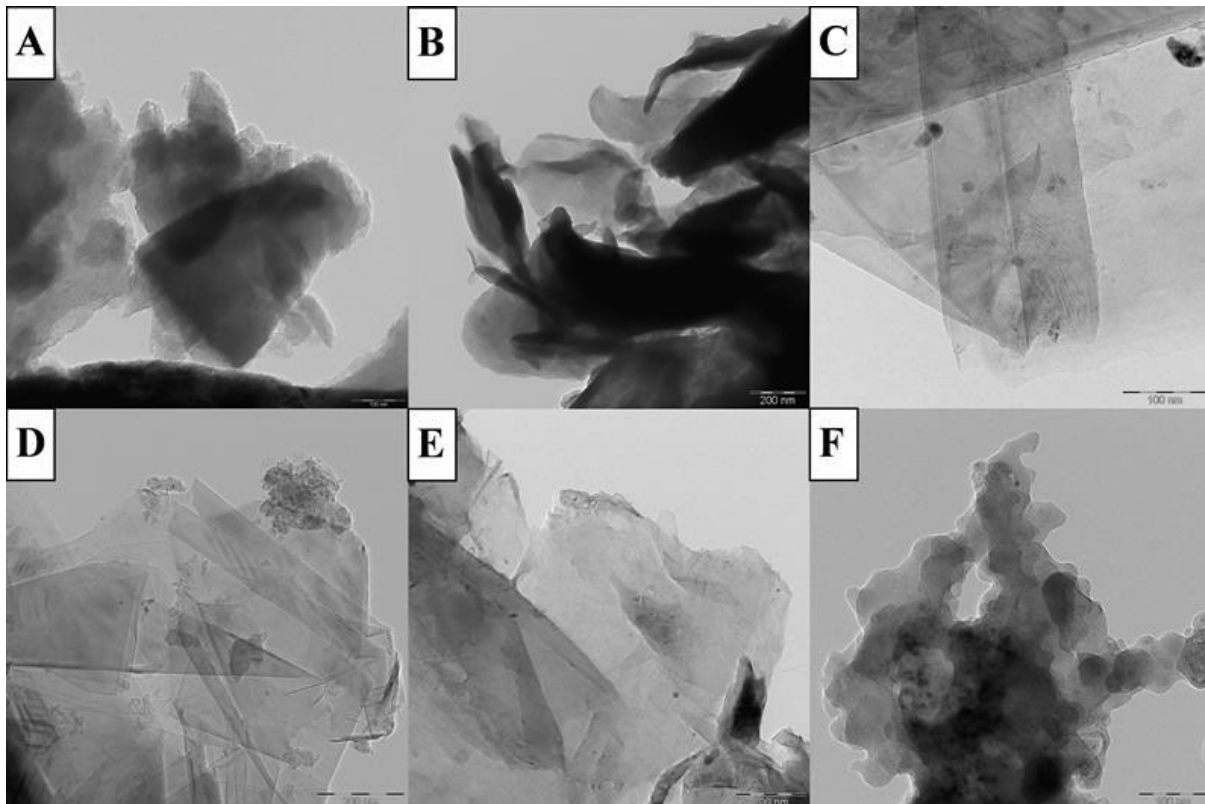


Fig. 4. Structural TEM characterization of arc discharge-exfoliated and reduced FLG: A – starting CF_x ; B – starting electrode, test 5; C – run #1; D – run #2; E – run #4; F – run #6

There is definitely the profound difference between the morphology of starting CF_x (A, B) and the product (C-F). The arc discharge exfoliated CF_x looks like a transparent thin sheet with few folds within its plane. The micrographs of as prepared FLG show randomly aggregated sheets. This is quite different from the graphene sheets obtained via conventional thermal exfoliation, which generally look like a wrinkled thin paper-like structure with many folds. This suggests that arc discharge is a more effective route to remove functional groups (than the commonly used thermal exfoliation and post-reduction) thus yielding the FLG. Hydrogen atmosphere definitely intensifies the de-fluorination process (C, D, E) comparing to He environment (F).

To further access the nature of products, XRD analysis was carried out (Fig. 5).

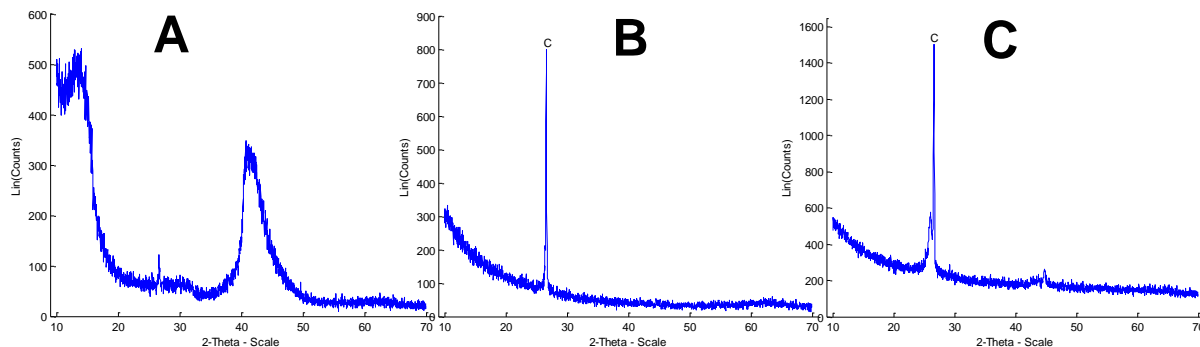


Fig. 5. XRD patterns of structural characterization of arc discharge-exfoliated and reduced FLG: A – starting CF_x ; B – run #2; C – run #4

It is evident from the comparison of XRD spectra between starting polymer (A) and the products (B, C) that a profound transformation of the CF_x into well-graphitized FLG has occurred. The patterns B and C are typical for graphitic materials with large ordering in c direction due to the presence of very well defined (002) reflection at 26.5° . The (100) and (101) peaks are absent (Fig 5B) or have very low intensity (Fig 5C). This observation shows that the ordering in the basal planes is weak. Interestingly, the (002) reflection in the sample obtained in run#4 is composed of two peaks. This finding indicates that this product comprises of graphitic phases of two distinct interlayer distances.

Raman spectroscopy is considered to be a fingerprint characterization for graphene and carbon materials. The representative Raman spectra are shown in Figure 6.

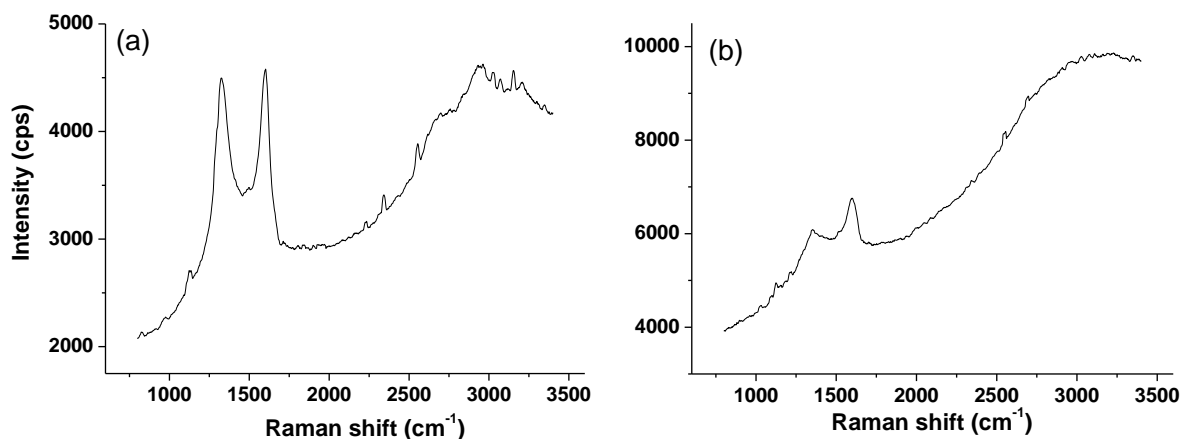


Fig. 6. Raman spectra of products obtained in run#1 (a) and run#6 (b).

Two typical first order bands appear, i.e. the G band (located at 1590 cm^{-1}) and the D band (at 1350 cm^{-1}). The first spectral feature is related to stretching vibrations of C-C bonds in hexagonal graphitic lattice. The second band is due to disorder and defects. Importantly both spectra are influenced by relatively strong fluorescence. This effect plausibly originates from the presence of polycyclic aromatic hydrocarbons, which could be synthesized during the arc plasma processing of fluorine-containing electrodes. The fluorescence can be also related with fluorine containing small hydrocarbon compounds. The second order 2D (ca. 2700 cm^{-1}) peak is absent on each spectrum. This observation along with the moderately low G/D ratio shows that the synthesized carbon materials do not have high

degree of graphitization. Moreover, the spectra in Figure 6 do not resemble the typical spectrum of single layer graphene. These spectra are similar to spectra reported for low-graphitized few-layer graphene [20]. In fact, this statement is coherent with electron microscopy images (Figure 3).

In summary, we have coined an effective arc plasma route for the reduction/exfoliation of CF_x to bulk amount of FLG as shown in Fig. 7. The optimization and further study is, however, required. The following research will concentrate on the further splitting of the produced FLG into singular graphene sheets.

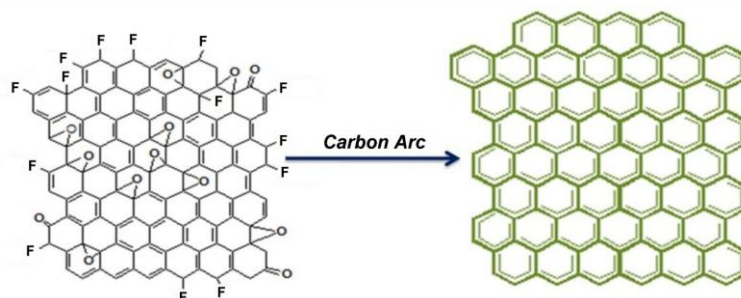


Fig. 7. Efficient and smooth plasma transformation of CF_x to FLG within minutes

Acknowledgement. This work was supported by NCN Grant No. 2012/05/B/ST5/00709. We are also grateful to Mr. M. Soszyński for the XRD measurements.

4. References

- [1] A.K. Geim et al., *Nat. Mater.*, **6**, 2007, 183-191
- [2] K.S. Novoselov et al., *Science*, **306**, 2004, 666-669
- [3] P. Avouris P., C. Dimitrakopoulos, *Materials Today*, **15**, 2012, 86-90.
- [4] F. Bonaccorso et al., *Materials Today*, **15**, 2012, 564-595.
- [5] Q.K. Yu et al., *Appl. Phys. Lett.*, **11**, 2008, 113103-113106
- [6] A. Reina et al., *J. Phys. Chem. C*, **112**, 2008, 17741-17745.
- [7] C. Berger et al., *Science*, **312**, 2006, 1191-1196
- [8] J. Robertson, *Phys. Status Solidi RRL*, **3**, 2009, A77-80.
- [9] Li D. et al., *Nat. Nanotechnol.*, **3**, 2008, 101-105.
- [10] T. Ramanathan et al., *Nat. Nanotechnol.*, **3**, 2008, 327-331.
- [11] M.J. McAllister et al., *Chem. Mater.*, **19**, 2007, 4396-4404.
- [12] W. Kraetschmer et al., *Nature*, **347**, 1990, 354-358.
- [13] X. Zhao et al., *Carbon*, **35**, 1997, 775-781
- [14] O. Łabędź et al., *J. of Physics, Conf. Ser.*, 511, 2014, 012068.
- [15] Z.-S. Wu et al., *ACS Nano*, **3**, 2009, 411-417.
- [16] H. Lange et al., *Rev. Sci. Instrum.*, **68**, 1997, 3723-3727.
- [17] M. Bystrzejewski et al. *Powder Technology*, **246**, 2013, pp. 70-15
- [18] H. Lange et al., *Spectroscopy Letters*, **29**, 1996, 1215-1228.
- [19] L.M. Malard et al., *Physics Reports*, 2009, 473, 51-87
- [20] H. Myriano et al., *Carbon*, **56**, 2013, Pages 339-350

BREAKDOWN VOLTAGE CURVES AND VOLT-AMPERE CHARACTERISTICS OF WATER VAPOR IN MICROGAPS

Marija Radmilović-Radjenović¹, Štefan Matejčik², Matej Klas²,
Branislav Radjenović¹

¹*Institute of Physics, University of Belgrade, Pregrevica 118, 11080 Belgrade, Serbia*

²*Department of Experimental Physics, Comenius University, Mlynski dolina F2, 84248 Bratislava, Slovakia*

E-mail: marija@ipb.ac.rs

Although the physics for breakdown initiation in gases is generally well understood, the process of breakdown initiation in liquids is much less clear. We studied the mechanism which determines the electrical breakdown and the formation of a plasma channel in water vapor based on the experimental results for the breakdown voltage curves and volt-ampere (V-I) characteristics. Measurements were performed for the pressures of 24.15 Torr, 20.85 Torr and 14.55 Torr with the gap size ranging from 40 μm to 900 μm in order to establish a relationship between the discharge structure and the electrical properties in a wide range of discharge currents for steady-state conditions. Having in mind that the atmospheric pressure sources operate in ambient air which unavoidably contains water vapor it is of great importance to study the basic processes and properties of discharges in water vapor.

1. Introduction

In the past few decades, a considerable number of studies on liquid discharges and discharges in the gas and vapor phase in and around liquids have been made due to a wide range of potential applications such as water decontamination or purification [1], microorganism destruction [2], biomedical and environmental applications [3]. The overall electrical breakdown and streamer physics in liquids is quite complicated. Two competing theories of liquid breakdown have been discussed in the literature: a bubble-initiated breakdown process [6] and an electronic impact-ionization process within the bulk liquid [7]. Despite of growing demand for better understanding of water vapor breakdown, existing data on breakdown and discharge properties are scarce and often not well documented. Most of the previous measurements of the breakdown voltage curves for water vapor span a very limited range of conditions [8,9] without the data for a minimum breakdown potential. An exception is the recently published data for the breakdown voltage curves for direct-current (DC) breakdown of water vapor over a full range of pd product [10]. In the case of microgaps, although results for the DC electrical breakdown characteristics in water exist [11], there are no such data for water vapor. Actually, the fundamental knowledge of the electric breakdown in water vapor has not kept pace with these increasing interests, mostly due to the complexity of the phenomenon related to the plasma breakdown process.

We studied the mechanism which determines electrical breakdown and the formation of a plasma channel in water vapor based on the experimental results for the breakdown voltage curves and volt-ampere (V-I) characteristics. Measurements were performed for the pressures of 24.15 Torr, 20.85 Torr and 14.55 Torr with the gap size ranging from 40 μm to 900 μm . The breakdown voltage curves were recorded near or slightly below the pressure of water vapor at room temperature. For the gas pressure of 24.15 Torr, the breakdown minimum voltage was found to be 575V at a pd value of around 0.36 Torr x cm. At pressures of 20.85 Torr and 14.55 Torr, the values of the minimum are higher (627V and 618 V) and shifted toward higher pd values. The primary aim was to establish a relationship between the discharge structure and the electrical properties in a wide range of discharge currents for steady-state conditions, but also in transient stages during formation of the discharge.

2. Experimental arrangements

The experimental system was similar to the one presented in [12,13] and it is shown in Figure 1. The discharge system consists of two planar tungsten electrodes of 2mm in diameter. The gap distance is possible to adjust between 40 μm to 900 μm with an accuracy of 1 μm . The vacuum chamber itself consists of three parts: positioner for centering the electrode position in three directions and tilting the upper electrode which is located in the upper part. In the middle part there is a glass crux with four fused silica windows. In the bottom part there is also positioning system for tilting electrode as well as an improved system for very ultrafine tilting. The electrode is fixed in the cradle with micrometric screw enabling to achieve parallelism of the electrodes with an accuracy of 1 μm . One of the electrodes was fixed and the other was movable continuously with micrometer scale linear feed-through. The 0 μm separation of the electrodes was established by checking the electrical contact between the electrodes and then the movable electrode was pulled away by the means of the micrometer screw. The electrodes gap was varied in the range from 40 μm to 900 μm . The vacuum was generated by the turbo-molecular pump and membrane pump. The low pressures were measured by the ionization gauge (Pfeiffer Vacuum, PKR 261) and the vapor pressures were measured by the capacitance gauge (Pfeiffer Vacuum, PCR 260).

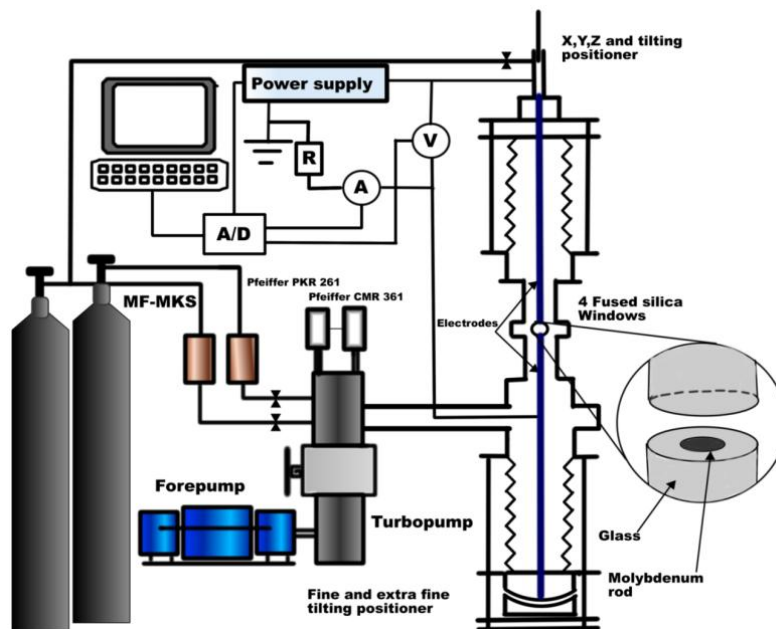


Fig. 1. The general layout of the experimental arrangement used for the measurements of the breakdown voltage and volt-ampere characteristics in water vapor.

Two types of electrodes were used: electrodes with Bruce profile for recording the right-hand side of the breakdown voltage curve and electrodes melted in glass for measuring the breakdown voltage in the whole range shown on the left- and on the right-hand side of Figure 2, respectively. The image on the left of Figure 2 shows that at the left-hand side of the Paschen curve the discharge burns on the edges stressing the importance of the isolation of the electrodes for the Paschen curve measurements. The electrodes were mechanically polished and chemically cleaned in ultrasonic bath. The water vapor was prepared from bi-distilled water, which was subjected to several pump freeze-thaw procedures. By applying a very slowly rising potential to one of the electrodes (ramp speed 0.05V/s), the potential across the discharge tube was increased until the breakdown occurred and the potential across the discharge tube decreases rapidly. The DC breakdown voltage was determined based on the maximum potential achieved across the discharge gap. The images were recorded by camera connected to a microscope. For recording voltage current characteristics, we used AD card (National Instruments NI

USB-6211) with sampling frequency 10 kHz and averaging 200 or 10 samples. The discharge current was limited to 2mA for protection electrode. In most cases, R1 was 300 k Ω and sometimes 5M Ω , resistor R2 was always 520 Ω .

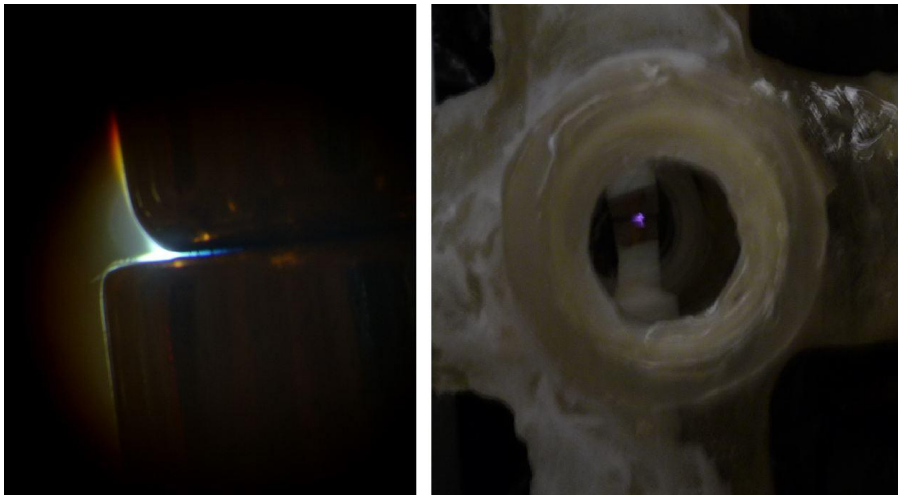


Figure 2. Electrodes with Bruce profile (left) and melted in the glass (right).

There are several key issues in the experimental measurements of electrical breakdown potentials in liquids. The first one is ensuring that the lowest voltage limit associated with Townsend discharge formation is observed, rather than the higher voltage associated with streamer, is detected. Here this is overcome by observing the light emission from the gap region and more specifically the axial emission profile. The second is related with the water vapor stems from gases dissolved in the liquid water, condensation on surfaces and hydration of charged particles in the gas phase. It is thus necessary to ensure that the water vapor is devoid of any dissolved oxygen and other volatile constituents.

3. Results

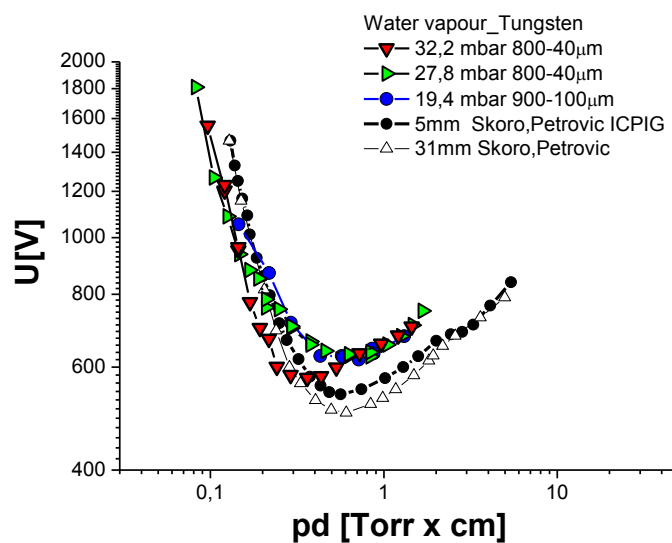


Figure 3. The breakdown voltage as a function of pd product. Red, green and blue symbols represent results obtained at the pressure of 24.15 torr, 20.85 torr and 14.55 torr, respectively.

The dependence of the breakdown voltage on the pd product (pressure times the electrode gap) for various gas pressures is shown in Figure 3. Red symbols represent the data obtained near the pressure of water vapor at room temperature by varying the gap size from 40 μm to 800 μm . The curve displays a minimum voltage of about 575V at pd of the order of 0.36 torr · cm. At lower pressures of 20.85 torr (green symbols) and 14.55 torr (blue symbols), the minimum breakdown voltages have higher values (627V and 618 V, respectively) and shifted toward higher pd values (0.63 torr · cm and 0.72 torr · cm). On the left-hand branch, all three Paschen curves have the same trend and breakdown voltage values agree well within the experimental errors. Discrepancies are noticeable around the minimum and probably caused by condensations of water on the electrode surfaces. At lower pressures, our measurements are in good agreement with the previously published experimental results [10]. The establishment of the connection between V-I characteristics and the structure of the discharge permits us to identify the main processes that participate in the breakdown and the discharge processes. As an illustration, we show V-I characteristics of the discharge at fixed pressure, but at different gap sizes with corresponding images of the discharge for typical regimes of non-equilibrium discharges in water vapor. As can be seen from Figure 4, at a pressure of 20.85 torr and a gap of 400 μm , an interesting behavior was observed on the right side of the Paschen curve. Up to a current of 500 μA an oscillating regime exists. With the further increase of the current, the discharge became stable (some kind of plateau region in V-I characteristics) which was observed optically as a contraction of the discharge and electrically as a small voltage drop.

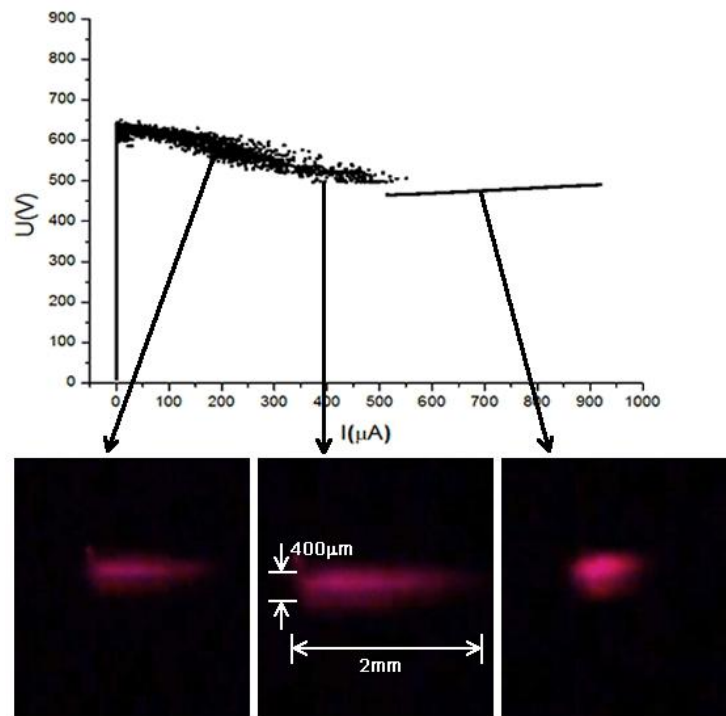


Figure 4. V-I characteristics and images of the contraction of discharges at 20.85 torr and 400 μm .

The breakdown in time at the same pressure but at a gap size of 80 μm is depicted in Figure 5. The applied voltage was increased and the current-voltage characteristics was recorded. When the breakdown occurred, the discharge immediately came to oscillating regime. With the increase of the voltage, the current continues to increase. Thus, the discharge spreads and the voltage remains in the same range of oscillation. As the discharge current increases sharply, simultaneously, the voltage across the discharge gap drops below extinction voltage within a very short time, thus ending the discharge. Subsequently, the potential difference between electrodes again increases until the firing voltage of spark discharge is achieved as given in Figure 6. Regions of spark creepage in which the charges are predominantly of one sign induce charges of opposite sign on the surface of the dielectric, as a result of which the spark channels spread over the surface of the dielectric. Figure 7 clearly demonstrates columns observed in glow discharges.

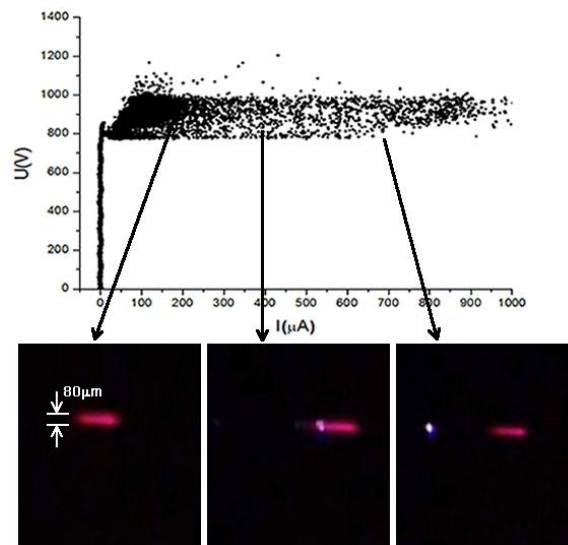


Figure 5. V-I characteristics and images of the spreading of discharges at 20.85 torr and 80 μm .

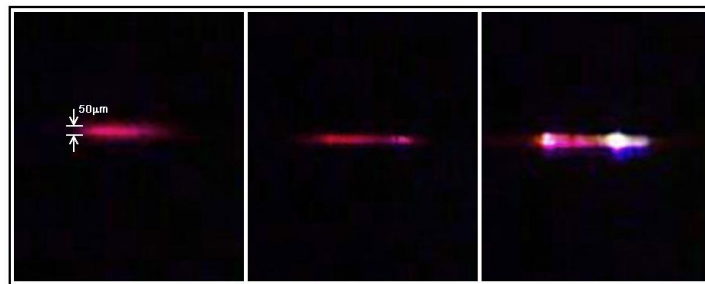


Figure 6. Sparking observed at the gap size of 50 μm and the gas pressure of 24.15 torr.

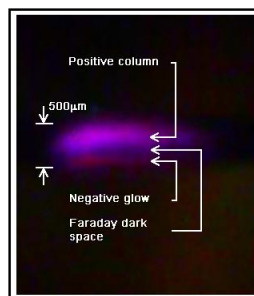


Figure 7. Columns observed in glow discharge.

4. References

- [1] Shannon M A, Bohn P W, Elimelech M, Georgiadis J G, Mariñas B J and Mayes A M 2008 *Nature* **452** 301.
- [2] Du C M, Wang J, Zhang L, Li H X, Liu H and Xiong Y 2012 *New Journal of Physics* **14** 013010.
- [3] Stalder K R, Nersisyan G and Graham W G 2006 *J. Phys. D: Appl. Phys.* **39** 3457.
- [4] Bruggeman P and Leys C 2009 *J. Phys. D: Appl. Phys.* **42** 053001.
- [5] Bruggeman P, Schram D, Gonzalez M A, Rego R, Kong M G and Leys C 2009 *Plasma Sources Sci. Technol.* **18** 02501.
- [6] Hara M, Kaneko T and Honda K 1985 *Cryogenics* **27** 93.

- [7] Lewis T J 1985 *IEEE Trans. Electr. Insul.* **EI-20** 123
- [8] Prasad N and Craggs J D 1960 *Proc. Phys. Soc.* **76** 223.
- [9] Hackam R 1971 *J. Phys. D: Appl. Phys.* **4** 1134.
- [10] Skoro N, Maric D, Malovic G, Graham WG, Petrovic ZLj 2011 *Phys. Rev. E* **84** 055401.
- [11] Schoenbach K, Kolb J, Xiao S, Katsuki S, Minamitani Y and Joshi R 2008 *Plasma Sources Sci. Technol.* **17** 024010.
- [12] Klas M, Matejčić Š, Radjenović B and Radmilović-Radjenović M 2011 *Europhysics Letters* **95** 35002.
- [13] Klas M, Matejčić Š, Radmilović-Radjenović M and Radjenović B 2012 *Europhysics Letters* **99** 57001.

ION MOBILITY SPECTROMETRY FOR THE DETECTION OF TOXIC GASES– OVERVIEW OF THE TECHNOLOGY AND IMPROVEMENTS

Walte Andreas, Bert Ungethüm, Wolf Münchmeyer

Airsense Analytics GmbH, Hagenower Str. 73, 19061 Schwerin Germany

E-mail: walte@airsense.com

Different ion mobility spectrometers (IMS) are reviewed and the limitations regarding the detection of toxic gases are discussed. Actual and future solutions of IMS systems as well as their relevant components, especially their ion sources, will be presented.

1. Introduction

First responders need instrumentation that is capable to detect hazardous gases instantly. Besides the detection also identification or at least a first hint of the nature of the released chemical is required. The most common and toxic chemicals transported in Germany are listed in the ETW list (Einsatz-Toleranz-Werte) with values similar or identical to the AEGL-2 (Acute Exposure Guideline Levels) for 4 hours exposure [1]. The instrumentation should detect the 44 compounds of the list and should also be capable to detect the most common chemical warfare agents (CWA). Portable, easy to use and fast responding (in a few seconds) instruments are required.

Ion mobility spectrometry (IMS) is already widely used in military applications for detection of chemical warfare agents and also for trace detection of explosives at airports. It is the most promising technology which could fulfill the requirements. This article will show the advantages and disadvantages of IMS for the detection of the toxic chemicals. Different solutions for improvement will be shown with a special focus on different ionization technologies.

2. IMS- Overview of Main Components

The main components of an IMS are an inlet, an ion source, a device for separation of the ions at atmospheric pressure and an ion detector. Portable instruments usually have a small pump for guiding the toxic gases to the inlet, which usually consists of a membrane or a switching valve. The toxic gases entering the ionization chamber are then ionized, usually by a radioactive ion source. Depending on the toxic gas positive and negative ions, in form of ion clusters containing molecular ions or fragments ions, are produced. The separation of the ions is performed by applying electric fields in a drift gas consisting of filtered air. Detection of the ions is done by a Faraday plate.

The main advantage of IMS when comparing it to sophisticated laboratory instruments, such as mass spectrometry, is that no vacuum system is required, permitting the development of really portable and hand-held instruments. This advantage is also its disadvantage, because the ionization is always accompanied by complex chemical reactions at atmospheric pressure.

3. Common Ion Sources for IMS

The most common ion sources are radioactive sources using ^{63}Ni , ^{241}Am or ^3H (Tritium). The sources are stable and do not require external power, but often need special permits and licensing procedures. With radioactive sources the high energy electrons emitted by the β -source (e.g. ^{63}Ni) will first hit and ionize the nitrogen in the air. The electrons will continue to ionize the main molecules in air until they lose their kinetic energy. Due to collisions at ambient pressure the charge is transferred to a water cluster $\text{H}^+(\text{H}_2\text{O})_n$ which is called the reactant ion. Usually the humidity of the drift gas in the IMS is kept at very dry conditions (a few ppm) such that the reactant ion consists of 2 or 3 water molecules ($n=2..3$). Negative ions are formed by thermalized or low energy electrons which attach to oxygen. Through collisions a negative reactant ion containing oxygen and water clusters is formed: $\text{O}_2^-(\text{H}_2\text{O})_n$.

After a while the reactant ions will hit the unknown molecules (toxic gases) in order to produce a product ion. Positive reactant ions will produce a product ion through association or transfer of a proton to the analyte molecule. The proton affinity of the analyte molecule plays an important factor. The higher the proton affinity of the analyte molecule compared to the reactant ion the higher the probability that the charge is transferred. Aromatic amines, amines and phosphorous compounds (such as nerve gases) have the highest proton affinities. Negative reactant ions will produce a hydrated adduct ion between the negative oxygen and the analyte molecule. Reactions by charge transfer and proton abstraction may also occur. Similar to the proton affinity for positive ions the electro negativity of the analyte will provide an indication if the analyte will keep the charge and can be detected by the IMS. It is important to keep in mind that in complex mixtures only the molecules with the highest proton affinities or the highest electro-negativities will be seen.

4. Separation of Ions by DC and AV voltages

First “time of flight” IMS (ToF-IMS) systems appeared in the 70s and used drift tubes for separation of ions in weak electric fields. Ions from the ion source are injected into a drift tube by an ion gate. The ion gate often consists of wires with alternating polarity (Bradbury-Nielsen design). By switching off the voltage from the shutter gate during micro seconds the ions are attracted by the electric field from the drift chamber and are injected into the drift tube. The drift tube consists of a series of electrodes building up a homogeneous field with field strength of about 200 to 300V/cm. Fig. 1 shows a sketch of a ToF-IMS.

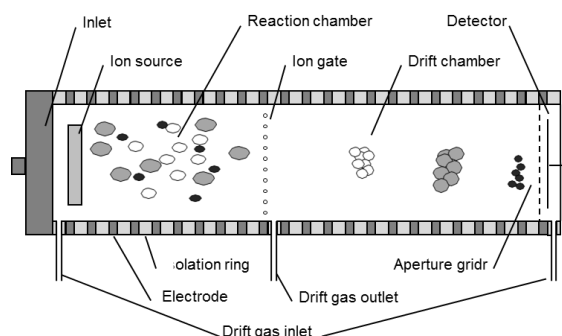


Fig. 1. Main components in a ToF-IMS.

The ions collide constantly with the molecules of the drift gas and reach the faraday cup in milliseconds. Different ions arrive at different times at the detector. The polarity of the drift tube has to be changed in order to measure positive and negative ions.

The drift velocity v is directly proportional to the electric field E (eq.1). The different shape and mass of the ions is reflected in the mobility factor K .

$$v = K \cdot E \quad (1)$$

The mobility factor also depends on the temperature and the pressure. For comparison purposes the temperature and pressure compensated mobility value K_0 is used ($K_0 = K \cdot (273\text{K}/T) \cdot (p/1013\text{hPa})$). The IMS spectrum consists of a graph showing the ion current (in pA) as a function of the time of flight (in ms). Fig. 2 shows a spectrum of a toxic gas (toluene diisocyanate).

Typically portable ToF-IMS have resolutions of 15 to 40. A resolution of 30 to 40 is enough for most of the toxic gases of the ETW list, but not for all. Benzene for example cannot be detected by a low or medium resolution IMS because the product ion co-elutes with the positive reactant ion.

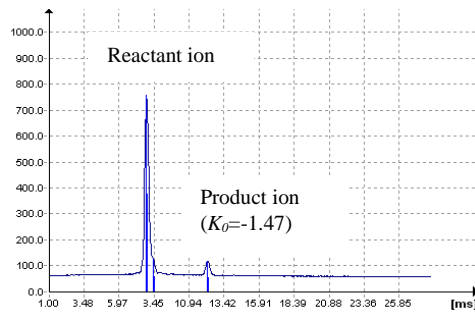


Fig. 2. Time of flight IMS spectrum of 0.2ppm toluene diisocyanate (negative ions)

When increasing the electric field by some orders of magnitude the linear equation (1) is not valid anymore because nonlinear effects start to dominate the equation, which can be expressed by equation (2).

$$v = K(E) \cdot E \quad (2)$$

with

$$K(E) = K + k_1 \cdot E^2 + k_2 \cdot E^4 + \dots \quad (3)$$

When an asymmetric alternating electric field, having high field strength during a short time and low field strength during a long time, is applied a separation of different ions can be achieved because of the non-linearity of equation (3). Fig. 3 shows the main components of a Field Asymmetric IMS (FAIMS) also known as Differential Mobility Spectrometer (DMS) including the path ways of three different ions in the alternating electric field.

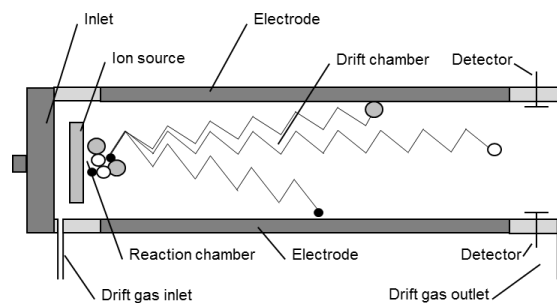


Fig. 3. Main components in a FAIMS.

Positive and negative ions from the ion source are transported by a constant gas flow through two parallel electrodes from the drift gas inlet to the drift gas outlet. By applying an asymmetric voltage between the electrodes the ions can be separated depending on the substance specific mobility coefficients. The mean velocity of the ions is directed to one electrode if the mobility value at high electric fields is higher than the mobility value at low electric fields. The mean velocity is directed to the other electrode if the mobility value at high electric fields is lower than the mobility value at low electric fields. In order to avoid the loss of ions at the electrodes a DC compensation voltage is applied. By changing the amplitude of the compensation voltage with time a spectrum can be achieved. Fig. 4 shows a spectrum of a FAIMS at fixed amplitude of the AC voltage. It can be seen that with the dimensions of the actual spectrometer a compensation voltage of ca. -10V is needed in order to guide the product ions to the detector. It is important to emphasize that the separation of ions is based on the differences of the mobilities at low and high electric fields. Therefore the separation is different to the time of flight based IMS systems and can be considered as an orthogonal detection system.

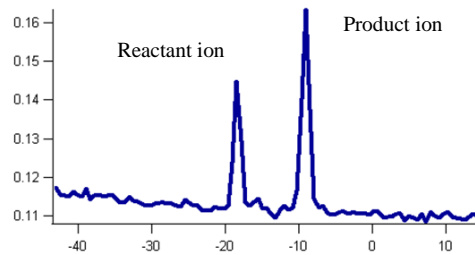


Fig. 4. Field asymmetric IMS spectrum of 1ppm sulfur dioxide (negative ion, ACV=1000V)

If after each scan, where the compensation voltage is changed, the amplitude of the AC voltage is also changed a so called dispersion plot can be generated. The next Fig. 5 shows a dispersion plot of sulfur dioxide (negative ions). With this dispersion plots more information can be gathered with the drawback that some minutes are needed for the acquirement of the data.

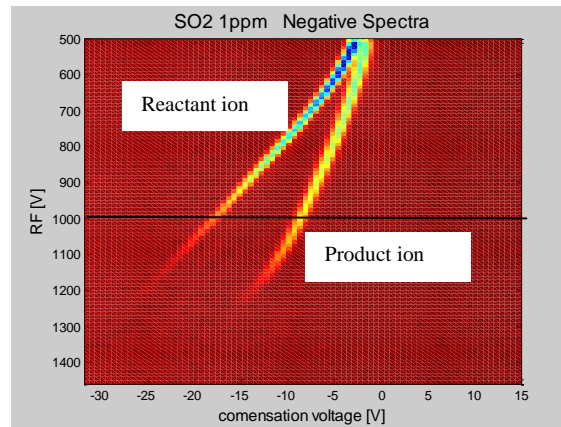


Fig. 5. Dispersion plot of 1ppm sulfur dioxide generated by a series of FAIMS spectra (negative ions, ACV=500 to 1500V). The black line shows the position of the spectrum of Fig. 4.

5. Detection of Toxic Gases with IMS and Comparison of Separation Techniques

The list of toxic compounds was analyzed with two IMS systems, a FAIMS (DMS) system from Sionex (SVAC with a 370MBq ^{63}Ni source) and a ToF-IMS from Airsense (GDA2 with a 100MBq ^{63}Ni source), both IMS systems had the same gas inlet (membrane inlet). Additionally also simulants for warfare agents were measured. The next examples show some of the main differences in the detection of the toxic gases.

The detection of benzene is not possible with a ToF-IMS with low or medium resolution, because the product ion has nearly the same time of flight than the reactant ion. The FAIMS system can clearly separate the benzene ion as shown in the dispersion plot in Fig.6.

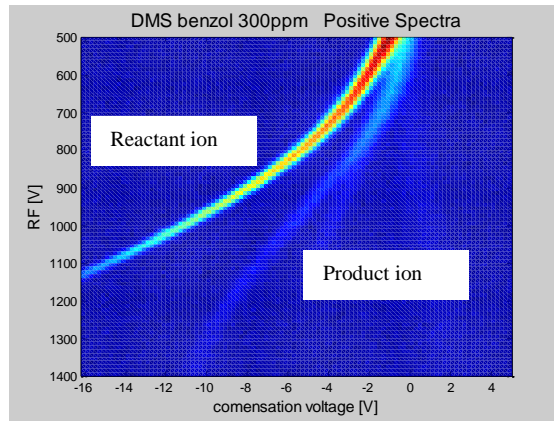


Fig. 6. Dispersion plot of 300ppm benzene (positive ions).

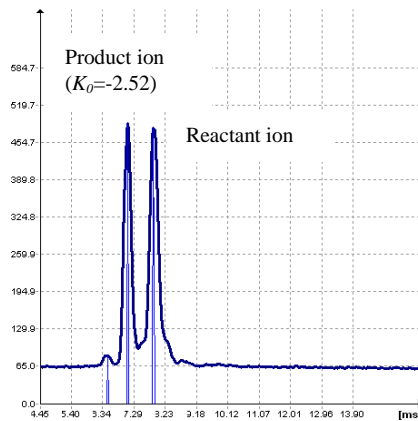


Fig. 7. ToF-IMS spectra of 1ppm cyanogen chloride (negative ions)

Fig.7 shows the ToF-IMS spectrum of cyanogen chloride. The cyanide fragment ion can be seen at the left side of the negative reactant ion. Fig. 8 shows the dispersion plot and the spectrum at a fixed AC voltage. The response of both systems is similar.

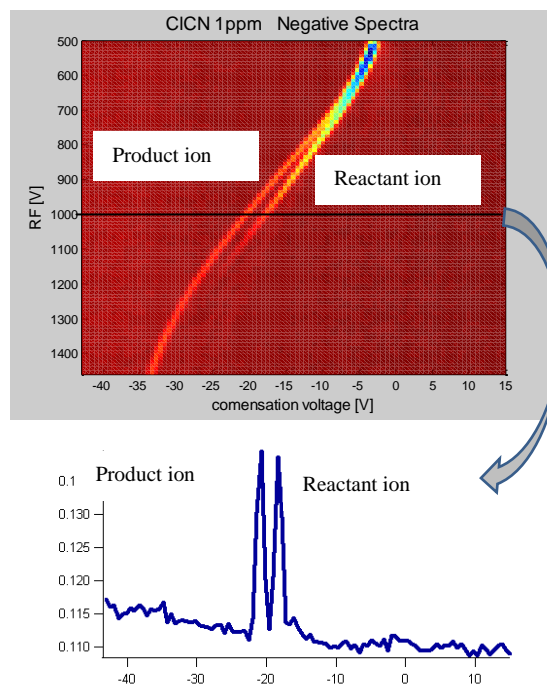


Fig. 8. Dispersion plot and FAIMS spectrum (at 1000V) of 1ppm cyanogen chloride

The last example shows in Fig.9 ToF-IMS spectra of two nerve gas simulants, one is diisopropyl methyl phosphonate (DIMP, a phosphor organic compound) and the other is dipropylene glycol monomethyl ether (DPM).

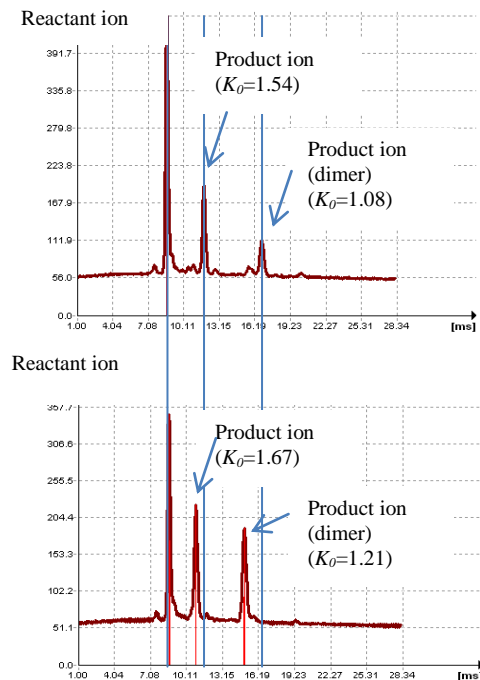


Fig. 9. ToF-IMS spectra of 0.1ppm of DIMP (upper spectrum) and 0.1ppm DPM (positive ions).

When comparing the ToF-IMS spectra both compounds can be clearly distinguished. Fig.10 shows the FAIMS spectra at the same concentration. It can be seen that the resolution of the FAIMS system is not high enough in order to distinguish both compounds.

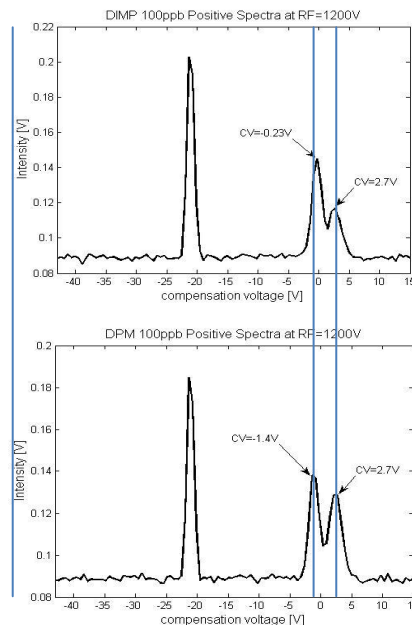


Fig. 10. FAIMS spectra of 0.1ppm of DIMP (upper spectrum) and 0.1ppm DPM (positive ions, ACV=1200V)

When comparing the systems with similar gas inlets it can be concluded that for small molecules (ions with high mobility) FAIMS seems to be better. The drawback is that for a clear discrimination often a

time consuming dispersion plot is needed. For bigger molecules, such as the warfare simulants a better resolution is possible with the ToF-IMS.

Although there are differences in the two independent ion separation technologies, they have also same advantages and disadvantages. Both technologies use the same ion sources and therefore have similar detection limits but also the same problems. Molecules with lower proton affinities or electro negativities than the water clusters cannot be measured. In complex mixtures only the toxic gases with the highest proton affinities or highest electro negativities can be detected. This means that for example high concentrations of acetone will prevent the detection of aromatics such as benzene. Some toxic compounds cannot be measured with both systems, examples are carbon monoxide, phosphine and arsine.

6. Methods to Improve IMS Technology

Very low detection limits in the low ppb region can be achieved with IMS due to the ionization at ambient pressures. The drawback is that also complex ion reactions occur in the ion source making it impossible to detect some toxic gases with IMS. Therefore the technology is not optimal for the detection of compounds in complex mixtures. Problematic is also the use of radioactive sources as ion sources.

Non-radioactive sources are also available, but they require additional power and are less stable. Examples are electron gun sources, corona discharge and photoionization. Electron gun sources are new non-radioactive sources which behave exactly like radioactive sources. Electrons are produced in vacuum by a heated filament. The electrons are accelerated by a high voltage in order to hit a thin membrane, which separates the vacuum from the atmospheric pressure. The electrons have enough energy in order to trespass the membrane and to undergo the ionization processes explained above. Another version of the electron gun uses membranes which are coated with a metallic layer in order to generate soft X-rays, which can also be used as ion sources.

All other ion sources do not produce the same spectra as the radioactive ion sources. Corona discharge or barrier discharge produces also nitrogen oxides (air is usually used as drift gas) which have a high electro negativity leading to problems for the detection of some negative product ions because of the high electro negativity of nitrogen oxides.

With photoionization ultraviolet light is used in order to ionize molecules directly. Glow discharge lamps with energies of 10.6 eV (VUV-light) can be used for example in order to directly ionize molecules with lower ionization potentials (IP), such as aromatic hydrocarbons. With this ion source no reactant ions are produced and different spectra, with only positive ions, is generated. In complex mixtures only molecules with the lowest IP can be seen, because also here charge will be transferred from molecules with higher IP to molecules with lower IP during collisions. Some VUV-light sources are also used to generate photoelectrons by illumination of metallic surfaces. The electrons can then be used to ionize compounds by electron attachment (negative ions, e.g. explosives).

The following table Tab.1 shows some of the compounds from the ETW list and some ionization mechanisms which could be used to detect them. It shows that the combination of different ionization techniques can be used to improve detection capabilities but it also shows that not all compounds can be detected with an IMS.

Tab. 1: Selection of compounds from the ETW list and ionization capabilities of β -radiation and VUV radiation

Name	β -radiation / electron impact	VUV radiation (10.6eV)
Acetic acid	✓(+/-)	no
Acetone	✓(+)	✓(9.7eV) (+)
Acrolein	✓(+)	✓(10.1eV) (+)

Ammonia	✓(+)	✓(10.2eV) (+)
Benzene	✓(+)	✓(9.25eV) (+)
Phosgene	✓(-)	no
Chlorine	✓(-)	no
Cyanogen chloride	✓(-)	no
Hydrogen cyanide	✓(-)	no
Carbon monoxide	no	no
Ethylenoxide	✓(+)	✓(10.57eV) (+)
Methanol	✓(+)	no
Phosphine	no	✓(9.87eV) (+)
Sulfur dioxide	✓(-)	no
Toluene diisocyanate	✓(-)	✓(?eV) (+)

(+)= positive ions, (-) =negative ions, (+/-) =positive and negative ions

As shown in the chapters before, ToF-IMS and FAIMS are orthogonal detection techniques. A combination of both technologies could increase the selectivity considerably. A solution was presented 2005 at the ISISM conference in Paris by Eiceman et.al. and published in 2007 [2]. The construction was basically a planar FAIMS system as shown in Fig. 3, with the difference that two ToF-IMS (one for positive, the other for negative ions) were positioned instead of the detection electrodes. The next Fig. 11 shows the results obtainable with such a system. At a fixed AC voltage a two dimensional graph is displayed showing the compensation voltage of the FAIMS system against the time of flight of the ToF-IMS system. Measuring acetone shows that a monomer and a dimer peak are present, even at relatively low concentrations. The monomer peak is normally not seen with portable ToF-IMS systems, but is now separated due to the FAIMS.

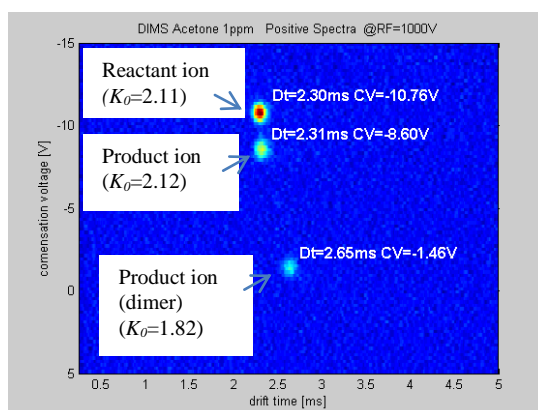


Fig. 11 2D-Plot of Acetone (1ppm) measured with a FAIMS-ToF-IMS² system.

FAIMS and especially the tandem FAIMS-ToF-IMS systems are very suitable for detecting toxic compounds which are known a priori. In case of emergencies the first responder normally does not know what he has to look for. Due to the time required for obtaining dispersion plots with actual FAIMS systems, which can take minutes, the technology is not ideal for first responders. ToF-IMS systems are much faster, providing results in seconds.

As mentioned before IMS technology cannot detect all toxic gases, therefore the Gas Detector Array GDA system was developed by Airsense. It consists of a combination of ToF-IMS with a photo ionization detector (PID), an electrochemical cell (EC) and two metal oxide sensors (MOS). The next Fig. 12 shows the newest version, the GDA-X system, which is also suitable for detection of explosives through a wipe desorption unit which has to be connected to the front of the system.

By combining different gas detectors also compounds which cannot be detected with IMS can be detected now. Phosphine at very low concentrations for example will react with the electrochemical cell and the metal oxide sensors. Carbon monoxide will only react with the MOS sensors. Benzene will give a sensitive response on the PID.

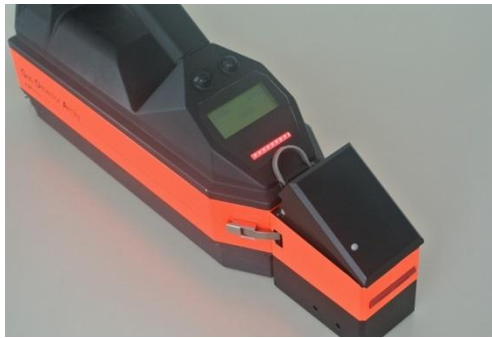


Fig. 12 The new GDA-X based on a combination of ToF-IMS and other detectors suitable for the trace detection of TICs, CWA and with the new desorption tool also for explosives.

Besides the improvement in detection capabilities the additional detectors can be also used to improve selectivity. The next Fig.13 shows ToF-IMS spectra of two very toxic compounds: hydrogen cyanide and cyanogen chloride. Both gases cannot be distinguished by portable ToF-IMS. Interesting is, that only one of the two gases also reacts with the electrochemical cell.

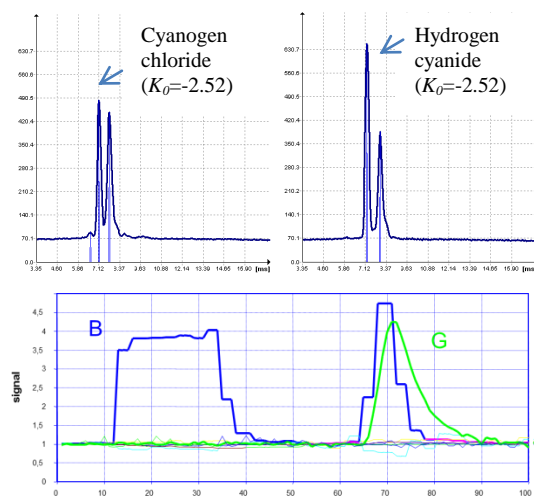


Fig. 13 The upper picture shows the ToF-IMS spectra of ClCN und HCN. The negative ions have the same mobility. The lower picture shows the response of the IMS (B=blue line) and the response of the electrochemical cell (G=green line) after exposure to the gases.

This example shows that the response of the other sensors can be used to improve identification.

A detection of the toxic compounds is performed in only a few seconds. The polarity of the IMS tube is switched very fast so that positive or negative spectra are available every 1.5 seconds.

As mentioned before in complex mixtures the identification of toxic gases is often very difficult. In this situation a gas chromatographic (GC) separation is often helpful. A combination of GC with a ToF-IMS and further detectors was developed during the research project DACHS [3] funded by the German Federal Ministry of Education and Research.

The prototype instrument has an array of 2 electrochemical cells, a PID, 3 metal oxide sensors and a new ToF-IMS. The IMS consists of two tubes with an unique ion injection system in order to measure positive and negative ions simultaneously, which is important when placing an IMS behind a GC-column. With this system complex mixtures can be separated by a short GC-column and the eluted gases can be analyzed by the detector array. A special inlet system allows the utilization of the detector similar to a GDA system for instant detection. In case of detecting something a further GC separation and analysis can be started in order to validate the results.

7. Conclusions

First responders need portable instrumentation that detects and alarms in case of release of toxic gases such as industrial gases or warfare agents. IMS is a promising technology suitable to fulfil many of the requirements. Some gases cannot be measured with IMS, therefore further detectors are required. ToF-IMS and FAIMS are IMS technologies suitable for the task, but they have some advantages and disadvantages. In case of a release of unknown compounds fast detection is a necessity which is one of the reasons why ToF-IMS is preferred by the authors. Resolution for bigger molecules is also better with ToF-IMS. In the near future gas detector array systems using ToF-IMS with an optional GC seem to be the optimal solution, but the GC increases the complexity of the systems. Further work is necessary to replace existing radioactive ion sources. In terms of IMS resolution FAIMS-ToF-IMS tandem systems seem to be the optimal IMS-solution, but the speed of analysis has to be increased considerably.

8. References

- [1] Vfdb 10-01en 2013, *Evaluation of Harmful Concentrations in Fire Service Operations (Guidelines of Vereinigung zur Förderung des Deutschen Brandschutzes –vfdb)*
- [2] G. Eiceman, et.al., 2008 *Miniature DMS-IMS detector for enhanced revolving power, IJIMS 10, 1-5*
- [3] B. Ungethüm, A. Walte, 2012 *Joint project: Detector array with a gas chromatograph for identification of toxic substances (DACHS) – Project: Development of a detection system for fast identification of toxic compounds, Ref. No. 13N9530, Final Report (BMBF)*

SELECTIVE-REAGENT-IONIZATION MASS SPECTROMETRY (SRI-MS): ADVANCEMENTS IN INSTRUMENTATION AND NOVEL APPLICATIONS

Matteo Lanza^{1,2}, W. Joe Acton³, Kostiantyn Breiev^{1,2}, Simone Jürschik¹, Rene Gutmann¹, Alfons Jordan¹, Eugen Hartungen¹, Gernot Hanel¹, Jens Herbig¹, Lukas Märk¹, Chris A. Mayhew⁴, Tilmann D. Märk^{1,2} and Philipp Sulzer¹

¹ IONICON Analytik GmbH., Eduard-Bodem-Gasse 3, 6020 Innsbruck, AUSTRIA

² Institut für Ionenphysik und Angewandte Physik, Leopold-Franzens Universität Innsbruck, Technikerstr 25, 6020 Innsbruck, AUSTRIA

³ Lancaster Environment Centre, Lancaster University, LA1 4YQ, Lancaster, UK

⁴ School of Physics and Astronomy, University of Birmingham, Edgbaston, Birmingham, B152TT, UK

E-mail: philipp.sulzer@ionicon.com

Here we present a compact review of some of the most recent technological advancements in Proton-Transfer-Reaction Mass Spectrometry (PTR-MS), now termed Selective-Reagent-Ionization Mass Spectrometry (SRI-MS), because it is no longer limited to ionization via PTR using H_3O^+ as the reagent ion. The reported developments include measures for a considerably improved selectivity, such as a novel fastGC inlet system and changing the ion chemistry via switching of the reagent ions. Furthermore, we report on two new Time-Of-Flight (TOF) based SRI-MS instruments: the compact PTR-TOF 1000, which has already proven its ruggedness in a NASA flight campaign and the PTR-QiTOF, which is the most sensitive SRI-MS instrument ever, reaching up to 4,700 cps/ppbv sensitivity and a limit of detection of 750 ppqv. In addition to this short review, we present unpublished data from a case study focusing on the analysis of a new psychoactive substance ("designer drug") called ethylphenidate. These substances have dramatically grown in importance over the past few years, but only little scientific literature is available. The data we discuss here represent a useful contribution to harm reduction among users and an improvement to the general scientific knowledge about new psychoactive substances.

1. Introduction

In the recent past a series of technological advancements has revolutionized Proton-Transfer-Reaction Mass Spectrometry (PTR-MS). In the first ten years following the introduction of commercially available PTR-MS instruments in 1998 [1] the technical development focused on increasing the sensitivity and improving the Limit-of-Detection (LoD), while the principal instrumental setup remained unchanged: Water vapor originating from a reservoir containing distilled water enters a hollow cathode ion source. The combination of well-tuned plasma conditions in this source and a subsequent short recombination zone leads to the production of H_3O^+ ions with over 99% purity, thus making a mass filter for selecting the reagent ions obsolete. The hydronium and normal air containing the analytes are injected into a drift tube, where PTR takes place between H_3O^+ and all compounds which possess a higher Proton Affinity (PA) than water. Eventually, the product ions are separated according to their mass-to-charge (m/z) ratio in a quadrupole mass spectrometer and detected by a secondary electron multiplier. The advantages of this design are the possibility of direct gas injection without the need for sample preparation, real-time quantification capability and high sensitivity. In 2009 minor modifications on a "classic" PTR-MS setup considerably improved the performance and led to a sensitivity of close to 1,000 cps/ppbv and a LoD of 890 ppqv [2]. However, the same publication can also be considered as the starting point of a new PTR-MS era: a novel ion source was introduced, which is capable of switching the reagent ions between H_3O^+ , NO^+ and O_2^+ . At the same time Jordan *et al.* published a PTR-MS setup where the quadrupole mass filter is replaced by a Time-Of-Flight (TOF) mass spectrometer with a mass resolution of up to 7,000 $m/\Delta m$ [3]. That is, within one year two of the major drawbacks in PTR-MS had been eliminated: the restriction to compounds

possessing a higher PA than water and the inability of separating isobars due to the unit mass resolution of quadrupole filters. These developments had a noteworthy impact in the analytical community, which is for example reflected by the trend in the number of PTR-MS related publications, abstracts and scientific contributions per year (compare Fig. 1). According to Google Scholar [4] this number slowly increased over the years to about 350 in 2008, but experienced a persistent boost to 550 in 2009 and 1200 PTR-MS related publications per year in 2013. Thus, we believe that there is a strong demand of technological advancements in PTR-MS instrumentation and invested a considerable amount of development work in the recent past, which we will summarize here.

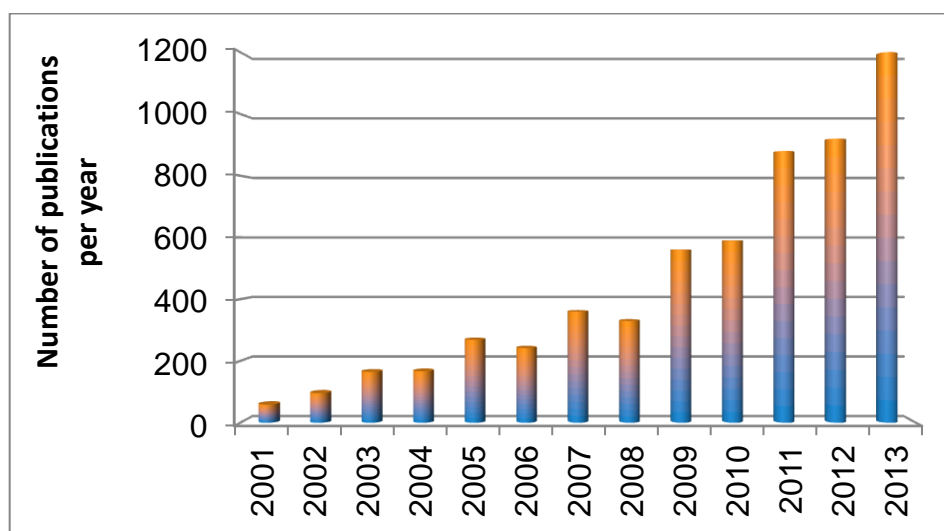


Fig. 1: Number of publications per year containing the term "PTR-MS" [4]

Moreover, from the very beginning environmental chemistry and atmospheric research, as well as food and flavor science and medical research have been the main fields of application for PTR-MS. With new instrumental developments and improved performance the applications grew more diverse. One field of particular note is the detection and identification of threat compounds, like *e.g.* explosives, chemical warfare agents, toxic industrial compounds, illicit drugs, etc. where PTR-MS appears to be ideally suited due to its high sensitivity and fast response. Very recently Ellis and Mayhew published a book where they give a detailed overview of both, the established and the emerging applications of PTR-MS [5]. Here, we present an extensive study on one of the latest PTR-MS applications: the analysis of new psychoactive substances (NPS). Over a time-span of three years we repeatedly purchased the NPS ethylphenidate, a strong stimulant that is not controlled in many countries, via the Internet and analyzed the variability of the different batches. This previously unpublished data can act as a scientific base for evaluating some of the dangers associated with NPS compared to those of well-known illicit drugs.

2. Instrumental Developments and Application Examples

Besides its continued use in the scientific community, the term PTR-MS is not appropriate any more for state-of-the-art instruments, because they are not limited to proton-transfer-reactions. Therefore, in 2012 Karl et al. [6] introduced the abbreviation SRI-MS (Selective-Reagent-Ionization Mass Spectrometry), which we have adopted and will use in the following, where we present the most recent instrumental developments including examples of their application.

2.1 Universality - SRI-MS

Chemical ionization of analytes via charge transfer reactions is energetically allowed when the Ionization Energy (IE) of the analyte is below the recombination energy of the reagent ion. Several molecules of high importance for environmental research (*e.g.* CH₄, CO, O₂, CO₂, etc.) possess IEs

between 12 and 14 eV, *i.e.* they cannot be ionized when O_2^+ or NO^+ is used as the reagent ion. Therefore, in 2012 we introduced a novel version of SRI-MS which is capable of switching reagent ions between H_3O^+ , NO^+ , O_2^+ and additionally Kr^+ and Xe^+ [7]. Kr has an IE of 14 eV, so that the above-mentioned molecules can be ionized and subsequently detected. In order to prove this detection capability we performed a study on laboratory air and the exhaust of gasoline and diesel cars in 2013 [8]. Fig. 2 represents two typical examples from this study. For the first 350 measurement cycles in the left diagram pure He is sampled by the instrument. Afterwards laboratory air is admixed to the helium stream and after a short settling phase of the mass flow controllers stable concentrations of O_2 (solid blue line) and CO_2 (dashed grey line) are visible (starting at about cycle 450). The obtained values of about 20.8% for O_2 and 770 ppmv for CO_2 , respectively, are in excellent agreement of what is expected to be found in an indoor working environment. The right diagram in Fig. 2 shows a CO analysis of gasoline (dashed orange line) and diesel (solid black line) engine exhaust. It should be noted that we did not follow a standardized car exhaust sampling procedure, thus the obtained concentrations cannot be directly compared to those reported in literature. However, gasoline engines are known to emit a considerable higher amount of CO than diesel engines, which is well reflected in our study.

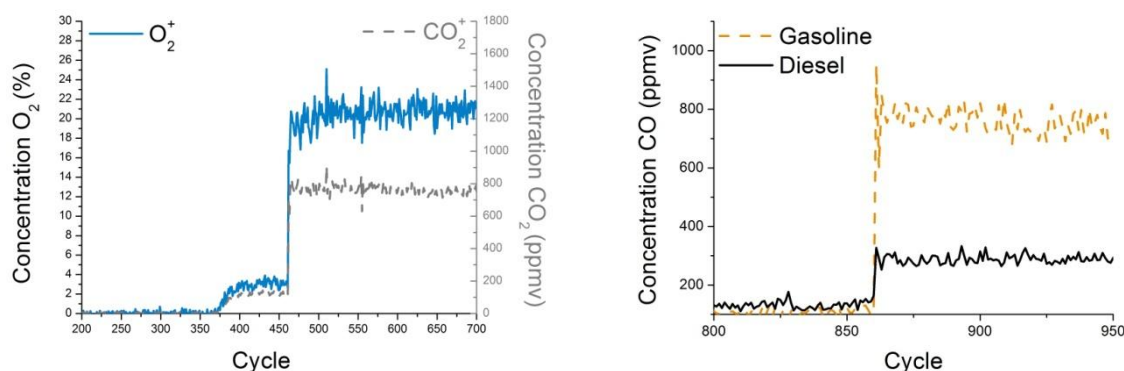


Fig. 2: Quantification of O_2 and CO_2 in lab air (left) and CO in gasoline and diesel car exhaust (right)

From these first proof-of-principle investigations we conclude that SRI-MS with H_3O^+ , NO^+ , O_2^+ , Kr^+ and Xe^+ as selectable reagent ions indeed transforms classic PTR-MS, which is limited to mostly organic compounds with PAs higher than the PA of water, to a universal trace gas analyzer. All advantages of the established H_3O^+ chemistry are preserved when the instrument is running in this mode. By simply switching the instrument to Kr^+ chemistry additionally most inorganic compounds can be detected.

2.2 Selectivity - E/N , SRI and fastGC

Although classic PTR-MS clearly outmatches Gas Chromatography (GC) in terms of speed of analysis and sample handling, GC is the analytical "gold standard" when it comes to selectivity. Thus, one of the main goals in the development of SRI-MS has been the improvement of selectivity using various strategies. An obvious advancement was the introduction of high mass resolution TOF mass spectrometers, which, in contrast to unit resolution quadrupole mass filters, enable the separation of isobaric compounds. However, even with very high mass resolution the technique remains one dimensional, *i.e.* substances are identified solely based on their exact m/z in the mass spectrum. Thus, probably the most promising way to increase the selectivity is to add additional data dimensions. In the following we present three ways of complementing m/z information with additional data, which all have already proven to be highly effective.

The E/N value can be changed by modifying the voltage applied across the drift tube and is virtually instantaneous, *i.e.* the real-time capability of SRI-MS is preserved. The product ion branching ratios of many molecules can be considered characteristic or even unique and thus can be utilized for substance identification. In some cases it might yet be sufficient to analyze the protonated parent ion yield in dependence of E/N . This procedure is exemplified here using the common solid explosive

pentaerythritol tetranitrate (PETN). In Fig. 3 a 3D diagram with the x-axis representing the m/z , the y-axis representing the applied E/N value and the z-axis representing the detected ion yield for the mass region around protonated PETN ($C_5H_8N_4O_{12}.H^+$; 317.02 Da) is shown. At the lowest E/N value of about 100 Td (1 Townsend = 10^{-17} V cm²) a strong signal at the exact m/z of PETN.H⁺ is observed, whereas at elevated E/N this signal virtually disappears. In [9] we reported the E/N dependence of another common explosive, trinitrotoluene (TNT). Interestingly the situation for TNT.H⁺ is the opposite of PETN.H⁺, *i.e.* the ion yield increases with increasing E/N . Thus, for both explosives (and many other compounds) the detection selectivity can be seriously increased by comparing the ion yields at the m/z of the protonated species at two (or more) E/N values.

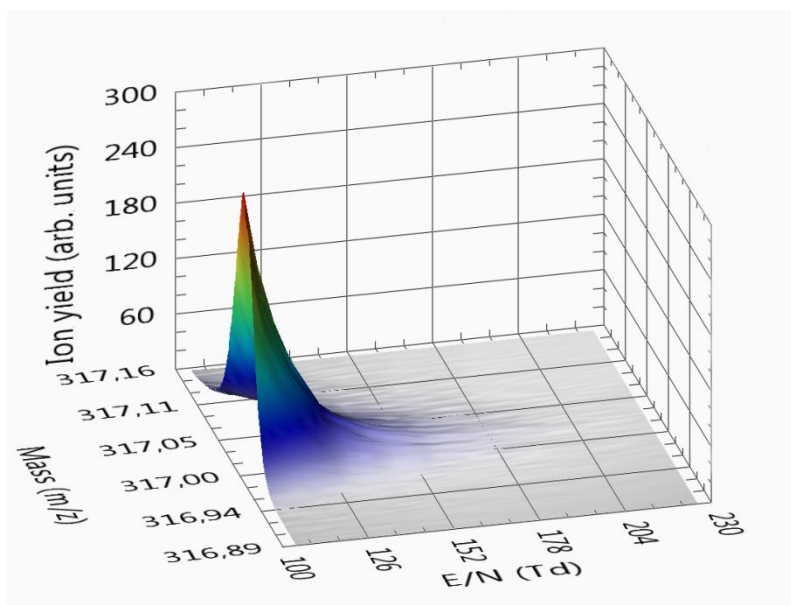


Fig. 3: Protonated parent ion yield for PETN in dependence of E/N

Changing the reagent ions and thus altering the ion chemistry in the drift tube has proven to be another powerful instrument for improving the selectivity in SRI-MS [10]. Prior to its ban in 2010 "mephedrone" (4-methylmethcathinone) had been one of the most popular NPS with effects that are described as a mixture of cocaine and MDMA. Therefore, it is not surprising that following this ban a whole series of substitutes has been introduced to the market, with the isomers 4-methylethcathinone (4-MEC) and N-ethylbuphedrone (NEB) being just two examples. For both isomers proton transfer ionization via H_3O^+ predominantly leads to the formation of the protonated parent ion at m/z 192.14, *i.e.* 4-MEC and NEB are indistinguishable. As soon as the SRI-MS instrument is switched to *e.g.* NO^+ reagent ions, this situation changes drastically: the most abundant product ion for 4-MEC is at m/z 72.08, whereas for NEB a product ion at m/z 86.10 appears (Fig. 4). That is, by switching the reagent ions from H_3O^+ to NO^+ the two isomeric compounds can be easily separated and identified. It is noteworthy that the switching process only takes some seconds and that NO^+ is simply produced using clean, charcoal filtered air.

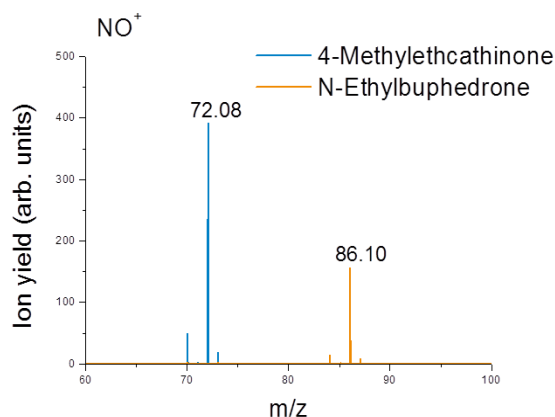


Fig. 4: Most abundant product ions upon ionization with NO^+ for 4-MEC and NEB, respectively

The most recent measure for selectivity improvement is the integration of a fastGC setup into the SRI-MS instrument's inlet system. Although GC has already been successfully coupled to PTR-MS in the past (*e.g.* [11]), the fastGC-SRI-MS setup can be considered as novel, because unlike previous realizations, the utilized column enables full GC spectra within a timeframe of about 1 min (fastGC) and the instrument can be rapidly switched between fastGC and normal inlet mode. That is, the SRI-MS instrument is normally being operated in direct injection, *i.e.* real-time, mode. However, in case the sample contains compounds that cannot be identified unambiguously (*e.g.* isomers) a fastGC run can be started, via simply pressing a button in the operating software that triggers some electronic valves in the inlet system, so that the sample air is loaded in a sample loop and subsequently injected into a fastGC column. Fig. 5 exemplifies this process while Manuka tea and spruce resin are analyzed, respectively. In direct injection mode for both samples a peak in the mass spectra appears at m/z 137.13, which can correspond to a multitude of monoterpenes that are not further distinguishable. After switching to fastGC mode the different compounds contributing to m/z 137.13 are separated according to their retention times in the column. The whole process is completed in less than 1 min, which is when the instrument can be switched back to direct injection mode. Thus, by performing an automated fastGC run every 10 to 60 mins (depending on the expected dynamics within the isomers) the two main advantages of SRI-MS and GC-MS are combined: real-time quantification and extremely high selectivity.

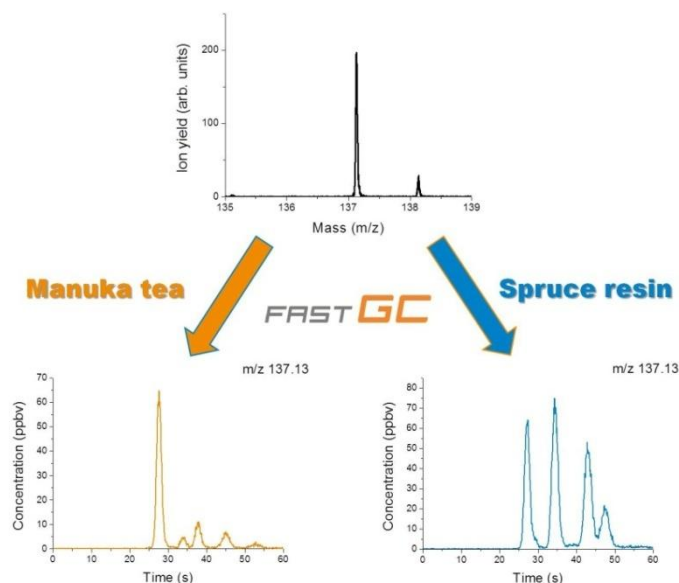


Fig. 5: Monoterpenes in Manuka tea (left) and spruce resin (right) separated by fastGC-SRI-MS

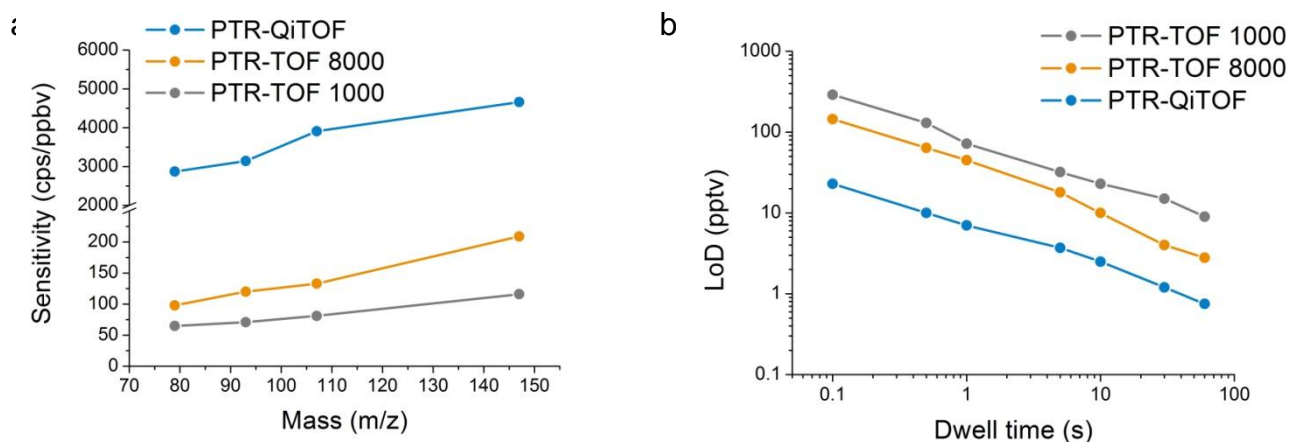
2.3 Compactness and Sensitivity - PTR-TOF 1000 and PTR-QiTOF

Depending on the field of application there are varying demands on the analytical instrument, such as increased sensitivity, high mass resolution, small size, low weight, etc. In some cases these demands can be conflicting (*e.g.* size and weight vs. instrumental performance) so that they cannot be combined in one universal device. Therefore, in 2014 we introduced two novel PTR-TOFMS instruments, which satisfy both extremes, *i.e.* the rugged and compact PTR-TOF 1000 and the extremely sensitive high mass resolution PTR-QiTOF. The abbreviation "Qi" in the latter stands for Quadrupole ion guide and indicates the feature point of this instrument: an improved transfer interface between the drift tube and the mass spectrometer which utilizes a quadrupole ion guide instead of the common lens system [12]. This results in a considerably reduced ion loss in the transfer region and optimized injection conditions into the TOF spectrometer, *i.e.* higher sensitivity and higher mass resolution, compared to state-of-the-art PTR-TOFMS devices (*e.g.* the PTR-TOF 8000 [13]).

On the other hand, the PTR-TOF 1000 originated from a collaborative project with the University of Innsbruck. The requirement for this project had been the development of a compact and rugged PTR-TOFMS instrument that can be installed in an aircraft for airborne missions, *i.e.* the instrument had to withstand shocks and vibrations, variable pressure and temperature in the cabin, etc. Meanwhile the developed prototype was successfully utilized in a NASA campaign, with the results recently published by Müller *et al.* [14] and based on this prototype the commercial PTR-TOF 1000 has been introduced.

In Fig. 6 the most important performance data of all three PTR-TOFMS models are compared. In Fig. 6a) the m/z dependent sensitivities are presented. It can be seen that for all TOF instruments the sensitivities increase with increasing m/z . However, the maximum sensitivities are about 120 cps/ppbv, 210 cps/ppbv and 4,700 cps/ppbv for the PTR-TOF 1000, PTR-TOF 8000 and the PTR-QiTOF, respectively. These values are reflected in the LoDs (Fig. 6b)), which have been calculated using the 3σ method (with σ being the standard deviation): 10 pptv, 3 pptv and 750 ppqv, respectively, after an integration time of 1 min. It should be noted, that for the PTR-QiTOF a LoD of 10 pptv is achieved with an integration time of 500 ms, thus making this instrument predestined for application where time per analysis is a critical issue (*e.g.* flux measurements or nose-space analysis in food and flavor research).

The measurement data displayed in Fig. 6c) prove that the calculated LoD values are indeed correct, as the linearity ranges of the three instruments are shown down to and even below the 10 s LoDs. Finally, Fig. 6d) gives a comparison of the maximum mass resolutions. Similar to the sensitivities, the mass resolution also increases with increasing m/z , so that at m/z 181 (protonated trichlorobenzene) the full-width half-maximum resolutions are: 1,700 $m/\Delta m$ (PTR-TOF 1000), 6,200 $m/\Delta m$ (PTR-TOF 8000) and 10,500 $m/\Delta m$ (PTR-QiTOF). Thus, these data underline that the newly developed PTR-QiTOF is the most sensitive high mass resolution SRI-MS instrument reported in literature so far. On the other hand, the compact and rugged PTR-TOF 1000 performs with an only somewhat reduced performance, compared to the established PTR-TOF 8000 as a reference standard.



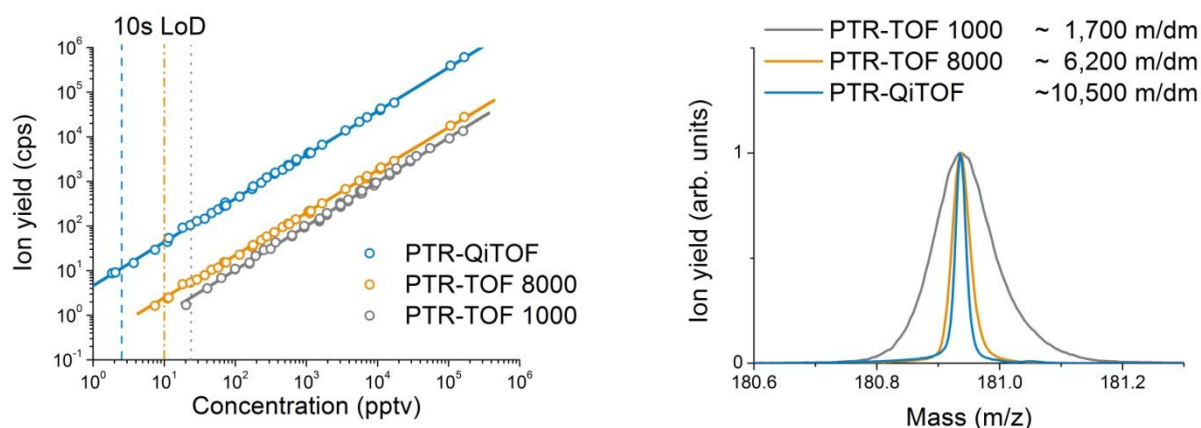


Fig. 6: Performance comparisons between the novel PTR-QiTOF, PTR-TOF 1000 and the established PTR-TOF 8000: a) sensitivity vs. mass, b) LoD vs. dwell time, c) linearity and d) mass resolution

3. Case Study on NPS Product Variability

New psychoactive substances is a generic term for various substances which induce drug-like effects in the human body, but do not belong to the group of common narcotics (*e.g.* cocaine, heroin, MDMA, etc.). Commonly referred to as "designer drugs" or "legal highs", NPS can also be found as "research chemicals" in the Internet. However, the reason for the existence of this kind of substances is rather simple: in most countries the laws for illicit drug possession are draconian, the substances are only available via the black market and the purity and composition of the drugs are completely unpredictable. Hence, there are people looking for a high or state of intoxication without getting into conflict with the law or the underworld and having some kind of quality control for the substances taken. These people are the target group for NPS vendors [15].

The major downside of NPS is that for most substances virtually no knowledge about toxicity and long term side actions exists. Recently, the time-span between the market release of novel NPS and the substance being controlled by drug laws and thus becoming illegal has significantly been shortened. This means that as soon as some knowledge about the dangers of a particular NPS has been gathered, it usually is made illegal and other, unexplored NPS enter the market. This prohibition policy has already led to fatalities [16], as in case of the NPS 5-EAPB, which is a replacement of the banned 5-APB, but is presumably much more toxic. Remarkably, a broad scene of internet forums has emerged, with users, chemists and physicians discussing the risks of NPS (*e.g.* [17], [18]). These not only provide profound resources for harm reduction but also act as information sources for scientists working with these kinds of substances.

Here we present results on a case study on product variability of the NPS ethylphenidate (EPH, $C_{15}H_{21}NO_2$), of which we purchased a series of samples between 2012 and 2014 from an online vendor. EPH is an exceptional NPS for two reasons: i) it has been readily available for several years and is still not controlled in many countries and ii) toxicity and side effects are rather well-known as it is formed as a byproduct of the prescription drug methylphenidate (aka Ritalin®) [19]. The targeted effects of EPH are according to user reports: increased focus, motivation, alertness, endurance and mood lift, while the main adverse effects are: vasoconstriction, tachycardia and long-lasting residual stimulation. Especially the (local) vasoconstrictive effects can be harmful as the preferred route of administration for EPH is insufflation, which can cause permanent damage to the nasal mucous membrane. This process is aggravated through the possible presence of irritant residuals of the synthesis process. To avoid these damages, some users recommend the administration of EPH via the sublingual, oral or rectal route [17]. However, even for the sensitive nasal route of administration reports about the resultant damage diverge, ranging from a light burning sensation during insufflation to permanent damage after only a few uses. While this can be partly attributed to the individual's constitution, it can also originate from varying levels of irritant impurities in different batches. Although, we do not provide any identification of the observed impurities (this would be beyond the scope of this

contribution), we want to give some indication on product variability of EPH during the past three years.

3.1 Experimental Setup

All experiments were performed utilizing a state-of-the-art PTR-TOF 8000 operated with H_3O^+ reagent ions at an E/N value of 130 Td. Each sample was analyzed shortly after purchasing using the following procedure. The inlet and outlet lines (1/16th inch PEEK tubing, internal diameter 1 mm) were inserted into a sealed glass vial containing a few milligrams of the compound. The inlet line was connected to a charcoal filter to provide a supply of pure air. The outlet line was connected to the instrument and maintained at a temperature of 110 °C in order to minimize adsorption of chemicals onto surfaces. The glass vial was kept at a temperature of 90 °C, in order to increase the dynamic headspace concentration and avoid any possible concentration variations, as a result of changes in the room temperature. An empty vial was used to measure the background spectra, which were subtracted from the respective sample spectra.

3.2 Three random samples

In a very recent publication [20] we showed that H_3O^+ reactions with EPH lead to the protonated molecular ion at m/z 248 (81%) and to two fragments at m/z 84 (18%) and m/z 165 (1%), respectively. In Figs. 7-9 these product ions are identified with the letter "E", with the exception of m/z 165, which is neglected here due to its low abundance. The sample from 2013 displayed in the middle panel of Fig. 7 represents the sample with the highest purity of our three year study. Only some minor product ions at nominal m/z 43, 45 and 63 cannot be attributed to the EPH molecule. In this mass range the samples from 2012 and 2014 show the same impurity products, although in considerable different abundances. However, the most remarkable difference between the samples from 2012 and 2014 is at a higher m/z range. For the 2012 sample (upper panel Fig. 7) we see a product ion at m/z 149, whereas for the 2014 sample (lower panel Fig. 7) products at m/z 151 and 156 appear, but none at m/z 149. From this result we conclude that most probably different synthetic methods have been used in the production of the 2012 and the 2014 sample, because of different residual impurities. The 2013 sample has been either synthesized with the highest accuracy or has been purified before dispatch (compare 3.3), as it contains virtually no impurities.

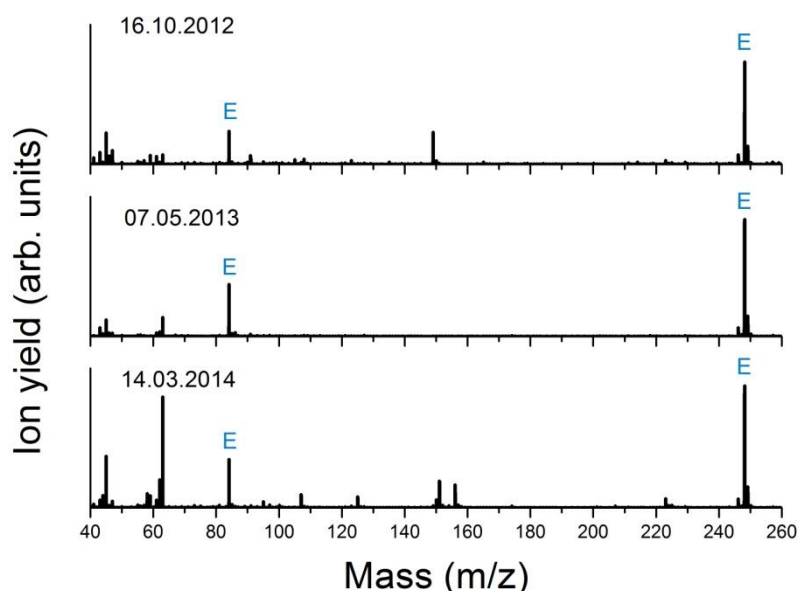


Fig. 7: Three samples of EPH purchased in 2012, 2013 and 2014, respectively. The letter "E" marks the mass spectral peaks previously identified as originating from EPH.

3.3 Powder vs. crystal EPH

Most Internet vendors offer EPH in two forms: fine powder and small crystals (although as of 2014 we have also spotted vendors offering "sugar-like" EPH and "rock" EPH, which consists of marble-sized crystals). The reason for this has been intensely discussed in forums. While some users assume that the crystal form should be of higher purity as the synthesis process allegedly would need more attention, the majority is convinced that powder EPH is just the milled version of crystal EPH. The latter one is usually being sold at a somewhat higher price, as some users presumably find some "coolness" in grinding up the crystals to a fine powder using a credit card prior to insufflation [17].

In Fig. 8 mass spectra of powder (upper panel) and crystal EPH (lower panel), which had been bought at the same time, are shown. It gets immediately clear that the two spectra cannot originate from one and the same sample with one being just the milled version. The ratios of most product ion yields are considerably different and for the crystal EPH some mass spectral peaks show up that are not present (or only in minute amounts) for the powder form: m/z 58, 107, 125 and 156. However, because we have shown in 3.2 that significant variations are observed between different EPH batches, we cannot exclude that powder EPH is simply the milled crystal EPH, because although as we have purchased both samples from the same vendor at the same time, this does not necessarily mean that the vendor packed them from the same batch.

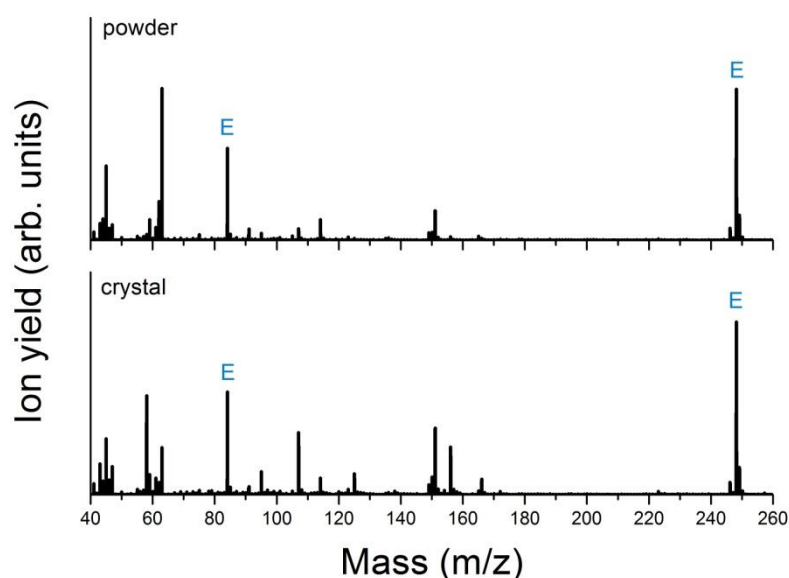


Fig. 8: Comparison of EPH mass spectra in powder (upper panel) and crystal form (lower panel). The letter "E" marks the mass spectral peaks previously identified as originating from EPH.

3.4 The "EPH crisis"

In December 2013 one Internet vendor after the other announced EPH being out of stock and in forums discussions about an EPH shortage arose. This is an indication that most vendors are just reselling NPS from a stock they have purchased from a wholesale laboratory. However, in January 2014 the vendor from whom we got our samples announced that he had synthesized EPH in his own lab, so that it would be available again. Reactions of people who had tried this new "home-made" batch read, *e.g.*, "feels wrong", "gives brain-zaps", "feels different" and reported adverse reactions included extreme burning sensations in the nose, headaches and a feeling of extreme physical exhaustion the day after consumption [17]. We purchased a sample during this period and present the mass spectrum in the upper panel of Fig. 9. It can be seen that this sample has by far the highest level of impurities with some product ions that had not appeared for any other batch. This indicates that this EPH was indeed produced in an at most semi-professional lab. Some of these "new" impurities include product ions at m/z 47 and 86 in the low mass region and very abundant products at m/z 174 and 220. The compounds corresponding to these product ions are likely being the cause of the very bad experiences with this sample reported in the forums.

However, assuming that the impurities are mainly (semi-)volatile residuals from the synthesis process, we placed some mg of the sample in an open glass vial, heated it to about 80°C and left it under the fume hood over night. The result of the analysis of this sample can be seen in the lower panel of Fig. 9. Virtually all impurities have disappeared and the mass spectrum is now comparable with the ones from the samples we considered as "pure". We conclude from this observation that heating a newly obtained sample to about 80°C for at least several hours could be a measure for harm reduction, as it minimizes toxic effects from possible residuals in the sample.

According to forums this "bad" batch disappeared at the end of February 2014, so we purchased a sample in March, which was indeed comparable to the previous ones and has already been discussed in 3.2.

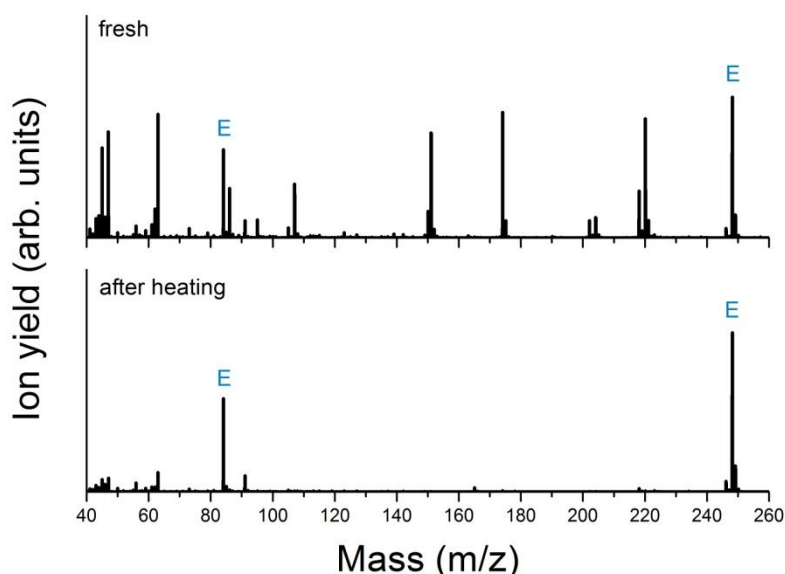


Fig. 9: Comparison of EPH mass spectra of a sample during the "EPH crisis". The upper panel represents the spectrum of the sample directly from the delivered bag, the lower panel shows the results of the same sample after one night of heating to 80°C. The letter "E" marks the mass spectral peaks previously identified as originating from EPH.

4. Conclusions

In this contribution we combine a compact review of recent technological advancements in PTR/SRI-MS and novel data on a NPS case study. Like every other existing technique PTR-MS has characteristic advantages, but also several drawbacks. Introducing SRI-MS, including a series of technological developments and add-ons, we are able to eliminate most drawbacks, while preserving the advantages of PTR-MS. Examples for such advancements are the switchable reagent ions, which not only enable the detection of a huge amount of additional substance classes, but also increase the selectivity because the ion chemistry in the drift tube can be changed, and a novel fastGC inlet system which enables a level of selectivity that previously could only be achieved with GC-MS.

Furthermore, the introduction of two novel SRI-MS instruments now covers a much broader variety of fields of application than before: the PTR-TOF 1000 is designed for applications where dimension, weight and ruggedness matter, whereas the PTR-QiTOF performs with a sensitivity (max. 4,700 cps/ppbv) and a mass resolution (max. 10,500 $m/\Delta m$) that has never been reported for an SRI-MS instrument so far. Thus, the latter instrument is ideally suited for fields of application that focus on sensitivity and speed.

In the second part of this contribution data on a three-year study of the NPS ethylphenidate are presented. All six samples purchased during this time definitely contain the advertised ingredient

ethylphenidate, which is remarkable as this is very often not the case for illicit drugs (*e.g.* the active ingredients of "ecstasy" pills, which often do not contain MDMA, but various other substances). However, we detected impurities in all samples, but in considerably different amounts. Additionally, the impurity compounds (product ions observed in the mass spectra) varied between different EPH batches, which is an indication that different synthesis routes are being used in the production of EPH, even if the product is purchased from the same vendor. This leads to the conclusion that one cannot assume if one batch of a particular vendor was pure, that the subsequent batches will be also nearly free from impurities, *i.e.* great care should be taken upon every new batch.

Finally, during an EPH shortage, we were able to obtain a presumably "home-made" batch in which we found the highest amount of impurities of all samples tested. This could be a possible explanation for the vast amount of negative comments from users in Internet forums on this particular batch. After one night of heating this sample to 80°C in an open vessel, the impurities could be considerably reduced. We conclude that this procedure could be a simple method for the reduction of harm caused by impurities, although it certainly does not reduce the harm caused by the active ingredient.

Acknowledgement

We gratefully acknowledge financial support for the technological developments by the FFG, Vienna. ML and KB have received funding through the PIMMS ITN which is supported by the European Commission's 7th Framework Programme under Grant Agreement Number 287382. WJA is in receipt of a BBSRC-Industrial CASE studentship in association with IONICON Analytik GmbH.

5. References

- [1] W. Lindinger, A. Hansel, A. Jordan, On-line monitoring of volatile organic compounds at pptv levels by means of Proton-Transfer-Reaction Mass Spectrometry (PTR-MS): Medical applications, food control and environmental research. *International Journal of Mass Spectrometry and Ion Processes* 173 (1998) 191-241.
- [2] A. Jordan, S. Haidacher, G. Hanel, E. Hartungen, J. Herbig, L. Märk, R. Schottkowsky, H. Seehauser, P. Sulzer, T.D. Märk, An online ultra-high sensitivity Proton-transfer-reaction mass-spectrometer with switchable reagent ion capability (PTR+SRI-MS). *International Journal of Mass Spectrometry* 286 (2009) 32-38.
- [3] A. Jordan, S. Haidacher, G. Hanel, E. Hartungen, L. Märk, H. Seehauser, R. Schottkowsky, P. Sulzer, T.D. Märk, A high resolution and high sensitivity proton-transfer-reaction time-of-flight mass spectrometer (PTR-TOF-MS). *International Journal of Mass Spectrometry* 286 (2009) 122-128.
- [4] <http://scholar.google.com> (24.09.2014)
- [5] A.M. Ellis, C.A. Mayhew, *Proton Transfer Reaction Mass Spectrometry: Principles and Applications*, John Wiley & Sons, Ltd, Chichester, UK (2014). doi: 10.1002/9781118682883.
- [6] T. Karl, A. Hansel, L. Cappellin, L. Kaser, I. Herdinger-Blatt, W. Jud, Selective measurements of isoprene and 2-methyl-3-buten-2-ol based on NO⁺ ionization mass spectrometry. *Atmospheric Chemistry and Physics* 12 (2012) 1-8.
- [7] P. Sulzer, A. Edtbauer, E. Hartungen, S. Jürschik, A. Jordan, G. Hanel, S. Feil, S. Jaksch, L. Märk, T.D. Märk, From conventional proton-transfer-reaction mass spectrometry (PTR-MS) to universal trace gas analysis. *International Journal of Mass Spectrometry* 321-322 (2012) 66-70.
- [8] A. Edtbauer, E. Hartungen, A. Jordan, G. Hanel, J. Herbig, S. Jürschik, M. Lanza, K. Breiev, L. Märk, P. Sulzer, Theory and practical examples of the quantification of CH₄, CO, O₂ and CO₂ with an advanced proton-transfer-reaction/selective-reagent-ionization instrument. *International Journal of Mass Spectrometry* 365-366 (2014) 10-14.
- [9] P. Sulzer, F. Petersson, B. Agarwal, K.H. Becker, S. Jürschik, T.D. Märk, D. Perry, P. Watts, C.A. Mayhew, Proton Transfer Reaction Mass Spectrometry and the Unambiguous Real-Time Detection of 2,4,6-Trinitrotoluene. *Analytical Chemistry* 84 (2012) 4161-4166.
- [10] M. Lanza, W.J. Acton, S. Jürschik, P. Sulzer, K. Breiev, A. Jordan, E. Hartungen, G. Hanel, L. Märk, C.A. Mayhew, T.D. Märk, Distinguishing two isomeric mephedrone substitutes with

- selective reagent ionisation mass spectrometry (SRI-MS). *Journal of Mass Spectrometry* 48 (2013) 1015-1018.
- [11] C. Lindinger, P. Pollien, S. Ali, C. Yeretizian, I. Blank, T.D. Märk, Unambiguous Identification of Volatile Organic Compounds by Proton-Transfer Reaction Mass Spectrometry Coupled with GC/MS, *Anal. Chem.* 77 (2005) 4117-4124.
- [12] P. Sulzer, E. Hartungen, G. Hanel, S. Feil, K. Winkler, P. Mutschlechner, S. Haidacher, R. Schottkowsky, D. Gunsch, H. Seehauser, M. Striednig, S. Jürschik, K. Breiev, M. Lanza, J. Herbig, L. Märk, T.D. Märk, A. Jordan, A Proton Transfer Reaction - Quadrupole interface Time-of-Flight Mass Spectrometer (PTR-QiTOF): High speed due to extreme sensitivity. *Int. J. Mass Spectrom.* 368 (2014) 1-5.
- [13] P. Sulzer, S. Jürschik, B. Agarwal, T. Kassebacher, E. Hartungen, A. Edtbauer, F. Petersson, J. Warmer, G. Holl, D. Perry, C.A. Mayhew, T.D. Märk, Designer Drugs and Trace Explosives Detection with the Help of Very Recent Advancements in Proton-Transfer-Reaction Mass Spectrometry (PTR-MS). *Communications in Computer and Information Science* 318 (2012) 366-375.
- [14] M. Müller, T. Mikoviny, S. Feil, S. Haidacher, G. Hanel, E. Hartungen, A. Jordan, L. Märk, P. Mutschlechner, R. Schottkowsky, P. Sulzer, J.H. Crawford, A. Wisthaler, A compact PTR-ToF-MS instrument for airborne measurements of VOCs at high spatio-temporal resolution. *Atmos. Meas. Tech. Discuss.* 7 (2014) 5533-5558.
- [15] B. Wersé, C. Morgenstern, How to handle legal highs? Findings from a German online survey and considerations on drug policy issues. *Drugs and Alcohol Today* 12/4 (2012) 222 - 231.
- [16] <http://www.theguardian.com/uk-news/2013/sep/01/festivalgoer-death-drug-warning-brownstock> (06.11.2014)
- [17] <https://www.ukchemicalresearch.org/> (06.11.2014)
- [18] <http://www.bluelight.org/vb/forum.php> (06.11.2014)
- [19] J.S. Markowitz, B.K. Logan, F. Diamond, K.S. Patrick, Detection of the novel metabolite ethylphenidate after methylphenidate overdose with alcohol coingestion. *Journal of Clinical Psychopharmacology* 19/4 (1999) 362-366.
- [20] W.J. Acton, M. Lanza, B. Agarwal, S. Jürschik, P. Sulzer, K. Breiev, A. Jordan, E. Hartungen, G. Hanel, L. Märk, C.A. Mayhew, T.D. Märk, Headspace analysis of new psychoactive substances using a Selective Reagent Ionisation-Time of Flight-Mass Spectrometer, *International Journal of Mass Spectrometry* 360 (2014) 28-38.

IONIZATION CHARACTERISTICS OF AMINO ACIDS IN DIRECT ANALYSIS IN REAL TIME MASS SPECTROMETRY USING ATMOSPHERIC PRESSURE HELIUM PLASMA

Kanako Sekimoto, Mitsuo Takayama

Graduate School of Nanobioscience, Yokohama City University

E-mail: sekimoto@yokohama-cu.ac.jp

The positive and negative ionization characteristics of 20 different α -amino acids were investigated using Direct Analysis in Real Time (DART) mass spectrometry using an atmospheric pressure helium plasma source. Almost all of the amino acids M were ionized to generate the (de)protonated analytes $[M \pm H]^\pm$ via proton transfer reactions with the typical background ions $H_3O^+(H_2O)_n$ and O_2^- and resonant electron capture by M. The application of DART to amino acids also resulted in oxidations involving oxygen attachment and hydrogen loss, and formation of adducts $[M + R]^-$ with negative background ions R^- (O_2^- , HCO_2^- , NO_2^- and $C_3H_5O_3^-$), depending on the physicochemical and/or structural properties of individual amino acids. The relationship between each amino acid and the ionization reactions observed suggested that oxidation and $[M + R]^-$ adduct formation originated from reactions with active oxygens such as hydroxyl radicals HO, indicating that the typical background neutral species involved in analyte ionization in DART mass spectrometry contain HO.

1. Introduction

The recent development of ambient desorption/ionization (ADI) mass spectrometry offers numerous advantages, including direct analysis of solids and liquids under ambient conditions with little or no sample preparation. For these reasons, ADI sources have become important tools in cleaning validation, forensic analysis, and drug discovery. Although several different types of ADI sources have been developed so far, a large amount of interest has been placed on direct analysis in real time (DART) using an atmospheric pressure helium plasma source [1], which is the origin of ADI sources. DART combines separate desorption and ionization processes into a single method. The desorption is carried out using hot helium gases, whereas the ionization goes through an atmospheric pressure chemical ionization (APCI)-like process with reactions involving excited helium. It has been reported that DART is a soft ionization technique forming abundant (de)protonated analytes $[M \pm H]^\pm$ via proton transfer from background ions such as $H_3O^+(H_2O)_n$ and O_2^- to the analytes M, while analytes with certain specific features can be ionized to form additional analyte ions. For instance, DART ionization of nonpolar compounds such as alkanes leads to the production of analyte ions originating from hydride abstraction, oxygen attachment, or hydrogen loss, instead of $[M \pm H]^\pm$. The mechanism of formation of those analyte ions is not well understood, although the involvement of NO^+ , one of the background ions in DART gas flow, has been suggested. A lack of knowledge concerning the ionization characteristics in DART results in difficulty in the interpretation of DART mass spectra, and limits its analytical utility. In order to overcome these issues, it is necessary to investigate the ionization characteristics of DART in detail, i.e., to identify the background ionic and neutral species formed in DART sources and to systematically understand the influence of these individual background compounds on analyte ionization.

Herein, the positive and negative ionization characteristics of 20 different α -amino acids were investigated by DART mass spectrometry. The amino acids used have a wide variety of physicochemical and/or structural properties originating from their side chains, including the nonpolarity associated with aliphatic or aromatic character, and the polarity due to the presence of specific functional groups (hydroxyl, amino, carboxyl and thiol groups). All of the amino acids except for arginine were positively and negatively ionized via various different reactions including (de)protonation, oxygen attachment, hydrogen loss, and the formation of adducts with negative background ions. The relationship between the physicochemical and/or structural properties of the individual amino acids and ionization reactions observed contributes to the understanding of the formation of background ionic and neutral species and the resulting effects on analyte ionization in DART [2].

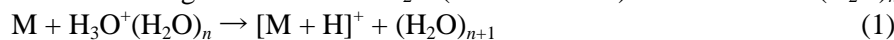
2. Experimental

All mass spectra were acquired with an LCQ ion-trap mass spectrometer (Thermo Fisher Scientific, San Jose, CA) equipped with a DART-SVP source (IonSense, Saugus, MA). The DART-SVP source was operated with a needle voltage of 5000 V and an exit grid electrode voltage of 350 V. Helium (He) at 350 °C was used for the DART gas at the factory-preset flow rate (2.5 Lmin⁻¹). The DART source exit was directed toward the orifice of the mass spectrometer, separated by a gap of ≈ 10 mm. The analytes used were the 20 standard α -amino acids, purchased from Sigma-Aldrich (Tokyo, Japan). Analyte desorption and ionization was accomplished by an insertion of a 1.5 mm i.d. glass tube containing the analyte in the He gas flow between the DART source exit and the mass spectrometer orifice. The resulting gas-phase analyte ions were introduced into the orifice. The orifice was heated at 275 °C and applied a voltage of 20 V. The ions were focused onto the skimmer and the tube lens and were transported into the ion-trap analyzer through ion guides consisting of a quadrupole, gate lens, octapole and entrance lens. The voltages applied to the skimmer and tube lens were 0 and 50 V, respectively. The applied RF voltages on the quadrupole and octapole were 400 V peak-to-peak. The gate lens regulating the ion injection into the ion-trap analyzer utilized an applied voltage of 16 V, whereas the voltage on the entrance lens for the eventual focusing of the transported ions was 30 V.

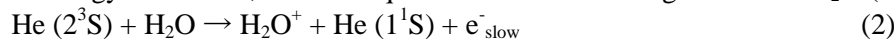
3. Results and discussion

3.1 (De)protonation

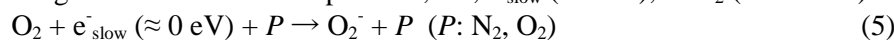
The positive- and negative-ion DART mass spectra of L-aspartic acid (Asp) shown in Figure 1 are representative examples. The mass spectra show the dominant ion peaks of the (de)protonated analytes [Asp \pm H] ^{\pm} , which are the major ion species commonly observed when ionizing various other amino acids. The protonated analytes [M + H]⁺ are most likely produced via proton transfer reactions involving H₃O⁺(H₂O)_n, the typical positive background ions in DART (reaction 1). Proton affinities of analytes M used are higher than that of H₂O (691.0 kJ mol⁻¹) and its clusters (H₂O)_n.



The reactant ions H₃O⁺(H₂O)_n can be formed via a Penning ionization to form H₂O⁺ (reaction 2), due to the energy transfer from an excited He with 19.8 eV excitation energy, He(2³S), to H₂O having an ionization energy of 12.6 eV, and subsequent reactions involving additional H₂O (reactions 3 and 4).



In contrast, the formation of deprotonated analytes [M - H]⁻ are most likely attributed to two different processes, i.e., proton transfer from analytes M to the negative background ions O₂⁻ and resonant electron capture by M. The O₂⁻ ions are formed via attachment of thermal electrons having kinetic energies at the ambient temperature, i.e., e⁻_{slow} (≈ 0 eV), to O₂ (reaction 5):



where *P* represents common air constituents such as N₂ and O₂ corresponding to a third body. Slow electrons e⁻_{slow} with low kinetic energies can be produced via Penning ionization (reaction 2) and/or the following surface Penning ionization (reaction 6).



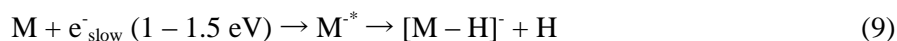
The electrons formed via reaction 6, e⁻_{fast}, are rapidly thermalized by collisions with common air constituents *P* (reaction 7).



The collision of O₂⁻ with analytes M efficiently brings about the formation of [M - H]⁻ via proton transfer from M to O₂⁻ (reaction 8), due to higher proton affinity of O₂⁻ (1477 \pm 2.9 kJ mol⁻¹) rather than [M - H]⁻.



The slow electrons having kinetic energies over the range of 1 - 1.5 eV, e⁻_{slow} (1 - 1.5 eV), can also resonantly attach to analytes M and subsequent dehydrogenation leads to produce [M - H]⁻ (reaction 9).



The formation of deprotonated amino acids $[M - H]^{-}$ via reaction 9 has been previously reported by numerous studies regarding resonant electron capture and dissociative electron attachment using low energetic electrons. On the basis of those previous studies, the $[M - H]^{-}$ ions resulting from reaction 9 have carboxylate anion structures occurring via either electron capture into the π^* orbital of the carboxylic group or hydrogen-atom tunneling through the barrier that separates a dipole-supported minimum and repulsive valence state.

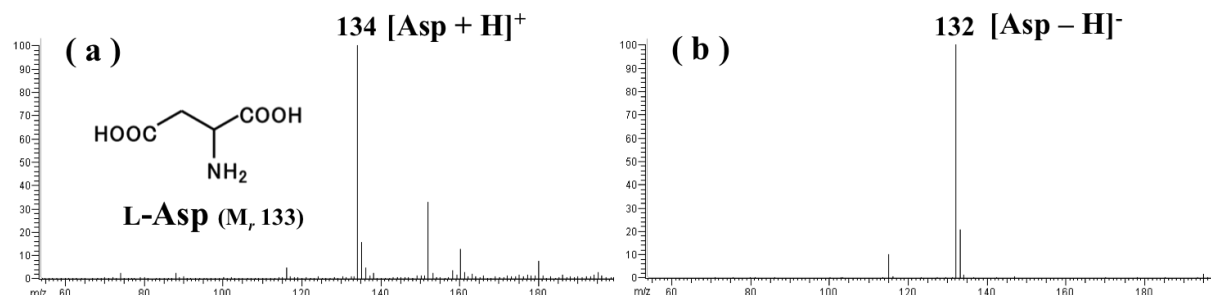


Fig. 1. (a) Positive- and (b) negative-ion DART mass spectra of L-aspartic acid (Asp).

3.2 Oxidation

DART ionization resulted in the formation of (de)protonated analytes with the addition of one and/or two oxygens, $[M \pm H + nO]^{\pm}$ ($n = 1, 2$), for sulfur-containing, aromatic, and aromatic heterocyclic amino acids such as Met, Phe, Tyr, Trp and His (see Figure 2a). It has been previously reported that these five amino acids can be easily oxidized with oxygen attachment due to hydroxyl radical HO as a strong oxidizing species, formed in ozonated solutions or via Fenton reactions and/or radiolysis in aqueous solutions. The oxidation of Met with HO results in the formation of sulfoxide. Reactions of HO with the aromatic rings in Phe and Tyr lead to the addition of HO to the rings, and subsequent reactions of the radical species with oxygen generate 2-amino-3-(hydroxyphenyl)propanoic acid and dihydroxyphenylalanine, corresponding to the monoxides of Phe and Tyr, respectively. It has been reported that aromatic amino acids are oxidized to form quinones, e.g., 2-amino-3-(3,4-dioxocyclohexa-1,5-dienyl)-propanoic acid which is a quinone structural oxidation product for Tyr. However, no observation of ions related to quinones in the mass spectra of Phe and Tyr indicates less occurrence of quinone formation in DART. Trp and His can be oxidized at the conjugated double bond moiety with HO to form oxindole-3-alanine ($[Trp + O]$), *N*-formylkynurenine ($[Trp + 2O]$) and 2-oxo-histidine ($[His + O]$). The oxidation reactivity for individual amino acids *M* can be estimated using relative abundances of $[M \pm H + nO]^{\pm}$. The reactivity order obtained here is $Trp > Met > Phe > Tyr > His > \text{other amino acids} \approx 0$. This order is in agreement with the previous report using ozonated solutions with pH 5.8: $Met > Trp > Tyr > His > \text{other amino acids}$ [3]. In the case of higher pH conditions, oxidation of Cys to form trioxide products $[Cys + 3O]$ proceeds most dominantly. Taking into account the results obtained, the oxidation with oxygen attachment reactions occurring in DART most likely originate with HO in the ionization area under relatively acidic conditions.

In negative-ion DART, deprotonated analytes with two hydrogen loss, $[M - 2H - H]^{-}$, were observed when analyzing Gly, Ala, Val, Leu, Ile, Ser, Thr, Asn, Cys, Met and Phe, which have aliphatic or non-ionic side chains (see Figure 2b). The peak abundances from $[M - 2H - H]^{-}$ were rather low compared to the abundances of $[M - H]^{-}$. Such $[M - 2H - H]^{-}$ ions have also been observed in the negative-ion DART of aliphatic compounds such as hexanes, heptanes, cyclohexane and hexatriacontane, although the precise mechanism of the 2H loss reactions in DART and its dependence on the structural properties of the analytes have not yet been clarified. It has been previously reported that deprotonated Ser in aqueous solution with HO and O₂ loses two hydrogens from the backbone of Ser via sequential oxidation reactions, as shown in Scheme 1. This scheme could be applied to the reactions observed here, i.e., the gas-phase 2H loss from deprotonated analytes for various amino acids including Ser. In contrast, the ion peaks of $[M - 2H - H]^{-}$ have been observed in the mass spectra of Gly and Val resonantly capturing low energetic electrons (≈ 1.5 eV). It is likely,

therefore, that the 2H loss reactions occurring in DART can be interpreted in terms of alternative oxidation processes due to HO and/or involvement of slow electrons e^-_{slow} (≈ 1.5 eV) formed via reactions 2 and 7.

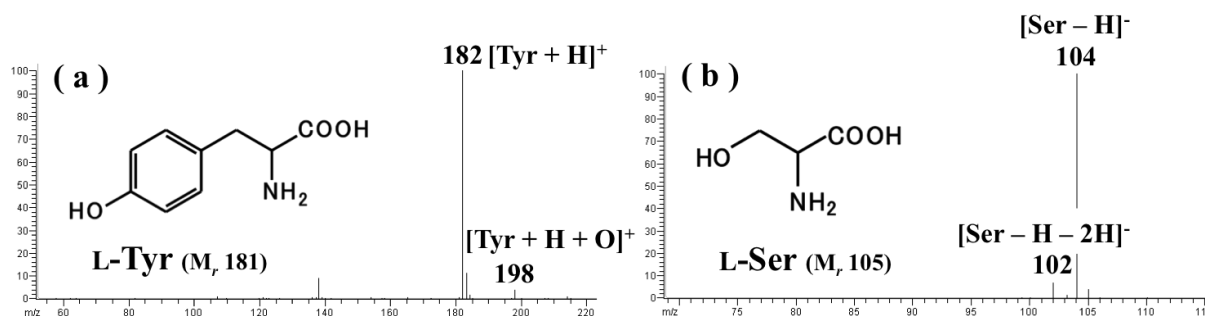
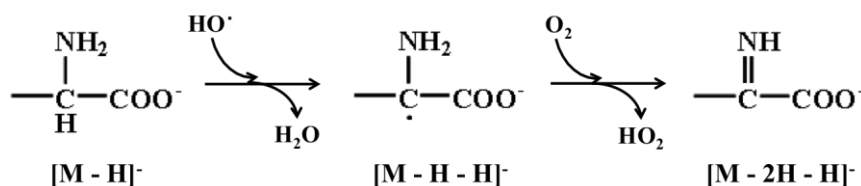


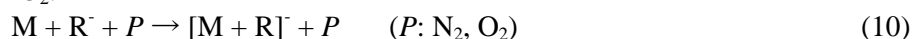
Fig. 2. (a) Positive-ion DART mass spectrum of L-tyrosine (Tyr). (b) Negative-ion DART mass spectrum of L-serine (Ser).



Scheme 1. Reaction of deprotonated amino acids with HO and O₂ to lose two hydrogens.

3.3 Formation of adducts with negative background ions

All of the amino acids M, except for acidic and amidic amino acids such as Asp, Glu and Gln, formed negative ion adducts $[\text{M} + \text{R}]^-$ with background ions R⁻, such as O₂⁻ (m/z 32), HCO₂⁻ (m/z 45), NO₂⁻ (m/z 46) and/or C₃H₅O₃⁻ (m/z 89). Those ions R⁻ are typical negative backgrounds formed in DART. The adduct ions $[\text{M} + \text{R}]^-$ were most likely formed via three-body reactions with a third body P such as N₂ or O₂.



The results obtained showed that whether $[\text{M} + \text{R}]^-$ are formed or not varies with each combination of R⁻ and M, which are not dependent upon the chemical properties of M, such as whether the analyte is aliphatic or aromatic, or has certain functional groups. The results obtained suggest that the formation of the $[\text{M} + \text{R}]^-$ adducts is attributed to the affinity or ability of complexation between individual R⁻ and M, although the factors determining its affinity or ability can not be readily proven. Similar phenomena have been also observed in atmospheric pressure corona discharge ionization (APCDI) [4, 5].

3.4 Ionization characteristics of DART

The notable reactions observed in DART were oxidations involving oxygen attachment and hydrogen loss. As described above, those oxidation processes in DART are most likely attributable to reactions with HO. It can be presumed, therefore, that the analyte ionization area between the DART source exit and the mass spectrometer orifice includes a number of active oxygens such as HO. Figure 3 shows the proposed sequential reactions for the formation of HO in DART involved excited He, He(2³S) having 19.8 eV, as an energy source. Collisions of He(2³S) with O₂ can occur homolytically and heterolytically in terms of bond dissociation to form an O atom in a ground-level triplet state, O(³P), and the O⁻ ion, respectively (reactions c and a in Figure 3). The oxygen atom O(³P) can combine rapidly with O₂ to generate ozone O₃ (reaction d in Figure 3), whereas O⁻ ion reacts with H₂O resulting in the formation of HO and HO⁻ ion (reaction b in Figure 3). It has been reported that O₃ molecules can dissociate with an energy above 3.87 eV to produce an O atom in an excited singlet state, O(¹D),

which is likely achieved involving $\text{He}(2^3\text{S})$ (reaction e in Figure 3). Subsequent reaction of $\text{O}(^1\text{D})$ with H_2O leads to the formation of HO (reaction f in Figure 3). The radical species HO can also be formed via reactions of H_2O with $\text{He}(2^3\text{S})$ and via reactions forming H_3O^+ (reaction g and h in Figure 3, respectively). It is most likely that the sequential reactions shown in Figure 3 can occur inside a DART source, and the resulting HO are introduced into the analyte ionization area by the He gas flow, independent of the polarity of the voltage applied to the grid electrode of the DART source exit. Therefore, the oxidation reactions due to HO can occur easily in both positive- and negative-ion modes.

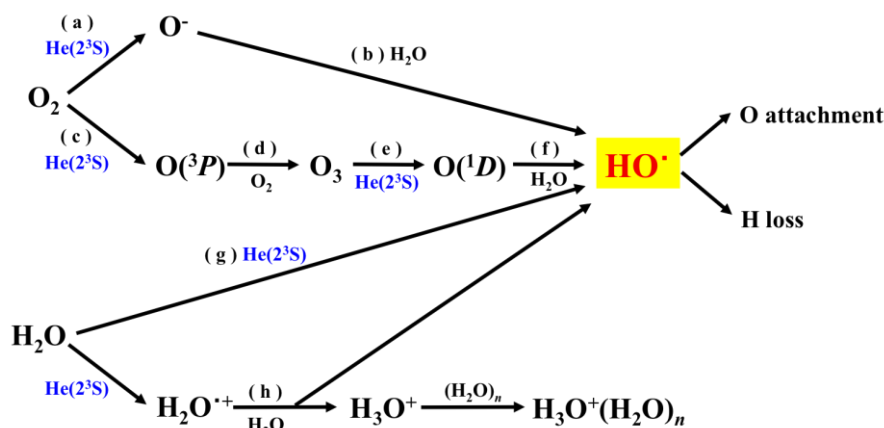


Fig. 3. Proposed sequential reactions for the formation of HO in DART using helium plasma.

4. Conclusions

The positive and negative ionization characteristics of 20 different α -amino acids were investigated in Direct Analysis in Real Time (DART) mass spectrometry using an atmospheric pressure helium plasma. All of the amino acids except for L-arginine (Arg) were ionized via various reactions depending on the physicochemical and/or structural properties of the individual amino acids, as follows:

- 1) (De)protonation for almost all of amino acids except for Arg via proton transfer reactions with the typical background ions $\text{H}_3\text{O}^+(\text{H}_2\text{O})_n$ and O_2^- and resonant electron capture by M.
- 2) Oxygen attachment for sulfur-containing, aromatic and aromatic heterocyclic amino acids.
- 3) Hydrogen loss for aliphatic or non-ionic amino acids.
- 4) Attachment of negative background ions R^- (O_2^- , HCO_2^- , NO_2^- and $\text{C}_3\text{H}_5\text{O}_3^-$) for almost all of the amino acids to form $[\text{M} + \text{R}]^-$.

Oxygen attachment and hydrogen loss can be interpreted as oxidation processes involving active oxygens such as hydroxyl radical HO. The results suggest, therefore, that analyte ionization in DART can be oxidatively influenced by HO.

5. References

- [1] Cody R B, Laramee J A and Durst H D 2005 *Anal. Chem.* **77**, 2297.
- [2] Sekimoto K, Sakakura M, Kawamukai T, Hike H, Shiota T, Usui F, Bando Y and Takayama M 2014 *Analyst* **139** 2589.
- [3] Kotiaho T, Eberlin M N, Vainiotalo P and Kostianen R 2000 *J. Am. Soc. Mass Spectrom.* **11**, 526.
- [4] Sekimoto K, Sakai M and Takayama M 2012 *J. Am. Soc. Mass Spectrom.* **23** 1109.
- [5] Sekimoto K, Matsuda N and Takayama M 2013 *Mass Spectrom.* **2** A0020.

DIRECT LIQUID SAMPLING FOR CORONA DISCHARGE ION MOBILITY SPECTROMETRY

Martin Sabo¹, Michaela Malásková¹, Olga Harmathová¹, Jasna Hradsky²,
Marian Masár² and Štefan Matejčík¹

¹*Department of Experimental Physics, Faculty of Mathematics, Physics and Informatics, Comenius University, Mlynska dolina F2, 842 48 Bratislava, Slovakia*

²*Department of Analytical Chemistry, Faculty of Natural Sciences, Comenius University,*

Mlynska dolina, 842 15 Bratislava, Slovakia

Martin.Sabo@gmail.com

In this work we will present new technique developed of direct liquid sampling for Ion Mobility Spectrometry (IMS) equipped with corona discharge (CD) ionization source. The direct liquid sampling for CD-IMS will be demonstrated on explosives (TNT, RDX, PETN, C4 and SEMTEX) and on amino acids and dipeptides.

1. Introduction

Already for half century are IMS instruments important tool in the security area, especially detection of explosives, illicit drugs and gas ware agents[1]. To main advantages of these instruments belong their compact design, high sensitivity fast response and high reliability. The IMS spectrometers are easy to use for detection of volatile and semivolatile compounds[1]. However, the analysis of liquid samples becomes more challenging task. One solution of this problem was the implementation of the electrospray ionization (ESI) method for IMS [2]. The implementation of ESI to IMS puts additional demands on construction of the instruments [2]. Additionally, in the ESI solvents like methanol, formic acid, etc. are used, which unfluence the nature of the detected analytr ions and in decrease of the sensitivity of the instrument. In this work we will for the first time present new direct liquid sampling (DLS) technique suitable for IMS instrument equipped with CD ionization source. The DLS technique was successfully demonstrated for detection and analysis of explosives, aminoacids and dipeptids.

2. Experiment

The IMS instrument used in this work was developed at Department of Experimental Physics, in collaboration with MaSaTECH. The picture of the instrument is shown in Figure 1. The IMS is constructed from stainless steel rings isolated by the Teflon. IMS was equipped with CD ionization source. The length of the IMS drift tube was 11,05 cm, the drift electric field intensity was 582 V/cm. The drift gas flow of purified air was 1 L/min and sample gas flow (atmospheric air) was 0,6 L/min. The instrument was operated in reverse gas flow mode [3] where the gas outlet was located behind the CD. The instrument was operated in both negative and positive polarity. The negative polarity was used for detection of explosives while the positive one was used for analysis of aminoacids and dipeptids.

The CCl₄ was used as a dopant gas[4] in the negative polarity in order to generate Cl⁻ reactant ions for explosives detection.

The explosives: TNT, RDX, PETN, C4 and SEMTEX were obtained from Slovak ministry of defense with purity up to 99 %. The small amount of explosives was diluted in methanol or in methanol/aceton mixture. The solution was in next step diluted with the pure methanol in order to reach sufficient concentration.

The aminoacids Glycine, Leucine, Iso-leucine, Phenylalanine, Serine and dipeptids Glycine-Alanine and Aspartame were ordered from SigmaAldirch. The aminoacids and dipeptids was diluted in deionised water.

The liquid samples were introduced to DLS unit by syringe pump (Kent Scientific). The liquid flow rate used in this experiment was in range from 20 to 200 $\mu\text{L}/\text{min}$.

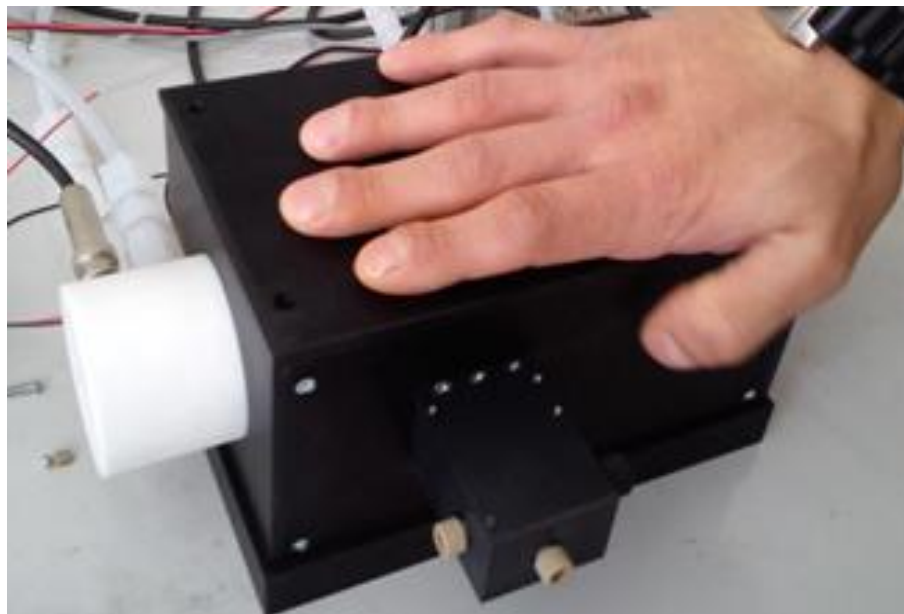


Fig. 1. The photograph of IMS instrument used in this work

3. Results and discussion

The IMS spectrum of most common explosives TNT, RDX and PETN analyzed directly from the liquid solution via the DLS unit is depicted in Figure 2.

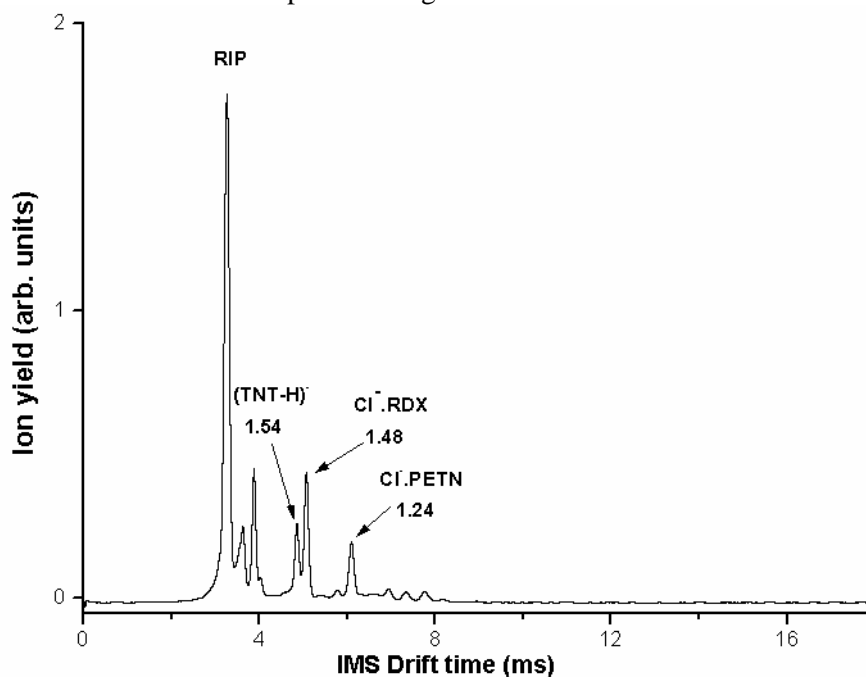


Fig. 2. The IMS spectrum of TNT, RDX and PETN

The reduced ion mobilities of the ions associated with the explosives were $1.54 \text{ cm}^2 \cdot \text{V}^{-1} \cdot \text{s}^{-1}$ for TNT, $1.48 \text{ cm}^2 \cdot \text{V}^{-1} \cdot \text{s}^{-1}$ for RDX and $1.24 \text{ cm}^2 \cdot \text{V}^{-1} \cdot \text{s}^{-1}$ for PETN. These values were in very good agreement with the values reported in literature [5]. The IMS supported by the DLS unit also allowed detection of explosives from solution like diesel fuel. Figure 3. Demonstrating detection of RDX, C4, PETN and SEMTEX directly from the diesel fuel.

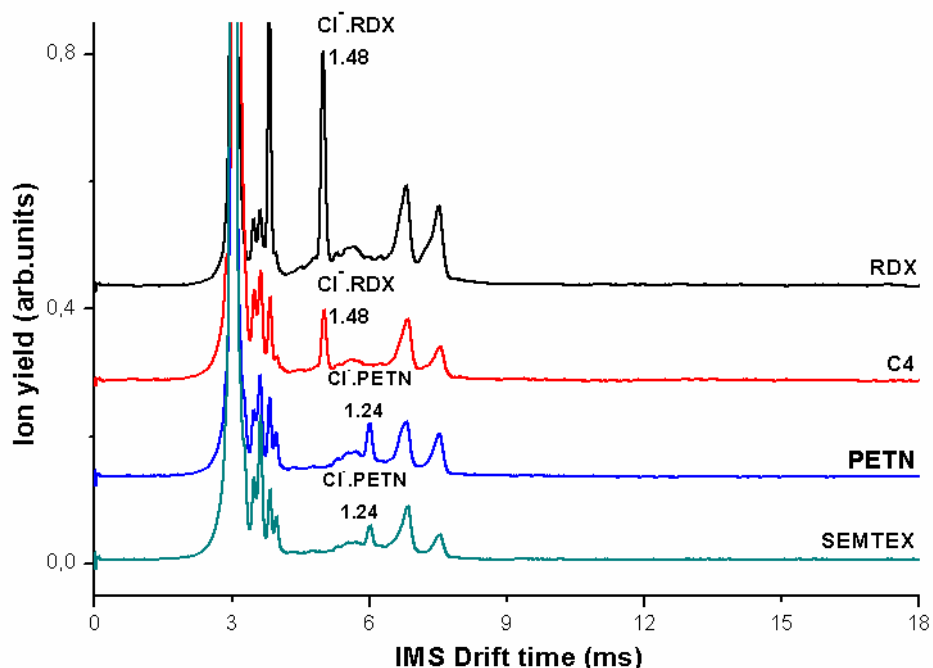


Fig. 3. The IMS spectrum of RDX, C4, PETN and SEMTEX detected directly from the oil sample.

The DLS method with CD IMS was also used for the study of aminoacids and dipeptids. The aminoacids glycine, leucine, iso-leucine, phenylalanine and serine were dissolved in deionised water. The water sample was in next step directly introduced to the DLS unit for analysis via the IMS. Here we see the main advantage of DLS compare with ESI. While the ESI requires for spray stabilisation special solutions (usually the methanol is used for stabilisation of ESI) the liquid sample introduced to DLS can be analysed without any further treatment. The IMS spectrum of investigated aminoacids is shown in Figure 4.

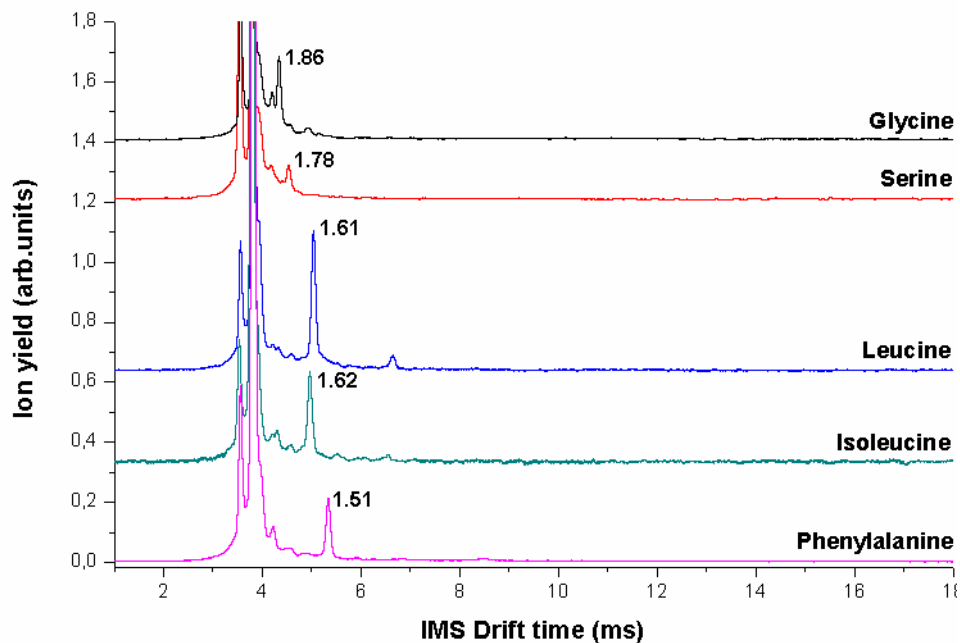


Fig. 4. IMS spectrum of investigated aminoacids

The aminoacids were investigated in the positive polarity. The reduced mobilities of the aminoacids were $1.86 \text{ cm}^2 \cdot \text{V}^{-1} \cdot \text{s}^{-1}$ for Glycine, $1.78 \text{ cm}^2 \cdot \text{V}^{-1} \cdot \text{s}^{-1}$ for Serine, $1.61 \text{ cm}^2 \cdot \text{V}^{-1} \cdot \text{s}^{-1}$ for Leucin, $1.62 \text{ cm}^2 \cdot \text{V}^{-1} \cdot \text{s}^{-1}$ for Isoleucine and $1.51 \text{ cm}^2 \cdot \text{V}^{-1} \cdot \text{s}^{-1}$ for Phenylalanine. As in positive polarity $\text{H}_3\text{O}^+ \cdot (\text{H}_2\text{O})_n$ ions are the maior reactant ions we assume that M.H^+ species were the products ions of interaction between reactant ions and samples. In order to confirm this assignment, we have to perform in future IMS-MS study on these samples.

The DLS technique was also used for detection of dipeptides, the results of this study we plan to present at the conference.

4. Conclusion

In this work we have demonstrated the new liquid sampling technique DLS suitable for CD-IMS. The ability of this technique was demonstrated on applications in two different fields. In the area of detection of explosives as well as for biochemical applications with analysis of aminoacids and dipeptides.

5. Acknowledgement

This work was supported by Slovak research and development agency project APVV-0259-12.

6. References

- [1] Karpas Z and Eiceman G A 2005 *Ion mobility spectrometry 2nd edition*, CRC Press.
- [2] Wittmer D, Chen Y H, Luckenbill B K and Hill H H 1994 *Anal.Chem.* **66** 2348-2355.
- [3] Sabo M, Matuska J and Matejčík Š 2011 *Talanta* **85** 400-405
- [4] Sabo M, Malásková M and Matejčík Š 2014 *Plasma Sources Science and Technology* **23** 015025.
- [5] Ewing R G, Atkinson D A, Eiceman G A and Ewing G J, 2001 *Talanta* **54** 515-529.

MICROCHIP ELECTROPHORESIS IN THE ANALYSIS OF BIOLOGICAL AND ENVIRONMENTAL SAMPLES

Marián Masár¹, Jasna Hradski¹, Martin Sabo², Štefan Matejčík²

¹*Department of Analytical Chemistry, Faculty of Natural Sciences, Comenius University in Bratislava, Mlynská dolina CH2, SK-84215 Bratislava, Slovakia*

²*Department of Experimental Physics, Faculty of Mathematics, Physics and Informatics, Comenius University in Bratislava, Mlynská dolina F2, SK-84248, Bratislava, Slovakia*

E-mail: masar@fns.uniba.sk

This contribution deals with application possibilities of microchip electrophoresis in the analysis of complex biological and environmental samples. Microchip electrophoresis was performed on a polymethylmethacrylate microchip with coupled separation channels and integrated conductivity detection. Various application areas of microchip electrophoresis, e.g., analysis of drinking waters, as well as biofluids are shown.

1. General aspects of MCE

One of the fastest growing separation methods in the field of miniaturized analytical systems, also called as lab-on-chip (LOC), is microchip electrophoresis (MCE). A common feature of LOC is integration of sample preparation, separation and detection of the analytes, as well as sample handling into one compact miniaturized system. This system enables a high level of automatization of analytical procedure, decrease of the overall analysis time and significant reduction of financial costs, and also the reduction of (toxic) waste produced during the analysis. An analytical use of MCE in practice is still limited in terms of availability of appropriate resources for miniaturized sample preparations and new technologies for miniaturized detection systems. In this context, a technology of coupling the separation channels (CC), known in conventional electrophoretic systems as the technique of column coupling, can be seen as a very efficient tool for integration of sample preparation with MCE separation of analytes in terms of the LOC concept [1]. In addition, a coupling MCE to miniaturized spectrometric detection systems, e.g., ion mobility spectrometry, could have a high analytical potential for the analyses of environmental and biological samples.

2. Practical applicability of MCE

Some theoretical and practical aspects of microchip electrophoresis (MCE), as a dominant method in LOC analytical systems, are to be discussed. MCE has shown a rapid development over the past few years. This technology, compared to the conventional capillary electrophoresis (CE) systems, has significant advantages in terms of high speed, high throughput, easy integration, low sample consumption and automation. However, a routine analytical use of MCE is still limited because of some serious problems resulted from downscaling [2].

The analytical possibilities of MCE with on-line conductivity detection in the analysis of complex environmental and biological samples have to be shown in this respect. Various types of sample pre-treatment techniques integrated prior to the MCE separations are to be discussed, as well. On-line combinations of electrophoresis methods can be considered as very promising tools in integrating sample pre-treatment with the electrophoretic separations on the microchips. Therefore, we pay a special attention to this topic with a focus on the combinations that integrate (electrophoretic) sample pre-treatment with the electrophoretic separations on the microchip.

In this context, the use of different electrophoresis methods combined on-line on the microchip with coupled channels, e.g., isotachopheresis (ITP) – capillary zone electrophoresis (CZE), ITP-CZE and CZE-CZE in the analyses of complex biological samples are to be demonstrated [1]. Application possibilities of MCE separation systems with integrated conductivity detection are to be shown on a set of analytical methods suitable for rapid monitoring and analysis of complex environmental and biological samples, e.g., ITP-CZE determination of pesticide – glyphosate in drinking water [3], ITP-CZE determination of nitrate and nitrite [4] as biomarkers of various neurological diseases in the

cerebrospinal fluid, CZE-CZE determination of metabolic organic acids in body fluids [5] and sequential CZE separations of cations and anions in various body fluids [6].

3. Instrumentation for MCE

Separations were carried out on polymethylmethacrylate (PMMA) CC microchip with integrated conductivity sensors (IonChip™ 3.0, Merck, Darmstadt, Germany, Fig. 1a). MicroCE analyzer consisted of electrolyte and electronic unit (Fig. 1b, c). Main components of an electrolyte unit were peristaltic micropumps and membrane driving electrodes. Peristaltic micropumps were used to transport BGE and sample solutions to the microchip. The membrane driving electrodes were used to suppress disturbances due to the bubble formation during the separation run. An electronic unit delivered the stabilized driving current to the counter-electrode, drove the peristaltic micropumps and interfaced the MCE analyzer to a PC. This unit also included the measuring electronics of the contact conductivity detectors. Monitoring of the analysis, as well as collecting the data from conductivity detectors and their evaluation were done using MicroCE Win software, version 2.4 (Merck).

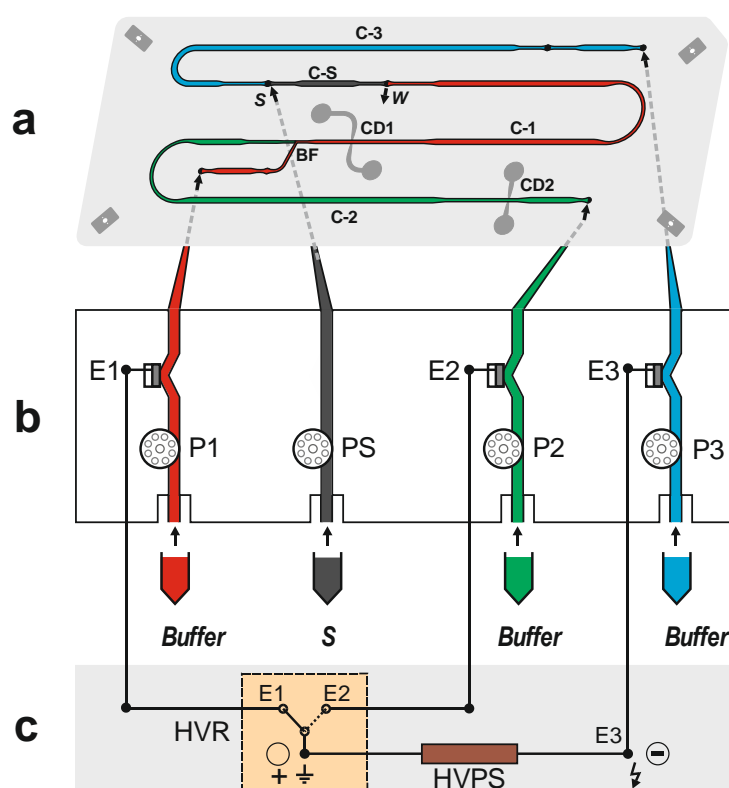


Fig. 1. Scheme of MCE equipment with CC microchip and contact conductivity detection.

(a) Arrangement of CC chip channels: C-S, sample injection channel with $0.9 \mu\text{L}$ volume; C-3, a non-separative part of the first separation channel; C-1, the first separation channel ($4.5 \mu\text{L}$ volume; $59 \times 0.2\text{--}0.5 \times 0.14\text{--}0.2\text{ mm}$ [length \times width \times depth]); C-2, the second separation channel ($4.3 \mu\text{L}$ volume; $56 \times 0.2\text{--}0.5 \times 0.14\text{--}0.2\text{ mm}$); CD1, CD2, conductivity sensors; BF, bifurcation section; S, sample solution; W, waste channel. Arrows indicate inlets for buffers and S into the chip channels and outlet hole from the chip channels to W.

(b) Electrolyte unit: P1, P2, P3, PS, peristaltic micropumps for filling C-1, C-2, C-3 and C-S channels with buffers and S, respectively; E1, E2, driving electrodes for the C-1 and C-2 separation channels, respectively; E3, the driving electrode connected to a high voltage pole of HVPS.

(c) Electronic unit: HVPS, high-voltage power supply ($0\text{--}50 \mu\text{A}$, $0\text{--}7\text{ kV}$); HVR, high-voltage relay. Driving current passed between the electrodes E1 and E3 (the first channel) or E2 and E3 (both the first and the second separation channels).

4. Acknowledgment

This work was supported by the Slovak Research and Development Agency (APVV-0259-12).

5. References

- [1] Kaniansky D, Masár M, Bodor R, Žúborová M, Olvecká E, Joehnck M and Stanislawski B 2003 *Electrophoresis* **24** 2208-2227.
- [2] Henry C S 2006 *Microchip Capillary Electrophoresis: Methods and Protocols* Humana press Totowa.
- [3] Horčíčiak M, Masár M, Bodor R, Danč L and Bel P 2012 *J Sep Sci* **35** 674-780.
- [4] Troška P, Chudoba R, Danč L, Bodor R, Horčíčiak M, Tesařová E and Masár M 2013 *J Chromatogr B* **930** 41-47.
- [5] Danč L, Bodor R, Troška P, Horčíčiak M and Masár M 2014 *Electrophoresis* **35** 2146-2154.
- [6] Hradski J, Bodor R and Masár M 2014 *Chromatographia* **77** 1461-1468.

ION MOBILITY SPECTROMETRY APPARATUS WITH RADIOACTIVE IONIZATION SOURCE

Bartosz Michalczuk, Karol Wnorowski, Antoni Jówko, Wiesława Barszczewska

Siedlce University, Faculty of Natural Sciences, Department of Chemistry,

3 Maja 54, 08-110 Siedlce, Poland

E-mail: bartosz.michalczuk@uph.edu.pl

Ion mobility spectrometry (IMS) is a highly sensitive, very fast and inexpensive analytical technique for detection and monitoring many kinds of volatile organic compounds. There are many known ion sources used in the IMS, but the radioactive source has the advantage, that there is no need for an additional power source. In our laboratory we have launched a new ion mobility spectrometry apparatus with radioactive ion source (^{238}Pu). We present the first results obtained for a few tested compounds.

1. Introduction and experimental

IMS allows the detection and monitoring of trace amounts of volatile organic compounds in the sample after its ionized. The most commonly used ionization sources in the IMS is a corona discharge. Other used methods include photoionization, electrospray ionization, laser-based ionization, surface ionization, flames, plasma and radioactive sources [1]. The advantage of this latter is stable and reliable ionization of the sample, with no need for additional power and damaging parts, which significantly affects on the cost of research/analysis and quality of the results. The most commonly used radioactive sources are ^{63}Ni , ^{241}Am and ^3H .

In our laboratory we have launched an ion mobility spectrometry apparatus with radioactive ionization source, which is the ^{238}Pu . The IMS was home made with broad participation and collaboration with the Faculty of Experimental Physics of the Comenius University in Bratislava. The schematic view of experimental set-up is shown in Fig. 1.

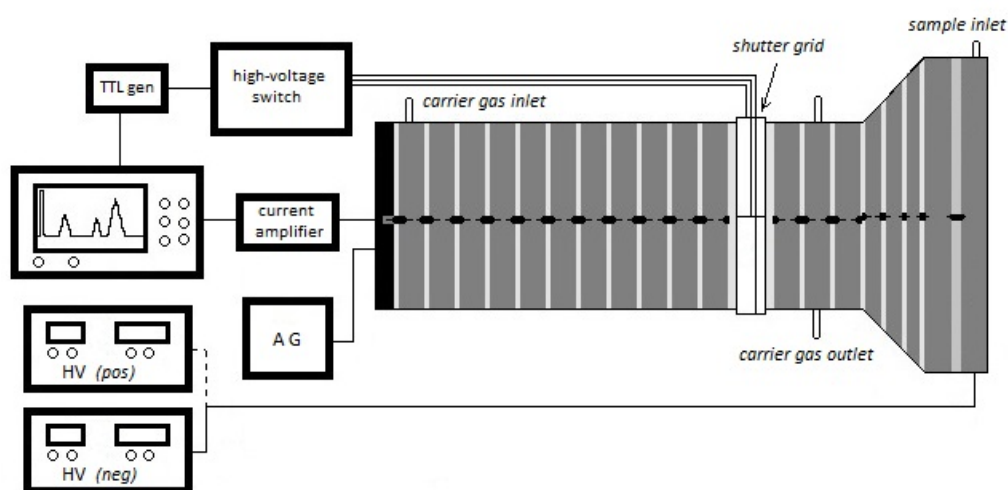


Figure 1. Schematic view of the IMS apparatus.

The ionization region consist the seven cone-shaped rings isolated by Teflon. Inside, between the first and second rings (made of aluminum ,diameter 14 cm), is placed a ring containing the alpha particles source (diameter 9 cm). Alpha particles are emitted in the plane of the ring (inside diameter 8.5 cm). The sequence of the other five rings of stainless steel allows the movement of ions to the

shutter grid (SG). The distance between the ionization source and the shutter grid is 6.5 cm. The Bradbury-Nielsen type SG was manufactured using tungsten wires (diameter 100 μm) separated by a distance 0.7 mm and it was located at the ninth ring. The opening time of shutter grid was 80 μs . The drift tube consist the 17 stainless steel ring electrodes (diameter of 6.5 cm) isolated by Teflon. The distance between the SG and ion collector is 18.6 cm. The ion collector is shielded by an aperture grid (AG). The ion current measured at the ion collector is amplified using a current to voltage of $2 \times 10^9 \text{ V A}^{-1}$ (FEMTO Messtechnik). To record the IMS spectra we use digital oscilloscope (Tektronix). The SG is controlled by a fast high-voltage transistor switch and is triggered by a TTL generator. Electric potential is reduced by resistors placed between them, and the last electrode was connected to a grounded plate. Electric field intensity of the IMS is 422.8 V cm^{-1} . The experiments were performed at room temperature and atmospheric pressure.

2. Results

To check whether the spectrometer is working properly we have measured pure nitrogen IMS spectrum (Fig. 2).

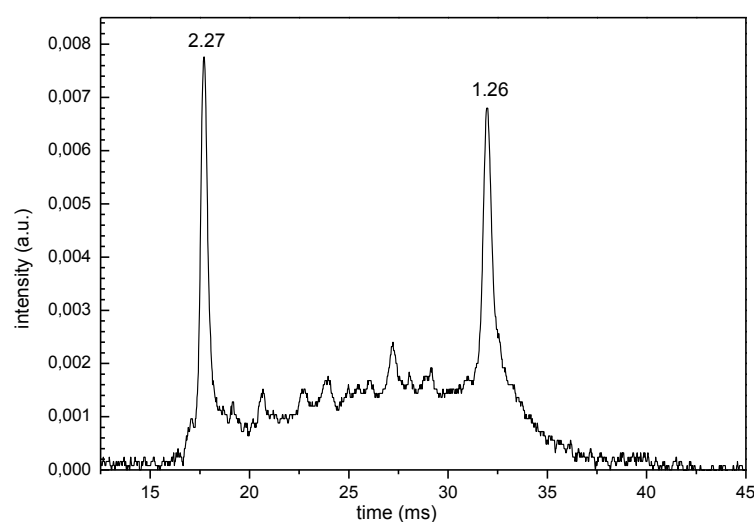


Figure 2. Ion mobility spectrum observed in pure nitrogen.

We observe two very intense signals with drift time 17.7 ms and 39.4 ms. The corresponding reduced ion mobilities of these peaks are $2.27 \text{ cm}^2\text{V}^{-1}\text{s}^{-1}$ and $1.26 \text{ cm}^2\text{V}^{-1}\text{s}^{-1}$. The reduced ion mobility for the first peak corresponds to a literature one [2]. Several smaller peaks may be the result of impurities detection.

We also have measured IMS spectra for a few organic compounds include benzene derivatives to form the base of output spectra for further studies of different organic and bioorganic molecules, for example amino acids, amines, etc.

The sample results for a few of investigated molecules are presented on Fig 3.

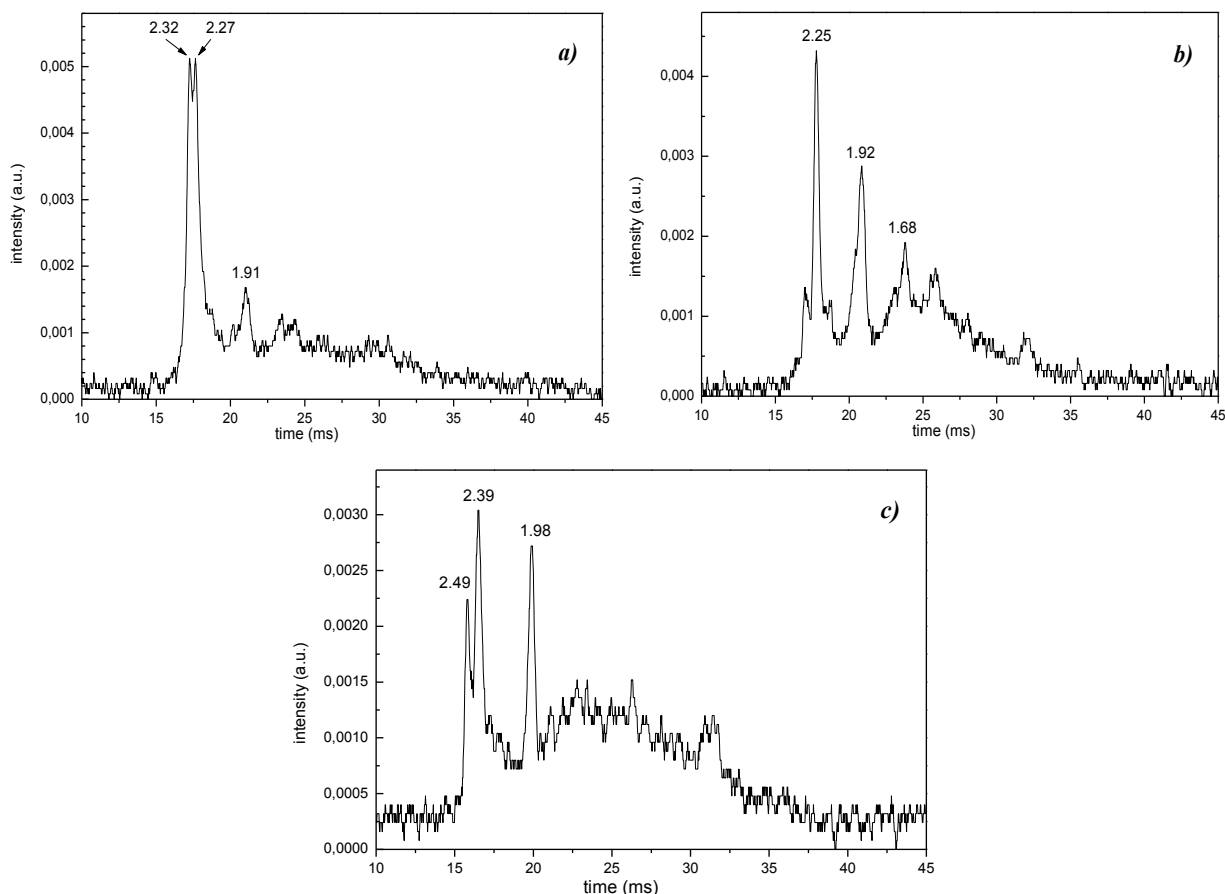


Figure 3. Ion mobility spectra registered for: *a)* nitrobenzene, *b)* bromobenzene, *c)* benzonitrile.

It seems that our spectrometer with radioactive ionization source is a good tool to determine the ion mobilities. The spectra obtained for the benzene derivatives allow for the distinction of generated ions. Further investigation for different kind of compounds will be continued.

3. Acknowledgments

Special thanks to S. Matejcik and M Stano for their help, the design and successful cooperation in the development and launch of our device.

4. References

- [1] G. A. Eiceman, Z. Karpas, H. H. Hill Jr., „*Ion Mobility Spectrometry*”, CRC Press, Taylor & Francis Group, Boca Raton, FL 33487-2742, 2014.
- [2] M. Sabo, Y. Okuyama, M. Kucera, S. Matejcik, *Int. J. Mass Spectrom.* 334 (2013) 19-26.

REACTION AND TRANSPORT OF PLASMA-GENERATED REACTIVE SPECIES IN LIQUID

Kazumasa Ikuse and Satoshi Hamaguchi,

*Center for Atomic and Molecular Technologies, Graduate School of Engineering,
Osaka University, Osaka, Japan.*

E-mail: hamaguch@ppl.eng.osaka-u.ac.jp

When a low-temperature plasma generated in ambient air is exposed to a liquid surface, reactive species are generated in the liquid through the plasma-liquid interface. Such reactive species in the liquid are generally qualitatively and significantly different from those generated in the gas phase by the same plasma. In this study, dynamical equations of mass transport of charged and charge-neutral chemically reactive species in pure water were solved numerically in one-dimension (in the direction of depth) under the assumption that the water surface is exposed to a flux of incident reactive species in the gas phase at room temperature. The model incorporates 37 species and 111 chemical reactions. It has been found from the numerical simulation that a thin boundary layer of a thickness 100 nm ~ 1 μ m is formed just below the water surface, where highly reactive species in the gas phase exist and rapidly generate less reactive species, which are then transported to the bulk liquid by diffusion. Chemical reactions that take place in this layer (which may be called a "reaction boundary layer") play important roles that control generation of less reactive (and therefore long-lived) chemical species in the liquid phase. If biological systems such as bacteria or living tissues exist in liquid, it is such long-lived and less reactive species that may cause biological reactions in those systems.

1. Introduction

Low temperature plasmas have been applied to a wide range of industrial processes such as fabrication of micro and nano-scale structures on the surfaces of semiconductor chips and thin film deposition for surface coating of various materials. Recently, as one of such applications, use of low-temperature plasmas for medical treatment and material processing for medical applications has attracted much attention in the plasma research community. This subfield of plasma science and technology is now collectively called "plasma medicine." Atmospheric-pressure plasma (APP) at room temperature formed in ambient air can produce various species such as ions and free radicals in air. Effects caused by such species on living tissues and cells have been widely studied in the field of plasma medicine.

One of such effects on bacteria is sterilization [1-4]. Including commercial products such as plasma-based air purifiers, plasma sterilization has seen much technological development in recent years in areas beyond medical equipment although the fundamental mechanisms of bactericidal effects by plasmas have yet to be understood better. Furthermore, there are other sources for infectious diseases that are still difficult to remove by plasmas, such as spore forming bacteria, viruses, and prions, and inactivation of them is still a topic of active research. Usually difficulty of treating such pathogens by plasmas lies in the fact that, in reality, removal of them needs to be done without damaging the environments (such as human bodies or medical equipment) where they exist, and often in a cost effective manner.

Chemically reactive species generated by low-temperature APP are also known to have some therapeutic effects such as blood coagulation, angiogenesis, prevention of organ adhesion, and wound healing [5] if they are directly applied to animal or human bodies. Under typical discharge conditions in air, plasma efficiently generates reactive oxygen species (ROS) /reactive nitrogen species (RNS) such as atomic oxygen O, hydroxyl radical OH, hydroperoxyl (or perhydroxyl) radical HOO, singlet oxygen $^1\text{O}_2$, and nitric oxide (or nitrogen monoxide) NO. Such chemically reactive species are often generated from endogenous sources in living bodies and play crucial roles in controlling cell signalling pathways and maintaining homeostasis. In this sense, perhaps it is not surprising that externally

generated ROS/RNS by plasmas can have some significant effects on living cells and tissues under certain conditions.

2. Simulation Model

We have developed a simplified computational model that governs reactions and transport of various chemical species in water facing a gas-phase plasma. The conceptual diagram of the system we consider in this study is shown in Fig. 1. In the model, fluxes of gas-phase species are given as boundary conditions (as functions of time in general). In this study it has been assumed that a plasma is generated in air whose composition is constant in time and uniform in space at the plasma-water interface, so that the system can be modelled as a one-dimensional system in the direction normal to the plasma-water interface (i.e., water surface). At time $t = 0$, gas phase species are assumed to be exposed to the water surface suddenly and concentrations of chemical species that are transported from the gas phase to water as well as those generated in water are evaluated by the numerical simulation. Charge neutral species are assumed to enter water at their thermal velocities whereas fluxes of charged species are specified by their current densities. Typically charged species are assumed to enter water with charge neutrality of water should be maintained. In this study, we usually use data of gas phase species from published literatures (such as [6-8]).

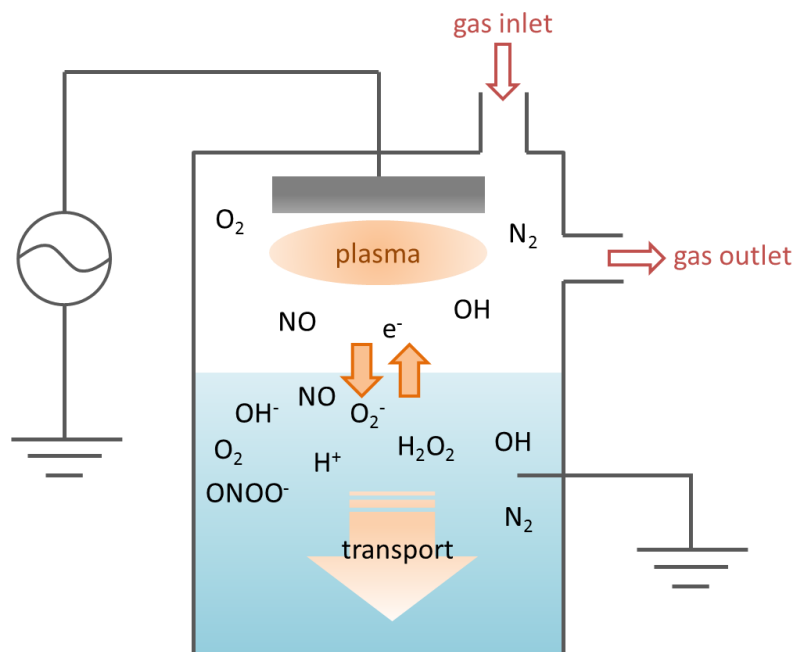


Fig. 1. Conceptual diagram of the system

The governing for reactive species may be derived in the following manner. The concentration of chemical species A is denoted by

$$n_A(t, x) = [A]$$

as functions of time and space. Here the x coordinate represents the direction of depth. Equations of the mass and momentum conservations are then given by

$$\frac{\partial n_A}{\partial t} + \nabla \cdot (n_A \mathbf{v}_A) = R_A$$

$$m_A n_A \frac{d\mathbf{v}_A}{dt} = -k_B T \nabla n_A + q_A n_A \mathbf{E} - \nu_A m_A n_A (\mathbf{v}_A - \mathbf{v}_C)$$

where \mathbf{v}_A and R_A denote the fluid velocity and reaction rates of species A and $m_A, k_B, T, q_A, \mathbf{E}, \nu_A$, and \mathbf{v}_C denote the atomic or molecular mass of species A , Boltzmann constant, water temperature, electrical charge of species A , electric field, collision frequency of species A and water molecules, and the convective flow velocity of water. Here we assume that temperature T is room temperature and uniform in space and constant in time. It should be noted that parameters m_A, q_A, ν_A are also constants and the water velocity \mathbf{v}_C is given (as a function of time and space in general). The above equations are coupled to Poisson's equation

$$\varepsilon \nabla \cdot \mathbf{E} = \sum_k q_k n_k$$

where ε is the dielectric constant of pure water and the right hand side represents the total charge density obtained from the sum of charges of all charged species.

If collisions of chemical species with water are sufficiently frequent, the inertia of the momentum conservation can be ignored, i.e.,

$$d\mathbf{v}_A/dt = 0$$

and then the fluid velocity of chemical species may be written as

$$\mathbf{v}_A = \mathbf{v}_C + \mu_A \mathbf{E} - \frac{D_A}{n_A} \nabla n_A$$

where μ_A and D_A are the mobility and diffusion coefficient, which are related with the parameters defined above as

$$\mu_A = \frac{q_A}{\nu_A m_A} \quad \text{and} \quad D_A = \frac{k_B T}{\nu_A m_A} .$$

From the derivation above, it is clear that Einstein's relation

$$\frac{D_A}{\mu_A} = \frac{k_B T}{q_A}$$

holds between μ_A and D_A . Assuming that the water flow is incompressible, i.e.,

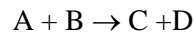
$$\nabla \cdot \mathbf{v}_C = 0$$

and combining the mass conservation equation above with the expression of velocity \mathbf{v}_A above, we obtain

$$\frac{\partial n_A}{\partial t} = R_A - \mathbf{v}_C \nabla n_A - \mu_A \nabla \cdot (n_A \mathbf{E}) + D_A \Delta n_A \quad (1)$$

which is the governing equation of our simulation.

The reaction rate R_A is given in the same manner as that in the global simulation given in, e.g., Ref. [9]. For example, if species A is lost through a chemical reaction



with a rate constant k , then we may write

$$R_A = -kn_A n_B + \dots$$

and \dots represents other source and loss terms for species A .

The outward flux of chemical species from water to the gas phase is determined based on the assumption that, in steady state, it balances with the influx of the same species via Henry's law. The gaseous species entering water are assumed to be dissolved into water without any barrier (e.g. with no reflection from the water surface). In other words, the sticking coefficients of gaseous species at the water surface are assumed to be unity. The rate constants of reactions are cited from NIST online database and other references on biology, pulse radiolysis, and tropospheric chemistry.

The simulations have been performed as a one-dimensional model in the direction from the water surface to the bottom. The model incorporates 37 species and 111 chemical reactions in water at room temperature. The initial condition of the liquid is assumed to be pure water (pH=7) with dissolved oxygen and nitrogen in equilibrium with air at 1 atm. The simulation has been parallelized with Message Passing Interface (MPI) based on the domain decomposition to simulate for many seconds of physical time within the reasonable computational time. Details of reaction rates and other transport coefficients will be published elsewhere.

3. Simulation Results

As a sample simulation, we have evaluated generation and transport of chemical species in pure when 6 gaseous species H_2O_2 , HO_2 , NO , NO_2 , NO_3 , and O_3 that are known to be generated by low-temperature APP enter the water surface for one second. In an actual plasma, many other species, including charged species such as ions and electrons are also generated in the gas phase, we only consider these 6 species for the sake of simplicity. The gas-phase densities of these species at the plasma-water interface assumed for the simulation are summarized in Table 1, where the references from which these densities are quoted from are also listed. Of course, these densities are not derived from a single plasma generated in a particular experiment but the values used here are considered to be within a range of realistic densities of a typical low-temperature APP. All gaseous species are in thermal equilibrium at room temperature and enter the water surface at their thermal velocities. Therefore the dissolving rates given in Table 1 are the same as their fluxes at the plasma-water interface. In the simulation presented here, it is also assumed that there is no water convection, i.e., $\mathbf{v}_c = 0$ and no external electric field is applied. As mentioned earlier, water begins to be exposed to the plasma at $t = 0$.

Figure 2 shows the depth profile of all chemical species present in water at $t = 1$ sec. The horizontal axis represents the position in the direction of depth measured from the water surface in linear scale and the vertical axis represents the concentration of each species in water. It is seen that there are far more species generated in water than those initially supplied to the water surface from the gas phase. It is seen that the dominant species in water are hydrogen peroxide H_2O_2 and nitric acid H^+ and NO_3^- . Charge neutrality is clearly satisfied and the diffusion of charged species such as H^+ , NO_3^- , O_3^- , O_2^- , and OH^- follows the ambipolar diffusion. Since the profiles seen in this figure are expected to expand to the deeper region if the water continues to be exposed to the same gaseous species, the solution is shown to become acidic with a rising concentration of H^+ .

Tab. 1. Gaseous species assumed in the simulation.

species	gas density (mol/L)	references	dissolving rate (mol/cm ² /s)
H ₂ O ₂	1.66 × 10 ⁻⁷	[6]	1.79 × 10 ⁻⁶
HO ₂	4.98 × 10 ⁻¹²	[7]	5.46 × 10 ⁻¹¹
NO	1.66 × 10 ⁻⁸	[6]	1.91 × 10 ⁻⁷
NO ₂	1.33 × 10 ⁻⁸	[8]	1.23 × 10 ⁻⁷
NO ₃	1.66 × 10 ⁻⁸	[8]	1.33 × 10 ⁻⁷
O ₃	1.66 × 10 ⁻⁶	[6]	1.51 × 10 ⁻⁵

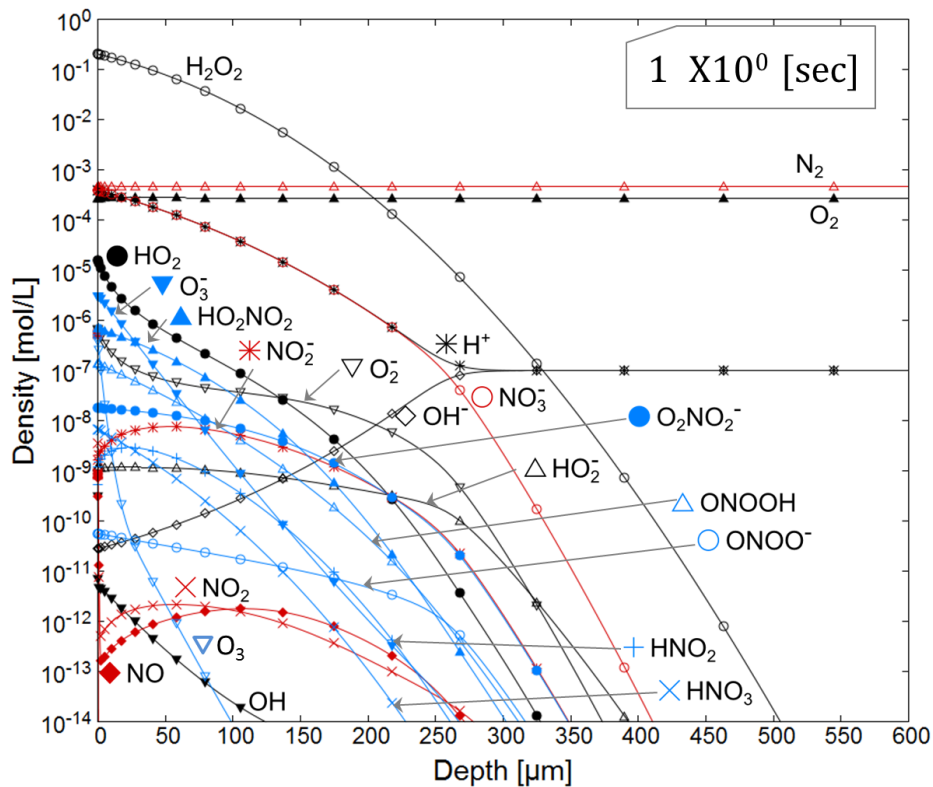


Fig. 2. Concentration profiles of chemical species at $t = 1$ sec. when the water surface has been exposed to the gaseous species given in Tab. 1 since $t = 0$. The horizontal axis represents the depth in linear scale. It should be noted that NO_3 , which is supplied from the gas phase, is not seen at all in this scale.

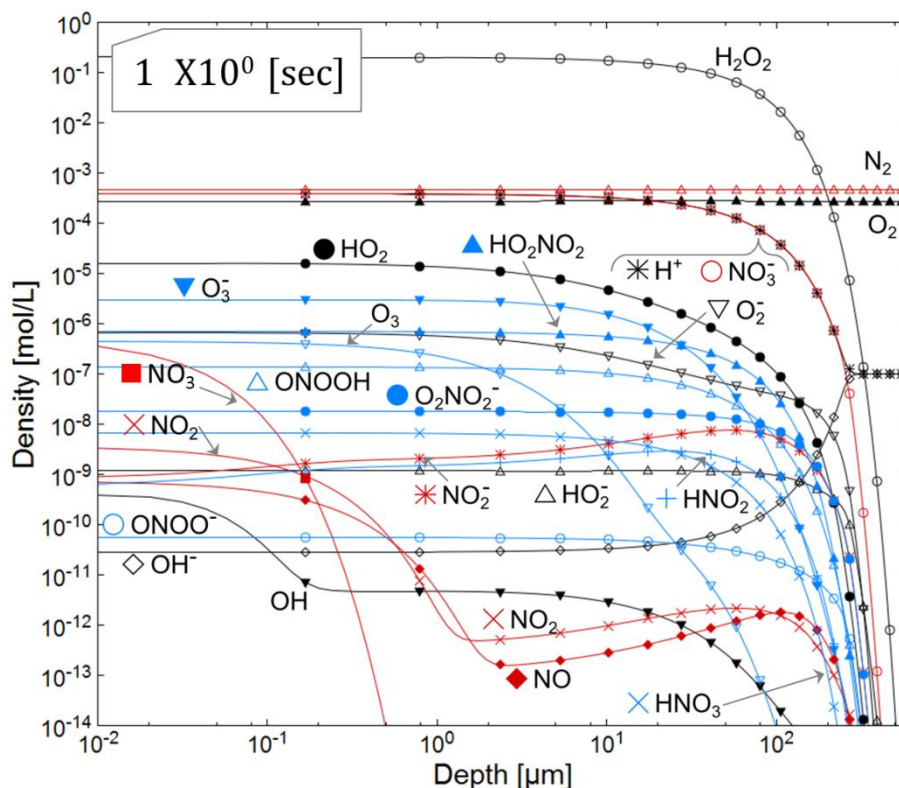


Fig. 3. The same concentration profiles as those shown in Fig. 2. The horizontal axis represents the depth in logarithmic scale. It is seen that concentrations of highly reactive species such as NO_3 , NO_2 , and NO falls quickly in a thin layer of a thickness of 100 nm ~ 1 μm below the water surface. Beyond this layer, which we call the “reaction boundary layer,” NO_3 and NO_2 are generated by different reactions. It is also seen that OH are generated in this system.

Although NO_3 gases are supplied to water, NO_3 is not seen at all in Fig. 2. Also the concentrations of NO and NO_2 , which are supplied from the gas phase, are very low at the plasma-water interface and rise along depth. This indicates that NO and NO_2 at the deeper region are generated by some chemical reactions rather than transported from the surface. It should be also noted that the concentrations of O_3^- , HO_2NO_2 , O_2^- , and ONOOH at the plasma-water interfaces are relatively large and decrease along depth although they are not supplied from the gas phase. This indicates that they are formed in water at or near the water surface. Peroxynitrous acid ONOOH [10,11] is known as a source of OH radicals via homolysis of its O-O bond, i.e.,

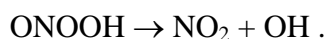


Figure 3 plots the same concentrations of chemical species shown in Fig. 2 with the horizontal axis represented in logarithmic scale. It is seen that concentrations of highly reactive species such as NO_3 , NO_2 , and NO falls quickly in a thin layer of a thickness of 100 nm ~ 1 μm below the water surface. We call this layer the “reaction boundary layer” as most chemical reactions involving highly reactive

species supplied from the gas phase take place in this layer. Beyond this layer, NO_3 and NO_2 are generated by chemical reactions in water.

4. Conclusions

Numerical simulations of chemical reactions and diffusion of reactive species in water exposed to an APP have been performed based on one-dimensional reaction-diffusion equations. When a living tissue is exposed to a low-temperature APP, there is almost always a liquid layer, such as blood, lymph, or other body fluid, that separates the gas phase and the tissue. Therefore charged and chemically reactive species generated by the plasma are transported through the liquid before reacting with the tissue surfaces. The aim of this research is to understand how and where such chemically reactive species that affect biological matters are generated and transported through a liquid. While a variety of ions, excited atoms and molecules as well as chemically reactive charge-neutral species (including free radicals) are generated in the gas phase, the majority of highly reactive species may decay or be converted to more stable species before reaching the liquid surface. On the other hand, charged species and highly reactive charge-neutral species generated in the gas phase near the plasma-liquid interface are likely to be adsorbed by the liquid surface and to generate highly reactive species in a very thin layer (with a thickness of $100 \text{ nm} \sim 1 \text{ }\mu\text{m}$) of liquid just below the liquid surface. In the simulation, gas phase species generated by APP are assumed to enter pure water at their thermal velocities and dissolved without any barrier. The model incorporates 37 species and 111 chemical reactions in water at room temperature. The simulation has indicated the presence of such a thin liquid layer (which we call a “reaction boundary layer”) at the plasma-liquid interface, only in which highly reactive species (such as NO_3 in our sample simulation) exist and rapidly generate less reactive species (such as NO_3^-), which are then transported to the bulk liquid by diffusion.

References

- [1] J. Ehlbeck, U. Schnabel, M. Polak, J. Winter, Th. von Woedtke, R. Brandenburg, T. von dem Hagen, and K.-D. Weltmann, *J. Phys. D, Appl. Phys.* **44** (2011) 013002.
- [2] M. Laroussi, *Plasma Process. Polym.* **2** (2005) 391.
- [3] S. Ikawa, K. Kitano, and S. Hamaguchi, *Plasma Process. Polym.* **7** (2010) 33.
- [4] H. Yasuda, T. Miura, H. Kurita, K. Takashima, and A. Mizuno, *Plasma Process. Polym.* **7** (2010) 301.
- [5] G. Lloyd, G. Friedman, S. Jafri, G. Shultz, A. Fridman, and K. Harding, *Plasma Process. Polym.* **7** (2010) 194.
- [6] R. Sensenig, S. Kalghatgi, E. Cerchar, G. Fridman, A. Shershevsky, B. Torabi, K. P. Arjunan, E. Podolsky, A. Fridman, G. Friedman, J. A. Clifford and A. D. Brooks, *Ann Biomed Eng.* **39** (2011) 674.
- [7] D. X. Liu, P. Bruggeman, F. Iza, M. Z. Rong and M. G. Kong, *Plasma Source Sci. Technol.* **19** (2010) 025018.
- [8] T. Murakami, K. Niemi, T. Gans, D. O'Connell and W. G. Graham, *Plasma Sources Sci. Technol.* **22** (2013) 015003.
- [9] S. Hamaguchi, *AIP Conf. Proc.* 1542 Eighth International Conference on Atomic and Molecular Data and Their Applications ICAMDATA-2012 (ed. by John D. Gillaspay, Wolfgang L. Wiese, and Yuri A. Podpaly) (2013) 214.
- [10] G. Merényi and J. Lind, *Chem. Res. Toxicol.* **11** (1998) 243.
- [11] S. Goldstein and G. Merényi, *Meth. Enzymol.* **436** (2008) 49.

NOVEL INSIGHTS IN THE DEVELOPMENT OF DIELECTRIC BARRIER DISCHARGES

Ronny Brandenburg

¹*Leibniz Institute for Plasma Science and Technology (INP Greifswald)*
E-mail: brandenburg@inp-greifswald.de

Dielectric Barrier Discharges (DBDs) are self-sustaining electrical discharges between at least two electrodes, with the space between these electrodes containing an insulating (dielectric) material and are a typical example of non-thermal (or non-equilibrium) plasmas generated at elevated pressure (i.e. at or around normal pressure). Initially developed for the generation of ozone they have opened up many other fields of application, e.g. surface treatment, degradation of pollutant molecules, pumping of gas lasers, construction of plasma displays and generation of excimer radiation. They have been developed for the biological decontamination of medical devices, air flows, and tissues and are considered as sources for the electric wind in gas flow and aerodynamic control systems. Furthermore, DBD-like plasmas have a great importance for energy transmission networks as so-called partial discharges.

The generation and structure of DBDs is controlled by processes in the discharge volume as well as on surfaces. Depending on the operation conditions filamentary or diffuse discharge regimes can be obtained [1]. The breakdown and discharge development of single discharges can be influenced by means of residual active species (ions, electrons, excited states) in the discharge space. This will be discussed for pulsed operated single DBDs in nitrogen/oxygen gas mixtures [2]. Furthermore, the role of residual surface discharges on the discharge generation and the mechanisms leading to diffuse DBDs will be discussed [3, 4, 5].

- [1] Kogelschatz U 2010 *J. Phys: Conf. Ser.* **257** 012015.
- [2] Höft H, Kettlitz M, Becker M M, Hoder T, Loffhagen D, Brandenburg R and Weltmann K-D 2014 *J Phys D: Appl Phys* **47** 465206.
- [3] Grosch H, Hoder T, Weltmann K-D and Brandenburg R 2010 *Eur. Phys. J. D* **60** 547-553.
- [4] Bogaczyk M, Wild R, Stollenwerk L and Wagner H-E 2012 *J Phys D: Appl Phys* **45** 465202.
- [5] Brandenburg R, Bogaczyk M, Höft, Nemschokmichal S, Tschiersch R, Kettlitz M, Stollenwerk L, Hoder T, Wild R, Weltmann K-D, Meichsner J and Wagner H-E 2013 *J Phys D: Appl Phys* **46** 464015.

RAPE TREATMENT BY THE LOW PRESSURE MICROWAVE PLASMA DISCHARGE AND GLIDING ARC PLASMA

Pavel Olšan¹, Pavel Kříž², Zbyněk Havelka¹, Andrea Bohatá³, Monika Strejčková³, Petr Bartoš^{1,2}, Petr Špatenka^{2,4}

¹*Department of Agricultural machinery and services, Faculty of Agriculture, University of South Bohemia in Ceske Budejovice, Czech Republic*

²*Department of Applied Physics and Technology, Faculty of Education, University of South Bohemia in Ceske Budejovice, Czech Republic*

³*Department of Plant production, Faculty of Agriculture, University of South Bohemia in Ceske Budejovice, Czech Republic*

⁴*Department of Materials Engineering, Faculty of Mechanical Engineering, Czech Technical University in Prague, Czech Republic*

E-mail: pavel.olsan@gmail.com

Low pressure microwave and atmospheric plasma discharge can be used in agricultural applications. Seeds are often contaminated by fungi and their secondary products – mycotoxins. Plasma treatment can reduce the contamination, but germination of seeds is also affected. This paper deals with application of low pressure microwave plasma discharge and atmospheric plasma discharge of Gliding Arc type to influence germination rate of the rape seeds.

1. Introduction

Almost 25 % of the crops is contaminated by fungi and their secondary products mycotoxins. Contamination can be transferred from seeds to feed stuff and food products [1, 2]. There are well known some methods of post-harvesting seed treatment to decontaminate the seeds, such as application of various chemical agents, radiation illumination, ozonation, thermal treatment, gas treatment by chloric oxide or other [3, 4]. Low temperature plasma treatment can be applied as alternative to the chemical and other treatment. Low temperature plasma generates chemical active radicals and high-energy UV radiation which are well known for their sterilization effect [5-8]. The layer of seeds behave as porous material. The reactive particles generated in plasma can easily penetrate through the gaps between individual seeds and interact with the surface of seeds in deeper layer. Thus it is possible to kill various pathogens and their spores with non-equilibrium plasma [9, 10]. Plasma on its own can also sterilize surgical tools [11] and foodstuffs [12]. Therefore the aim of the paper is focused on application two different types of plasma discharge on rape seeds germination. The treatment with better results was also used for consequent pilot field experiment.

2. Experiment

The two types of plasma discharge were used, plasma discharge of Gliding Arc type burned at atmospheric pressure (APD) and microwave plasma discharge generated at low pressure (LPMD). The experimental setup based on APD used in experiments was described in detail in [13]. High voltage transformer (10 kV) with power input 750 W was used as power source operated with frequency of 50 Hz. Compressed air was used as a carrying gas. The overpressure of the flowing gas was maintained at the values about 600 kPa by the air compressor. The air flowmeter Omega was used for sustaining of the carrying gas flow. It is capable to change the air flow in the range from 10 to 100 SCFH (gas flow 1 Nm³.h⁻¹ corresponds to 35.3 SCFH). The airflow was set to 30 SCFH in the experiments. Two stainless steel electrodes are placed into the atmospheric plasma jet. The shape of electrode was rectangular with one rounded corner with diameter of 6 mm. The minimal gap between the electrodes was 2 mm. Electric field distribution in the vicinity of electrodes was in detail described in [14]. The distance between electrodes edges and treated samples was set to 10 cm in the experiments.

Because of completely new electrodes of the plasma jet in the equipment it was necessary to perform some characterization of the plasma. The emission spectrum overview was captured for verifying of

the reactive species presence. Some experiment with distilled water was also performed for proving of the reactive species effect on distilled water pH. The pH of the treated water was measured after every 30 s of treatment duration up to 5 min treatment. Subsequently H_3O^+ ions concentration was calculated. Due to the fact that temperature plays crucial role in the treatment of biological materials some temperature measurement of the plasma discharge was also carried on to determine the adequate temperature distribution along the longitudinal axis of the working gas flow.

LPMD is commonly used for polymeric powder treatment and surface modification (scheme is in Fig. 1). The characteristics of the system were described in detail in [15]. The device consists of stainless steel vacuum chamber of cylindrical shape with inner diameter of 250 mm. Upper and lower side is equipped with a standard ISO K 250 flange. Chamber contains stainless steel blender with a horizontal propeller stirrer. The stirrer axis is placed through a vacuum through-out at the bottom of the reactor. Outside the reactor the electrical engine is placed and moves the stirrer with vertical shaft. The engine adjusts the stirrer speed to approximately one revolution per second. MKS mass flow controllers and VAT regulating valve are used to control the working gas and the working pressure. The microwave plasma is generated from pulsed microwave power unit MNG 1K-08 by Radan Ltd. The air was used as carrier gas with flow of 100 sccm. The working pressure was sustained at the value 100 Pa.

The both types of plasma devices were used to test the treatment influence on the germination of the seeds. The rape seeds were used as model corns. The treatment time was the same for seeds treated by both types of discharges, 3, 5, and 10 min. The amount of the untreated seeds germinated after 7 days after start of experiment was taken as reference value (100 %). The percentage of germinated seeds 7 days was determined with relation to the untreated seeds.

Results proved that the LPMD has a better effect on the germination rate. Therefore LPMD was used for consequent field experiment with the same type of seeds. Three variants of the samples were prepared and sowed in the field. 4 min treated, 8 min treated and untreated variants were sowed in the minimal area of half hectare for each one. The growth of the plants was monitored during the whole vegetation season and per hectare yields were calculated after harvest in the summer.

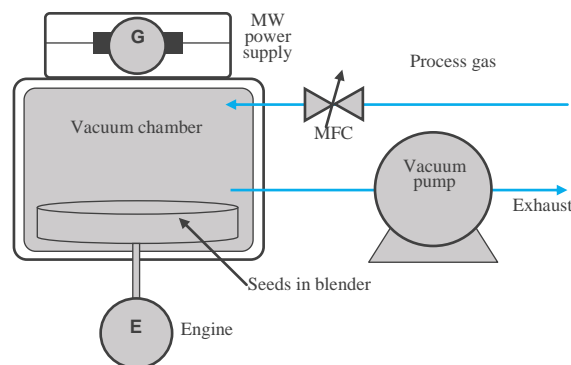


Fig. 1. The scheme of LPMD.

3. Results and discussion

3.1 Atmospheric plasma device characterization

The results of verifying of the reactive species presence and their effect on distilled water are shown in Figs. 2, and 3. Typical spectrum overview of the APD system is shown in Fig. 2. It is evident that the device can be used as source of highly reactive species as OH^\cdot , ozone or atomic oxygen and not only as a source of strong UV light. For example the typical peak corresponding to OH^\cdot band can be seen around the value of 310 nm. Next Fig. 3 shows the H_3O^+ ions concentration in treated distilled water in the dependence on treatment time. It is obvious that treatment has substantial influence on the H_3O^+ concentration and it is increasing almost linearly with the treatment duration.

The results of temperature measurements are demonstrated in Figs. 4, and 5. In Fig. 4 the temperature dependence on distance from electrodes edges is shown. It is evident that for gas flow 30 SCFH the working gas temperature is rapidly decreased with the distance from electrodes and in the distance of 6 cm dropped to approx. half of the value corresponded to 2 cm distance. The downtrend of the temperature with the distance from electrodes is also visible for other flows but it is not as rapid as for 30 SCFH. Fig. 5 shows the analogous situation in case of temperature dependence on working gas flow for various distances from the jet. The very fast temperature fall is well visible in the case of the shortest distance from the jet whereas the temperature downtrend is not so fast for longer distances. Hence it is possible to adjust the temperature of the plasma process by the suitable choices of appropriate working gas flow and distance from the jet.

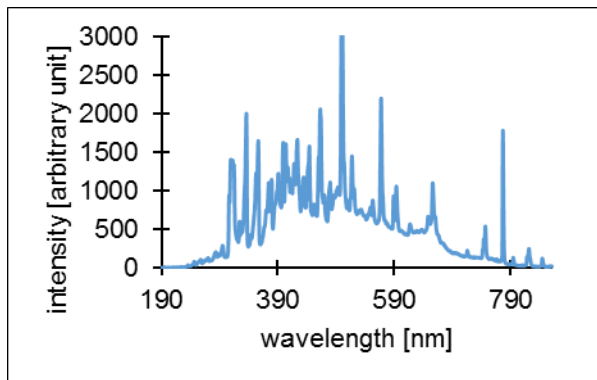


Fig. 2. The spectrum overview of the APD.

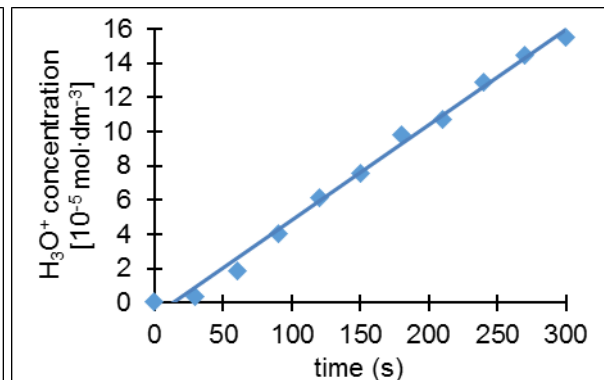
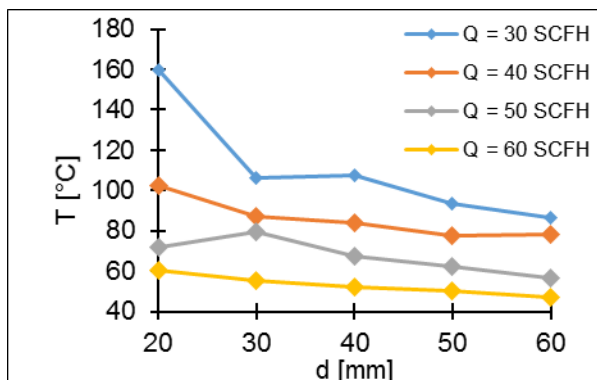
Fig. 3. H_3O^+ concentration dependence on treatment time.

Fig. 4. The temperature dependence on the distance.

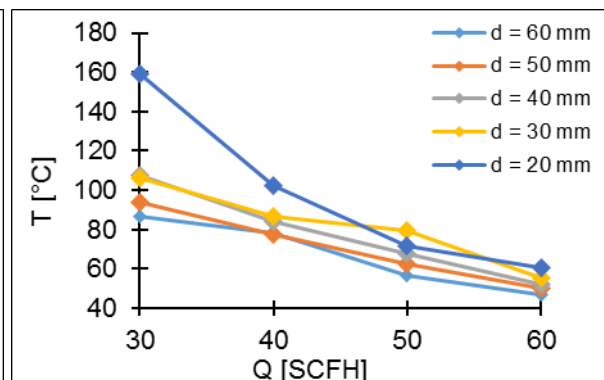


Fig. 5. The temperature dependence on the gas flow.

3.2 Application of plasma on rape seeds

The result of the experiment focused on comparison of both types of plasma discharges is depicted in Fig. 6. The results discovered that the APD markedly reduces the germination rate of rape seeds. It can be caused by relatively high temperature of the plasma jet (see Figs. 4, and 5), which can strongly affect the seeds, mainly oilseeds. The different situation could be in case of cereals treatment but these experiments are the aim of the research in progress in this time.

On the other hand the LPMD shows slight improvement of the germination rate in comparison with untreated seeds. It reaches about 18 % for 5 min or about 6 % for 10 min treatment. It can be very promising for higher yields after harvest. Due to this result LPMD was selected as a main type of plasma discharge for the field experiment.

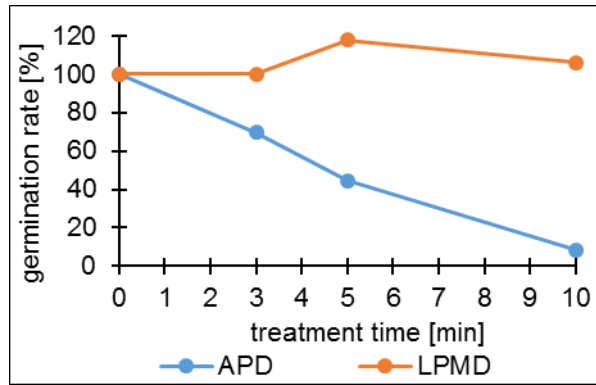


Fig. 6. The germination rate dependence on treatment time for both types of plasma.

Some photos of the area sown by the rape are in Fig. 7. The left side is a snapshot of the field taken in autumn approx. 3 months after sowing. The snapshot does not prove any significant difference between the treated samples and the untreated one (untreated rape on the left, 8 min treated in the middle, 4 min treated on the right). The snapshot of the same field in spring is on the right side of Fig. 7. The boundary line between untreated rape and 8 min treated is well visible. The flowers of rape plants have much more yellow petals on the left side (untreated rape) in comparison with treated rape. It was caused by accelerated growth and plant formation after winter. The plants from treated seeds already lost blossoms and they started to create the seed pods whereas the plants from untreated seeds were only in phase of full blossom.



Fig. 7. The photos of the rape field (left in autumn, right in spring).

The comparison of the per hectare yields is shown in Fig. 8. It is evident that LPMD treatment has a positive effect on the per hectare yield of the rape. The maximal yield was achieved in case of 4 min treated rape and it was about 10 % higher than for untreated rape. In case of 8 min treatment the yield was not so high but it still was about 5 % higher in comparison with untreated one. It is in very good agreement with the test of germination (see Fig. 6) where longer treatment time has not as positive effect as shorter treatment.

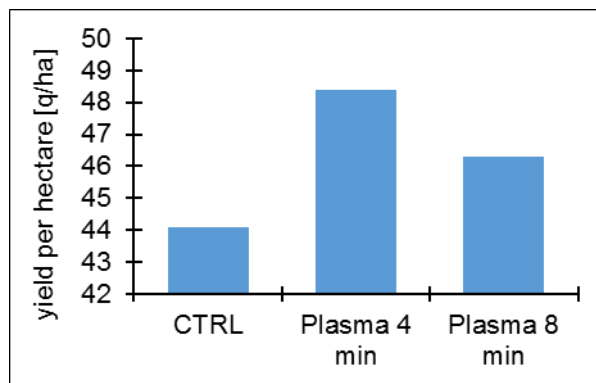


Fig. 8. Per hectare yields after harvest. (CTRL) untreated sample, (plasma 4 min) 4 min treatment, (plasma 8 min) 8 min treatment.

Due to the very good results of the field experiment we decided to repeat it to avoid some anomalies. The rape seeds were treated by LPMD as last year but only for 4 min. In addition some treated seeds were covered by biological substances of two types. The first of them features phytopathogenic activity against fungi (coating 1) the second one features entomopathogenic effect against insects (coating 2). Five variants of the seeds were prepared: raw untreated, only plasma treated, plasma treated and subsequently covered by coating 1, untreated covered by coating 2, and plasma treated and subsequently covered by coating 2. The worst germination rate was achieved in variant that was plasma treated in combination with phytopathogenic coating 1.

The standard laboratory germination test (100 seeds in 2 replicates) was performed for each variant and adequate germination rates after 3 days and 7 days of experiment were determined. The results are depicted in Fig. 9. It is obvious that untreated seeds have very good germination. The third day two variants (only plasma treated and untreated covered by coating 2) have even better germination. The seventh day the germination rate of untreated sample and plasma treated sample without any coating is comparable and it is no longer significant difference. On the other hand plasma treatment combined with coatings noticeably slows down the germination.

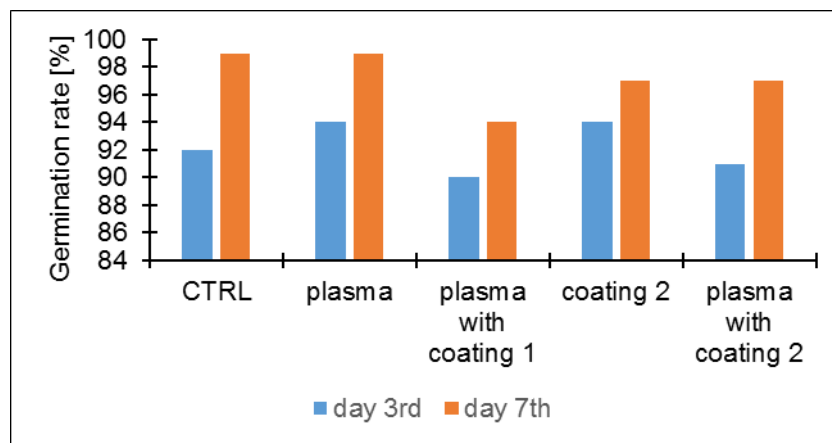


Fig. 9. Three-day and seven-day day germination rate of the rape seeds. (CTRL) untreated, (plasma) only plasma treated, (plasma with coating 1) plasma treated and subsequently covered by phytopathogenic substance, (coating 2) only covered by entomopathogenic substance, (plasma with coating 2) plasma treated and subsequently covered by entomopathogenic substance.

Each of prepared variant is sown in the field in recent time and their growth is monitored. The yields per hectare will be calculated again after harvest in the summer next year and it will be compared to the results obtained this year.

4. Conclusion

The APD has a strong negative effect on the germination of the rape seeds. On the other hand decrease of the germination can be related to better plasma effect on seed decontamination and protection against fungi (the research in this field of interest is in intensive progress in recent time). It can be very important in application for treatment of the seeds intended as man food or animal feed.

The LPMD has a positive effect on germination of the rape seeds. It causes that the germination rate increases up and this leads to higher yields during the harvest. The germination rate is higher in case of the only plasma treatment in comparison to combination with any biological coating.

5. Acknowledgement

This work has been supported by the Technology Agency of the Czech Republic – grant number TA04021252, and by the Grant Agency of University of South Bohemia – projects 102/2013/S and 020/2013/Z. The lend of the Surface Treat, Inc. facilities is highly appreciated.

6. References

- [1] K. Lancová, et al., *Food Additives & Contaminants: Part A*, vol. 25, pp. 732-744, 2008.
- [2] M. Kostelanska, et al., *Journal of Agricultural and Food Chemistry*, vol. 57, pp. 3187-3194, 2009.
- [3] R. Bhat, et al., *Comprehensive reviews in Food Science and Food Safety*, vol. 9, pp. 57-81, 2010.
- [4] P. Karlovsky, et al., *Applied Microbiology and Biotechnology*, vol. 91, pp. 491-504, 2011.
- [5] O. Kylian, et al., *Journal of Physics D: Applied Physics*, vol. 41, 2008.
- [6] K. Stapelmann, et al., *Journal of Physics D: Applied Physics*, vol. 41, 2008.
- [7] M. Moisan, et al., *Pure and Applied Chemistry*, vol. 74, pp. 349-358, 2002.
- [8] G. Fridman, et al., *Plasma Process and Polymers*, vol. 5, pp. 503-533, 2008.
- [9] M. Laroussi, et al., *IEEE Trans. Plasma Sci.*, vol. 30, pp. 1501-1503, 2002.
- [10] L. F. Gaunt, et al., *IEEE Trans. Plasma Sci.*, vol. 34, pp. 1257-1269, 2006.
- [11] T. C. Montie, et al., *IEEE Trans. Plasma Sci.*, vol. 28, pp. 41-50, 2000.
- [12] M. Vleugels, et al., *IEEE Trans. Plasma Sci.*, vol. 33, pp. 824-828, 2005.
- [13] P. Kříž, et al., in *Proceedings of the International Conference on Optimization of Electrical and Electronic Equipment (OPTIM)*, pp. 1337-1340, 2012.
- [14] P. Bartoš, et al., in *Proceedings of the International Conference on Optimization of Electrical and Electronic Equipment (OPTIM)*, pp. 999-1004, 2014.
- [15] J. Hladík, et al., *Czechoslovak Journal of Physics*, vol. 5, pp. 1120, 2006.

UNDERSTANDING OF HYBRID PVD-PECVD PROCESS WITH AIM TO CONTROL GROW OF NANOSTRUCTURED COMPOSITE COATINGS

Petr Vasina¹, Tereza Schmidtova¹, Pavel Soucek¹, Radek Zemlicka¹,
Petr Vogl², Mojmír Jilek²

¹*Department of Physical Electronics, Faculty of Science, Masaryk University,
Kotlářská 2, CZ-61137, Brno, Czech Republic*

²*Platit a.s., Průmyslová 3, CZ-78701, Šumperk, Czech Republic*

E-mail: vasina@physics.muni.cz

Hybrid PVD-PECVD process is used for preparation of superhard metal carbon nanocomposites or low-friction low-stress DLC layers. The aim of this paper is to describe and understand non-monotonous dependence of cathode voltage, discharge current and other quantities on acetylene supply which was observed to take place at both laboratory scale device with planar magnetron and industrial scale device with rotating cylindrical cathodes.

Hybrid Physical Vapour Deposition – Plasma Enhanced Chemical Vapour Deposition (PVD-PECVD) process of titanium sputtering in argon and acetylene atmosphere combines aspects of both conventional techniques: sputtering of titanium target (PVD) and supply of acetylene gas into the plasma-chemical deposition chamber as a source of carbon (PECVD). This process can be used for preparation of metal carbon nanocomposites (n-TiC/a-C(:H)) or DLC layers doped with metal (DLC:Ti). Typically optimized n-TiC/a-C(:H) coatings show hardness over 40 GPa, reduced Young's modulus over 300 GPa and internal stress lower than -1 GPa [1]. High carbon content coatings (DLC:Ti) show friction coefficient lower than 0.1 and wear rate below $2 \cdot 10^{-7}$ mm³/Nm [2]. The deposition rate of the hybrid PVD-PECVD process is satisfactory comparing to low deposition rates at co-sputtering experiments and moreover, the hybrid PVD-PECVD process shows many advantages such as the possibility to easily prepare gradient layers at high deposition rates or to switch the industrial deposition process conventionally used for the production of TiN coatings to preparation of n-TiC/a-C:H layers simply by changing the reactive gas. For the specific case of the titanium target sputtering in hydrocarbon containing atmosphere there exists variety of papers that are focused on the influence of process parameters on properties of deposited coating. Deposition process features are however often omitted.

Behaviour of the hybrid PVD-PECVD process was compared to the conventional reactive magnetron sputtering. Even though the addition of the hydrocarbon is very similar to the adding of oxygen or nitrogen as a reactive gas in reactive sputtering, it was found [3] that hysteresis behaviour typical for reactive magnetron sputtering described by Berg model [4] was completely suppressed during the hybrid PVD-PECVD process. Therefore, the hybrid PVD-PECVD depositions do not require complex feedback control. The absence of the hysteresis region was explained [3] by the capability of surfaces to be covered by thick carbon rich layers. In these thick carbon rich layers the carbon atoms can be bound mutually in contrary to metal oxides/nitrides formation on surfaces during classical reactive magnetron sputtering where oxygen/nitrogen can be bound only to the metal. Nevertheless, the target covering by these carbon rich layers during the hybrid PVD-PECVD process is still similar to the target poisoning by a reactive gas, because it prevents the sputtering of the metal. So for description of both the processes the phrases 'target poisoning' and 'target cleaning' can be understood and used.

The aim of this paper is to describe and understand elementary processes influencing the hybrid PVD-PECVD process and to use the knowledge to control the deposition process at both laboratory

and industrial scale. Laboratory measurements were performed using laboratory magnetron sputtering system Alcatel SCM 650. A planar titanium target (purity 99.99%) 20 cm in diameter was mounted on a well balanced magnetron head and sputtered in mixture of argon (purity 99.999%) and acetylene (purity 99.6%). DC generator operated in constant power mode was used to drive the deposition plasma. Figure 1 shows the dependences of cathode voltage on the acetylene supply flow for 2 kW DC power applied on the magnetron target. The full black square points denote the measured values with increasing acetylene flows - on the way from the clean target. When measuring with the decreasing acetylene flows, the cleaned target was exposed for 3 min to 30 sccm of C₂H₂ for full poisoning; the hollow red circle points denote measured values with decreasing acetylene flows - on the way from the poisoned target. Fig. 1 demonstrates that the hybrid PVD–PECVD process does not exhibit hysteresis behaviour typical for reactive magnetron sputtering [3,4]. The discharge voltage is however non-monotonous; three zone behaviour with a certain local minimum is observed [5].

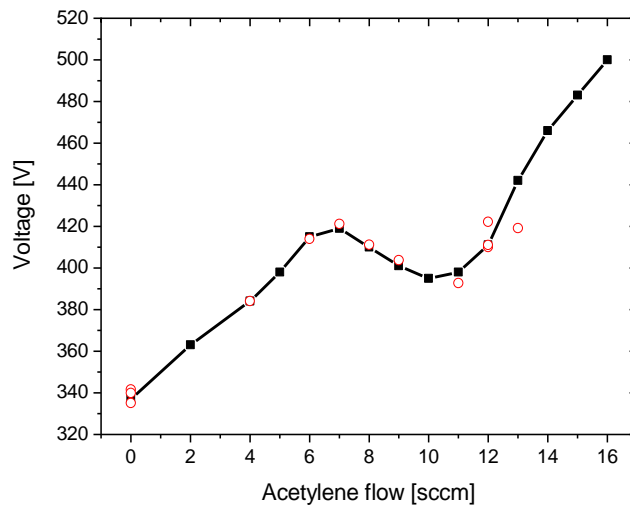


Fig. 1: Evolution of discharge voltage with acetylene supply, planar magnetron.

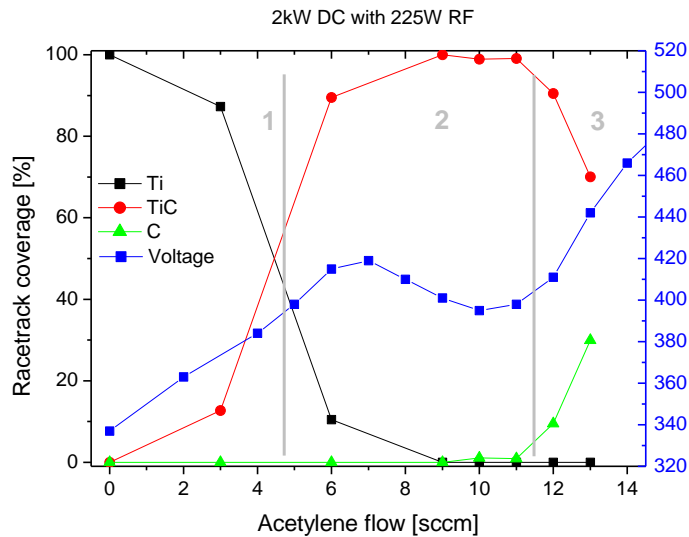


Fig. 2: Racetrack coverage by Ti, TiC and C as a function of acetylene supply. Voltage characteristics with three zones behaviour is correlated with plotted racetrack coverage, planar magnetron.

For reactive magnetron sputtering, it was reported [6] that the discharge voltage is related to the state of the target; the target poisoning by a compound (oxide or nitride) of different coefficient of secondary electron emission from the original target material results in a change in the target voltage. In classical reactive magnetron sputtering the cathode voltage decreases/increases monotonously with the partial pressure of the reactive gas as the target gets monotonously covered by compound. However the discharge voltage plotted in Fig. 1 shows distinctive evolution on the acetylene flow. A characteristic local minimum was observed. The pressure was observed to evolve only a little with C_2H_2 supply, so its influence on the electrical characteristics should be negligible and the presence of the local minimum should be related to the evolution of the state of the target in a different way during hybrid PVD-PECVD process than during classical reactive magnetron sputtering.

In the following set of experiments, the hybrid PVD-PECVD process was operated at constant acetylene supplies and after the steady state was reached, the chamber was opened and the target surface was photographed. Typically, the photograph revealed that the target was covered by three differently 'coloured' regions. The following can be distinguished: a metallic region, a black region, and a grey region. The metallic region is of the same colour as the original titanium target, so it is denoted as titanium (Ti). The black layer which was easily removable by hand or an abrasive resembles the soots and so it is denoted as carbon (C). The grey region which is matt, compact and very difficult to remove by an abrasive is a transition between the metallic and black regions. It is similarly coloured to titanium carbide so this region is denoted as titanium carbide (TiC). Calculation of the relative target racetrack coverage by Ti, TiC and C parts was performed by the software counting of pixels of corresponding colours. Figure 2 shows the racetrack coverage percentages together with discharge voltage evolution as a function of the acetylene supply. At the range of C_2H_2 supply from 0 to 6 sccm, Ti regions are diminishing on behalf of TiC regions. Between 6 and 12 sccm of C_2H_2 the racetrack is composed mainly by TiC region. For higher flows of C_2H_2 the TiC parts are overtaken by C, the racetrack becomes carbon rich. Combining information from discharge voltage characteristics with the racetrack coverage we can conclude that the voltage increase between 0 and 6 sccm of C_2H_2 is connected with the creation of TiC on the target racetrack. Between 6 and 12 sccm of C_2H_2 presence of local minimum in the discharge voltage should be related with the evolution of TiC. Invoking the phase diagram of Ti-C, we suppose the voltage decrease to be caused by the evolution of the TiC stoichiometry in the racetrack region from the substoichiometric TiC (at 6 sccm of C_2H_2) to stoichiometric TiC (around 11 sccm of C_2H_2). The rapid voltage increase at acetylene flows higher than 12 sccm is clearly related to the carbon formation in the racetrack. Qualitative analyses of the target composition evolution by EDX technique agreed well with the proposed explanation [5].

Hybrid PVD-PECVD process of Ti sputtering in mixture of Ar and C_2H_2 was also studied performing experiments with an industrial coating machine developed by the Platit company. A single central rotating cylindrical titanium cathode (size $\varnothing 110 \times H 510$ mm) was driven by 20 kW DC power. Fig. 3 depicts the evolution of the cathode voltage and pressure in the deposition chamber with acetylene supply. Increasing the acetylene supply from 0 to 25 sccm caused the the cathode voltage to increase. Further increase in the acetylene supply led to the slow cathode voltage decrease, probably in response to the pressure increase. At a critical acetylene supply of approximately 55 sccm, a sudden drop in the cathode voltage is observed, and further increase in the acetylene supply leads to another gradual decrease of the cathode voltage. To compensate for the reduction of the observation-window transparency during the long deposition process, the line-intensity ratios of Ti (521 nm) to Ar (750 nm) and H (656 nm) to Ar (750 nm) were monitored. The drop in the cathode voltage is accompanied by a drop in the Ti/Ar line-intensity ratio; however, the H/Ar line-intensity ratio reaches a maximum at this moment, see Fig 4. At the same moment, the increasing trend of the pressure with the increasing acetylene supply terminates, and after the drop of the cathode voltage, the pressure decreases as the acetylene supply increases. We suppose that when the critical acetylene supply is reached, the whole target surface undergoes a phase transition from Ti/TiC to TiC, according to the phase diagram. As the phase composition of the target surface changes, the secondary electron emission coefficient also changes, and to sustain the magnetron discharge at the desired power, a lower voltage must be applied. The phase-composition change from Ti/TiC to TiC leads to lower sputtering of titanium atoms from the magnetron target, which is indicated by the drop in the optical emission spectral lines of titanium. During the voltage drop, the coating composition changes from titanium rich to carbon rich [7], and the amorphous carbon matrix grows extensively alongside the TiC phase. The a-C matrix can

accommodate hydrogen into the coating, which causes a decrease in the hydrogen optical emission and also in the pressure itself.

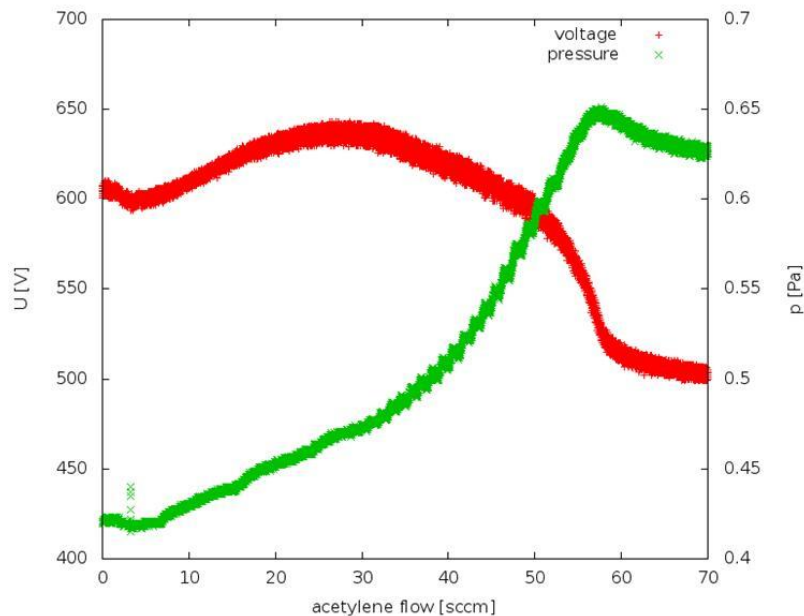


Fig. 3: Evolution of discharge voltage and pressure for sputtering of titanium target while acetylene supply was slowly linearly increased from 0 to 70 sccm at rate of 0.15 sccm/min, rotating cylindrical magnetron.

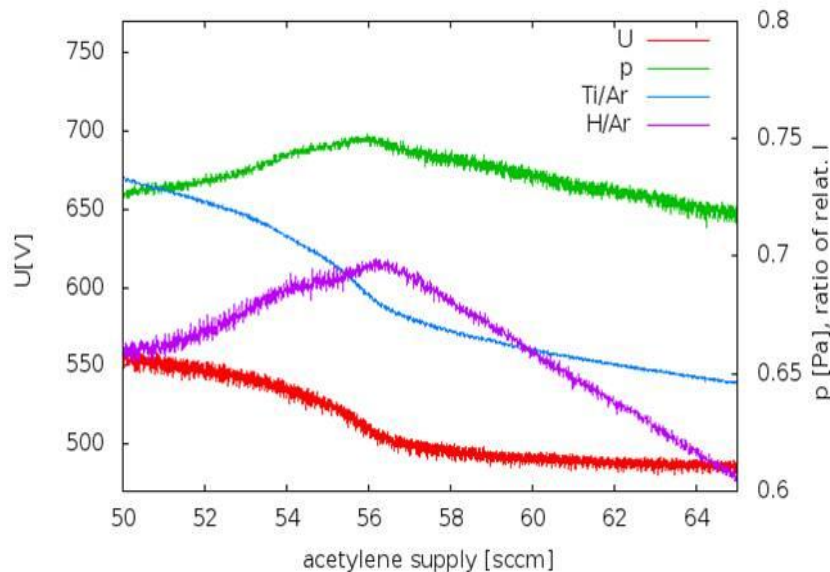


Fig. 4: Evolution of discharge voltage, pressure and ratios of Ti(521 nm) /Ar(750 nm) and H(656 nm)/Ar(750 nm) optical emission lines while acetylene supply was slowly linearly increased from 50 to 65 sccm at rate of 0.3 sccm/min, rotating cylindrical magnetron.

The sudden drop in the cathode voltage observed in Figs 3,4 for central rotating cylindrical titanium cathode resembles the observed evolution illustrated in Fig. 1 for planar magnetron; however, in the case of sputtering of the cylindrical magnetron, the voltage drop was very sudden, while in the case of sputtering with a planar magnetron, a gradual decrease in the cathode voltage was observed. This difference in behaviour can be explained as follows. In a hybrid PVD-PECVD process, the target is exposed to a flux of carbonaceous species originating from acetylene dissociation, which causes the poisoning of the titanium target with carbon. Simultaneously, the target is being sputter cleaned by Ar-ion bombardment. A cylindrical rotating target is equally influenced by target cleaning and target

poisoning over almost its entire profile, and the average target composition is expected to be constant over the entire target surface. Consequently at certain critical acetylene supply, the whole target surface can undergo a phase transition from Ti/TiC to TiC and as the phase composition of the target surface changes, the secondary electron emission coefficient also changes, and to sustain the magnetron discharge at the desired power, a lower voltage must be applied. However, in the case of a planar magnetron, there exists a position-dependent evolution of the target's surface composition from the racetrack centre, which is very intensively sputter cleaned, to its edges, which become poisoned even at very low acetylene supplies. Thus, the gradual evolution of the process parameters observed for the planar magnetron are caused by the gradual change of the phase composition of the target surface, while in the case of a rotating cylindrical magnetron, this phenomenon manifests as a sudden change in the process parameters caused by a sudden change in the phase composition of the entire target surface. The non-monotonous behaviour of the process is used to determine the optimal supply of acetylene gas to always lead the process to the required state to growth hard titanium-carbon coatings at an industrial scale device.

This research has been supported by GACR contract 205/12/0407 and project R&D center for low-cost plasma and nanotechnology surface modifications CZ.1.05/2.1.00/03.0086 funded by the European Regional Development Fund.

References

- [1] P. Souček, et al. *Surf Coat. Technol.* 211 (2012) 111
- [2] J. Musil et al., *J. Vac. Sci. Technol. A* **28**, (2010) 244
- [3] T. Schmidtová et al. *Surf Coat. Technol.* **205** (2011) S299
- [4] S. Berg et al. *Thin Solid Films* **476** (2005) 215
- [5] T. Schmidtová et al., *Surf Coat. Technol.* **232** (2013) 283
- [6] D. Depla et al., *Thin Solid Films* **517** (2009) 2825
- [7] R. Žemlička et al. *Surf Coat. Technol.* (2014) accepted

INVESTIGATION OF METAL COATED HIGHLY ORDERED PYROLITIC GRAPHITE

Stefan Ralser¹, Stefan Raggl¹, Martina Harnisch¹, Paul Scheier¹

¹*Institute of Ion Physics and Applied Physics, University of Innsbruck, A-6020, Innsbruck, Austria,
E-mail: Stefan.ralser@uibk.ac.at*

In this work tungsten coated HOPG (highly ordered pyrolytic graphite) surfaces were investigated by means of scanning tunnelling microscopy. The coating was performed via magnetron sputtering deposition. Previous works [1, 2] showed, that other materials like silicon or titanium could easily be manipulated with the help of the STM tip, whereas the tungsten layer is not affected at all during the manipulation process, even under extreme tunnelling conditions.

1. Motivation

High melting metals like tungsten or molybdenum are used in a wide range of applications. Especially tungsten is planned to be used as a plasma facing component in the fusion reactor ITER [3, 4]. In this application, the tungsten surface has to withstand a high heat load and evaporation processes of surface material have to be minimized in order to not contaminate and cool down the fusion plasma. On the other hand, thin metal or semiconducting films are used in wafer production where the nanoscale-surface structure and its physical properties play an important role. Especially for thin-film transistor liquid crystal displays (TFT-LCD) and as the contact material for high efficiency solar cells molybdenum turned out to be an interesting material. In this work we investigate such surfaces and concentrate on local heat load deposition with the help of an STM tip.

2. Experimental Setup

The experiment consists of two parts. In the preparation chamber the HOPG sample is placed in front of a low pressure DC magnetron sputter source and is coated for several minutes at a sputter current of up to 70mA. This leads to a thin layer of tungsten clusters with a radius of about 2-3 nm on the HOPG surface. As a sputter target material we use 99.97% pure tungsten (Plansee Group). The prepared surface is then transferred into an Omicron[®] variable-temperature STM without breaking the vacuum, and measured with the help of a tungsten STM tip. As shown in [1], a local heat load can be applied to the sample by using high tunnelling currents which enables the investigation of cluster evaporation processes.

3. Results

Figure 1 shows three measurements of the tungsten-coated sample under different tunnelling conditions. The size of the images is 100 nm x 100 nm each. For the different images, tunnelling conditions were constantly raised from low (a) to extremely high (c) tunnelling currents.

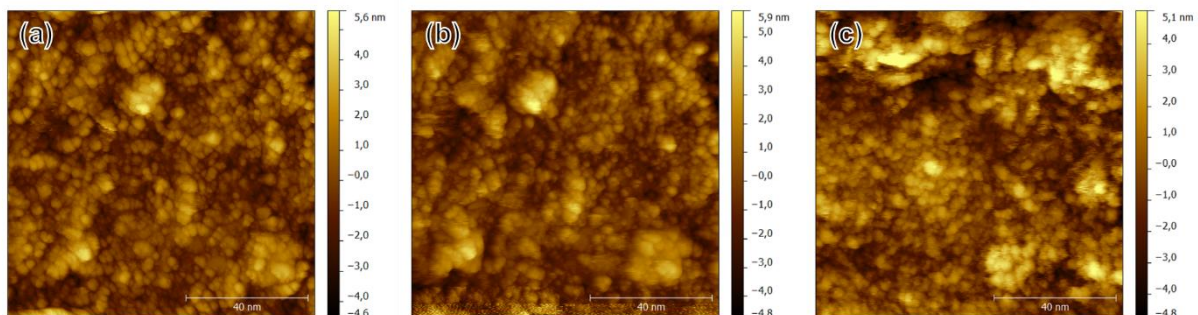


Fig. 1. STM topographs of a tungsten coated HOPG sample under different tunnelling conditions. The size of the images are 100 nm x 100 nm. Even very high tunnelling currents do not result in a manipulation of the surface. The bias voltages were -0.6 V for images (a) and (c) and -2.7 V for image (b). The tunnelling currents were 20 pA (a), 1 nA (b) and 100 nA (c).

In the case of a silicon-coated sample evaporation of surface material could already be achieved with a bias voltage of 2.7 V and a tunnelling current of 1 nA. Depending on the manipulation time, it was possible to remove a few monolayers of the material up to the entire silicon film, and to resolve the underlying HOPG structure atomically. These conditions correspond to image (b) in figure 1. It can be seen, that no manipulation has been taken place. The tungsten layer remains unaffected, even when very high currents of up to 100nA were applied during the manipulation process. Further raising of the current resulted in a demolition of the STM tip rather than a surface manipulation. The measurements underline the high heat resistance of the tungsten layer and show that even a locally applied heat load does not result in material evaporation. Similar experiments are currently investigated with molybdenum coated HOPG.

4. References

- [1] Hager M. et al. 2013 *Chemical Physics* 425 141–147.
- [2] Schrittwieser R. et al. 2010 *J. Plasma Physics*, vol.76, 655–664.
- [3] Bartels H.-W. 2000 *Fusion Engineering and Design* 51 – 52 401 – 408.
- [4] Aymar R. et al. 2002 *Plasma Phys. Control. Fusion* 44 519–565.

ELECTRICAL CHARACTERIZATION OF HYDROGEN MICRODISCHARGES FROM DIRECT CURRENT UP TO 13.56 MHz

Matej Klas¹, Ladislav Moravský¹, Štefan Matejčík¹

¹Department of Experimental Physics, Comenius University, Mlynská dolina F-2, 842 48 Bratislava, Slovakia

E-mail: matej.klas@gmail.com

This paper we present results of experimental investigations of the direct current up to radio frequency (RF) breakdown voltage curves in hydrogen. Electrical characterization (Paschen curves, V/I waveforms) were collected for low frequency and high frequency at different condition of pressure and distances. All measurements were performed with a molybdenum parallel-plane electrodes melted in glass separated from $2.5\mu\text{m}$ to $100\mu\text{m}$ for the pressures range from 40mbar up to 930mbar. Additionally, optical emission spectroscopy analyses were obtained.

1. Introduction

Radio frequency low pressure plasma is extensively used as a source of energetic ions, chemically active species, radicals and also energetic neutral species in many industrial processes including microelectronics, semiconductors, aerospace or biology [1-3]. In recent years, RF driven atmospheric-pressure glow discharge APGD plasmas have received an increasing amount of attention as an alternative to low pressure glow discharges. However, with increasing pressure and frequency, discharge are much more susceptible to rapid transition into a constricted γ - mode. Essential parameters for a control transition from α -mode into γ -mode and sustained glow discharge at higher pressure is a frequency and electrode distance [4,5]. Breakdown of gases at micrometer separation at radio frequency is still not well known thus the aim of the present research is to extend investigations of the RF discharges at high pressure towards the microdischarges generated from $2.5\mu\text{m}$ up to $100\mu\text{m}$ from low up to atmospheric pressure.

2. Experimental setup

The experimental apparatus consisted of two parallel molybdenum cylinders (diameter of 2mm) melted in glass. Fig. 1 The plasma was maintained by supplying AC/DC power to the bottom electrode, while the top electrode was grounded. A current and voltage IV probe was attached directly to the source, eliminating any cable connections, which might add inductance to the system. Probes were connected to an oscilloscope (Agilent DSO5032A) a calibrated with procedure to ensure accurate phase and power measurements [6].

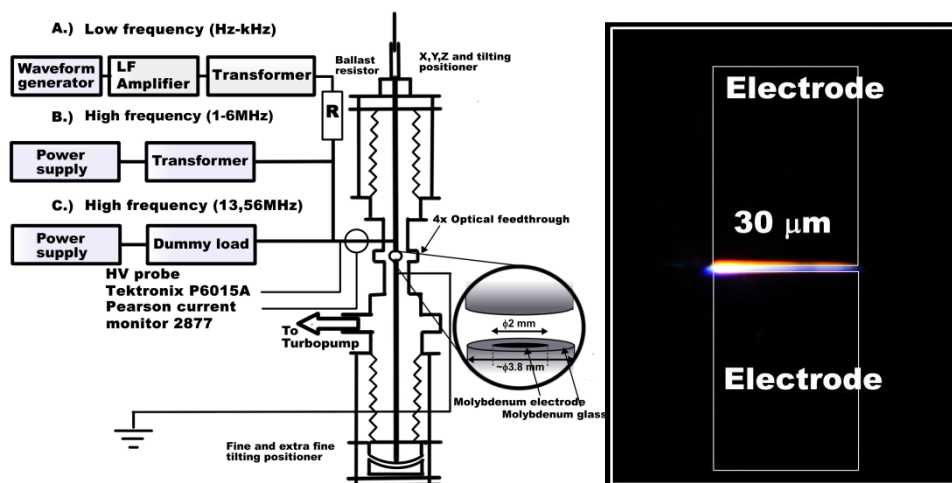


Fig.1 Schematic of the experimental apparatus (left) and picture of hydrogen discharge at $f=4.3\text{MHz}$, $p=930\text{mbar}$ and $d=30\mu\text{m}$

3. Results and Conclusion

In Fig. 2 are shown the Paschen curves at atmospheric pressure (930mbar) from DC up to 13.56 MHz for electrode distance ranging from 2.5 μm up to 100 μm . The general shape of AC curves agrees with that obtained for dc discharge. At low frequencies (100Hz -10kHz), breakdown process is basically the same as in case of static field due to short transit time of electrons cloud compare to the period of the field. Thus, breakdown voltages obtained for low frequencies are identical with DC measurements. For higher frequencies a significant lowering of voltage can be observed explained by the incomplete removal of the electrons and ions from the gap during half period of the field [7].

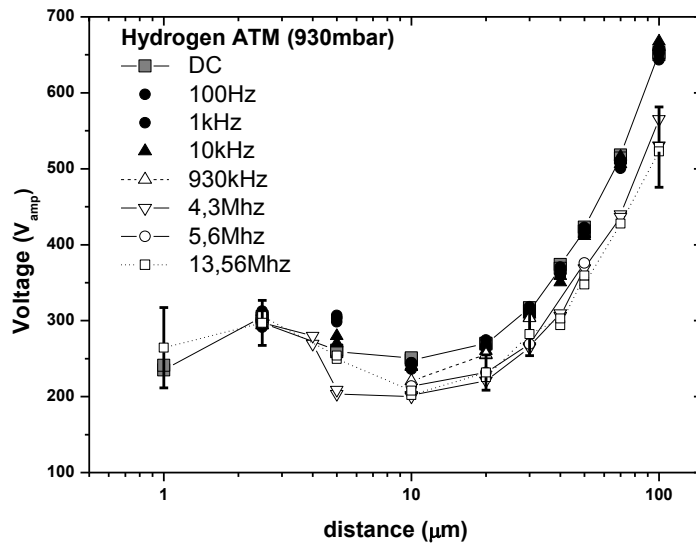


Fig.2 Paschen curve for Hydrogen at 930mbar and different electrode separation

In Fig. 3 we present current and voltage waveforms for 5 μm and 100 μm electrode separation at 4,3MHz. Both waveforms show the process at the beginning of the discharge breakdown. Immediately after breakdown a ringing occurs with a self frequency of $\sim 70\text{MHz}$ due to parasitic capacitance and inductance of wires and probes within chamber. Stabilization of discharge is only visible in case of 100 μm probably due to space limitation and fast losses of charge particles with electrode walls at electrode distance of 5 μm . From V-I waveform it is clearly seen a distortion of voltage due to formation of space charge between electrodes with similar behavior observed in low pressure glow discharges.

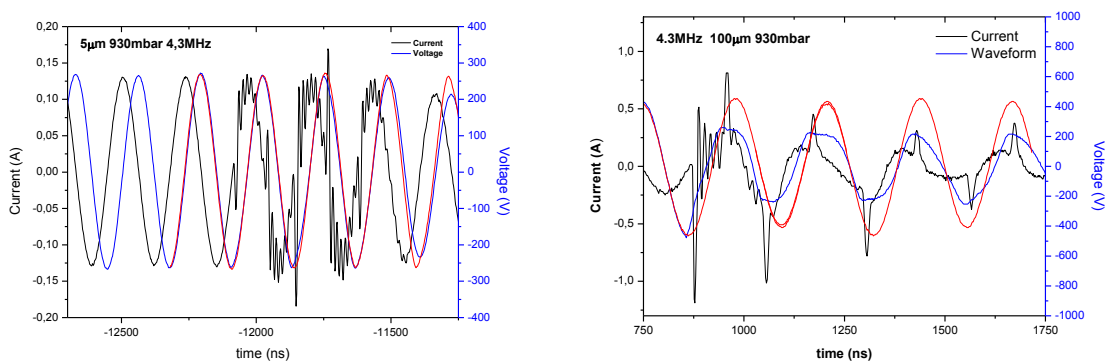


Fig. 3 V-I waveform for different electrode distances at frequency of 4.3MHz

Acknowledgements

This work was supported by Slovak Research and Development Agency, project Nr. APVV-0733-11 and VEGA 1/0514/12.

4. References

- [1] K.H. Becker, U. Kogelschatz, K.H. Schoenbach, R.J. Barker 2005 *Non-equilibrium Air Plasmas at Atmospheric Pressure* Institute of Physics Publishing, Bristol
- [2] E. Valderrama, M. Favre, H. Bhuyan, H.M. Ruiz, E. Wyndham, J. Valenzuela, H. Chuaqui. 2010 *Surf. Coat. Technol.*, **204**
- [3] M.L. Hoey, J.B. Carlson, R.M. Osgood, B. Kimball, W. Buchwald 2010 *Appl. Phys. Lett.*, **97**
- [4] Walsh, J.L., Iza, F. And Kong, M.G., 2008 *Applied Physics Letters*, **93** 251502
- [5] Muehe Ch, 1965 *AC Breakdown in Gasses*, M.I.T. Lincoln Laboratory
- [6] Spiliopoulos, 1996 *Journal of Vacuum Science and Technology* **A14**, 2757
- [7] Llewellyn Jones, *Electrical discharge*, 1953

CHARACTERIZATION OF A NON-EQUILIBRIUM ATMOSPHERIC PRESSURE PLASMA JET DRIVEN BY NANOSECOND VOLTAGE PULSES

Marco Boselli¹, Vittorio Colombo^{1,2}, Matteo Gherardi², Romolo Laurita², Anna Liguori², Paolo Sanibondi², Emanuele Simoncelli², Augusto Stancampiano²

¹*Interdepartmental Center for Industrial Research – Advanced Applications in Mechanical Engineering and Materials Technology (I.C.I.R.-A.M.M.), Alma Mater Studiorum-Università di Bologna, via Saragozza 8, Bologna 40123, Italy*

²*Department of Industrial Engineering (D.I.N.), Alma Mater Studiorum-Università di Bologna, via Saragozza 8, Bologna 40123, Italy*
E-mail: matteo.gherardi4@unibo.it

The contribution reports on the characterization of a cold atmospheric pressure plasma jet driven by high-voltage pulses with rise time and duration of few nanoseconds. As diagnostic techniques, iCCD imaging was employed to investigate the discharge structure, Schlieren imaging for the study of the jet fluid-dynamic behaviour and Optical Emission Spectroscopy (OES) to qualitatively evaluate the chemical composition of the discharge. Moreover, plasma plume temperature was measured by means of fiber optic temperature sensors and total UV irradiance through a UV power meter. Results attest the suitability of the plasma source for biomedical applications.

1. Introduction

Atmospheric pressure plasma jets (APPJs) are widely investigated for plasma assisted medical therapies due to their versatility, granted by the diverse possible combinations of driving power supply, gas employed and source architecture [1-5].

In this work, a single electrode (SE) plasma jet driven by voltage pulses with nanosecond rise time and pulse duration in the order of few tens of nanoseconds is characterized; this plasma source has been previously used for the treatment of polymer solutions to improve their electrospinnability [6-7] and to increase nanoparticle dispersion [8]. Here a set of diagnostic techniques is adopted to get deeper insights on the correlation between the plasma structure and fluid-dynamic behaviour of the jet (by means of iCCD and high-speed Schlieren imaging) and to assess the compatibility of the plasma jet for the treatment of thermo-sensible materials and for biomedical applications (by means of temperature measurements, Optical Emission Spectroscopy and UV absolute radiometry).

2. Experimental setup

The plasma source adopted in this work is a single electrode plasma jet developed in our laboratory and previously reported in [6-9], as shown in Fig. 1. The high voltage single electrode is a stainless steel sharpened metallic needle with a diameter of 0.3 mm; the electrode protrudes from a quartz capillary (outer diameter of 1 mm) by 3 mm. The plasma is ejected through a 1 mm orifice [6,9] and in this work helium (He) is used as plasma gas. The plasma source is driven by a commercial pulse generator (FID GmbH - FPG 20-1NMK) producing high voltage pulses with a slew rate of few kV/ns, pulse duration around 30 ns, a peak voltage (PV) of 7-20 kV and an energy per pulse of 50 mJ at maximum voltage amplitude into a 100-200 Ω load impedance.

A Schlieren imaging setup in a Z configuration [9], composed of a 450 W Ozone Free Xenon Lamp (Newport-Oriel 66355 Simplicity Arc Source), a slit and an iris diaphragm, two parabolic mirrors with a focal length of 1 m, a knife edge positioned vertically and a high-speed camera (Memrecam K3R-NAC Image Technology, operated at 4000 fps and 1/50000 s shutter time), has been adopted to visualize refractive-index gradients generated in the region downstream the plasma source outlet by the plasma gas mixing with the surrounding ambient air.

An iCCD camera (Princeton Instruments PIMAX3) was used to investigate the temporal evolution of the plasma discharge. A pulse generator (BNC 575 digital pulse/delay generator) has been used to synchronize the generator, the oscilloscope (Tektronix DPO 40034) and the iCCD camera. Two

configurations of the iCCD camera have been adopted: in the first configuration, several sequential frames at time steps of 0.25 ns and with an exposure time of 3 ns (50 accumulations collected on the CCD sensor for each frame) have been acquired in order to track the temporal evolution of the plasma discharge during the high-voltage pulse; in the second configuration, a single frame with exposure time of 35 ns covering the entire voltage pulse has been acquired with the aim of comparing the discharge structure and the fluid-dynamic behavior of the jet observed through Schlieren imaging.

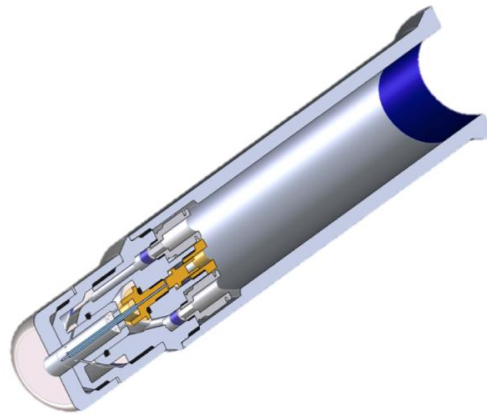


Fig. 1. Three dimensional cross-section representation of the plasma source adopted in the experiments [6].

Plasma jet temperature has been measured by means of fiber optic sensors (OPSENS OTP-M) since they are immune from electro-magnetic interferences [10]; sensor head was positioned coaxially with the source orifice during the measurements.

An iCCD camera (PIMAX3, Princeton Instruments) mounted on a 500 mm spectrometer (Acton SP2500i, Princeton Instruments) has been adopted to collect spatially resolved optical emission spectra in the ultraviolet (UV), visible (VIS) and near infrared (NIR) regions. Details of the experimental setup can be found in [6]. Exposure time has been set at 20 μ s and for each spectrum a set of 50 accumulations has been collected on the CCD sensor.

UV irradiance has been measured using the UV power meter Hamamatsu C9536/H9535-222 (measurement range of 0.001 mW/cm^2 – 200 mW/cm^2 , high spectral response in the range 150-350 nm). The sensor head, covered with a quartz disk to avoid direct exposure to the plasma jet, has been positioned downstream the plasma source outlet. The protecting quartz disk (thickness = 0.5 mm, diameter = 35 mm) is characterized by an integral UV transmission of 93% across the sensor spectral range.

3. Results

The structure of the plasma jet and its evolution in time have been investigated for the following set of operating conditions: peak voltage 25 kV, pulse repetition frequency 1000 Hz and mass flow rate 3 slpm He. The iCCD camera was set to scan the voltage pulse with a exposure time of 3 ns. The iCCD gate opening for the first recorded frame of each scan was set at the start of the voltage pulse and subsequent frames were recorded at fixed time steps of 0.25 ns; therefore two consecutive frames overlap for 2.75 ns.

A sequence of representative frames is shown in Fig. 2a where the time values reported on top of each frame are indicative of the time lapse between the start of the voltage pulse and the corresponding opening of the iCCD gate. For the sake of clarity, the exposures of the most relevant frames depicted in Fig. 2a are reported, together with the high-voltage pulse waveform, in Fig. 2b.

The plasma plume appears 4.5 ns after the start of the voltage rise, which corresponds to a voltage in the range 5-10 kV, and it can be observed in all the subsequent frames taken during the voltage pulse. Nevertheless, its intensity and extension seem to fluctuate during the high-voltage pulse with a period (5 ns). Considering only the brightest frame in each fluctuation, a progressive elongation of the plasma plume is clearly visible. Moreover, it is possible to see that the final part of the plasma jet is at first distorted (frames at 11 and 11.25 ns in Fig. 5) and then branched in several fronts connected to the plasma source by converging tails characterized by weaker emission (frames at 16 and 16.25 ns). This aspect, as well as the subsequent branching of the plasma jet front, is probably related to

hydrodynamic instabilities of the He gas flow, which result in turbulent mixing of He species with the surrounding ambient air; to investigate the correlation between gas flow instabilities and discharge structure, further investigations exploiting Schlieren imaging have been conducted.

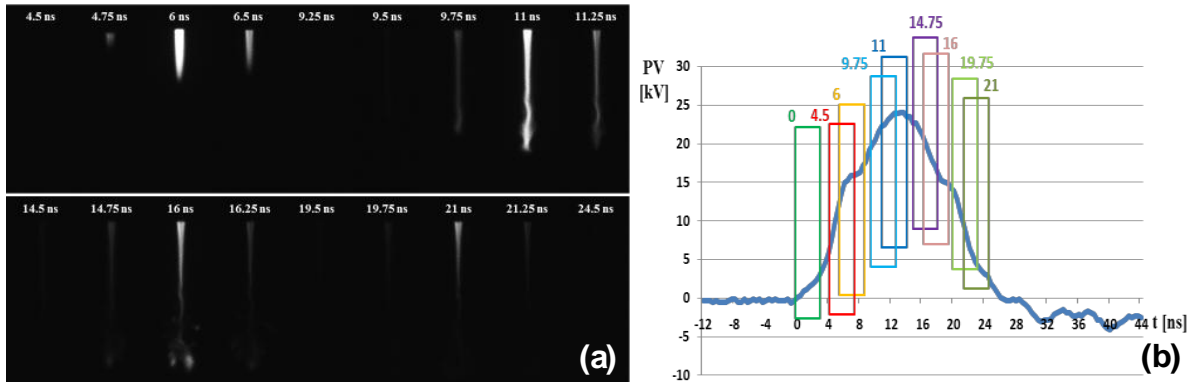


Fig. 2. a) iCCD frames (3ns exposure time, 50 accumulations); b) Voltage waveform with superimposed exposures for relevant iCCD frames. The time values reported on top of each exposure and frame are indicative of the time lapse between the start of the voltage pulse and the corresponding opening of the iCCD gate.

Schlieren high-speed recordings of the fluid-dynamic behaviour of the plasma jet and iCCD images of the discharge structure have been acquired for the different operating conditions of the plasma source. Results are here reported for He flow rate and pulse repetition frequency kept fixed at 3 slpm and 1000 Hz, respectively, while the peak voltage was set to 17 kV or 30 kV. Since the duration of the high-voltage pulse driving the plasma source is less than the time span of each Schlieren high-speed camera frame (0.25 ms at 4000 fps), the fluid-dynamic phenomena occurring during the voltage pulse are observed in a single frame. This frame has been reported in Fig. 3 together with the corresponding iCCD acquisition performed with an exposure window of 35 ns to collect light emitted during the whole high-voltage pulse.

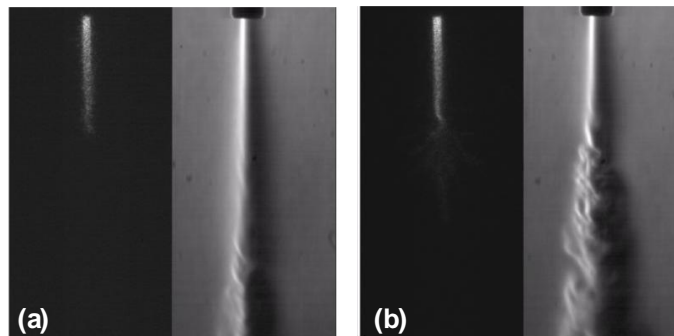


Fig. 3. Comparison of synchronized iCCD (left) and Schlieren (right) acquisitions of the plasma jet operated at: a) He flow rate 3 slpm, pulse repetition frequency 1000 Hz and peak voltage 17 kV; b) He flow rate 3 slpm, pulse repetition frequency 1000 Hz and peak voltage 30 kV.

From Schlieren images, it can be noted that the flow at the source outlet is almost laminar while fluid-dynamic instabilities can be observed in a more downstream position. With peak voltage increasing from 17 to 30 kV, the length of the laminar region becomes shorter and fluid-dynamic instabilities of higher intensity can be observed. From iCCD images, it can be noted that the length of the plasma plume is increased as the peak voltage is increased. From the comparison of Schlieren frames and iCCD images, a clear correspondence between fluid-dynamic instabilities and branching of the plasma plume can be observed. Branching appears in the ending part of the plasma plume in the cases in which the operating conditions induce the plasma plume to propagate into the spatial region where the flow is turbulent. This phenomenon is mostly evident for the case peak voltage 30 kV; on the contrary, in the cases with peak voltage 17 kV, the plasma plume is propagating in the laminar region only and no branching of the front is observed.

Plasma jet temperature has been measured during operation with pulse repetition frequency set at 1000 Hz, peak voltage in the range 17-25 kV and He flow rate at 1 or 3 slpm. Axial temperature profiles

(with the axial position defined as the distance measured from the sensor tip to the source outlet; so axial position = 0 mm corresponds to the source outlet) are presented for four different operative conditions in Fig. 4. Three different measurements have been carried out for each operating condition. It should be noted that in all the investigated cases the maximum gas temperature measured by means of fiber optic sensors in the region downstream the source outlet is lower than 45 °C.

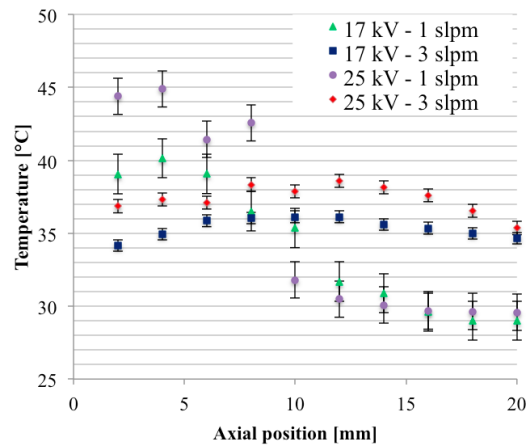


Fig. 4. Axial temperature profile of the plasma jet at constant pulse repetition frequency (1 kHz) for different values of peak voltage (17 and 25 kV) and He flow rate (1 and 3 slpm). Room temperature during measurements: around 29 °C. Axial position = 0 mm corresponds to source outlet.

Optical emission spectra in the UV-VIS-NIR regions as a function of both the wavelength and the distance from the source outlet are shown in Fig. 5 for the plasma jet operated with a peak voltage of 20 kV, a pulse repetition frequency of 125 Hz and a He gas flow rate of 3 slpm.

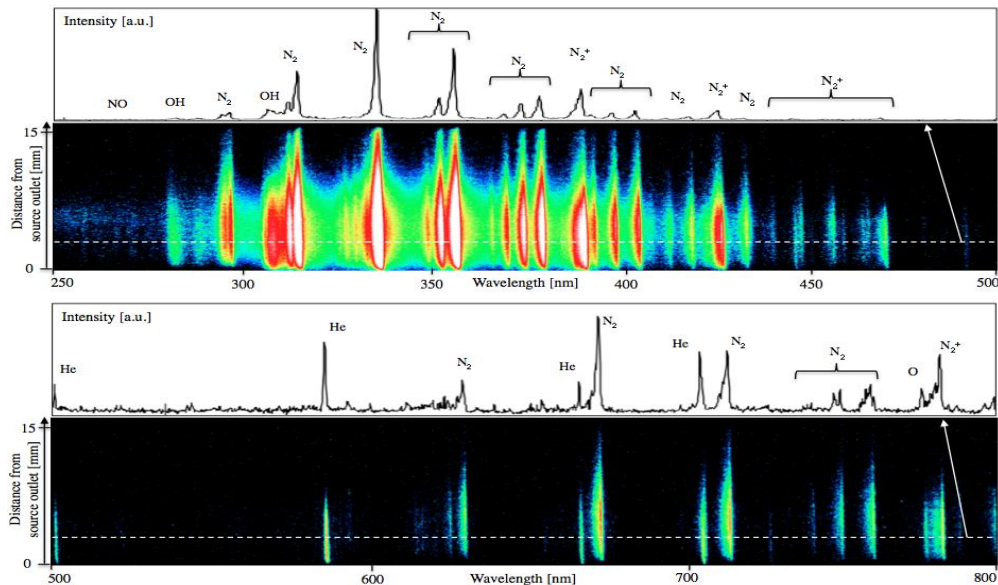


Fig. 5. Optical emission spectra in UV-VIS (top) and VIS-NIR (bottom) range as a function of both the wavelength and the distance from the source outlet. Plasma jet operated with PV = 20 kV, PRF = 125 Hz and He flow rate = 3 slpm.

Optical radiation is emitted mainly in the UV-VIS region, where bands of excited molecular nitrogen (Second Positive System of N_2), OH radicals in the UVB region, First Negative System of N_2^+ are detected. A faint emission in the UVC region between 250 and 280 nm due to NO radicals was also observed. In VIS-NIR only few lines of He and O and the second order diffractions of N_2 and N_2^+ systems can be observed. He lines and emission of atomic oxygen were also observed. Spectral bands observed between 675 and 760 nm are generated by second order diffractions of the monochromator and are related to N_2 emission bands. As the plasma gas is He, at the axial position corresponding to the outlet of the plasma source only the emission from He lines is observed. At higher distance from the source outlet, the surrounding air is diffusing into the plasma gas and the emission bands of excited N_2 , OH and NO can be observed, which are characterized by maximum intensity positioned

approximately at 6 mm downstream the source outlet. A qualitatively similar emission spectrum can be observed also for other operating conditions, which have been investigated; in particular, emission intensity was observed to increase for higher values of peak voltage and He gas flow rate. The reactive species of oxygen (ROS) and nitrogen (RNS) observed are widely known to play an important role in bacterial decontamination or in the interaction with living tissue [11-12].

An indirect measurement of the influence of different operating parameters on the total irradiance in the UV range of the plasma plume is reported in Tab. 1; this was performed by measuring the distance at which an irradiance of $1 \mu\text{W}/\text{cm}^2$ can be detected using a UV power meter: the higher is the distance at which UV irradiance = $1 \mu\text{W}/\text{cm}^2$, the higher is the plasma total UV irradiance. The values obtained for our plasma jet are below those reported in literature for several similar non-equilibrium atmospheric pressure plasma sources, which range between $10 \mu\text{W}/\text{cm}^2$ and $1 \text{mW}/\text{cm}^2$ [4,13-15].

Plasma gas flow rate	Pulse repetition frequency	Peak voltage	Distance from source outlet at which UV irradiance = $1 \mu\text{W}/\text{cm}^2$
1 slpm He	83 Hz	17 kV	<3 mm
1 slpm He	83 Hz	20 kV	<3 mm
3 slpm He	83 Hz	17 kV	<3 mm
3 slpm He	83 Hz	20 kV	9 mm
3 slpm He	125 Hz	17 kV	7.5 mm
3 slpm He	125 Hz	20 kV	12 mm
3 slpm He	1000 Hz	20 kV	15 mm

Tab. 1. UV irradiance measurements for different plasma jet operating conditions

4. Conclusions

The discharge generated by an APPJ developed by the Authors and driven by high-voltage pulses with rise time and duration of few nanoseconds has been investigated. Depending on the operating conditions, the plasma plume was reported to present a single front or several branched sub-fronts; comparing results from Schlieren and iCCD imaging, it was observed that branching of the plasma jet front occurs in spatial regions where the flow is turbulent. Moreover, oscillations both in light emission intensity and plume length were observed during the temporal evolution of the plasma discharge. The plasma plume spectrum, measured by OES, was characterized by N_2 , N_2^+ , NO, OH spectral bands as a consequence of mixing with ambient air. UV irradiance of the APPJ and temperature of the plasma plume were also measured and found to be compatible with biomedical applications.

5. References

- [1] Stoffels E, Flikweert A J *et al.* 2002 *Plasma Sources Sci. Technol.* **11** 383.
- [2] Robert E, Barbosa E *et al.* 2009 *Plasma Process. Polym.* **6** 795.
- [3] Laroussi M and Lu X 2005 *Appl. Phys. Lett.* **87** 113902.
- [4] Weltmann K D, Kindel E *et al.* 2009 *Contrib. Plasma Phys.* **49** 631.
- [5] Bianconi S, Colombo V *et al.* 2014 *IEEE Trans. Plasma Sci.* **42** 2746.
- [6] Colombo V, Fabiani D *et al.* 2014 *Plasma Process. Polym.* **11** 247.
- [7] Colombo V, Fabiani D *et al.* 2013 IEEE International Conference on Solid Dielectrics (ICSD) 358.
- [8] Colombo V, Fabiani D *et al.* 2013 IEEE International Conference on Solid Dielectrics (ICSD) 718.
- [9] Boselli M, Colombo V *et al.* 2014 *Plasma Chem. Plasma Process.* **34** 853.
- [10] Wertheimer M R, Saoud B *et al.* 2012 *J. Appl. Phys.* **100** 201112.
- [11] Dobrynin D, Fridman G *et al.*, 2009, *New J. Phys.* **11** 115020.
- [12] Boxhammer V, Morfill G E *et al.*, 2009 *New J. Phys.* **11** 115013.
- [13] Dobrynin D, Arjunan K *et al.* 2011 *J. Phys. D: Appl. Phys.* **44** 075201.
- [14] Klampfl T G, Isbary G *et al.* 2012 *Appl. Env. Microbiol.* **78** 5077.
- [15] Shimizu T, Steffes B *et al.* 2008 *Plasma Process. Polym.* **5** 577.

6. Acknowledgements

Work partially supported by COST Action MP1101 “Biomedical Applications of Atmospheric Pressure Plasma Technology” and COST Action TD1208 “Electrical discharges with liquids for future applications”.

GLIDING ARC SUBJECTED TO HYPERGRAVITY

Lucia Potočňáková¹, Jiří Šperka¹, Petr Zikán¹, Jack J.W.A. van Loon²,
Job Beckers³, Vít Kudrle¹

¹ *Department of Physical Electronics, Masaryk University, Kotlářská 2, 61137 Brno, Czech Republic*

² *Dutch Experiment Support Center, ACTA-VU-University and University of Amsterdam, Amsterdam, The Netherlands*

³ *Faculty of Applied Physics, Eindhoven University of Technology, P.O. Box 513, 5600 MB Eindhoven, The Netherlands*

E-mail: kudrle@sci.muni.cz

Glide arc in four noble gases was studied under normal and hypergravity conditions. Here, we present the details of hypergravity influenced glide arc motion, frame by frame images of arc ascending in various g -levels, the distribution of maximum heights achieved in individual experiments and the discussion of flow pattern differences in high gas flow and hypergravity.

1. Introduction

Arc and glide arc discharges operated at atmospheric pressure are both good examples of plasma employed widely in industry. Wool surface treatment, decontamination of bacterial-contaminated water [1,2] or dry methane reforming [3] are only a few of many industrial fields where they are exploited. Their industrial applicability and also their theoretical fundamentality predestined the arc discharges to be intensively studied under variety of operating conditions, including extreme cases of hyper- and micro-gravity. One of the first to be investigated in that way was the arc discharge in free fall [4,5]. Recently, carbon species were synthesized in microgravity [6] in the 28th ESA Parabolic Flight Campaign. Single-walled carbon nanotubes were produced by arc discharge method in hypergravity [7] and also microgravity [8,9]. The flow phenomena in metal-halide arc discharge lamps were intensively investigated under varying gravity conditions [10,11,12]. Although the arc applications surely profit from the gravity oriented research, a hypergravity plasma research is also of direct importance to safety precautions in space flight (high g -levels during the take off alters the behaviour of various forms of discharges that might arise from malfunction in electric systems), ion thrusters design or understanding of plasma related processes in atmospheres of other planets, where the gravity is significantly different from that on Earth.

In this paper, we present the results of experimental studies of glide arc in laboratory (normal 1g gravity) conditions as well as in hypergravity conditions (1g-18g) achieved at Large Diameter Centrifuge (LDC) [13] in ESA ESTEC centre (Noordwijk, The Netherlands).

The mechanisms that govern glide arc are very similar to those of more known stable arc discharge. Both can be easily produced by applying the voltage high enough for gas electrical breakdown between two electrodes. After a breakdown, electric current starts to flow in previously non-conductive working gas. Due to its electrical resistance, the plasma channel is intensively heated and the difference in mass density of the heated gas in the discharge column and the cold surrounding atmosphere gives a rise to buoyant force. Buoyancy lifts up the arc and it assumes a typical arc-like curved shape. In gliding arc, the electrodes typically have divergent slanted shape promoting the upwards movement of contact points of arc to electrodes, thus creating typical gliding motion, from which also the glide arc name is derived. The plasma properties are changing during the rise of the gliding arc channel, as the length of the plasma column increases to its maximum extent. When the power requirements needed for further sustainment of the elongated plasma channel can not be satisfied, the discharge extinguishes and a new arc forms between the nearest points at the two electrodes. This discharge evolution cycle then repeats itself.

The gliding arc is can be operated without any gas flow, or in a flow regime, which is the more often case. In flow regime, the working gas is blowing into the discharge volume and the flow is usually oriented in the same direction as buoyancy. In such case, the arc is not only lifted up by buoyancy, but also a gas drag contributes to its movement. Consequently, the higher the gas flow, the faster the arc moves. As the role of gas drag and buoyancy are essentially similar, one should expect the same effect to accompany the increase of buoyant force. The buoyancy is closely related to the

gravitational force and thus the increase of buoyant force can be achieved by placing the discharge into a hypergravity environment.

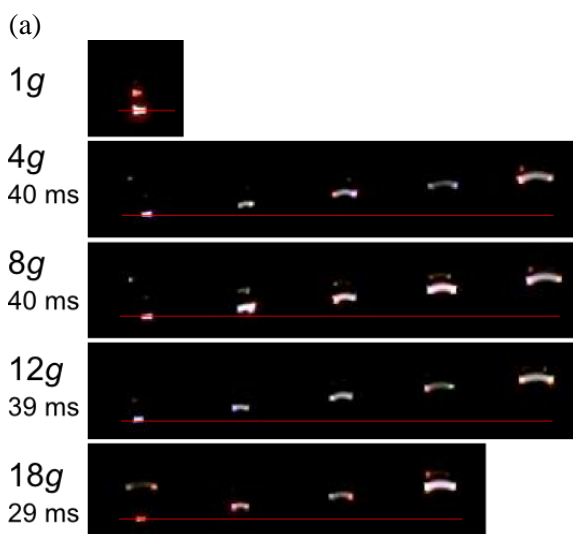
2. Experimental

The glide arc was ignited between slanted copper electrodes with a minimum distance of 4.5 mm and an initial angle between them of 36° . These electrodes were connected to a current limiting high voltage transformer supplying 0-10 kV at 50 Hz AC. The configuration was enclosed in nonconductive discharge chamber with 2 dm^3 inner volume. Front and back walls were made of heat resistant glass allowing direct optical observation by digital cameras. More detailed description of the experiment can be found in [14,15].

3. Results

As already outlined in introduction, it was found out, that increased gravity has similar effects on glide arc as increased gas flow – the velocity of arc channel rises, height and maximum extension of channel are reduced and thus the increase of gliding frequency is even bigger. As the movement of gliding arc generally determines its behaviour to a great extent, other parameters exhibit similar dependencies on gravity. These results were already briefly reported in our previous papers [14,15,16]. In this paper we will present the details of hypergravity glide arc motion, frame by frame images of its ascending in various g -levels, the distribution of maximum heights achieved in individual runs and the discussion of flow pattern differences in high gas flow and high gravity.

In Fig. 1, there are frame by frame images of glide arc in helium, neon and argon at $1g$, $4g$, $8g$, $12g$ and $18g$ as taken by the fast camera. The time delay between each two images in rows is 0.01 s for (a) helium and (b) neon and 0.03 s for (c) argon, except for the last photo in each row, where the time delay may be shorter. It can be seen, that for helium and neon the arc is stable (not gliding) for low g -levels. However, it started to move upwards after the increase of artificial gravity, when buoyancy force became strong enough to evoke such movement. For helium it was already at $4g$, while glide arc in neon started to glide at g -levels above $8g$, but one must keep in mind that the gas flow conditions were more favourable for helium than for neon. The glide arc in argon is gliding for each gravity condition. Glide arcs in all three gases show the same attribute of shortening of duration of one glide-cycle in hypergravity. For glide arc in helium, this length decreased from 40 ms (in $4g$) to 29 ms (in $18g$), in neon from 139 ms (in $12g$) to 89 ms (in $18g$) and in argon the length of duration of one full glide-cycle decreased continuously from 260 ms (in $1g$) to 63 ms (in $18g$). From Fig. 1 (b) it can be seen, that the velocity of upwards movement is not constant during the one glide-cycle. The ascending is much faster in second half of the period, while the movement is only reluctant in the first one. The decrease of maximum height can be seen the most evidently in Fig. 1 (c), where the maximum height in $18g$ is less than one half of original maximum height in $1g$.



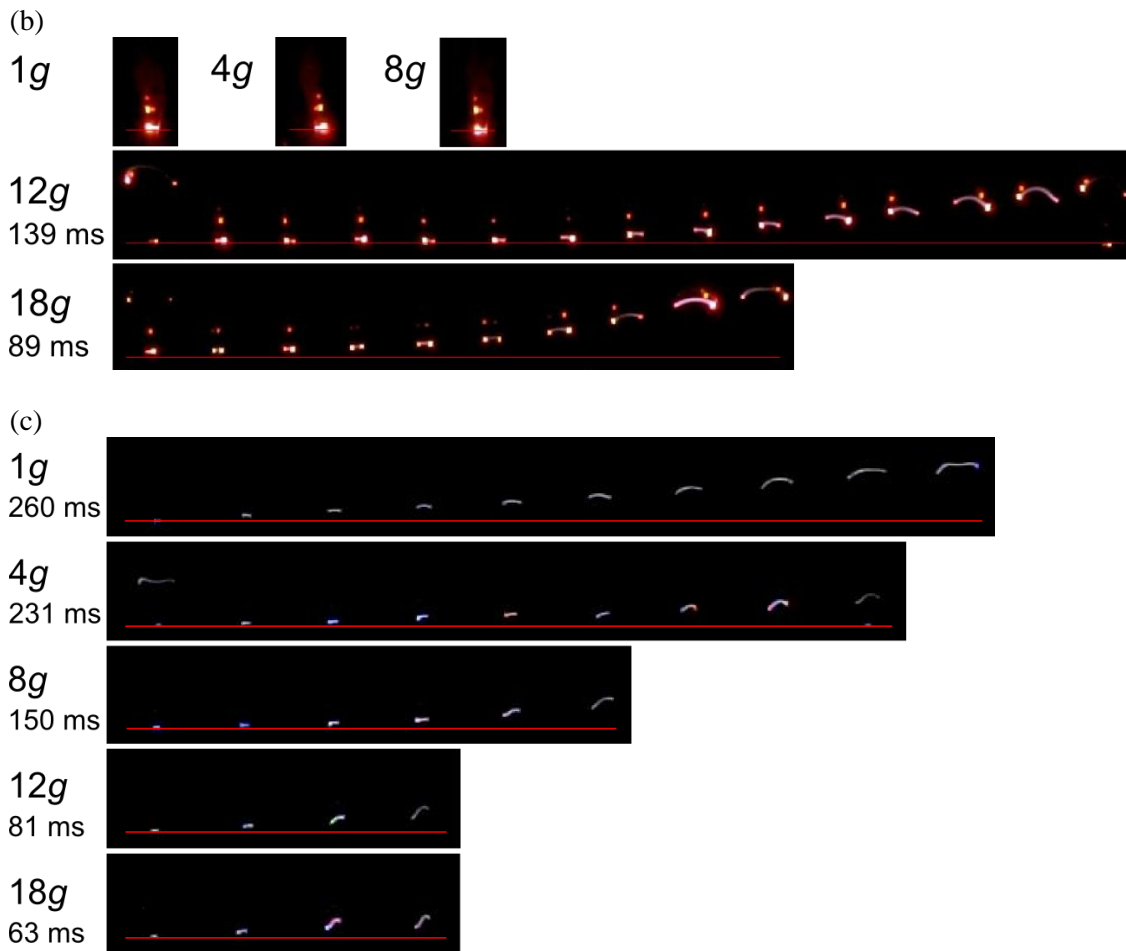


Fig. 1. Images of one glide arc glide-cycle at 1g, 4g, 8g, 12g and 18g in (a) helium (gas flow 0.65 slm, discharge voltage 8 kV, time delay between each two images in rows 0.01 s), (b) neon (gas flow 0.15 slm, discharge voltage 4 kV, time delay between each two images in rows 0.01 s) and (c) argon (gas flow 0.15 slm, discharge voltage 4 kV, time delay between each two images in rows 0.03 s), as taken by the fast camera.

However, the above presented Fig. 1 describes only individual glides with no statistical value. Glide arc is a very complex system, extremely sensitive on experimental conditions and even with signs of hysteresis. Not only is its behaviour significantly different for different input conditions, but also for the same conditions each glide is unique. Therefore we present also the distribution of maximum heights reached by the individual arcs, which can be seen in Fig. 2. The working gas in this experiment was krypton, the gas flow was 0.4 slm and the discharge voltage was 4 kV. The maximum height in 1g is around 12-13 cm, the maximum height reached in 18g is around 1-2 cm. The decrease of maximum height occurs mostly in the range of few g , where the maximum heights are dispersed significantly. Before this region (1-4g) and after this region (12-18g) the dispersion is relatively low, as the height of individual arcs deviates only ± 1 cm. However, in the middle of the transition region (8g) the maximum heights are distributed almost homogenously between 13.5 and 2 cm.

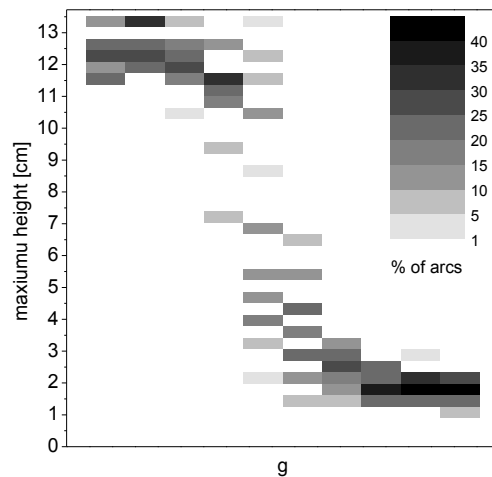
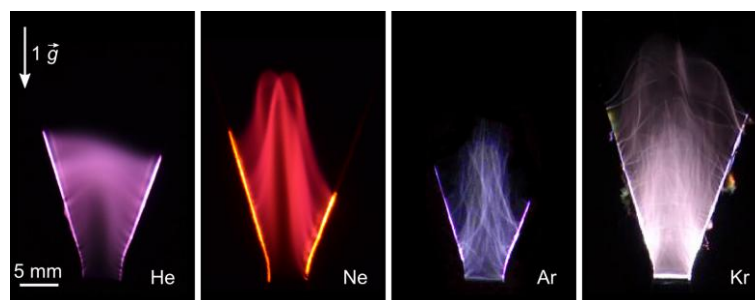


Fig. 2. The distribution of maximum heights reached by glide arc in krypton (gas flow 0.4 slm, discharge voltage 4 kV) in various g -levels just before quenching.

Finally, in Fig. 3 we present the long exposure photographs of glide arc in helium, neon, argon and krypton. The upper set of photographs (a) represents the glide arc at high gas flow conditions, while the lower set was taken during hypergravity experiments from inside the centrifuge gondola at $18g$. At both high gas flow and high gravity conditions, the upwards force was very strong and the gliding frequency was very high, so each photograph comprises of many individual glides overlaying each other and thus carrying also statistical information, eliminating the importance of random irregularities. It can be seen from the upper set of photographs, that the influence of gas flow is not homogeneously spread in the discharge chamber space, resulting in turbulent flow and plasma channel deformation. The deformation of arc by the gas drag became evident predominantly in the lower parts of inter-electrode region, where the flux of gas is the strongest. Occasionally, individual arcs were able to escape this turbulent region. In those cases, the arc then could expand to its maximum elongation as in the case of low gas flow, with almost non-deformed appearance in the upper parts.

In contrast with effects of increased gas flow, the deformation of the arc in hypergravity wasn't so evident (see Fig. 3 lower set). The disruption of regularity wasn't concentrated in the discharge axis, nor restricted to lower part. The deformation of arc shape consisted rather of random warping, creating small undulations. The origin of the hypergravity-induced deformation could consist in local temperature variation in arc channel. While these deviations from homogeneity throughout the plasma channel might not be significant enough to cause a major deformation in normal gravity, their influence becomes intensified in higher g -levels, which then results in uneven force acting on colder/hotter sections of the arc channel and finally the arc deformation. The consequence of gravity being homogeneous in the whole volume of the discharge chamber (unlike the gas drag which is strongest at the bottom) can further be seen in the absence of seldom break out of arc to the full expansion for high g -levels.



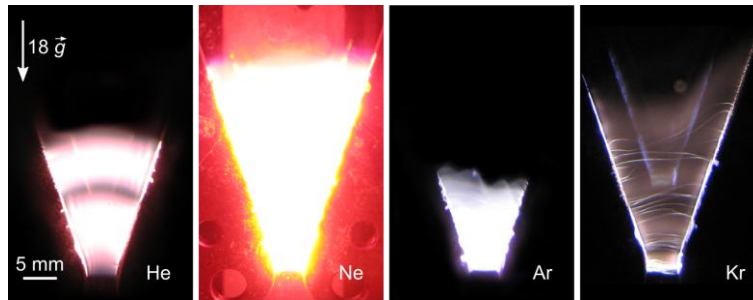


Fig. 3. Long exposure photographs of glide arc in helium, neon, argon and krypton. Upper set of photographs - normal gravity conditions, high gas flow; lower set of photographs – 18g hypergravity, low gas flow.

4. Conclusion

In this paper, we presented some results of hypergravity glide arc study performed in ESA ESTEC centre in The Netherlands. Glide arc in four noble gases (helium, neon, argon, krypton) was studied in artificial gravity ranging from 1g to 18g. It was found out, that the increase of gravity dependent buoyancy results in faster glide arc movement and lower maximum height, which is achieved before extinguishing of the arc. Frame by frame study of high speed video revealed the uneven velocity of the upwards movement, which seems to accelerate in higher positions. Many of the hypergravity effects on glide arc are similar to those of increased gas flow, but the different nature of gas flow and hypergravity reveals itself for example in differences in the flow pattern and the arc deformation.

5. References

- [1] Burlica R, Kirkpatrick M J and Locke B R 2006 *Journal of Electrostatics* **64** 1.
- [2] Du Ch M, Wang J, Zhang L, Li H X, Liu H, Ziong Y, Strnad O, Novak L 2012 *New Journal of Physics* **14**.
- [3] Bo Z, Yan J, Li X, Chi Y, Chen K, Strnad O, Novak L 2008 *International Journal of Hydrogen Energy* **33** 20.
- [4] Steenbeck M 1937 *Z. Tech. Phys.* **18** 593.
- [5] Kenty C 1939 *J. Appl. Phys.* **10** 714.
- [6] Pletser V 2004 *Acta Astronaut.* **55** 829.
- [7] Tan G D, Mieno T 2010 *Thin Solid Films* **518** 3541.
- [8] Kawanami O, Sano N, Miyamoto T, Mineshige A, Murakami T, Harima H 2007 *Appl. Phys. A* **89** 929.
- [9] Alford J M, Mason G R, Feikema D A 2006 *Rev. Sci. Instrum.* **77** 074101.
- [10] Stoffels W W, Flikweert A J, Nimalasuriya T, Van der Mullen J, Kroesen G M W, Haverlag M 2006 *Pure Appl. Chem.* **78** 1239.
- [11] Flikweert A J, Nimalasuriya T, Kroesen G M W, Haverlag M, Stoffels W W 2009 *Microgravity Sci. Technol.* **21** 319.
- [12] Nimalasuriya T, Flikweert A J, Haverlag M, Kemps P C M, Kroesen G M W, Stoffels W W, Van der Mullen J 2006 *J. Phys. D* **39** 2993.
- [13] Loon J J W A, Krause J, Cunha H, Goncalves J, Almeida H, Schiller P 2008 *Proc. Of the Life in Space for Life on Earth Symposium (Angers, France 22-27 June 2008)*, ESA SP-663.
- [14] Sperka J, Soucek P, Loon J J W A, Dowson A, Schwarz Ch, Krause J, Kroesen G M W, Kudrle V 2013 *European Physical Journal D* 67 12.
- [15] Potocnakova L, Sperka J, Soucek P, Zikan P, Beckers J, Kroesen G M W, Loon J J W A, Kudrle V 2013 *Proceedings of International Masaryk Conference* 2013.
- [16] Potocnakova L, Sperka J, Zikan P, Loon J J W A, Beckers J, Kudrle 2014 *IEEE Transactions on Plasma Science* **42** 10

INTERACTION OF FREE ELECTRONS WITH NANO-SOLVATED BIOMOLECULES

Michael Neustetter¹, Julia Aysina¹, Paul Scheier¹, Stephan Denifl¹

¹*Institute of Ion and Applied Physics, University of Innsbruck, Technikerstrasse 25, 6020 Innsbruck, Austria*

E-mail: Michael.Neustetter@uibk.ac.at

We investigate the interaction of free electrons of different energies with various nano-solvated biologically relevant molecules. In this context we present our results of mixed biomolecule/water clusters ionized via electron impact as well as electron attachment.

In recent years there has been a significant interest in the understanding of damage processes of DNA, also induced by low energy electrons. It has been suggested that ionizing radiation releases a large number of secondary electrons in human cells. These electrons achieve kinetic energies in the range of up to a few of tens of eV [1, 2]. In this energy range electron ionization and electron attachment processes may cause chemical transformation of biological matter. The studies by Sanche and co-workers [3, 4] demonstrated that these low energy electrons can induce single and double strand breaks in a film of plasmid DNA upon dissociative electron attachment (DEA). In DEA an electron attaches resonantly and the transient negative ion formed may decay via dissociation of the molecule. This dissociation can be fast and often has only spontaneous electron emission as competitive channel. A large number of studies on electron ionization and electron attachment to various simple biomolecules (e.g. DNA bases, sugars, amino acids) in the gas phase have been carried out [5, 6]. Thereby, it turned out that biomolecules often substantially decompose upon electron collisions. In addition, DEA is a very bond and site selective process, i.e. only certain bonds are cleaved in a molecule after capture of an electron with specific kinetic energy [7].

However, for applications like in radiotherapy it is highly important to understand how the fragmentation process of biomolecules is modified by surrounding environment. For example, it was shown that electron attachment to nucleobases embedded in helium droplets is strongly modified in terms of the molecular fragmentation pattern compared to the isolated molecule [8, 9]. In this case extensive and slow fragmentation processes have been quenched effectively in the droplet, while direct dissociations via repulsive potential energy surface upon DEA remain.

The studies with doped helium droplets represent a very first approach to investigate the effect of environment. Living cells consist of up to 70% water. To account for more realistic conditions in comparison to a living cell, we are using clusters of biomolecules solvated with several water molecules. Therefore, we built up a cluster source producing the mixed biomolecule/water clusters.

In the present study we are investigating pyrimidine which is a derivative of the nucleobases cytosine, thymine and uracil. Hence, pyrimidine ($C_4H_4N_2$) is often used as a model system for collision studies on radiation damage. Compared to those nucleobases, pyrimidine has a much higher vapour pressure and thus it is experimentally easier to create the clusters of interest. These clusters are produced via supersonic expansion into vacuum of both components water and pyrimidine. To enhance the cluster efficiency we use argon as seeding gas. The filament of a Nier type ion source provides the free electrons with a tuneable kinetic energy in the range of interest (0 to 70 eV). To identify the created ions we are using a double focusing sector field mass spectrometer which additionally allows us to measure metastable products. In this context we present results of electron attachment as well as electron impact ionisation to pyrimidine/water clusters.

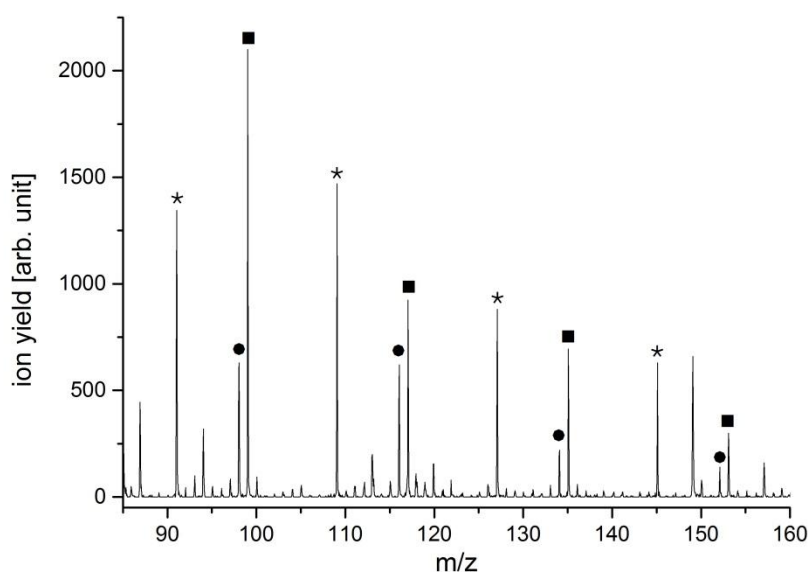


Fig. 1. Detailed view of an electron ionization mass spectrum of pyrimidine/water clusters in the range between pyrimidine monomer (80 amu) and dimer (160 amu). For the mixed clusters the protonated series (■) as well as un-protonated series (●) are visible. Additionally, one can see the well-known protonated pure water clusters (*).

In the case of cations we mainly observe the bare pyrimidine $(C_4H_4N_2)^+$, whereas about 30% of the signal is due to gas phase pyrimidine present in the cluster beam. Furthermore, un-protonated clusters $(C_4H_4N_2)(H_2O)_n^+$ as well as the protonated clusters $(C_4H_4N_2)(H_2O)_nH^+$ ($n = 1 - 4$) were created as shown in figure 1. Other observed ions are protonated water clusters $(H_2O)_mH^+$ ($m = 5 - 8$). Larger clusters like pyrimidine dimer solvated, un-solvated, protonated and un-protonated respectively, were also produced, but to avoid confusion are not shown in figure 1. During the measurements we were not able to detect water clusters attached to pyrimidine fragments. These fragment clusters are also not present in the negative ion measurements. In striking contrast to measurements of gas phase pyrimidine and water-solvated pyrimidine, where no anionic monomers are detectable, we are able to measure $(C_4H_4N_2)^-$ as a fragmentation product in pure pyrimidine clusters. Furthermore we see evidence that water is preventing the ring fragmentation of the pyrimidine.

Acknowledgment: This work is partially supported by FWF, Vienna (P22665, P24443) and J. Aysina acknowledged a Lise Meitner grant from the FWF (M1445-N20).

References

- [1] C. von Sonntag 1987 *The Chemical Basis for Radiation Biology*, Taylor and Francis: London.
- [2] A. F. Fuciarelli et al. 1995 *Radiation Damage in DNA: Structure/Function Relationships at Early Times*, Battelle Press: Columbus.
- [3] B. Boudaiffa et al. 2000 *Science* **287** 1658.
- [4] F. Martin et al. 2004 *Phys. Rev. Lett.* **93** 068101.
- [5] I. Bald et al. 2008 *In. J. Mass. Spec.* **277** 4.
- [6] I. Baccarelli et al. 2011 *Physics Reports - Review Section of Physics Letters* **508** 1.
- [7] S. Ptasinska et al. 2005 *Phys. Rev. Lett.* **95** 093201.
- [8] S. Denifl et al. 2006 *Phys. Rev. Lett.* **97** 043201.
- [9] S. Denifl et al. 2008 *ChemPhysChem.* **9** 1387.

QUANTITATIVE DIAGNOSTICS OF INDUCTIVE PLASMAS IN Cl₂, O₂ AND Cl₂/O₂ MIXTURES

Jean-Paul Booth, Mick  el Foucher, Daniil Marinov and Pascal Chabert

LPP-CNRS, Ecole Polytechnique, Palaiseau, France

E-mail: jean-paul.booth@lpp.polytechnique.fr

Inductively-coupled plasmas in molecular, electronegative gases are widely used for plasma processing of surfaces, for instance in CMOS manufacture. The complexity of these systems is such that they can only be described by multi-physics models which describe both the plasma physics and the molecular collisional processes. However, there has been little rigorous validation of these models by comparison to quantitative measurements of particle densities over a wide range of parameter space. We have chosen to study the Cl₂/O₂ system partly because of the industrial process relevance but also because methods exist to measure the density of many of the particles present. Electron densities were measured by microwave hairpin resonator. Absolute Cl and O atom densities were determined by Two-photon Absorption Laser-Induced Fluorescence. We have constructed a new ultra-low noise broadband UV-visible absorption bench, which allows the measurement of the densities of ground state Cl₂ molecules and Cl_xO_y reaction products, as well as vibrationally excited states of Cl₂ and O₂.

1. Introduction

Radiofrequency-excited inductively-coupled plasmas in low-pressure (0.2-10 Pa) halogen-containing diatomic molecules (for example Cl₂ and HBr) are an archetype for the study of the dynamics of plasmas in simple molecular electronegative gases, and are well-suited for model validation because techniques exist to measure the absolute densities of the majority of stable and transient species (molecules, atoms, ions and electrons) occurring in them. Simultaneous measurements of these densities over a large range of operating conditions (gas pressure and composition, injected RF power) provides a stringent test of models. In addition to steady-state measurements, the kinetics of creation and destruction of transitory species can be probed by time-resolved measurements in pulse-modulated plasmas. Such plasmas are also of great industrial importance as they are widely used for plasma etching of nanostructures in semiconductor materials, an essential step in the fabrication of nano-devices such as integrated circuits and photonic devices. Electronegative plasmas are equally of current interest for the development of ion-ion plasma thrusters.

Understanding these systems involves not only treating the charged particle dynamics but also the collisional processes of the atoms and free radicals created by electron-molecule collisions. For instance, the Hybrid Plasma Equipment Model (HPEM[1]) developed over many years by Prof Kushner of Michigan (with whom we are collaborating) treats the motion of electrons and ions under the influence of applied electromagnetic fields using a hybrid fluid/Monte-Carlo approach, and couples this to a fluid chemical kinetics model. While the validity of the HPEM approach is well established, a recent study at LPP of Cl₂ plasmas[2], using state-of-the-art laser and microwave diagnostic measurements, showed that the physico-chemical model of Cl₂ used in HPEM is naive, leading to wildly inaccurate predictions (for instance, underestimation of such basic parameters as the electron density by a factor of 3 under some circumstances). Inclusion of processes such as electron collisional vibrational excitation[3] of Cl₂ (followed by v-T transfer), and spin-orbit excitation[4] and quenching, is under study and appears to substantially improve the model agreement.

2. Experimental Techniques

The cylindrical plasma chamber (diameter 55cm, height 10cm) is excited at 13.56 MHz (20-500 W) by a 4-turn planar spiral antenna placed on a top window made of alumina. All other surfaces are hard anodised aluminium. Gases are supplied via a showerhead in the top of the reactor (typically 50 sccm) and evacuated by a turbo-molecular pump with a throttle valve to set the pressure between 2 and 100 mTorr. The electron densities are determined using the floating microwave hairpin resonator technique as described by Piejak et al.[5], with correction for the floating sheath around the probe[6].

Measurements were taken at the reactor centre unless otherwise stated. Atom densities were determined at the reactor centre by two-photon laser-induced fluorescence. Chlorine atoms were excited at 233.2nm by means of a pulsed tuneable dye laser with frequency doubling, and absolute densities were obtained by 355nm photolysis of Cl_2 molecules without plasma [7]. Spin-orbit excited chlorine atoms were also detected by TALIF [8], and their density was added to that of the ground state. Oxygen atoms were excited at 225.6nm, and calibrated by comparison with the TALIF at 224.3 nm from a known sample of Xe [9].

A novel broadband UV absorption bench was constructed, in order to permit the measurement of weak absorption features over wide spectral ranges. The setup and technique used is similar to that used by Booth et al. [10], but with the following improvements: 1) the Xe arc light source was replaced by a laser-produced plasma source (EQ 99 from Energetiq); this source provides broad continuum radiation (200-800nm) from a point less than 100 μm in diameter with higher irradiance and far higher stability than a Xe arc lamp, 2) Only reflective optics (parabolic and planar mirrors) are used, eliminating all chromatic aberrations, 3) transmitted light is dispersed by an aberration-corrected spectrograph (Acton Isoplane 320) with a choice of three gratings (300, 1200 and 2400l/mm) onto a 1024 element photodiode array detector (Hamamatsu S3904-1024Q). This setup allows spectra over ranges of 240nm, 60nm or 30nm to be measured with shot noise and base-line stability better than 5×10^{-5} with signal averaging over a few minutes.

3. Results in pure O_2

Figures 1 and 2 show how the electron density and oxygen atom density vary with gas pressure and radiofrequency power in a pure oxygen discharge. The electron density increases monotonically (and almost linearly) with RF power, whereas with pressure it reaches a broad peak around 30-40mTorr, and decreases slowly thereafter. Radial scans show that the electron density is always centre-peaked, decaying slowly towards the reactor edges. In contrast, the oxygen atom density increases sub-linearly with radiofrequency power, nearing saturation at 500W with a dissociation degree (atom density divided by the density of O_2 present before plasma) of about 20%, almost independent of pressure. Why this should saturate, far from 100%, when the electron density is continuing to rise, will be discussed below.

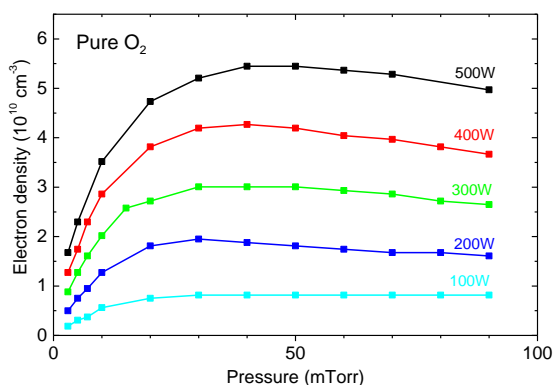


Fig. 1. Electron density in pure O_2 plasma.

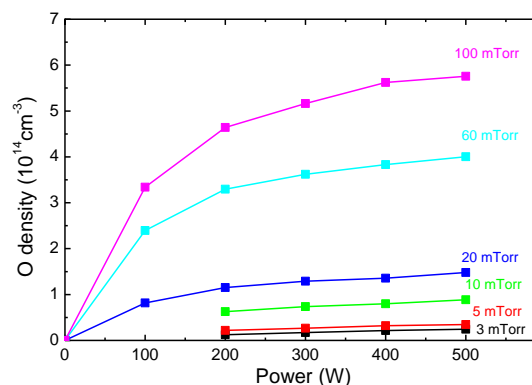


Fig. 2. Oxygen atom density in pure O_2 plasma.

Pure oxygen does not show significant absorption for wavelengths above 200nm. However, we did observe significant complex absorption bands in O_2 plasmas, as seen in Fig. 3. We could assign these features to Schumann-Runge bands from highly vibrationally excited O_2 molecules; fitting of the spectra gives a vibrational temperature of around 10,000K! However, these excited molecules only represent about 3% of the total gas density; therefore the distribution is not a simple Maxwellian. To our knowledge, this is the first time that such vibrationally excited O_2 molecules have been observed in such low-pressure plasmas; we attribute this to the extremely high sensitivity (low baseline noise) of our absorption setup. There are several mechanisms that can be responsible for the creation of these highly-excited molecules. Firstly, electrons can cause vibrational excitation, either via temporary negative-ion resonance states at low electron energy, or via electronically-excited states above 10eV [11]. Secondly, recombination of oxygen atoms at surfaces may produce highly vibrationally-excited

molecules[12]. However, modelling and further experiments are necessary to fully understand the mechanism. High resolution measurements of the $0 \leftarrow 13$ band allows the rotational structure to be observed. Fitting of this structure gives the rotational temperature (in equilibrium with the translational temperature), which reaches 600K. Since the reactor is operated at constant pressure, the total gas density is reduced by up to a factor of two by this gas heating, compared to cold (no plasma) gas at 300K. This effect is therefore a major factor in the saturation of oxygen atom density with RF power presented above. Furthermore, higher gas temperature will greatly increase the loss rate of atoms by recombination at the reactor walls, by increasing the diffusion coefficient (scales with $T^{3/2}$) and the kinetic mean velocity (scales with $T^{1/2}$).

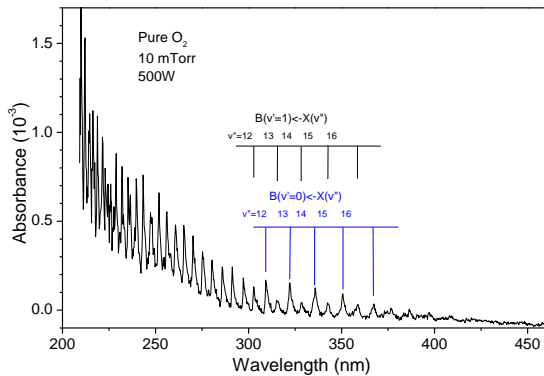


Fig. 3. Absorption spectrum of pure O₂ plasma.

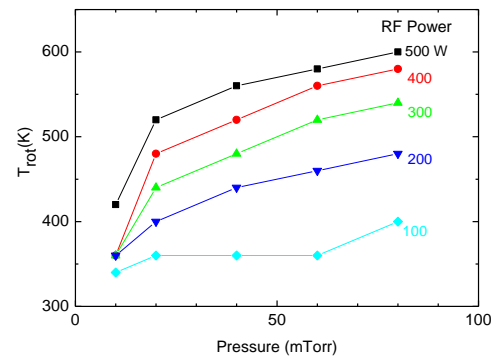


Fig. 4. O₂ rotational temperature from absorption

4. Results in pure Cl₂

The variation of the electron and chlorine atom density with Cl₂ pressure and RF power in a pure Cl₂ discharge is shown in Figs 5 and 6. The same qualitatively similar behaviour is seen as for oxygen plasmas; the electron density increases almost linearly with RF power. However, with pressure it peaks at 10-20 mTorr then drops sharply. Radial scans show that this drop in the (central) electron density corresponds to the onset of significant plasma-non-uniformity: the peak plasma density moves to a doughnut-shaped region under the spiral antenna. The atom density again increases sub-linearly with RF power, tending to saturate. However, the level at which the “dissociation degree” saturates is pressure-dependent, reaching far higher values at low Cl₂ pressure, but only reaching around 5% at pressures above 10 mTorr.

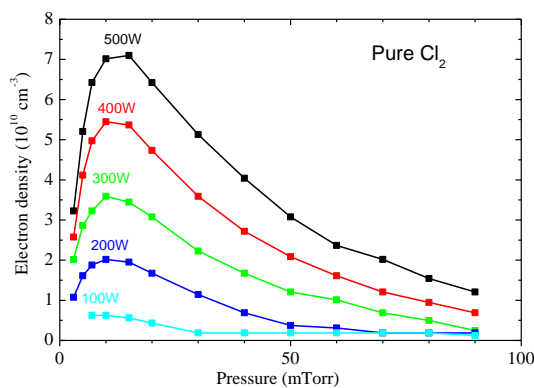


Fig. 5. Electron density in pure Cl₂ plasma.

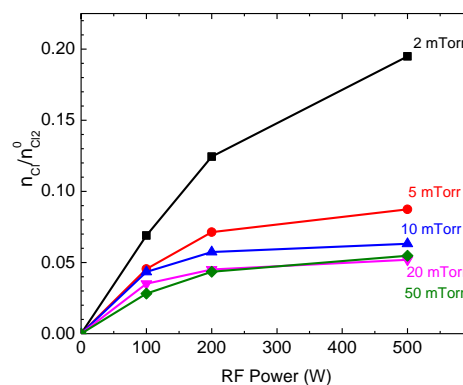


Fig. 6. Dissociation degree in pure Cl₂ plasma.

Broadband absorption spectroscopy was used to measure the density of Cl₂ molecules in the ground [13] and vibrationally excited levels. However, in this case there is much less evidence of vibrational excitation, the maximum vibrational temperature observed being in the region of 1000K. The absorption spectrum of Cl₂ is a continuum that does not allow the rotational temperature to be determined. Therefore we estimated the temperature from the Doppler broadening of transitions of argon metastable atoms (added in small quantity), measured by infrared diode-laser absorption

spectroscopy[14]. This indicated that the gas translational temperature reaches up to 1200K, much higher than in the case of O₂ plasmas. At the same time, the absorption spectra show that the Cl₂ is not depleted by more than 50% by the plasma. However, the absorption measurements are line-integrated, whereas the TALIF measurements are made at the reactor centre. This apparent paradox is the result of strong spatial gradients in the reactor: cold, un-dissociated gas resides at the reactor edge, whereas in the centre the gas is hot and more strongly dissociated.

5. Results in O₂ / Cl₂ mixtures

We investigated the behaviour of plasmas in Cl₂/O₂ mixtures as a function of composition at 10 mTorr and 500W. An example of the absorption spectra in a 20% Cl₂/ 80% O₂ plasma is shown in Fig. 6. This spectrum is composed of Cl₂ absorption (centred at 330nm), ClO radicals (centred at 270nm) and OClO (bands between 300 and 450nm). De-convolution of these spectra, and adding the TALIF data, allows the gas composition to be determined as a function of O₂ fraction in the feed-gas, as shown in Fig. 8

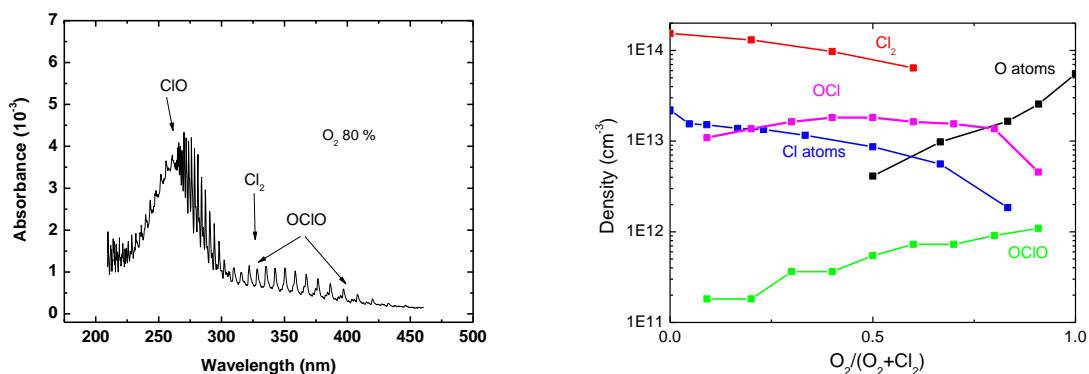


Fig 6. Absorption spectrum in 10mTorr O₂/Cl₂ plasma. Fig 8 Densities as a function of O₂ fraction.

6. Discussion and Conclusion

In this work we have made a comprehensive set of measurements of transient species densities in plasmas of O₂, Cl₂ and mixtures, as a function of gas pressure, RF power and composition. Many similarities are seen between O₂ and Cl₂: electron densities pass through a maximum with pressure, and increase linearly with RF power. Atom densities rise less than linearly with RF power, as a consequence of substantial gas heating, and saturate at values far lower than would be expected if the gas were cold and fully dissociated. O₂ plasmas show high vibrational excitation, and rotation-translation temperatures reaching 600K. In contrast, Cl₂ shows vibrational distributions close to equilibrium with rotation-translation temperatures, which reach up to 1200K. High-sensitivity ultra-broadband absorption spectroscopy is shown to be a powerful technique, allowing many molecular species, and their energy distributions, to be measured. Comparison of these results to 2-dimensional hybrid fluid/Monte-Carlo models is in progress.

7. References

- [1] Kushner, M.J. *HPEM*. Available from: <http://uigelz.eecs.umich.edu/Projects/HPEM-ICP/index.html>.
- [2] Booth, J.P., Y. Azamoum, N. Sirse, and P. Chabert, 2012, *J. Phys. D: Appl. Phys.*, **45**,
- [3] Gregorio, J. and L.C. Pitchford, 2012, *Plasma Sources Science & Technology*, **21**,
- [4] Wang, Y., O. Zatsarinny, K. Bartschat, and J.-P. Booth, 2013, *Physical Review A*, **87**,
- [5] Piejak, R., J. Al-Khuzee, and N.S. Braithwaite, 2005, *Plasma Sources Sci. Technol.*, **14**,

- [6] Piejak, R.B., V.A. Godyak, R. Garner, B.M. Alexandrovich, and N. Sternberg, 2004, *Journal of Applied Physics*, **95**,
- [7] Booth, J.P., Y. Azamoum, N. Sirse, and P. Chabert, 2012, *Journal of Physics D: Applied Physics*, **45**,
- [8] Sirse, N., J.P. Booth, P. Chabert, A. Surzhykov, and P. Indelicato, 2013, *Journal of Physics D: Applied Physics*, **46**,
- [9] Niemi, K., V. Schulz-von der Gathen, and H.F. Dobeles, 2005, *Plasma Sources Science & Technology*, **14**,
- [10] Booth, J.P., G. Cunge, F. Neuilly, and N. Sadeghi, 1998, *Plasma Sources Science & Technology*, **7**,
- [11] Laporta, V., R. Celiberto, and J. Tennyson, 2013, *Plasma Sources Science and Technology*, **22**,
- [12] Cacciatore, M., M. Rutigliano, and G.D. Billing, 1999, *Journal of Thermophysics and Heat Transfer*, **13**,
- [13] Neuilly, F., J.P. Booth, and L. Vallier, 2002, *Journal of Vacuum Science & Technology a-Vacuum Surfaces and Films*, **20**,
- [14] Cunge, G., R. Ramos, D. Vempaire, M. Touzeau, M. Neijbauer, and N. Sadeghi, 2009, *Journal of Vacuum Science & Technology A*, **27**,

INTEGRATED MODELLING ACTIVITIES FOR TOKAMAKS

Denis Kalupin^{1,2}, Stefan Matejcik³, Feodor Zaitsev⁴

¹*EUROfusion – Programme Management Unit, Boltzmannstrasse 2, 85748 Garching, Germany*

²*Institute of Energy and Climate Research – Plasma Physics, Forschungszentrum Jülich, Trilateral Euregio Cluster, D-52425 Jülich, Germany, www.fz-juelich.de/iek/iek-4*

³*Slovak Fusion Association CU, Comenius University, Bratislava, Slovakia*

⁴*FUSION, Advanced Research Group, s.r.o., Slovak Fusion Association CU, Slovakia*

E-mail: denis.kalupin@euro-fusion.org; Stefan.Matejcik@fmph.uniba.sk; feodor@zajcev.eu

Abstract

Development of the operating scenario for future fusion reactor requires the integrated modelling approach addressing the critical reactor issues: plasma heating and fuelling, radiation from impurities, MHD stability and etc. In order to demonstrate the successful operational scenario all above mentioned physics need to be a part of a single simulation, which would also cover synergies between various elements of the system. This task is not obvious and requires the development of the generic modelling platform for coupling of individual validated physics codes into scientific workflows. Such technology was developed in the frame of the Integrated Modelling Task Force. It provides the user of the platform with the: data base structured on consistent physics objects (CPOs); the universal access layer to this object and the engine to generate the workflows. There is also the assistance to the users, and particularly to newcomers, on the technical aspects of the platform use. This approach allows to build highly flexible (in terms of physics and sophistication degree) complex scientific workflows.

The European Transport Simulator (ETS) is an outstanding example, where the integration of very different physics is done into single discharge simulator. The ETS workflow couples individual modules e.g. calculating the plasma magnetic equilibrium, transport of energy and particles and their depositions by external auxiliary heating systems, impurity radiation, MHD, and allows for several options of different physics fidelity for each of physics components. Previously, the ETS was verified and used to analyse data from the existing tokamaks, and recently it has been applied to study the possible scenario in a reactor scale machine.

General approach for solution of the inverse problems of plasma diagnostics with the epsilon-net technique and its use in the European modelling activities will be discussed briefly.

Contributed paper will present the overview of the platform elements, the examples of the use of the platform based on the ETS discharge simulator. It will also discuss the plans for future developments, particularly focusing on the areas, where the activities from Slovakian association might be contributed.

ATMOSPHERIC PRESSURE PLASMA CO-POLYMERIZATION OF MALEIC ANHYDRIDE AND ACETYLENE IN DIELECTRIC BARRIER DISCHARGE

Lenka Zajíčková^{1,2}, Anton Manakhov², Marek Eliáš^{1,2}, Miroslav Michlíček^{1,2},
Adam Obrusník^{1,2}, Petr Jelínek^{1,2}, Josef Polčák³

¹*Department of Physical Electronics, Faculty of Science, Masaryk University, Brno, Czech Republic*

²*Plasma Technologies, Central European Institute of Technology - CEITEC, Masaryk University, Brno, Czech Republic*

³*Central European Institute of Technology - CEITEC, Brno University of Technology, Brno, Czech Republic*

E-mail: lenkaz@physics.muni.cz

Maleic anhydride and acetylene diluted in argon were co-polymerized in atmospheric pressure dielectric barrier discharge (6.6 kHz driving frequency). Coating contained about 11 % of COOH groups. Gas dynamics of argon in the DBD system was modelled in 3D for a possible improvement of the coating uniformity.

1. Introduction

Surfaces with amine or carboxyl functional groups find applications in adhesion promotion [1], immobilization of biomolecules [2,3], biosensors [4] and tissue engineering [5,6]. The problem of amine polymers is their stability at air and after immersion in water. Amine-rich plasma polymerized allylamine thin films showed a significant decrease in nitrogen concentration (N/C decreasing from 0.22 to 0.06) [7,8] and film thickness loss up to 90% after the immersion [9]. Although the optimization of deposition conditions can lead to significant improvements in the water stability [10,11] the reactivity of amine groups with water vapours and carbon dioxide makes it difficult to prepare amine coatings by atmospheric pressure plasma discharges. Carboxyl (COOH) functional groups are very stable at air and even in water media, especially if these groups are embedded into the organosilicon matrix. This became possible thanks to the pulsed plasma copolymerization of maleic anhydride (MA) and vinyltrimethoxysilane (VTMOS). As reported, up to 25% of carboxyl groups per carbon atoms can be deposited even by atmospheric pressure dielectric barrier discharge (DBD) [12]. The immersion in the de-ionised water during three hours did not induce the degradation of COOH intensity monitored by infrared spectroscopy.

Atmospheric pressure DBD is often used for plasma processing of soft materials. It can be operated either in filamentary or homogeneous mode [13]. Homogeneous DBD, which was discovered and studied within last 20 years, brought new possibilities into DBD applications. If obtained in He or Ne it is called atmospheric pressure glow discharge (APGD) [14,15]. Another type of homogeneous DBD can be obtained in nitrogen and it is called atmospheric pressure Townsend-like discharge (APTD) [16]. The homogeneous DBD discharge is more suitable for homogeneous plasma treatment of heat sensitive polymers or for homogeneous deposition [17] but in varying deposition mixtures it is difficult to avoid the filaments completely.

In this work, maleic anhydride (MA) and acetylene (C₂H₂) precursors were co-polymerized in nearly homogeneous DBD plasma. The aim was to prepare plasma polymers containing a high concentration of carboxyl groups that could be used in soft tissue engineering, i.e. without metallic element like Si. The role of acetylene as a second precursor is in an enhancement of the plasma coating stability if immersed in water or cell medium because a key issue is the deposition of durable and stable coating with sufficient concentration of COOH.

2. Experimental Details

The depositions were carried out in an atmospheric pressure DBD ignited by a sinusoidal high voltage (6.6 kHz) supplied with a tunable generator providing 12 W power input. The DBD electrodes were two copper rectangular plates covered by Al₂O₃ dielectrics with the thickness of 1 mm. The gap between the ceramic dielectrics was 1.65 mm. The bottom metallic electrode had the dimensions of

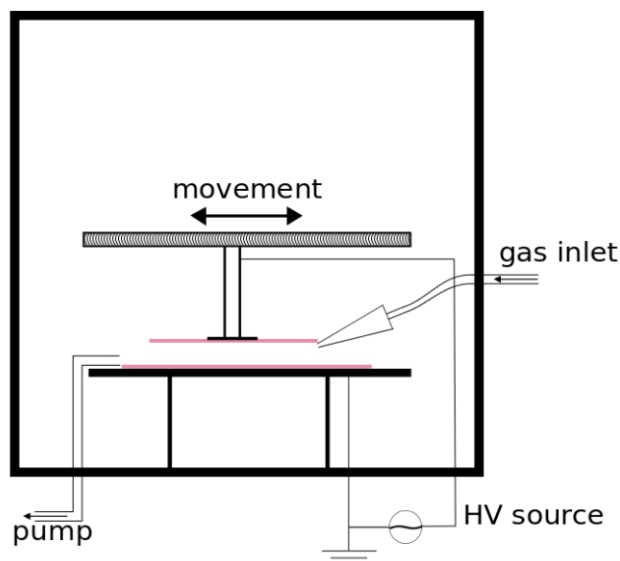


Fig. 1 Schematic drawing of the atmospheric pressure DBD set-up used for the deposition of carboxyl-containing plasma polymers from maleic anhydride.

150 mm × 60 mm, whereas the upper 20 mm × 60 mm. The upper electrode was connected to the high voltage and the bottom electrode was grounded. The deposition mixture was fed by a slit positioned at the upper electrode. The deposition uniformity was improved by moving the upper electrode with the gas supply horizontally above the bottom electrode with the substrate. The whole set-up, schematically depicted in Figure 1, was enclosed in a metallic cube with the side dimensions of 500 mm. The metallic chamber could be pumped by a rotary pump in order to ensure controlled atmosphere of the deposition process.

Plasma copolymer layers were deposited in nearly homogeneous mode of DBD from the mixture of MA and C₂H₂ diluted

in Ar. The MA vapours were delivered into the discharge by Ar flowing through a bubbler with solid MA pellets. The flow rate of MA was 0.40 sccm as calculated from the Ar flow of 1.8 slm through the bubbler. The acetylene flow rate was set to 3.0 sccm. Before starting the experiment the discharge chamber was pumped down to a pressure of 100 Pa and then filled with gases in the same ratio as for deposition up to the pressure of 96 kPa. The deposition time was 10 minutes for all samples.

Characterization of surface chemistry of the deposited films was performed by X-ray photoelectron spectroscopy (XPS) using the Omicron X-ray source (DAR400) and electron spectrometer (EA125) fitted on a custom built UHV system. The narrow scan measurements were performed at pass energies of 25 eV and the X-ray gun power was set to 270 W. The electrons take off angle was 50°. The maximum lateral dimension of the analyzed area was 1.5 mm. The quantification was carried out using XPS MultiQuant software [18]. The XPS C1s and N1s signals were fitted with the Casa XPS software after subtraction of the Shirley-type background. The XPS data curve fittings were performed in accordance with the available literature on binding energies (BE) of different carbon environments [19]. The fitting employed Gaussian–Lorentzian (G-L) peaks with the fixed G-L percentage 30%. The full width at half maximum (FWHM) was set to 1.85 ± 0.05 eV for all the peaks.

Atomic force microscopy (AFM) was measured by a commercial ambient scanning probe microscope (NT-MDT Ntegra Prima) in a semicontact mode using commercial silicon cantilevers NSG-10 (NT-MDT).

3. Results of Plasma Co-polymerization

According to the AFM measurements, the surface roughness of MA-C₂H₂ plasma copolymers deposited on silicon wafer characterized by root mean square of heights (rms) was around 50 nm. XPS analysis provided insight into the surface chemistry. Except hydrogen that can be determined by XPS the film surface was composed of 72 at.% of carbon and 27 at.% of oxygen. The concentration of oxygen in the deposited layers is relatively high compared to the atomic composition of the gas mixture supplied into the plasma. The ratio of MA to C₂H₂ in the gas mixture is equal to 1:7.5 that corresponds to O/C ratio of 0.16. Hence, the incorporation of the oxygen species into the plasma copolymer layer is more efficient compared to the hydrocarbon species.

Further investigation of the surface chemistry was based on the fitting of the XPS C1s peak that revealed details about the carbon chemical environment (Figure 2). The C1s signal was fitted as a sum of five components, (i) aliphatic carbon CH_x at 285.0 eV, (ii) carbon with single bond to oxygen (C-O) chemical shifted by 1.45 eV with the respect to 285.0 eV, (iii) carbon with a double bond to

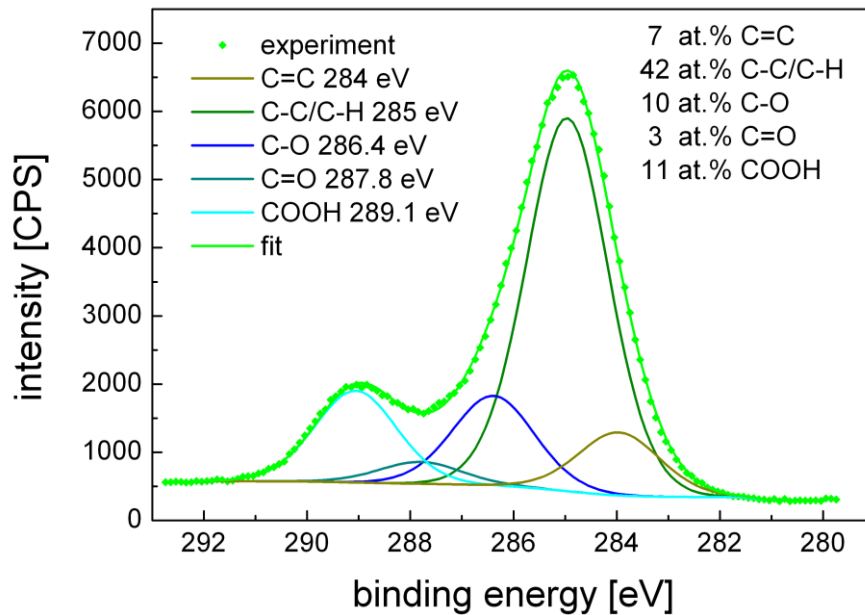


Fig. 2 Fitting of XPS C1s peak measured on the MA and C₂H₂ plasma copolymers deposited on silicon substrate.

oxygen (C=O) chemical shifted by 2.85 eV, (iv) carbon in carboxyl group (COOH) with the chemical shift of 4.1 eV and (v) an additional component with the chemical shift of -1.0 eV. The latter peak was attributed to the unsaturated carbon (C=C) related to an incomplete polymerization of acetylene, i.e. only one π -bond opening. The C-O and C=O environments are the result of MA degradation, as these moieties are not presented in the monomer structure. The density of COOH groups (11 at.%) is comparable with the previously reported results of MA or acrylic acid plasma polymerization using atmospheric pressure DBD [12,20-22]. It has been also reported in our previous work that this coating can be successfully applied to electrospun polycaprolactone nanofibrous foils without damaging the fibrous structure [23].

4. Modelling of DBD Process

Although the uniformity of the deposition was experimentally optimized by modification of gas inlet position or shape and the upper electrode was moving horizontally above the substrate the results were not completely satisfactory. Since experimental improvements require many trials without a good understanding of the process the modelling of the gas flow and even better of the deposition process is required. Therefore, we started developing a numerical model of the DBD reactor, using the expertise achieved by modelling atmospheric-pressure plasma jets and torches [24,25]. So far, the model is capable of describing the gas flow and the heat transfer in the device and since the device does not possess only plane symmetries, the equations have to be solved in full 3D. The velocity field is obtained from the Navier-Stokes equations while the temperature is calculated by solving the heat equation. These equations are solved self-consistently.

The first modelling results were obtained for an improved geometry of the DBD that is depicted in Figure 3. The upper electrode consists of two copper plates mounted to a thin dielectric plate and connected to the generator. The gas supply system starts with a plastic supply pipe connected to a rectangular buffer chamber. On the other side of the buffer chamber, there is a narrow slit, through which the gas mixture escapes. The upper ceramics is located 1 mm above the bottom ceramics plate with the grounded electrode.

Even the simple gas dynamics model has already delivered some interesting application-relevant findings. For instance, Figure 4 shows a 2D cross section through the device. It is evident that the velocity magnitude has three maxima, one in the middle of the slit (i.e. directly underneath the inlet tube) and two more at the ends of the slit. These additional maxima are a result of complex flow patterns in the buffer chamber. Figure 5 illustrates these flow patterns using velocity streamlines. It is apparent that the complex flow patterns follow from the fact that the diameter of the inlet pipe is much

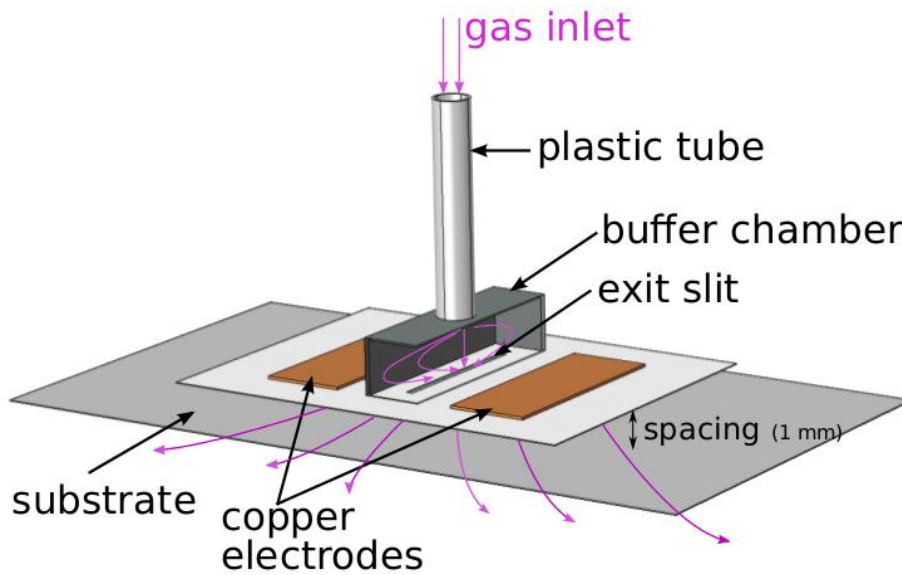


Fig. 3 A schematic view of the DBD upper electrode and gas inlet that was suggested for improvements of the deposition uniformity.

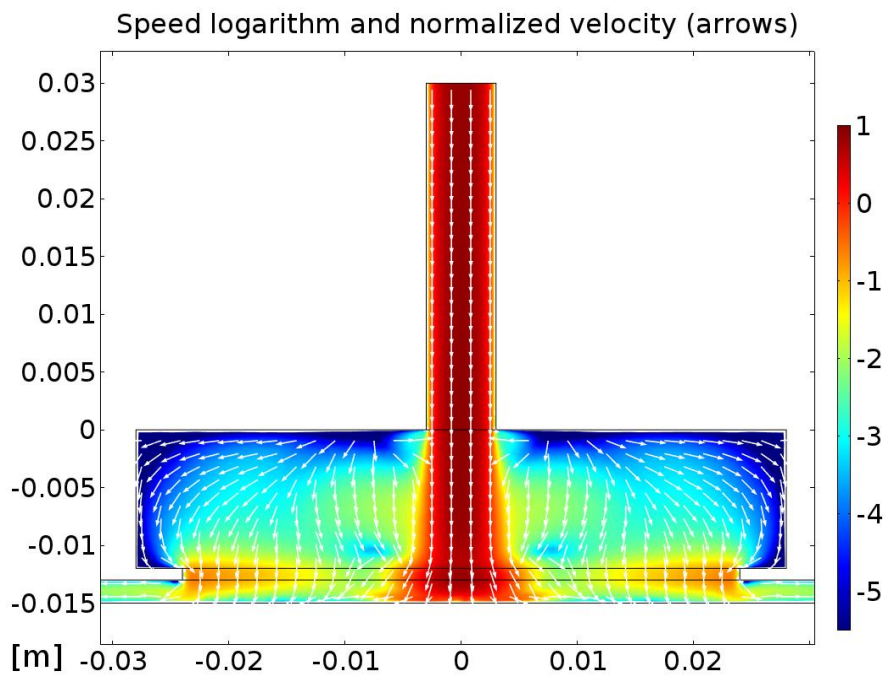


Fig. 4 Simulated gas flow velocity in the DBD reactor for the Ar flow rate of 1550 sccm.

larger than the width of the slit. The model also suggests that the recirculation makes the gas velocity along the slit more uniform. There is, however, still room for improvement which could be achieved for example by changing the shape of the buffer chamber.

Acknowledgements

This work was supported by the COST CZ project LD14036 financed by the Ministry of Education of the Czech Republic and BioFibPlas project No.3SGA5652 financed from the SoMoPro II Programme that has acquired a financial grant from the People Programme (Marie Curie Action) of the Seventh Framework Programme of EU according to the REA Grant Agreement No. 291782 and was further

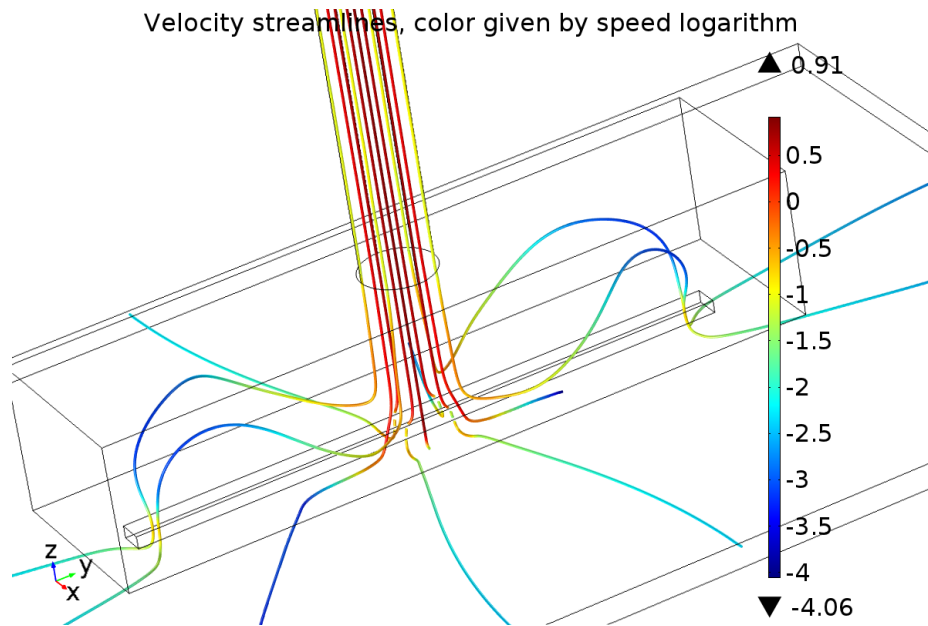


Fig. 5 Gas velocity streamlines demonstrating the 3D flow in the buffer chamber for Ar flow rate of 1550 sccm.

co-financed by the South-Moravian Region. The research was also supported by the projects “CEITEC — Central European Institute of Technology” (CZ.1.05/1.1.00/02.0068) from the European Regional Development Fund. The authors would like to acknowledge also the COST Actions, MP1101 "Biomedical Applications of Atmospheric Pressure Plasma Technology" and MP1206 "Electrospinning Nanofibers". This publication reflects only the author's views and the Union is not liable for any use that may be made of the information contained therein

5. References

- [1] Borris J, Thomas M, Klages C, Faupel F, Zaporojtchenko V 2007, *Plasma Process. Polym.* **6**, S258.
- [2] Siow K, Britcher L, Kumar S, Grieser H 2006, *Plasma Process. Polym.* **3**, 392.
- [3] Sasai Y, Matsuzaki N, Kondo SI, Kuzuya M 2008, *Surf. Coat. Technol.* **202**, 5724
- [4] Manakhov A, Skládal P, Nečas D, Čechal J, Polčák J, Eliáš M, Zajíčková L 2015, *Phys. Status Solidi A* **211(12)**, 2801.
- [5] Chua K-N, Chua K-N, Chai C, Lee P-C, Tang Y-N, Ramakrishna S, Leong K, Mao H-Q 2006, *Biomaterials* **27**, 6043.
- [6] Guex A, Kocher F, Fortunato G et al. 2012, *Acta Biomater.* **8**, 1481.
- [7] Finke B, Schroder K and Ohl A 2009, *Plasma Process. Polym.* **6**, S70.
- [8] Jarvis K and Majewski P 2013, *ACS Applied Materials and Interfaces* **5**, 7315.
- [9] Abbas A, Vivien C, Bocquet B, Guillochon D and Supiot P 2009, *Plasma Process. Polym.* **6**, 593.
- [10] Manakhov A, Zajíčková L, Eliáš M, Čechal J, Polčák J, Hnilica J, Bittnerová Š, Nečas D 2014, *Plasma Process. Polym.* **11**, 532.
- [11] Manakhov A, Nečas D, Čechal J, Pavliňák D, Eliáš M and Zajíčková L 2014, *Thin Solid Films* in press <http://dx.doi.org/10.1016/j.tsf.2014.09.015>
- [12] Manakhov A, Moreno-Couranjou M, Boscher N D, Roge V, Choquet P and Pireaux J J 2012, *Plasma Process. Polym.* **9**, 435.
- [13] Tendero C et al. 2006, *Spectrochim. Acta B* **61**, 2.
- [14] Kanazawa S, Kogoma M, Moriwaki T and Okazaki S 1988, *J. Phys. D: Appl Phys.* **21**, 838.
- [15] Trunec D, Brablec A and Buchta J 2001, *J. Phys. D: Appl. Phys.* **34**, 1697.
- [16] Gherardi N, Gouda G, Gat E, Ricard A and Massines F 2000, *Plasma Sources Sci. Technol.* **9**, 340.
- [17] Trunec D, Zajíčková L, Buršíková V, Studnička F, Sťahel P, Prysiazny V, Peřina V, Houdková J, Navrátil Z and Franta D 2010, *J. Phys. D: Appl. Phys.* **43**, 225403

- [18] Mohai M 2004, *Surf. Interface Anal.* **36**, 828.
- [19] Beamson G, Briggs D 1992, *High Resolution XPS of Organic Polymers*, Wiley&Sons, Chichester, England.
- [20] Moreno-Couranjou M, Manakhov A, Boscher N D, Pireaux J J and Choquet P 2013, *Appl. Mater. Interfaces* **5**, 8446.
- [21] Morent R, De Geyter N, Trentesaux M, Gengembre L, Dubruel P, Leys C and Payen E 2010, *Appl. Surf. Sci.* **257**, 372.
- [22] Beck A J, Short R D, Matthews A 2008, *Surf. Coatings Technol.* **203**, 822.
- [23] Michlíček M, Manakhov A, Eliáš M, Pavliňák D, Polčák J and Zajíčková L 2014, *Proceedings of NANOCON conceference*, Brno, Czech Republic
- [24] Voráč J, Obrusník A, Procházka V, Dvořák P and Talába M 2014, *Plasma Sources Sci. Technol.* **23**, 025011.
- [25] Synek P, Obrusnik A, Hübner S, Nijdam S and Zajíčková L, *Plasma Sources Sci. Technol.* submitted

COST TD1208
Workshop on Application of Gaseous Plasma with Liquids

Poster Presentations

HIGH FREQUENCY DISCHARGE BETWEEN SOLID AND LIQUID ELECTRODES

Al. F. Gaisin¹, R. Sh. Sadriev², I. Sh. Abdullin³, V. S. Zheltuhin³

¹Kazan National Research Technical University named after A.N.Tupolev

²Branch of Kazan Federal University in Naberezhnye Chelny

³Kazan National Research Technological University

E-mail: almaz87@mail.ru

We present the experimental results on burning of the high frequency discharge between a copper pin electrode and technical water, in air, within the ranges of the voltage $U = 28\text{--}75$ kV, the frequency $f = 40\text{--}100$ MHz, and the inter-electrode space $l = 2\text{--}20$ mm. We have revealed the essential influence of the pulse repetition frequency and the inter-electrode space on the development, the shape, and the structure of the high frequency discharge between the copper electrode and the technical water. We have also revealed the transition of the weakly glowing micro-discharges inside the high frequency discharge into the multichannel spark discharge. We have discovered a temperature decrease below room temperature in the inter-electrode gap of the high frequency discharge with the technical water.

1. Introduction

Over the last two decades, the multitude of papers and conferences on non-equilibrium low temperature plasmas of electrical discharges with liquid electrodes has accentuated the increasing interest in this field of plasma physics and chemistry [1]. Study of the electrical discharges in the liquids between the metal electrodes as well as between the metal and the liquid electrodes poses new problems in the face of investigators and gives the new technological opportunities. A number of applications approaching the wide practical use have already been developed: the plasma scalpel for surgery [2], the lithotripsy (special waves causing breaking the cystic calculus) [3], and a miniaturized chemical analyzer of liquid composition [4, 5]. The discharges in liquids and outside liquids produce high-power UV-radiation, shock waves, and the intensive radicals (OH, atomic hydrogen, hydrogen peroxide, etc.). This is the main reason why the above plasma types have been widely investigated over the past few decades. However, due to the essential complexity of the plasmas of electrical discharges with liquid electrodes, a profound understanding of their fundamental physics has still not been achieved. By now, only experimental investigation of discharge ignition is primarily performed and the characteristics of the DC-discharge between the solid and the liquid electrode are determined [6–10].

High frequency discharges with liquid electrodes are applied in air and water disinfection and might be used in other fields of industry. Nonetheless, the study of HF-discharges with liquid electrodes is still at its beginning [10]. Investigations of the high frequency discharge between the solid and liquid electrodes are infact absent.

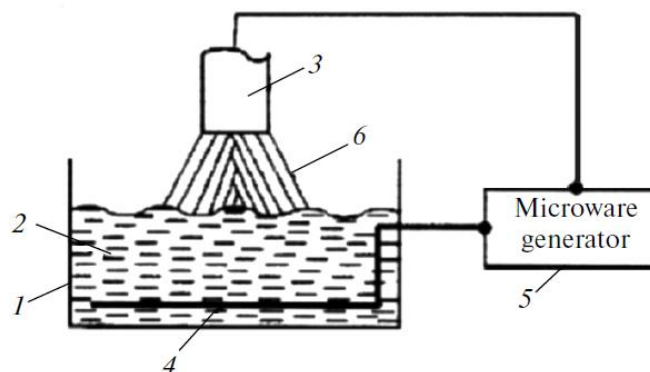


Fig. 1. Layout of the experimental facility to study the high frequency discharge between the pin and the liquid electrodes.

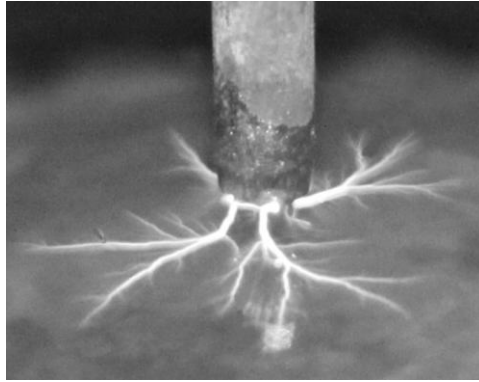


Fig. 2. Spark multichannel discharge between the copper electrode and the technical water in air, at atmospheric pressure; the interelectrode space $l = 11$ mm, the electrode diameter $d = 5$ mm.

The present work is aimed at study of the microwave electrical discharge within the ranges of the voltage $U = 28\div 75$ kV, the frequency $f = 40\div 100$ MHz, and the inter-electrode space $l = 2\div 20$ mm, between a copper pin electrode and technical water, in the air at atmospheric pressure.

2. Experimental facility and the measurement technique

We investigated the high frequency discharge between the pin cylindrical electrode and the technical water using a microwave generator adjusted to the frequencies of $40\div 100$ MHz. Figure 1 shows the functional layout of the facility. It consists of the electrolytic bath 1, the electrolytic electrode 2, the solid electrode 3, and the metal plate 4 to supply the potential to the electrolyte, the high frequency generator 5 ($f = 40\div 100$ MHz). The microwave electrical discharge 6 burns between the solid electrode and the technical water. We measured the voltage by means of the KVTs-120 kilovolt meter intended to measure the DC and the AC voltages up to 120 kV. The kilovolt meter display shows the values of the effective, the amplitude, and the averaged voltages simultaneously thus making it possible to estimate the shape and the distortion of the measured voltage. We registered the discharge by means of a Sony HDR-SR72E video camera with a single frame exposition of 0.04 s. We measured the temperature distribution by means of the TemPro300 infrared pyrometer with the error within $\pm 1.5^\circ\text{C}$.

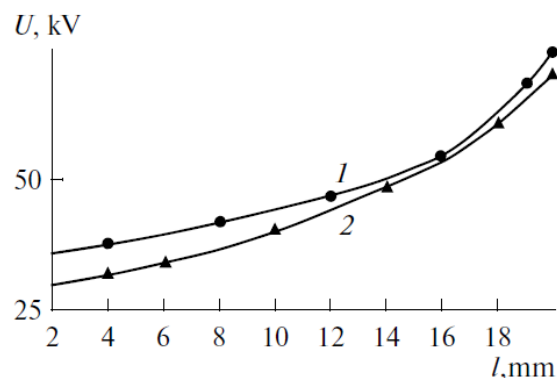


Fig. 3. Dependencies of the high frequency discharge voltage on the inter-electrode space:
1, $f = 40$ MHz, 2, $f = 100$ MHz.

3. Discussion of the experimental results

Figures 2–4 show the experimental results.

Figure 2 shows the burning of the high frequency discharge 6 between the solid cylindrical electrode 3 and the technical water 2. Here burning are the spark discharges with the developed rootage 7 on the technical water surface. Analysis of the experimental data shows that, within the l range from 14 mm to 20 mm, a multichannel micro-discharge is burning with a weak glow in the inter-electrode gap, whereas at the l below 14 mm or above 20 mm, spark discharges begin to occur.

We revealed that the multichannel micro-discharge transfers gradually into the multichannel spark discharge between the copper pin electrode and the technical water.

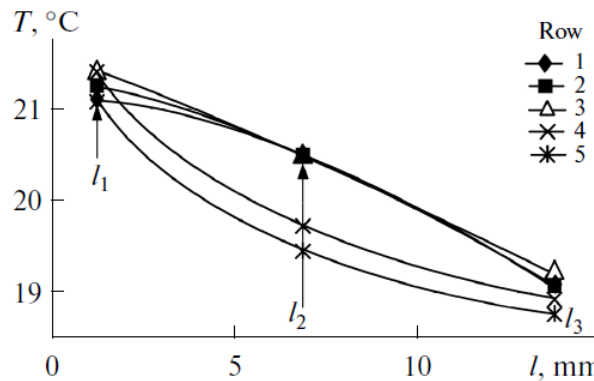


Fig. 4. Temperature distribution between the pin electrode and the technical water in air, at atmospheric pressure, $f=40$ MHz, the inter-electrode space $l = 15$ mm, the room temperature $T_r = 22^\circ\text{C}$. In the cross sections $l_1 = 1$ mm, $l_2 = 7$ mm, $l_3 = 14$ mm and in the rows 1–5 (see Fig. 5).

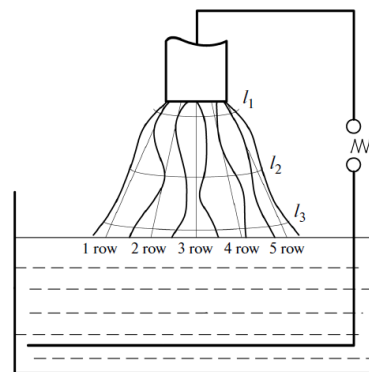


Fig. 5. Layout of measurement of the high frequency discharge temperature distribution between the pin electrode and the technical water in air, at atmospheric pressure, at $l = 15$ mm, in the cross sections l_1-l_3 and the rows 1–5.

Figure 3 shows the dependencies of the high frequency discharge on the inter-electrode space for the different frequencies of the microwave generator. Within the space range 2–14 mm, the voltage increases almost linearly, whereas within the range from 14 mm to 20 mm, the $U = f(l)$ dependency becomes nonlinear. This is caused by the transition of the multichannel spark discharge to the stable weakly glowing micro-discharges. The channels of the spark discharge move chaotically over the electrode surfaces; however, for the multichannel micro-discharge, such movement is not observed. Comparison of curves 1 and 2 in Fig. 3 shows that the U value decreases within the investigated range of the inter-electrode space, $l = 2-16$ mm, with a pulse repetition frequency increase from 40 MHz to 100 MHz. Analysis of the experimental data shows the essential influence of the pulse repetition frequency and of the inter-electrode space on the development, the shapes, and the structures of the multichannel high frequency discharge between the copper pin electrode and the technical water.

We investigated experimentally the temperature distribution in the inter-electrode gap of the high frequency discharge. Figure 5 shows the layout of the high frequency discharge temperature measurement. The experimental data are presented in the tab. 1. The temperature was measured in different cross sections, l_1-l_3 , of the inter-electrode gap.

Figure 4 and the table show that the minimal temperature $\sim 19^\circ\text{C}$ is observed near the technical water surface; it is by $\sim \Delta T = 3^\circ\text{C}$ below the room temperature (22°C). The temperature increases up to 21.5°C in the direction to the copper electrode. In the middle cross section ($l_2 = 7$ mm), the temperature varies from 20.5°C to 19.5°C ; it is higher from the left side (rows 1 and 2). The temperature decrease below room temperature is caused by the fact that, in the process of the

multichannel high frequency discharge burning, plasma-chemical reactions with heat absorption take place.

Tab. 1. Temperature distribution in the high frequency discharge between the copper cylindrical electrode and the technical water.

	1 row	2 row	3 row	4 row	5 row
$l_1 = 1 \text{ mm}$	21	21.1	21.2	21.2	21
$l_1 = 7 \text{ mm}$	20.5	20.5	20.5	19.8	19.6
$l_1 = 14 \text{ mm}$	19.1	19.1	19.2	19	18.9

4. Conclusions

(1) We have studied the electrical and temperature characteristics of the high frequency discharge between a copper pin cylindrical electrode and technical water in air at the atmospheric pressure, for various values of the inter-electrode space and the generator frequency.

(2) We have shown the influence of the generator pulse repetition frequency and of the inter-electrode space on the development, shapes, and the structure of the high frequency discharge between the solid and the liquid electrodes.

(3) We have revealed the transition, depending on the inter-electrode space, of the weakly glowing microwave micro-discharges to the spark discharge between the solid electrode and the technical water.

(4) We discovered the temperature decrease below the room temperature in the inter-electrode gap caused by the plasma-chemical reactions.

Reference

- [1] Bruggeman, P. and Chrystophe, L. *J. Phys. D: Appl. Phys.*, 2009, vol. 42, p. 053001.
- [2] Stalder, K.R., Mcmillen, D.F., and Woloszko, J., *J. Phys. D: Appl. Phys.*, 1728, vol. 38, p. 1728.
- [3] Sunka, P., *Phys. Plasmas*, 2001, vol. 8, p. 2587.
- [4] Jo, K.W., Kim, M.G., Shin, S.M., and Lee, J.H., *Appl. Phys. Lett.*, 2008, vol. 92, p. 011503.
- [5] Mitra, B., Levey, B., and Gianchandani, Y.B., *IEEE Trans. Plasma Sci.*, 2008, vol. 36, p. 1913.
- [6] Gaisin, Al.F. and Son, E.E., *High Temp.*, 2010, vol. 48, no. 3, p. 447.
- [7] Gaisin, Al.F. and Son, E.E., *High Temp.*, 2010, vol. 48, no. 5, p. 747.
- [8] Shakirova, E.F., Gaisin, Al.F., and Son, E.E., *High Temp.*, 2011, vol. 49, no. 3, p. 325.
- [9] Mustafin, T.B. and Gaisin, Al.F., *High Temp.*, 2011, vol. 49, no. 4, p. 615.
- [10] Gaisin, A.F., *High Temp.*, 2013, vol. 51, no. 6, p. 863.

LOW TEMPERATURE PLASMA OF ELECTRIC DISCHARGES WITH LIQUID ELECTROLYTE ELECTRODES IN THE SURFACE TREATMENT PROCESS

F.M. Gaisin¹, Al. F. Gaisin, F. Shakirova², G. T. Samitova²

¹*Kazan National Research Technical University named after A.N.Tupolev*

²*Zelenodolsk Institute for Engineering Industry and Information Technology*

E-mail: almaz87@mail.ru

In the paper presented results of electric steel surface treatment by low temperature plasma of electric discharges in the electrolyte. The results of forms and structure of discharge, voltage and current waveforms, discharge spectrum in the UV-range, metallographic analysis, surface roughness analysis, sclerometer analysis are presented in the paper.

1. Introduction

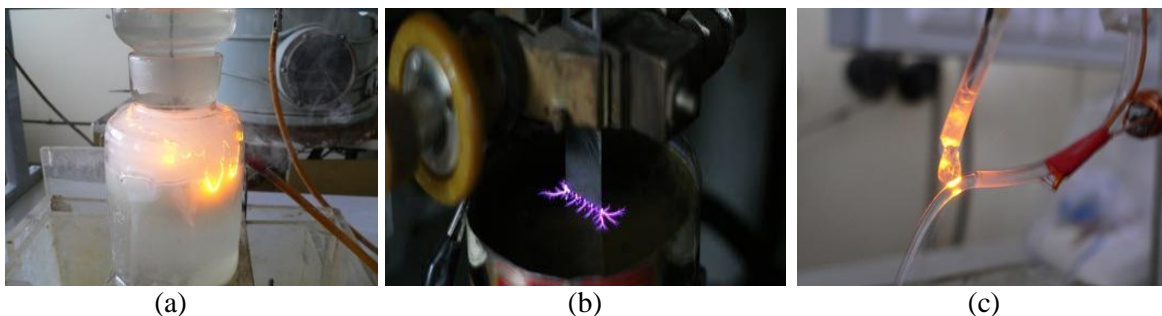
Gas discharges with liquid electrodes are known more than a hundred years. But still now there is no general fundamental theory which describes these discharges. Physics of processes in such kind of discharges are very dynamic. Low temperature plasma of electric discharges with liquid electrolyte electrodes finds wide application in different branches of industry. Electric discharges with liquid electrolyte electrodes are used for different materials surface treatment, air and liquids sterilization. Therefore the purpose of this work is to research the parameters of the discharge in the electric steel surface treatment process.

2. Experiment and results

To achieve the purpose has been developed the experimental set-up which includes high-frequency current generator which tuned to frequency 13.56 MHz, discharge chamber, electrolytic cell and diagnostic equipment (Fig.1). Figure 2 shows different forms of electric discharges with liquid electrolyte electrodes. The main contribution to surface treatment is due to anodic dissolution and ion impact. Steam gas shell with micro discharges cover and treat the sample surface. Cathode spots appear on the electrolyte surface. The main contribution to surface treatment is due to anodic dissolution and ion impact. Figure 3 shows electric steel surface microrelief before and treatment. Figure 4 shows results of steel surface roughness analysis.



Fig.1 Experimental set-up



(a)

(b)

(c)

Fig.2 Electric discharge forms: (a) - steam-gas, (b) – between solid and electrolyte, (c) – between electrolytes.

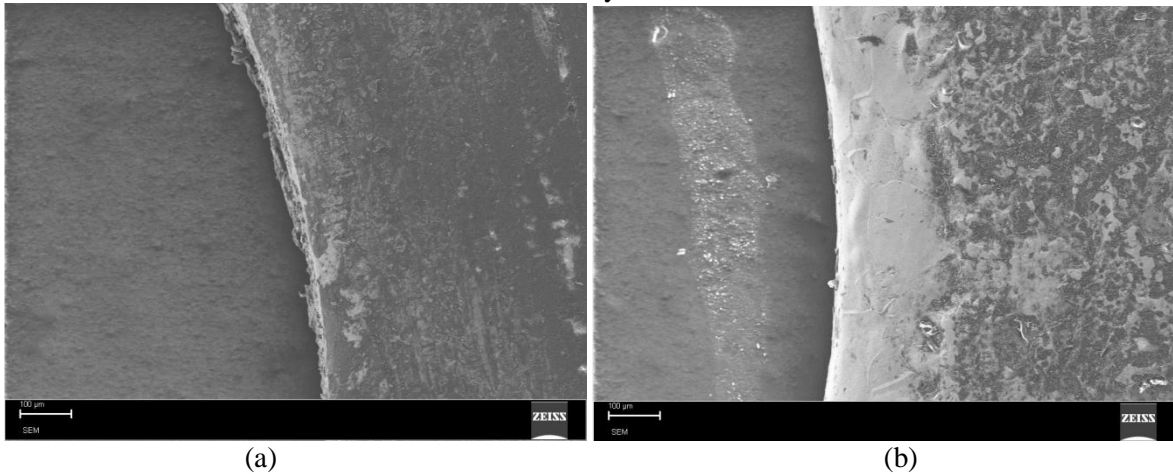


Fig. 3 Electric steel surface microrelief: (a) – before treatment, (b) – after treatment.

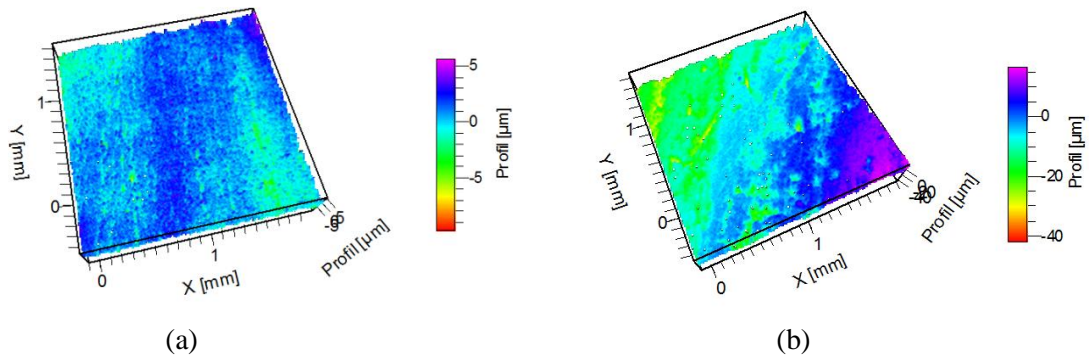


Fig.4 Electric steel surface roughness analysis: (a) – before treatment, (b) – after treatment.

3. Reference

- [1] Bruggeman, P. and Chrystophe, L. *J. Phys. D: Appl. Phys.*, 2009, vol. 42, p. 053001.
- [2] Stalder, K.R., Mcmillen, D.F., and Woloszko, J., *J. Phys. D: Appl. Phys.*, 1728, vol. 38, p. 1728.
- [3] Sunka, P., *Phys. Plasmas*, 2001, vol. 8, p. 2587.
- [4] Jo, K.W., Kim, M.G., Shin, S.M., and Lee, J.H., *Appl. Phys. Lett.*, 2008, vol. 92, p. 011503.
- [5] Mitra, B., Levey, B., and Gianchandani, Y.B., *IEEE Trans. Plasma Sci.*, 2008, vol. 36, p. 1913.
- [6] Gaisin, Al.F. and Son, E.E., *High Temp.*, 2010, vol. 48, no. 3, p. 447.
- [7] Gaisin, Al.F. and Son, E.E., *High Temp.*, 2010, vol. 48, no. 5, p. 747.
- [8] Shakirova, E.F., Gaisin, Al.F., and Son, E.E., *HighTemp.*, 2011, vol. 49, no. 3, p. 325.
- [9] Mustafin, T.B. and Gaisin, Al.F., *High Temp.*, 2011, vol. 49, no. 4, p. 615.
- [10] Gaisin, A.F., *High Temp.*, 2013, vol. 51, no. 6, p. 863.

PLASMA TREATMENT OF HOLLOW OBJECTS USING SURFACE DBD WITH LIQUID ELECTRODES

David Pavliňák, Oleksandr Galmiz, Antonín Brablec, Vít Kudrle, Mirko Černák

Department of Physical Electronics, Masaryk University, Kotlářská 2, 61137 Brno, Czech Republic

E-mail: kudrle@sci.muni.cz

A novel type of surface dielectric barrier discharge using water-solution electrodes is presented. It generates thin layers of visually diffuse plasmas along the treated polymer surfaces. The technique has been designed particularly to perform a plasma treatment of surfaces of polymeric tubes and other hollow bodies which is currently a serious challenge for atmospheric pressure plasma processing. As an example, the results of plasma treatment of PTFE tubes are discussed.

1. Introduction

Electrical discharges generated at atmospheric pressure in and around liquids have attracted wide scientific interest [1-4]. The water based electrolytes are the most often studied as they are promising for a wide range of potential applications. Plasmas generated in liquid vapours have already demonstrated their potential for surface modification of polymer materials [5-7] and are currently tested for their capability to generate selectively functionalised polymer surfaces [7].

Dielectric barrier discharge (DBD) technology is well established and widely used in industry for various purposes. Surface DBDs (SDBDs) typically generate thin layers plasma over the dielectric barrier surface. Eg. the diffuse coplanar surface barrier discharge (DCSBD) is extremely suitable [8-10] for plasma surface treatment of many materials as it produces visually diffuse plasma.

In this paper we describe a newly developed [11] device, combining both approaches. The technique has been aimed particularly to achieve uniform atmospheric pressure plasma treatment of inner surfaces of polymeric tubes and other hollow bodies for applications [12] as cleaning, sterilisation, activation and coating of biomedical devices, surface modification of microfluidic channels, etc. To illustrate the application potential of such liquid electrode SDBD and its basic physical properties we present the example of permanent hydrophilisation of inner and outer surfaces of polytetrafluoroethylene (PTFE) tubes.

2. Experimental

A schematic diagram of the experimental set-up is shown in Fig. 1a. A common laboratory PTFE tube with an outer diameter of 8 mm and inner diameter of 7 mm was selected as a sample to be treated, as PTFE is widely used in engineering but its hydrophobic properties often limits biomedical applications. The polymer sample to be treated forms also the DBD dielectric barrier.

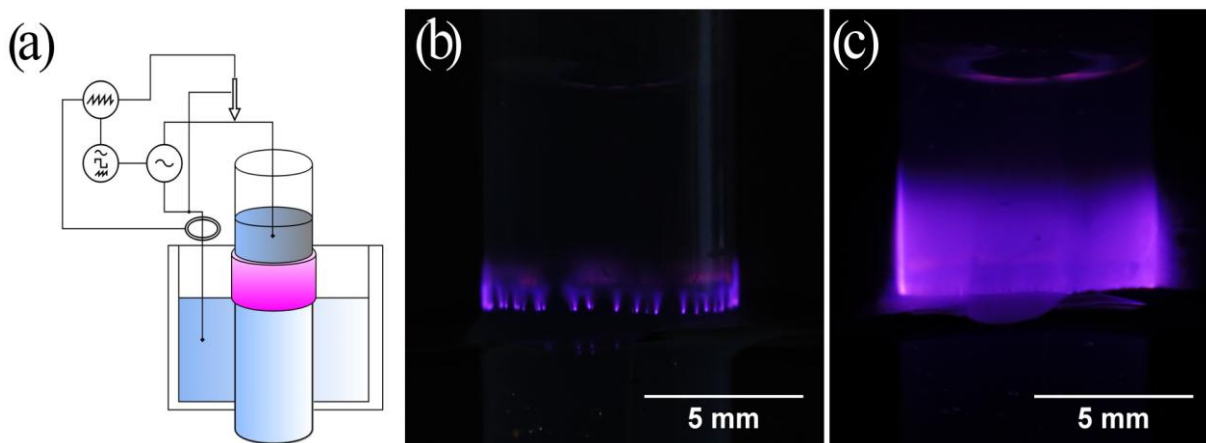


Fig.1. Schematic drawing of the experimental set-up for a treatment of the outer tube surface (a) and the discharge photographs taken at the discharge power of 3 W (b) and 9 W (c).

The oxalic acid solution inside and outside the tube serve as liquid electrode. The SDBD is generated between uneven levels of the liquid inside and outside of the tube. The discharge was excited by a sinusoidal alternating current (AC) high voltage power supply with the amplitude of 15-20 kV and the frequency of 25-30 kHz.

To simulate the intended application (an industrial plasma treatment of PTFE tubes) the tube was moved vertically with the speed of 10 cm/min continuously during the plasma treatment.

The photographs of the discharge generated on the outer tube surface are presented in Fig. 1b and Fig. 1c.

3. Results and discussion

The discharge uniformity increases with the input power as demonstrated in Fig. 1(b) and Fig. 1(c). For the surface treatment applications it is very important feature of the discharge. A similar behaviour was observed in diffuse coplanar surface barrier discharges (DCSBDs) [8-10]. In contrast, in the atmospheric pressure glow discharges (APGDs) the increasing discharge power causes a transition from the homogeneous glow discharge mode to that of visually non-uniform filamentary discharge.

The Fig. 2 shows the temporal evolution of the discharge current during both positive and negative polarity. The waveforms for the discharges generated over inner vs. outer tube surfaces were very similar to each other.

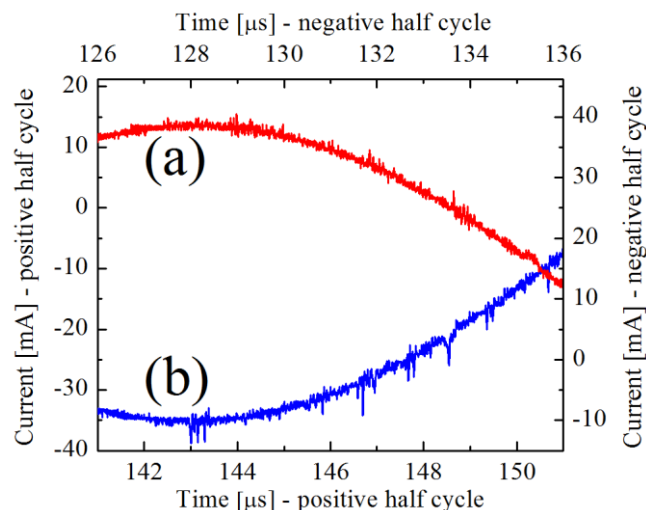


Fig. 2. Discharge (over outer surface of the tube) current waveforms taken at the negative (a) and positive (b) half cycle maximum.

Although the plasma in Fig. 1(c) appears as an uniform diffuse discharge, in reality the discharge consists of many short (<10 ns) micro-discharges, forming the peaks on the current waveforms in Fig. 2. Several micro-discharges randomly form and disappear during each half cycle of the applied voltage. The existence of these micro-discharges was confirmed also by high speed imaging [11]. Their formation is influenced [13] by the extremely high electric field at a line of contact between the air, water surface and PTFE surface [14]. This local field can be enhanced even more by the AC electrowetting effect [15].

Static contact angle measurements were carried out on untreated and plasma-treated inner and outer surfaces of the PTFE tubes. After the surface curvature corrections the results obtained for the inner and outer surfaces were practically the same. The obtained contact angles were less than 90° and permanent (negligible ageing effect) as demonstrated in Fig. 3. These results are comparable to those of a low-pressure water plasma treatment of PTFE, which induces relatively deep surface modification preventing polymer chain reorientations [16].

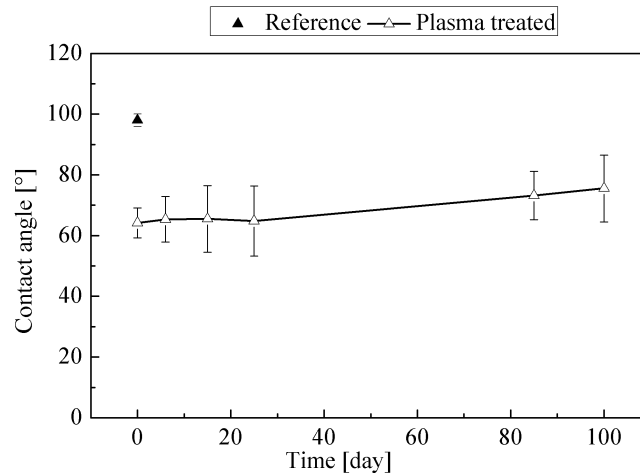


Fig. 3. Effect of the plasma treatment of PTFE and its ageing during 100 days, as demonstrated by changes in contact angle.

4. Conclusion

The technique using liquid electrodes to generate surface dielectric barrier discharge is viable and technically simple technique to plasma treat a dielectric hollow object. The experimental results for PTFE tubes show its ability to operate in continuous mode and treat both inner and outer surfaces without the use of any expensive equipment or gases. The contact angle after the plasma treatment is comparable to other techniques and does not degrade with time.

5. Acknowledgements

The authors acknowledge support by the project CZ 1.05/2.1.00/03.0086 (*CEPLANT - R&D center for low-cost plasma and nanotechnology surface modifications*) funded by European Regional Development Fund.

6. References

- [1] J. S. Clements, M. Sato and R. Davis, *IEEE Trans. Ind. Appl.* **23**, 224 (1987).
- [2] B. Jiang, J. Zheng, S. Qiu, M. Wu, Q. Zhang, Z. Yan, Q. Xue, *Chem. Eng. J.* **236**, 348 (2014).
- [3] R. Joshi, S. Thagard, *Plasma Chem. Plasma Process.* **33**, 1 (2013).
- [4] P. Bruggeman, C. Leys, *J. Phys. D: Appl. Phys.* **42**, (2009).
- [5] A. Brablec et al, *Czech. J. Phys. Suppl. D* **52**, 491 (2002).
- [6] A. Y. Nikiforov, C. Leys, *Plasma Chem. Plasma Process.* **26**, 415 (2006).
- [7] R.S. Joshi, J.F. Friedrich, and M.H. Wagner, *Eur. Phys. J. D* **54**, 249 (2009).
- [8] M. Simor, J. Rahel, P. Vojtek, M. Cernak and A. Brablec, *Appl. Phys. Letters* **81**, 2716 (2002).
- [9] M. Cernak et al, *Plasma Phys. Control. Fusion* **53**, 124031 (2011).
- [10] T. Homola et al, *Plasma Chem. Plasma Process.* **33**, 881 (2013).
- [11] D. Pavliňák et al, *Applied Physics Letters* **105**, 154102-3 (2014).
- [12] M. Cernak et al, Czech Patent Application, PV 2013-1045, (submitted 19th December 2013)
- [13] A R Hoskinson, N Hershkowitz, *J. Phys. D: Appl. Phys.* **43**, 065205 (2010).
- [14] N. M. Jordan et al, *J. Appl. Phys.* **102**, 033301 (2007).
- [15] H. Lee, S. Yun, S. H. Ko and K. H. Kang, *BIOMICROFLUIDICS* **3**, 044113 (2009).
- [16] R. C. Chatelier, X. Xie, T. R. Gengenbach and H. J. Griesser, *Langmuir* **11**, 2576-2584 (1995).

THE EFFECT OF THE PLASMA NEEDLE ON THE WOUND HEALING PROCESS

Ihor Korolov¹, Barbara Fazekas², Márta Széll^{2,3}, Lajos Kemény^{2,4}, Kinga Kutasi¹

¹*Wigner research centre for physics Institute for Solid State Physics and Optics, Wigner Research Centre for Physics, Hungarian Academy of Sciences, Konkoly-Thege Miklos str. 29-33, H-1121 Budapest, Hungary*

²*University of Szeged, Faculty of Medicine, Department of Dermatology and Allergology, 6720 Szeged, Korányi fasor 6.*

³*Institute of Medical Genetics, Faculty of Medicine, University of Szeged, Szeged, Hungary*

⁴*MTA-SZTE Dermatological Research Group, University of Szeged, Szeged, Hungary*

E-mail: kutasi.kinga@wigner.mta.hu

We performed the direct treatment of HPV-immortalized human keratinocytes, protected by a layer of phosphate buffered saline (PBS) solution, with the plasma generated in flowing helium with a plasma needle. A 4 mm scratch made on the cell culture served as the model for a wound. The conducted systematic study has shown, that there is a maximum in the wound reduction as a function of the plasma input power and treatment time, while the closing speed changes with the elapsed time.

1. Introduction

The recognition that non-thermal plasmas can be useful tools for medicine has triggered numerous investigations aiming to understand the effect of discharge plasmas on human cells. The application of plasmas in medicine first of all target the chronic wounds, which constitute a serious problem for the society, as millions suffer poorly healing chronic wounds [1]. Several types of atmospheric plasma sources have been developed, such as argon plasma jet [2], plasma needle [3,4], dielectric barrier discharge [5] and investigated its antibacterial effect [6] and the plasma species effect on cells [1,3,7,8]. With our studies we aim to contribute to the understanding of the plasma effect on the keratinocyte cells, which participate in the wound healing process.

2. Experimental

In the present study the effect of the plasma on the wound healing process has been studied through the treatment of HPV-immortalized human keratinocyte cells, protected from desiccation by phosphate buffered saline (PBS) solution, with the non-equilibrium plasma generated by a plasma needle [4,9].

2.1. Plasma Needle

As its name infers, in the case of the plasma needle the discharge is ignited at the tip of a needle. In the present case the needle consists of a central electrode that is made of wolfram and is 0.3mm in diameter. The needle is covered by a slightly larger ceramic tube, leaving 2 mm of the needle free, both being placed in a glass tube of 4 mm inner and 6 mm outer diameter. The needle body is made of Teflon. Helium is flowing between the ceramic and the glass tube. We used flow rates of 1 and 1.45 slm (standard liters per minute). The central electrode is powered by a 13.56 MHz power generator (KJLC R601) through a matching network. Plasma is ignited between the needle and a grounded electrode, here served by the support of the plates, which contain the cell culture, as shown in Fig. 1.

We conducted two types of the experiments, which required the use of two different types of plates. In the first case, in the wound-healing assay treatment we used a 24-well plate, which has wells of 16 mm diameter and 20 mm height. Here the cells attached to the bottom of the well are covered with a PBS layer of 1.5 mm thickness, and the needle is approached to 3 mm distance to the PBS surface. In this case the tip of the needle is in line with the end of the glass tube. Consequently, the inter-electrode distance is 5 mm. In this case the visible plasma glow, shown in Fig. 2, covers a 5 mm

diameter circular area of the sample. During these treatments a glass lid was also used in order to limit the treatment environment to predominantly helium, as shown in Fig.1.a.

In the proliferation experiments a 96-well plate has been used, which belongs to the xCELLigence microelectronics biosensor system for cell-based assays, which provides dynamic, real-time, label-free cellular analysis. The wells have 6 mm diameter and 10 mm height. In this case PBS layer 3.5 mm. In order to be able to reach the PBS surface the 2 mm tip length of the needle was pushed out of the glass tube, as illustrated in Fig.1.b. Consequently, the distance between the tip of the needle and the PBS surface was around 4.5 mm, while the inter-electrode distance 8 mm.

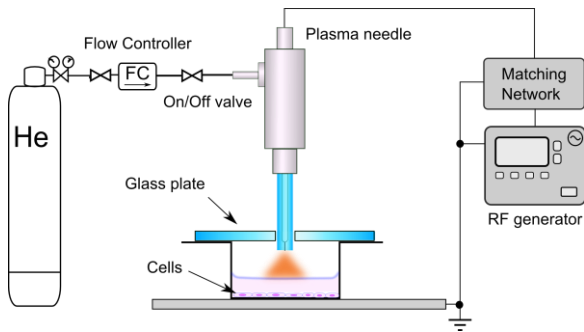


Fig.1.a. Schematic representation of the experimental set-up used in scratched cell assay experiments.

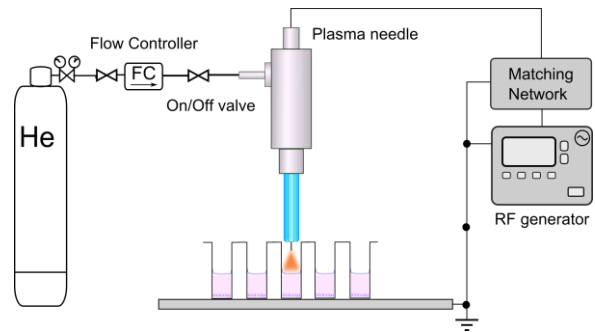


Fig.1.b. Schematic representation of the experimental set-up used in proliferation experiments with cells treated in 96-well plates.



Fig.2. Image of the plasma needle glow.

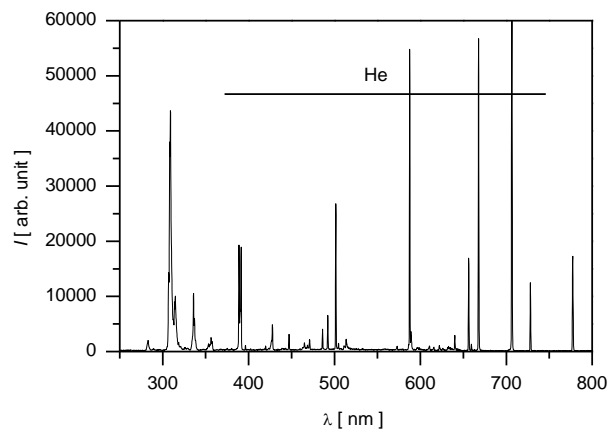


Fig.3. Spectra of the plasma needle ignited in the well covered with a glass lid, which assures predominantly helium environment.

2.2. Scratch Assay

HPV-immortalized human keratinocytes (HPV-KER clone II/15) according to the procedure described in Ref. [10,11] were seeded in serum-free keratinocyte basal medium (KER-SFM, Gibco, Thermo Fisher Scientific Inc, Waltham, MA USA) supplemented with L-glutamine and antibiotic/antimycotic solution containing penicillin, streptomycin and amphotericin B (Sigma-Aldrich, USA). Keratinocytes were grown at 37 °C in a 5% CO₂ atmosphere. With 48 h before the experiment 1×10⁵ cells were seeded into the 24-well plate (Corning, Sigma-Aldrich, USA). Before treatment a scratch wounding was performed with a cell scraper of 4 mm width according to a well-established *in vitro* wound-healing assay [12], as shown in Fig.4. For plasma treatment the medium covering the keratinocytes was replaced with PBS. The size of the scratch was observed by microscopy and recorded subsequently by measurement of the scratch width using Adobe Photoshop. Scratch width reduction was calculated by subtraction of scratch width at t = n hours from scratch width at t = 0 h.

For the proliferation experiments 5×10^3 cells were seeded into the 96-well plate.

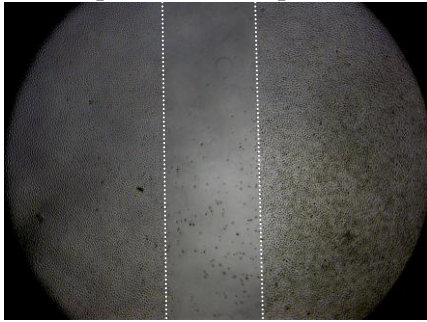


Fig.4. Image of the scratch on the cell culture.

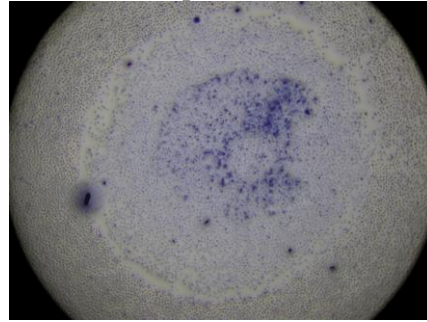


Fig.5. Cell death and detachment caused by plasma treatment, when cells are protected with 200 μ l PBS, equivalent to 1 mm thick layer, visualized by staining the dead cells with Methylene blue.

3. Results

As a first step we investigated the viability of the cells under different discharge and treatment conditions, which includes the needle configuration, plasma input power, protecting PBS layer thickness. These studies were conducted on cells seeded into 24-well plates, as well as 6-well plates with well diameters of 16 mm and 48 mm, respectively. It has been found that in the 24-well plate a PBS layer thicker than 1 mm is necessary to protect the cells. This is illustrated on Fig.5., where the death of the cells can be observed on the plasma treated area in case of 1 mm PBS layer. The distribution of the dead and detached cells show the structure of the plasma, presumably the distribution of active species. Repeating the same experiment in the 6-well plate found that due to the complex chemistry of the system the effect depends not only on layer thickness, but also the volume of the solution, since in the 6-well plate the 1 mm layer appeared to protect the cells from death.

On the second step we performed the treatment of scratched assays using 300 μ l PBS in the 24-well plates. The evolution of the scratch has been monitored along 40 h after plasma treatment, microscopy images being recorded at 17 h, 24 h and 40 h. Fig.6.a.-c. show the measured scratch width reduction as a function of plasma input power for different treatment times at the three elapsed times. The evolution of the control assay is also shown here. At each condition we took the average of the results of three separate samples. It can be seen that at majority of conditions the scratch width reduction is higher than in the case of the untreated assay. At higher elapsed times the best results are obtained at the lowest investigated input power. In case of higher powers the increased proliferation obtained right after the plasma treatment slows down with time. A similar effect can be observed also in the proliferation experiments. Fig.6.c. shows the time evolution of the cell index monitored with the xCELLigence biosensor for selected conditions.

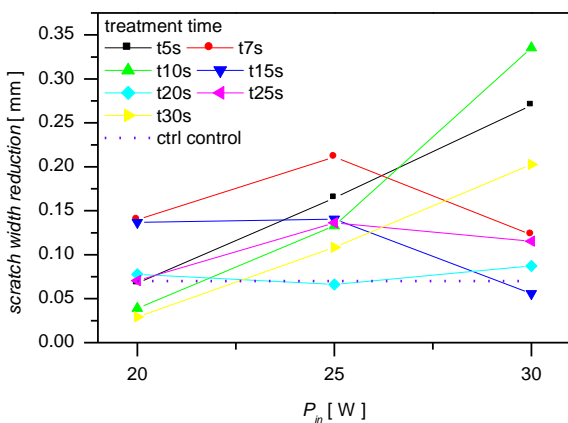


Fig.6.a. The reduction of the scratch width with 17 h after plasma treatment.

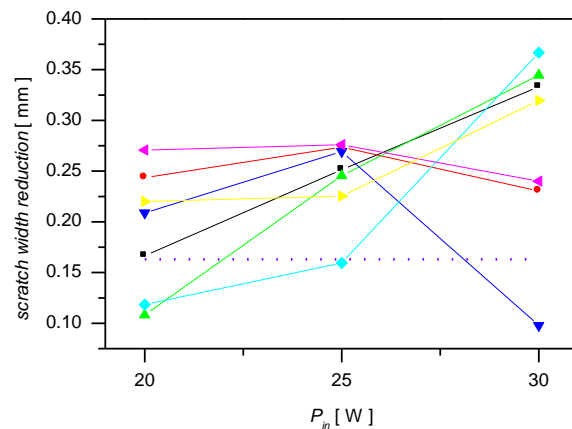


Fig.6.b. The reduction of the scratch width with 24 h after plasma treatment.

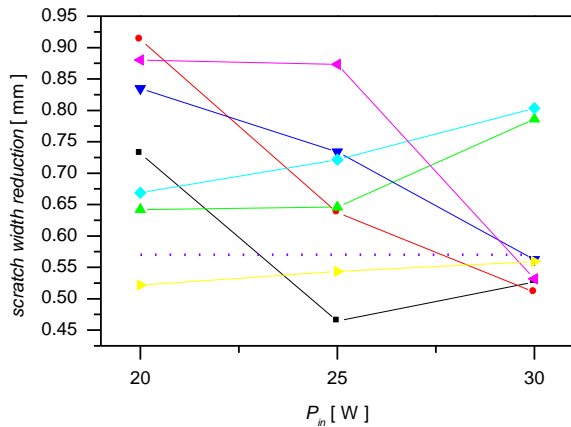


Fig.6.c. The reduction of the scratch width with 40 h after plasma treatment.

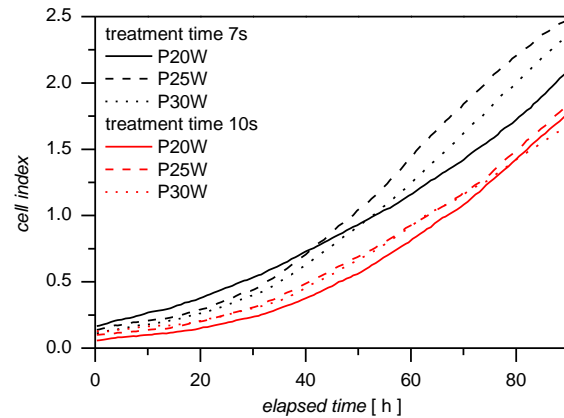


Fig.6.d. Cell index indicating the cell proliferation as a function of time as measured with the xCELLigence microelectronics biosensor.

4. Conclusions

The effect of the plasma needle on the wound healing process has been investigated using HPV-immortalized human keratinocytes. The wound was modeled with a scratch made on the cell culture. The cells protected by a layer of phosphate buffered saline (PBS) solution were directly treated with the plasma generated in flowing helium with a plasma needle. We have shown that the minimum thickness of PBS layer, which protects the cells during treatment depends on the volume of the solution used, i.e. in larger wells thinner layer appeared to protect the cells from death. Monitoring the reduction of the scratch width after plasma treatment for 40 h, we have found that there is a maximum in the wound reduction as a function of the plasma input power and treatment time, while the closing speed changes with the elapsed time.

Acknowledgement

This work has been financially supported by the Hungarian Scientific Research Fund, via Grant OTKA K104531. The authors acknowledge also the support of COST Action MP1101 and TD1208.

5. References

- [1] Wende K. *et al.* 2010 *IEEE Trans. Plasma Sci.* **38** 2479.
- [2] Reuter S. *et al.* 2012 *Plasma Sources Sci. Technol.* **21** 034015.
- [3] Kieft I. E., Kurdi M. and Stoffels E. 2006 *IEEE Trans. Plasma Sci.* **34** 1331.
- [4] E. Stoffels, A. J. M. Roks, L. E. Deelman 2008 *Plasma Process. Polym.* **5** 599.
- [5] Fridman G *et al.* 2006 *Plasma Chem. Plasma Process.* **26** 425.
- [6] van Gils C. A. J. *et al.* 2013 *J. Phys. D: Appl. Phys.* **46** 175203.
- [7] Dobrynin D, Fridman G, Friedman G and Fridman A 2009 *New J. Phys.* **11** 115020
- [8] M. Miletic *et al.* 2013 *J. Phys. D: Appl. Phys.* **46** 345401.
- [9] N. Puac *et al.* 2006 *J. Phys. D: Appl. Phys.* **39** 3514.
- [10] Polyanka H. *et al.* 2011 *J. Invest. Dermatol.* **131** (Suppl.2) S70.
- [11] Fazekas B. *et al.* 2014 *J Photochem Photobiol B.* **140** 215.
- [12] K. Matsuura, T. Kuratani, T. Gondo, A. Kamimura, and M. Inui 2007 *Eur. J. Pharmacol.* **563** 83.

PLASMA GUN DECONTAMINATION OF BACTERIA IN LIQUID SUSPENSIONS

Marco Boselli², Francesca Cavrini², Vittorio Colombo¹⁻², Matteo Gherardi¹,
Romolo Laurita¹, Anna Liguori¹, Emanuele Simoncelli¹, Augusto Stancampiano¹,
Luca Viola¹

¹ *Department of Industrial Engineering (D.I.N.), Alma Mater Studiorum-Università di Bologna, via Saragozza 8, Bologna 40123, Italy*

² *Interdepartmental Center for Industrial Research – Advanced Applications in Mechanical Engineering and Materials Technology (I.C.I.R.-A.M.M.), Alma Mater Studiorum-Università di Bologna, via Saragozza 8, Bologna 40123, Italy*

E-mail: emanuele.simoncelli@unibo.it

The contribution reports on the antibacterial efficacy of a *Plasma Gun*, which produces a non-equilibrium atmospheric pressure plasma that propagates through a flexible dielectric channel. The antibacterial activity was assessed by treating liquid suspensions contaminated with *Staphylococcus aureus*. Optical Emission Spectroscopy (OES) of the produced plasma plume was performed in order to qualitatively analyse its chemical composition. The results here presented for different operating conditions prove the suitability of the *Plasma Gun* source for antibacterial applications.

1. Introduction

Atmospheric pressure non-equilibrium plasma sources able of propagating plasma through dielectric capillaries over distances of tens of centimeters (*Plasma Guns*) [1-3] are raising great interest for their potential in a wide range of biomedical applications, such as cancer cells treatment and endoscopic therapies [4-5].

Since in the field of Plasma Medicine it's nowadays established the importance of plasma induced liquid chemistry that acts on cells (both prokaryotic and eukaryotic), such as in the decontamination of living tissue [6-7], in the present work the antibacterial efficacy of a non-equilibrium atmospheric plasma was evaluated on bacteria suspended in a liquid solution in order better simulate a realistic clinical environment.

In particular, the antibacterial activity of a wire electrode flexible *Plasma Gun*, driven by a high voltage micropulsed generator, was investigated by treating liquid suspensions contaminated with *Staphylococcus aureus* and quantitatively evaluating the associated reduction of bacterial load; various operating conditions were considered, in order to evaluate the effect of varying peak voltage and treatment time. Furthermore, as Plasma Gun sources are known to generate guided ionization waves (GIWs) that produce reactive species of oxygen (ROS) and nitrogen (RNS), holding a key role in antibacterial efficacy of plasma treatment, when interacting with ambient air [8], Optical Emission Spectroscopy (OES) analysis of the produced plasma plume was performed in order to evaluate its chemical composition.

2. Experimental setup

Plasma Gun source

The plasma source adopted in this work is a wire electrode *Plasma Gun* developed in our laboratory. The high voltage electrode is a tungsten wire with a diameter of 1 mm and a length of 50 mm; as the outer electrode, a 25 mm width grounded aluminium foil wrapped around the dielectric channel was used. Plasma generation is confined in a 100 mm long borosilicate glass tube, with inner and outer diameters of 4 mm and 6 mm, respectively; the borosilicate glass is connected to a 200 mm long PTFE flexible tube, transparent in the visible region of light spectrum, with the same diameters of the previous one, where the plasma propagates, eventually producing a plasma plume at the tube outlet.

The working gas used is 99.999% pure helium. The plasma device is driven by a micropulsed generator producing high voltage sinusoidal pulses; in the experiments, the pulse width was set at 600 μs and the duty cycle at 6%.

In order to identify the reactive species produced by *Plasma Gun* source, an iCCD camera (PIMAX3, Princeton Instruments) mounted on a 500 mm spectrometer (Acton SP2500i, Princeton Instruments) was adopted to collect optical emission spectra in the ultraviolet (UV), visible (VIS) and near infrared (NIR) regions. Exposure time was set at 20 μs and for each spectrum a set of 50 accumulations was collected on the CCD sensor.

Bacterial liquid solution

The antibacterial activity was investigated testing the gram positive *Staphylococcus aureus*, which is a common cause of skin and wound infections, but it is associated also to soft tissue, bone, joint, endovascular and respiratory infections. For the experiments, a *S. aureus* suspension was prepared in NaCl 0.9% from an overnight culture. The bacterial suspension was adjusted to approximately 10^7 - 10^8 CFU (Colony Forming Units) ml^{-1} based on McFarland turbidity standards and quantitative dilution technique. The bacterial suspension was then introduced and plasma treated in 96-wells plates (50 μl of bacteria suspension per well). Immediately after treatment the samples were serially diluted in NaCl 0.9%, plated on tryptone soy agar plates and incubated for 24h at 37°C to quantify the number of viable bacterial cells. The number of bacterial cells recovered after plasma treatment was compared to bacterial cells number of untreated samples (control). Each test was performed in duplicate.

Plasma treatment

Plasma Gun treatment of contaminated suspensions was performed for various operating conditions, in order to evaluate the effects of varying peak voltage and treatment time; results here reported refer to only three sets of operating conditions, as reported in Tab. 1. Briefly, all treatments were carried out at fixed pulse frequency (25 kHz), He flow rate (3 slpm) and distance between the *Plasma Gun* outlet and the liquid surface (7 mm); meanwhile, treatment time was varied between 3 min and 5 min, peak voltage between 9.5 kV and 11 kV. A schematic of the experimental setup is reported in Fig. 1.

Tab. 1. Selected operating conditions. All treatments have been carried out fixing the pulse frequency at 25 kHz, the He flow rate at 3 slpm and the distance between plasma propagation zone outlet and the liquid surface at 7 mm.

Treatment	Time [min]	Peak Voltage [kV]
1	3	9.5
2	3	11
3	5	9.5
Control	----	----

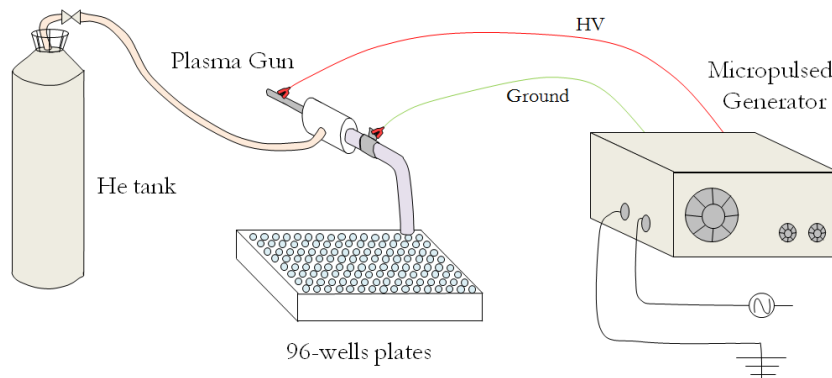


Fig. 1: Schematic of the experimental setup.

3. Results

Results for the *Plasma Gun* decontamination of bacteria solutions are reported in Fig. 2 and in Fig. 3; in particular, results for different scalar dilutions of treated and untreated suspensions are reported in Fig. 2; as can be observed for the control case in Fig. 2a, the undiluted suspension was plated twice on two separate region of the upper Petri dish. The suspension was then diluted five times and plated thrice after each dilution; for a certain dilution, samples were plated adjacent to each other. In this way, each line of three circular bacterial colonies in the Petri dishes reports on results for a single dilution; the number that can be read behind the circular bacterial colonies is the dilution order (for all the operating condition reported, dilutions were plated in the same order). For all the evaluated operating conditions, a decrease of bacterial load in the suspension contaminated with *Staphylococcus aureus* is observed; for a treatment time of 3 min, results for two different values of peak voltage (9.5 kV and 11 kV) are presented: while only a 1 log reduction was achieved at peak voltage (Fig. 2b), complete inactivation was observed for peak voltage 11 kV (Fig. 2c). As expected, increasing treatment time from 3 min to 5 min for the case with peak voltage 9.5 kV is shown to enhance the antibacterial efficacy of plasma treatment, resulting in a bacterial load reduction of 3.5 log (Fig. 2d). Quantitative measurements of the bacterial load before and after plasma treatment are reported in Fig. 3.

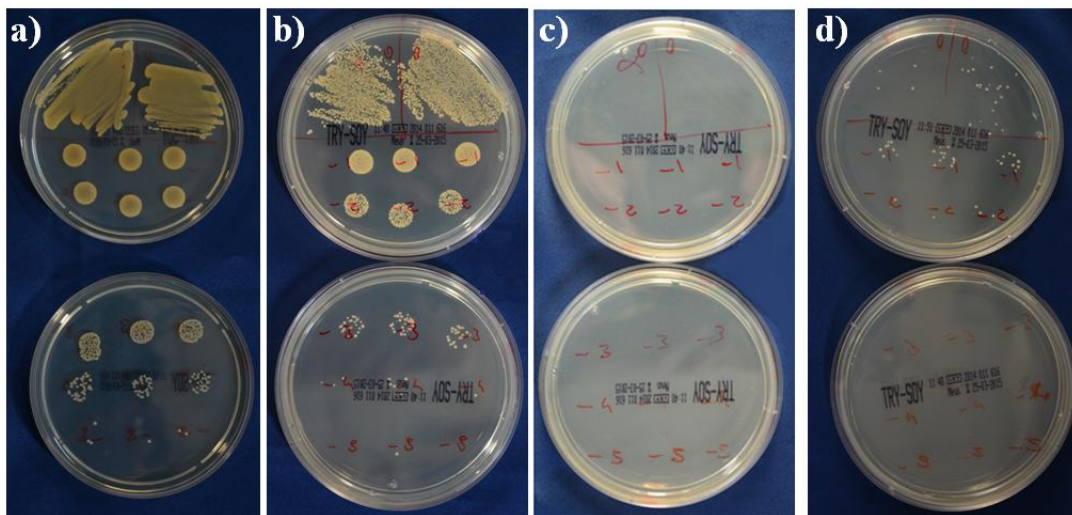


Fig.2: Colony Forming Units grown on Agar plates from untreated and treated suspensions in different operating conditions (different scalar dilutions plated on the same agar plates): a) Control; b) peak voltage = 9.5 kV and treatment time = 3 min; c) peak voltage = 11 kV and treatment time = 3 min; d) peak voltage = 9.5 kV and treatment time = 5 min.

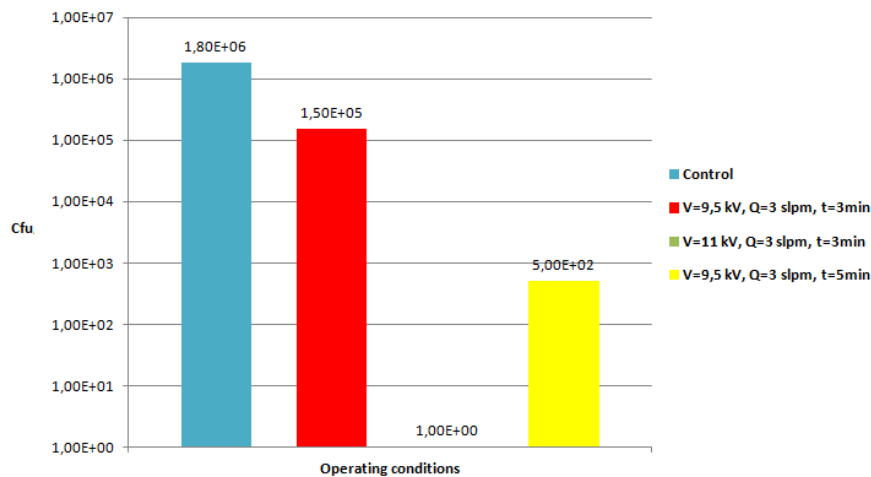


Fig. 3: Bacterial load after plasma treatment.

The lower antibacterial efficacy observed when the *Plasma Gun* was operated at 9.5 kV can be related to the lower intensity of the plasma generated, as can be observed comparing Fig. 4a and Fig. 4b where the plasma produced at 11 kV is characterized by a stronger light emission. Moreover, in the case with lower voltage the plasma was clearly visible only inside the dielectric tube and a the plasma plume formed at the source outlet was only faintly emitting; on the other hand, for the case with higher voltage the formation of a plasma plume at the outlet of the *Plasma Gun* was evident.

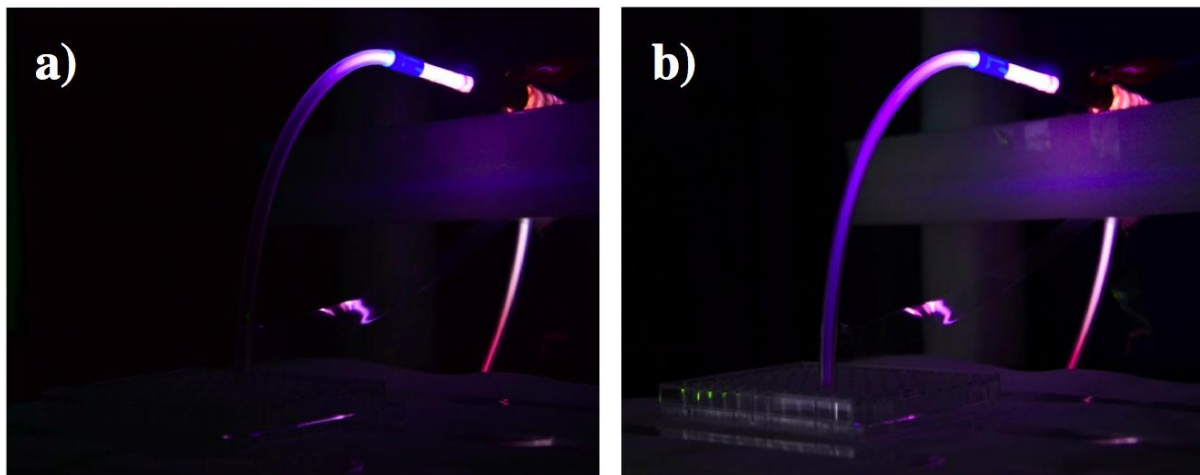


Fig. 4: Camera images of the *Plasma Gun* during the treatment: a) He flow rate 3 slpm, pulse frequency 25 kHz, peak voltage 9.5 kV; b) He flow rate 3 slpm, pulse frequency 25 kHz, peak voltage 11 kV. Images recorded with identical camera settings.

In order to get some qualitative information on the reactive species produced in the plasma plume at the outlet of the *Plasma Gun* and that interact with the contaminated liquid, optical emission spectra in the UV, visible (VIS) and near infrared (NIR) regions have been collected. The UV-VIS spectrum for the *Plasma Gun* source operated with a peak voltage of 9.5 kV is shown in Fig. 6. The OES analysis shows that the main components of optical radiation are in the wavelength region between 280-450 nm, where the bands of excited molecular nitrogen and OH radicals are detected. Future studies will focus on the analysis of the chemical species forming in the liquid suspension during plasma treatment, in order to better understand the physical and chemical mechanisms behind the *Plasma Gun* inactivation process.

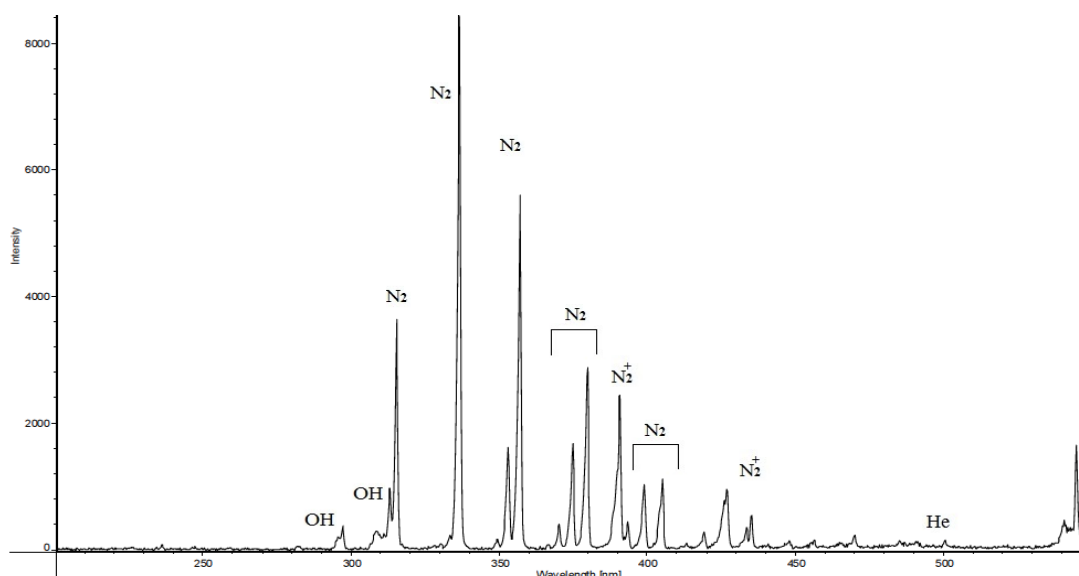


Fig. 6: Optical emission spectrum of the plasma plume; operating conditions: He flow rate 3 slpm, pulse frequency 25 kHz, peak voltage 9.5 kV.

4. Conclusions

The antibacterial efficacy of a flexible *Plasma Gun*, developed by the Authors and driven by microsecond pulse generator, onto *Staphylococcus aureus* contaminated suspensions was investigated. Different operating conditions were selected with the aim of evaluating the effect of a variation of peak voltage and treatment time in the decontamination process. Results highlight that for a peak voltage of 11 kV, total decontamination after only 3 min of plasma exposure is achieved; on the other hand, for a peak voltage of 9.5 kV, bacteria load reductions of 1 log and 3.5 log were observed for 3 and 5 min treatments. Moreover, OES results highlight the presence of N_2 , N_2^+ , NO and OH in the plasma plume region, as a consequence of mixing with the surrounding air, which are widely known to hold an extremely relevant role in the decontamination of liquid suspensions [9].

Future studies will be aimed at the investigation of the effects of varying gas flow rate and pulse frequency on the efficacy of the developed *Plasma Gun* in the decontamination of bacterial suspensions.

5. References

- [1] Robert E, Sarron V *et al.* 2012 *Plasma Sources Sci. Technol.* **21** 034017.
- [2] Robert E, Barbosa E *et al.* 2009 *Plasma Process. Polym.* **6** 795.
- [3] Xiong Z, Robert E *et al.* 2012 *J. Phys. D: Appl. Phys.* **45** 27.
- [4] Robert E, Vandamme M *et al.* 2013 *Clin. Plasma Med.* **1** 2.
- [5] Robert E, Barbosa E *et al.* 2009 *Plasma Process. Polym.* **6** 795.
- [6] Boxhammer V, Morfill G E *et al.* 2012 *NJPh.* **14**.
- [7] Boekema B K H L, Hofmann S *et al.* 2013 *J. Phys. D: Appl. Phys.* **46** 422001.
- [8] Lu X, Naidis G V *et al.* 2014 *Phys. Rep.* **540** 3.
- [9] Boxhammer V, Morfill G E *et al.* 2009 *New J. Phys.* **11** 115013.

6. Acknowledgements

Work partially supported by COST Action MP1101 “Biomedical Applications of Atmospheric Pressure Plasma Technology” and COST Action TD1208 “Electrical discharges with liquids for future applications”

20th Symposium on Application of Plasma Processes

Poster Presentations

COMPARISON OF RESULTS FROM ELECTRON INDUCED FLUORESCENCE STUDY OF DEUTERIUM AND HYDROGEN MOLECULE

Marián Danko¹, Anita Ribar¹, Juraj Országh^{1,2}, Štefan Matejčík¹

¹ *Comenius University, Faculty of Mathematics, Physics and Informatics, Bratislava, Slovak Republic*

² *Empa - Swiss Federal Laboratories for Materials Science and Technology, Thun, Switzerland*

E-mail: stefan.matejcik@fmph.uniba.sk

Hydrogen and deuterium molecules were investigated by the electron induced fluorescence method in a cross-beam apparatus. Emission spectra induced by electrons with energy of 14 eV and 25 eV were obtained. We also measured emission functions of D₂ molecule at 230, 360, and 650 nm in the electron energy range of 0-100 eV. Only continuum radiation of D₂ ($a^3\Sigma_g^+ \rightarrow b^3\Sigma_u^+$) is supposed to be present there. Our results were compared to our hydrogen molecule measurements. Only minor distinctions were observed between the spectra and the emission functions of the two molecules.

1. Introduction

Deuterium and hydrogen molecules are of the simplest molecules and thus their study is of interest for comparison of theoretical methods with experiments and for fundamental knowledge [1, 2]. These molecules are very important also in many industrial branches. Astrophysicists need knowledge of D₂ and H₂ to study different objects such as stars, interstellar matter, atmospheres of planets and solar wind [2,3,4]. The characteristics of the molecules and their interactions are applied also in diagnostics of different industrial plasmas, including thermonuclear fusion plasmas in tokamaks [5, 6].

Both hydrogen and deuterium molecule were extensively studied. Extensive spectroscopic research works were published by Richardson [7], Finkelnburg [8], Dieke [9] and his co-worker Crosswhite, who edited Dieke's lifetime research into two spectroscopic tables containing tens of thousands of emission lines of H₂ f10g and D₂ [11].

Preliminary electron induced fluorescence measurements of deuterium molecule are presented in this paper and the obtained data are compared with the measurements of hydrogen molecule. Study of electron induced fluorescence radiation provides important information about collision processes such as electron induced excitation of a molecule, electron induced ionization and excitation, electron induced dissociative excitation, and electron induced dissociative ionization and excitation. The present paper is focused on the fluorescence spectrum induced by electrons with energy of 14 eV and 25 eV, in the wavelength range of 200-680 nm, and on the emission functions of the $a^3\Sigma_g^+ \rightarrow b^3\Sigma_u^+$ transition in D₂ and H₂ in the range of electron energy 0-100 eV.

2. Experiment

The emission spectra and emission functions of deuterium and hydrogen molecule were acquired using a cross-beam apparatus, depicted in Figure 1. The reaction took place in a stainless steel vacuum chamber, since high vacuum was required for the experiment. The vacuum chamber was pumped down to $\sim 10^{-8}$ mbar and the ambient pressure in the chamber during the experiment was $\sim 1.5 \times 10^{-4}$ mbar. We performed a check if single collision conditions were maintained. This was done by measuring of the linearity of spectral line intensity to pressure dependence [12].

The electron beam was formed obtained by thermal emission from a tungsten hairpin filament and formed by electrodes of a trochoidal electron monochromator (TEM) [13]. The electron beam was energetically analyzed in a dispersion region by applied perpendicular electric field (0-10 V) and parallel magnetic field (5×10^{-3} T). The fields were perpendicular to each other. The energy distribution was intentionally worsened (~ 500 meV) to obtain higher electron current and thus measurable fluorescence signal. The beam was then focused and accelerated to desired energy by electron lenses

into the reaction chamber, where it collided with a molecular beam formed by effusive flow through a capillary ($d = 0.5$ mm). The electron current (typically $I \sim 10^2$ nA) was measured on a Faraday cup by a Keithley 6485 picoammeter, after it passed the reaction chamber.

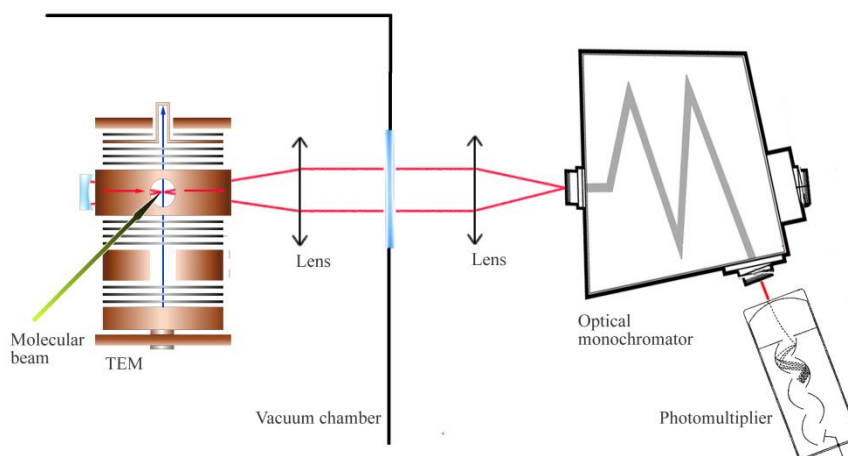


Fig. 1. Cross-beam apparatus equipped with a trochoidal electron monochromator (TEM). The fluorescence radiation is analyzed by a Czerny-Turner $\frac{1}{4}$ m optical monochromator together with a photomultiplier

The electron induced fluorescence processes that take place at the crossing of the beams, allow us to study optically forbidden excitations, since molecular states of a different multiplicity can be excited by an electron, while it cannot be achieved by a photon. The fluorescence photons emitted by deuterium and hydrogen molecules were gathered by UV grade silica lens, and guided through an MgF_2 window and another UV grade silica lens, to the entrance slit of the Oriel Cornerstone 260 Czerny-Turner $\frac{1}{4}$ m optical monochromator. Some of the dispersed signal was returned to the gathering optics by a spherical mirror with UV enhanced aluminium coating placed opposite to the first UV grade silica lens (see Fig.1). After analyzing of the signal by the optical monochromator, the intensity at the set wavelength (usually in the order of 10^0 - 10^1 photons per second) was detected by a low-noise (0.5-2 cps), Peltier-cooled R4220P Hamamatsu photomultiplier working in the range of 190-700 nm.

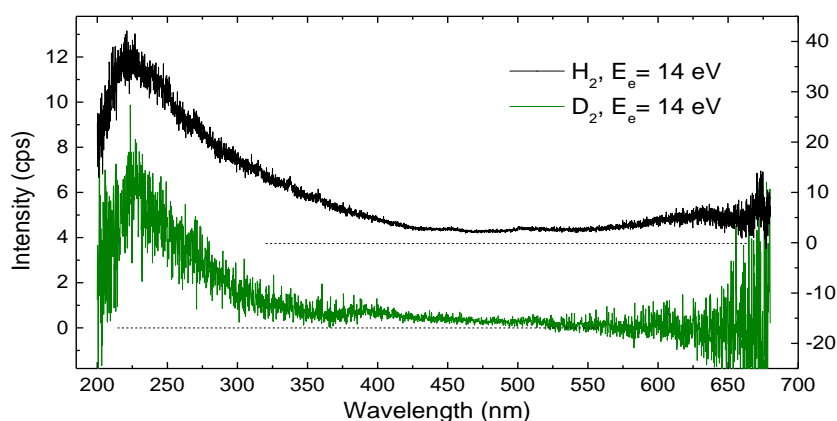


Fig. 2. Comparison of hydrogen and deuterium fluorescence spectrum induced by electrons with the energy of 14 eV. At this energy the dissociative excitation process $\text{H}_2(a \rightarrow b)$ and $\text{D}_2(a \rightarrow b)$ dominate the spectrum. The spectrum was corrected for spectral response of the apparatus.

3. Results and discussion

Preliminary measurements of deuterium molecule were done in the cross-beam apparatus described above, and the obtained data were compared with the measurements of hydrogen molecule.

Our interest was focused on the fluorescence spectrum at 14 eV and 25 eV in the wavelength range of 200-680 nm, and on the emission functions of the $a^3\Sigma_g^+ \rightarrow b^3\Sigma_u^+$ transition in the range of electron energy 0-100 eV. The spectra were corrected for the apparatus functions. The emission functions were energy calibrated by the peak intensity position of the 2nd positive system (0,0) of N₂ line at 337 nm, which lies at 14.1 eV [14].

The spectrum of D₂ and H₂ induced by electrons with energy of 14 eV is formed purely by the $a^3\Sigma_g^+ \rightarrow b^3\Sigma_u^+$ transition, which results in a continuum depicted in Figure 2, since the state $b^3\Sigma_u^+$ is repulsive. It is supposed, that the continuum spans in the range of 120-500 nm [2, 4], though our measurements of emission functions for both molecules (see Figure 4) suggest that it spans at least to 670 nm. It may be interesting to study possible presence of the hydrogen / deuterium continuum in the near IR region. The shape of D₂ and H₂ continuum is similar. However, there exist a differences at 400 nm, where D₂ continuum exhibits a low peak, while H₂ not and vice versa at 460 nm. These differences may be caused by a different of Franck-Condon factors of the involved states at the particular molecules, as well as the noise level of the D₂ measurement. To resolve this uncertainty, further measurements are needed.

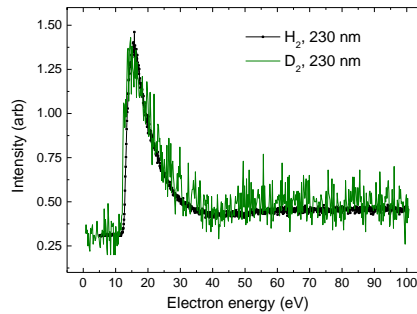


Fig. 3. Comparison of hydrogen and deuterium emission functions of $a^3\Sigma_g^+ \rightarrow b^3\Sigma_u^+$ transition at 230 nm induced by electron impact. The observed shapes are identical.

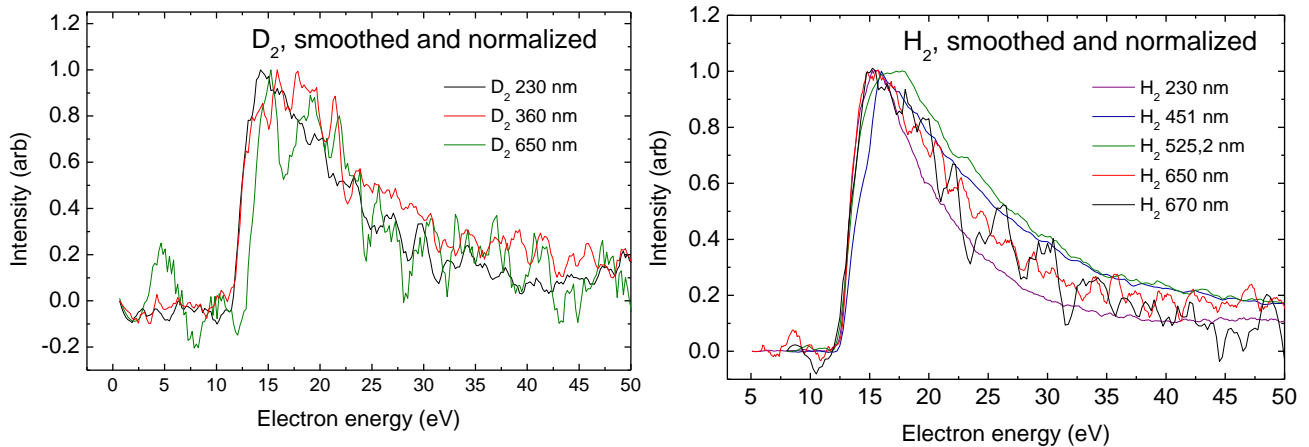


Fig. 4. Emission functions of transition $a^3\Sigma_g^+ \rightarrow b^3\Sigma_u^+$ measured at different wavelengths in H₂ and D₂ molecule.

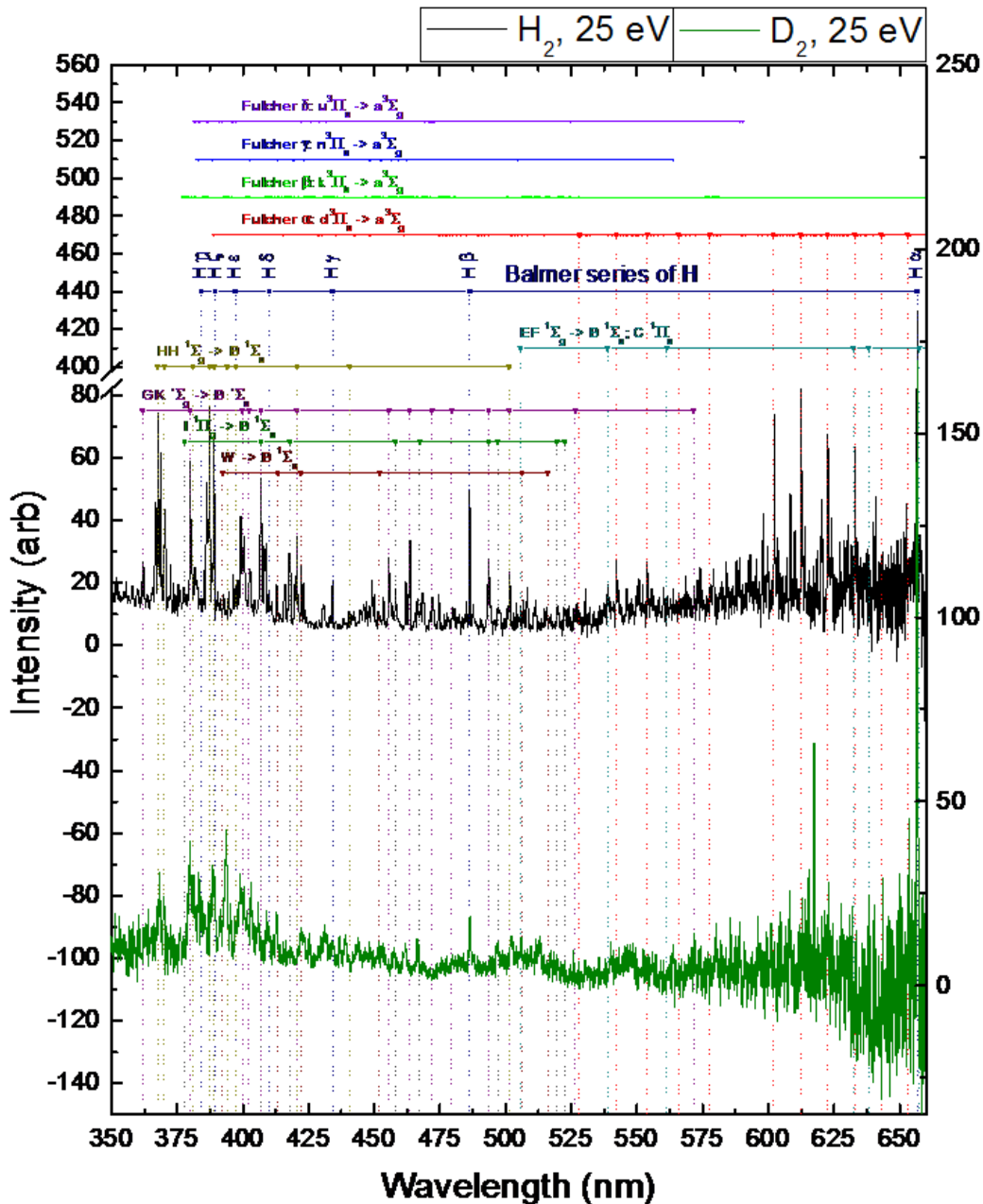


Fig. 5. Hydrogen and deuterium fluorescence spectrum induced by electrons with the energy of 25 eV. The comparison of the presence of molecular bands exhibits significant differences.

Emission functions at 230 nm of the deuterium and hydrogen continuum resulting from $a^3\Sigma_g^+ \rightarrow b^3\Sigma_u^+$ transition in the molecules correspond well in shape and mutual position (see Figure 3). Measurements of higher quality are needed to estimate the threshold energies, though the preliminary results correspond well with the theoretical value of excitation from the ground state of H_2 $X^1\Sigma_g^+$ to the $a^3\Sigma_g^+$ state. The estimate from the molecular constants of Herzberg [15] is 11.8 eV. We also measured emission functions of the continuum at different wavelengths from 230 nm up to 670 nm, where our detection limit lies. This was done to find out, if the continuum region ends at 500 nm as mentioned above. Our measurements for both H_2 and D_2 proved, that the continuum spans further towards the IR region, at least up to 670 nm. This conclusion was deduced from the shape and mutual position of the emission functions depicted in Figure 4.

Fluorescence spectrum induced by electrons with the energy of 25 eV was also measured both in D_2 and H_2 . The results are depicted in Figure 5. The descriptions of emission lines in the Figure 5 correspond to the lines of H_2 molecule that were indentified with the help of [3, 16]. The preliminary comparison of D_2 and H_2 emission lines shows good agreement of the mutual positions of some of the lines (e.g. Balmer's atomic lines and some Fulcher a molecular lines). Both spectra are very complex with mixed lines of different rovibronic transitions. This is caused by the small moment of inertia of the molecules [9]. Some molecular lines observed in the H_2 spectrum are not observed in D_2 and vice versa (see Figure 5), while some lines appear to be shifted. This is expected [9] and except for other factors may be caused by the different moment of inertia of the studied molecules. The mass difference between the molecules is close to the factor of 2, thus higher moment of inertia of D_2 may be a cause for compression of rotational emission lines. Further study of spectra with lower noise level and higher resolution are needed to prove our suggestions.

4. Conclusion

Deuterium molecule was studied by the electron induced fluorescence method using a cross-beam apparatus. Preliminary results were compared to our hydrogen molecule measurements. Fluorescence spectra of D_2 and H_2 induced by electrons with energy of 14 eV were compared. Only continuum radiation of $a^3\Sigma_g^+ \rightarrow b^3\Sigma_u^+$ was present and a slight difference in shape was observed. Emission functions of the continuum were measured at different wavelengths (230 to 670 nm). The shapes of D_2 and H_2 functions were considered identical and a conclusion was derived, that the continuum spans at least to 670 nm, not only up to 500 nm as mentioned by previous works. Fluorescence spectra of D_2 and H_2 induced by electrons with energy of 25 eV were also obtained. There were some discrepancies observed between the molecular lines of deuterium and hydrogen present in the spectra.

5. Acknowledgments

Financing of this work was by the Slovak Grant Agency VEGA-1/0514/12. This work was supported by the Slovak Research and Development Agency, project Nr. APVV-0733-11. This work was conducted within the framework of the COST Action CM1301 (CELINA).

6. References

- [1] Kramida A E 2010 *Atomic Data and Nuclear Data Tables* **96** 586.
- [2] Ajello J M, Shemansky D E 1993 *The Astrophysical Journal* **407** 820.
- [3] Aguilar A, Ajello J M, Mangina R S, James G K, Abgrall H, Roueff E 2008 *The Astrophysical Journal Supplement Series* **177** 388.
- [4] Lavrov B P, Melnikov A S, Käning M, Röpcke J 1999 *Physical Review E* **59** 3526.
- [5] Khakoo M A, Segura J 1994 *Journal of Physics B: Atomic Molecular and Optical Physics* **27** 2355.
- [6] Fantz U, Heger B, Wunderlich D 2001 *Plasma Physics and Controlled Fusion* **43** 907.
- [7] Richardson O W 1925 *Proceedings of the Royal Society of London A* **108** 553.
- [8] Finkelburg W 1929 *Zeitschrift für Physik* **52** 27.
- [9] Dieke G H 1958 *Journal of Molecular Spectroscopy* **2** 494.
- [10] Crosswhite H M: *The Hydrogen Molecule Wavelength Tables of Gerhard Heinrich Dieke*, John Wiley & Sons, Inc., New York, 1972.
- [11] Freund R S, Schiavone J A, Crosswhite H M 1985 *Journal of Physical and Chemical Reference Data* **14** 235.
- [12] Filippelli A R, Lin C C, Anderson L W and McConkey J W 1994 *Advances in Atomic, Molecular, and Optical Physics* **33** 1.
- [13] Matúška J, Kubala D and Matejčík Š 2009 *Meas. Sci. Technol.* **20** 015901.
- [14] Zubek M 1994 *Journal of Physics B: Atomic Molecular and Optical Physics* **27** 573.
- [15] Herzberg G: *Molecular Spectra and Molecular Structure*, vol. 1 – Spectra of Diatomic Molecules, 2nd edition, 8th printing, D. Van Nostrand Company, Princeton, 1963.
- [16] James G K, Ajello J M, Pryor W R 1998 *Journal of Geophysical Research* **103** 20,113.

DISSOCIATIVE ELECTRON ATTACHMENT TO CARBON AND NITROGEN RICH MOLECULES: DEVELOPMENTS FROM QUEEN'S UNIVERSITY BELFAST

Thomas Gilmore, Tom Field

Centre for Plasma Physics, School of Mathematics and Physics, Queen's University Belfast
E-mail: tgilmore02@qub.ac.uk

Investigations into carbon- and nitrogen-rich molecules have yielded new absolute cross sections for the processes of dissociative electron attachment and electron-impact ionization. New absolute cross sections for dissociative electron attachment to HCCCN (cyanoacetylene or propiolonitrile) in the range of 0–10 eV electron energy have been determined from a new analysis of previously reported data (Graupner et al 2006 New J. Phys. 8 117). The highest cross sections are observed for the formation of CN⁻ at 5.3 eV and CCCN⁻ at 5.1 eV; approximately 0.06 Å² and 0.05 Å² respectively. As part of the re-analysis, it was necessary to determine absolute total cross sections for electron-impact ionization of HCCCN with the binary-encounter Bethe method; the maximum value was found to be ~6.6 Å² at ~80 eV. Dissociative electron attachment cross sections for the three diazine molecules, the isomers of C₄H₄N₂, have also been measured. R-Matrix calculations for electron attachment to CO and CS have been completed and will be presented here.

1. Overview

Carbon- and Nitrogen-rich molecules have been observed in a number of environments outside of Earth, such as comets, nebulae and in the atmosphere of Saturn's moon Titan. A very recent paper by the team at Atacama Large Millimeter/submillimeter Array (ALMA) identified and mapped out the distribution of HCN and HCCCN in Titan's atmosphere. In particular, HCCCN "is abundant at a [broad] range of altitudes", from 70-600km above Titan's surface. This information, along with the revelation that a large number of negative ions exist in Titan's atmosphere (Cordiner, M. A., et al. 2014 *ApJL* 795.2 L30), highlights the importance of having cross sections for electron scattering processes for a complete understanding these alien environments.

Graupner et al (2006 New J. Phys. 8 117) has previously presented dissociative electron attachment spectra for this molecule, which identified the electron energy resonance bands where negative ions are found and the relative abundances of these ions. These measurements were made using ERIC, the electron radical interaction chamber, which has been described previously (Field, T. A., et al. 2005 J. Phys. B 255). In light of recent demands for better data pertaining to gaseous and plasma processes, a reanalysis of Graupner et al's data was done. Using some straight forward inference methods, absolute cross sections for dissociative electron attachment to HCCCN were obtained. As part of the re-analysis, it was necessary to determine absolute cross sections for electron-impact ionization of HCCCN with the binary-encounter Bethe method. Full details are available in Gilmore and Field 2015 J Phys B (in press).

Similar work has been carried out for the azines, the isomers of C₄H₄N₂. Pyridimine, the most well-known of the azines, is a component of the nucleobases Thymine, Cytosine and Uracil. R-Matrix scattering calculations for the azines are available for comparison and thus benchmarking of the code. CN⁻ was found to be the dominant dissociation channel for these molecules, occurring at approximately 5.1 eV and 8.2 eV electron impact energies for all the azines. Hydrogen anion formation was also observed. Further details, including cross sections and theory comparisons, will be available in "Absolute cross sections for dissociative electron attachment to the azines" (in preparation).

Using the R-matrix codes via Quentemol-N, potential energy curves were calculated for the CS and CO molecules. For CS, 17 bond-lengths from 1.1 to 2.7 Angstroms were analysed (Varambha 2010), while for CO 20 bond-lengths from 0.8 to 2.4 Angstroms were analysed. These curves were correlated with various distinct appearance potentials for the dissociative electron attachment at various energies (5.43 eV, 6.40 eV and 6.70eV for CS, 9.63 eV, 9.8 eV and 10.88 eV for CO).

ION INDUCED WATER RELEASE FROM ACETURIC ACID

Janina Kopyra¹, Jaroslav Kocisek², Rudy Delaunay², Bernd A. Huber², Patrick Rousseau², Alicja Domaracka²

¹*Chemistry Department, Siedlce University, 3 Maja 54, 08-110 Siedlce, Poland*
²*CIMAP, UMR 6252, Bd. Henri Becquerel, BP 5133, 14070 Caen Cedex 5, France*
E-mail: kocisek@ganil.fr

We present the combined experimental and theoretical study of resonant electron transfer between the aceturic acid molecule and slow O^{6+} ions. Rich fragmentation is observed upon single and multiple ionization of the molecule in the gas phase which is dominated by CH_3COOH^+ and $COOH^+$ fragment ions, respectively. On the contrary, the metastable parent ion dissociates exclusively by the release of neutral water molecules. In the present contribution we focus on the nature of the metastable parent ion as well as the dissociation process. We assign the observed slow decay of the parent ion to the high stability of the *cis* peptide bond conformer of the ion in contrast to the stable *trans* peptide bond conformer of the neutral. The observation can have significant implications on the energy distribution in peptides as well as on the related chemistry.

1. Introduction

The interaction of multiply charged ions with biomolecules has gained significant interest in the last years. This is directly linked to the growing number of ion beam applications for cancer treatment [1]. Typical ion beams used in these therapies are proton and carbon beams. However, new therapies based on ions such as oxygen are also under development [2].

Even though the physics and chemistry of ion beam interactions with living organisms is understood on a level that allows for the clinical use of ion beams, further progress in the cancer treatment by ion irradiation can be expected only when the underlying processes are described at the molecular level. Therefore, a variety of processes including both primary and secondary particles, formed during the ion passage through the living organism, has been studied. Frequent targets are DNA and the corresponding building blocks, since their damage is one of the main causes for cell damage. However, it is now widely accepted that this kind of damage is provided by secondary species such as electrons and radicals [3,4]. The mean free paths of these species in living organisms are rather short and, therefore, primary ions have to pass in close vicinity of the DNA. In general, this is not the case, due to the low fluence of the clinical beams. Hence, the question arises how cell constituents, other than DNA, are influenced by ion beam irradiation and how this may lead to the cancer cell death. An important cell constituents are peptides. Several studies concerning the interaction of secondary species with amino acids, as the peptide building blocks (see e.g. [5] [6]). Recently, we have studied also the interaction of slow ions with neutral aminoacids in the gas phase and amionacid clusters [7,8]. The present contribution extends our previous works which aims to understand ion induced processes in peptides.

Aceturic acid is the simplest system that allows the study of peptide bond behavior. By the use of slow ions in the present study, we have been able to selectively study the resonant electron exchange between the molecule and the incoming ion. The resonant electron exchange is an important reaction pathway in the ion interaction with living matter. The nature of this interaction is of long range and its cross section rises with the charge state of the ion. Thus, the resonant electron exchange is of fundamental importance for novel ion beam therapies which use heavy ions (e.g. [2]).

In this contribution we will discuss how peptide bond isomerization can significantly influence the stability of the molecule after ionization by slow ions. The observed effect can significantly modify the energy balance in the complex biomolecular systems as well as their reactivity.

2. Experiment

The experiment was carried out at the COLIMACON end-station [9] placed on ARIBE (Accélérateurs pour les Recherches avec les Ions de Basses Energies) ion beam facility in Caen. COLIMACON is equipped with a linear time of flight mass spectrometer which can be combined with a variety of molecular and cluster sources. In the present study, a simple heated reservoir has been used to evaporate the molecules at temperatures of $\sim 360\text{K}$ forming an effusive beam of acetic acid in the gas phase. This target was irradiated by pulsed beam of $^{16}\text{O}^{6+}$ ions at a kinetic energy of 48keV and mass spectra of the cationic products were detected. The experiments were carried out under the coincidence conditions, thus each obtained mass spectrum consist only the products of single ion – molecule interaction event. COLIMACON TOF mass spectrometer was designed as a Wiley-McLaren spectrometer with an extraction region optimized for the detection of large mass range detection. The elongated design (11 cm) results in long residence times of ions in the extraction region (up to several microseconds). This fact can be used to analyze long lifetimes of ionic states in the way similar to ion trap - mass spectrometer instrument.

3. Results

A sample mass spectrum is shown in Fig. 1. On the top of the Fig. 1 raw data are presented including the background contribution. On the bottom of the Fig. 1 integrated intensities of the peaks after the background subtraction are compared to the electron ionization mass spectra obtained from the NIST database [10]. The most intense fragment after ion collision is $m/z = 43$ (OCNH^+ , CH_3CO^+) in contrast to $m/z = 30$ after EI (CH_2O^+ , NH_2CH_2^+ [10]). Formation of $m/z=30$ ions after electron ionization requires significant fragmentation and can not be easily linked to the peptide dissociation. On the other hand O^{6+} ions seem to be highly effective in the peptide bond cleavage that results in the formation of CH_3CO^+ ion. Another contribution to the $m/z=43$ signal is coming from the dissociation of multiply charged ions as revealed by coincidence mass spectrometry. These ions could be assigned to the OCNH^+ structure on the basis of fragment kinetic energy analysis. The most intense channel of the dication dissociation is then $m/z = 45$ (COOH^+).

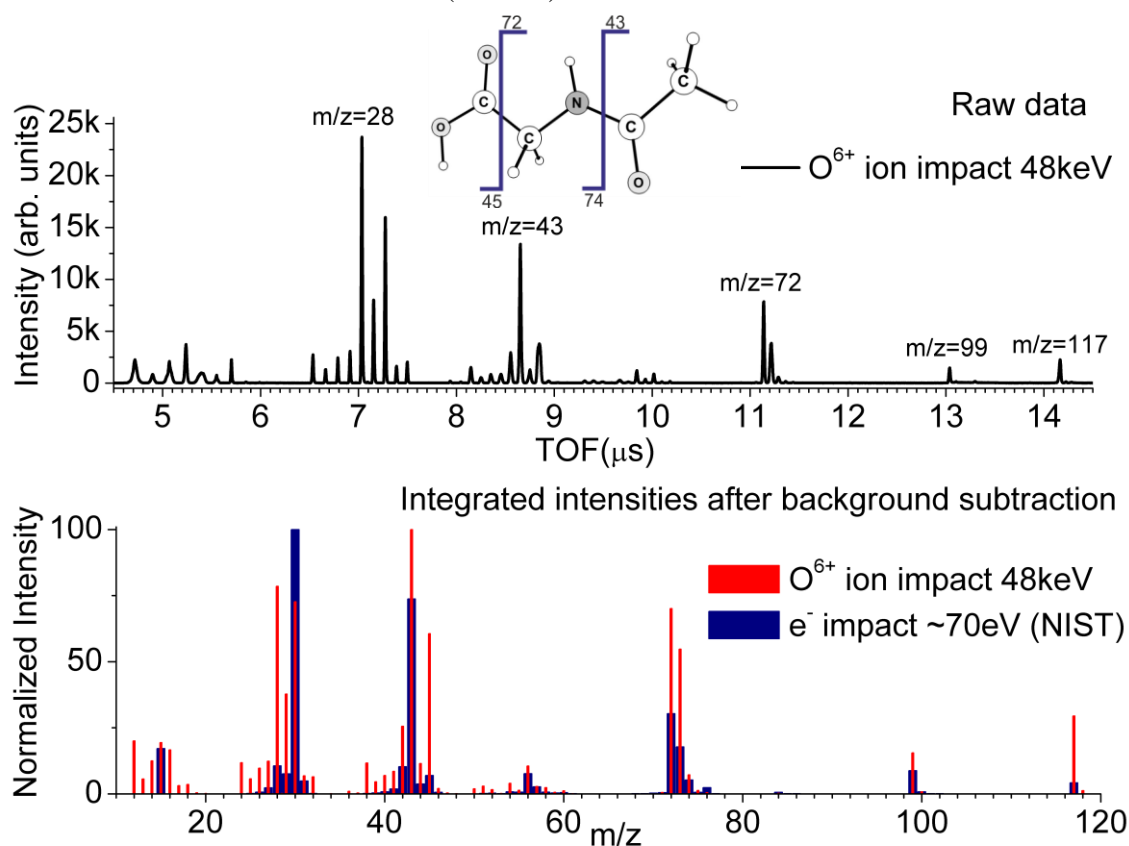


Fig. 1: Mass spectrum of the acetic acid after ionization by O^{6+} ion impact at 48keV and comparison of the mass spectra to the spectra after electron ionization from the nist database (bottom) [10].

The most intriguing result of the study is related to the neutral water release channel:



The signal of $m/z = 99$ ion formed in the mentioned process has long tail up to higher masses (see Fig.2). Such tail is the typical sign for the metastable decay of a heavier ion mass towards the $m/z = 99$ fragment in the extraction region of the TOF mass spectrometer. The analysis of length of the tail confirms that the dissociation occurs from the parent ion of aceturic acid ($m/z=117$) in the reaction (1). We subtract the direct dissociation signal and background signals from the data and transforms the observed TOF to the residence time of metastable parent ion in the extraction region. The fit indicates the exponential decay of metastable ion intensity with the time constant of $\sim 1.2 \mu\text{s}$. However, the quality of fit is low and, therefore, we can only conclude that we observe the metastable ion with lifetimes longer than $1 \mu\text{s}$.

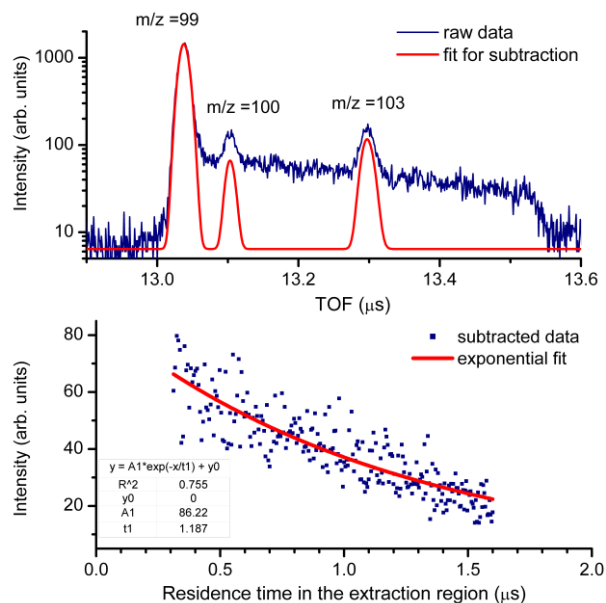


Fig. 2: Shape of the $m/z = 99$ ion signal in the mass spectra, that indicates a metastable decay of the parent ion. The bottom figure is the residence time of the metastable ion in the extraction region calculated from the data shown on the upper part of the figure.

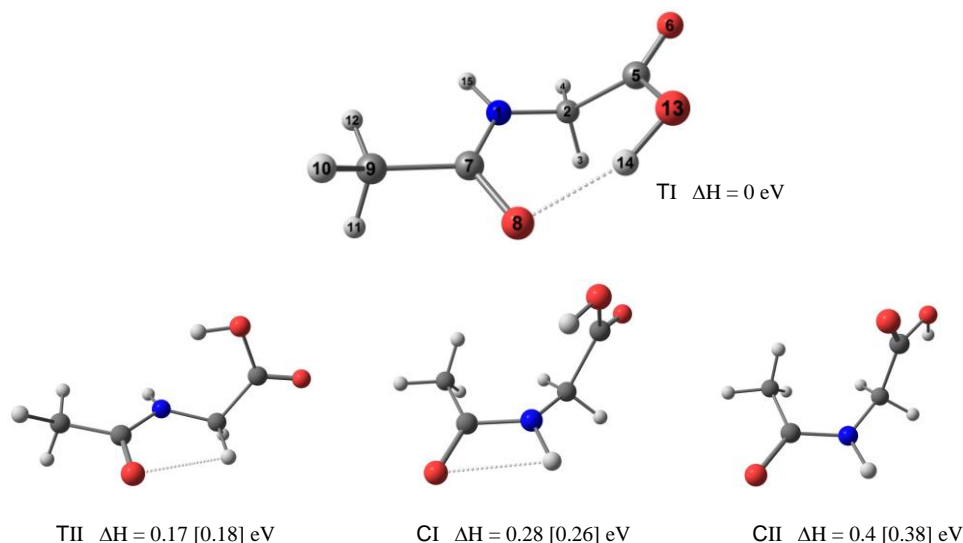


Fig. 3: The conformers of aceturic acid chosen for the study. Sequential numbers of atoms are indicated on the TI conformer picture. Relative enthalpies of formation obtained at B3LYP/6-311++G(2df,2pd) and [G4MP2] level of theories are indicated.

To explore the nature of the reaction (1) and corresponding metastable parent ion, we perform supporting calculations by using the GAUSSIAN 09 quantum chemistry package [11]. At first, we did simple conformational search to find the most stable conformers of molecule in the gas phase. The potential energy curves for the (5,2,1,7), (1,2,5,6) and (8,7,1,15) dihedral angle rotations (see Fig. 3) were calculated by the density functional theory at B3LYP/3-21G level and the local minimum configurations were optimized at the same level of theory. In this way, the 12 minimum energy configurations have been reduced into 8 stable conformers.

For the further analysis, we used the two most stable conformers corresponding to the *trans* form of the peptide bond and two most stable conformers corresponding to the *cis* form of the peptide bond.

These were re-optimized at the B3LYP/6-311++G(2df,2pd) level of theory and the validity of the solution was further verified by G4MP2 calculation.

The optimized structures of the conformers are presented in Fig. 3. The conformers corresponding to the *trans* form of the peptide bond are labeled TI and TII and conformers corresponding to the *cis* form are labeled CI and CII. The values of relative energies of the found neutral conformers indicate that the *trans* form of the molecule is extremely stable in the gas phase. We also found that the hydrogen bonding between OH (13-14) and O(8) significantly stabilizes the molecule and therefore the TI conformer is more stable in the gas phase than any other conformer. Since the cross section for slow ion interaction is not significantly influenced by the molecule conformation, we can conclude that the ion molecule interaction in our present experiment is dominated by the ion interaction with conformer TI.

In the second step we calculate the reaction enthalpies of nearly complete set (21 reactions) of the possible reaction channels of the reaction (1) at the B3LYP/3-21G level of theory. The reaction enthalpies of the energetically most favorable channels were recalculated on B3LYP/6-311++G(2df,2pd) level of theory. Out of these, 4 reaction channels have been found to be exothermic in respect to vertically ionized TI structure. The optimized structures of the $m/z=99$ fragment ion with the indication of H_2O dissociation positions is on the Fig. 4. The energetically most favorable channel results in the formation of cyclic ion with *cis* structure of the atoms corresponding to the peptide bond in the neutral molecule. The combination of the fact that the *trans* form of the peptide bond is the mark of the dominant reactant and the *cis* form of the peptide bond is the mark of most favorable product suggests the hypothesis that the underlying reaction paths of the reaction (1) are:

1. Fast - direct dissociation process after vertical ionization of TI neutral which results to the type 2) or type 4) fragment ion formation according to Fig. 4.
2. Slow - indirect dissociation process of TI neutral which include *trans* – *cis* isomerization of the parent ion and results in the formation of the type 1 fragment ion. Alternatively, that includes the proton transfer reaction between the OH group and O(8) oxygen and results in the type 3 ion formation according to the Fig. 4.

To support our hypothesis, we perform the series of ADMP (Atom centered Density Matrix Propagation molecular dynamic) calculations to explore the behavior of the parent ion. In the first study we run ADMP B3LYP/3-21G calculations for vertically ionized conformers from the Fig. 3 with only negligible amount of the total nuclear kinetic energy $\sim 0.27\text{eV}$. The 20 trajectories were computed for each ion giving a first impression about the final behavior. The trajectories were calculated with 0.1fs step to secure the adiabatic evolution and the total length of the trajectory calculation was set for 1ps. The most of the *trans* conformer trajectories results in CO_2 release upon fast proton transfer from OH group to O(8) oxygen. Due to sympathetic orientation of conformer TI the proton transfer is much

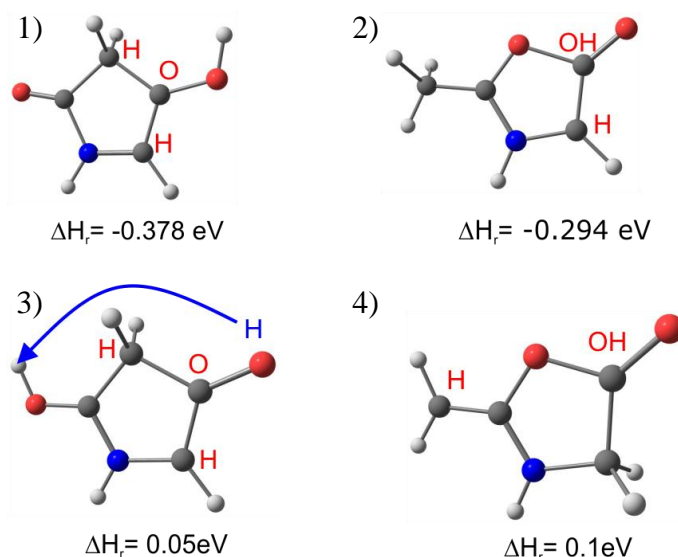


Fig. 4: Four structures of $m/z=99$ fragment ion corresponding to the energetically most favorable channels of the reaction (1). Enthalpy of the reaction (1) is indicated under the appropriate structure and it was calculated with respect to the most stable parent ion conformer at B3LYP/6-311++G(2df,2pd) level of theory. Red letters represent the positions of individual O and H atoms of the released water molecule.

faster than in the case of conformer TII and takes only 50 fs. Conformer TII dissociates in the same process under 200 fs. On the other side, all *cis* conformers remain stable for the whole 2ps period. Clearly the stability of *cis* conformer in the ionic state is much higher than that of the *trans* conformer. At the moment, more sophisticated calculations of the full reaction path of the reaction (1) and *cis* – *trans* isomerization process are running to confirm our hypothesis.

4. Conclusions

Interaction of acetic acid with slow multiply charged ions was studied for the first time. The ionization by 48keV O^{6+} results in a rich fragmentation spectrum. The relatively high abundance of the high mass fragments, in comparison to the electron ionization, means that the electron transfer process is surprisingly soft in its nature and most probably all the chemistry is driven only by the unstable nature of the formed parent ion and the electrostatic repulsion within multiply charged molecules. We also observed the formation of metastable parent ions, which dissociate exclusively by neutral water release. The water release reaction indicates that the metastable parent ion has *cis* peptide bond configuration. The stability of the *cis* ion in comparison to the *trans* form was confirmed also by ADMP calculations.

5. Acknowledgement

We would like to acknowledge R. Čurík for providing us with the access to the computational facilities at the J. Heyrovsky Institute of Physical Chemistry in Prague and S. Díaz-Tendero and D. Piekarski for the discussion of the computational results. Financial support from INCa-ITMO (N° PC201307) within the Programme Plan Cancer 2009-2013 (Inserm) and from the XLIC COST action (CM1204) is gratefully acknowledged.

6. References

- [1] See the map of operational and planned proton therapy centers worldwide at the web page : <http://www.proton-cancer-treatment.com/proton-therapy/proton-therapy-around-the-world/>
- [2] Kurz C et al. 2012 Phys. Med. Biol. **57** 5017
- [3] Nguyen J et al. 2011 Proceedings of the National Academy of Sciences of the USA **108** 11778
- [4] Rezaee M et al. 2013 Radiation Research **179(3)** 323
- [5] Kocisek J et al. 2010 Journal of Physical Chemistry A **114(4)** 1677
- [6] Papp P et al. 2012 The Journal of Chemical Physics **137(10)** 105101
- [7] Domaracka A et al. 2012 J. Phys.: Conf. Ser. **373** 012005
- [8] Maclot S et al. 2011 ChemPhysChem **12(5)** 930
- [9] Capron M et al. Chem. Eur. J. **18** 9321
- [10] Linstrom P and Mallard W 2011 NIST, Gaithersburg MD - <http://webbook.nist.gov>
- [11] Gaussian 09, Revision D.01 Frisch MJ et al. 2009 Gaussian, Inc., Wallingford CT

STUDY OF OZONE THERMAL DECOMPOSITION ON METAL SURFACES

Zdenka Kozáková, František Krčma, Michal Procházka, Radka Veverková,
Eliška Krejsková

Brno University of Technology, Faculty of Chemistry, Purkyňova 118, 612 00 Brno, Czech Republic
E-mail: krcma@fch.vutbr.cz

The paper deals with ozone decomposition on selected metal surfaces (copper and iron) at temperature varying from 10 to 85°C. Ozone concentration was determined by spectral absorption at 253.65 nm. In the stationary regime, ozone decomposition proceeded exponentially, and it was substantially enhanced by increasing temperature. Higher decomposition was observed on iron surfaces. Rate constants of ozone decomposition at various conditions were calculated.

1. Introduction

Nowadays, utilization of ozone in various industrial processes is very wide and thus efficiency of its production and transport is demanded as high as possible. Ozone is an instable gas which is very easily decomposed to atomic oxygen especially when it can react with some compound or solid surface. Another important parameter influencing ozone decomposition is temperature. Moreover, liquid ozone is explosive. Therefore, storage of ozone is a quite difficult process, and thus ozone generators are often used directly at the place of further ozone application. However, in all cases it is important to choose appropriate material for ozone transportation from the generator to the place of ozone consumption. Such material should not catalyse ozone decomposition and thus decrease its production efficiency. Moreover, interaction between ozone molecules and solid materials might differ with respect to the temperature.

The most inert material with regard to ozone decomposition is glass. However, its disadvantage concerning construction of devices for ozone utilization is its high fragility. Other convenient materials could be found among plastic materials, especially based on fluorinated polymers such as PTFE [1]. On the other hand, using of rubber as a pipeline or packing is almost dangerous because it actively reacts with ozone and it could be even ignited [1, 2]. Also using of polystyrene is impossible for ozone transportation or storage [3]. Nevertheless, these materials still require further investigation. Metals have been the most common materials utilized for pipelines. However, a lot of them are strongly oxidized by ozone and thus these materials easily corrode. Some of them are even used as catalysts for ozone decomposition in silica gel, for example silver [4] or cobalt ions [5]. This work presents results obtained for two common construction metals: iron, and copper.

Concerning ozone thermal decomposition, it is primary described by standard kinetic laws. For decomposing reaction $2\text{O}_3 \rightarrow 3\text{O}_2$, the experimentally verified equation of ozone decrease is

$$-\frac{dc_{\text{O}_3}}{d\tau} = k_{c(\text{O}_3)} \cdot c_{\text{O}_3}^2 \cdot c_{\text{O}_2}^{-1} \quad (1)$$

where c_{O_3} and c_{O_2} is ozone and oxygen concentration in time τ , and $k_{c(\text{O}_3)}$ is the rate constant dependent on temperature [6]. In a plasma reactor, ozone is also decomposed by heterogeneous reactions on reactor walls, and such reactions are stimulated by elevated temperature. At sufficiently low temperature, ozone decomposition is only negligible. Ozone maximal production is reached at approximately 30°C. Exceeding this value, decomposition reactions prevail ozone synthesis [7].

This paper is focused on temperature effect influencing ozone decomposition on copper and iron surfaces with different specific dimensions in order to estimate contribution of surface heterogeneous reactions and bulk reactions on this process.

2. Experimental set-up

Experimental apparatus was constructed according to the scheme presented by Fig. 1. It consisted of a commercial ozone generator Lifepool (Lifetech, maximal ozone production from pure oxygen was 0.5 g/hour), a specially constructed device for ozone spectral detection, a UV lamp and a spectrometer connected to the PC. Oxygen with purity of 99.5 % was used for ozone generation. Its constant gas flow rate of 500 ml/min was controlled by a mass flow controller Omega FMA-A2407. As demonstrated in Fig. 1, gas from the pressure bomb was led through the mass flow controller (8) and the ozone generator (9) into a special cuvette (4) serving for ozone detection in a stationary regime (Fig. 2). An optical cable (11) from the low pressure mercury lamp Sterilight (10; 253.56 nm) was mounted to this cuvette at its axis while another cable was connected on the other side and led into the spectrometer Ocean Optics HR4000 (12) and PC (13). The device for ozone detection itself (Fig. 2) consisted of a tube made of selected metal material (copper or iron) with the length of 100 mm and the inner diameter of 4 or 8 mm. A new tube was used in every experiment in order to prevent effect of partial surface oxidation cause by ozone interaction within the previous measurement. Both ends of the tube were closed by PTFE fronts (3) equipped by gas inlet and outlet valves and by quartz windows. Optical cables leading from the UV lamp and to the spectrometer were mounted to these windows. The metal tube was further wrapped into a copper plate (4) which served for the heat transfer from a water bath (7) into which the device could not be fully immersed because of its limited water tightness. Therefore, only the copper plate was immersed in water of appropriate temperature. Temperature inside the tube was measured by a thermocouple (type K) installed directly in the gas phase in the tube. The measured temperature showed out only a 10% uncertainty comparing to the set water bath temperature.

The whole experimental procedure started with the water bath tempering to the required temperature. In this work, ozone decomposition at 10, 25, 40, 55, 70, and 85°C was studied. When temperature inside the tube reached the desired value, the constant flow rate of oxygen was adjusted, and the ozone generator was switched on at its maximal value. After ten minutes, both inlet and outlet valves of the measuring cuvette were closed. Thus a defined amount of ozone was stored inside it. Simultaneously, UV light transmitted through the cuvette was recorded by the spectrometer using a grid with 2400 grooves per mm and software Spectra Suite.

Ozone amount in the cuvette was evaluated from the spectra obtained in the range of 240–350 nm. Especially, the spectral line at 253.65 nm was observed, and its integral intensity was used for calculation of ozone concentration according to the Lambert-Beer's law:

$$T = \frac{I}{I_0} = e^{-c \cdot x \cdot \varepsilon} \quad (2)$$

where T is the light transmission through the cuvette, I is intensity of transmitted light, I_0 is intensity of light from the UV lamp, c is the determined ozone concentration, x is the length of the tube and ε is the absorption coefficient for ozone (305.24 cm^{-1} at 253.65 nm [8]). In all studied conditions, ozone concentration decreased more or less exponentially as follows:

$$c = c_0 \cdot e^{-k \cdot t} \quad (3)$$

where c is ozone concentration in time, c_0 is the initial ozone concentration, k is the rate constant, and t is time. Therefore, rate constants of ozone decomposition were calculated from the linear parts of curves $\ln c = f(t)$.

Ozone decomposition was studied in the stationary regime when the gas mixture containing original oxygen and ozone formed in the ozone generator was closed in the cuvette made of selected metal material. For comparison, two materials (copper and iron) were used. Further, the testing tubes were of two diameters in order to obtain significantly different reaction surface to volume ratio. In the case of the smaller diameter of 4 mm, the ratio is approximately 10 while it is only 5 when the bigger diameter of 8 mm is used. This enables revealing the contribution of volume or heterogeneous surface reactions on ozone decomposition in this system. The comparison is given for six temperature values in the range from 10 to 85°C.

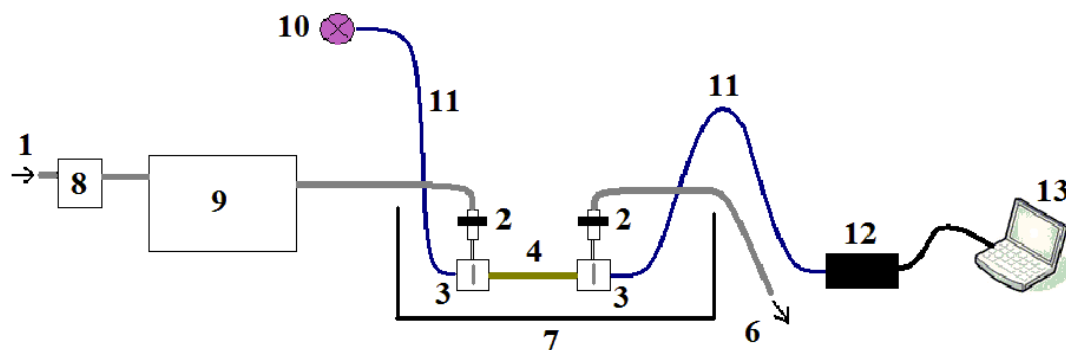


Fig. 1. Scheme of experimental set-up: 1 – gas inlet to the cuvette, 2 – gas inlet/outlet valve, 3 – PTFE front with quartz window, 6 – gas outlet from the cuvette, 7 – water bath, 8 – mass-flow controller, 9 – ozone generator, 10 – UV lamp, 11 – optical cable, 12 – spectrometer, 13 – PC.

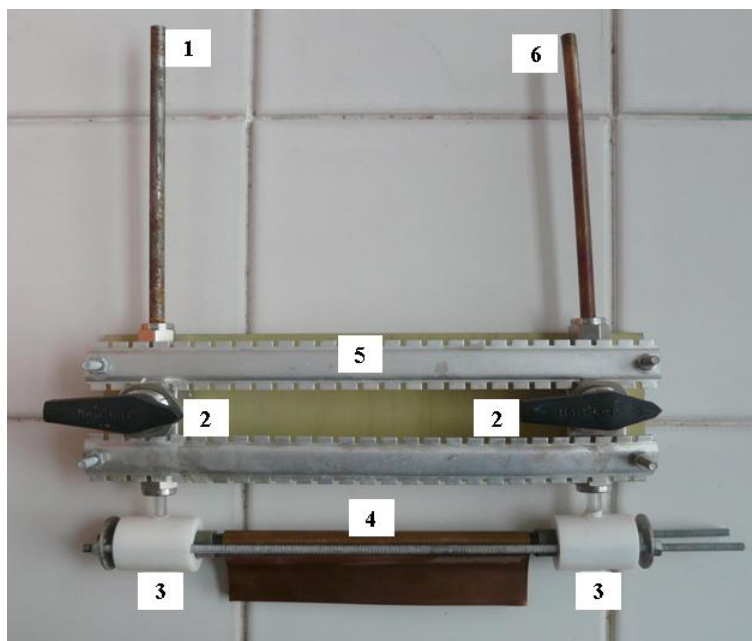


Fig. 2. The device for spectral ozone detection: 1 – gas inlet, 2 – valve, 3 – PTFE front with quartz window, 4 – metal tube wrapped into a copper plate, 5 – system of holders, 6 – gas outlet.

3. Results

Ozone concentration in the cuvette was determined from the UV light absorption at 253.56 nm providing by the mercury lamp, and it was measured continually. Due to the spectral broadening of the measured line, an integral intensity of mercury line was used for further comparisons.

At the beginning of each measurement when ozone concentration was maximal, no light intensity was recorded because it was fully absorbed by ozone molecules. As ozone concentration decreased due to its decomposition, light intensity increased. According to the speed of this increase, the rate of ozone decomposition can be estimated in the dependence on experimental conditions.

Time evaluations of mercury line intensity transmitted through the gas mixture in the copper tube are given in Fig. 3 for both smaller diameter of 4 mm (left) and bigger diameter of 8 mm (right). Moreover, the comparison is given for reaction temperature of 10, 25, 40, 55, 70, and 85°C. The same experimental conditions were set in the case of iron tubes, and the appropriate results are demonstrated in Fig. 4.

In all tested metal tubes, ozone decomposition represented by the increase of mercury line intensity is accelerated by temperature enhancement. However, the effect of this phenomenon is different from the viewpoint of the tube material. Generally, ozone was decomposed faster in both iron tubes comparing

to the copper ones. On the other hand, the thermal effect is dependent on the tube diameter as well as on the material.

Concerning the copper tubes, velocity of light intensity enhancement reached at the same temperature is slower for the bigger diameter, i.e. for the lower surface-volume ratio (Fig. 3). This fact indicates that the main process of ozone decomposition is its heterogeneous decay on the tube walls and no homogeneous decay in the bulk gas mixture. In the case of iron, the situation is significantly different. The whole degradation is substantially faster, but it is much faster when the bigger diameter is used (Fig. 4). This means that homogeneous volume reactions in the gas phase should not be omitted for this material although we change the surface-volume ratio. Therefore, it is necessary to create a simple numeric model describing a time evaluation of ozone concentration which will be our future task.

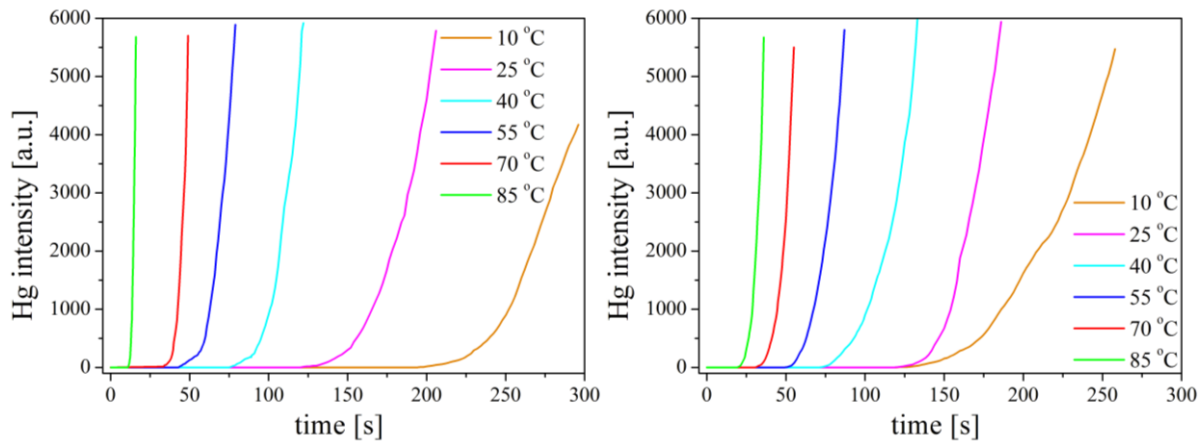


Fig. 3. Time evaluation of mercury (Hg) integral intensity (line at 253.56 nm) representing ozone decomposition in copper tubes with inner diameter of 4 (left) and 8 mm (right) in the dependence on temperature.

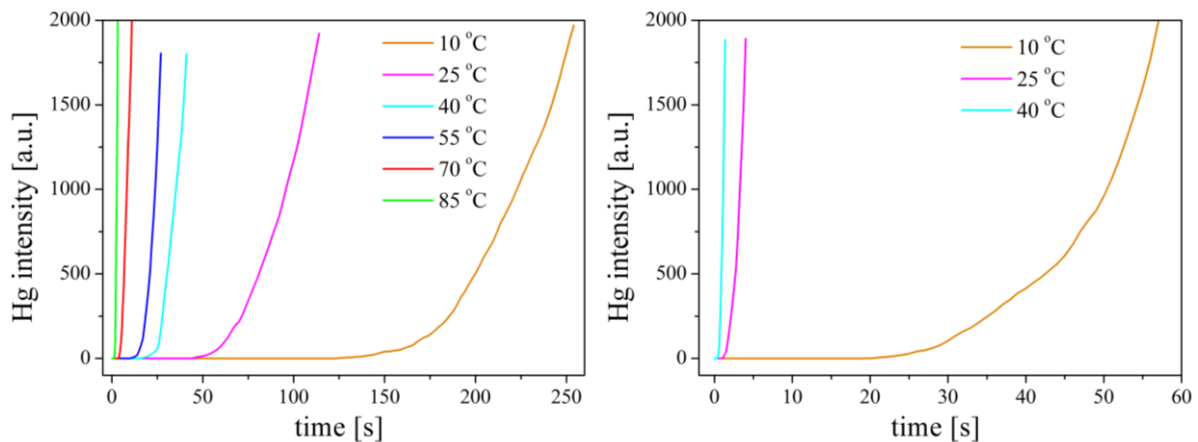


Fig. 4. Time evaluation of mercury (Hg) integral intensity (line at 253.56 nm) representing ozone decomposition in iron tubes with inner diameter of 4 (left) and 8 mm (right) in the dependence on temperature.

As it was already mentioned above, ozone decomposition has two main reaction mechanisms: the homogeneous decay in the gas phase and the heterogeneous decay on the solid surface (the tube wall). The main homogeneous process in the vicinity of the metal wall is ozone reaction with oxygen molecules:



The rate constant of this reaction is in the order of $10^{-20} \text{ cm}^3 \cdot \text{s}^{-1}$ [9]. However, rate constants evaluated in this study are in the order of about $10^{-3} \text{ cm}^3 \cdot \text{s}^{-1}$. Therefore, it is evident that the contribution of the homogeneous process to the whole ozone decomposition should be only negligible and the heterogeneous decay should be the dominant process as it was confirmed in the copper tubes. Rate constants estimated for different experimental conditions (selected material of the tube, dimensions of the tube and temperature) are summarized in Table 1.

Tab. 1. Rate constants of ozone decomposition for selected materials, dimensions and temperatures. (k_{Cu-4} and k_{Cu-8} means the rate constant for the copper tube with the inner diameter of 4 and 8 mm, respectively, k_{Fe-4} and k_{Fe-8} means the same for the iron tubes.)

T [°C]	k_{Cu-4} [$10^{-3} \text{ cm}^3 \cdot \text{s}^{-1}$]	k_{Cu-8} [$10^{-3} \text{ cm}^3 \cdot \text{s}^{-1}$]	k_{Fe-4} [$10^{-3} \text{ cm}^3 \cdot \text{s}^{-1}$]	k_{Fe-8} [$10^{-3} \text{ cm}^3 \cdot \text{s}^{-1}$]
10	0.80 ± 0.18	0.60 ± 0.15	0.6 ± 0.2	1.6 ± 0.3
25	1.3 ± 0.2	1.0 ± 0.2	1.7 ± 0.3	20 ± 4
40	1.6 ± 0.3	1.1 ± 0.2	2.9 ± 0.4	62 ± 7
55	2.5 ± 0.3	2.4 ± 0.4	4.5 ± 0.6	124 ± 14
70	3.7 ± 0.4	3.1 ± 0.5	5.7 ± 0.5	140 ± 14
85	15.0 ± 3.0	4.1 ± 0.6	38 ± 5	150 ± 16

4. Conclusion

Ozone decomposition was studied in the dependence on temperature, and from the viewpoint of interaction with selected metal surfaces (in the form of metal tubes with different inner diameter in order to obtain different surface-volume ratio). Ozone concentration was determined from the light absorption at 253.56 nm. Subsequently, rate constants for different experimental conditions were evaluated.

It was proved that enhanced temperature accelerated ozone decomposition in both copper and iron tested tubes. Generally, the decomposition was faster when iron tubes were used. However, the dominance of heterogeneous processes contributing to ozone decomposition was evident only in the case of copper surfaces. The comparison of the rate constants for different conditions did not reveal obvious participation of homogeneous bulk reactions or heterogeneous reactions of ozone with metal surfaces. Therefore, a new numeric model combining experimental data with theoretical assumptions is contemporarily under development.

Acknowledgements

This work was supported by the Technical Agency of the Czech Republic, project No. TA 03010098.

5. References

- [1] Horváth M, Bilitzky L and Hüttner J 1985 *Ozone* Budapest: Akadémiai Kiadó 350.
- [2] Tausch M and von Wachtendonk M 2001 *CHEMIE 2000+* Bamberg: C.C. Buchner 78.
- [3] Obvintseva A D, Klimuk A I et al. 2007 *Russian J Appl Chem* **81** (4) 593.
- [4] Konova P, Naydenov A et al. 2008 *Catalysis Today* **137** (2-4) 471.
- [5] Ennan A, Rakitskaya T L et al. 1999 *Catalysis Today* **53**.
- [6] Bartovská L 2008 *Chemická kinetika* Praha: VŠCHT (in Czech).
- [7] Orszagh J, Skalný J D et al. 2007 *International Workshop on Ozotech* Bratislava 44.
- [8] Daumont D, Brion J et al. 1992 *J Atm Chem* **15** (2) DOI: 10.1007/BF00053756.
- [9] Chemical Kinetics Database 2000 NIST: <http://kinetics.nist.gov/kinetics>.

ELECTRON INDUCED DISSOCIATION ON DICYCLOHEXYL PHTHALATE

Michal Lacko, Peter Papp, Štefan Matejčík

*Department of Experimental Physics, Faculty of Mathematics, Physics and Informatics,
Comenius University, Mlynska dolina, 84248 Bratislava, Slovakia*
E-mail: m.lacko@fmph.uniba.sk

The investigation of creation a positive and negative ions from dicyclohexyl phthalate molecule is presented. Using a trochoidal electron monochromator and quadrupole mass spectrometer we estimated a positive mass spectrum. For production of negative ions, the relative cross sections are presented.

1. Introduction

Phthalatic acid esters (“phthalates”) are molecules used in polyvinyl chloride production as plasticizer. The structural form of a general phthalate molecule is show in fig. 1, where R and R’ are hydrocarbons defining the different phthalate molecules. European Union in Directive 2005/84/EC created limits for concentration of phthalates in toys for children under 3 years old. This regulation contains DEHP (diethylhexyl phthalate), DBP (dibutyl phthalate), BBP (benzyl butyl phthalate), DINP (Diisonyl phthalate), DIDP (Diisodecyl phthalate) and DNOP (di-n-octyl phthalate) [1]. Moreover, the European Chemical Agency tagged phthalates (DHP, DPP, DIPP, DMEP, DIBP, BBP, DEHP, DBP and n-pentyl-isopentyl phthalate) as “toxic for reproduction” [2]. The health risk of phthalates is investigated continuously for decades and the results indicated a potential threat not only for children and humans [3-7], but also for environment [8-11]. Analyses denote a decreasing number of products with concentration of phthalates over recommended or enactment concentrations [12-16]. Those concentration limits are unfortunately not created for many human products (like a food cover) and also many countries don’t limit phthalates concentrations.

The investigation of phthalates concentration in plastics is very often made via gas chromatography method, which is frequently accompanied by mass spectrometry. Analysis of phthalates positive mass spectra shows an intensive product at $m/z = 149$ amu, which is dominant almost for all phthalates. However those peaks which could lead to a clear determination of phthalates from each other are much weaker. George and Prest [17] presented a gas chromatography study connected with different ionization method than electron induced ionization, the positive chemical ionization using ammonia reagent gas.

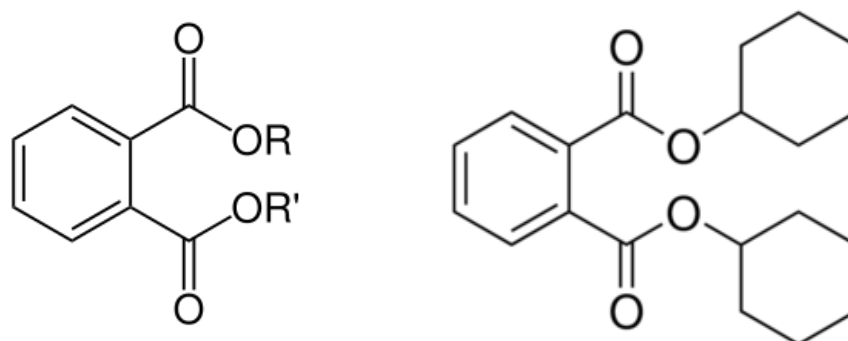
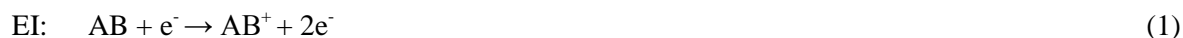


Fig. 1. The general structure of phthalates molecules, where R and R’ are hydrocarbons defining the different phthalate molecules (left) and the schematic structure of dicyclohexyl phthalate (right).

In this study we present electron induced processes on dicyclohexyl phthalate (DCP), schematically show in fig. 1. Although DCP is not one of the phthalates forbidden in the European Union, but still can be considered as dangerous. Moreover, this molecule is one of a few of phthalates which are at normal conditions in solid state.

The electron induced processes, investigated in this work are divided into two parts. First, formation of positive ions *via* electron ionization (EI, 1) and corresponding dissociative ionization (DI, 2), and second, formation of negative ions *via* electron attachment (EA, 3) and corresponding dissociative electron attachment (DEA, 4).



The experimental investigation of the electron induced processes on DCP was performed using crossed electron and molecular beam apparatus (fig. 2), located at Department of Experimental Physics of Comenius University in Bratislava [18]. The molecular beam is created by sublimation of the vapours of the solid DCP sample via a small capillary into the reaction region. There it collides with the electron beam, which has perpendicular orientation to the molecular beam. Electron beam is formed using a trochoidal electron monochromator, with the resolution of electron energy used in this study of around 200 meV. The calibration of the electron energy scale was made for EI using Ar^+/Ar reaction with threshold at 15.76 eV [19] and for EA and DEA studies using the SF_6/SF_6 reactions with peak at ~ 0 eV [20]. A weak electric field extracts the produced ions from the reaction region into the ion optics of the quadrupole mass analyzer. The mass separated ions (according to m/z) are detected with the electron multiplier.

Two different modes of operation of the experiment were applied, the first one, the mass spectrum was recorded at constant electron energy. For positive ions standard mass spectrum was recorded at electron energy ~ 70 eV. In the case of negative ions the mass spectra depend more strongly on the energy of the electrons due to resonant character of the reactions in the energy scale (0–13 eV), therefore the knowledge of the positions of the resonances for EA and DEA reaction for particular molecule is important. In the second mode, we have measured the ion efficiency curves for particular ions (for given m/z) as function of the incident electron energy, both for positive and negative ions.

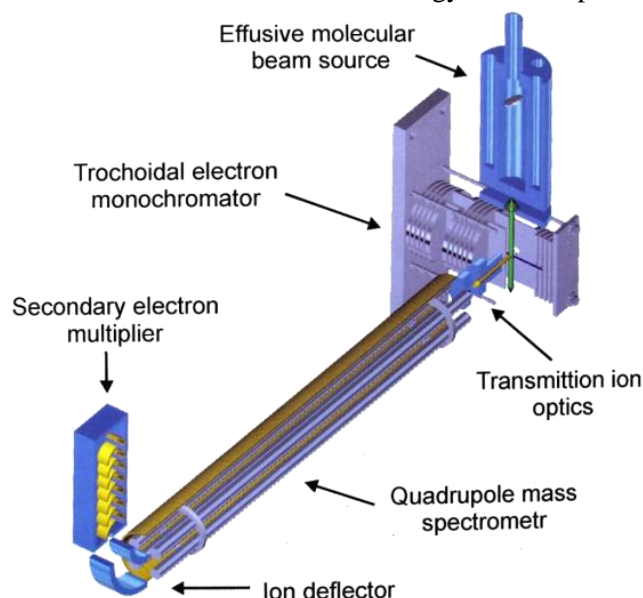


Fig. 2. The schema of electron – molecular beam experiment.

2. Results and discussion

The investigation of creation of positive ions via EI and DI resulted into a mass spectrum shown in fig. 3. The dominant peak at 149 amu, observed at almost all phthalates mass spectra's [21–22], represents the dissociation of both (R and R') hydrocarbons and one oxygen atom from phthalate molecule. The residual positive ion does not carry information about phthalate type. As well, the peak at 167 amu is observed in more cases, it represents the dissociation of DCP into a

$\text{COOH}(\text{C}_6\text{H}_4)\text{C}(\text{OH})_2^+$ ion. The positive ion with $m/z = 249$ amu is a result of loss of one cyclohexyl group wherein two hydrogen atoms from cyclohexyl remain on the ion. The ion at 83 amu is created by similar process, but there a positive charge remains on cyclohexyl. The intensive peaks below 83 amu (67, 55 and 41 amu) are probably created by dissociation of cyclohexyl, because the position is similar with cyclohexane (69, 56 and 41 amu) [19]. The positive ion of parent DCP was not detected.

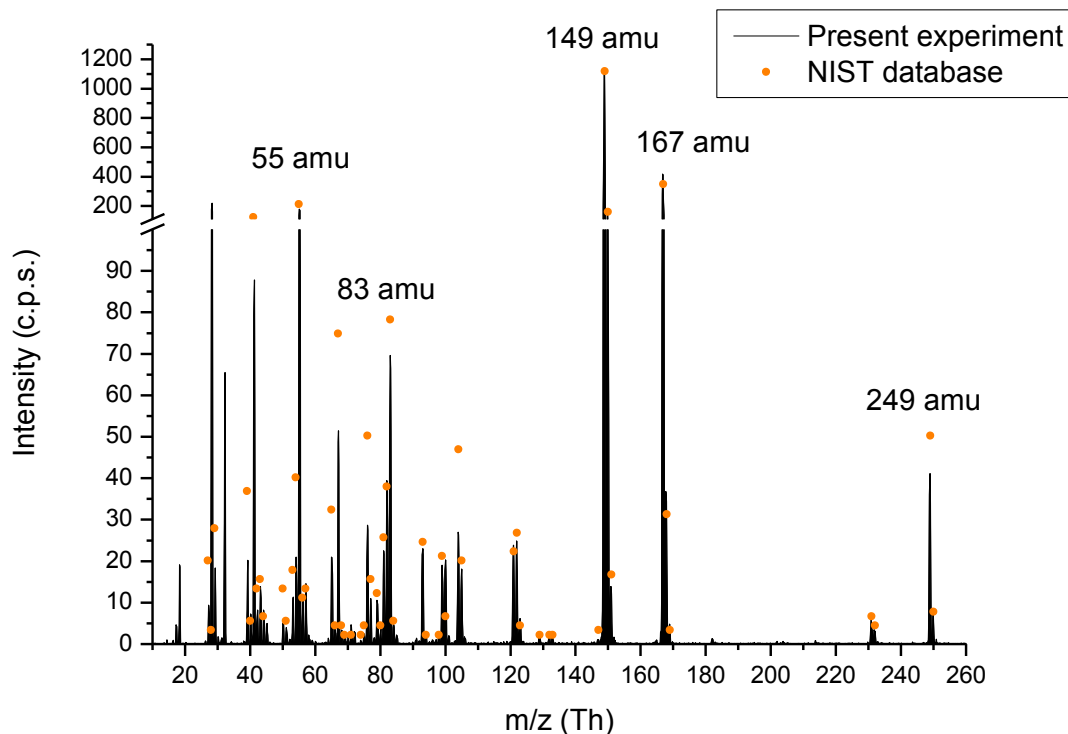


Fig. 3. The mass spectrum of dicyclohexyl phthalate at incident electron energy 70 eV.

The relative cross sections of DEA to DCP are present in fig. 5. Here, contrary to positive ions, production of DCP^- is the most intensive process, where the energy of incident electrons is close to 0 eV. At the same energy we observed products with m/z 148 and 45 amu. These ions are generated via dissociative electron attachment as single-particle resonance process. The ion with $m/z = 148$ amu have a similar character as positive ion with $m/z = 149$ amu. In case of negative ion, the hydrogen located on oxygen atom is replaced by entrapped electron. Mazurkiewicz and Deinzer [23] observed this ion as well, for different phthalates. Finally, the negative ion at 45 amu can be described as dissociation of COO part between benzene centre and characteristic part of phthalate (R or R'), where the hydrogen is added probably from cyclohexyl, resulting to COOH^- product. From the DEA processes discussed above we can expect that the captured electron is located on one of the oxygen atoms.

There exist other negative ions via DEA to DCP at higher energies which are associated with core excited resonances. Except the ion with m/z 247 amu, all of them have the threshold situated at ~ 4.5 eV. Here, the production of ion at 148 amu is also visible. Moreover, other new ions with m/z 77 and 121 amu were detected, both represented by dissociation of benzyl group where one hydrogen atom is added from cyclohexyl and dissociation of benzyl group with one COO part, where also one hydrogen atom is transferred from cyclohexyl, respectively. The resonance combined from 99 and 97 amu products is presented as well. This combination was conducted as a result of using a worse mass resolution during the experiment. The cross section of separated ions is not presented, but measurements indicate a similar position of resonances for both products. For mass 99 amu, the cyclohexyl with one oxygen atom is produced, where a negative charge is probably located on oxygen. The negative charge can be spontaneously transferred into a cyclohexyl ring where is delocalized, that can lead to creation of double bond between oxygen and cyclohexyl carbon, whereby the two

hydrogen atoms are dissociated. This process leads to creation of a negative ion at 97 amu. The negative ion at 247 amu is a result of dissociation of cyclohexyl from parent molecule. This product is formed by two resonances with thresholds at ~ 2 eV and ~ 6 eV.

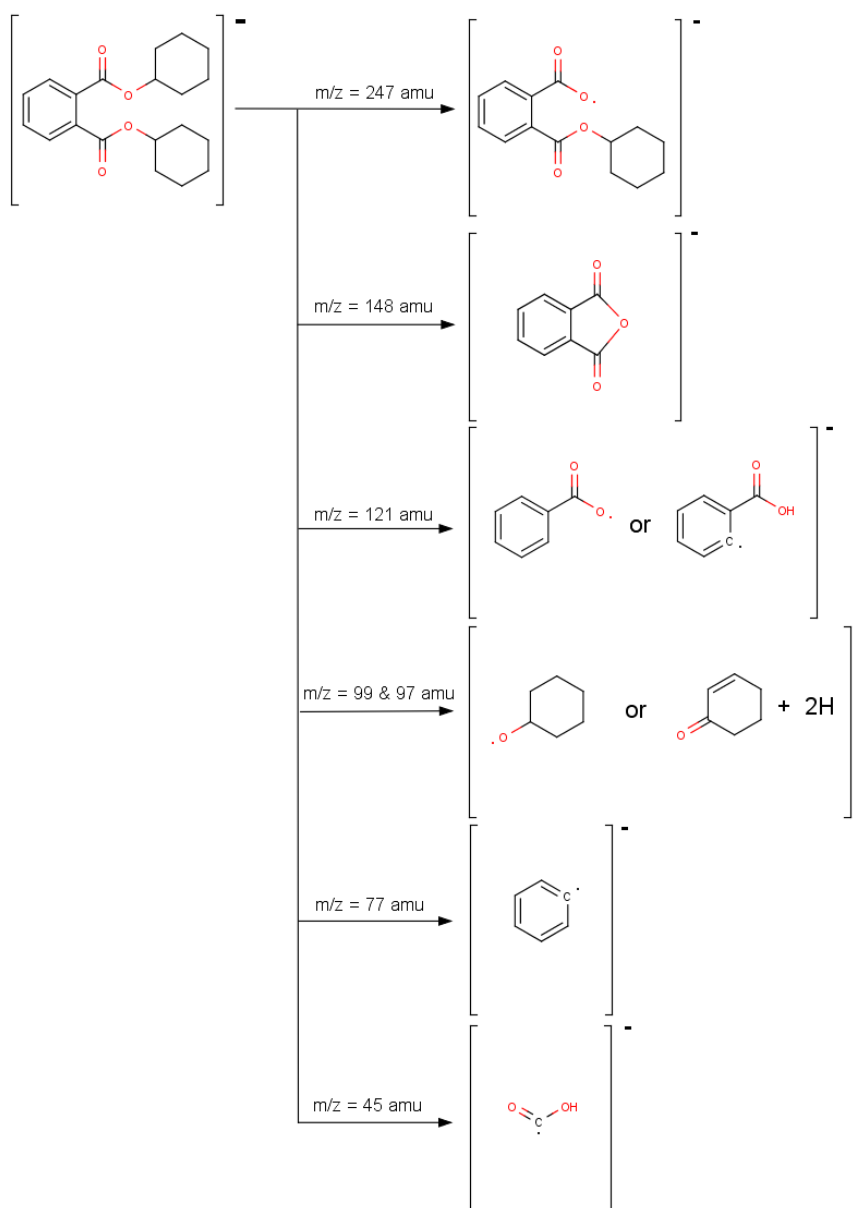


Fig. 4. The visual schema of negative ion products detected by crossed – beam experiment

Mazurkiewicz and Deinzer [23] presented negative ion resonances for 7 *o*-phthalates. Resonance maxima of production of negative parents are localized mostly around 0.5 eV followed by second resonances around 1 eV. A relative cross section for *o*-methyl phthalate and *o*-butyl cyclohexyl phthalate indicated that resonances are mostly localized into region from 0 to 2 eV. This contrast can be associated with difference bond strength between oxygen atom and cyclohexyl and with different electron affinity of products. The expected negative ion at 164 amu was not observed in our case, where both cyclohexyl's would be dissociated.

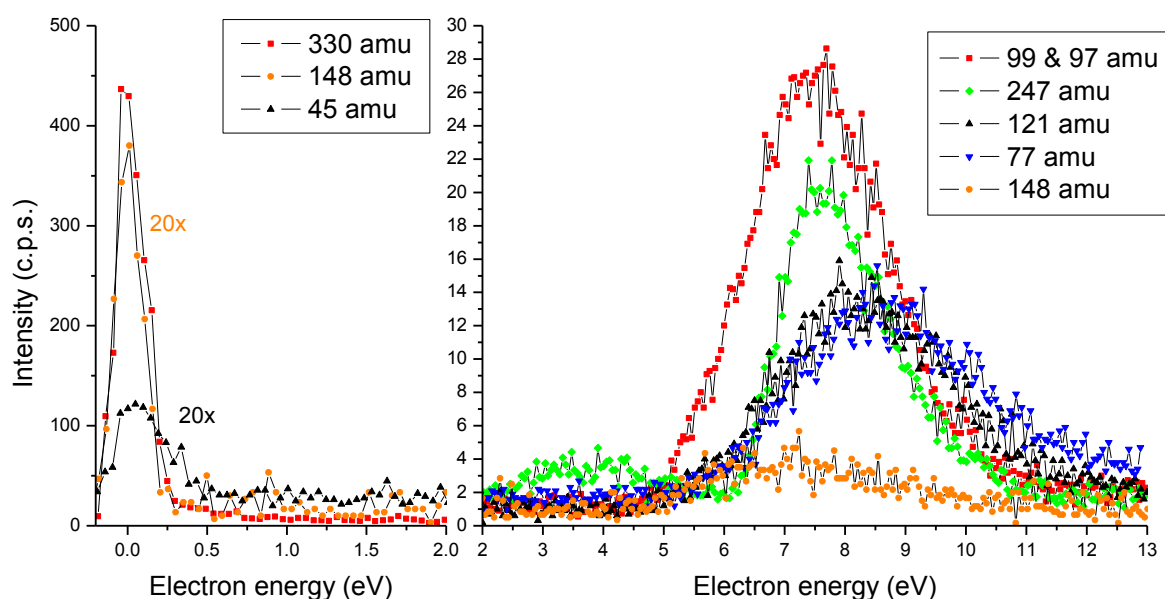


Fig. 5. The energy dependence of creation of negative ions.

3. Acknowledgments

Financing of this work was by the Slovak Grant Agency VEGA-1/0514/12. This work was supported by the Slovak Research and Development Agency, project Nr. APVV-0733-11 and the Comenius University student grant program no. UK/528/2014.

4. References

- [1] Directive 2005/84/EC of the European Parliament and of the Council of 14 December 2005
- [2] EHCA – European Chemicals Agency, Candidate List of Substances of Very High Concern of Authorisation, <http://echa.europa.eu/candidate-list-table/-/substance/>
- [3] North M L, Takaro T K et al. 2014 *Ann. Allergy. Asthma. Immunol.* **112** (6) 496-502.
- [4] Halden R U 2010 *Annu. Rev. Public Health* **31** 179.
- [5] Earls A O, Axford I P and Braybrok J H 2003 *Journal of Chromatography A* **983** 237-246.
- [6] Heise S and Litz N 2004 *Deskstudy PHTHALATES* German Federal Environmental Agency, Berlin, Germany, Horizontal.
- [7] Johnson S, Saikia N et al. 2010 *Phthalates in Toys* Investigation study of Centre for Science and Environment in New Delhi CSE/PML/PR-34/2009
- [8] Foster P M D, Mylchreest E et al. 2001 *Hum. Rep. Update* **7** (3) 231-235
- [9] Jobling S, Reynolds T et al. 1995 *Env. Health Persp.* **103** (6) 582-587
- [10] Ohtani H, Mikura I and Ichikawa Y 2000 *Env. Health Persp.* **108** (12) 1189-1193
- [11] Wams T J 1987 *Sci. Total Env.* **66** 1-16
- [12] Ionas A C, Dirtu A C et al. 2014 *Environm. Int.* **65** 54-62.
- [13] Korfali S I, Sabra B et al. 2013 *Arch. Environ. Contam. Toxicol.* **65** (3) 368.
- [14] Özer E T and Güçer Ş 2011 *Talanta* **84** 362-367.
- [15] Shen H Y 2005 *Talanta* **66** 734-739.
- [16] Rastogi S C 1998 *Chromatographia* **47** 784.
- [17] George C and Prest H 2002 *LCGC North America* **20** (2) 142-151.
- [18] Stano M, Matejčík Š 2003 *J. Phys. B: At., Mol. Opt. Phys.* **36** 261.
- [19] Lias S G Ion energetic data, in: NIST Chemistry WebBook, NIST Standard Reference Database 69, <http://webbook.nist.gov/chemistry/> [cited 2014 December].
- [20] Christophrou L G and Olthoff L G 2000 *J. Phys. Chem. Ref. D* **29** 267-330.
- [21] Leung S C and Giang B Y 1993 *Bull. Environ. Contam. Toxicol.* **50** 528-532.
- [22] Yinon J 1988 *Org. Mass Spectr.* **23** 755-759.
- [23] Mazurkiewicz P H and Deinzer M L 1999 *J. Am. Chem. Soc.* **121** 3421-3427.

DETERMINATION OF THE NITROGEN ATOM WALL RECOMBINATION PROBABILITY IN LATE AFTERGLOW

Věra Mazánková¹, David Trunec², František Krčma¹

¹*Faculty of Chemistry, Brno University of Technology, Purkyňova 118, Brno 612 00, Czech Republic*

²*Masaryk University, Kotlářská 2, 611 37 Brno, Czech Republic*

E-mail: mazankova@fch.vutbr.cz

The reaction kinetics in nitrogen flowing afterglow was studied by optical emission spectroscopy. The DC flowing post-discharge in pure nitrogen was created in a quartz tube at the total gas pressure of 1000 Pa and discharge power of 130 W. The optical emission spectra were measured along the flow tube. Three nitrogen spectral systems - the first positive, the second positive, and the first negative were identified. It was found that N atoms are the most important particles in this late nitrogen afterglow, their volume recombination starts a chain of reactions which produce excited states of molecular nitrogen. In order to explain the decrease of N atom concentration, it was also necessary to include the surface recombination of N atoms to the model. The surface recombination was considered as a first order reaction and wall recombination probability $\gamma = (2.16 \pm 0.07) \times 10^{-6}$ was determined from the experimental data.

1. Introduction

In flowing nitrogen afterglows (post-discharges) at low pressure, a large number of nitrogen atoms is created in the discharge or in the short-lived (pink) afterglow during collisions of nitrogen molecules with electrons, vibrationally excited nitrogen molecules and metastable states. The nitrogen atoms are lost by volume and wall recombination [1]. The probability of volume recombination (a three-body collision) tends to be lower than the wall recombination probability γ . The probability γ is the ratio between the number of atoms effectively recombining at the surface over the number of atom-wall collisions [2]. Nitrogen late afterglow is characterized by a visible emission in the yellow part of the spectrum, associated with the recombination of the nitrogen atoms in the gas phase.

Nitrogen post-discharges are widely used for various industrial applications such as nitriding [3], plasma surface modification [4] or plasma sterilization [5]. Besides laboratory and technological plasmas, the nitrogen post-discharge is studied also in connection with the kinetics of the upper Earth atmosphere (corona borealis [6]) and the processes occurring in nitrogen post-discharges are also taken into account in some extraterrestrial systems, for example in the Titan atmosphere [7].

This paper presents a method for obtaining the atomic nitrogen recombination probability (γ). It is based on the measurement of 11-7 transition intensity in first positive nitrogen spectral system (FPS).

2. Experimental set-up

The flowing configuration of nitrogen DC discharge was used for the experimental study. This experimental set-up was already used for our previous study with nitrogen [8, 9]. A simplified schematic drawing of the experimental set-up is given in Fig. 1. The active discharge was created in a quartz discharge tube with the inner diameter of 12 mm at the constant total gas pressure of 1000 Pa and the discharge power of 130 W. Hollow molybdenum electrodes were placed in the side arms (at the interelectrode distance of 120 mm) of the main discharge tube to minimize their sputtering and also to minimize the influence of the light emitted in the electrode regions. The nitrogen gas was of 99.9999 % purity and it was further cleaned by Oxiclear and LN₂ traps. The reactor system was pumped continuously by a rotary oil pump separated from the discharge tube by another LN₂ trap. The gas flow of 800 sccm was automatically controlled by the Bronkhorst mass flow controller. The total gas pressure in the discharge tube was measured by a capacitance gauge connected to the end of the discharge tube. The gas temperature was 300 K.

The bulk flow velocity v_g of nitrogen in the tube was calculated from the continuity equation and the state equation for ideal gas. The calculated velocity v_g was 12 ms⁻¹. The flow analysis was performed in the same way as in previous studies using flowing afterglow [10, 11].

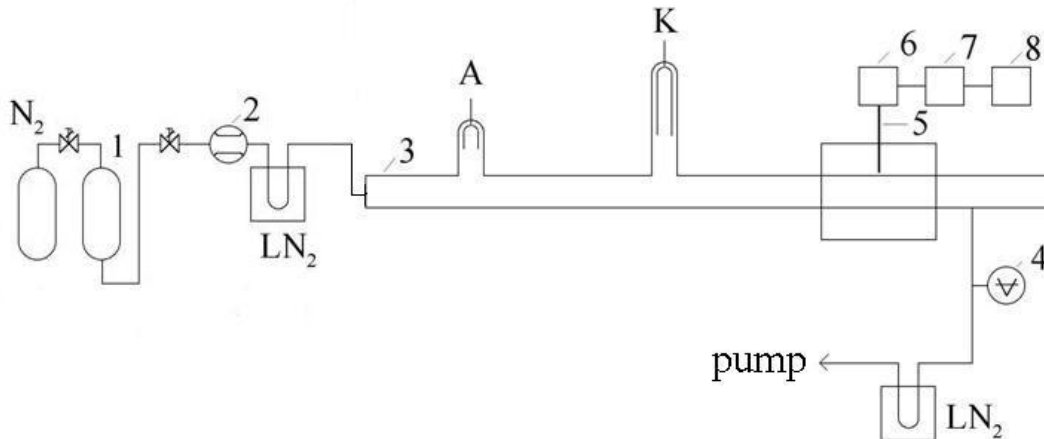


Fig. 1. Scheme of the experimental setup. 1- catalyzer Oxiclear; 2- mass flow controller; 3- quartz discharge tube; 4-capacitance gauge; 5-quartz optical fiber; 6-monochromator Jobin Yvon Triax 550; 7-CCD; 8-PC.

The distance d needed to develop a full parabolic velocity profile is given by $d = 0.277 a R$, where a is the flow tube radius (0.6 cm) in cm and R is the Reynolds number. For our experimental conditions, the Reynolds number R is equal to 184, which gives $d = 31$ cm. Furthermore, our experimental setup introduced perturbations into the flow pattern at the side arms and at the nitrogen inlet. So, the flow will be in transition between plug and parabolic flows and in this case the bulk flow velocity can be used for the calculation of the decay time. This approach was found to be correct in previous studies [8-10]. In present experiment the line intensities (which are proportional to the exited particle concentrations) were measured across the diameter of the flow tube. Bolden et al. [12] have experimentally demonstrated that this is equivalent to monitoring the concentration at the center of the tube for fully developed parabolic flow conditions.

The optical spectra were measured by Jobin Yvon monochromator TRIAX 550 with CCD detector. The 300 gr/mm grating was used for overview spectra in the range from 300 nm to 600 nm. The emitted light was led to the entrance slit of the monochromator by the multimode quartz optical fiber movable along the discharge tube.

3. Results

The optical spectra were measured as a function of position along the flow tube in the distances 30 – 52 cm from the active discharge. An example of the typical recorded post-discharge spectrum is shown in Fig. 2. The nitrogen late afterglow emission is dominated by the



band of the first positive system at 580 nm [13], see also Fig. 2. This band is correlated with the three-body recombination process with the rate constant $k_{\text{vol}} = 4.4 \times 10^{-33} \text{ cm}^6 \text{ s}^{-1}$ taken from [14]



As the $\text{N}_2(\text{B}, \nu=11)$ state can de-excite either radiatively to the A state with a global frequency ν_{rad} or collisionally by quenching with the nitrogen molecules (k_q), the emitted intensity can be written as

$$I_{11-7} \propto [\text{N}_2(\text{B}, \nu = 11)] \propto \frac{k_{\text{vol}}[\text{N}]^2[\text{N}_2]}{\nu_{\text{rad}} + k_q[\text{N}_2]} \quad (3)$$

where the values $\nu_{\text{rad}} = 1.7 \times 10^5 \text{ s}^{-1}$ and $k_q = 5 \times 10^{-11} \text{ cm}^3 \text{ s}^{-1}$ were taken from [15]. So it appears that the evolution of the N atom concentration can be followed monitoring I_{11-7} . For pressures higher than 133 Pa is $k_q[\text{N}_2] \gg \nu_{\text{rad}}$ and equation (3) reduces to

$$[\text{N}] \propto \sqrt{I_{11-7}}. \quad (4)$$

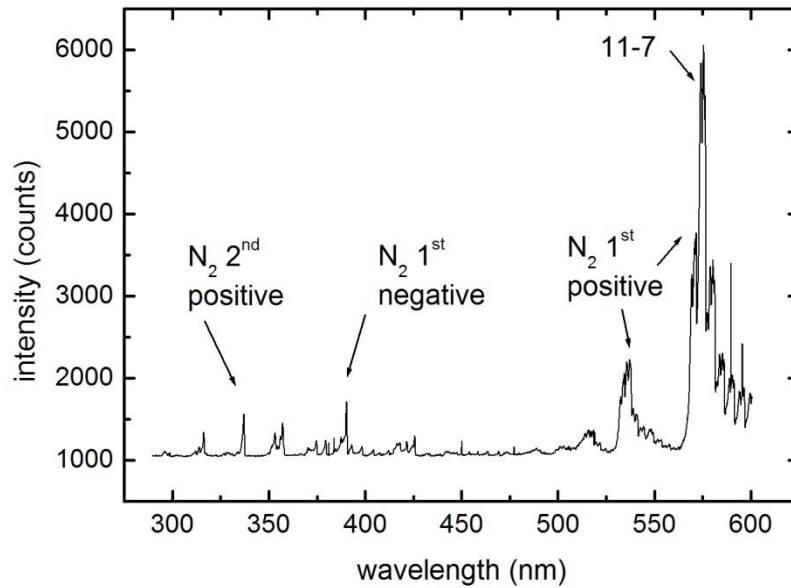


Fig. 2. Overview spectrum of nitrogen post-discharge.

The N atom concentration determined from this equation is shown in Fig. 3 as a function of decay time. These N atom concentrations were multiplied by a constant so that they can be coincident at $t = 0$ s (distance 30 cm from active discharge) with absolute N atom concentration determined in previous study by NO titration [16].

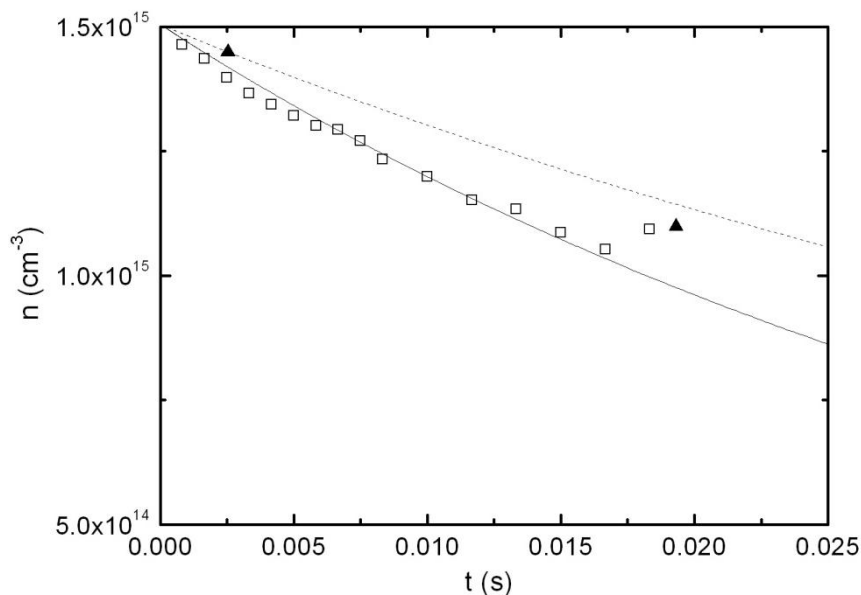


Fig. 3. Time dependence of nitrogen atom concentration. Squares – concentrations determined from Eq. (4); triangles – concentrations determined by NO titration [16]; full line – calculation from the model with $\gamma = 2.16 \times 10^{-6}$; dashed line – calculation from the model with $\gamma = 1.35 \times 10^{-6}$.

The kinetic model of nitrogen late afterglow developed previously [9] was used to fit measured data using least square method. The value $\gamma = (2.16 \pm 0.07) \times 10^{-6}$ was obtained from this method. However, the N atom concentrations determined from measurement of FPS intensity decreases faster than the N atom concentration determined by NO titration and also faster than calculated N atom concentration from the model in previous study [9] with the value $\gamma = 1.35 \times 10^{-6}$. This discrepancy could be caused by incorrect determination of 11-7 transition intensity in FPS due to overlap of this band with neighboring vibrational bands.

4. Conclusion

The recombination of N atoms in nitrogen late afterglow was studied in flowing afterglow experiment at pressure of 1000 Pa. The optical emission spectra were measured at different positions along the quartz flow tube (and hence at different times of afterglow). The spectra were dominated by 11-7 band of the nitrogen first positive system. This band is correlated with three body (volume) recombination of atomic nitrogen and thus it is possible to determine the relative concentration of N atoms from band intensity. Then the wall recombination probability γ for N atoms was calculated from the decrease of N atom concentration along the flow tube and the value $\gamma = (2.16 \pm 0.07) \times 10^{-6}$ was obtained.

5. Acknowledgments

The present work was supported by the project "R&D center for low-cost plasma and nanotechnology surface modifications" (CZ.1.05/2.1.00/03.0086) funding by the European Regional Development Fund and by the Czech Science Foundation, contract No. 13-24635S.

6. References

- [1] Guerra V, Sa P A and Loureiro J 2004 *Eur. Phys. J. - Appl. Phys.* **28** 125.
- [2] Rouffet B, Gaboriau F and Sarrette J P 2010 *J. Phys. D: Appl. Phys.* **43** 185203.
- [3] Bockel S, Belmonte T, Michel H and Ablitzer D 1997 *Surf. Coat. Technol.* **97** 618.
- [4] Junkar I, Vesel A, Cvelbar U, Mozetic M and Strnad S 2009 *Vacuum* **84** 83.
- [5] Kutasi K, Pintassilgo C D, Coelho P J and Loureiro J 2006 *J. Phys. D: Appl. Phys.* **39** 3978.
- [6] Ashrafi M, Lanchester B S, Lummerzheim D, Ivchenko N and Jokiah O 2009 *Ann. Geophys.* **27** 2545.
- [7] Horvath G, Krcma F, Polachova L, Klohnova K, Mason N J, Zahoran M and Matejcik S 2011 *Eur. J. Phys. D: Appl. Phys.* **53** 11001.
- [8] Mazankova V, Trunec D and Krcma F 2013 *J. Chem. Phys.* **139** 164311.
- [9] Mazankova V, Trunec D and Krcma F 2014 *J. Chem. Phys.* **141** 154307.
- [10] Kolts J H and Setser D W 1978 *J. Chem. Phys.* **68** 4848.
- [11] Piper L G, Velazco J E and Setser D W 1973 *J. Chem. Phys.* **59** 3323.
- [12] Bolden R C, Hemsworth R S, Shaw M J and Twiddy N D 1970 *J. Phys. B* **3** 45.
- [13] Noxon J F 1962 *J. Chem. Phys.* **36** 926.
- [14] Krivonosova O E, Losev S A, Nalivaiko V P, Mukoseev Y K and Shatalov O P 1991 *Reviews of Plasma Chemistry vol. 1* ed. B M Smirnov (New York: Consultants Bureau) p 9.
- [15] Gordiets B and Ricard A 1993 *Plasma Sources Sci. Technol.* **2** 158.
- [16] Mazankova V, Polachova L, Krcma F, Horvath G and Mason N. J. 2011 *Proceedings, 19th Symposium on Physics of Switching Arc*, Brno, ed. V Aubrecht and M Bartlova (Brno University of Technology) 283.

REACTION OF BENZYNE RADICAL ANIONS WITH ACETYLENE. A STEP TOWARDS THE FORMATION OF PAHS IN EXTRATERRESTRIAL ENVIRONMENTS?

Michaela Obluková, Miroslav Polášek, Ján Žabka

J. Heyrovský Institute of Physical Chemistry of the ASCR, Dolejškova 2155/3, 182 23 Prague 8, Czech Republic

The negative ions have already been found in various extraterrestrial environments such as coma of the comet Halley [1], ionosphere of the Saturn's moon Titan [2] and molecular envelopes of carbon stars [3-5]. Recently, a possible role of negative ions, namely the *ortho*-benzyne, in the formation of PAH's in the protoplanetary atmospheres has been discussed [6]. We have found that various hydrocarbon anions are formed in the acetylene low-pressure plasma, which is present in the chemical ionization ion source, where the acetylene molecules are bombarded by 100eV electrons. Besides expected acetylides $C_{2n}H^-$ ($n = 1-3$), also $C_6H_4^-$, $C_7H_4^-$, $C_8H_4^-$ anions were observed. Out of these, the $C_6H_4^-$ was identified as benzyne anion using structurally diagnostic methods of tandem mass spectrometry.

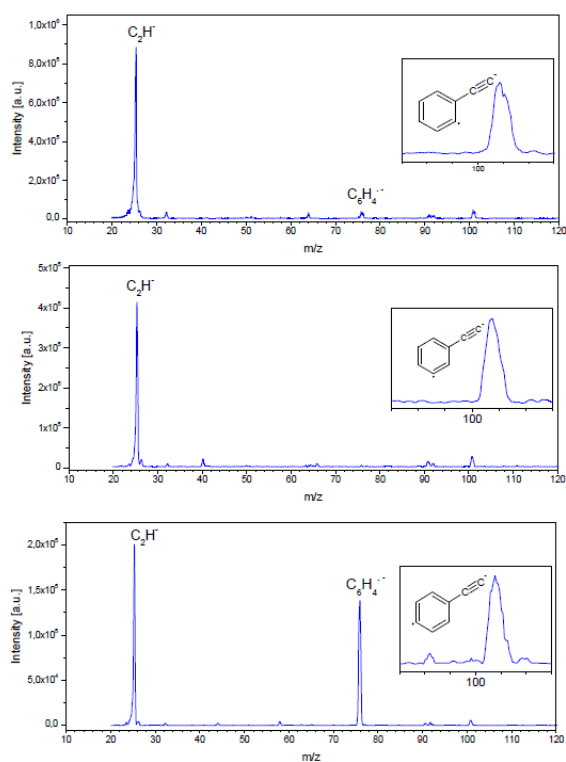


Fig.1.: Product ion mass spectra for reactions of (a) *o*- $C_6H_4^-$, (b) *m*- $C_6H_4^-$, (c) *p*- $C_6H_4^-$ with C_2H_2

Acknowledgment:

This work was supported by the Czech Science Foundation (grant No. 14-19693S) and the COST program, Action CM0805 "The Chemical Cosmos: Understanding Chemistry in Astronomical Environments".

References:

- [1] P. Chaizy *et al.*, *Nature* **349** (1991) 393
- [2] V. Vuitton *et al.*, *Planet. Space Sci.* **57** (2009) 1558
- [3] M.C. McCarthy *et al.* *Astrophys. J.* **652** (2006) L141
- [4] J. Cernicharo *et al.*, *Astronomy and Astrophysics.* **467** (2007) L37
- [5] S. Brünken *et al.*, *Astrophys. J.* **664** (2007) L43
- [6] F. Carelli *et al.*, *Mon. Not. R. Astron. Soc.* **415** (2011) 425

- (a) Following this observation suggesting the possibility of formation of benzyne anion from acetylene via negative ion/molecule chemistry, a reactivity of this interesting species with acetylene has been studied both experimentally and theoretically. For the *ortho*-benzyne we have found two major reaction channels: proton transfer $C_6H_4^- + C_2H_2 \rightarrow C_6H_5^- + C_2H^+$, (1), and C-C bond formation $C_6H_4^- + C_2H_2 \rightarrow C_8H_5^- + H^+$, (2). The exothermicities of the reactions (1) and (2) were found to be 25 kJ mol^{-1} and 75 kJ mol^{-1} , respectively. However, the branching ratio observed (5:1 in favor of proton transfer) does not follow the order of calculated reaction energies. Similar reactivity was observed also for *meta*- and *para*-benzyne. A detailed quantum chemical study of the molecular mechanism of these reactions revealed that this apparent discrepancy is most probably given by kinetic reasons.
- (b)
- (c)

LUMINESCENCE OF PHOSPHORS INDUCED BY ELECTRON IMPACT

Juraj Országh^{1,2}, Ivo Utke², Štefan Matejčík¹

¹*Department of Experimental Physics, Comenius University, Mlynská dolina F2, Bratislava, Slovakia*

²*EMPA, Swiss Federal Laboratories for Materials Science and Technology, Laboratory for Mechanics of Materials and Nanostructure, Feuerwerkerstrasse 39, Thun, Switzerland*

E-mail: orszagh@fmph.uniba.sk

Three commonly industrially used phosphors yttrium oxide doped by europium ($\text{Y}_2\text{O}_3:\text{Eu}$), cerium magnesium aluminate doped by terbium ($\text{CeMgAl}_{11}\text{O}_{19}:\text{Tb}$) and barium magnesium aluminate doped by europium ($\text{BaMgAl}_{10}\text{O}_{17}:\text{Eu}$) were selected to study their excitation by electron impact and test new experimental setup for luminescence of powders induced by electron impact. The 20kV electron beam of the scanning electron microscope was used to induce the phosphorescence of these compounds and the subsequent photon emission was detected by optical spectrometer.

1. Introduction

In general the term phosphor is most commonly used for inorganic synthesized phosphorescent compounds or in a broader sense it is used to describe any solid luminescent material. The phosphor research evolved dramatically after the World War II with the progress in the solid-state physics. Contemporary industrial applications of the phosphors can be divided into four categories: light sources – fluorescent lamps, display devices – cathode-ray tubes, detector systems – X-Ray screens and scintillators and other applications such as luminous paints, etc. [1].

Phosphors are usually composed of a transparent crystalline host compound and so-called activator which is an intentionally added impurity. The activator particles in the host compound create emission centres as the phosphor luminescence originates in the deexcitation transitions of the activator. From that it is evident that the efficient transfer of the excitation energy from an excited point in host crystal to the emission centre is a crucial process. In general the excitation energy can be transferred by migration of free particles (electrons, holes, pairs, etc.) or by quantum mechanical resonance. While the first type is observed mostly in semiconductor-like hosts that are often used in cathode-ray tubes the second type is active in phosphors with less mobile electrons and holes such as oxides [1].

The $\text{Y}_2\text{O}_3:\text{Eu}$ phosphor is mostly used in fluorescent lamps. Its strongest photon emission is in the spectral range between 450 and 720nm with the most intensive peak at approximately 611nm thus it is a red emitting phosphor. All the emission lines correspond to the deexcitation of activator Eu^{3+} ion [2]. In general this red phosphor is considered to be the one with the highest quantum efficiency of all lighting phosphors [3].

The $\text{CeMgAl}_{11}\text{O}_{19}:\text{Tb}$ phosphor is based on Ce^{3+} ions acting as sensitizers and Tb^{3+} ions acting as activators. The energy of from the outer source (usually UV or electron irradiation) is absorbed by cerium ions which then transfer the energy to the terbium ions. The energy from an excited cerium ion can be transferred to the six nearest neighbouring particles at 5.6Å [3]. For the complete quenching of the cerium ions the terbium concentration needs to be at least 33 mole percent. During the deexcitation the Tb^{3+} ions emit photons in the wavelength range from 475nm to 700nm with the strongest peak at approximately 545nm.

Blue emitting phosphor $\text{BaMgAl}_{10}\text{O}_{17}:\text{Eu}$ exhibits one broad peak in the emission spectrum between 410nm to 550nm with the maximum approximately at 450nm. This emission is caused by the deexcitation of the Eu^{2+} ions. This compound is often industrially used in the fluorescent lamps [3].

The aim of this work is to test the new experimental setup for optical emission spectroscopy of powders irradiated by electron beam. The phosphors were chosen as the first test candidates as their photon emission is strong.

2. Experiment and results

The experimental measurements were done in the chamber of the Hitachi S-3600N scanning electron microscope where the phosphor powder on the SiO_2 substrate was irradiated by the 20kV primary

electron beam. The electron current measured in the faraday cup reached approximately 2nA. For optical measurements of the emission spectra the Ocean Optics HR-2000+ES spectrometer and for photon collection near the irradiated sample Ocean Optics fibre with diameter of 600 μ m was used. The spectrum was measured in the range from 200nm to 1100nm and the collection time in each case was set to 110ms. In case of Y₂O₃:Eu and CeMgAl₁₁O₁₉:Tb phosphors such collection time led to saturation at the wavelength corresponding to the most intensive peak so its maximum is not visible in the shown spectra. This approach was chosen to better resolve less intense transitions in the spectra. The spectrum of the Y₂O₃:Eu is divided into three parts and it is shown in the following figures 1a – 1c. The transitions were identified and labeled according to [2]. It was possible to identify various transition of the Eu³⁺ ion from excitation levels ⁵D_i (i = 0, 1, 2) to levels ⁷F_j (j = 0, 1, 2, 3, 4). In the spectral region 450nm – 575nm (fig. 1a.) the deexcitations from levels ⁵D₂ and ⁵D₁ are mixed.

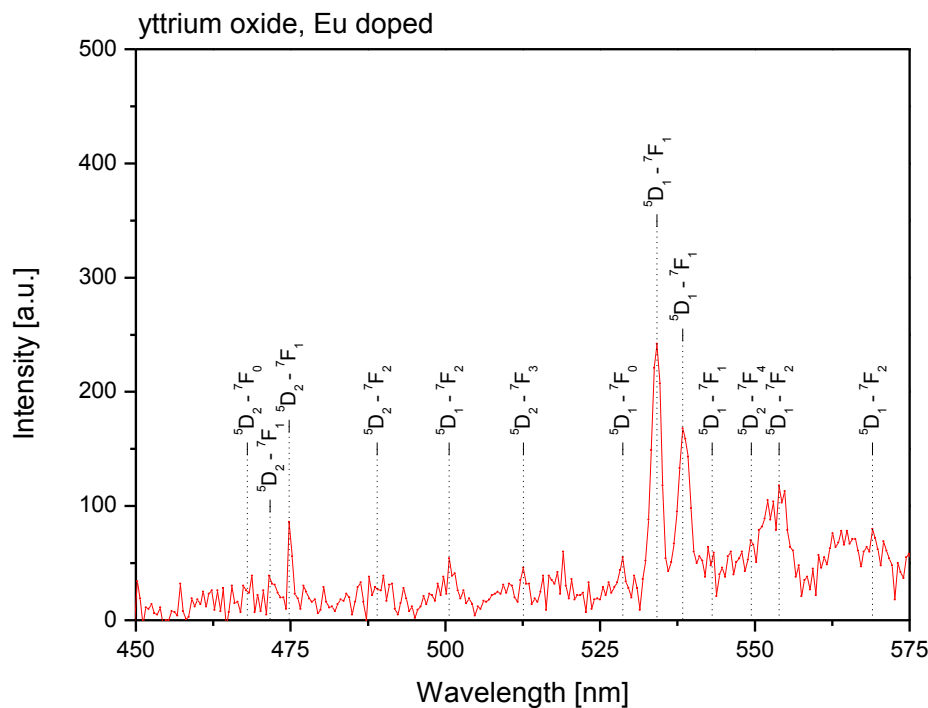


Fig. 1a. First part of the “red” phosphor Y₂O₃:Eu spectrum induced by electron impact. The peaks corresponding to the transition of the Eu³⁺ ion are shown.

In the next figure 1b the spectral region from 575nm to 635nm is shown. In this region the most intense radiation was detected with the strongest transition at approximately 611nm. The deexcitation ⁵D₀ – ⁷F₂ of the Eu³⁺ ion produces spectral peak with approximately 10x higher intensity in comparison to second most intensive transition Eu³⁺ (⁵D₀ – ⁷F₂) at approximately 632nm. In this wavelength region (fig. 1b.) the transitions mostly from excitation level ⁵D₀ with two weaker transitions from level ⁵D₁ to higher termination levels ⁷F₃ and ⁷F₄ are present.

In the last figure 1c the third part of the red phosphor spectrum is shown (635nm – 725nm). In this region only the transitions from level ⁵D₀ to higher terminating levels ⁷F₃ and ⁷F₄ are present.

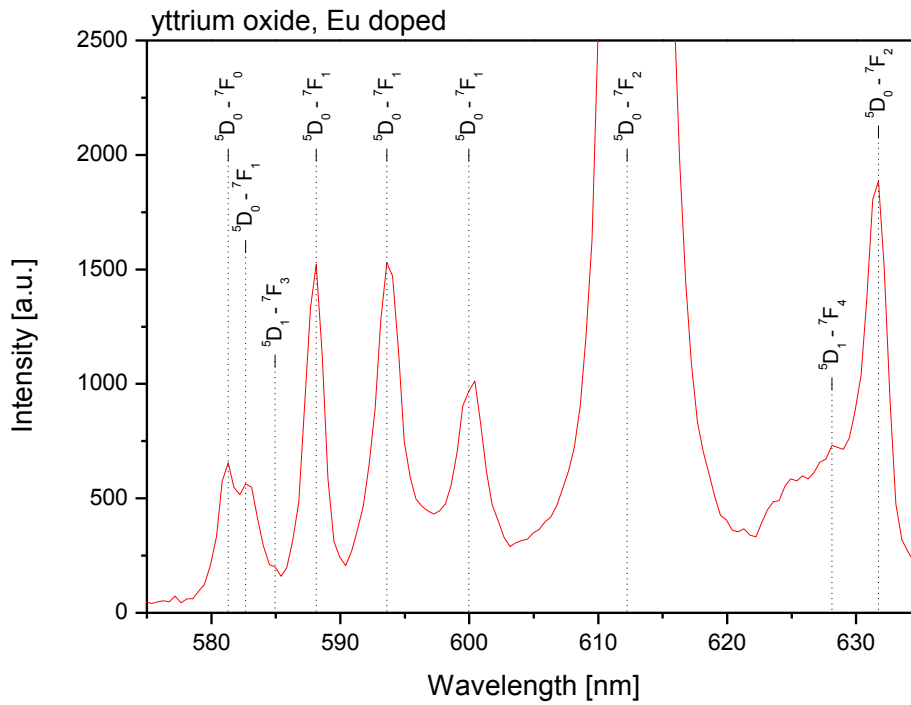


Fig. 1b. Second part of the “red” phosphor $\text{Y}_2\text{O}_3:\text{Eu}$ spectrum induced by electron impact. The peaks corresponding to the transition of the Eu^{3+} ion are shown.

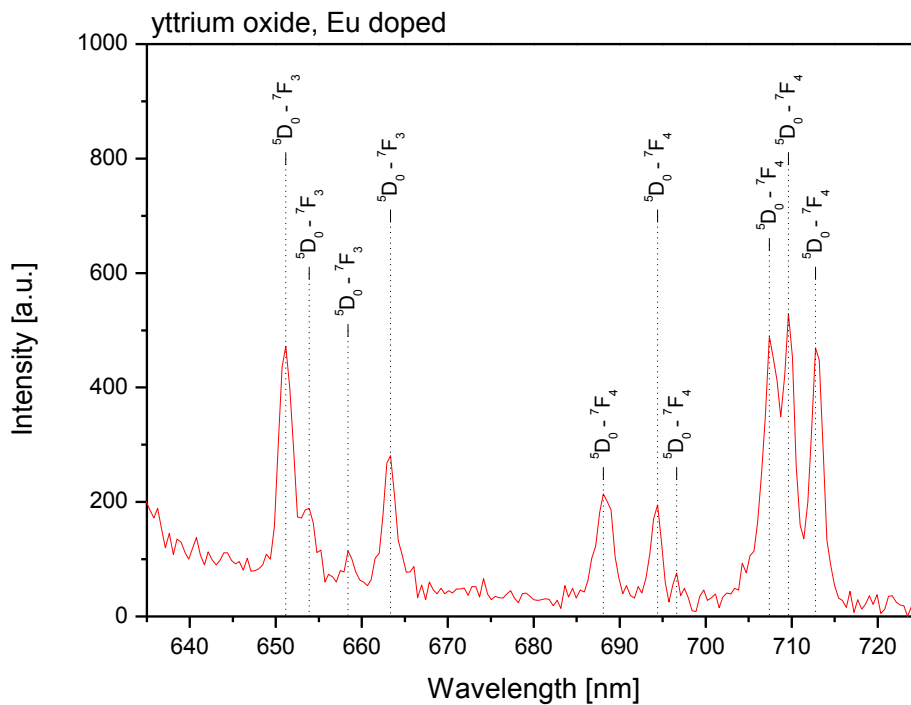


Fig. 1c. Third part of the “red” phosphor $\text{Y}_2\text{O}_3:\text{Eu}$ spectrum induced by electron impact. The peaks corresponding to the transition of the Eu^{3+} ion are shown.

The emission spectra of blue and green phosphors are shown in the following figures 2 and 3.

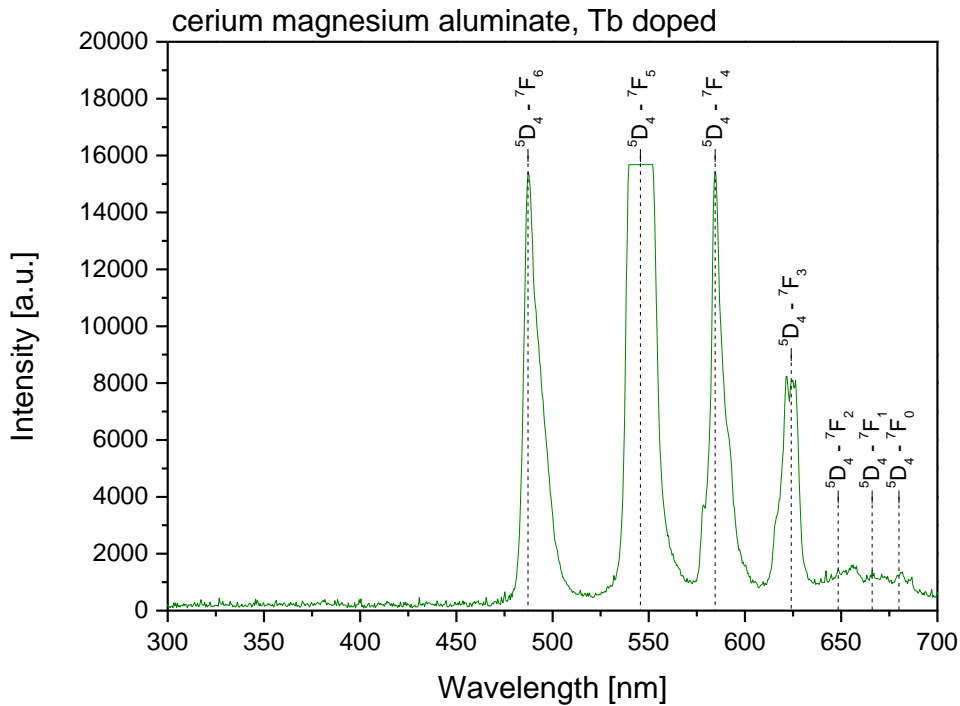


Fig. 2. Spectrum of the “green” phosphor cerium magnesium aluminate doped by terbium. The peaks corresponding to the transition of the Tb^{3+} ion are shown.

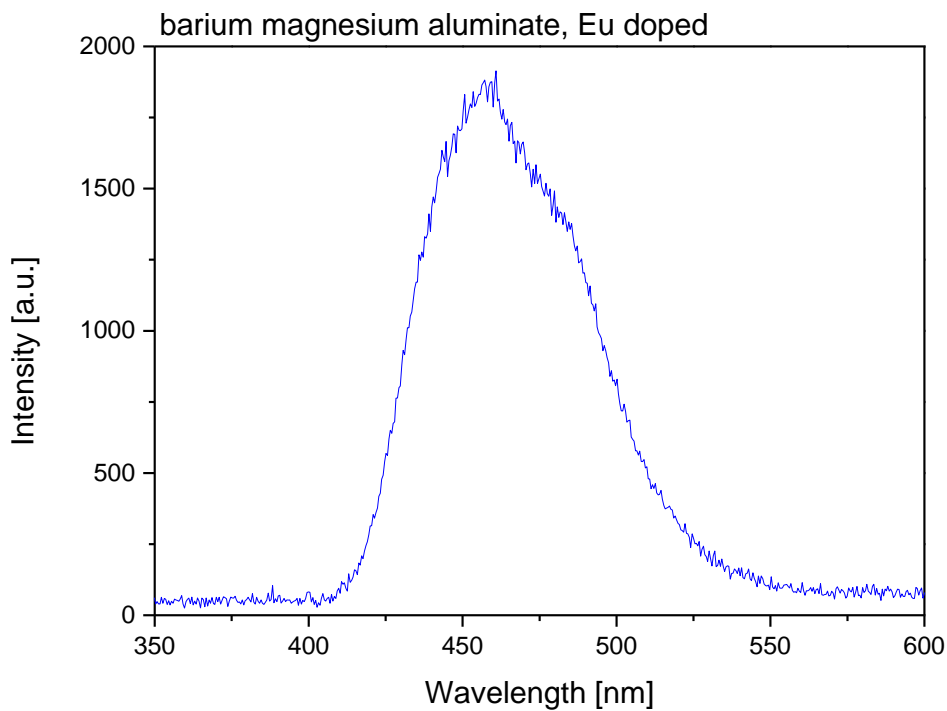


Fig. 3. Spectrum of the “blue” phosphor barium magnesium aluminate doped by europium. The band corresponds to the transition $5d - 4f$ of the Eu^{2+} ion.

The cerium magnesium aluminate doped by terbium in our experiments contained 37 mole percent of terbium. This composition is confirmed by our spectral measurements as there is no signal in the region below 400nm. In this region the emission of the Ce^{3+} ion can be detected if the terbium concentration is less than 33 mole percent. The transitions in the spectrum were identified according to [4] and [5]. They correspond to the deexcitations of the Tb^{3+} ion from the excitation level 5D_4 to 7F_j ($j = 0, 1, \dots, 6$). The most intense emission comes from the transition $^5D_4 - ^7F_5$ at approximately 545nm. The emission of the $BaMgAl_{10}O_{17}:Eu$ form one broad band between 410nm and 550nm with the maximum at 450nm. This radiation corresponds to the deexcitation of the Eu^{2+} ion from level 5d to level 4f [6], [7].

3. Conclusions

The new experimental setup for optical emission spectroscopy of the powders excited by the electron impact was tested with the common and industrially often used phosphors emitting in the visible spectral region. The spectra of yttrium oxide doped by europium, cerium magnesium aluminate doped by terbium and barium magnesium aluminate doped by europium were measured and matched to the corresponding transitions of the activator dopants.

4. Acknowledgments

This research was supported by the Sciex project 13.057, Slovak grant agency APVV-0733-11 and This work was conducted within the framework of the COST Action CM1301 (CELINA).

5. References

- [1] Yen W M, Shionoya S, Yamamoto H 2006 *Phosphors Handbook Second Edition* CRC Press Boca Raton, ISBN 0-8493-3564-7.
- [2] Chang N C and Gruber J B 1964 *J. Chem. Phys.* **41** 3227.
- [3] Srivastava A M and Ronda C R 2003 *The Electrochemical Society Interface* **12** 48.
- [4] Podhorodecki A, Nyk M, Misiewicz J and Strek W 2007 *Journal of Luminescence* **126** 219.
- [5] Nagpal J S, Godbole S V, Varadharajan G and Page A G 1998 *Radiation Protection Dosimetry* **80** 417.
- [6] Zhang S, Kono T, Ito A, Yasaka T and Uchiike H 2004 *Journal of Luminescence* **106** 39.
- [7] Yadav R S, Pandey S K and Pandey A C *Materials Sciences and Applications* **1** 25.

A COMPLEX STUDY OF ELECTRON IMPACT IONISATION AND DISSOCIATION OF METHYL-, DIMETHYL- AND TRIMETHYLPHENYLSILANE

Michal Lacko¹, Peter Papp¹, Amer Al Mahmoud Alsheikh², Jan Žídek³,
František Krčma², Štefan Matejčík¹,

¹ Department of Experimental Physics, Faculty of Mathematics, Physics and Informatics, Comenius University, Mlynská dolina F2, 84248 Bratislava, Slovakia

² Institute of Physical and Applied Chemistry, Faculty of Chemistry, Brno University of Technology, Purkyňova 464/118, 612 00 Brno, Czech Republic

³ Central European Institute of Technology "CEITEC", Brno University of Technology, Purkyňova 464/118, 612 00 Brno, Czech Republic

E-mail: m.lacko@fmph.uniba.sk

Electron impact ionization (EII) of methylphenylsilane (MPS), dimethylphenylsilane (DMPS) and trimethylphenylsilane (TMPS) was investigated using the crossed electron/molecular beam technique. For the fragmentation products from MPS and TMPS measured in this work the ionization energies and appearance energies were estimated and compared to the previous results of DMPS molecule with respect to the effect of methyl and hydrogen ligands substitutions.

1. Introduction

The fragmentation patterns are important in description of electron – molecular interactions in the gas phase for chemical reactions in plasma applications, as well as for development of new precursors. Organo - silicon molecules are in present time used in microelectronics [1] and food industry [2]. Plasma Enhanced Chemical Vapour Deposition (PECVD) application [3,4] is used with many new as precursors for preparation of thin films. For future applications these molecules could be used also in nanotechnological application such as Focused Electron Beam Induced Deposition (FEBID). Fragmentation of organosilicones by electron impact is the critical point with respect to plasma based CVD techniques. The presented study deals for the investigation of the role of organic content in organosilicones (see Fig. 1) that differ by number of CH₃ functional groups in their structure. Methylphenyl silane (MPS) and Trimethylphenyl silane (TMPS) molecules were studied and compared with the previously published results for Dimethylphenylsilane (DMPS) [5] obtained with the same apparatus in the past. In general the molecular ions are not too stable under electron impact and they rapidly form various fragments, see Fig. 2 for MPS and Fig. 3 for TMPS. The process after the ionization depends on the energy profile of bond dissociation. We describe the mechanism, where the bond dissociation, is preceded by electron impact ionization while radical-ion appears.

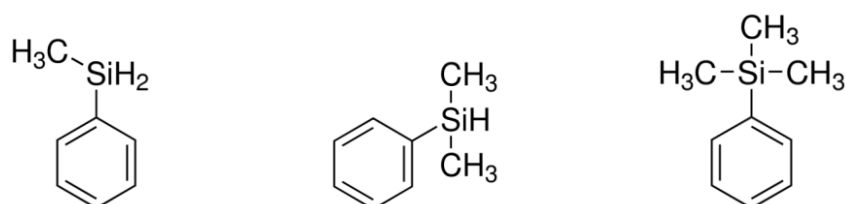


Fig. 1. Schematic structures [6] of: left - methylphenylsilane (MPS), middle - dimethylphenylsilane (DMPS) and right - trimethylphenylsilane (TMPS).

2. Experiment

The experimental study of the electron induced processes on MPS and TMPS was performed using crossed electron and molecular beam apparatus, located at Department of Experimental Physics of Comenius University in Bratislava [7]. The molecular beam is created by effusion of the vapours of the liquid MPS/TMPS sample via a small capillary into the reaction region. There it collides with the electron beam, which has perpendicular orientation to the molecular beam. The electron beam is formed using a trochoidal electron monochromator, with the resolution of electron energy used in this

study of around 300 meV. The calibration of the electron energy scale was made for EI using Ar⁺/Ar reaction with threshold at 15.76 eV [8]. A weak electric field extracts the produced ions from the reaction region into the ion optics of the quadrupole mass analyzer. The mass separated ions (according to m/z) are detected with the electron multiplier. Two different modes of operation of the experiment were applied, the first one, the mass spectrum was recorded at constant electron energy ~ 70 eV. In the second mode, we have measured the ion efficiency curves for particular ions (for given m/z) as function of the incident electron energy. The experimental thresholds for EI and DI processes have been evaluated, which is an important information about the energetics of reaction. The thresholds were evaluated using a fitting procedure based on generalized Wannier law [9] with the following function:

$$S(\varepsilon) = b; \varepsilon < AE; \quad S(\varepsilon) = b + a(\varepsilon - AE)^d; \varepsilon > AE$$

where ε represents electron energy and b, a, d are variable fitting parameters.

3. Results and Discussion

The ionization energies (IE) of MPS and TMPS were experimentally measured and estimated as 9.33 ± 0.25 eV and 8.97 ± 0.25 eV respectively. For MPS molecule we did not find any data in the literature but for TMPS we have two benchmark values; 8.81 ± 0.15 eV [10] and 9.05 ± 0.03 eV [11]. There are some previously published values of EI for DMPS molecule; 9.04 ± 0.06 eV [5], 8.92 ± 0.15 eV [10] and 8.72 ± 0.20 eV [12]. From all these data a minimal decrease of IE is observed with increasing number of methyl ligands in this group of molecules. However, according to the known data the IE of phenyl silane (PS) (9.09 eV [13]; 9.25 eV [14]; 9.1 eV [15]) does not fit in this tendency.

We have evaluated the appearance energies (AE) of measured ions for both molecules; these are summarized in table 1. The mass spectrum of MPS (fig. 2) shows typical patterns with dissociation of H and 2H atoms (or H₂) from MPS⁺, represented by two peaks at $m/z = 121$ and $m/z = 120$. Moreover, the formation of (MPS - H)⁺ ion is more efficient than that of the parent ion. The TMPS molecule does not show dehydrogenation reaction, we were not able to detect (TMPS - H)⁺ or (TMPS - 2H)⁺. The bond dissociation energies of Si - H in MPS⁺ can be calculated as $AE(\text{MPS}^+ - \text{H}) - AE(\text{MPS}^+) = 1.23$ eV, similarly 1.32 eV for the dissociation of two H atom from MPS⁺. These data are supported with our B3LYP/6-311++G(d,p) calculations where the first H atom loss appears with 1.49 eV bond dissociation energy, however the second H atom dissociation appears at 2.47 eV.

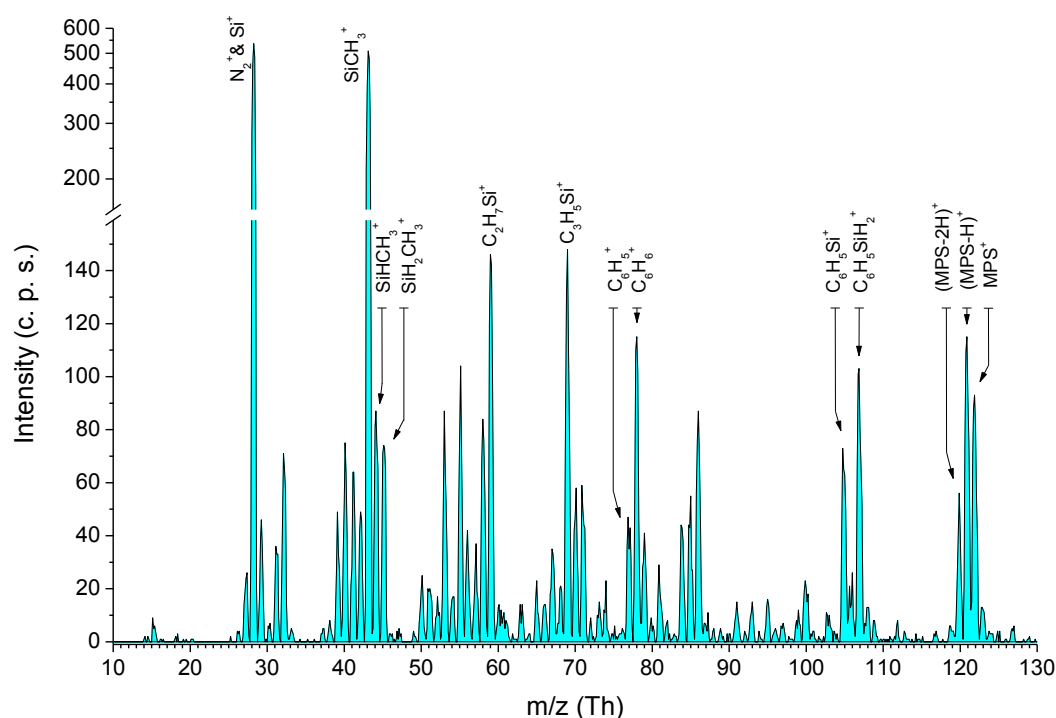


Fig. 2. Mass spectrum of methylphenylsilane (MPS) recorded at incident electron energy of ~ 70 eV, chemical formulas of fragments are listed above some of the peaks.

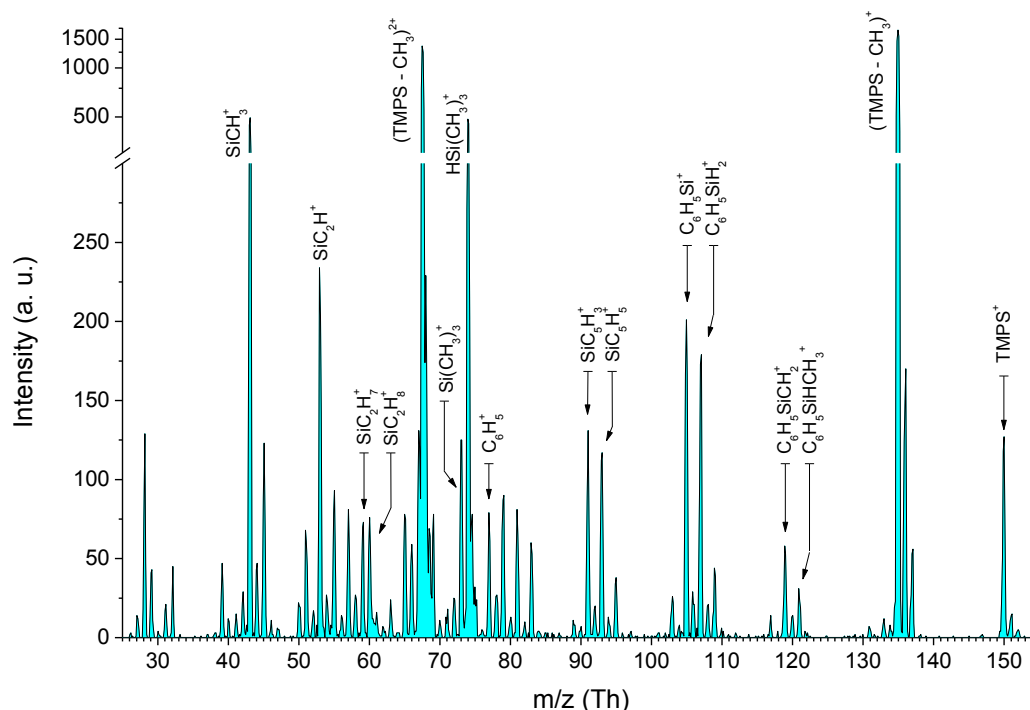


Fig. 3. Mass spectrum of dimethylphenylsilane (DMPS) recorded at incident electron energy of ~ 70 eV, chemical formulas of fragments are listed above some of the peaks.

In DMPS molecule only the $BDE(\text{DMPS}^+ - \text{H})$ of 1.38 eV [5] was determined, with a good agreement with our theoretical result 1.30 eV. These values are significantly lower than the Si – H BDE calculated for similar molecules but without the phenyl ligand ($\text{H}_3\text{Si-H}$, $\text{MeSiH}_2\text{-H}$, $\text{Me}_2\text{SiH-H}$, $\text{Me}_3\text{Si-H}$, BDE are around 3.8 eV) [16]. The CH_3 dissociation energy from MPS/DMPS/TMPS is decreasing with the number of methyl ligands on the molecule ($BDE(\text{MPS} - \text{CH}_3) = 2.01$ eV; $BDE(\text{DMPS} - \text{CH}_3) = 1.47$ eV [5]; $BDE(\text{TMPS} - \text{CH}_3) = 0.79$ eV). $(\text{TMPS}-\text{CH}_3)^+$ is the most intensive ion in its mass spectrum at m/z 135, see fig. 3. The same theory has been applied to compare the experimentally obtained BDEs, for the methyl loss from MPS^+ we have got 1.60 eV, from DMPS^+ 1.33 eV and from TMPS^+ 1.08 eV. In the mass spectrum of MPS molecule the demethylation is followed by the loss of both $2\text{H}/\text{H}_2$ from Si.

Table 2. The ionization energies for MPS, DMPS, and TMPS determined from experiment compared with the theoretical values from B3LYP/6-311++G(d,p) method.

m/z	ion	AE (eV)	m/z	ion	AE (eV)
122	MPS^+	9.33 ± 0.25	150	TMPS^+	8.97 ± 0.25
121	$(\text{MPS}-\text{H})^+$	10.56 ± 0.25	135	$(\text{TMPS}-\text{CH}_3)^+$	9.76 ± 0.25
120	$(\text{MPS}-2\text{H})^+$	10.65 ± 0.25	121	$\text{C}_6\text{H}_5\text{SiHCH}_3^+$	14 ± 1
107	$(\text{MPS}-\text{CH}_3)^+$	11.34 ± 0.25	119	$\text{C}_6\text{H}_5\text{SiCH}_2^+$	15.94 ± 0.5
105	$\text{C}_6\text{H}_5\text{Si}^+$	12.27 ± 0.50	107	$\text{C}_6\text{H}_5\text{SiH}_2^+$	14.54 ± 0.25
78	C_6H_6^+	9.46 ± 0.25	105	$\text{C}_6\text{H}_5\text{Si}^+$	16.93 ± 0.5
69	SiC_3H_5^+	18 ± 0.50	93	SiC_5H_5^+	17.27 ± 0.5
59	SiC_2H_7^+	11.31 ± 0.50	91	SiC_5H_3^+	15.44 ± 0.5
45	$\text{SiH}_2\text{CH}_3^+$	11.76 ± 0.50	77	C_6H_5^+	12.5 ± 0.5
44	SiHCH_3^+	11.28 ± 0.25	74	$\text{HSi}(\text{CH}_3)_3^+$	10.69 ± 0.5
43	SiCH_3^+	11.7 ± 0.50	73	$\text{Si}(\text{CH}_3)_3^+$	11.29 ± 0.5
			59	SiC_2H_7^+	11.13 ± 0.5
			53	SiC_2H^+	20.09 ± 1
			43	SiCH_3^+	11.5 ± 0.5

Similar products were observed for DMPS molecule, the reported ions are $(\text{DMPS} - 2\text{CH}_3)^+$ and $(\text{DMPS} - \text{H} - 2\text{CH}_3)^+$. TMPS molecule, however, has no intensive dissociation channel resulting into $(\text{TMPS} - 2\text{CH}_3)^+$ ion. Here, the dissociation channel result into creation $\text{C}_6\text{H}_5\text{SiHCH}_3^+$ and $\text{C}_6\text{H}_5\text{SiCH}_2^+$ and $\text{C}_6\text{H}_5\text{SiH}_2^+$ molecules. Finally, the dissociation of all three methyl groups from TMPS ion can be detected. From AE of this ion the bond energy of methyl group can be estimated as 2.65 eV.

On the other side the dissociation of phenyl group from MPS/DMPS/TMPS is dependent of hydrogenation of the central silicon atom. In the case of MPS/DMPS, the dissociation results in creation of $(\text{MPS/DMPS} - \text{C}_6\text{H}_5)^+$, $(\text{MPS/DMPS} - \text{C}_6\text{H}_6)^+$ and in parallel to creation of a C_6H_6^+ ion. Formation of $(\text{MPS/DMPS} - \text{C}_6\text{H}_6)^+$ ion is in both cases more effective and energetically more efficient than of $(\text{MPS/DMPS} - \text{C}_6\text{H}_5)^+$ ion. Only for MPS the C_6H_5^+ ion can be also visible. The loss of phenyl can be also visible in TMPS molecule. However, the dissociation of C_6H_6 was not recorded probably due to a missing hydrogen – silicon bond. Also the inversion process results in formation of C_6H_5^+ ion exclusively. Moreover, fragmentation of TMPS^+ results in intensive ions like $\text{HSi}(\text{CH}_3)_3^+$ (instead of the expected dissociation of phenyl and one methyl group), as well as SiC_2H_7^+ and SiC_2H_8^+ . Finally, the intensive ion of SiCH_3^+ was detected for all molecules.

The pure silicon ion was uniquely detected only for MPS molecule. However, the AE of this ion wasn't evaluated due to the presence of atmospheric nitrogen at the same mass with $\text{IE}(\text{N}_2) = 15.58 \text{ eV}$ [8] being lower than the threshold of Si^+ at the same mass.

4. Conclusions

The ionization energies and the appearance energies of some products of MPS and TMPS molecules were estimated. The DI of MPS molecule is mainly resulting in formation of SiCH_3^+ ion. The DI of TMPS molecule has intensive channels for $(\text{TMPS}-\text{CH}_3)^+$, $(\text{TMPS}-\text{CH}_3)_2^+$, $\text{HSi}(\text{CH}_3)_3^+$ and SiCH_3^+ ions. We have shown that dissociation of single CH_3 ligand from all three target molecules is less favourable for MPS molecule, probably due to a lower spatial repulsion between the ligands. The increase of CH_3 ligands on the Si atom causes the decrease of the Si- CH_3 BDE. Contrary, to this the loss of hydrogen atom is visible only for MPS and DMPS with comparable energetical demand.

5. Acknowledgments

Financing of this work was by the Slovak Grant Agency VEGA-1/0514/12, Slovak Research and Development Agency, project Nr. APVV-0733-11. This work was conducted within the framework of the COST Action CM1301 (CELINA). This work was supported by the project No. LO1211 "Materials Research Centre at FCH BUT- Sustainability and Development" supported by the National Programme for Sustainability I of Ministry of Education, Youth and Sports (MEYS).

6. References

- [1] C.H. Lin, H.L. Chen, L.A. Wang, *Microelectron. Eng.* 57-58 (2001) 555–561.
- [2] R. Morent, N.D. Geyter, et al, Payen, *Prog. Org. Coat.* 64 (2009) 304–310.
- [3] Kuritka I. Broza P et al, 2007 *Plasma Process. Polym.* 4 53-61.
- [4] Schauer F. Kuritka I et al, 2002 *Phys E* 14 272.
- [5] Kočíšek J. Stružinský O et al, 2012 *Plasma Proses. Polym.* 9 298-303.
- [6] Pictures taken from: <http://www.sigmaaldrich.com>
- [7] Stano M. Matejíček Š et al, 2003 *J. Phys. B: At. Mol. Opt. Phys.* 36 261.
- [8] Lias S G Ion energetic data. in: NIST Chemistry WebBook. NIST Standard Reference Database Number 69. <http://webbook.nist.gov/chemistry/> [cited 2014 June].
- [9] Wanier G H 1953 *Phys. Rev.* 90 817.
- [10] J.M. Gaidis, P.R. Briggs, T.W. Shannon, *J. Phys. Chem.* 75 (1971) 974–980.
- [11] T. Veszprémi, Y. Harada, K. Ohno, H. J. Mutoh, *J. Organomet. Chem.* 266 (1984) 9–16.
- [12] G. Dube, V. Chvalovský, *Collect. Czech. Chem. Commun.* 39 (1974) 2621–2629.
- [13] McLean R A N 1973 *Can. J. Chem.* 51 2089.
- [14] Pitt C G 1973 *J. Organomet. Chem.* 61 49.
- [15] Fujii T. Ishii H and Tokiwa H 1990 *J. Organomet. Chem.* 391 147-153.
- [16] Walsh R 1981 *Acc. Chem. Res.* 14 246-252.

ELECTRON IMPACT DISSOCIATIVE IONIZATION OF TETRAETHYL ORTHOSILICATE

Jelena Maljković¹, Peter Papp², Michal Lacko², Michal Stano², Aleksandar Milosavljević¹, Štefan Matejčík²

¹Laboratory for Atomic Collision Processes, Institute of Physics, University of Belgrade, Pregrevica 118, 11080 Belgrade, Serbia

²Department of Experimental Physics, Faculty of Mathematics, Physics and Informatics, Comenius University, Mlynská dolina, 84248 Bratislava, Slovakia
E-mail: jelenam@ipb.ac.rs

The dissociative electron ionization of tetraethyl orthosilicate (TEOS) molecule was studied; mass scans and appearance energy measurement at the threshold region were done. TEOS molecule is widely used with PECVD technique; its potential use is possible also as a target precursor considered for FEBID technique. The dissociation of one and three methyls, one and three ethyls, one and all ligands was observed.

1. Introduction

We have investigated the dissociative ionization of tetraethyl orthosilicate ($\text{Si}(\text{OC}_2\text{H}_5)_4$), TEOS, in the gas phase, by electron impact. This molecule is interesting as a potential precursor molecule for Focused Electron Beam Induced Deposition (FEBID) technique. In the past TEOS was already used by Bulla and Morimoto [1] for deposition of thick silicon oxide layers by Plasma Enhanced Chemical Vapour Deposition (PECVD), for integrated optical waveguide applications. TEOS has been used for microelectronic applications, silicon dioxide film (SiO_2) have been grown by PECVD method using liquid TEOS as Si source [2,3]. Zhang et al [4] have investigated residual stress measurements and fracture analysis in thick TEOS and silane-based PECVD oxide films.

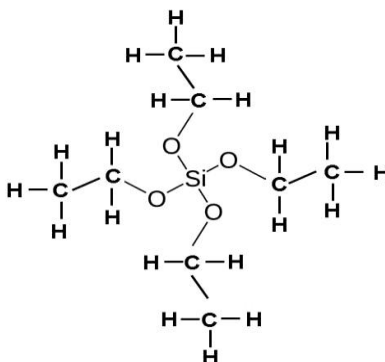


Fig. 1. Tetraethyl orthosilicate (TEOS) molecule.

2. Experimental setup

Measurements were performed with the crossed beams apparatus (CBA) [5,6] operated at the Comenius University in Bratislava. A trochoidal electron monochromator (TEM) and quadrupole mass analyzer (QMA) are used to generate the electron beam and detect the ionic products respectively. For the present experiment the TEM was operated with energy resolution ~ 250 meV and electron current up to $1\mu\text{A}$ at the Faraday cup placed after the reaction region. The molecular beam is obtained by effusion from a capillary installed close to the reaction region perpendicularly to the electron beam. Positive ions formed with electron molecular interactions are extracted by a small electric field and recorded mass spectrometrically by QMA. After being selected according to their mass charge m/z ratio by quadrupole, ions are detected by a multiplier. Two different modes of operation of the experiment were applied, the first one, the mass spectrum was recorded at constant electron energy ~ 70 eV. In the second mode, we have measured the ion efficiency curves for particular ions (for given m/z) as function of the incident electron energy. The experimental thresholds for EI and DI processes

have been evaluated, which is important information about the energetics of reaction. The thresholds were evaluated using a fitting procedure based on generalized Wannier law [7] with the following function:

$$S(\varepsilon) = b; \varepsilon < AE; \quad S(\varepsilon) = b + a(\varepsilon - AE)^d; \varepsilon > AE$$

where ε represents electron energy and b, a, d are variable fitting parameters.

3. Results

In the literature there is only one value for the ionization energy of TEOS molecule from photoelectron spectroscopy. The reported value measured by Green et al. [8] represents the vertical ionization, 9.77 eV. Our electron ionization value is close to 10.02 eV and could be also represented as a vertical ionization process. Beside the parent M^+ at m/z 208 many other positive ions are recorded in mass spectrum which is in good agreement with spectra that NIST proposed [9]. Fig. 2 demonstrates our measurements of mass spectra for different settings of the ion optics, optimized for the best signal for m/z 30, 80 and 120. In all spectra the region between m/z 60 and 100 is very intensive and populated with many fragments. As the mass of the OCH_2CH_3 ligand is 45 amu, it is obvious that the composition of ions in between m/z 60 and 100 is SiO_2^+ , SiO_3^+ , SiO_4^+ , and their hydrogenated alternatives.

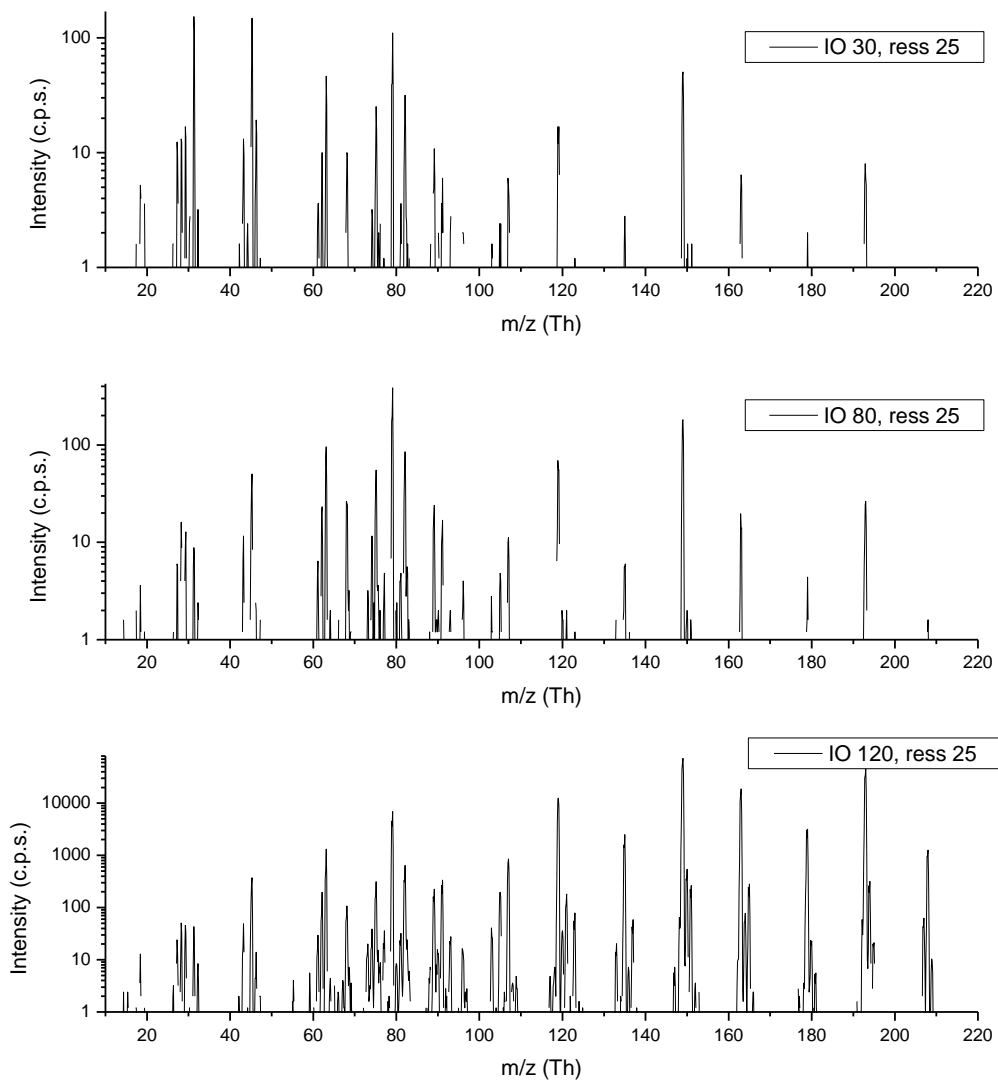


Fig. 2. Mass spectra of TEOS obtained for different ion optics settings with respect to optimized signal for m/z 30, 80 and 120.

There are four identical ligands which can be further fragmented either to one methyl or one ethyl group. We have noticed several possible ways of fragmentation of TEOS molecule via dissociation of ligand(s). First is a loss of a methyl group CH_3 (one or more), which is more prominent at m/z 193 than the TEOS^+ at m/z 208. On the other hand dissociation of more than one methyls from TEOS could be identified only at m/z 163, this could be either the loss of three methyls or one ligand from TEOS. Unfortunately the isotopic peaks around m/z 163 are not enough intensive to say that these ion is produced from one of the two proposed ways. The same can be seen for the loss of ethyl group CH_2CH_3 (one or more), this process was detected only at m/z 179 and 121, for the loss of one and three ethyls respectively. The competitive fragmentations are also not negligible, where a CH_3^+ was detected at m/z 15 and CH_2CH_3^+ at m/z 29. Contrary to these two similar processes, the multiple ligand loss from TEOS is characterised only by one OCH_2CH_3 or all four, at m/z 163 and 28 respectively. However the ion m/z 28 can be Si^+ (IE=8.15 eV [9]), N_2^+ (IE=15.58 eV [9]), C_2H_2^+ (IE=11.40 eV [9]), CO^+ (IE=14.01 eV [9]); the measured threshold around 10.88 eV is low enough to make a conclusion that this peak consists from Si^+ . Alternative fragmentation paths were detected at m/z 149, 119, 105 and 90. The dissociation of two methyls and one ethyl at m/z 149 is a very dominant reaction at this mass range. Other mentioned ions are associated with a ligand loss also, m/z 119 is produced by dissociation of one methyl, one ethyl and one ligand, m/z 105 by two ethyls and one ligand, m/z 90 by one methyl, two ethyls and one ligands.

4. Conclusion

The purpose of the present experimental investigation was to determine a fragmentation pattern of FEBID precursor tetraethyl orthosilicate. TEOS molecule was taken because according to our knowledge there is no results on gas phase electron interaction with this molecule. We have proposed several fragmentation ways including not only the Si-O bond break for ligand loss(es) but also the dissociation of ligand(s) via loss of one or more methyls, ethyls.

5. Acknowledgments

Financing of this work was by the Slovak Grant Agency VEGA-1/0514/12, Slovak Research and Development Agency, project Nr. APVV-0733-11, Ministry of Education and Science of Republic of Serbia (Project No. 171020). This work was conducted within the framework of the COST Action CM1301 (CELINA).

6. References

- [1] Bulla D A P and Morimoto N I 1998 *Thin Solid Films* **334** 60.
- [2] Mahajan A M, Patil L S, Bange J P, Gautam D K 2005 *Vacuum* **79** 194.
- [3] Mahajan A M, Patil L S, Bange J P, Gautam D K 2004 *Surface and Coatings Technology* **193** 295.
- [4] Zhang X, Chen K S, Ghodssi R, Ayón A A, Spearing S M 2001 *Sensors and Actuators* **91** 373.
- [5] Stano M, Matejčík S, Skalný J D, Märk T D 2003, *Jour. of Phys. B: Atomic, Molecular and Optical Physics*, **36** 261.
- [6] Ingólfsson O, Weik F and Illenberger E 1996, *Int. Jour. Mass. Spec.* **155** 1
- [7] Wanier G H 1953, *Phys. Rev.* **90** 817
- [8] Green M C, Lappert M F, Pedley J B, Schmidt W, Wilkins B T 1971, *J. Organomet. Chem.* **31** 55
- [9] taken from NIST Mass Spec Data Center, S. E. Stein, <http://webbook.nist.gov>

DIFFERENCES BETWEEN FLUORESCENCE SPECTRA OF VARIOUS HYDROCARBONS WITH EMPHASIS ON NITROMETHANE

Anita Ribar, Marián Danko, Juraj Országh and Štefan Matejčík

Faculty of Mathematics, Physics and Informatics, Comenius University Bratislava, Slovakia

E-mail: anita.ribar@fmph.uniba.sk

Relative intensities of measured fluorescence spectra of methane, acetylene, acetone and nitromethane in the spectral range between 300 – 490 nm have been compared in this paper. The spectra of the molecules were dominated by CH bands and hydrogen Balmer lines. Additionally CN bands in nitromethane spectrum, and strong indications for OH bands in nitromethane and acetone spectra were observed. Photon efficiency curves (PECs) were measured for CH ($B^2\Sigma^- \rightarrow X^2\Pi$) (0, 0) in methane and acetylene, CN ($B^2\Sigma^+ \rightarrow A^2\Pi$) (0, 0) in nitromethane and H β Balmer line in all three molecules.

1. Introduction

Methane, acetylene, acetone and nitromethane (Fig.1 and Fig.2) are simple hydrocarbons present in various media. A common feature of being exposed to low energy electrons in general makes them objects of interest for investigation of fluorescence induced by electrons.

Methane, CH₄, is the simplest hydrocarbon molecule, and its presence ranges from atmospheres of Solar system's planets and satellites [1], to plasmas in industrial technologies [2], it is used in energetics for the production of hydrogen [3], in CVD (chemical vapour deposition) for the growth of diamonds [4], and even in diagnostic of erosion of tokamak divertors [5].

Acetylene, C₂H₂, similarly as methane, can be found in atmospheres of planets, interstellar medium and on comets [6], it is used in diamond growth [4], diagnostics of divertors erosion [5], but its structural difference in respect to methane molecule, the π bond, makes it suitable for the examination of conjugated polymers containing great number of these bonds and are being used for example in semiconductor industry [7].

Acetone, (CH₃)₂CO, is the simplest ketone. It is a volatile organic compound widely used in different fields of chemistry and technology, typically as solvent, a starting material in synthesis of many other compounds building for example artificial fibers, explosives, etc. Acetone has an important feature which is dissolving acetylene, so the acetylene can be stored and transported without a risk of explosion. Nitromethane, CH₃NO₂, is the simplest nitro-compound and is widely used in industry as a solvent, degreaser and has characteristics typical for commonly used explosives and propellants [8]. It can also act as a human carcinogenic agent [9]. Further motivation for the research on nitromethane's interaction with low energy electrons is due to its abundance in the Earth's atmosphere, where it may influence local chemistry [10].

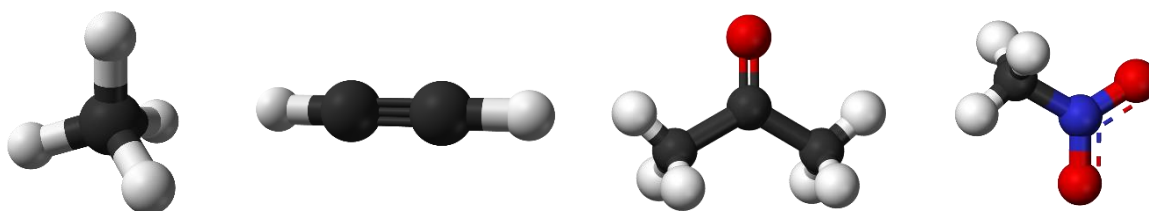


Figure 1. Ball models of methane, acetylene, acetone and nitromethane molecules (from left to right). Carbon – black, hydrogen – white, oxygen – red and nitrogen – blue. [11]

2. Experimental results and discussion

Emission spectra of methane, acetylene, acetone and nitromethane in the region 300 – 490 nm (Fig.2 and Fig.3) were obtained at 50 eV electron impact energy using Electron Induced Fluorescence

Apparatus (EIFA) [12] operating with optical resolution of ~ 0.8 nm. EIFA is a cross electron – molecular beam apparatus, operating at high vacuum (10^{-5} mbar) and low electron current (10^{-7} A). An effusive capillary producing the molecular beam and trochoidal electron monochromator or electron gun as the source of electrons are used for the single collision experiment. After the electron/molecule interaction, radiation from the reaction is observed through the optical system consisting of two MgF₂ windows, Czerny – Turner optical monochromator and photomultiplier with high quantum efficiency. With EIFA we can observe spectra of molecules by setting the electron impact energy and varying the observed wavelength (Fig.2 and Fig.3), or varying the electron impact energy at one wavelength so the excitation functions are being recorded (Fig.4 and Fig.5).

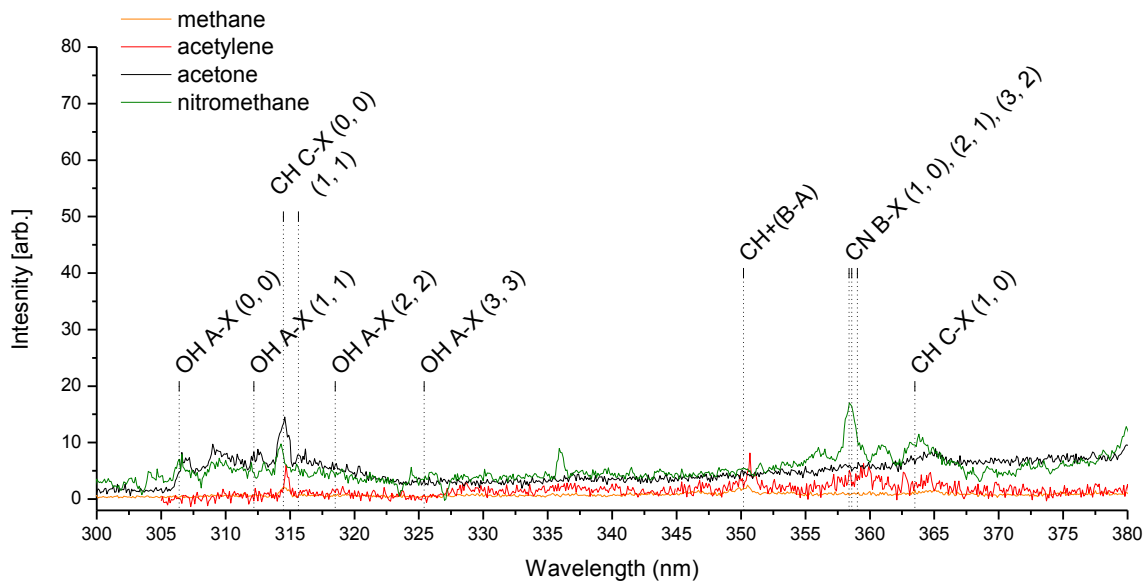


Figure 2. Emission spectra of methane (orange), acetylene (red), acetone (black) and nitromethane (green) molecules obtained at 50 eV electron impact energy spectral resolution of 0.8 nm (first part).

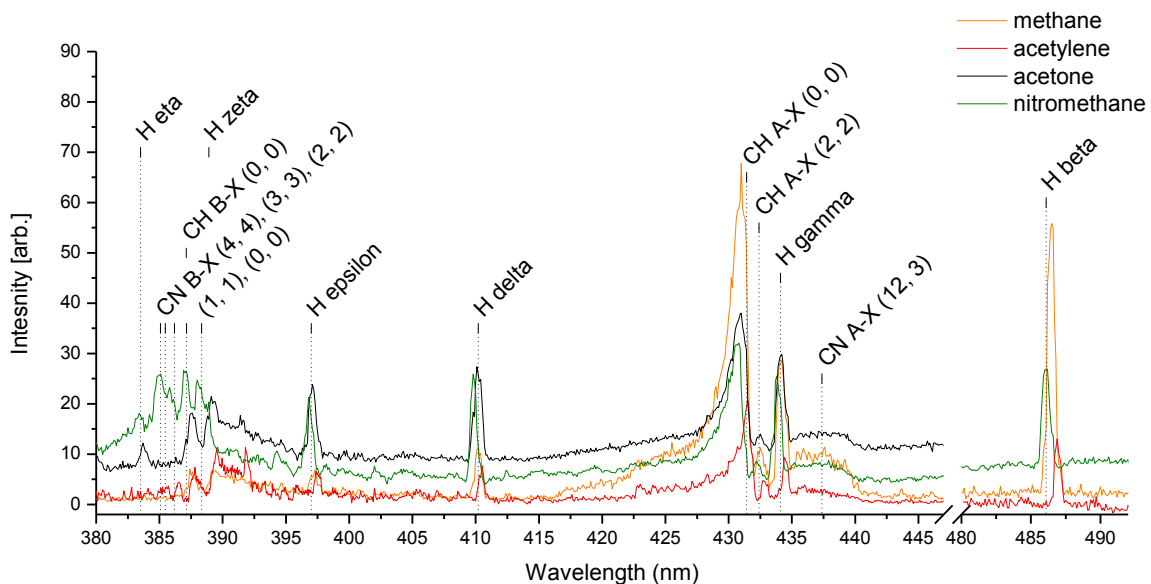


Figure 3. Emission spectra of methane (orange), acetylene (red), acetone (black) and nitromethane (green) molecules obtained at 50 eV electron impact energy spectral resolution of 0.8 nm (second part).

In the past we have published a detailed study of methane [13], acetylene molecule has been examined to large extent, and for acetone and nitromethane introductory measurements have been obtained. All

four molecules are hydrocarbons, so the mutual CH and H Balmer lines in region between 300 – 490 nm have been expected. Further, for acetone, which contains an oxygen atom, or rather CO functional group, additional lines and bands are contributing to the emission spectrum. Nevertheless, high intensity band heads originating from CO band heads are not dominant in the spectrum. In nitromethane CN band has strong contribution to the emission spectrum, in opposite to the CO group in acetone. Indications of OH violet band in acetone spectrum is observed, as well as in nitromethane spectrum in region between 306 – 326 nm and is marked on the graph (Fig.2).

Filament radiation has been subtracted from raw data and subsequently multiplied by the apparatus function so the final comparison on Figure 3 and Figure 4 could be done.

Nitromethane molecule has been studied further so the PEC for the band head of the CN violet band CN ($B^2\Sigma \rightarrow A^2\Pi$) (0, 0) at 389 nm has been recorded. It has been compared to the measurements taken at 387.5 nm in methane, and 387.8 nm in acetylene. In last two molecules PEC is ascribed to CH ($B^2\Sigma^- \rightarrow X^2\Pi$) (0, 0) with several thresholds determined by the dissociation route, while in nitromethane we can ascribe the first threshold at about 12 eV to CN violet band head (Tab.1). Low signal to noise ratio prevents us from determining the other thresholds. The electron energy resolution for the nitromethane measurements is 0.5 eV, but due to the low signal to noise ratio the uncertainty of the threshold value exceeds this value.

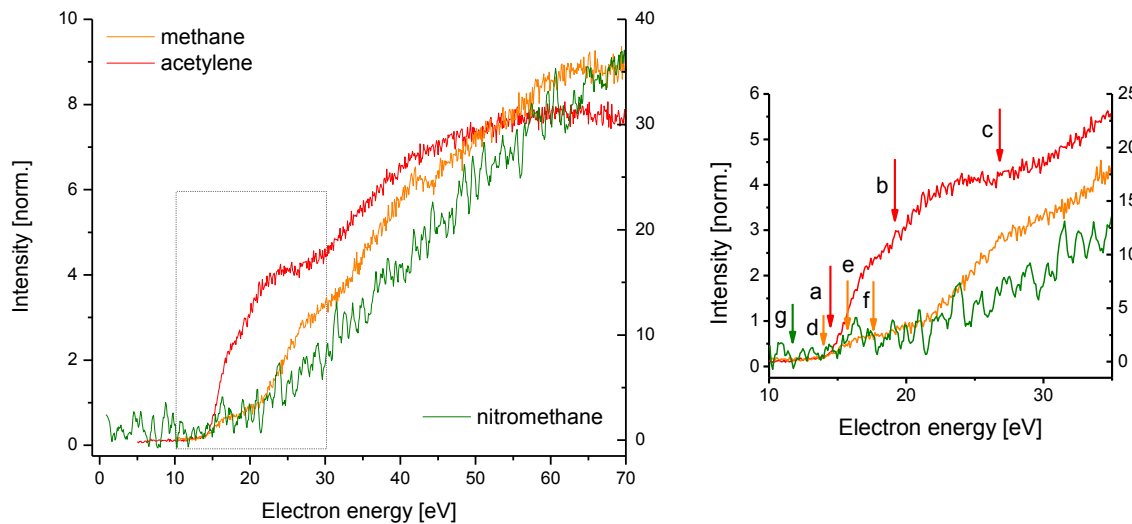


Figure 4. PECs of: 387.5 nm measured in methane (left axis), 387.8 nm in acetylene (left axis), and 389 nm in nitromethane (right axis) with intensities normalized to the 50 eV spectrum peaks (Fig.2). On right closer look on dashed area with thresholds (see Table 1).

Table 1. Threshold energies for the 387.8 nm PECs in acetylene corresponding to CH ($B^2\Sigma^- \rightarrow X^2\Pi$) (0, 0) transition, as well as 387.5 nm in methane and 389 nm in nitromethane corresponding to CN ($B^2\Sigma \rightarrow A^2\Pi$) (0, 0) obtained in the experiment. The present values are compared with values calculated for selected reaction channels from thermochemical data [13] [14] [15]

Molecule	Dissociation route	Calc. threshold	Exp. threshold
Acetylene	$e + C_2H_2 \rightarrow CH(B) + CH + e$	13.34 eV	14.22 eV (a)
	$e + C_2H_2 \rightarrow CH(B) + C + H + e$	16.87 eV	19.20 eV (b)
	$e + C_2H_2 \rightarrow CH(B) + C^+ + H + 2e$	28.13 eV	27.53 eV (c)
Methane	$e + CH_4 \rightarrow CH(B) + H + H_2 + e$	12.33 eV	14.1 eV (d)
	$e + CH_4 \rightarrow CH(B) + 3H + e$	16.91 eV	15.2 eV (e)
	$e + CH_4 \rightarrow CH(B) + 2H + H^+ + e$	30.52 eV	17.9 eV (f)
Nitromethane	$e + CH_3NO_2 \rightarrow CN(B) + H_2 + H + O_2 + e$	10.77 eV	12 eV (g)

At 486.2 nm where the peak of the H β Balmer in nitromethane is observed on the emission spectrum of nitromethane (Fig.3) we obtained the excitation function presented in green compared to the

corresponding measurements in methane (486.4 nm) and acetylene (486.7 nm). Signal to noise ratio in nitromethane is lower than in other two measurements and only one threshold is observed.

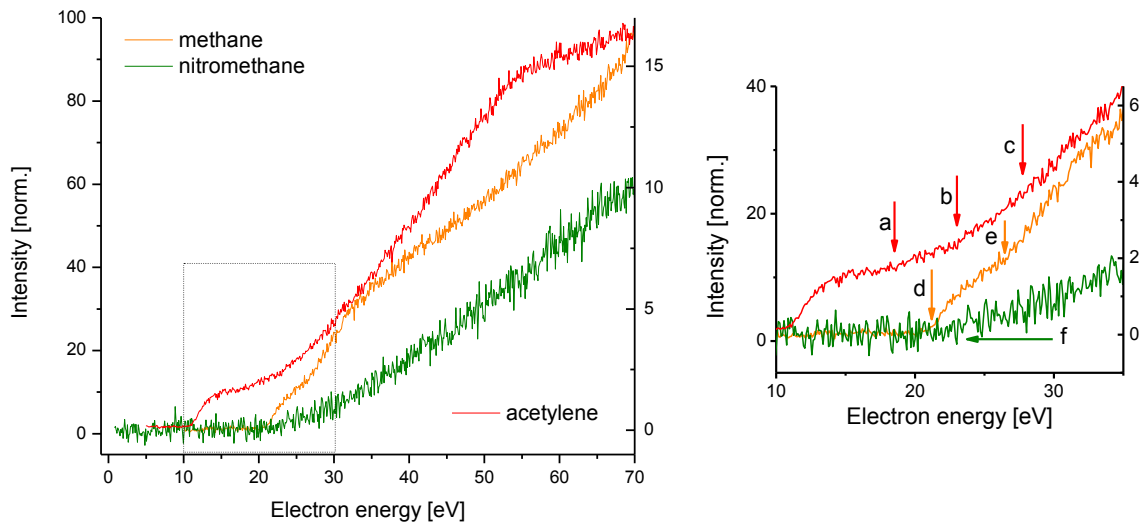


Figure 5. PECs of: 486.4 nm measured in methane (left axis), 486.7 nm in acetylene (right axis), and 486.2 nm in nitromethane (left axis) with intensities normalized to the 50 eV spectrum peaks (Fig.2). On right closer look on dashed area with thresholds (see Table 2).

Table 2. Threshold energies for the 486.7 nm in acetylene, 486.4 nm in methane and 486.2 nm in nitromethane obtained in the experiment corresponding to H β Balmer. The present values are compared with values calculated for selected reaction channels from thermochemical data [13] [14] [15]

Molecule	Dissociation route	Calc. threshold	Exp. threshold
Acetylene	$e + C_2H_2 \rightarrow H(n=4) + C_2H(A) + e$	18.08 eV	18.75 eV(a)
	$e + C_2H_2 \rightarrow H(n=4) + C_2 + H + e$	23.62 eV	23.04 eV(b)
	$e + C_2H_2 \rightarrow H(n=4) + C + CH + e$	26.27 eV	27.88 eV(c)
Methane	$e + CH_4 \rightarrow H(n=4) + CH_3(X) + e$	17.30 eV	21.0 eV (d)
	$e + CH_4 \rightarrow H(n=4) + H + CH_2(X) + e$	22.05 eV	27.10 eV (e)
Nitromethane	$e + CH_3NO_2 \rightarrow H(n=4) + CH_2NO_2 + e$	17.28 eV	23 eV (f)

3. Conclusion

In range between 300 – 490 nm emission spectra of methane, acetylene, acetone and nitromethane show similar structure with dominant CH bands and H Balmer lines. Methane and acetylene, composed only of hydrogen and carbon atoms, have the most similar relative emission spectra. Acetone and nitromethane show the indication of OH violet band, and relative intensities of the CH bands and H Balmer lines are more similar than compared with methane and acetylene. Characteristic CN violet band in nitromethane contributes to the emission spectrum in range between 385 nm – 389 nm. PEC at 389 nm was measured and the gained threshold at 12 eV is in correspondence with the CN ($B^2\Sigma^+ \rightarrow A^2\Pi$) (0, 0) calculated to be 10.77 eV. Comparison between H β Balmer in methane acetylene and nitromethane has been done, showing only one threshold in nitromethane (23 eV) compared with three in acetylene (18.75 eV, 23.04 eV, 27.88 eV) and two in methane (21 eV and 27.1 eV).

4. Acknowledgement

This work was partially supported by the Slovak Research Agency, project Nr. APVV-0733-11 and the grant agency VEGA project Nr. VEGA-1/0514/12. This work was conducted within the framework of the COST Action CM1301 (CELINA).

5. References

- [1] Lutz B L, Owen T and Cess R D 1976 *The Astrophysical Journal* **203** 541.
- [2] Motohashi K, Soshi H, Ukai M and Tsurubuchi S 1996 *Chemical Physics* **213** 369.
- [3] Abbott H L and Harrison I 2008 *Journal of Catalysis* **254** 27.
- [4] Childs M A, Menningen K L, Chevako P, Spellmeyer N W, Anderson L W and Lawler J E 1992 *Physics Letters A* **171** 87.
- [5] Fantz U, Meir S and ASDEX Upgrade Team 2005 *Journal of Nuclear Materials* **337** 1087.
- [6] Boyé S, Campos A, Douin S, Fellows C, Gauyacq D, Shafizadeh N, Halvick P and Boggio-Pasqua M 2002 *Journal of Chemical Physics* **116** 8843.
- [7] Lischka H and Karpfen A 1986 *Chemical Physics* **102** 77.
- [8] Klezenberg S, Eisenreich N, Eckl W and Weiser V 1999 *Propellants, Explosives, Pyrotechnics* **24** 189.
- [9] Takeuchi A, Nishimura Y, Kaifuku Y, Imanak T, Natsumeda S, Ota H, Yamada S, Kurotani I Sumino K and Kanno S 2010 *J. Occup. Health* **52** 194.
- [10] Taylor W D, Allston T D, Moscato M J, Fazekas G B, Kozlowski R and Takacz G A 1980 *Int. J. of Chem. Kin.* **12** 231.
- [11] <https://www.wikipedia.org/>
- [12] Országh J, Danko M, Ribar A and Matejčík Š 2012 *Nuclear Instruments and Methods in Physics Research B* **279** 76.
- [13] Danko M, Orszagh J, Ďurian M, Kočíšek J, Daxner M, Zöttl S, Maljković J B, Fedor J, Scheier P, Denifl S and Matejčík Š 2013 *J. Phys. B: At. Mol. Opt. Phys.* **46** 045203.
- [14] Danko M 2014 *PhD Thesis*
- [15] Melius C F 1995 *Journal de Physique IV* **5** 535.

ROTATIONAL TEMPERATURES IN HYDROGEN AND HYDROGEN-ARGON DC DISCHARGE

Mária Suchoňová¹, Jaroslav Krištof¹, Michal Anguš¹, Pavel Veis¹

¹*Department of Experimental Physics, Comenius University, Mlynska Dolina, 842 48 Bratislava, Slovakia*

E-mail: Pavel.Veis@fmph.uniba.sk

Ro-vibrational emission spectrum of Lyman system was simulated and studied. Rotational temperatures of Fulcher- α system, Lyman system of hydrogen and of the second positive system of nitrogen were compared. Gas temperature was 440K. Influence of heavy collisions on rotational temperature of hydrogen emission systems was considered at pressures 80 and 400 Pa. Changes of emission spectra with amount of argon in the discharge were observed because of resonance reactions with resonant state of argon.

1. Introduction

Discharges in hydrogen have wide applications in chemical vapour deposition growth of graphene [1, 2], diamonds [3], in formation thin layers [4] and many others. For all applications, diagnostics of plasma is very important and gas temperature is one of the most important parameter of plasma. Problem of hydrogen plasma is non-thermalized molecular states at low pressures [5] and difficulties with determination of gas temperatures from hydrogen emission spectra. We have studied emission spectra of Lyman system and Fulcher- α system and the second positive system of nitrogen. Gas temperature was determined from emission spectra of the second positive system and compared with Lyman and Fulcher- α system. Influence Ar on experimental spectra was observed.

2. Experimental set-up

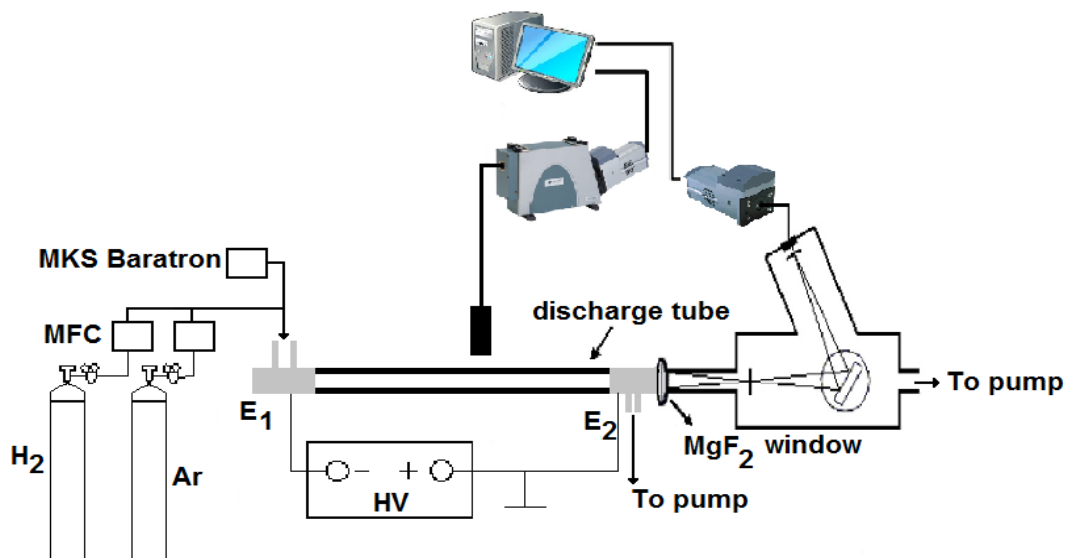


Fig. 1.: Experimental set-up. MFC – mass flow controller, E₁, E₂ – electrodes, MKS Baratron – pressure gauge.

The experimental set-up including the spectroscopic devices is shown in figure 1. The flowing plasma is sustained in a Simax tube (18mm inner diameter, 26 cm length). The discharge is ignited in H₂ and H₂-Ar mixtures (purity grades of 99.9990% and 99.996% for hydrogen and argon,

respectively). The gas is evacuated by an oil rotary pump. The total gas pressure is measured by a capacitive gauge MKS Baratron controlled by a throttle valve. The flow rates are controlled by mass-flow MKS and AERO controllers. The total flow rate is fixed to 22 sccm for gas pressure of 400 Pa and 4.4 sccm for gas pressure of 80 Pa. The distance between the electrodes is 26 cm. Electrodes are made from brass and they are used also as vacuum exchange labels. The discharge pulse is maintained by a DC voltage source providing up to -2 kV, 30 mA (ISEG). We have studied the hydrogen–argon plasma at 10 mA with different percentages of argon ranging from 0 to 90 in the mixture. The optical signal is collected by a quartz optical fibre placed perpendicular to discharge in the middle of tube. The collected signal is recorded with an Andor Mechelle-5000 spectrometer coupled with an Andor iStar intensified camera in the wavelength range 200–950 nm. Resolution of Mechelle spectrometer is $\lambda/\Delta\lambda = 4000$. The integral light emitted from the discharge in the axial direction came through MgF₂ window and the input slit of a VUV spectrometer. The MgF₂ window served for separation of discharge tube and VUV spectrometer (McPherson) with Andor iStar intensified camera. Instrumental function of VUV spectrometer has Gaussian profile with FWHM of 0.18 nm and wavelength range 115–300 nm.

3. Results and discussion

3.1 Rotational temperature of H₂ (d³Π_u⁻)

Rotational temperature of H₂ (d³Π_u⁻) is determined from Boltzmann distribution of rotational transitions of the vibrational (v' - v'' = 2-2, 1-1) of Fulcher-α band of Q-branch. Other branches, P and R are perturbed by higher Σ states [6]. Intensities of 5 rotational lines were fitted by Gaussian profile. Intensity of rotational line can be written as

$$I \sim (2\Gamma_{N'} + 1) S_{a_{N''}}^{d_{N''}} \exp\left(\frac{-E_{v'N'}(N'+1)hc}{kT_{rot}}\right) \quad (1)$$

Rotational constant is $B_v = B_e - \alpha_e\left(v + \frac{1}{2}\right)$ and $B_e = 30.364 \text{ cm}^{-1}$, $\alpha_e = 1.545 \text{ cm}^{-1}$ [7] for H₂ (d³Π_u⁻) state. It is taken in account total nuclear spin due to presence orto- ($\Gamma_{N'} = 1$) and para-states ($\Gamma_{N'} = 0$) of H₂. $\Gamma_{N'} = 1$ for N' even and $\Gamma_{N'} = 0$ for N' odd, respectively. $S_{a_{N''}}^{d_{N''}} = \frac{2N'+1}{2}$ is Hönl-London factor, T_{rot} is rotational temperature of the state.

3.2 Rotational temperature of N₂ (C³Π_u)

Low amount of impurities allows us to determine rotational temperature of N₂ (C³Π_u) state. Rotational temperature is determined by the best fit of synthetic and experimental spectra of the transition N₂ (C³Π_u, v' = 0 → B³Π_g, v'' = 2) and N₂ (C³Π_u, v' = 1 → B³Π_g, v'' = 3) using Specair program [8]. The typical accuracy is ±50 K.

3.3 Simulation of Lyman system of H₂ (B¹Σ_u⁺)

The theoretical construction of the H₂ spectra is based on the conventional description of the diatomic molecules spectra analysis, which can be found e. g. in [7, 9]. For intensity of rotational line can be written:

$$I_{v'j'j''}^{v''j''j''}(\lambda_i) \sim \frac{hc}{\lambda_{v'j'j''}} A_{v'j'j''}^{v''j''j''} \frac{S_{j''}^{j'}(\Gamma_{j''} + 1)}{\sum_{j'} \exp\left(\frac{-F_{v'}(j')hc}{kT_{rot}}\right) \sum_{v''} \exp\left(\exp\left(\frac{-G_{v''}hc}{kT_{vib}}\right)\right)} \times \exp\left(\frac{-F_{v'}(j')hc}{kT_{rot}} - \frac{G_{v''}hc}{kT_{vib}} - \frac{1}{2}\left(\frac{\lambda_i - \lambda_{v'j'j''}}{\sigma}\right)^2\right) \quad (2)$$

Lyman system consists from 2 branches, P ($\Delta J = -1$) and R ($\Delta J = +1$). We did not find this kind of simulation in any papers. But we could find several sets of different equilibrium constants available. To avoid of possible imprecise constants, we tried to use always experimental data for simulation as much as it was possible. Positions of rotational lines were taken from Abril et al. [10]. Wavelength of rotational lines is proportional to difference of energies upper and lower state. By suitable difference of two wavelengths is possible to determine requested energies $F_{v'}(J')$ and $G_{v'}$. $FWHM = \sigma\sqrt{8\ln 2}$ and Höln-London factors were calculated according formula (3)

$$S \sim \frac{A(2J'+1)A^B}{\text{band strength}} \quad (3)$$

Where A is Einstein coefficients and band strengths were taken from [11]. There is comparison of simulation and experimental spectra in fig.2.

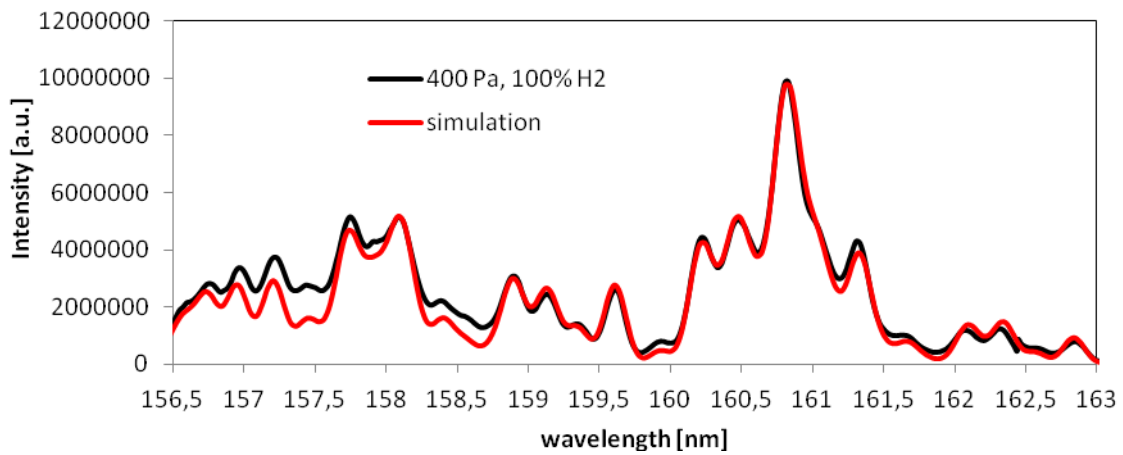


Fig. 2.: Comparison of experimental spectra (black) and simulation (red) of Lyman system.

3.4 Gas temperature

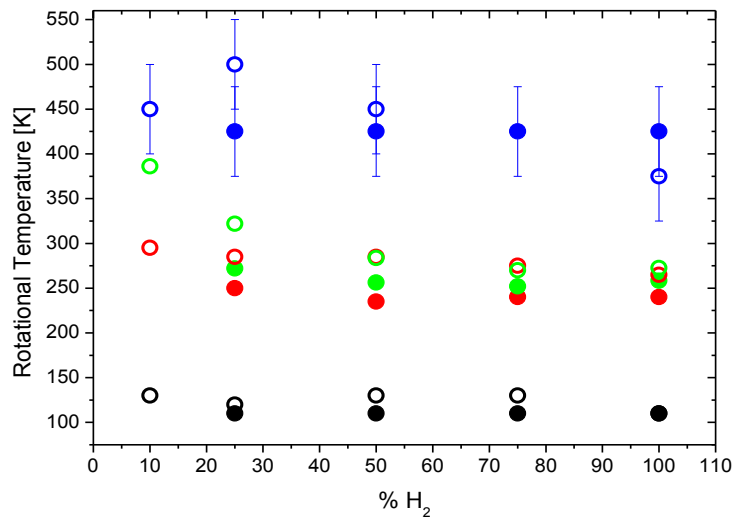


Fig. 3: Rotational temperatures at 80 Pa (full circles) and 400 Pa (empty circles) of $N_2(C^3\Pi_u)$ (blue), $H_2(B^1\Sigma_u^+)$ (black), $H_2(d^3\Pi_u, v'=1)$ (green), $H_2(d^3\Pi_u, v'=2)$ (red).

Rotational temperatures of $N_2(C^3\Pi_u)$ state at 80 Pa and 400 Pa are close to each other. Average value is 440 K for all measured concentration of H_2 . This value is assimilated with gas temperature. Rotational temperatures of $H_2(d^3\Pi_u, v'=1)$ and $H_2(d^3\Pi_u, v'=2)$ are also close to each other and equal to 250 K at 80 Pa and 290 K at 400 Pa and of $H_2(B^1\Sigma_u^+)$ equal to 110 K at 80 Pa and 130 at 400 Pa. Molecular hydrogen states are not thermalized because of short time of life but rotational distribution of $H_2(d^3\Pi_u^-)$ states are very often used for determination of gas temperature if rotational levels are populated mainly by electrons with Maxwell distribution. It is supposed that the rotational distribution of $H_2(d^3\Pi_u^-)$ copies rotational distribution of ground state $H_2(X^1\Sigma_g^+)$. Then it is assumed that rotational distribution of ground state $H_2(X^1\Sigma_g^+)$ is in equilibrium with gas temperature. Difference between both rotational energies ($H_2(X^1\Sigma_g^+)$ and $H_2(d^3\Pi_u^-)$) lies in rotational constant. So

$$T_{rot}(H_2(X^1\Sigma_g^+)) = (B_{vg}/B_v) \times T_{rot}(H_2(d^3\Pi_u^-)) = T_g. \quad (4)$$

Ratio of B_{vg}/B_v depends on vibration level of upper state and it is equal to 2.24 for $H_2(d^3\Pi_u, v'=2)$ state and equal to 2.11 for $H_2(d^3\Pi_u, v'=1)$. If this procedure is used at our conditions we would get 100-200 K higher gas temperature depending on pressure. Real ratio of $T_g/T_{rot}(H_2(d^3\Pi_u^-)) = 1.7$ at 80 Pa and 1.5 at 400 Pa. Ratio 1.7 was measured at 133 Pa by Tomasini et al. [12].

Emission spectrum of Lyman system consists from many overlapping vibrational bands and our resolution of spectrometer is not sufficiently low to resolve them. Technique of ratio of B_{vg}/B_v is probably not possible to use but further research have to be done, we observed ratio $T_g/T_{rot}(H_2(B^1\Sigma_u^+))$ 3.9 (80 Pa) and 3.4 (400 Pa).

Difference can be caused by lower values of rotational constants of upper state of Lyman transitions.

3.5 Relative density of $H_2(B^1\Sigma_u^+, v = 3)$

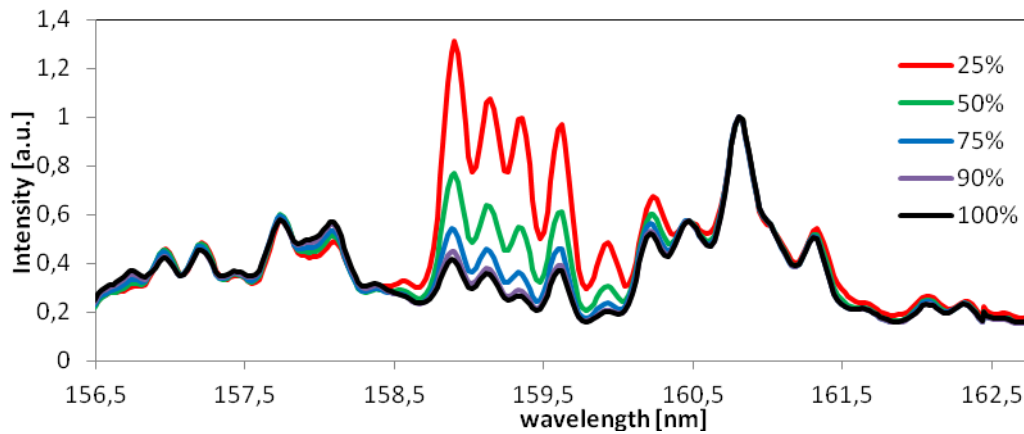


Fig. 4.: Emission spectra of $H_2(B^1\Sigma_u^+)$ in the mixture H_2 -Ar in dependence of concentration of H_2 .

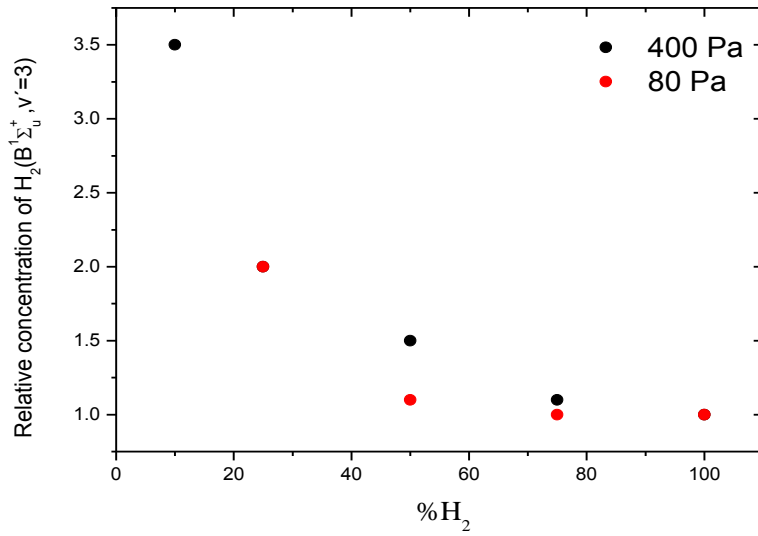
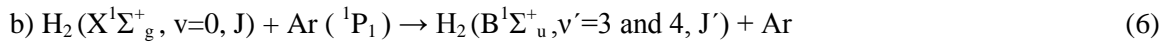
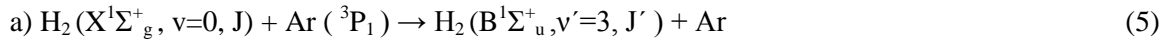


Fig. 5.: Evolution of concentration of $H_2(B^1\Sigma_u^+, v'=3)$ in the mixture H_2 -Ar in dependence of concentration of H_2 .

Argon has no influence on rotational temperature in studied range of Lyman system (156.5 – 163) nm. We observed increasing intensity of transition $H_2(B^1\Sigma_u^+, v'=3 \rightarrow X^1\Sigma_g^+, v=10)$. This behaviour can be explained by resonance reaction of $H_2(B^1\Sigma_u^+, v'=3)$ states with resonant states of argon $Ar(^3P_1, ^1P_1)$ [13]:



Relative density of $H_2(B^1\Sigma_u^+, v'=3)$ (normalized to density in pure hydrogen) is shown in fig. 6. We observed expected increasing of $H_2(B^1\Sigma_u^+, v'=3)$ because of increasing of concentration of resonant Ar states.

4. Conclusion

In this work, ro-vibrational spectrum of Lyman system was observed in hydrogen and hydrogen-argon mixture in continuous DC discharge at pressures 80 Pa and 400 Pa. We compared rotational temperatures of Lyman system, Fulcher- α system and the second positive system of nitrogen from nitrogen impurities. We concluded that rotational temperature of second positive system of nitrogen is equal to gas temperature 440 K at both pressures. States of molecular hydrogen were not thermalized. Standard procedure for determination of gas temperature from molecular hydrogen emission systems showed overestimation of temperature in comparison with gas temperature. This effect was observed in Fulcher- α system. We have not found simulation of Lyman system based on the conventional description of the diatomic molecules spectra analysis before, so further investigation has to be made for more precise conclusions. Increasing of $H_2(B^1\Sigma_u^+, v'=3)$ states with increasing of amount of argon was observed in emission spectra of Lyman system because of resonance reactions with resonant Ar species.

Acknowledgment

The authors thank for financial support from the Scientific Grant Agency of the Slovak Republic (VEGA) under the contracts No. 1/0914/14 and 1/0925/14. This work has been carried out within the

framework of the EURO fusion Consortium and has received funding from the European Union's Horizon 2020 research and innovation programme under grant agreement number 633053. The views and opinions expressed herein do not necessarily reflect those of the European Commission.

5. References

- [1] Vlasiouk I, Regmi M, Fulvio P, Dai S., Datskos P, Eres G, Smirnov S 2011 *ACS Nano* **5**(7) 6069.
- [2] Zhang X, Wang L, Xin J, Yakobson B I, Ding F 2014 *J. Am. Chem. Soc.* **136** (8) 3040.
- [3] Spear K E, Frenklach M 1994 *Pure&Appl. Chem.* **66**(9) 1773.
- [4] Chinthaginjala J K, Lefferts L 2009 *Carbon* **47**(14) 3175.
- [5] Farley D R, Stotler D P, Lundberg D P, Cohen S A 2011 *Journal of quantit. spec. & radiative transfer* **112** 800.
- [6] Kovács I, Lavrov B P, Tyutchev M V, Ustimov V I 1983 *Acta physica Hungarica* 54 161.
- [7] Herzberg G *Molecular spectra and molecular structure I. Spectra of diatomic molecules*. New York: Van Nostrand 1955.
- [8] <http://www.specair-radiation.net/>
- [9] Kovacs I., "Rotational Structure in the Spectra of Diatomic Molecules", Adam Hilger Ltd., London, 1969.
- [10] Abgrall H, Roueff E, Launay F, Roncin J-Y 1994 *Can. J. Phys.* **72** 856.
- [11] Allison A C, Dalgarno A 1970 *Atomic data* **1** 289.
- [12] Tomasini L, Rousseau A, Gousset G, Leprince P 1996 *Journal of Physics D* **29**(4) 1006.
- [13] McKenney D J, Dubinsky N 1997 *Chemical Physics* **26** 141.

KINETICS OF LOW ENERGY ELECTRON ATTACHMENT TO SOME CHLORINATED ALCOHOLS IN THE GAS PHASE

K. Wnorowski, J. Wnorowska, B. Michalczuk, W. Barszczewska

Siedlce University, Faculty of Natural Sciences, Department of Chemistry,

3 Maja 54, 08-110 Siedlce, Poland

E-mail: karol.wnorowski@uph.edu.pl

The results of thermal electron attachment investigations by chloroalcohols: $\text{CH}_2\text{ClCH}_2\text{OH}$, $\text{CH}_2\text{ClCH}_2\text{CH}_2\text{OH}$, $\text{CH}_2\text{ClCHOHCH}_2\text{Cl}$, $\text{CH}_2\text{ClCHClCH}_2\text{OH}$ and $\text{CH}_2\text{ClCHOHCH}_2\text{OH}$ in the gas phase are reported. The fundamental quantities such as rate coefficients (k 's) and activation energies (E_a 's) for the electron capture processes were determined. We have used Pulsed Townsend technique. Measurements were carried out in the temperature range 298K to 378K. The obtained rate coefficients depended on temperature in accordance to Arrhenius equation. From the fit to the experimental data points with function $\ln(k) = \ln(A) - E_a/k_B T$ the activation energies (E_a 's) were determined.

1. Introduction

Ionizing radiation contributes to the formation of many secondary species along its path, including among others large quantities of free electrons with a kinetic energy below 15 eV.

Since electron capture processes often occur at very low energy, they play an important role in pure and applied science, inter alia in plasma chemistry, atmospheric chemistry or in gaseous dielectrics. A detailed knowledge of these processes in isolated molecules is essential for the understanding of more complex reactions such as electron transfer as an elementary step in chemical reactions [1-2] or charge transfer reactions in solution (in electrochemical or biological systems). These studies are of particular interest, since electrons despite the fact that their energy is less than the ionization energy of many molecules, are reactive in contact with various substances ranging from small molecules such as O_2 [3] and ending at the components of DNA [4].

For several years, in our laboratory we have systematically studied the interaction of low energy electrons with molecules that are responsible for the destruction of the ozone layer in the atmosphere and global warming. To date, we have investigated halogenated derivatives of alkanes (10 methanes [5-8], 17 ethanes, 12 propanes and 3 butanes) [9-12], perfluoroethers (4 molecules) [13] and fluoroalcohols (4 molecules) [14]. The examination in the same method and in the same laboratory of the large number of molecules which have similar structure allows us to determine molecular parameters which are responsible for its ability to electron capture. It has been clearly established that in the mixtures of molecule with CO_2 or N_2 for the halomethanes (exception methyl bromide) includes attachment both by individual molecules and by van der Waals complexes, whereas for the other investigated molecules only two-body processes were observed. In the case of chloroalkanes and bromoalkanes the dependence of the electron capture rate constants on electronic polarizability of the accepting center of the molecule (that part of the molecule which is immediately connected with the attachment process) has been demonstrated.

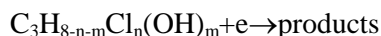
At present we have started the electron capture studies on the new group of compounds - chlorinated alcohols. Below, we present the data on the thermal electron attachment to $\text{CH}_2\text{ClCH}_2\text{OH}$, $\text{CH}_2\text{ClCH}_2\text{CH}_2\text{OH}$, $\text{CH}_2\text{ClCHOHCH}_2\text{Cl}$, $\text{CH}_2\text{ClCHClCH}_2\text{OH}$ and $\text{CH}_2\text{ClCHOHCH}_2\text{OH}$.

2. Results and discussion

The present data were obtained by using the recently established swarm method, known as the Pulsed Townsend technique. This technique allows us to study electron attachment processes at elevated temperature. The experimental procedure has been described in detail previously [8]. In brief, the electron acceptor was introduced into the chamber in the excess of carbon dioxide as a buffer gas. The electron swarm was produced at the cathode using laser. The electron swarm moved to the collecting electrode (anode) due to uniform electric field, through the gas mixture containing buffer

gas and an electron acceptor. The pressures of the electron attaching gases depended on their efficiency in attaching electrons and were chosen to reach the rate of the process equal to ca. 10^5 s^{-1} . The drifting electrons create a pulse change in the potential of the collecting electrode. The pulse signal is amplified, registered on an oscilloscope and saved in a computer memory. The electron attachment rate coefficients were determined from the shape of the output signal of the electron pulse.

We have measured the electron attachment rate coefficients (k 's) in the temperature 298 K for $\text{CH}_2\text{ClCH}_2\text{OH}$, $\text{CH}_2\text{ClCH}_2\text{CH}_2\text{OH}$, $\text{CH}_2\text{ClCHOHCH}_2\text{Cl}$, $\text{CH}_2\text{ClCHClCH}_2\text{OH}$ and $\text{CH}_2\text{ClCHOHCH}_2\text{OH}$ used as attaching gases diluted with carbon dioxide. With thermal electrons they react in a simple two-body process:



The rate coefficients obtained in the swarm experiment correspond to total attachment processes including all the reaction channels. All presented molecules are not very effective electron scavengers, but we have observed the influence of numbers of substituents on increase the value of the rate coefficients. All rate coefficients obtained for 298 K are presented in Tab. 1. To our knowledge they have been measured for the first time. We have also measured rate coefficients in the temperature range 298-378 K. The obtained results are shown in Fig. 1.

Tab. 1. Thermal electron attachment rate coefficients ($T=298 \text{ K}$) and activation energies (E_a 's) calculated from kinetic data, T_{range} - the temperature range applied for E_a 's determinations.

Molecule	$k_{298} (\text{cm}^3\text{s}^{-1})$	$E_a (\text{eV})$	$T_{\text{range}} (\text{K})$
$\text{CH}_2\text{ClCH}_2\text{OH}$	$4,9 \pm 0,7 \times 10^{-12}$	$0,26 \pm 0,01$	298-338
$\text{CH}_2\text{ClCH}_2\text{CH}_2\text{OH}$	$2,4 \pm 0,6 \times 10^{-12}$	$0,23 \pm 0,02$	298-368
$\text{CH}_2\text{ClCHOHCH}_2\text{Cl}$	$1,9 \pm 0,5 \times 10^{-11}$	$0,34 \pm 0,01$	298-378
$\text{CH}_2\text{ClCHClCH}_2\text{OH}$	$9,0 \pm 1,7 \times 10^{-11}$	$0,37 \pm 0,02$	298-358
$\text{CH}_2\text{ClCHOHCH}_2\text{OH}$	$1,3 \pm 0,1 \times 10^{-11}$	$0,39 \pm 0,03$	298-358

There are no data for thermal electron attachment for chlorinated alcohols therefore the examination of the obtained results will base mainly on their comparison with the kinetic data for other molecules of similar structure. For example since the rate coefficients for $\text{CH}_2\text{ClCH}_2\text{OH}$ and $\text{CH}_2\text{ClCH}_2\text{Cl}$ ($k=4,5 \cdot 10^{-12} \text{ cm}^3\text{s}^{-1}$ [15]), or $\text{CH}_2\text{ClCH}_2\text{CH}_2\text{OH}$ and $\text{CH}_2\text{ClCH}_2\text{CH}_2\text{Cl}$ ($k=2,0 \cdot 10^{-12} \text{ cm}^3\text{s}^{-1}$ [16]) are practically the same so we can conclude that replacement of chlorine atom by a hydroxyl group does not significantly affect the efficiency of electron-capture process. This confirm also data for isomers ($\text{CH}_2\text{ClCHOHCH}_2\text{Cl}$, $\text{CH}_2\text{ClCHClCH}_2\text{OH}$) and $\text{CH}_2\text{ClCHOHCH}_2\text{OH}$ where rate coefficients are, within the error limits, the same order of magnitude. The presence three substituents in the molecule at adjacent carbon atoms, regardless of whether it is chlorine or hydroxyl group having the same meaning with respect to the electron-capture process.

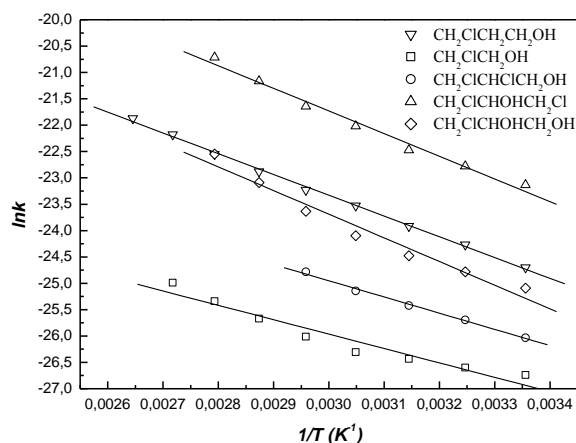


Fig. 1. The dependence of $\ln(k)$ vs. $1/T$ for all studied chlorinated alcohols.

In Tab. 1 and in Fig. 1 we summarize results of measurements for investigated molecules in the temperature range 298–378 K. In all cases we observed the increase of the rate coefficients with the temperature according to the Arrhenius-type behavior ($\ln(k)=\ln(A)-E_a/k_B T$) what suggest that the investigated processes require some activation energies. From the slopes of the lines shown in Fig. 1 we derived the activation energies (E_a 's).

All presented values were determined for the first time, similarly as rate coefficients. However it is unusual and surprising that higher values of rate coefficients are related with higher activation energies. First it should be considered the impact of pollutions on the increase in rate coefficient especially for lower temperatures. Such a case has been discussed in detail in our previous work [10]. For $\text{CH}_3\text{CHClCH}_2\text{CH}_3$ was observed two different slopes for dependence of k on temperature: one for lower (up to 340 K) and other one for higher temperatures and after purification (fractional distillation with a bubble-cap column) there was no visible attachment at room temperature. In the case of chlorinated alcohols we observed only one slope which denies the existence of significant amounts of pollutants in investigated samples.

The activation energy is identified with the crossing point between neutral and anionic potential curves where resonances are low in energy. However, due to the tunneling effect that can take place from vibrational level below the barrier it is likely that the activation energy of the process is slightly lower than the energy of the crossing point. The activation energy thus defines effective barrier energy for the electron attachment process.

In our previous paper [10-11, 13-14] we have shown the linear correlation between the thermal electron attachment rate coefficients (k 's) and activation energies (E_a 's) for chloroalkanes, bromoalkanes and fluorinated alcohols. In Fig. 2 we present thermal electron capture rate coefficients as a function of the activation energies for chloroalcohols investigated just now together with our previous data.

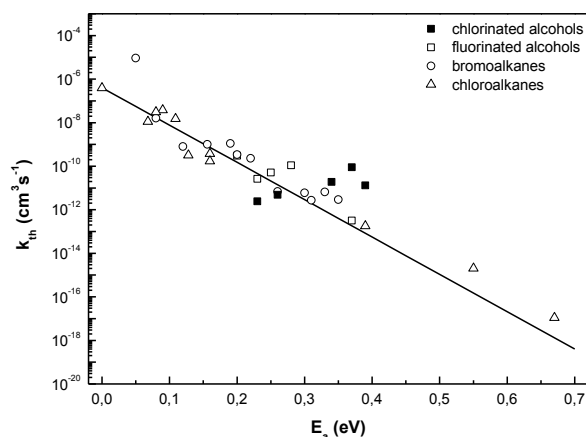


Fig. 2. Thermal electron capture rate coefficients as a function of the activation energies: present data, our previous data for some halogenated alkanes and fluorinated alcohols with literature one [9, 11, 14, 17-22].

As you can see most experimental data are located practically nearby the theoretical line. This fact proves that the activation energy is the main factor determining the rate coefficient for thermal electron capture. Set parameters (k , E_a) for chlorinated alcohols are spaced away the theoretical line. The better understanding of these cases that significantly deviate from the exponential relationship between k and E_a are needed.

3. Conclusions

- a) New set of the reaction rate coefficients and activation energies for electron capture by chloroalcohols (Tab. 1) have been completed.

- b) The dependence of the thermal electron attachment rate coefficients (k 's) on the activation energies (E_a 's) has been demonstrated.
- c) The simultaneous determination of the reaction rate coefficients and activation energy seems to elevate the reliability of the obtained values. On the other hand it can be treated as quality indicator of the experiment.

4. Acknowledgments

This work has been supported by the Polish Ministry of Science and Higher Education. Special thanks are due to prof. Mieczysław Foryś who was extremely dedicated researching electron attachment processes by halogenated alkanes.

5. References

- [1] L. G. Christophorou, „*Atomic and Molecular Radiation Physics*“, Wiley-Interscience, London, 1971.
- [2] L. G. Christophorou (Ed.), „*Electron-Molecule Interactions and Their Applications*“, Vols.I-II, Academic, Orlando, FL, 1984.
- [3] M. Kucera, M. Stano, J. Wnorowska, W. Barszczewska, D. Loffhagen, S. Matejcik, *Eur. Phys. J. D* 67 (2013) 234.
- [4] B. Boudaiffa, P. Cloutier, D. Hunting, M. A. Huels, L. Sanche, *Science* 287 (2000) 1658.
- [5] I. Szamrej, A. Jówko, M. Foryś, *Radiat. Phys. Chem.* 48 (1) (1996) 65.
- [6] I. Szamrej, W. Tchórzewska, H. Kość, M. Foryś, *Radiat. Phys. Chem.* 47 (2) (1996) 269.
- [7] I. Szamrej, H. Kość, M. Foryś, *Radiat. Phys. Chem.* 48 (1) (1996) 69.
- [8] J. Kopyra, A. Rosa, I. Szamrej, *J. Radioanal. Nuclear Chem.* 232 (1-2) (1998) 71.
- [9] J. Kopyra, W. Barszczewska, J. Wnorowska, M. Foryś, I. Szamrej, *Acta Physica Slovaca* 55 (5) (2005) 447.
- [10] J. Kopyra, J. Wnorowska, M. Foryś, I. Szamrej, *Int. J. Mass Spectrom.* 268 (2007) 60.
- [11] J. Kopyra, J. Wnorowska, M. Foryś, I. Szamrej, *Int. J. Mass Spectrom.* 291 (2010) 13.
- [12] K. Wnorowski, J. Wnorowska, B. Michalczuk, A. Jówko, W. Barszczewska, *Chem. Phys. Lett.* 586 (2013) 29.
- [13] J. Kopyra, J. Wnorowska, W. Barszczewska, S. Karolczak, I. Szamrej, *Chem. Phys. Lett.* 519-520 (2012) 25.
- [14] K. Wnorowski, J. Wnorowska, J. Kopyra, B. Michalczuk, I. Szamrej, W. Barszczewska, *Chem. Phys. Lett.* 591 (2014) 282.
- [15] H. Hotop, M. W. Ruf, J. Kopyra, T. M. Miller, I. I. Fabrikant, *J. Chem. Phys.* 134 (2011) 064303.
- [16] W. Barszczewska, J. Kopyra, J. Wnorowska, I. Szamrej, *J. Phys. Chem. A* 107 (2003) 11427.
- [17] T. M. Miller, J. F. Friedman, L. C. Schaffer, A. A. Viggiano, *J. Chem. Phys.* 131 (2009) 084302.
- [18] D. Smith, N. G. Adams, E. Alge, *J. Phys. B: At. Mol. Phys.* 17 (1984) 461.
- [19] D. Smith, C. R. Herd, N. G. Adams, *Int. J. Mass Spectrom. Ion Proc.* 93 (1989) 15.
- [20] Z. Lj. Petrovic, R. W. Crompton, *J. Phys. B: At. Mol. Phys.* 20 (1987) 5557.
- [21] E. Alge, N. G. Adams, D. Smith, *J. Phys. B: At. Mol. Phys.* 17 (1984) 3827.
- [22] D. Smith, C. R. Herd, N. G. Adams, J. F. Paulson, *Int. J. Mass Spectrom. Ion Proc.* 96 (1990) 341.

STUDY OF THE $\text{CH}_3^+ + \text{O}_2$ REACTION AT TEMPERATURES RELEVANT TO THE ATMOSPHERE OF TITAN

Ilia Zymak, Ján Žabka, Miroslav Polášek

*J. Heyrovský Institute of Physical Chemistry of the ASCR, Dolejškova 2155/3,
182 23 Prague 8, Czech Republic*

Large ions of hydrocarbons were found in the ionosphere of the Saturn's moon Titan [1, 2]. However, understanding of the observed data is not sufficient. Theoretical models of the Titan ionosphere do not agree with observations, especially in abundances of larger negative ions. This is due to a lack of knowledge of the rate constants of ion-molecule reactions. The overall precision of theoretical models of planetary atmospheres has unambiguously been shown to be highly sensitive to the uncertainties in chemical rates. The current data were obtained at room temperature and extrapolation to the temperature of Titan ionosphere ($\sim 80\text{K}$) is inaccurate and there are no data for the important anions.

Therefore, the SIFT apparatus was recently modified in our laboratory. This allows the experimental measurement of data necessary for the modeling of unique Titan's atmosphere.

The calibration reaction of CH_3^+ ions with the molecular oxygen $\text{CH}_3^+ + \text{O}_2 \rightarrow \text{HCO}^+ + \text{H}_2\text{O}$ was studied at $245 - 305\text{ K}$ using the Selected Ions Flow Tube (SIFT) apparatus with the flow tube thermoregulation system (see fig. 1). Ions and molecules of the reactant gas are cooled in collisions with the helium carrier gas. Typical He number densities in the flow tube are in the range of $10^{21} - 10^{23}\text{ cm}^{-3}$, so reactants are in the thermal equilibrium with reasonably good accuracy and the time of the thermalisation is negligibly short. Measured temperature gradient does not exceed the range of $\pm 5\text{ K}$ along the tube axis.

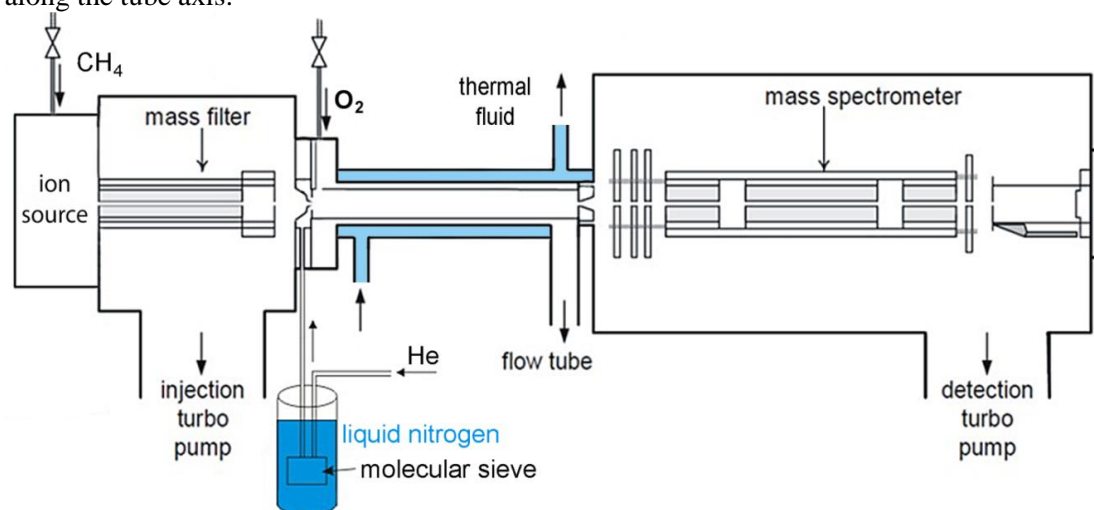


Fig. 1. Scheme of the Variable Temperature SIFT apparatus

Measured rate constant of the $\text{CH}_3^+ + \text{O}_2$ reaction ($k = (4.7 \pm 0.9) \cdot 10^{-11}\text{ cm}^3\text{s}^{-1}$ at $302 \pm 1\text{ K}$) is in agreement with the previous experiments [3], value slowly decreases at low temperatures ($k = (3.2 \pm 0.7) \cdot 10^{-11}\text{ cm}^3\text{s}^{-1}$ at $248 \pm 5\text{ K}$).

Acknowledgements

This work was supported by the Czech Science Foundation (grant No. 14-19693S) and the COST program, Action CM0805 "The Chemical Cosmos: Understanding Chemistry in Astronomical Environments".

References:

- [1] V. Vuitton et al., *Planet. Space Sci.* 57 (2009) 1558
- [2] V. Anicich et al., *J. Am. Soc. Mass Spectrom.*, 15, 8 (2004) 1148
- [3] W.T.Huntress, *Astrophys. J. Suppl. Ser.*, 33, 495 (1977)

ELECTROHYDRAULIC LEACHING OF ALKALI METALS FROM ZINNWALDITE MICA

Miloš Faltus², Václav Babický¹, Jiří Botula², Nguyen Hong Vu³
and Martin Člupek¹

¹ *Institute of Plasma Physics AS CR, v.v.i. Prague, Czech Republic*

² *VŠB - Technical University of Ostrava, Czech Republic*

³ *Institute of Chemical Technology Prague, Czech Republic*

E-mail: clupek@ipp.cas.cz

This study was designed to check possibility of leaching of alkali metals from zinnwaldite mica concentrate using electrohydraulic discharge technology. Electrical discharges are used in the field of the ore processing for fine grinding of ores. Use of mica as starting material offers the possibility to test the alkali metal leaching into solution assisted by electric discharge. Zinnwaldite mica concentrate was obtained from the tailings pond remaining after the mining and processing of Sn - W ores.

1. Introduction

1.1. Electrohydraulic technology

There are many physical and chemical phenomena occurring during the electrical discharge in water, active chemical substances are formed and intensive UV radiation is generated, thanks to discharge channel overheating, acoustic or even shock waves are formed.

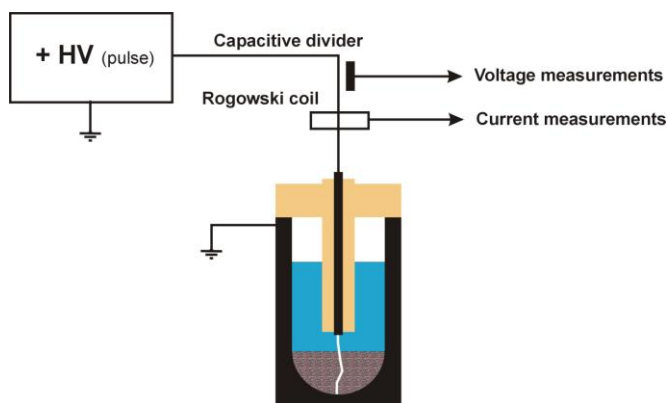
This complex process is usable in broad field of applications. Electrical discharges are used in laboratory conditions for decontamination [1] of water contaminated with organic pollutants and sterilization of water with microbial contaminants [2]. Generation of shock waves is also used in medical practice [3], e.g. non-invasive lithotripsy. Lastly, the shock waves can be used to disintegrate of minerals [4].

The process of disintegration (crushing, selective crushing, milling and ultra-fine milling) with help of the electrohydraulic effect was researched in past and is well described. Other applications of electrohydraulic effect are usable for hemolysis [5], cleaning of pipes or metallic casts [6], pressing of metallic parts, electrohydraulic drilling, electrohydraulic pumps, electrohydraulic propulsion [7] and others.

Only little research has been done on use of an electrohydraulic apparatus as a chemical reactor for leaching of desirable elements from different minerals. Information about leaching of alkali metals and alkaline earth metals from a mineral component of soil, originate from attempts to modify soils and electrohydraulic production of fertilizers [8]. These attempts also provided insights on how HNO₃ is formed in aerated water within an electrohydraulic apparatus and following bonding of nitrogen with organic matter.

2. Experiment

2.1. Impulse device description



The device used in research of impulse leaching is composed of:

- high voltage pulse source
- leaching container with 50 mm diameter, with two asymmetrical electrodes (needle electrode and grounded steel bottom of the container)

Distance between electrodes can be set in range of 0 to 50 mm

Fig. 1. Diagram of apparatus for electrohydraulic treatment of zinnwaldite concentrate

2.2. Methodology

Zinnwaldite concentrate was chosen as the most suitable candidate for experimental electrohydraulic activated leaching of alkali metals. The zinnwaldite concentrate was obtained by dry magnetic separation from tailings pond used in Sn – W ore mining and processing plant at Cínovec near Teplice, Czech Republic.

This material has been already studied by various departments with focus on extracting zinnwaldite concentrate [9] and alkali metals [10], mostly Li and Rb. Previous research of this material provide broad information about various methods of leaching alkali metals and their efficiency.

2.2.1. Zinnwaldite concentrate analysis

2.2.1.1 Granulometric analysis

Zinnwaldite concentrate sample was homogenized by mixing. Sample weighting 680 g was prepared by quartering and used in granulometric analysis, by sorting on sieves.

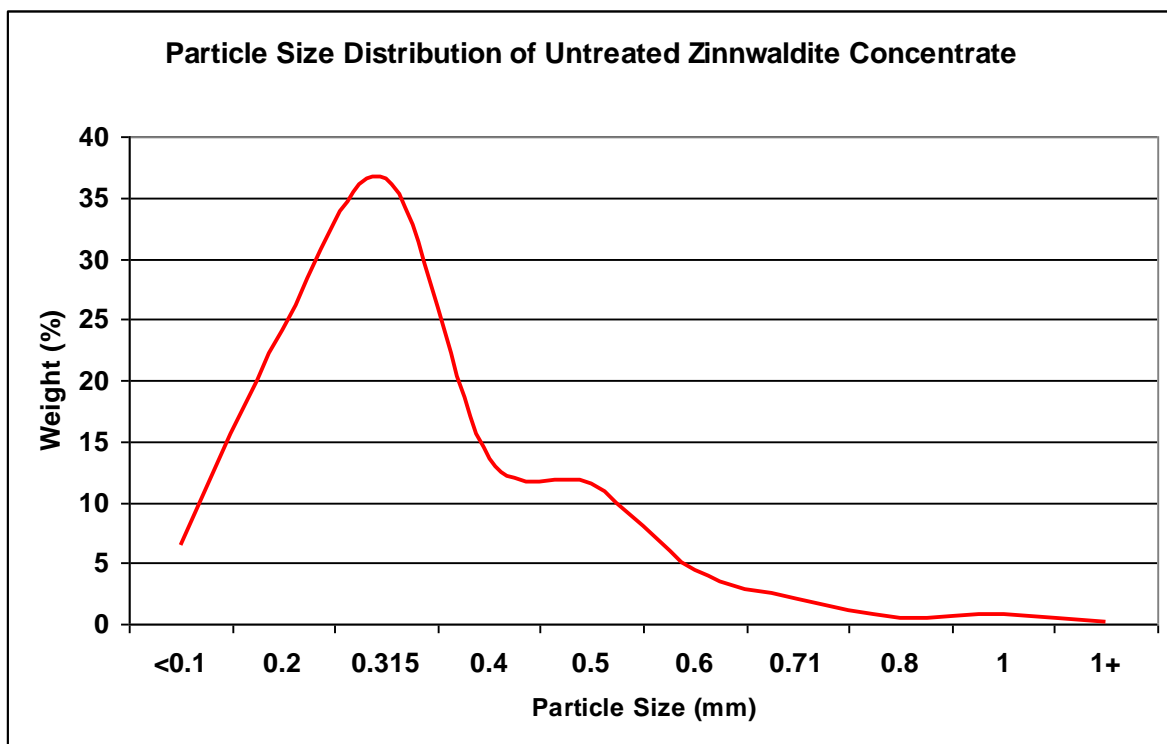


Fig. 2. Particle size distribution of untreated zinnwaldite concentrate

2.2.1.2. XRD structure analysis

Following the granulometric analysis, 2 g sample was separated from the sample prepared by quartering. The new sample was manually triturated in agate mortar to analytical fineness. This sample was then analyzed in powder X-ray diffraction analysis to determine crystalline mineral phases contents (presence of amorphous phases such as limonite is expected to be in negligible amount). XDR record was obtained with PANalytical XPertPRO MPD and the results were evaluated using X'Pert HighScore 1.0d, made by PANalytical B.V., Almelo, Netherlands.

2.2.1.3. Chemical analysis

50g sample was separated from the original sample used for granulometric analysis to determine content of alkali metals, Li, Rb, Cs and K. The sample was fully dissolved with standard laboratory methods and measured for content of the listed elements using Flame Atomic Absorption Spectrometry (FAAS) on flame absorption spectrophotometer VARIAN (type 200 HT).

2.3. Sample preparation

A whole mica concentrate sample (after conducting granulometric, XDR analysis and measuring of alkali metal content), was homogenized by mixing and separated to 100 samples weighting 10g, 20 samples weighting 5 g, 100 samples weighting 2 g and 100 samples weighting 1g. These samples serve as main batch for all experiments.

2.4. Conditions of electrohydraulic leaching

Demineralized water was used as a working medium. Experiments were conducted with voltages in range of 20 – 27 kV at 20 Hz repetition rate with distance of the electrodes in range of 10 to 15 mm. Experiments were conducted within range of 75 ml and 150 ml of demineralized water, with sample batches of 1 g, 2 g, 5 g and 10 g.

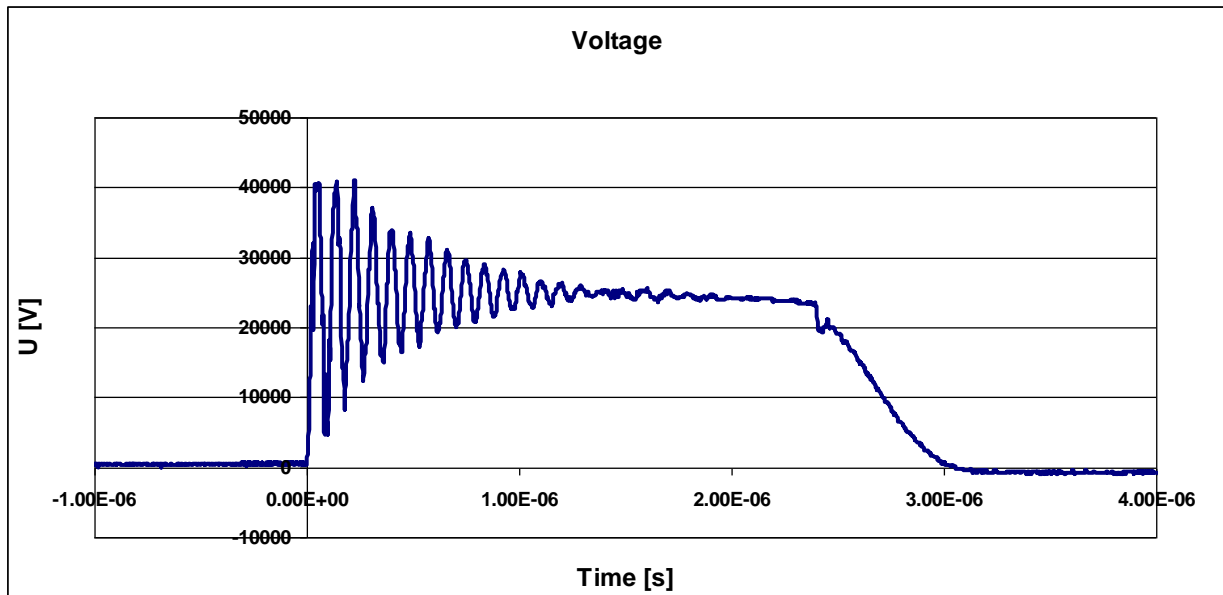


Fig. 3 – Typical voltage waveform at the discharge chamber

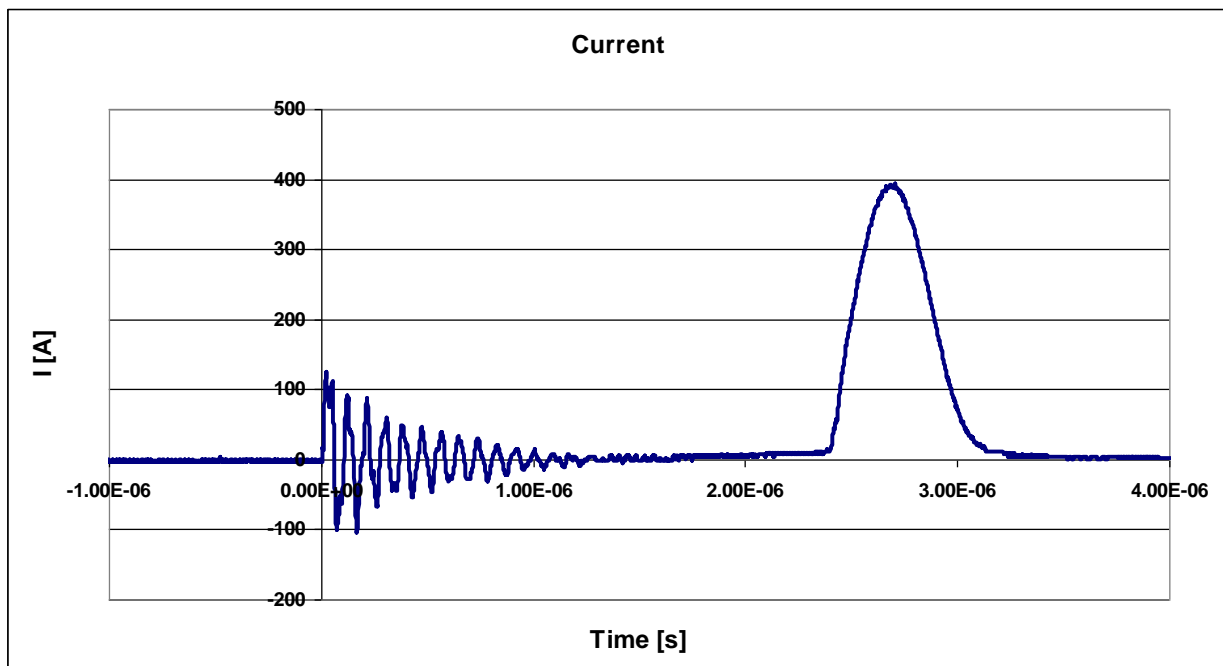


Fig. 4 Typical current waveform at the discharge chamber

2.4.1. Sample analysis after electrohydraulic treatment

Individual samples of the mica concentrate were filtered in order to separate the leachate and filter cake. Leachate was then analyzed with Flame AAS (FAAS) to measure content of K, Li, Rb. Yield of individual alkali metals was measured based on ratio of contained alkali metals leached out during the electrohydraulic leaching from zinnwaldite concentrate. Dried filter cake was then analyzed with laser granulometer Mastersizer 2000 by Malvern.

3. Experiment results

Zinnwaldite material used for experimental hydraulic leaching had determined phase composition with XRD and content of alkali metals by FAAS. Zinnwaldite concentrate used for this research of electrohydraulic leaching was composed of zinnwaldite, Fe- polyolithionite, quartz and kaolinite (detected by XRD powder analysis). Zinnwaldite and polyolithionite make up for approx. 85% weight percent of the concentrate and are source minerals for Li and other alkali metals of interest, mostly Rb and K.

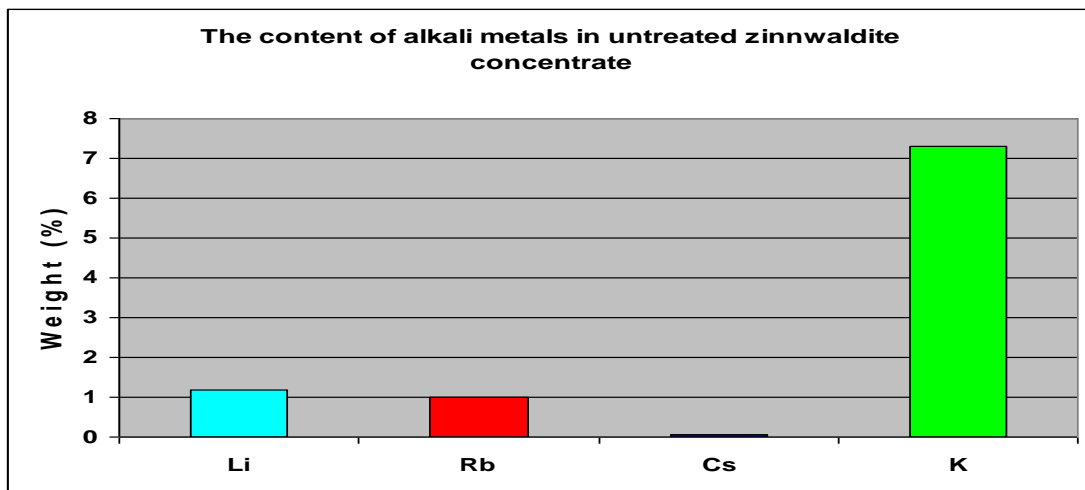


Fig. 5. The content of alkali metals in untreated zinnwaldite concentrate

Best leaching yields of alkali metals resulted from using 2g batch of zinnwaldite concentrate put in 150 ml of demineralized water at voltage of 26 kV, with 15 mm distance between electrodes and 20 Hz repetition rate of pulses, leached for 5 minutes.

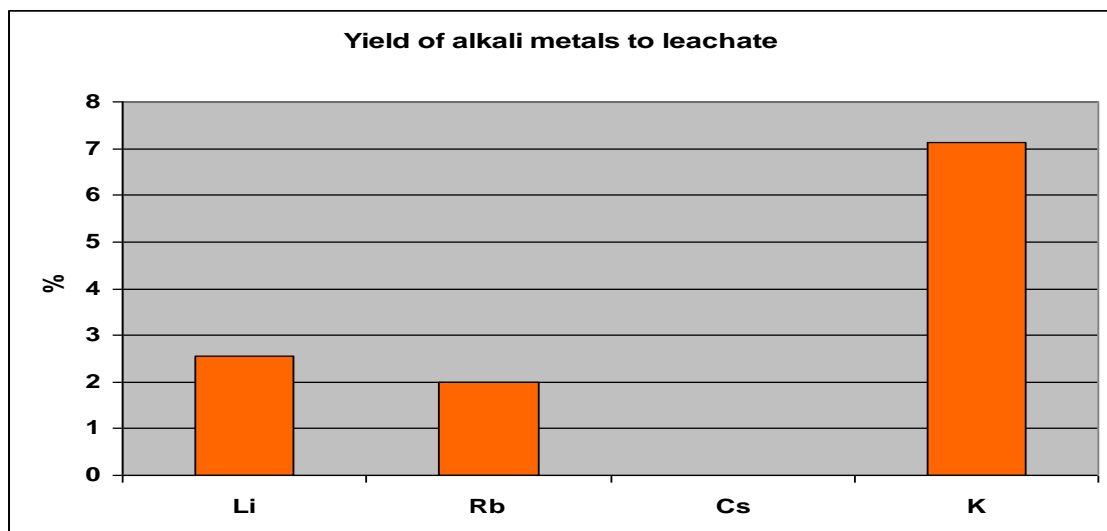


Fig. 6. Yield of alkali metals to leachate

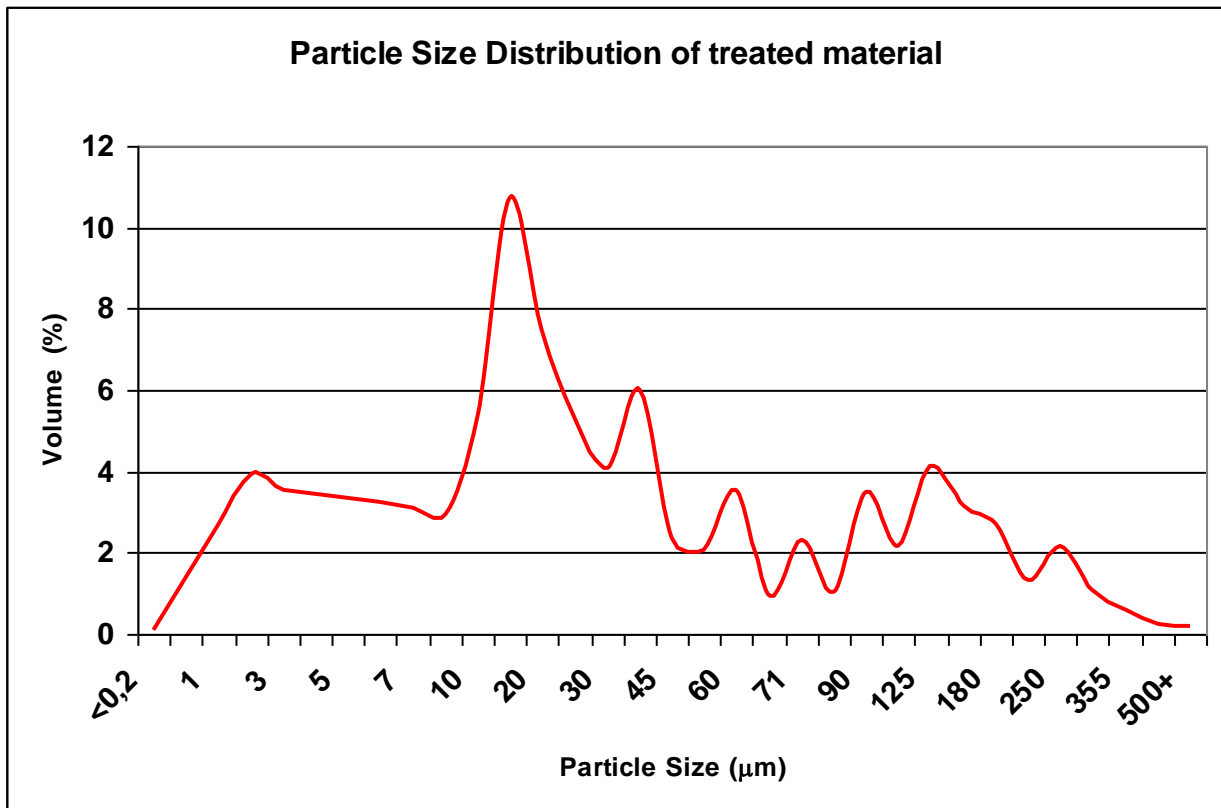


Fig. 7. Graph of particle size distribution of filtrate cake

During the electrohydraulic leaching of the sample, the zinnwaldite concentrate also became finer. Change in samples granularity is defined by coefficient of refinement, a ratio between mean value of granularity of sample before and after leaching. Finest material with coefficient of refinement about 12.6 was also achieved under the same conditions as the highest leaching yield to the leachate. The experiment in this sample created about 4 % (out of the whole mica concentrate) of very fine particles, with sizes under 1 μm .

4. Discussion and conclusion

Experiments have shown that effect of hydraulic leaching on yield of alkali metals from zinnwaldite concentrate and the changes in granularity increase with higher voltage and increasing distance between electrodes. Effect is also increased to certain degree by increasing duration of leaching and ratio of sample to working fluid. Reducing the amount of working fluid or increasing its conductivity proven to be decreasing the effectiveness of the process. During the batch regime, amount of leached sample is limited by increasing conductivity of the leachate, which affects the nature of discharge.

Acknowledgement: This work was supported by Ministry of Education, Youth and Sports of the Czech Republic; Project ID: COST CZ LD 14080 and COST Action TD 1208

References:

[1] Lukeš P., Člupek M., Babický V., Šunka P., Winterová G., Janda V. Non-thermal plasma induced decomposition of 2-chlorophenol in water. Proceedings of the 14th Symposium on Application of Plasma Processes. Liptovský Mikuláš: Military Academy, 2003 - (Šutta, P.; Muellerová, J.; Bruner, R.) p. 64-65. ISBN 80-8040-195-0.

- [2] **Lukeš P., Člupek M., Babický V., Šunka P., Špetlíková E., Říhová -Ambrožová J., Janda V., Vinklárková D., Maršálková E., Maršálek B.** Biological decontamination of water by high power DC diaphragm underwater discharge. Book of Contributed Papers of 12th International Symposium on High Pressure Low Temperature Plasma Chemistry (HAKONE XII). Bratislava: Comenius University, 2010 - (Országh, J.; Papp, P.; Matejčík, S.) p. 348-352. ISBN 978-80-89186-71-6.
- [3] **Šunka P., Fuciman M., Babický V., Člupek M., Beneš J., Poučková P., Souček J.** Generation of focused shock waves by multichannel el. discharged in water. Czech J Physics. (2002) 52: D397-D405
- [4] **Teslenko V., Rostovcev V., Lomanovich K., Drozzhin A., Medvedev R.** Electroexplosive desintegration of Cu – Ni ore with simultaneously particle separation according of the sizes, Fiziko – technologicheskie problemy razrabotky poleznych iskopaemych, 1, Publishing house of Siberian branch of Russian Academy of Science, Novosibirsk, 2007, p. 100 – 107, ISSN 0015-3273, (in Russian)
- [5] **Beneš J., Šunka P., Hani A.B.** Effect on hemolysis by shock waves created by a new method of multichannel discharge. Sb Lek. (2001) 102: 29-35.
- [6] **Meriin B.** Electrohydraulic treatment of engineering parts, Mashinostroenye, Moscow, 1985 (in Russian)
- [7] **Yutkin L.** The electrohydraulic efekt and his use in industry, Mashinostroenye, Moscow, 1986 (in Russian)
- [8] **Ořechová V.** Research of the impact of electrohydraulic impulse on the fertility of soils, Publishing house of Kuban State Agricultural University, Krasnodar, <http://aeli.altai.ru/nauka/sbornik/2010/st5.htm> (in Russian)
- [9] **Botula J., Rucký P., Řepka V.** Extraction of zinnwaldite from mining and processing wastes, Collection of scientific works of Technical University of Ostrava, Mining – geological group, Volume LI, No.2, p. 9-16, ISSN 0474-8476, Ostrava, 2005
- [10] **Jandová J., Konrád J., Vu H. N.** Overview of methods for the treatment of lithium-bearing waste raw material, Partial research work of project FF-P2/057, Institute of Chemical technology Prague, Prague, 2003

LOW PRESSURE PLASMA CHEMICAL TREATMENT FOR METAL ARTEFACTS - CONSERVATION APPROACH

Hana Grossmannová^{1,2}, František Krčma¹

¹Brno University of Technology, Faculty of Chemistry, Purkyňova 118, 612 00 Brno, Czech Republic

²Methodical Centre for Conservation Technical Museum in Brno, Purkyňova 105, 612 00 Brno, Czech Republic

E-mail: grossmannova@technicalmuseum.cz

Article examines the possibilities and conditions of the hydrogen plasma treatment application for the iron artefacts conservation from the conservation-restoration approach. Treatment of the large volume objects (kind of "mass conservation techniques") or big archaeological object was studied and some experiments were performed to understand the changes in material composition and migration of corrosion activators (chlorides, sulphates). Specific groups of samples were treated to describe the whole process – pure artificial minerals, model samples, real archaeological samples. Electron microscopy and XRD techniques were used to understand the transformation of ferrous compounds.

1. Introduction – technology and conservation

This work is dealing with the possibilities and conditions of the plasma treatment application for the iron artefacts conservation. Generally, it was proved that the application of hydrogen/argon plasma allows reduction of chlorinated products as well as oxides from the corrosion layers of archaeological objects [1]. Plasma chemical treatment has some advantages compare to the other methods, as abbreviation of the conservation procedures and relative regardful of the artefacts. The corrosion removal process is very complex and it is very important to understand well the treatment mechanisms and to find the optimal conditions for the whole procedure.

This technology itself is well defined and verified [2 – 4], but still some important tasks are related to the conservation issues. For these reasons, we cooperated with conservator specialists, to understand fully the process details and its specific parameters. Our apparatus, usable for the large amount of the treated objects (kind of "mass conservation techniques" could be applied) or for the big archaeological object such as swords or hatchets, needs to be studied for the plasma homogeneity (i.e. homogeneity of the process, represented by the sample temperature). Next important factor of this technique is how to combine effectively plasma with the conservation pre-treatment and/or after treatment. An important part of the experiments is performed also to understand the changes in material composition and migration of corrosion activators (chlorides, sulphates).

The plasma is produced in cylindrical reactor (0.75 m³) by 13.56 MHz generator at operating pressure of 30 Pa, total gas flow of 400 ml/min (200 ml/min H₂, 200 ml/min Ar). Reactor is equipped with gas inlets and mass flow controllers for hydrogen and argon and a pumping system. Whole technology is fully automatized, supplied by Programmable Logic Controller unit allowing a digital recording of all treatment parameters.

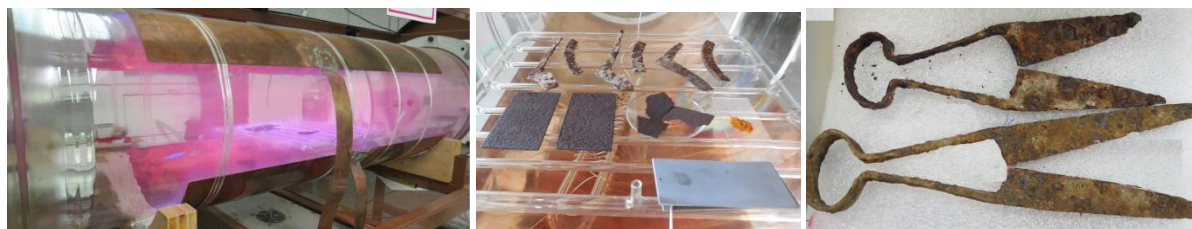


Fig. 1. Plasma reactor, model samples treated in plasma, example of treated object.

2. Experimental

Conditions and parameters

Model iron samples or newly excavated originals used for all the presented experiments were always pre-dried by molecular sieve only, treated in plasma reactor and cooled down in inert atmosphere. Optical emission spectrometer (Ocean Optics HR4000) was used to monitor the process during some measurements. Optical fibre was focused axially to the central part of the reactor. The OH radicals are generated during the plasma chemical treatment and can be used for the process monitoring [5].

We also tried to understand the desalination process induced by plasma. As the original artefacts are mostly contaminated by chlorides and sulphates, is quite challenging to determine and analyse the decrease of chlorides in metal samples (solution is to use higher volume of the samples or to use model samples with defined chloride concentration). Despite this, migration of chloride ions is confirmed by XRD analysis.

Sample temperature during the plasma treatment

Sample temperature during the plasma treatment is one of the most important parameters, because it is necessary to avoid the transformation of the metal phases during the eutectics transition. Moreover, the higher temperature corresponds to the activity of the chemical species and it also helps to the migration of contaminants. The temperature strongly depends on the supplied power, its mode (continuous or pulsed) and on the sample position in the reactor. Generally, it would basically be taken into account as the maximum allowed process temperature of the eutectic transformation for a particular metal - from the phase diagrams (Fe approx. 700 °C.). However, due to the object manufacturing technology (turbidity, carburising) specific phases are formed in the metal, which are very important for the authenticity of the object. This means it is very difficult to determine one exact value of the maximum allowed temperature. Because of various impurities etc., the most sensitive material, which should be the part of the object (verified at least by X-rays analysis before the treatment) must be taken into account. Thus contemporary practically used maximal temperature for iron objects should not exceed about 250 °C, only.

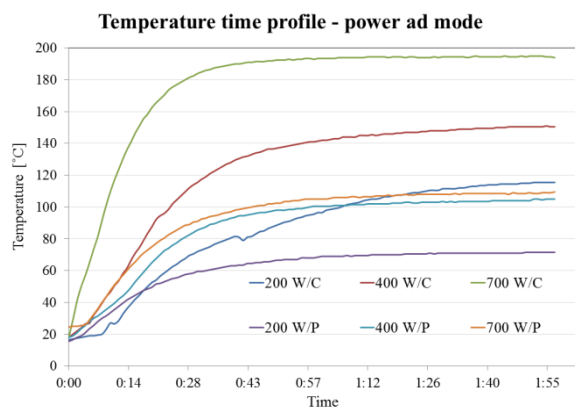


Fig. 2. Sample temperature during 2H H hhhdfsf h treatment. C – continuous, P – pulsed (duty cycle 50 %).

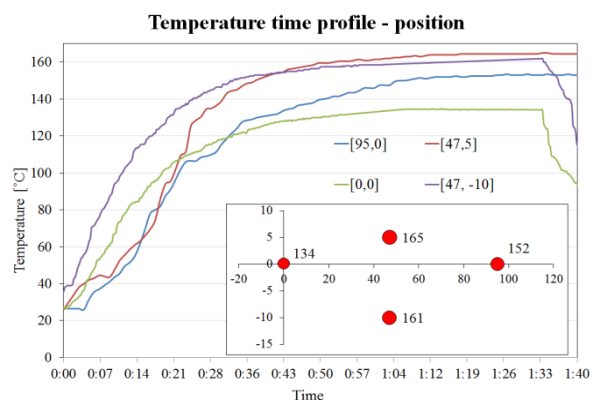


Fig. 3. Sample temperature during H H hhhdfsf90 min treatment, 400 W, continuous. Coordinates present the sample position in plasma.

The sample temperature contact monitoring system was developed and successfully tested. It allows measurement only at one spot, but simultaneously with plasma operation. The results give the information about typical temperature profile – growing up during about 2 hours of the process. The maximum temperature achieved under the different electrical parameters (RF discharge generation at 200–700 W in continuous and pulsed regime) was varied between 71 and 194 °C. The application of pulsed discharge regime could maintain the corrosion removal process at lower mean power and thus lower heating stress affected the treated samples. The use of pulsed regime helps to regulate the temperature but when the mean supplied power is similar (200 W/C versus 400 W/P) the achieved

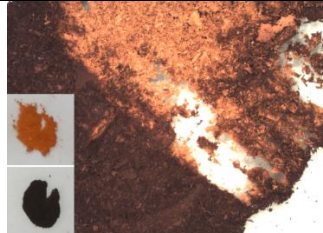
temperature is almost the same. The plasma reactor is 1.5 m long and outer electrodes surround the cylinder in the length 1 m around its centre. Active plasma can be visually observed particularly in the area between the electrodes, but its intensity is not homogenous. Due to this fact, we tried to determine this non-homogeneity on the samples treatment determined via their temperature. The samples located in several positions. Point [-20,0] presented the openings of the reactor, point [0,0] – X (start of the electrodes), Y - centre of the reactor diameter, point [100,0] – X (end of the electrodes), Y - centre of the reactor diameter (see the immersed sketch in Fig. 3). The highest maximum temperature was achieved at the reactor centre as it was expected. Based on the results shown in Fig. 2, it can be concluded that only the part of the reactor between the cylindrical electrodes can be used as the working space for the objects treatment.

3. Results and conclusions

Treatment of pure minerals

To verify the processes leading to the corrosion removal, the pure corrosion model samples were used. Pure lepidocrocite (β -FeOOH) was formed in laboratory, and treated together with the whole real samples (pieces of the agricultural tools), to understand the process of the Cl migration and mineral reduction. Lepidocrocite is an orange iron corrosion product that is close to tone of the mineral akaganeite. These two types of corrosion products are generally less stable compared to goethite (α -FeO(OH)) or magnetite (Fe_3O_4). Lepidocrocite creates a secondary corrosion coating in the neutral water during conservation (desalination process). These types of corrosion products are commonly found on the surface at points or sockets, and they are the typical products of the so-called chloride corrosion. Its colour allows approximately distinguish it from the black-brown corrosion products - oxides with hydrated forms $\text{Fe}_2\text{O}_3 \cdot \text{H}_2\text{O}$ and goethite. The plasma induced reduction of lepidocrocite and particularly of akaganeite, too, leads to the object mechanical stabilization. Experimental observation showed that treated lepidocrocite (amount of 1 g) is visually transformed to goethite on the powder sample surface; original lepidocrocite orange products remained unchanged in the powder bulk. Significant amount of chlorine containing mineral akaganeite is formed. This supports the theory of chloride ions trapping (from other real samples) at the lattice of akaganeite [6].

Tab. 1. Results of XRD analysis before and after plasma treatment of pure lepidocrocite.
L – lepidocrocite, L_h – lepidocrocite (homogenized L after treatment).

	Sample	Treatment	Lepidocrocite γ -FeO(OH)	Akaganeite β -FeO(OH,Cl)	Goethite α -FeO(OH)
	Pure L	No	100%	-	-
	Pure L _h	6h cycle	51,4 %	17,3 %	31,29 %

Treatment of model samples and archaeological samples

Two groups of samples were used for other series of experiments. At the first, the effect of the plasma treatment of artificial corrosion layer (without the core, chlorinated) was tested. Secondary, the effect of the plasma and separately of the temperature, only (at the same time profile as in plasma), was studied under 6 h treatment of model corrosion layers without any metallic core and corrosion on archaeological samples with metallic core. Archaeological samples were determined as parts of the sickles, excavated in Brno-Žebětín, track "U Újezda" extinct medieval village from 15th century. Layered artificial corrosion was powdered and analysed by XRD on a Bruker D8 Advance apparatus with Cu anode ($\lambda_{\text{K}\alpha} = 1.54184 \text{ \AA}$) and variable divergence screens at θ - θ Bragg-Brentano. The qualitative phase analysis was done to determine the phase (mineral) composition changes due to the plasma treatment. Simultaneously, part of the samples was analysed using a scanning electron microscope with an energy-dispersive micro analyser (SEM-EDX). Analytical work was carried out on electron microscope PHILIPS XL 30th. Surface micro analyses were performed on the analytical

complex PHILIPS-EDAX. On the real samples, detailed microscopy of the chloride and sulphate nests was performed.

Tab. 2. Comparison of XRD analysis results in dependence on the treatment procedure.

	Corrosion layer (before)	Corrosion layer (plasma)	Arch. sample (before)	Arch. sample (plasma)	Arch. sample (temperature)
Lepidocrocite $\gamma\text{-FeO(OH)}$	3,5 %	-	1,5 %	-	-
Akaganeite $\beta\text{-FeO(OH,Cl)}$	3,7 %	4,2 %	-	-	-
Goethite $\alpha\text{-FeO(OH)}$	50,3 %	44,2 %	58,9 %	69,3 %	66,0 %
Magnetite Fe_3O_4	42,5 %	51,6 %	9,5 %	21,8 %	13,6 %
Silica SiO_2	-	-	17,4 %	6,0 %	11,9 %
Albite $\text{NaAlSi}_3\text{O}_8$	-	-	7,3 %	2,9 %	6,6 %
Microcline KAlSi_3O_8	-	-	5,4 %	-	-

Analysing XRD data (see Table 2), it was confirmed that the influence of the plasma results in the transformation of corrosion products. The significant increase of magnetite concentration, both in model and real samples, was observed. For model samples, lepidocrocite and goethite are transformed in to magnetite. The results for original archaeological objects are affected by a high content of soil silicate minerals and thus it is difficult to precede the correct methodology of the sampling for the XRD analysis. Data are distorted by different percentage of soil minerals, but calculating the ratio of ferrous compounds without the soil minerals confirms the formation of magnetite also for these samples. Decreasing lepidocrocite concentration confirms the results obtained during the treatment of the pure mineral. To better understanding these chemical processes, new experimental series using samples of other pure minerals will be prepared.

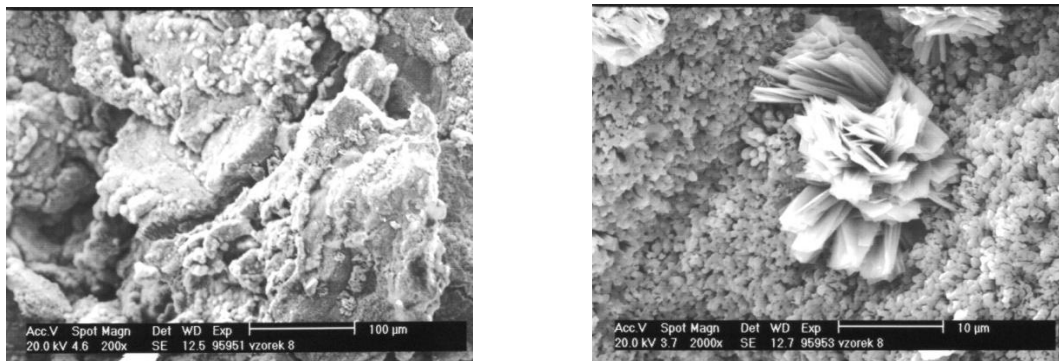


Fig. 4. Left - clumps of chloride corrosion on the surface crusting, right - tabular sulphate crystals.

As it is shown on the Fig. 4, optical microscope helps to identify chloride nests on the surface of sickles. Macroscopically, it is a hollow space in the corrosion layer filled with tiny crystals shining brownish coloration. Observing these spots by electron microscopy and EDX microanalysis was determined that it is the sulphate crystals. Chloride corrosion products were laid outside the nest. Plasma treatment significantly decreased the concentrations of sulphates, chlorides were not identified by SEM-EDX. In future experiments, we would like to focus on the effect of plasma applications on the sulphate concentration. An important research would be also performed on the artificially prepared pure corrosion minerals to understand well the effect of the transformation and migration process.

4. References

- [1] Patscheider J and Vepřek S 1986 *Studies in Conservation* 31 29.
- [2] Sázavská V, Krčma F, Šimšová T and Zemánek N 2010 *Journal of Physics: Conference Series* **207** 1742.
- [3] Schmidt-Ott K and Boissonnas V 2002 *Studies in Conservation* **47** 81.
- [4] Vepřek S, Eckmann Ch and Elmer J Th 1988 *Plasma Chemistry and Plasma Processing* **4** 445.
- [5] Rašková Z, Krčma F, Klíma M and Kousal J 2002 *Czechoslovak Journal of Physics* **52** 927.
- [6] Kotzamanidi I, Vassiliou P, Sarris Em, Anastassiadis A, Filippakis L, Filippakis S E 2002 *Anti-Corrosion Methods and Materials* **49** 256.

Acknowledgement

The work was supported by the Ministry of Culture of the Czech Republic, project No. DF11P01OVV004.

PLASMA NEEDLE DECOLOURISATION OF DIRECT RED (DR 28) DIAZO DYE

Tatjana Mitrović^{1,2}, Nikola Božović², Nataša Tomić¹, Zorana Dohčević-Mitrović¹, Dejan Maletić¹, Saša Lazović¹, Gordana Malović¹, Uroš Cvelbar³ and Zoran Lj. Petrović^{1,4}

¹ *Institute of Physics, University of Belgrade, Pregrevica 118, 11080 Belgrade, Serbia*

² *Institute for development of water resources "Jaroslav Černi", Jaroslava Černog 80, 11226 Belgrade, Serbia*

³ *Jožef Stefan Institute, Jamova cesta 39, 1000 Ljubljana, Slovenia*

⁴ *Academy of Sciences and Arts of Serbia, 11001 Belgrade Serbia*

E-mail: lazovic@ipb.ac.rs

We investigate decolourisation of Direct Red 28 (DR 28), diazo dye by plasma needle. UV-VIS spectroscopy is employed to measure decolourisation rates. Argon flow rate of 1, 4, and 8 slm is used and its influence on decolourisation rates is investigated. We find that the increase of the argon flow rate increases the colour removal rate. Complete decolourisation is achieved after 210 min of treatment. This study is performed in order to investigate the prospects of using a small size, low power consumption, non-thermal plasma source, which operates at atmospheric pressure, to perform oxidation of organic pollutants in the water.

1. Introduction

Textile industry effluents can contain high concentrations of colorants and therefore have significant carcinogenic influence on human health. This caused more stringent world regulations which indicate that a complete removal of the dyes from the wastewaters is required before its disposal into the environment. Azo-dyes represent the major class of all dyes used in textile industry and more than 15 % of them end up in its effluents [1]. Their oxidation is very complex because of the presence of one or more aromatic rings and sulfonate groups which typically makes them resilient to conventional biological, physical and chemical water treatment processes. Direct red (DR 28) diazo dye, a very toxic, mutagenic, and carcinogenic substance, has been used in dyeing process for many years [2]. As already mentioned, standard wastewater purification processes did not accomplish effective results and other methods had to be included [3].

The advanced oxidation processes (AOPs) are reported to be highly efficient in oxidizing organic dye pollutants. They demonstrated high capability for decomposition of organic matter due to generation of hydroxyl radicals (OH[•]) which have a very high oxidation potential (2.8 V) [1]. Plasma is considered as one of the AOPs and represents a novel method for water treatment which is based on abundant production of reactive species. One of the plasma sources of a simple design that can efficiently produce reactive species at atmospheric pressure is a plasma needle.

In our previous work we investigated decolourisation and degradation of azo dye Reactive orange 16 (RO 16) using a plasma needle [4]. Decolourisation was achieved by breaking a -N=N- bond and a complete colour removal was achieved after 60 min of treatment. In this work we investigate decolourisation process of DR 28 diazo dye which has a different chemical structure than RO 16.

2. Experimental setup

Plasma needle consists of a body made of Teflon, a central electrode made of copper, and a glass tube. The argon gas is fed through the glass tube and a kHz power source is used to generate plasma [4]. The dye sample is prepared with distilled water (50 mg/l, 50 ml). Molecular formula of DR 28 is given on Fig. 1. The needle tip is placed about 4 millimetres above the sample. Magnetic stirrer (300 rpm) is used to provide sample homogeneity. We use different argon flow rates (1, 4, and 8 slm).

Decolourisation is monitored by UV/VIS spectrophotometry by measuring the solution absorbance at 498.5 nm after the plasma treatment.

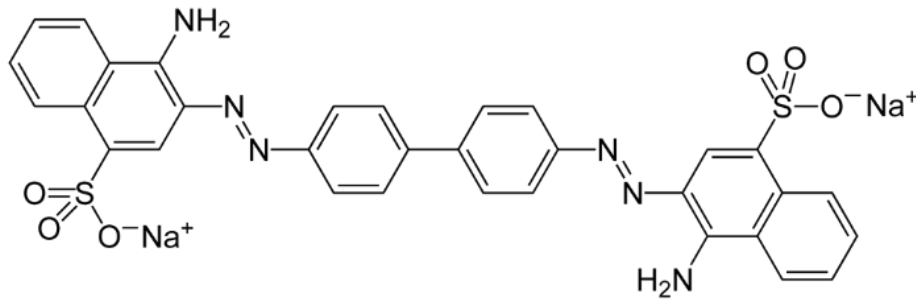


Fig. 1. Molecular formula of DR 28

3. Results and discussion

We investigate the influence of feed gas flow rate on decolourisation kinetics of DR 28 using a plasma needle. Decolourisation process can be interpreted with a kinetic model of a reaction which follows the pseudo-first order kinetics:

$$-\frac{dA}{dt} = kt \quad (1)$$

$$-\ln\left(\frac{A}{A_0}\right) = kt \quad (2)$$

where k is pseudo-first order constant rate, t the treatment time and A is dye absorbance. Decolourization rates for different gas flows are given on Fig. 2. and the corresponding rate constant in Tab. 1.

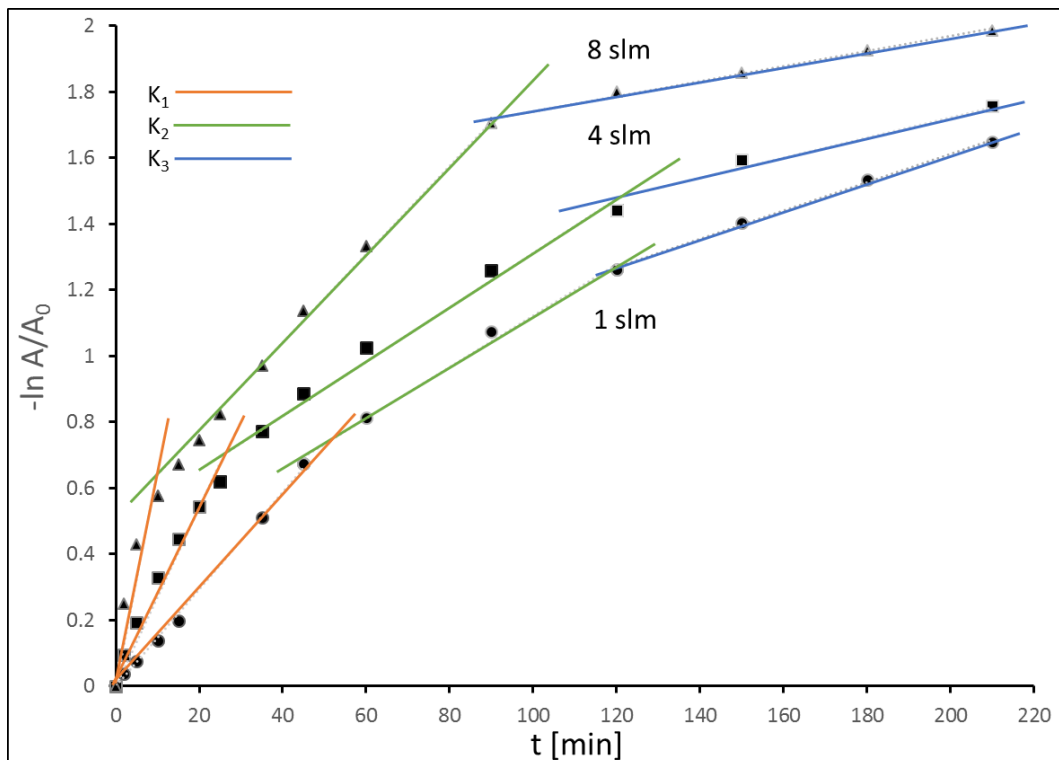


Fig. 2. Effects of different flow rates of argon on the decolourisation rate.

With the increase of flow rate the volume of the plasma and the production of reactive species increases. Increased radical production consequently leads to the more efficient decolourisation (mainly OH[•]). The constant rates increase from $14.7 \times 10^3 \text{ min}^{-1}$ to $65.3 \times 10^3 \text{ min}^{-1}$ when the flow rate is increased from 1 to 8 slm (see Tab.1. for the corresponding rate constants). Furthermore, we can see that the rate of decolourisation is decreasing with treatment time in all cases and we can identify three distinct regions where we apply the pseudo first order kinetic model. Rate constants for a fixed flow of 1 slm are $14.7 \times 10^3 \text{ min}^{-1}$, $7.8 \times 10^3 \text{ min}^{-1}$, and $4.3 \times 10^3 \text{ min}^{-1}$ respectfully. In the case of higher flow rates, for example 8 slm, the differences are being more pronounced and constant rates decrease from $65.3 \times 10^3 \text{ min}^{-1}$ to $13.4 \times 10^3 \text{ min}^{-1}$ to $2.3 \times 10^3 \text{ min}^{-1}$.

Tab. 1. Decolourisation rate constants for different argon flow rates of plasma treatment

Constant rates	Argon feeding gas flowrates		
	1 slm	4 slm	8 slm
$K_1 \cdot 10^3 (\text{min}^{-1})$	14.7	24.8	65.3
$K_2 \cdot 10^3 (\text{min}^{-1})$	7.8	8.2	13.4
$K_3 \cdot 10^3 (\text{min}^{-1})$	4.3	3.1	2.3

4. Conclusion

In this article we demonstrate that the plasma needle can be an efficient method for decolourisation of the direct red DR 28 diazo dye but requires further optimization of the treatment parameters such as gas composition, flow rate, distance from the sample surface, etc. We find that argon flow rate has a significant effect on the decolourisation rate. The increase of the flow rate leads to a faster decolourisation. Pseudo first order kinetic model is used to calculate rate constants. It is found that the decolourisation is fastest in the initial stages of the plasma treatment and slows down as the treatment continues. The dyestuff is characterized by two azo groups as chromophores ($-\text{N}=\text{N}-$) which gives very intensive colour to the substance. As a consequence, decolourisation process is significantly slower than for RO 16 which has only one chromophore.

Authors acknowledge the support by MESTD, Republic of Serbia, project number OI41017 and III41011, and NATO Science for Peace and Security Programme, project number EAP.SFP 984555.

5. References

- [1] Ay F, Catalkaya E C, Kargi F 2009 *Journal of Hazardous Materials* **162** 230–236
- [2] Bafana A, Jain M, Agrawal G, Chakrabarti T 2009 *Chemosphere* **74** 1404–1406
- [3] Hairoma N H H, Mohammadb A W, Kadhum A A H 2014 *Journal of Water Process Engineering* **4** 99–106
- [4] Mitrović T, Maletić D, Tomić N, Lazović S, Malović G, Nenin T, Cvelbar U, Dohčević-Mitrović Z and Petrović Z Lj 2014 *27th Summer School and International Symposium on the Physics of Ionized Gases, August 26 – 29, Belgrade, Serbia* 443

DEPOSITION AND ANALYSIS OF HARD AND MODERATELY DUCTILE MO₂BC COATINGS BY PULSED DC SPUTTERING

Vratislav Peřina¹, Pavel Souček², Petr Vašina², Vilma Buršíková², Vladimír Havránek¹

¹*Nuclear Physics Institute, Academy of Sciences of the Czech Republic, v.v.i., Řež 130, CZ-25068, Řež, Czech Republic*

²*Department of Physical Electronics, Faculty of Science, Masaryk University, Kotlářská 2, CZ-61137 Brno, Czech Republic*
E-mail: perina@ujf.cas.cz

Superhard Mo_xB_yC_z coatings with promising mechanical properties were prepared by pulsed DC magnetron sputtering. Structure information obtained from XRD is not enough to optimize the deposition process to reach stoichiometric Mo₂BC film. EDX and WDX technique does not show sufficient resolution to distinguish Mo and B in the spectra. Rutherford back scattering is very suitable technique to evaluate chemical composition of the whole of prepared coatings and it was used for optimization of the coating stoichiometry.

1. Introduction

Nowadays, in the field of protective coatings traditionally coatings like TiN, TiAlN, c-BN or Al₂O₃ are often used to enhance tool life of cutting tools. While having high stiffness and hardness, often brittle deformation behaviour of these coatings is observed. Crack initiation and propagation significantly decrease the tool life and increase the cost.

Prospective coatings showing high hardness, stiffness and moderate ductility are sought for next generation protective coatings. Such an unusual combination of properties was recently reported in nanolaminated coatings, where often alternating layers of low and high electron densities are observed [1,2]. Mo₂BC in bulk form was synthesized and studied since 1960s [3], but the studies were mostly motivated only by the superconducting properties of this bulk material [4]. Mo₂BC in the form of a thick film was theoretically proposed and prepared at extreme conditions of very high temperatures [5] or at a single setting of HiPIMS deposition [6]. Mo₂BC exhibits rather large unit cell in an orthorhombic structure [3,7] and similarities to MAX phases like high aspect ratio of unit cell [8]. Formation of solid lubricant Mo-Magnéli phases in tribological contacts in the presence of oxygen may be expected in addition to high hardness, stiffness and moderate ductility, making these coatings promising in the future of protective coatings. A recently published study [9] theoretically proposes an enhancement of the materials properties if molybdenum is replaced by tantalum or tungsten.

2. Experimental details

All depositions utilized a sputtering device equipped by four confocally arranged magnetrons accommodating 3 inch sputtering targets. All magnetron heads are aimed at a rotatable biasable substrate holder that can be heated up to 750°C. Molybdenum, carbon and B₄C targets were co-sputtered simultaneously. Molybdenum and B₄C targets were DC powered, while carbon target was connected to Advanced Energy Pinnacle+ pulsed DC generator capable of pulsing up to frequency of 350 kHz. Powers to magnetrons were kept constant as well as the total pressure was kept constant at 0.1 Pa, bias and pulsing frequency were varied in order to tune the ion flux to the growing film. All the depositions were carried out for one hour.

The chemical composition was measured by Oxford Instruments EDX detector connected to TESCAN Mira FEG SEM and RBS.

The RBS was measured by proton projectiles with energy 1740 and 2700 keV impinging vertically on samples and backscattered protons analysed at 170 deg scattering angle. The energy is characteristic for mass of struck atoms and is also diminished by energy losses by passing into and out of the layer material [10]. The type of atoms and their depth are detectable. The analyses of MoBC layers with classical Rutherford backscattering highlight heavy elements due to the Z^2 proportion. This leads us to use energies with enhanced non Rutherford cross sections. The advantage is the increased sensitivity for the light elements in heavy elements matrixes.

Dual head Hysitron TI 950 TriboIndenter was used to study the mechanical properties of MoBC coatings. The nanoscale measuring head with resolution of 1nN and load noise floor less than 30nN was used for this study. Several testing modes were used in the range of indentation loads from 0,25 to 10mN, namely quasistatic nanoindentation, quasistatic nanoindentation with several unloading segments and nanodynamic mechanical analysis (nanoDMA) in the range from 0,1 up to 300Hz. Crystalline structure was investigated by X-ray diffractometer Rigaku Smartlab F with copper x-ray tube in Bragg-Brentano configuration.

3. Results and discussion

In order to prepare stoichiometric composition a precise characterization of the chemical composition is necessary. However, analysis of chemical properties of MoBC type films poses a challenge. Standard EDX/WDX methods are somewhat limited when quantifying amount of carbon due to electron beam interaction with carbon contamination on the surface of the sample in ex-situ measurements or in the residual atmosphere in the microscope. So that carbon content is often overestimated by these methods. Moreover the analysis of the EDX spectra of MoBC films can be a source for error. The overall spectra depicted in Fig.1a show clearly distinct Mo L-lines, C K-line and B K-line. However, if we enlarge the area of low energy, we can see a very significant overlap of B K-line and Mo M_{γ} -line (see Fig. 1b). This overlap coupled with relatively low resolution of EDX makes EDX estimate of Mo, B and C content impossible. The problem with resolution can be overcome by utilizing WDX equipped with special crystal for light element (Be, B) measurements. However, relatively high uncertainty for light element quantification together with carbon quantification overestimation still leads to rough estimates of the chemical composition only. Thus a more powerful method of chemical analysis must be used in order to pinpoint the precise composition.

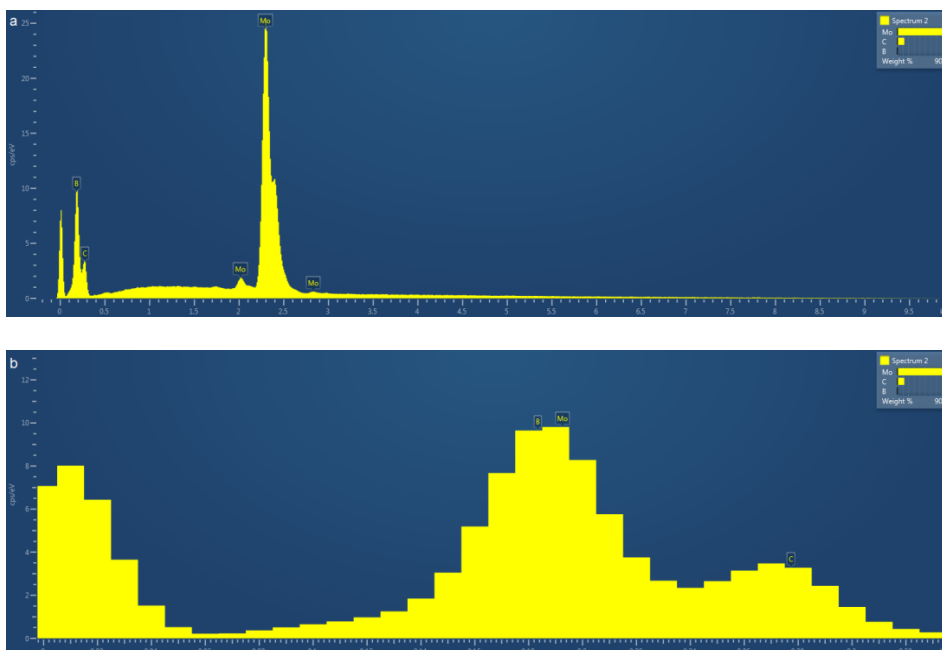


Fig. 1. a) Overall EDX spectra of MoBC film. b) Detail of low energy region showing overlap of Mo and B lines.

The reason for simultaneously measurements with proton energies 1.74 and 2.7 MeV is seen from Fig 2. The optimal measurements of carbon content at proton energy 1.74 MeV is visible on Fig. 3 and for boron at energy 2.7 MeV on Fig. 4. The relatively new values for non-Rutherford cross-sections proton-boron are used [11]. Other values of cross-sections are taken from [12]. The limits of observation; estimation and accuracy of boron and carbon depend on ratio of signals to signal of Si substratum at proper energy. Spectra were evaluated by SIMNRA code [13].

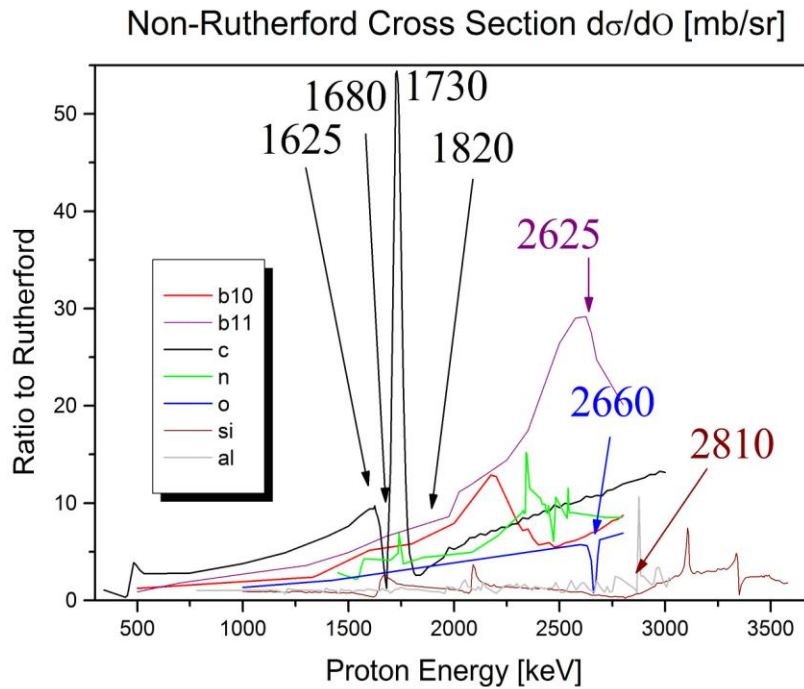


Fig. 2: Non-RBS cross-sections for protons. The areas around 1.74 MeV where C-crs are favourable for carbons and around 2.7 MeV where B-crs are favourable for boron are used for RBS measurements.

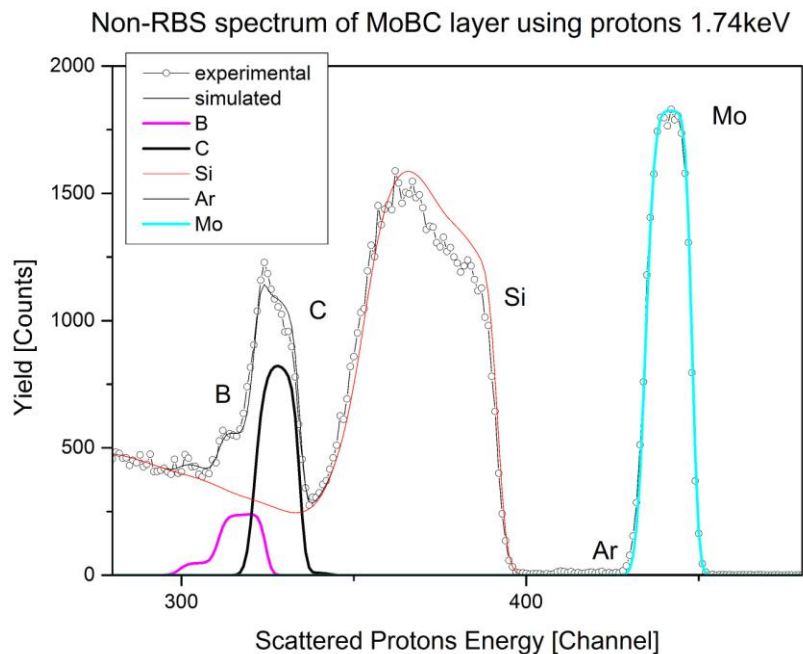


Fig. 3: RBS spectra for protons energy 1.74 MeV

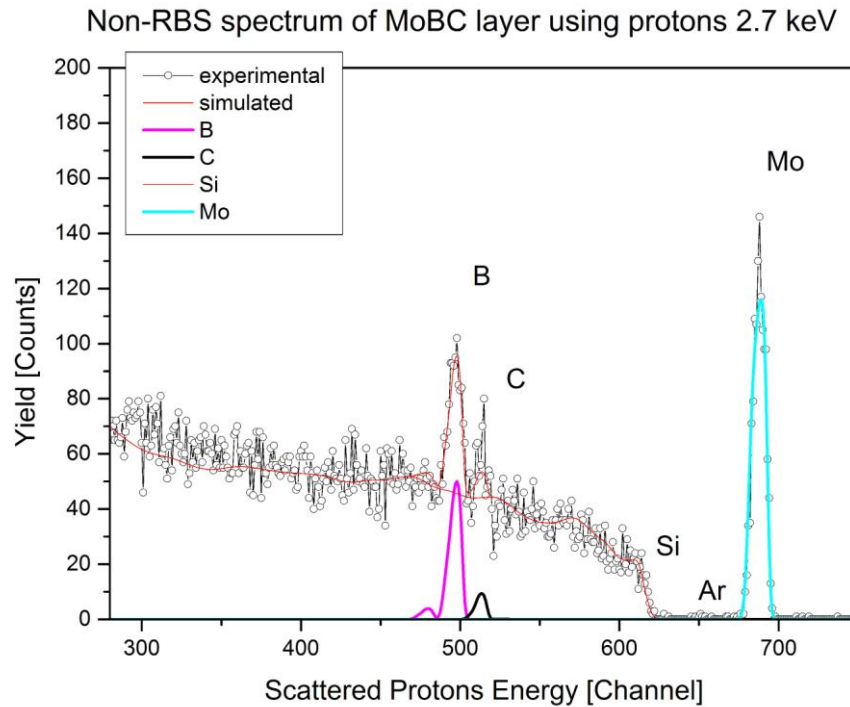


Fig. 4: RBS spectra for protons energy 2.7 MeV

The structure of the films was characterized by XRD. Comparison of XRD patterns of coatings prepared at different pulsing and bias conditions are plotted in Fig. 5. Positions amorphous (A) and crystalline (C) phase are reported to be 37° and 42° for stoichiometric Mo_2BC phase [6]. The presence of crystalline Mo_2BC phase was proven for different deposition conditions utilizing pulsed DC sputtering as well as DC even without the need of high temperatures.

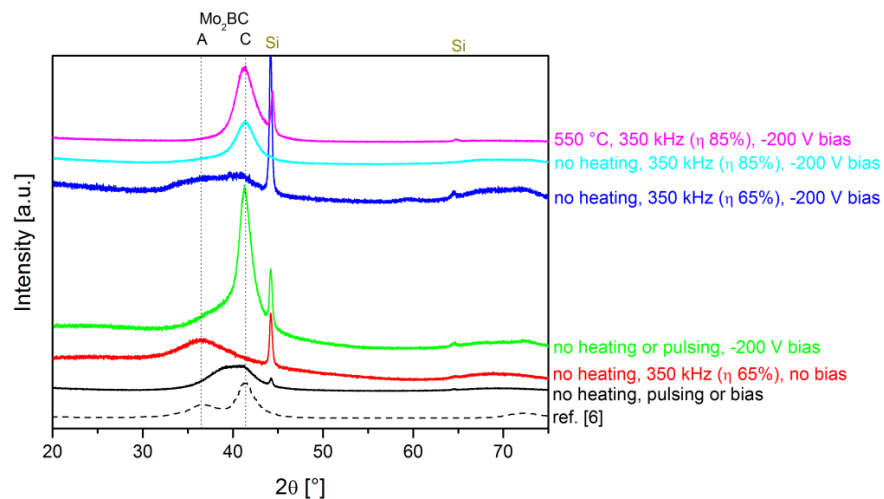


Fig. 5: XRD patterns of samples prepared at the constant magnetron powers with differing heating, pulses and bias. Positions of (A) amorphous and (C) crystalline Mo_2BC phase are emphasized.

Samples prepared at conditions with lowest ion bombardment – no heating, pulsing or biasing – and at highest ion bombardment with heating – 550°C , 350 kHz (85% duty cycle) and -200 V bias were

chosen for analysis of mechanical properties. Low measurement loads (500 μN and less) were used due to low thickness (< 500 nm) of the coatings. Use of such low loads was possible because of low average roughness < 0.5 nm. The sample prepared at the most gentle conditions with no heating, pulsing or biasing had hardness of 44 ± 5 GPa with elastic modulus of 400 ± 20 GPa ($H/E = 0.113$, $H^3/E^2 = 0.570$) and was composed of 8.1 at.% B, 22.4 at.% C and 69.5 at.% Mo as determined by RBS. RBS proved that the sample is of poor stoichiometry. Further enhancement of the mechanical properties is possible by optimization of the coating stoichiometry using RBS technique to evaluate the coating composition. The sample prepared at harshest conditions exhibited hardness of 55 ± 5 GPa with elastic modulus of 430 ± 10 GPa ($H/E = 0.128$, $H^3/E^2 = 0.900$) and was composed of 29.3 at.% B, 18.6 at.% C and 52.1 at.% Mo, again leaving space for possible optimization of stoichiometry and enhancing its properties. Thus very hard coatings were prepared at conditions of high ion bombardment of the growing thin film. Also H/E and H^3/E^2 ratio values are very promising for achievement of moderate ductility and tribological performance.

4. Conclusions

$\text{Mo}_x\text{B}_y\text{C}_z$ coatings with promising mechanical properties were prepared by pulsed DC magnetron sputtering. Structure determined by XRD does not provide enough information to optimized deposition process to reach stoichiometric Mo_2BC film. However, RBS characterization of chemical composition proved to be necessary for further optimization of the deposition condition to get closer to ideal stoichiometry. Superhardness with good H/E and H^3/E^2 ratios were reached, promising good mechanical and tribological performances are expected.

5. Acknowledgment

This research has been supported by GACR contract 205/12/0407 and R&D centre project for low-cost plasma and nanotechnology surface modifications CZ.1.05/2.1.00/03.0086 funded by European Regional Development Fund. The RBS analyses were realized at CANAM (Center of Accelerators and Nuclear Analytical Methods) LM 2011019.

6. References

- [1] D. Music, J.M. Schneider, *JOM* 59/7 (2007) 60-64.
- [2] D. Music, J.M. Schneider, *J. Phys.: Condens Matter*. 20 (2008) 055224
- [3] W. Jeitschko, H. Nowotny, F. Benesovsky, *Monatsh. Chem.* 94/3 (1963) 565-568
- [4] P. Lejay, B. Chevalier, J. Etourneau, P. Hagenmuller, P. Peshev, *Synthetic Met.* 4/2 (1981) 139-145
- [5] J. Emmerlich, D. Music, M. Braun, P. Fayek, F. Munni, J.M. Schneider, *J. Phys. D: Appl. Phys.* 42 (2009) 185406
- [6] H. Bolvardi, J. Emmerlich, S. Mráz, M. Arndt, H. Rudigier, J.M. Schneider, *Thin Solid Films* 542 (2013) 5-7
- [7] J.O. Bovin, M. O'Keefe, L. Stenberg, *J. Solid State Chem.* 22 (1977) 221-231
- [8] W. Jeitschko, H. Nowotny, *Monatsh. Chem.* 98 (1967) 329-337
- [9] H. Bolvardi, J. Emmerlich, M. to Baben, D. Music, J. Von Appen, R. Dronsowski, J.M. Schneider, *J. Phys.: Condens, Matter* 25 (2013) 045501
- [10] Y. Yang, M. Nastasi, *Handbook of Modern Ion Beam Materials Analysis*, Material Research Society, Pitsburg, 2009.
- [11] M. Chiari et al. *Nucl. Instr. Meth. B* 184 (2001) 309
- [12] <http://www-nds.iaea.org/iband/>
- [13] M. Mayer, *SIMNRA User's Guide*, Forschungszentrum Julich, Inst. fur Plasmaphysik, 1998.

ATMOSPHERIC PRESSURE PLASMA JET SURFACE CLEANING, SURFACE MODIFICATION AND NANOCOATING

Péter Urbán

PhD student, University of Miskolc, Institute of Metallurgical and Foundry Engineering

E-mail: onturban@uni-miskolc.hu

Several experiments were performed with atmospheric pressure plasma jet to develop a novel and environmentally friendly surface cleaning and treating technology without the use of chemical detergents in the Laboratory of Surface Techniques at the Institute of Metallurgical and Foundry Engineering. To this end steel specimens were artificially contaminated with dimethyl-sulfoxide and then cleaned with plasma jet in specified number of scans. A glow discharge optical emission spectrometer (GD-OES) was used for the determination of the efficiency of plasma cleaning. The results of this experiment proved that this novel technology outperforms the traditional (for ex. aqueous based) surface cleaning technologies.

1. Introduction

Atmospheric pressure plasma (APP) treatments have already gained some ground in several traditional materials processing as well as in different new high-tech industries. However, their applications in many fields of surface treatments and engineering like atmospheric pressure surface cleaning and plasma-polymerization are still in a developing phase, which has encouraged us to study their possible further technical applications towards corrosion protection and surface treatments and developing protective coatings on metals, especially on common grade and relatively cheap unalloyed carbon steels. Cold-rolled steels, for example, are always surface pre-treated and then often coated as well by different means, where there is also much place for further investigations to test the applicability of possible novel variants of the APP treatment techniques [1].

For our cleaning experiments, an atmospheric pressure plasma treating equipment, the Plasmatreater AS400 was used, which was bought from Germany and was installed in a laboratory of the Institute of Metallurgy and Foundry. The acquisition was induced by the plan of doing experiments in the field of different procedures by plasma flame. One of the most important possibilities for its application is cleaning surfaces of different solid products, among them even metallic surfaces from organic contaminants. The plasma generator is FG5000. It has a double resonance system, a state-of-the-art IGBT and Power-MOSFET semiconductor for pulse-pause modulation and wide voltage control [2].

Measurement of cleanliness by GD-OES

For the measurement of cleanliness of steel samples, a recently installed Glow Discharge Optical Emission Spectrometer (GD-OES) was applied. The equipment is capable to determine elemental composition profile of solid materials vs. depth. A Horiba JobinYvonGDProfiler2 analyser was used for the investigation of the samples as multi-layered coating systems by the advantages of its special features:

- Depth profile analysis of solid conductive and non-conductive samples down to $\sim 200 \mu\text{m}$ is allowed
- Bulk analysis of specimens is also possible to measure multi-layered or coated material systems
- With its polychromator, 46 elements can be simultaneously measured in a very short period of time and among them there are C, H, O, N, P, S, etc. which are major elementary components of organic substances.
- With its monochromator, further elements can be detected and measured

The GD OES measuring method chosen for determining the surface carbon contamination had the following parameters: Power: 25 W, Argon pressure: 500 Pa [3].

2. Results and discussion

The prepared steel (brushed and polished) specimens were cleaned in acetone by ultrasonic treatment for 25 min at 35 degrees Centigrade. Then they were etched in a 5% HCl solution for 120 s in order to clean the surface and increase the wetting ability, rinsed by distilled water and dried on paper wipes in ambient conditions. Without etching, the DMSO does not wet the surface well but ran off and coalesced.

As for the artificial surface contamination, a thin DMSO layer was obtained thru dipping the steel specimens into the liquid DMSO then wiping up its excess. In this way we were aiming at developing an artificial contaminant layer reproducibly. The thickness of the so prepared DMSO coverage was approximately 0.6 μm determined by profilometric analysis [4].

The DMSO was obtained from KAT CHEM Ltd. It is weakly acidic mild oxidant. As a polar aprotic solvent it dissolves both nonpolar and polar substances also as surface contaminants. Furthermore, it is a good surfactant which was even used as a solvent of electrolytes for measuring the corrosion properties of HCl on steel [5].

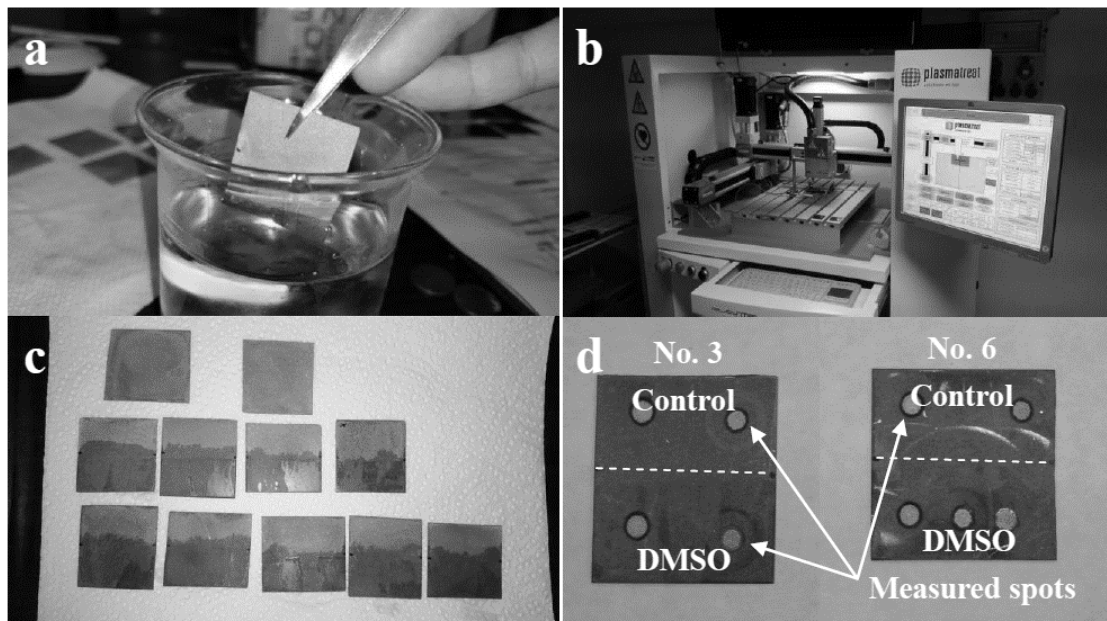


Fig. 1. Dipping in DMSO (a), Plasmatreater AS400 (b), dipped specimens before drying (c), plasma cleaned and GD-OES measured samples No.3 and No.6 (d)

As our GD-OES equipment is not sensitive enough for sulphur, the measurements were based on the well detectable carbon. The surface of each specimen was divided into two areas, one part was dipped into DMSO, the other was left untreated, and two additional samples were set aside for comparison. The initial surface carbon content of the untreated sides of the specimens were all determined before commencing the plasma treatments on their other sides in order to get a feedback about the effectiveness of the cleaning procedure (Figure 1).

The main plasma settings were the followings:

- Frequency: 15 kHz
- Distance: 9 mm
- Jet slide velocity: 1 m/min
- Airflow: 2 $\text{m}^3 \cdot \text{h}^{-1}$

These settings were chosen based on our huge range of tests performed with the Plasmatreater® 400 AS. We treated our specimens 1, 3, 5 and 10 times with plasma. Figure 2. shows the results of GD-OES analysis of 10 times plasma treated specimens. The 1 and 3 times treated specimens did not bring satisfactory results, but anyway shows the effect of plasma.

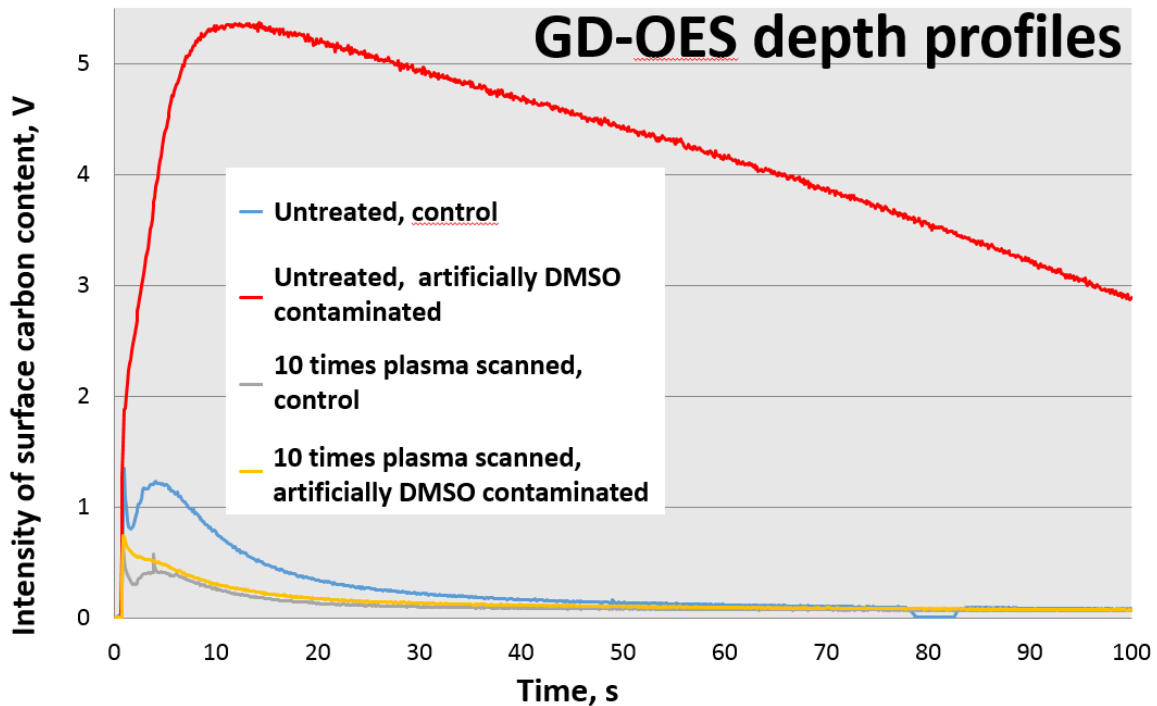


Fig. 2. GD OES depth profile of the plasma cleaned steel sample No.6 with different surface conditions

As a result of the measurements, all the artificially surface loaded DMSO contaminants were cleaned off from the steel specimens by the atmospheric air plasma jet working with a frequency of 15 kHz. The 5 times plasma treated specimens were even cleaner than in the initial stage obtained after careful traditional cleaning. In the case of those samples which were not dipped into the liquid DMSO, the plasma treating yielded lower surface carbon contamination compared to the initial stage. Both of the initial surfaces were cleaner after plasma cleaning than in the original untreated surface state. We did not detect significant differences between the contaminated and untreated samples after plasma cleaning. There was no further surface purification on the surface of the control samples between 5 and 10 times subsequent plasma treatments.

3. References

- [1] Atmospheric plasmas: A review. Tendero, C. 2006, *Spectrochimica Acta Part B*, 61. pages: 2-30.
- [2] www.plasmatreater.com 17.01.2014.
- [3] www.pprc.org/pubs/techreviews/measure/metypes.html 01.11.2014.
- [4] Schütze A., Jeong J.Y., Babayan S.E., Park J., Selwyn G.S 1998: Hicks R.F. *The Atmospheric-Pressure Plasma Jet: A Review and Comparison to Other Plasma Sources. IEEE Transactions on Plasma Science* 26(6) 1687-1694
- [5] Rastogi R.B., Singh M.M., Singh K., Maurya J.L. 2010: Electrochemical behaviour of mild steel in dimethyl sulphoxyde containing hydrochloric acid. *Portugaliae Electrochimica Acta* 28(6) 359-371

EXPERIMENTAL AND MODELING STUDIES OF LOW-PRESSURE CAPACITIVE OXYGEN PLASMAS EXCITED BY TAILORED VOLTAGE WAVEFORMS

A. Derzsi¹, T. Lafleur², I. Korolov¹, J. P. Booth², Z. Donkó¹

¹*Institute for Solid State Physics and Optics, Wigner Research Centre for Physics,
Hungarian Academy of Sciences, 1525 Budapest, POB. 49, Hungary*

²*LPP-CNRS, Ecole Polytechnique, 91128 Palaiseau, France*

E-mail: derzsi.aranka@wigner.mta.hu

We report experimental and particle-based kinetic simulation studies of low-pressure capacitively excited oxygen plasmas driven by tailored voltage waveforms that consist up to four harmonics of the base frequency of 13.56 MHz. We find that a DC self bias develops over the plasma due to the asymmetry of the waveform, which provides a control over the flux-energy distribution functions of the ions at the electrodes. The simulation results confirm the experimental observations and aid their understanding by allowing access to the space-time dynamics of different discharge characteristics, like particle densities, fluxes, heating and reaction rates.

1. Introduction

Capacitively coupled plasmas (CCPs) operated in various gases are important in several high-tech applications, such as etching and deposition techniques and modification of surface properties (see e.g. [1]). In most of these applications the *flux* and the *energy* of the ions reaching the electrode (target) surfaces are of primary importance. During the past years a number of schemes for controlling these ion properties separately (excitation of the plasma by two or more frequencies, use of hybrid sources, etc.), have been proposed. One way to optimize this separate control is to use "customized" or "tailored" voltage waveforms, which influence the density distributions and the dynamics of charged particles.

Here we report a combined experimental + simulation study of a low-pressure oxygen CCP, which is excited by tailored voltage waveforms that consist of a base harmonic and a number of additional higher harmonics. The resulting "peaks" and "valleys" waveforms lead to the generation of a DC self bias via the Electrical Asymmetry Effect (EAE) [2]. We follow the evolution of the discharge characteristics with increasing number of applied harmonics, up to four, and compare selected simulation results with experimental data. The experimental setup is described in section 2, while the simulation method is presented in section 3. The experimental and simulation results are presented and compared to each other in section 4.

2. Experimental

Experiments are performed in the DRACULA CCP plasma reactor previously described in [3] and shown schematically in figure 1. The cylindrically symmetric reactor has aluminium electrodes with a diameter of 50 cm, and separated by a distance of $L = 2.5$ cm. The bottom electrode is powered, while the top electrode is grounded. The plasma between the electrodes is radially bounded by a large Pyrex cylinder and a thick Teflon dielectric, thus ensuring that the plasma "sees" almost equal electrode areas. The chamber is pumped with a rotary/turbomolecular pump system, and the pressure is measured using both ion and Baratron gauges. Oxygen is injected into the reactor via a side port in the chamber, and the flow rate is adjusted using a mass flow controller. The powered electrode is connected to a class A, broad band, RF power amplifier via a 4.5 nF bias capacitor. The amplifier is controlled using an arbitrary function generator and a PC with a LABVIEW program that creates and sends the desired voltage waveforms. The frequency response of the reactor and the plasma impedance in general distort this waveform, and so a Fourier transform feedback technique [3,4] is used to ensure that the desired waveforms can be produced on the powered electrode. A SOLAYL voltage-current probe (described in detail in Ref. [5]) is placed between the powered electrode and the bias capacitor,

and is used to monitor the discharge current and power. The discharge voltage and DC self bias are measured with a 100:1 high-voltage probe connected directly to the powered electrode.

The ion flux-energy distribution function (IFEDF) is measured with a HIDEN EQP mass/energy spectrometer. The spectrometer entrance orifice is embedded in the grounded electrode and is aligned with the axis of the reactor. In order to avoid the need to know the ion energy dependent transmission function (which requires trajectory simulations) [6,7], the focussing electrodes are turned off and only ions in a narrow acceptance angle of about 2° are measured.

The experimental system also allows the determination of the electron density (with a hairpin probe) and the flux of the ions to the grounded electrode (with probes embedded in the electrode). The results obtained for these characteristics will be discussed elsewhere, here we only present data for the electrical characteristics (self-bias voltage) and the flux-energy distribution of ions, and compare these characteristics to simulation results.

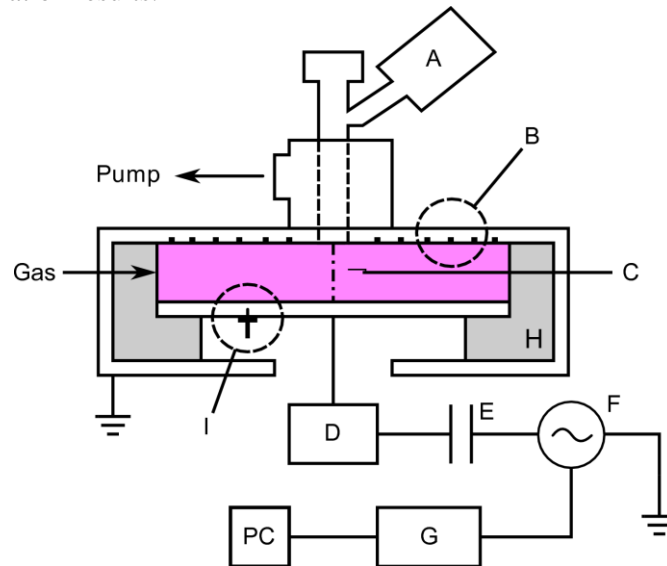


Figure 1. Schematic of the DRACULA plasma reactor, showing the Hiden Mass Spectrometer (A), ion flux probe array (B), hairpin resonator probe (C), SOLAYL VI probe (D), blocking capacitor (4.5 nF; E), RF power amplifier (F), arbitrary function generator (G), dielectric spacers between the powered and grounded electrodes (H), and high-voltage probe (I).

3. PIC/MCC simulation

The discharge is described by a Particle-in-Cell simulation code incorporating Monte Carlo treatment of collision processes (PIC/MCC) [8]. Our code is one-dimensional in space and three-dimensional in velocity space. The chemistry of oxygen plasmas is fairly complicated due to the high number of important species and reaction channels. There are different recommended sets of processes and related cross sections / rate coefficients available in the literature [9-12]. These sets differ in many respects: in the number of species and reaction processes considered, in the values of cross sections, and in the handling of different processes. Most of the models consider electrons, O_2^+ ions, and O^- ions, as important charged species. The collision processes between electrons and O_2 molecules include elastic scattering, excitation to rotational, vibrational and electronic levels, ionization, dissociative excitation, and dissociative attachment. For O^- ions we consider elastic scattering with O_2 , detachment in collisions with electrons and O_2 molecules, and – identified as the dominant loss channel – mutual neutralization with O_2^+ ions. Another important loss process of O^- ions is via their collisions with singlet delta oxygen molecules, $O_2(a^1\Delta_g)$, of which the density may be significant in CCPs. Unfortunately, it is difficult to estimate the $O_2(a^1\Delta_g)$ density self-consistently, therefore we neglect this process. One has to bear in mind that, consequently, our calculations may overestimate the positive and negative ion densities, which are unfortunately not accessible in the experiment (because the hairpin probe only measures the electron density). For O_2^+ ions the charge transfer collision with O_2 is included. The presence of O^- ions results in the formation of an electronegative bulk plasma,

where the positive and negative ions are present with comparable densities. Under such conditions the plasma density is determined by the balance of the negative ions, as these cannot escape to the electrodes. In our work we adopt the reaction and cross section set proposed in [9] (also known as the 'xpdpl' cross section set), with some modifications. Compared to the original set (i) we replace the elastic collision cross section with the elastic momentum transfer cross section of [13] and use isotropic scattering in our code, and (ii) we adopt the charge transfer cross section of [10] to model ion transport more realistically, which is crucial for the reproduction of the IFEDF at the electrodes.

The excitation (generator) voltage waveform consists of N harmonics ($N = 1 \dots 4$) having amplitudes and phase angles, ϕ_k and Θ_k ($k = 1 \dots N$), respectively, as

$$\phi(t) = \sum_{k=1}^N \phi_k \cos(2\pi k f_1 t + \Theta_k), \quad (1)$$

where f_1 is the base frequency, and the amplitudes of the individual harmonics are set according to the following equations, to achieve the greatest self bias:

$$\phi_k = \phi_0 \frac{N-k+1}{N} \quad ; \quad \phi_0 = \frac{2N}{(N+1)^2} \phi_{PP}, \quad (2)$$

where ϕ_{PP} is the peak-to-peak voltage. The "peaks" voltage waveforms are generated by setting all phase angles to zero, while "valleys"-type waveforms are obtained by changing the phase angles of all the even harmonics to $\Theta_k = \pi$. Figure 2(a) illustrates "peaks"-type voltage waveforms given by (1) for different number of harmonics, for $\phi_{PP} = 150$ V. Note that the need for a balance of fluxes of positive and negative particles on time average to either of the electrodes will shift this voltage waveform by a constant DC self bias η .

4. Results

Here we present the experimental and simulation results for $p = 50$ mTorr pressure. The base harmonic frequency is $f_1 = 13.56$ MHz. We used peak-to-peak voltages of $\phi_{PP} = 150$ V and 200 V. Figure 2(b) shows the measured and calculated values of the DC bias. Here the bias is given in a normalized value, as η / ϕ_{PP} . For the "peaks"-type waveforms we find a negative bias, while "valleys"-type waveforms result in $\eta > 0$. The magnitude of the normalized bias increases with increasing number of harmonics.

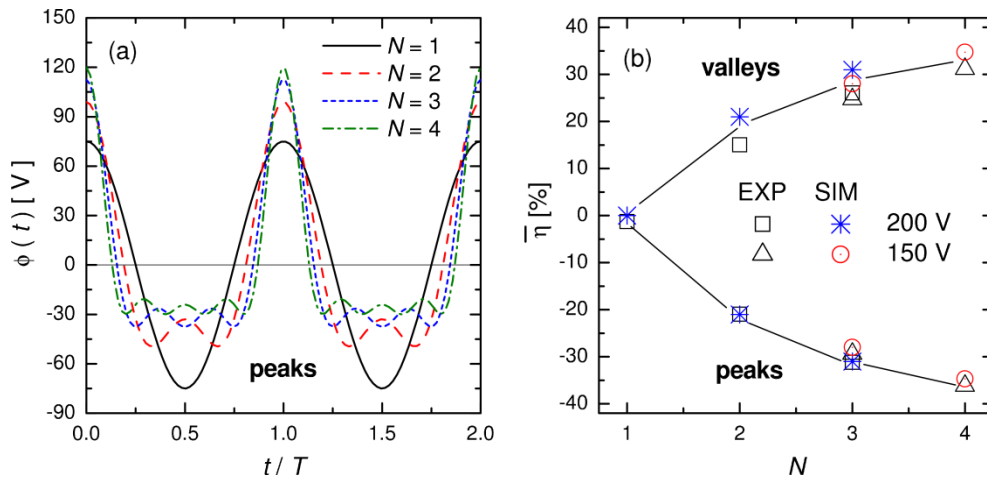


Figure 2. (a) "Peaks"-type voltage generator waveforms (note that the discharge voltage includes the additional self bias for $N > 1$), for $\phi_{PP} = 150$ V. (b) Measured (EXP) and calculated (SIM) values of the normalized DC self bias for different numbers of harmonics (N). In panel (b) the lines intend to guide the eyes only.

Figure 3 presents the spatial distribution of charged particles in the single frequency case ($N = 1$, with $\phi_{PP} = 200$ V, in (a)) and in the case of four harmonics ($N = 4$, with $\phi_{PP} = 150$ V, "peaks"-type waveform, in (b)). In the former case we obtain a spatially symmetrical distribution of the densities. At $N = 4$ the sheath at the powered electrode (situated at $x = 0$) expands and the density peaks are shifted towards the grounded electrode (situated at $x = L$). In both cases, and in the other cases that we have studied, the plasma is always found to be strongly electronegative: the negative ion density largely exceeds the electron density. Panels (c) and (d) display the spatiotemporal distribution of the electron heating rate, for the two cases. We observe two important contributions to electron heating: (i) at the expansion of the sheaths electrons are accelerated towards the bulk plasma thereby gaining energy – this is the well-known α -mechanism that is dominant in most CCPs; (ii) due to the high electronegativity of the plasma a relatively strong electric field has to build up in the bulk, which accelerates electrons significantly; this mode is termed as the Ω -mode, e.g. [14]. The symmetry of the heating and cooling patterns observed in the single-frequency case (figure 3(c)) breaks down at $N > 1$. The α -heating becomes very strong in the vicinity of the powered electrode (at $x = 0$), due to the very fast expansion of that sheath forced by the specific waveform, while at the grounded side heating is much weaker during the expansion phase (see figure 3(d)). Heating in the bulk also occurs mainly when the sheath at the powered electrode is expanding.

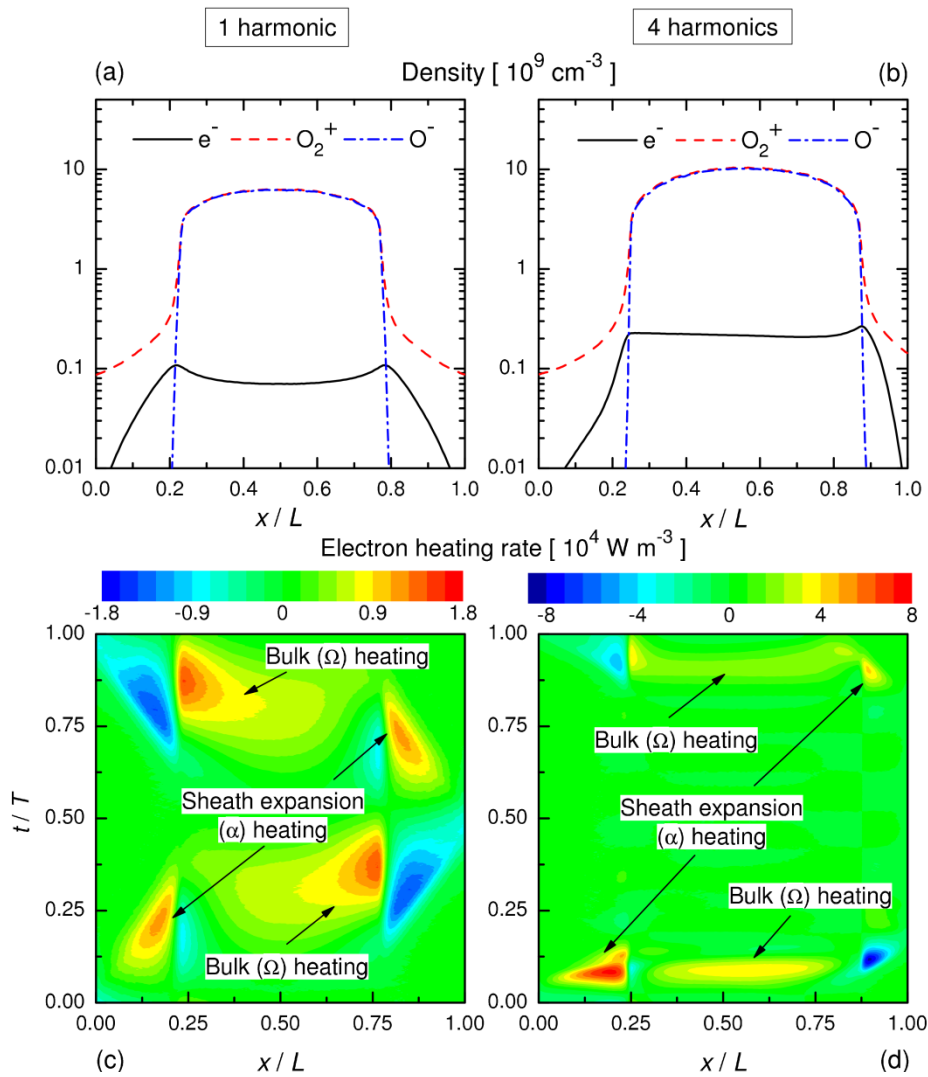


Figure 3. Spatial distribution of charged particles: (a) single frequency case ($N = 1$, $\phi_{PP} = 200$ V) and (b) with four harmonics ($N = 4$, $\phi_{PP} = 150$ V, "peaks"-type waveform). Corresponding space- and time-resolved electron heating rates (c) and (d), with important contributions indicated. The powered electrode is situated at $x = 0$.

Finally we compare the flux-energy distributions of the O_2^+ ions at the grounded electrode, for different conditions. Figure 4 shows both experimental data and simulation results, for the case of 3 harmonics and $\phi_{pp} = 150$ V. At the low pressure (50 mTorr) considered here, the sheaths are weakly collisional, so that a significant fraction of the ions arrives at the electrodes with an energy corresponding to the maximum sheath voltage. The experimental and simulation results are in good agreement. The IFEDF can be changed to a great extent by varying the excitation waveform, in particular a change between the "peaks" and "valleys" waveforms changes the maximum ion energy by a factor of 3 in the case of use of three consecutive harmonics in the excitation waveform, as shown in figure 4. The small differences in the locations and the shapes of the peaks are due to the imperfections of the model.

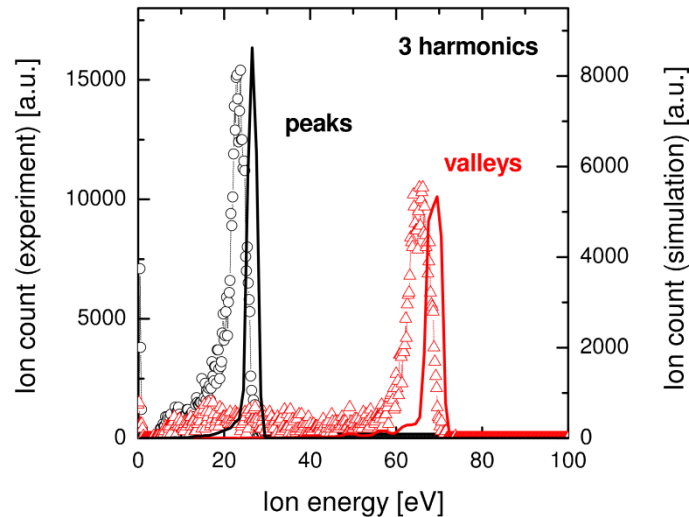


Figure 4. Measured (symbols) and calculated (solid lines) ion flux-energy distributions at $\phi_{pp} = 150$ V, with an excitation waveform consisting of three harmonics.

This work was supported by the Hungarian Fund for Scientific Research (OTKA) via the grant K105476, and by Agence Nationale de la Recherche project "CLEANGraph (ANR-13-BS09-0019).

5. References

- [1] Makabe T and Petrovic Z Lj 2006 *Plasma Electronics: Applications in Microelectronic Device Fabrication* (London: Taylor and Francis); Lieberman M A and Lichtenberg A J 2005 *Principles of Plasma Discharges and Materials Processing* 2nd edn. (New York: Wiley-Interscience)
- [2] Heil B G, Czarnetzki U, Brinkmann R P and Mussenbrock T 2008 *J. Phys. D: Appl. Phys.* **41** 165202; Donkó Z, Schulze J, Heil B G and Czarnetzki U 2009 *J. Phys. D: Appl. Phys.* **42** 025205; Schulze J, Schuengel E and Czarnetzki U 2009 *J. Phys. D: Appl. Phys.* **42** 092005
- [3] Delattre P A, Lafleur T, Johnson E V and Booth J P 2013 *J. Phys. D: Appl. Phys.* **46** 235201
- [4] Patterson M M, Chu H Y and Wendt A E 2007 *Plasma Sources Sci. Technol.* **16** 257
- [5] Lafleur T, Delattre P A, Booth J P, Johnson E V and Dine S 2013 *Rev. Sci. Instrum.* **84** 015001
- [6] Hamers E A G, van Sark W G J H M, Bezemer J, Goedheer W J and van der Weg W F 1998 *Int. J. Mass Spectrom. Ion Process.* **173** 91
- [7] O'Connell D, Zorat R, Ellingboe A R and Turner M M 2007 *Phys. Plasmas* **14** 103510
- [8] Birdsall C K 1991 *IEEE Trans. Plasma Science* **19** 65; Verboncoeur J P 2005 *Plasma Phys. Control. Fusion* **47** A231; Matyash K, Schneider R, Taccogna F, Hatayama A, Longo S, Capitelli M, Tskhakaya D and Bronold F X 2007 *Contrib. Plasma Phys.* **47** 595
- [9] Vahedi V and Surendra M 1995 *Computer Phys. Commun.* **87** 179
- [10] Bronold F X, Matyash K, Tskhakaya D, Schneider R and Fehske H 2007 *J. Phys. D: Appl. Phys.* **40** 6583

- [11] Schuengel E, Zhang Q-Z, Iwashita S, Schulze J, Hou L-J, Wang Y-N and Czarnetzki U 2011 *J. Phys. D: Appl. Phys.* **44** 285205
- [12] Gudmundsson J T, Kawamura E and Lieberman M A 2013 *Plasma Sources Sci. Technol.* **22** 035011
- [13] Biagi-v8.9 database (Cross sections extracted from PROGRAM MAGBOLTZ, VERSION 8.9 March 2010), www.lxcat.net, retrieved on November 25, 2014.
- [14] Schulze J, Derzsi A, Dittmann K, Hemke T, Meichsner J and Donkó Z 2011 *Phys. Rev. Lett.* **107** 275001

RADIOFREQUENCY AND DIRECT CURRENT BREAKDOWN IN HYDROGEN: EXPERIMENT AND KINETIC SIMULATIONS

Ihor Korolov¹, Zoltan Donkó¹

¹*Wigner research centre for physics Institute for Solid State Physics and Optics, Wigner Research Centre for Physics, Hungarian Academy of Sciences, Konkoly-Thege Miklos str. 29-33, H-1121 Budapest, Hungary*

E-mail: korolov.ihor@wigner.mta.hu

We report on an experimental and modelling study of the breakdown of hydrogen in static (DC) and radio-frequency (RF = 13.56 MHz) electric fields. For the simulation of the breakdown event, a simplified model is used, where only electrons are traced by Monte Carlo simulation. The experimental data of DC breakdown are used for determination of the effective secondary electron emission coefficient. A very good agreement between the experimental and the calculated breakdown characteristics is found for the RF case.

1. Introduction

The complex phenomenon of gas breakdown has been attracting considerable attention from the beginning of gas discharge research [1]. For DC excitation the details of the underlying processes are quite well understood, thanks to a large number of experimental and theoretical studies for different gases and conditions, e. g. [2-5]. In the case of RF excitation both the experiments, as well as the calculations are more complicated compared to the DC scenario. For conditions when the electron oscillation amplitude in the RF field is smaller than the electrode gap, gas phase charge reproduction is dominant and the effects of surface processes (electron reflection and secondary electron emission) are negligible. When the oscillation amplitude and the gap size become comparable (at low pressure and/or lower frequency), surface processes start playing a role too.

The electrical breakdown and discharges in hydrogen have been a subject of intense research due to the wide usage in a various technological processes: thin-film deposition, etching, cleaning, etc. [6-7]. The breakdown in hydrogen has been previously studied both for DC [8,9] and RF fields [10,11]. More recent studies of direct-current gas discharges also concentrated on micro plasma sources for which the breakdown phenomena at small electrode gaps was investigated [12]. The measured breakdown characteristics in the RF field can be also used for the determination of the electron-drift velocity in hydrogen [13].

Our aim here is to carry out a study of the breakdown phenomena in hydrogen, both experimentally and by kinetic simulations based on the Monte Carlo (MC) technique [14], to provide a deeper understanding of the relevant effects. Most of similar studies for RF fields were reported for noble gases in ref. [15] and for synthetic air in our previous work [16]. As far as we know there is no published work using the same approach for the case of hydrogen.

2. Experimental

The schematic of the experimental set-up is shown in figure 1. The geometrically symmetric discharge cell consists of two stainless steel electrodes (diameter: $D = 7.5$ cm) placed inside a glass cylinder at a distance of $L = 1.0$ cm from each other. The cell is completely geometrically symmetric and connected to a vacuum system using 6 mm inner diameter and 30-40 cm long glass tubes in order to minimize stray capacitances that could introduce an asymmetry and, thus, influence the measurements. Before the experiments, the cell is pumped down to $< 10^{-6}$ Torr by a turbo molecular pump (TMP). We use 5.0 purity hydrogen gas ($H_2O \leq 3$ ppm, $O_2 \leq 2$ ppm, $C_nH_m \leq 0.5$ ppm, $N_2 \leq 5$ ppm) at a slow flow (2-6 sccm), regulated by a flow controller. For further purification a cryogenic trap (filled with liquid nitrogen) is used. Before starting the breakdown measurements, the electrode surface is cleaned by running (~ 5 mA) DC discharges with both polarities for about 10 min. To check the cleanliness of the cell, the DC discharge emission spectra was recorded in a wide spectral range (250-800 nm). No

noticeable traces of water vapour (OH bands) were observed. For the DC measurements the high voltage is established by a PS325 (Stanford Research Systems) power supply, interfaced with a computer via GPIB. For the radiofrequency measurements ($f = 13.56$ MHz) we have built a high-voltage push-pull oscillator similar to that described in ref. [17]. In the experiment the two electrodes are driven by the generator with potentials $U_1 = U_0 \sin(2\pi f t)$ and $U_2 = -U_0 \sin(2\pi f t)$, respectively. When the breakdown event occurs, the breakdown voltage is defined as the peak value of the difference of two potentials, $V_{BR} = 2U_0$. The actual voltage on the cell is measured by two voltage divider probes (Agilent 10076B), connected to two inputs of a digitizing oscilloscope (PicoScope 6403B). The breakdown event is detected by several methods: (a) the detection of the light of the plasma using a broad band photodiode (58-262 Edmund Optics). (b) A change of frequency of the high voltage oscillator (or sudden drop of the voltage amplitude) due a change of the impedance of the cell. (c) Observing an increase of the power consumption of the RF oscillator. More detailed information about the experimental set-up and the measurements methods can be found elsewhere [16].

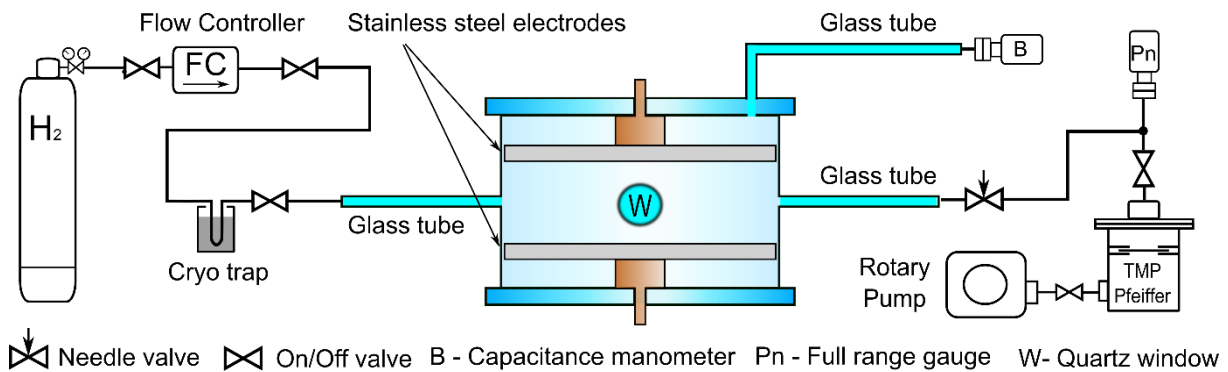


Fig. 1. Schematic of the breakdown cell and the vacuum system

3. Simulations

DC case

For DC breakdown, surface processes play a critical role and cannot be neglected. Different species such as photons, electrons, ions and metastable can contribute to secondary emission at the cathode. For the conditions covered here ions are expected to have the major impact. Unfortunately, the data availability for an energy dependent electron yield for H_2^+/H^+ ions and different metals is very limited. Therefore, we have combined the experimental and modelling studies to derive the effective secondary electron yield, γ^* , defined as a ratio of the electron current to ion current at the cathode and it basically accounts for the contributions of the other species (electrons, photons, metastables). In our simulation code only electrons are traced using Monte-Carlo technique [14], which provides a fully kinetic description under the condition of nonlocal transport. The simulation is three dimensional in velocity space and one dimensional in real space. We trace electrons emitted from the cathode along their path to the anode. The initial number of electrons is 3×10^3 . The cross section used for $e^- - H_2$ collisions are taken from ref. [18]. The reflection probability of electrons from the electrode surface is taken to be $\rho = 0.2$ [19]. Following the additional electrons created in ionizing collisions, we simulate a high number of complete electron avalanches to reach a good level of statistics. In the simulation, it is assumed that all ions created between the electrodes reach the cathode due to their directed motion caused by the electric field. The simulations are executed for the experimentally measured values of breakdown voltage and pressure to determine the secondary yield as ratio between the number of emitted electrons and incoming ions.

RF case

In contrast to the DC case, in RF simulations the time dependent evolution of the electron density is followed. To greatly reduce the computational time, here we still trace electrons only. In the RF field,

ions due to their mass respond only to the time-averaged field, which is zero (no space charges are presented). Thus, the motion of the ions in the cell can be taken as diffusive. Considering only the lowest order of the diffusion mode in the cylindrical geometry, the fraction of ions, f_i , that reaches the electrodes can be easily estimated. When ion is created a new electron is emitted from one of the electrodes with a probability γf_i in the next RF cycle at a random time. At the beginning, for a fixed set of conditions, we seed 3×10^3 electrons in the centre of the electrode gap. The simulation time is set to 500 RF cycles and the number of electrons is continuously monitored. The time dependent density during the last 250 cycles is then fitted by a straight line. The breakdown event is recognized when the slope of the line is near zero.

4. Results

DC case

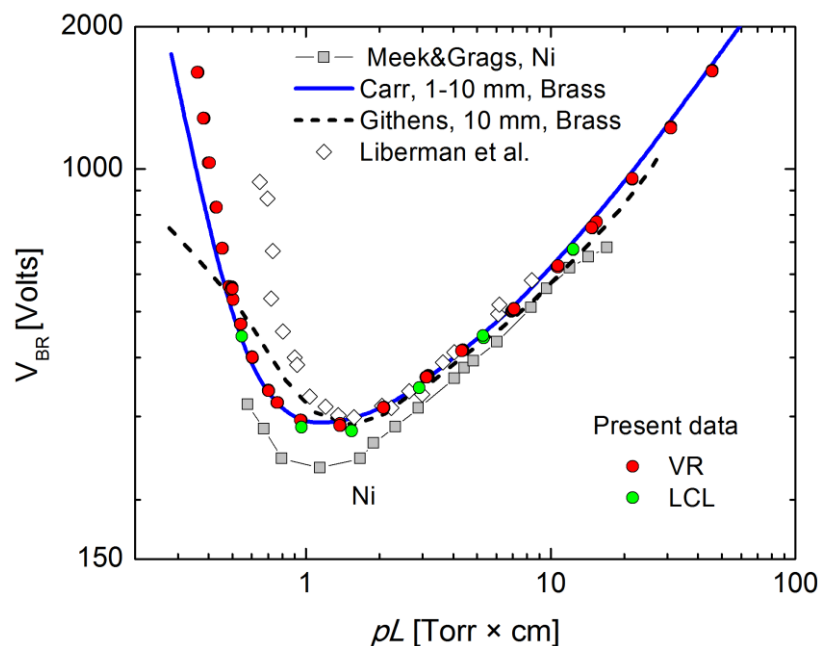


Fig. 2. Breakdown voltages obtained in the experiments in DC mode by two different methods (VR – voltage ramp and LCL – low current limit). Paschen curves obtained in previous studies [7-9,11] for different electrode materials are also plotted.

Figure 2 shows the experimental data obtained in DC mode and data obtained in some earlier works. Two methods were applied in the measurements of the breakdown curve: (i) VR – voltage ramp method, where for the given pressure voltage is slowly increased ($0.5-1.5 \text{ V s}^{-1}$) until the breakdown event occurs; (ii) LCL – low current limit method, proposed by Phelps and Jelenkovic [20], where the breakdown voltage is determined as a sustaining voltage of a Townsend discharge in the limit of zero current. The data obtained by these methods show a high degree of consistency results. It can be clearly seen that the right part of the curve is also in good agreement with results of previous works. Usage of different electrode materials and their cleanliness can explain deviations at the left part of the Paschen curve. The measurement gives a location of the Paschen minimum at $V_{BR,\min} = 290 \text{ V}$ and $pL = 1.2 \text{ Torr}\times\text{cm}$, which is comparable to that obtained by Carr [9]. The main purpose of the measurements is to obtain the effective electron yield, γ^* , as a function of E/p using our simulation code. Calculated values of the yield are shown in figure 3. The smallest γ^* (~ 0.008) is obtained for low E/p and it increases significantly towards to high E/p values. The present data are quite different from those obtained by Klas et al. [12] for molybdenum electrode and small gaps. The deviation can be explained by dependence of the effective yield on the electrode material and on the gap size as at high E/p , e.g., field emission from the cathode cannot be neglected.

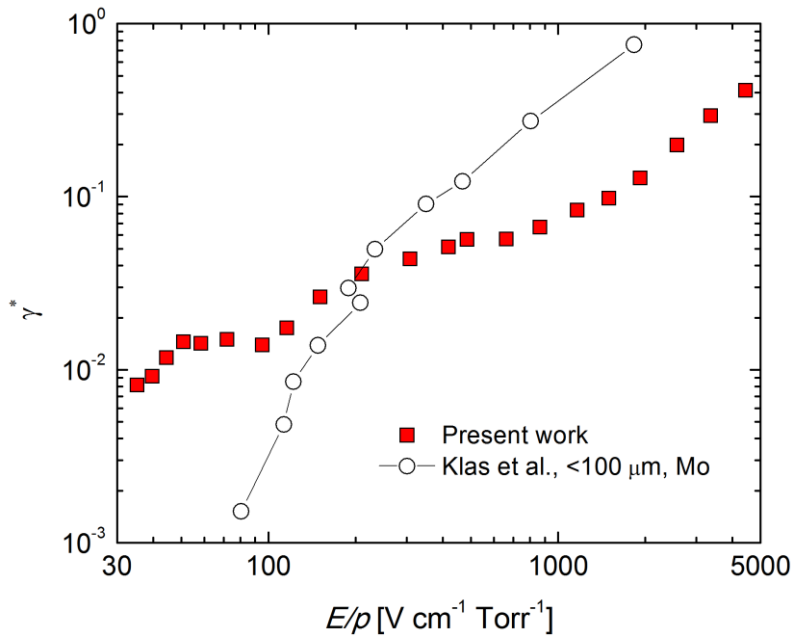


Fig. 3 Effective electron yield, γ^* , as a function of E/p . The open circles represent data studied for small gaps and molybdenum cathode by Klas *et al* [12].

RF case

The experimental breakdown curve measured at $f = 13.56$ MHz together with data measured in earlier studies are shown in figure 4. The shape of the curve can be explained in the following way: (i) at high pressures the amplitude of electron oscillations is smaller than the gap size and, therefore, the properties of the electrodes do not play a role. For precise description of this region only gas-phase processes have to be taken into account. (ii) At lower pressures, when the amplitude of the oscillations becomes comparable with the gap length, electrons can reach the surfaces and only a small fraction of them can be reflected back and create avalanches towards the opposite electrode. The bending point at $p = 3$ Torr and $V_{BR} = 350$ V shows the region where the ion impact electron emission becomes dominant. A more detailed analysis of the breakdown curve behavior for different gasses, gaps and frequencies can be found elsewhere [8,16,21].

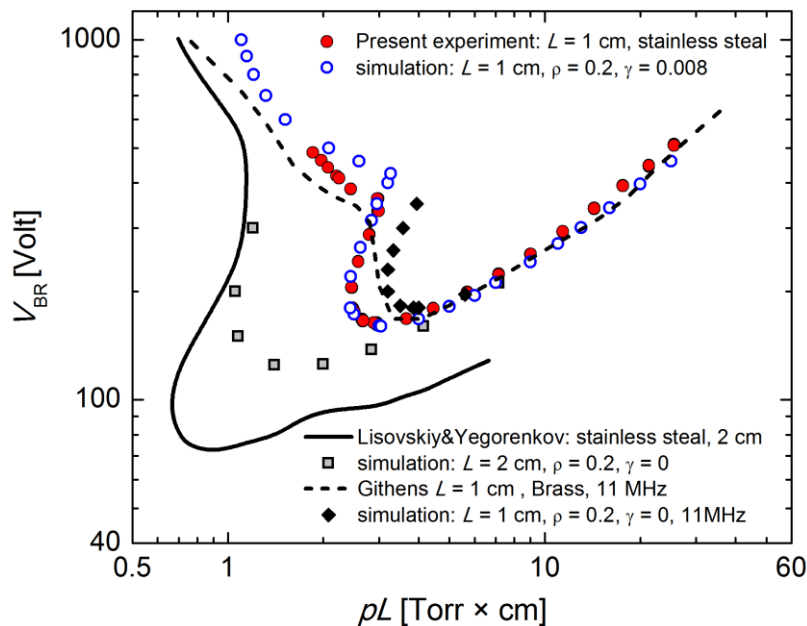


Fig.4 Comparison of the experimental breakdown voltage values with simulation results. The dashed line represents experimental results measured by Githens [11] at $f = 11$ MHz and $L = 1$ cm. The solid line is from Lisovskiy and Yegorenkov [10] at $f = 13.56$ MHz and $L = 2$ cm.

As it has been mentioned before, the motion of ions in the RF field can be taken as diffusive and, therefore, $\gamma^*(E/p)$ at $E/p \rightarrow 0$ are expected to be applicable. In the simulations to reproduce the measured BD curve, the secondary electron yield is taken to be $\gamma^* = 0.008$ - the lowest value of γ^* obtained for the DC case. The results obtained from the simulation (see figure 4) show that, despite of the simplifications of our model, the measured curve can be accurately reproduced up to the bending point ($pL = 3 \text{ Torr}\times\text{cm}$ and $V_{BR} = 350 \text{ V}$). The slight deviation from the measured data at this point can be explained by the fact that hydrogen ions are quite light and apparently can gain some energy from the electric field and the energy dependence of γ has to be taken into account.

Considering only gas-phase processes and reflection of the electrons from the electrodes we could also precisely reconstruct the experimental curve (for $pL > 3 \text{ Torr}\times\text{cm}$) measured by Githens [11] at $f = 11 \text{ MHz}$. The horizontal shift of the 11 MHz curve toward higher pressures (with respect to the curve corresponding to 13.56 MHz) is due to the fact that at lower frequencies electrons oscillate with higher amplitude and, thus, more of them can be absorbed at the electrode surface. By increasing a gap size the effect is opposite to the low frequency scenario, here less electrons can reach the electrodes and the breakdown curve shifts to the low pressure direction (see, Figure 4). The large deviation of the measured curve by Lisovski and Yegorenkov [10] from the calculated curve for $L = 2 \text{ cm}$ is not clearly understood. According to the simulation results, at $pL > 2 \text{ Torr}\times\text{cm}$, the charge reproduction is dominated by gas phase reactions only and the breakdown voltage is not dependent on the surface parameters. Taking into account this fact, the deviation can be explained only by some systematic error or by presence some impurities in the measurements.

5. Conclusions

We have carried out a combined experimental and kinetic simulation study of the breakdown in hydrogen under DC and RF (13.56 MHz) excitation. The experiments have been performed for pressures up to 30 Torr and with $L = 1 \text{ cm}$ gap size, using a glass cell with plane parallel stainless steel electrodes.

A simulation model has been developed that traces the electrons at the kinetic level. Based on this model the effective electron yield, as a function of the reduced electric field, $\gamma^*(E/p)$, has been determined from the measured DC Paschen curve. Despite the simplifications used in the model, the simulations showed that the whole breakdown curve can be quite accurately reproduced adopting a constant effective electron yield $\gamma^* = 0.008$.

Acknowledgement

This work has been financially supported by the Hungarian Scientific Research Fund, via Grant OTKA K105476. Thanks are due to Scott Anderson for discussions on the construction of the high-voltage RF generator.

6. References

- [1] J.M. Meek and J.D. Graggs, 1953 *Electrical breakdown of gases*, Oxford, Clarendon Press.
- [2] A.V. Phelps and Z. Petrović, 1999 *Plasma Sources. Sci. Technol.* **8** R21.
- [3] P. Hartmann, Z. Donkó, G. Bánó, L. Szalai, and K. Rózsa, 2000, *Plasma Sources. Sci. Technol.* **9** 183.
- [4] M. Klas, Š. Matejčík, B. Radjenović and M. Radmilović-Radjenović, 2011 *EPL*, **95** 35002;
- [5] G. Malović, A. Strinić, A. Živanov, D. Marić and Z. Lj. Petrović, 2003, *Plasma Sources Sci. Technol.* **12** S1.
- [6] P. K. Chu, X. Lu 2014 *Low temperature plasma technology*, CRC Press Taylor & Francis Group.
- [7] M. Lieberman and A. J. Lichtenberg 2005 *Principles of plasma discharges and materials processing*, Hoboken, New Jersey, John Wiley & Sons, Inc.
- [8] J. M. Meek and J. D. Craggs 1953 *Electrical Breakdown of Gases* (Oxford: Clarendon Press)
- [9] R. Carr 1903 *Phil. Trans. R. Soc.* **201** 403
- [10] V. A. Lisovski and V.D. Yegorenkov 1998 *J. Phys. Appl. Phys* **31** 3349
- [11] S. Githens, 1940 *Phys. Rev.* **57** 822
- [12] M. Klas, Š. Matejčík, B. Radjenović and M. Rdmilović-Radjenović, 2014, *Physics of Plasmas*, **21** 103503; M. Radmilović-Radjenović, B. Radjenović, Š. Matejčík, M. Klas 2013 *EPL* **103** 45002
- [13] V. Lisovkiy, J-P. Booth, K. Landry, D. Douai, V. Cassagne and V. Yegorenkov 2006 *J. Phys. D: Appl. Phys.* **39** 660

- [14] A. Tran Ngoc, E. Marode, P.C. Johnson 1977 *J. Phys. D: Appl. Phys.* **10** 2317; S. Dujko, Z.M. Raspopović and Z. Lj Petrović Z 2005 *J. Phys. D: Appl. Phys.* **38** 2952; S. Longo 2006 *Plasma Sources Sci. Technol.* **15** S181; Z. Donkó 2011 *Plasma Sources Sci. Technol.* **20** 024001
- [15] Z. Lj. Petrović, J. Sivos, M. Savić, N. Skoro, M. Radmilović-Radenović, G. Malović, S. Gocić and D. Marić 2014 *J. Phys.: Conf. Ser.* **514** 01204; M. Savić, M. Radmilović-Radjenović, M. Suvakov and Z. Lj. Petrović 2014 *27th Summer School and Int. Symp. on the Physics of Ionized Gases (Belgrade, Serbia, 26–29 August 2014)* p 411
- [16] I. Korolov, A. Derzsi, Z. Donkó 2014 *J. Phys. D: Appl. Phys.* **47** 475202
- [17] R. M. Jones, D. Gerlich, S.L. Anderson 1997 *Rev. Sci. Instrum.* **68** 3357; R. M. Jones and L. S. Anderson 2000 *Rev. Sci. Instrum.* **71** 4335
- [18] A.V. Phelps http://jila.colorado.edu/~avp/collision_data/electronneutral/
- [19] R. Kollath 1956 *Encyclopedia of Physics* vol **21** (Berlin: Springer)
- [20] A. V. Phelps and B. M. Jelenković 1988 *Phys. Rev. A* **38** 2975
- [21] V. Lisovski, J-P. Booth, K. Landry, D. Douai, V. Cassagne, V. Yegorenkov 2008 *EPL*, **82** 15001

FORCE BALANCE OF DUST PARTICLES IN RF+DC DISCHARGES

N. Kh. Bastykova¹, A. Zs. Kovács², S. K. Kodanova¹, T. S. Ramazanov¹,
I. Korolov², P. Hartmann², Z. Donkó²

¹*IETP, Al-Farabi Kazakh National University, 71 Al-Farabi av., Almaty 050040, Kazakhstan*

²*Institute for Solid State Physics and Optics, Wigner Research Centre for Physics,
Hungarian Academy of Sciences, 1525 Budapest, POB. 49, Hungary*

E-mail: bastyk_nuriya@mail.ru

Experiments and particle-based kinetic simulations were performed to obtain the equilibrium levitation height of dust particles in plane parallel electrode discharges in low pressure argon gas, established by combined RF and DC excitation. The computed values were compared to experimental data. The good overall agreement of the simulation results and the experimental data serves as verification of our gas discharge, dust charging, as well as dust force balance models.

1. Introduction

Layers of dust particles are routinely generated in low-pressure gas discharges and many of their properties (structure, phase transitions, collective excitations, and transport properties) have thoroughly been investigated. For a range of conditions (properties of the dust particles and characteristics of the discharge plasma) a single layer of dust particles can be levitated, the position of which is defined by the balance of the forces acting on the particles. This position can be tuned by changing the characteristics of the plasma that surrounds the particles and serves as a source of charging of the dust [1-4].

The position of the dust layer can easily be determined experimentally by side-on observation of the system. Parallel to experiments, theoretical models of the dust charging, combined with a discharge model, make it possible to calculate this position. Our aim is here to examine the validity of such a model via measuring and calculating the position of a dust layer in a radiofrequency (RF) discharge in the presence of an additional DC bias that allows manipulation of the equilibrium position.

2. Experiment

In our experiments two flat aluminium electrodes with a diameter of $D = 170$ mm were placed horizontally, at a distance of $L = 55$ mm from each other, inside a glass cylinder, as shown in Figure 1. The lower electrode was powered via a coaxial feedthrough by an RF power supply operating at $f_{\text{RF}} = 13.56$ MHz. We applied a peak-to-peak voltage $V_{\text{pp}} = 200$ V at $p = 1.8$ Pa argon pressure and $V_{\text{pp}} = 175$ V at $p = 3.6$ Pa, at a gas flow of approx. 0.1 sccm. A separate power supply, connected to the powered electrode via a RF choke made it possible to introduce an *external* DC bias. We note that due to the high degree of symmetry of the electrode configuration the DC *self bias* of the plasma was below 1 V.

Melamine-formaldehyde (MF) spherical micro-particles with a radius of $r_d = 2.19$ μm were dropped into the discharge plasma through a small opening in the centre of the upper, grounded electrode. This opening was covered with a 400 lines per inch stainless steel mesh, to confine the plasma between the electrodes and to provide a proper boundary condition for the modeling studies. The particle cloud was illuminated through a side window with a vertical light sheet from a 532 nm, 200 mW laser source. We used a Jai Pulnix RM-1405 CCD camera, which was equipped with a 50 mm focal length photographic lens that imaged the light scattered from the dust particles. The levitation height was determined from the recorded images after performing a pixel to mm length calibration.

Conditions for reproducible measurements were reached after applying a daylong pumping followed by 10 minutes DC discharges with both positive and negative voltages applied to the lower electrode, with approximately 7 mA current. These DC discharges served to pre-condition the aluminium electrodes by sputtering, as this material has a high affinity for surface oxidation, resulting in large and unpredictable variations of the surface properties, like secondary electron emission yield

and electron reflection ability. This preparatory procedure provided the necessary cleanliness of the system, which had a base pressure of about 2×10^{-6} mbar.

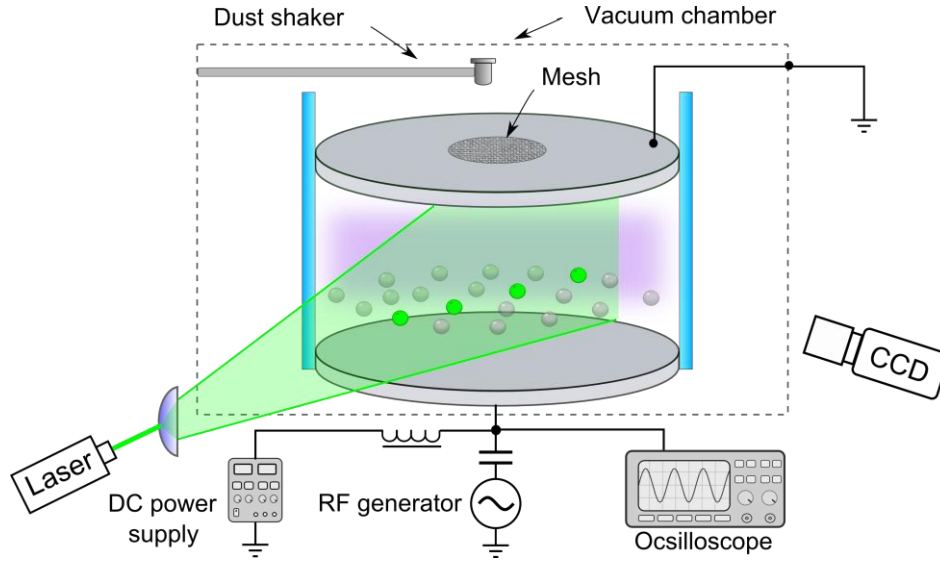


Fig. 1. Schematics of the experimental setup

3. PIC/MCC simulation

The discharge was described by Particle-in-Cell simulation incorporating Monte Carlo treatment of collision processes (PIC/MCC) [5-8]. The code considers one spatial dimension and traces about 2×10^5 superparticles, representing electrons and argon ions. We assume that the density of the dust is low, i.e. the presence of the dust has no influence on the discharge characteristics. This approach – although it breaks the complete self-consistency – avoids the problems that arise because of the extremely different timescales of the motion of electrons, ions, and the dust particles [9,10]. For the interactions of charged particles with electrode surfaces we account for secondary electron emission (with $\gamma = 0.15$) and the reflection of electrons (with probability of $\eta = 0.5$).

The main aim of our simulations is to determine the position x_d , where the dust layer settles in the discharge. We expect this position to be in the vicinity of the sheath / bulk boundary above the lower electrode of the discharge, at a position defined by the balance of the vertical forces acting on the particles (we neglect the dust-dust interaction, due to the low dust density, so only vertical forces are important). We contemplate the following three forces to be important: gravity, electrostatic, and ion drag forces.

- The force due to gravity is given as

$$F_g = m_d g, \quad (1)$$

where m_d is the mass of the dust particles.

- The electrostatic force is

$$F_{el} = \langle E(x) \rangle q_d, \quad (2)$$

where $\langle E(x) \rangle$ is the time-average of the electric field at position x (as obtained from the PIC/MCC simulation of the discharge without dust) and q_d is the dust charge. The calculation of this force needs the determination of the charge of the dust particles, q_d . For that, the first step is to calculate the floating potential, ϕ_d . For the determination of ϕ_d we apply the method of [11], which is based on the interaction (collisions) between electrons and ions with the dust particles, described by cross sections that correspond to the Orbital Motion Limited (OML) approximation. We assume that a dust particle is

located at each grid point (x_k) in the simulation and carry out calculations for the floating potential at all grid points. We emphasize that this is only needed to determine one of the forces, F_{el} , as a function of x , and finally the real position of the dust layer will be determined by the balance of the three forces listed above. The calculation of the floating potential, φ_d , proceeds in the following way: we run the PIC/MCC simulation for one RF cycle, and meanwhile calculate the electron and ion fluxes to dust particles (Γ_e and Γ_i), by summing for all electrons and ions, respectively:

$$\Gamma_e(x_k) \propto \sum_p W_e v_p n_d(x) \sigma_{ed}[\varepsilon_p, \varphi_d(x_k)], \quad (3)$$

$$\Gamma_i(x_k) \propto \sum_p W_i v_p n_d(x) \sigma_{id}[\varepsilon_p, \varphi_d(x_k)], \quad (4)$$

where W denotes the superparticle weight, v_p is the velocity of the p -th electron or ion, n_d is the dust density, σ_{ed} and σ_{id} are the electron-dust and ion-dust collision (“collection”) cross sections [12]. The floating potential of the dust particles is found iteratively, by the requirement that (3) and (4) become equal in the stationary state, at all positions. $\varphi_d(x_k)$ is changed by ± 0.05 V after each RF simulation cycle at each position to reach the above mentioned requirement. Having obtained $\varphi_d(x_k)$ the equilibrium dust charge is found adopting the simple “capacitor model” according to which:

$$q_d = 4 \pi \varepsilon_0 r_d \varphi_d(x_k). \quad (5)$$

From this known value of the charge we can calculate the electrostatic force, with spatial dependence, $F_{el}(x)$.

□

- Ion drag force.

This force results from the momentum transfer from the ions flowing to the dust particles [13]. It consists of two parts: (i) ions absorbed by the dust particles, and (ii) ions deflected by the charge of the dust particles. The two corresponding force components are called the “collection force” and the “orbit force”:

$$F_i(x) = F_{i, \text{coll}}(x) + F_{i, \text{orb}}(x). \quad (6)$$

The usual way to handle these processes is to adopt the binary collision model. We proceed with the calculation based on the model of [13]. The required data (drift and mean velocities of the ions) are readily available from the PIC/MCC simulation.

Finally the equilibrium position of the dust particles is derived from the force balance:

$$F_{\text{tot}} = F_{el}(x_d) - F_g - F_i(x_d) = 0. \quad (7)$$

4. Results

First we illustrate the general characteristics of the discharge plasma. Figure 2 shows the spatial distribution of the ion density, obtained from the PIC/MCC simulation, for $V_{pp} = 200$ V, at $p = 1.8$ Pa. Besides the “base case” when the discharge is driven by a pure harmonic RF voltage waveform, we also display simulation results for two cases, when a DC voltage is superimposed at the driven electrode (external DC bias). While in the “pure” RF case the density profile is symmetrical, a superimposed DC bias shifts the peak as the sheath expands at the negatively biased electrode. As a consequence of the increased sheath length the bulk region of the plasma shrinks and the peak density decreases.

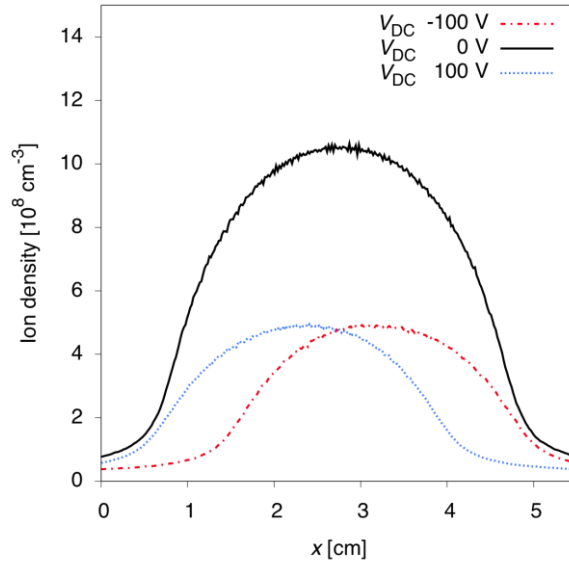


Figure 2. Ion density profiles of the RF and the RF+DC plasmas, for $V_{pp} = 200$ V, at $p = 1.8$ Pa.

Next we illustrate (in Figure 3) the spatial dependence of the different force components described above, for conditions $V_{pp} = 200$ V, at $p = 1.8$ Pa, with $V_{DC} = 0$ V and $V_{DC} = -100$ V. The panels of the figures show only a part of the electrode gap, where the model is expected to be valid. (We note that the OML theory breaks down deep inside the sheath, leading to non-physical solution.) Among the components of the ion drag force (6), the orbit force is found to be dominant, and the collision force is negligible. The equilibrium levitation position at $V_{DC} = 0$ V – found as $F_{tot}(x_d)=0$ – is $x_d = 0.86$ cm. When a negative DC bias is applied, the levitation height clearly increases as dictated by the increased sheath length at the powered electrode. The levitation position at $V_{DC} = -100$ V becomes $x_d = 1.69$ cm. The floating potential and the charge of the dust particles at the levitation height was found to be $\varphi_d \approx -9$ V, and $q_d \approx 13800$ C, respectively.

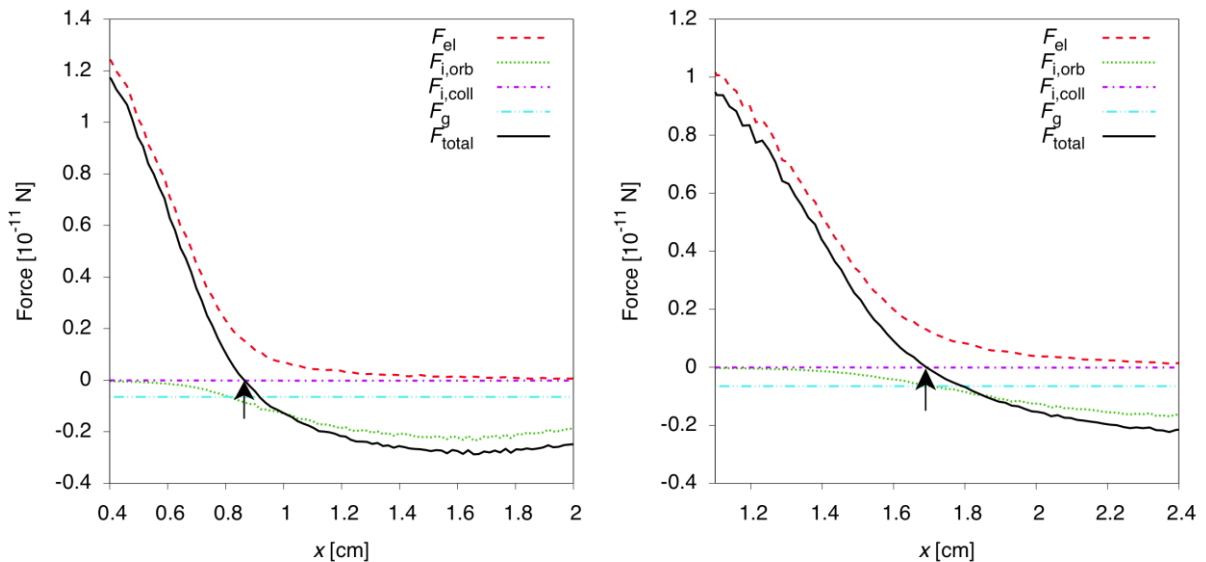


Figure 3. Spatial dependence of the different force components, for conditions $V_{pp} = 200$ V, at $p = 1.8$ Pa, $V_{DC} = 0$ V (left panel) and $V_{DC} = -100$ V (right panel). The arrows indicate the equilibrium levitation positions for the respective conditions.

In the experiment as well as in the simulation the DC bias was scanned over a wide range. The results of these scans, carried out at the two different gas pressures, are given in Figure 4.

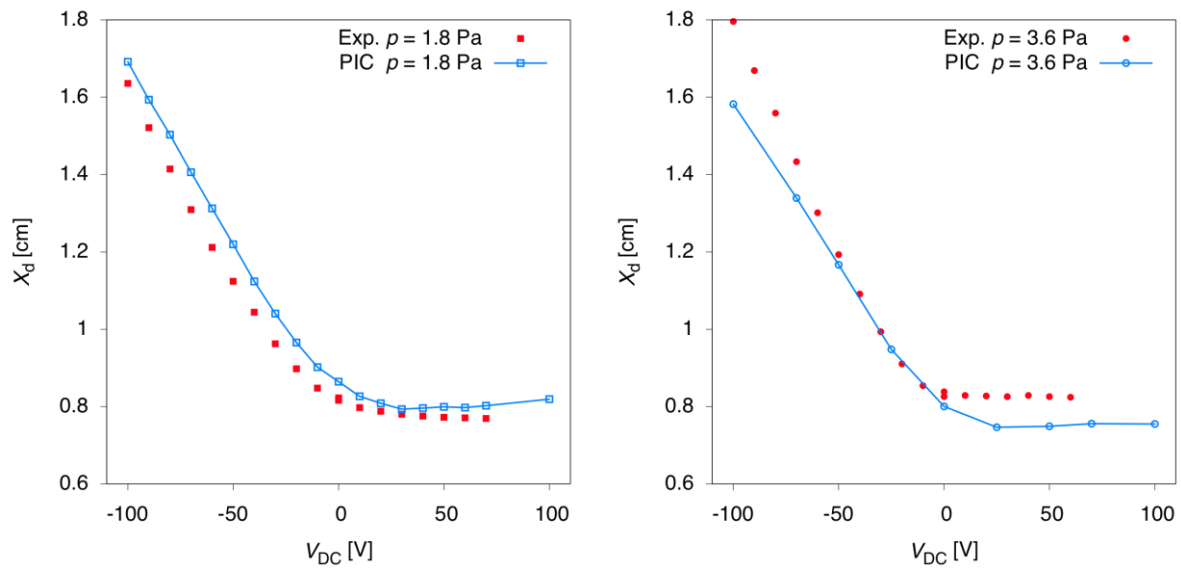


Figure 4. Equilibrium position of the dust layer as a function of the DC bias, V_{DC} , for conditions: $V_{pp} = 200$ V at $p = 1.8$ Pa (left panel) and $V_{pp} = 175$ V at $p = 3.6$ Pa (right panel).

We find a good agreement between the experimental and calculated values of the levitation height for both sets of data obtained at the different gas pressures. This agreement confirms that the simulation method (and code), as well as the charging and force balance models adopted in the work describe the plasma + dust system considerably well, and that they are applicable for the range of conditions covered here. Moreover, we confirm that the external DC bias is found to provide a solid control over the position of the dust layer.

This work has been supported by the Hungarian Fund for Scientific Research (OTKA) via grants K105476 and NN103150.

5. References

- [1] Klindworth M, Melzer A, Piel A and Schweigert V A 2000 *Phys. Rev. B* **61** 8404.
- [2] Nosenko V, Goree J and Piel A 2006 *Phys. Plasmas* **13** 032106.
- [3] Nosenko V, Ivlev A V and Morfill G E 2010 *Phys. Plasmas* **17** 123705.
- [4] Iwashita S, Schüngel E, Schulze J, Hartmann P, Donkó Z, Uchida G, Koga K, Shiratani M, and Czarnetzki U 2013 *J. Phys. D: Appl. Phys.* **46** 245202.
- [5] Birdsall C K 1991 *IEEE Trans. Plasma Sci.* **19** 65.
- [6] Matyash K, Schneider R, Taccogna F, Hatayama A, Longo S, Capitelli M, Tskhakaya D, and Bronold F X 2007 *Contrib. Plasma Phys.* **47** 595-634.
- [7] Longo S, Capitelli M, and Hassouni K 1997 *J. Phys. IV France* **07** C4-271-C4-281.
- [8] Donkó Z 2011 *Plasma Sources Sci. Technol.* **20** 024001.
- [9] Matyash K, Schneider R, and Kersten H 2005 *J. Phys.: Conf. Series* **11** 248-253.
- [10] Land V, Matthews L S, Hyde T W, Bolser D 2010 *Phys. Rev. E* **81** 056402.
- [11] Alexandrov A L, Schweigert I V, and Peeters F M 2008 *New J. Phys.* **10** 093025.
- [12] Khrapak S A and Ivlev A V 2010 in *Complex and Dusty Plasmas* (CRC Press, ed. by Fortov V E and Morfill G E)
- [13] Barnes M S, Keller J H, Forster J C, O'Neill J A, and Coultas D K 1992 *Phys. Rev. Lett.* **68** 313

A PHOTOELECTRIC FRANK-HERTZ EXPERIMENT AND ITS KINETIC SIMULATION

Péter Magyar, Ihor Korolov, Zoltán Donkó

*Institute for Solid State Physics and Optics, Wigner Research Centre for Physics
Hungarian Academy of Sciences, Konkoly-Thege Miklos str. 29-33, H-1121 Budapest, Hungary
E-mail: magyar.peter@wigner.mta.hu*

We have developed an experimental Franck-Hertz cell, which operates on the basis of photoemission. The electrical characteristics of this cell have been measured in argon gas over a wide range of pressure. The experiment, and in particular the electron kinetics, is analyzed via Monte Carlo simulation. A good agreement is obtained between the cell's measured and calculated electrical characteristics, the peculiarities of which are understood by the simulation studies.

1. Introduction

It was about 100 years ago when James Franck and Gustav Ludwig Hertz carried out their famous experiment [1] that demonstrated the quantized nature of atomic energy levels. Their work was awarded with the Nobel Prize in Physics in 1925.

In their experiment Franck and Hertz studied the behavior of electrons under the effect of electric fields, in the presence of mercury vapor. Their experimental cell had a cathode-grid-anode configuration. They launched electrons from a thermionic cathode in the first region of their experimental cell and accelerated them by a variable voltage ($V_{cg} > 0$). In the second region of the cell, which was separated from the first region by a wire grid, a decelerating voltage ($V_{ga} < 0$) was applied. Franck and Hertz measured the anode current I_a as a function of V_{cg} at a constant value of V_{ga} . The measured current had a peak-valley structure with a periodicity of $V_{cg} = 4.9$ V. This nature of the $I_a(V_{cg})$ characteristic was explained by the multiple excitation processes by individual electrons. Light emission from Hg vapor at $\lambda = 253.7$ nm has also been observed, which wavelength corresponds to an excitation energy of 4.9 eV.

The correct description of the Franck-Hertz (FH) experiment, which intends to go beyond qualitative explanations, requires a treatment at the level of the kinetic theory [2] due to the appearance of *nonequilibrium* effects [3] in the electron transport. Considering the fact that all previous works, that we are aware of, have dealt either with an experiment (without a rigorous kinetic analysis) or with the kinetic description of the phenomena taking place in FH cells (without a rigorous comparison to a recent experiment), a combined experimental and kinetic modeling study could provide a more complete physical picture of the electron kinetics in FH cells. Our aim is to carry out and present such a study [4].

2. Experiment

The scheme of our experimental setup is shown in Fig. 1. Our experiment differs in one major aspect from the original FH setting: We use the photoelectric effect to emit electrons from the cathode. To induce photoemission we use a frequency-quadrupled diode-pumped MPL-F-266 nm-3 mW laser providing $\lambda = 266$ nm radiation with a single-pulse energy of $1.5 \mu\text{J}$, in ~ 6 nsec pulses, at 2 kHz repetition rate. By eliminating the need for a heated cathode we can ensure a uniform gas density distribution inside the FH cell, which makes modeling more straightforward.

The cathode and anode electrodes are made of aluminium; they have a diameter of 61 mm and a thickness of 8 mm. A magnesium disk with 15 mm diameter is inserted into the center of the cathode, to serve as the source of photoelectrons, due to its high quantum efficiency, $\eta_{\text{Mg}} \approx 5 \times 10^{-4}$. To suppress photoemission (originating from scattered light) from the cathode outside the Mg disk, as well as from the anode, these surfaces are covered with thin ($50 \mu\text{m}$) molybdenum plates, expected to

have a significantly lower photoelectric yield than Al ($\eta_{\text{Al}} \approx 3 \times 10^{-5}$) when the Mo surface is not treated.

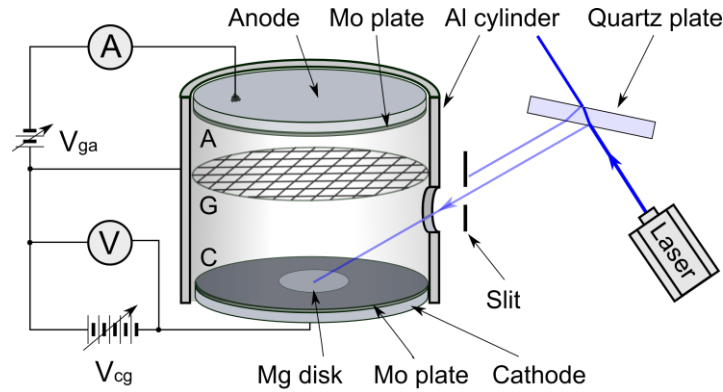


Fig. 1. Schematic of the experimental set-up

The grid (wire mesh) is held at $x_g = 14.9 \pm 0.2$ mm height above the cathode surface by an Al cylinder, to which it is electrically connected. This cylinder surrounds the cathode and the anode, and holds the latter, by ceramic spacers, at a distance $d_{\text{ga}} = 7 \pm 0.2$ mm above the grid. Using a proper mesh is crucial in the experiments. We use a rectangular Ni mesh with $T = 90\%$ geometric transmission, with square openings and 70 lines/inch density, manufactured by Precision Eforming LLC (type MN17). A high transmission is needed for acceptable signal intensity. A high density minimizes the effect of uneven potential distribution in the plane of the mesh and the penetration of the electric field from either side of the grid into the other side. Such effects have a smoothing effect on the FH characteristics and would complicate the treatment of the grid in the simulation. The thickness of the mesh is about $7 \mu\text{m}$.

The FH cell is situated in a vacuum chamber (described in details in Ref. [5]). To enhance the purity of the system: (1) the vacuum part of the apparatus is pumped down by a turbo-molecular pump to $\sim 10^{-7}$ mbar and is heated to $\sim 100^\circ\text{C}$ by heating tapes, for several hours, preceding the measurements, (2) the experiments are conducted using 6.0 purity argon gas with a slow flow (< 10 sccm), and (3) prior to entering the vacuum chamber, the gas is fed through a cold trap filled with liquid nitrogen.

With direct illumination of the cathode by the laser beam we observed the effect of Coulomb collisions of photoelectrons that showed up as a smoothing effect (decreased modulation) of the FH characteristics due to the energy spreading of the electrons. To avoid this effect we use for illumination a beam of the laser reflected from a quartz plate, resulting in $\sim 10\%$ of the initial intensity. The voltage V_{ga} is set to a fixed value -3.05 V, while V_{cg} is scanned between 0 and 55 V. The anode current I_a is first amplified by a Keithley 427 current amplifier (shown schematically as a current meter in Fig. 1) and is sampled by the National Instruments (USB-6251) card controlled by LabView software running on a personal computer. During the course of measurements data obtained for 80 000 pulses are averaged at each value of V_{cg} . We measure the FH characteristics in relative units, as it was not possible for us to carry out an accurate absolute calibration of the system.

3. Simulations

The kinetic analysis of the experiment is based on Monte Carlo (MC) simulation (see, e.g., Ref. [6]), in which a high number of electrons is traced as they proceed under the effect of the electrostatic field and under the effect of collisions with the atoms of the background gas.

The electrostatic potential distribution U inside the discharge cell has a cylindrical symmetry. In the calculation of U the fine structure of the grid is not resolved and a zero mesh thickness is assumed.

The electrons emitted due to the photoeffect are assumed to have Gaussian initial energy distribution centered at 0.5 eV and having a standard deviation of 0.15 eV, constrained between 0 and 1 eV. The direction of the initial velocity of photoelectrons is randomly chosen over a half sphere. Typically 10^5

primary electrons are released from the cathode for each set of simulation conditions. We assume the gas temperature to be 300 K.

The electrons move (in three-dimensional space) under the effect of the electric field $\mathbf{E} = -\nabla U$ between the collisions with the background gas atoms and with the surfaces. The simulation employs a fixed time step Δt in the integration of the equation of motion. The probability of a collision between each electron and the gas atoms (using the cold gas approximation),

$$P = 1 - \exp[-n\sigma_{\text{tot}}(\varepsilon)v\Delta t], \quad (1)$$

is checked in each time step (see, e.g., Ref. [6]). Here σ_{tot} is the total cross section of the electron with an energy ε at time t , n is the density of the background gas and v is the velocity of the electron. Using the cross sections of Hayashi [7] we take into account the elastic scattering of electrons from Ar atoms, electron impact excitation to 25 electronic levels, as well as ionization. The collision kinematics follows the procedures given by Nanbu [8]. Electrons created in ionization processes are also followed in the same way as the ‘‘parent’’ electrons. Quantities of interest (velocity distribution, mean electron energy, etc.) are sampled in each time step.

The electrons are traced until they get absorbed by any of the surfaces: at the cathode, at the anode, at the confining cylinder, or at the mesh. The reflection from all these metal surfaces is assumed to be elastic and to have a probability that depends on the angle of incidence (θ):

$$R(\theta) = R_0 \exp[c(1 - \cos(\theta))], \quad (2)$$

where c is constant chosen in a way that $R(90^\circ) = 1$. Our calculations indicate that the best agreement with the experimental data can be obtained when $R_0 = 0.7$ is used.

The effect of the mesh can be accounted for in the simulation in a simple manner, by assigning a transmission coefficient T . We take T to be the geometric transmission (90%). Whenever an electron crosses the mesh plane it is transmitted with a probability T and a reflection process [characterized by a reflection coefficient given by (2)] takes place with a probability $1 - T$.

4. Results

The FH characteristics have been measured in the pressure range between $p = 0.25$ and 4 mbar. A series of these characteristics (comprising five different pressure values) are shown in Fig. 2. Before discussing our results we first comment on the accuracy of the measurements. Within recording one series of FH characteristics we have rechecked points when data collection was accomplished. With this procedure we confirmed that our system was stable within $\pm 2\%$ over the data recording period for the whole series of FH characteristics. When we checked the day-to-day reproducibility of the measured data we have observed some change of the magnitudes of the FH characteristics, most likely due to the slow change of the quantum yield of the Mg disk used as the photocathode. The ratios between the characteristics measured at different pressures (at given voltages), however, were found to remain within $\pm 10\%$. Note that, as we measure the FH characteristics in arbitrary units, it is their *ratios* that are the important quantities.

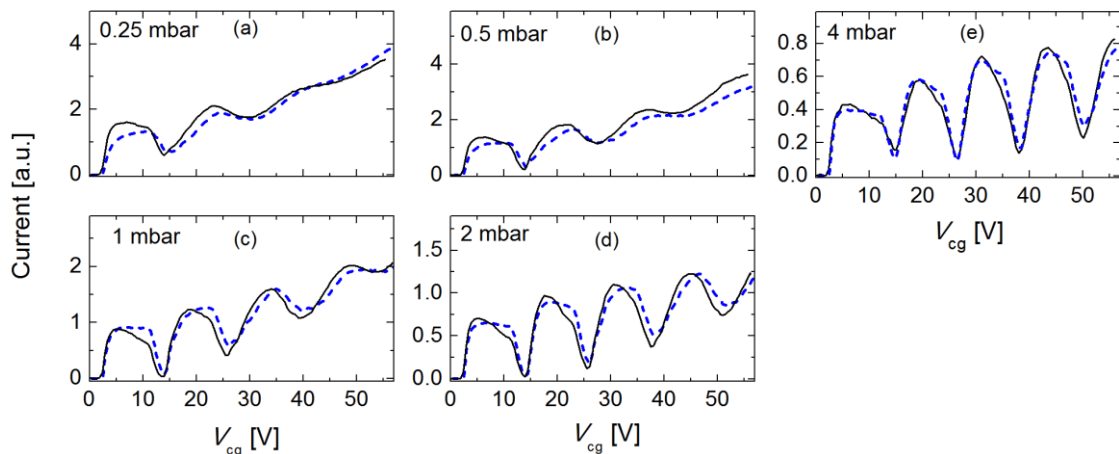


Fig. 2. Comparison of the measured (solid lines) and calculated (dashed lines) Frank-Hertz current-voltage characteristics at different pressures.

A general feature of the FH characteristics is a sharply increasing current when V_{cg} approaches $|V_{ga}|$. As the initial energy of photoelectrons is between 0 and ~ 1 eV (the UV photon energy is the 4.7 eV, while the work function of Mg is 3.7 eV) anode current starts to flow at $V_{cg} \approx |V_{ga}| - 1$ V. Following a domain of high current we observe a sudden drop of the current that can be associated with the excitation of the first energy level of Ar. The highest value of relative drop of the current near the first excitation energy is observed at 1 and 2 mbar. The qualitative explanation for this observation is aided by considering the values of the electric fields in the FH cell.

At the highest pressure of 4 mbar the accelerating reduced electric field E/n is quite low (e.g., $E/n \approx 7$ Td at $V_{cg} = 10$ V, $1 \text{ Td} = 10^{-21} \text{ Vm}^2$), so the elastic collision causing low energy loss is the dominant process. At medium pressures less energy is deposited in elastic collisions, but the excitation occurs primarily only to the lower-lying levels of Ar. Therefore at these conditions peaks in the electron energy spectrum are expected to be sharp, resulting in a high modulation depth of the FH curves. At the lower pressures (where E/n reaches values up to ~ 600 Td at the highest V_{cg}) ionization takes place as well, and this, together with the excitation of a higher number of levels results in a significant broadening of the electron energy spectrum and in a decrease of the modulation of the FH curves, especially at higher accelerating voltages.

The calculated FH current-voltage characteristics, at all different pressure values covered in the experiment, are also shown in Fig. 2. In the simulation the anode current is measured in arbitrary units, as the ratio of the number of electrons absorbed at the anode and the number of photoelectrons leaving the cathode. As the current is also measured in arbitrary units in the experiment, a scaling factor F is used here to match the two current values; i.e., we compare the values of $F I_{a,calc}$ to those of $I_{a,meas}$. Note that we use the same scaling factor for all the conditions (pressure, cathode-grid voltage), and we do not use any additional fitting parameters to match the experimental and simulation results. Repetitive calculations resulted in FH characteristics that differ less than 2% from each other at any pressure and voltage values.

A very good general agreement is obtained between the two sets of curves, which verifies our model and justifies its assumptions. Furthermore, it is this agreement that gives confidence in the additional simulation results for which no direct comparison with experimental data is possible. In the following we will present such results characterizing the electron kinetics in the FH cell.

Figure 3. shows the dependence of the mean energy of the electrons, the electron-impact excitation rate S_{exc} and the electron-impact ionization rate S_{ion} on the spatial position (x) and accelerating voltage (V_{cg}) at pressure values of 0.25 mbar and 4 mbar. These distributions represent radially averaged quantities.

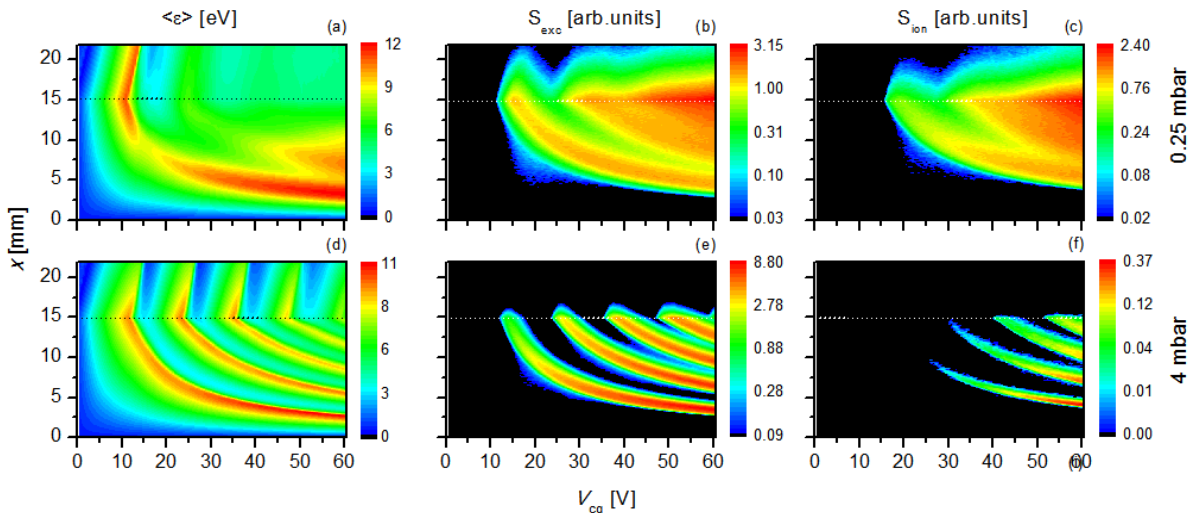


Fig. 3. The mean energy of the electrons (left column), the electron-impact excitation rate (middle column) and the electron-impact ionization rate (right column) as a function of position measured from the cathode (x) and the accelerating voltage (V_{cg}) calculated for two pressures: 0.25 mbar (top row) and 4 mbar (bottom row). The position of the grid, $x_g = 14.9$ mm, is indicated by dotted horizontal lines.

At the pressure of 4 mbar the patterns of all distributions are much more regular than those at the pressure of 0.25 mbar. Under the relatively low E/n conditions here, excitation occurs mostly to the few lowest-lying levels of Ar atoms, and the ionization rate is very small (note the different color scales in the panels of Fig. 3.). At this pressure the mean energy of the electrons at the grid and at the anode is strongly modulated by V_{cg} , in agreement with the deep modulation of I_a , observed in Fig. 2(e). At the lowest pressure the patterns of the excitation and ionization rates widen and the modulation on the mean energy decreases strongly. At this pressure and high V_{cg} values (i.e., at the highest E/n values) S_{exc} and S_{ion} take comparable values, and, as electrons are born in a wide spatial domain, the periodic modulation in I_a disappears, as seen in Fig. 2(a).

Figure 4. shows the rate of the different types of inelastic collisions taken into account in the simulations as a function of the accelerating voltage V_{cg} . The Ar excited levels are indicated by the values of $N_{Ar} = 1 \dots 25$, ionization is indicated by $N_{Ar} = 26$. At the pressure of 4 mbar the majority of the inelastic collisions correspond to the excitation of the levels with $N_{Ar} < 5$ and the ionization has a low probability. At the pressure of 0.25 mbar the excitation occurs to the higher-lying levels of Ar and the ionization becomes the dominant process at high V_{cg} .

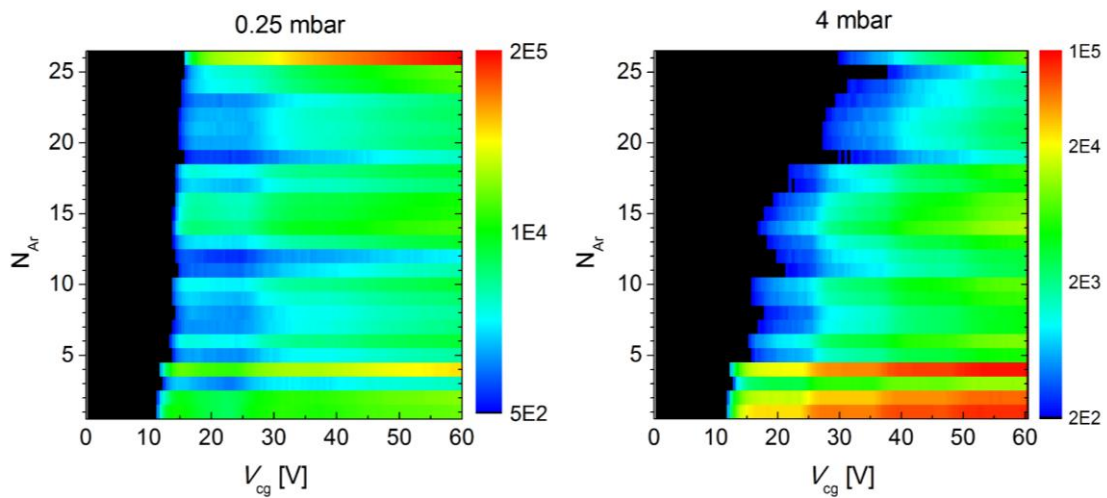


Fig. 4. Relative number of inelastic collision leading to excitations of Ar atoms to different levels ($N_{Ar} = 1-25$), as a function of the accelerating voltage, V_{cg} . $N_{Ar} = 26$ corresponds to the ionization process of argon atoms.

5. Conclusions

We have carried out a combined experimental and theoretical (modeling) study on a Franck-Hertz cell with plane-parallel electrode configuration. Our experimental cell operated on the basis of photoemission.

In the experiment we have recorded the anode current-accelerating voltage characteristics of the cell in argon gas, at different pressures between 0.25 and 4 mbar. This range of pressure covered highly collisional conditions with significant elastic collisional energy losses (high pressures) as well as conditions when the ionization rate becomes comparable to the excitation rate (low pressure and high V_{cg}).

Our modeling study has been based on Monte Carlo simulation, which provided an exact description of the electron kinetics under nonequilibrium (nonhydrodynamic) conditions for electron transport, typical for FH settings.

The experimental cell characteristics have been reproduced rather accurately by the modeling calculations. The cold cathode operation achieved in the experiment allowed the assumption of a uniform gas density distribution in our modeling studies. The simulations made it possible as well to obtain the spatial variation of the energy distributions of the electrons, their transport parameters, and the rates of excitation and ionization processes.

Acknowledgement

This work has been financially supported by the Hungarian Scientific Research Fund, via Grant OTKA K105476.

6. References

- [1] J. Franck and G. Hertz, 1914 *Verh. Deut. Phys. Ges.* **16** 457.
- [2] R. Winkler, S. Arndt, D. Loffhagen, and D. Uhrlandt, 2004 *Contrib. Plasma Phys.* **44** 437.
- [3] L. C. Pitchford, J.-P. Boeuf, P. Segur, and E. Marode, 1990 in *Nonequilibrium Effects in Ion and Electron Transport*, edited by J. W. Gallagher, New York, Plenum.
- [4] P. Magyar, I. Korolov, Z. Donkó, 2012 *Physical Review E* **85** 024001.
- [5] A. Derzsi, P. Hartmann, I. Korolov, G. Bánó, J. Karácsony, and Z. Donkó, 2009 *J. Phys. D* **42** 225204.
- [6] Z. Donkó, 2011 *Plasma Sources Sci. Technol.* **20** 024001.
- [7] M. Hayashi, *Nagoya Institute of Technology Report IPPJ-AM-19* (unpublished).
- [8] K. Nanbu, 2000 *IEEE Trans. Plasma Sci.* **28** 971.

STUDY OF MICRODISCHARGES IN HYDROGEN

¹L. Moravský, ¹M. Klas and ¹Š. Matejčík

¹ *Department of Experimental Physics, Comenius University, Mlynská dolina F-2, 842 48 Bratislava, Slovakia*

E-mail: ladislav.moravsky@fmph.uniba.sk

A comparative experimental study of the high pressure direct current (DC) and alternative current (AC) microdischarges over wide range of frequencies in Hydrogen have been carried out in this work. In a high vacuum chamber filled with pure Hydrogen gas the microdischarges have been generated between two plan-parallel molybdenum electrodes. The breakdown voltages from the Paschen curves were measured as a function of the gas pressure (from 50 mbar up to 930mbar) and the frequency range (from 100Hz up to 13.56MHz) while the electrode distance was constant at 100 μm .

1. Introduction

In many applications, the non-equilibrium plasma sources operating in the glow mode, are highly desired [1, 2]. However, at high pressure, the stable diffuse glow discharge can transit to an arc [3, 4]. In order to stabilize such a high-pressure plasma, one of the ways is to spatially confine it to the dimensions below 1 mm [4]. Plasma in these dimensions we call microplasma. Many mechanisms and phenomena occurring in microdischarges are not clearly understood. Especially AC microdischarges are not examined enough. The microdischarges have been applied in different fields of technology in recent years. The most applied field are chemical synthesis, material processing, plasma medicine etc. [5-7]. Therefore the knowledge of the physical phenomena occurring in the microdischarges, are very important [8-12]. The Paschen's law describes the electric breakdown of the discharge. In this law the breakdown voltage depends on the product of pressure and the distance between electrodes - pd . In microdischarges different mechanism responsible for electric breakdown in gases, start to play a role in comparison to standard macroscopic discharges [10-12]. These processes are related to the high electric fields and thus deviations from Paschen law are observed. The main goal of this work is to study the breakdown phenomena of high pressure microdischarges over wide range of frequencies in Hydrogen. Comparison to the breakdown phenomena between low frequency AC and high frequency AC discharges are presented.

2. Experimental apparatus

In Figure 1, the schematic view of the experimental apparatus is shown. It consists of vacuum chamber with four glass window and two xyz and tilting manipulators of electrodes. The electric discharge was generated in hydrogen with purity 99.999% between two plan-parallel molybdenum electrodes covered by glass. The diameter of the electrodes was 3.8 mm respectively.

The distance between the electrodes was set by micrometer linear feedthrough. The Paschen curves and the Current-Voltage waveforms were measured by 300MHz oscilloscope (Agilent Technologies DSO5032A), connected to high-voltage probe (Tektronix P6015A) and to current probe (Pearson 2877) for frequency range from 100Hz up to 13,56MHz. For such a wide range of frequencies three different power supplies were used. For the frequency range from 100Hz to 10kHz the power supply consists of wave generator connected to an acoustic amplifier and then through the high voltage transformer and 100k Ω resistor to the discharge tube. For the frequencies between 10kHz and 4.3 MHz homemade high frequency generator was used. The third source was a high frequency generator (400W) connected with Dummy load for 13.56MHz. Moreover, direct current (DC) measurements were carried out for comparison to AC microdischarges.

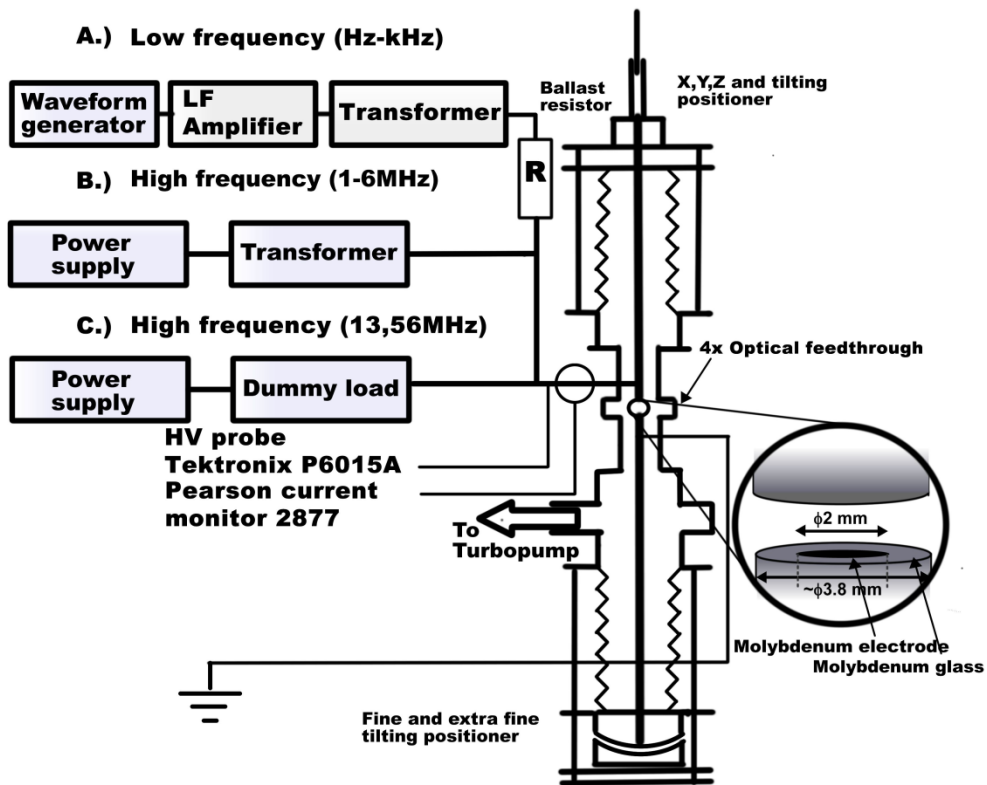


Figure 1: Vacuum chamber for microdischarges with different type of sources.

3. Results and discussion

The breakdown voltages of the microdischarges were studied in this experiment according to three parameters (pressure, distance between electrodes and frequency). In Figure 2, the breakdown voltage has been measured as function of pressure and frequency at constant electrode distance of 100 μm .

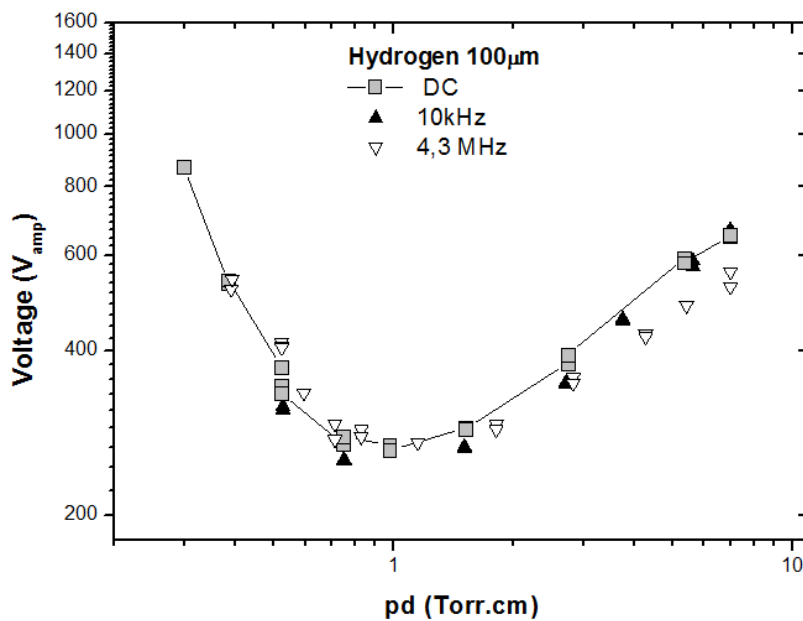


Figure 2: Breakdown voltages V_{amp} for different pressures at the electrodes distance of 100 μm .

As it is seen from the figure, the highest values of the breakdown voltages were measured for the DC electric field if V_{amp} was taken for the AC discharges. If we consider the AC voltage amplitude, the breakdown voltage for DC and AC are more or less identical, if the frequency is not very high and the breakdown voltage is weakly dependent on the frequency. But at higher frequency the electrons with high drift velocities are lost on the walls but the ions are trapped in the gap since their drift velocity is significantly lower than of the electrons [13]. In Fig. 3 is shown the typical current-voltage waveform of the discharge at 4,3MHz and in Fig. 4 you can see the comparison of current-voltage waveforms before and after the breakdown at 10 kHz. We compared the waveforms at 350 mbar at constant electrode distance of 100 μm . The dash waveform represents the current and voltage when discharge is off, and the strong lines represent waveforms when discharge is on. The waveform indicates a capacitive discharge.

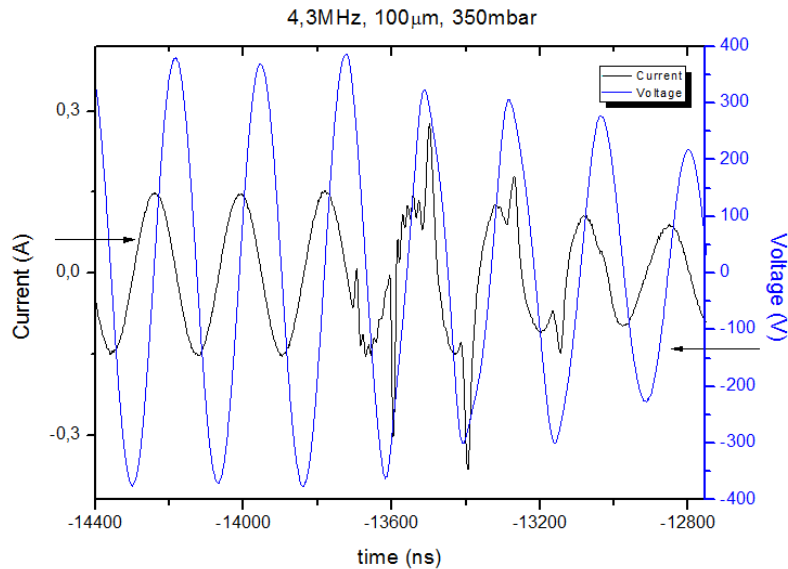


Figure 3: The current-voltage waveform of the discharge at frequency 4.3 MHz.

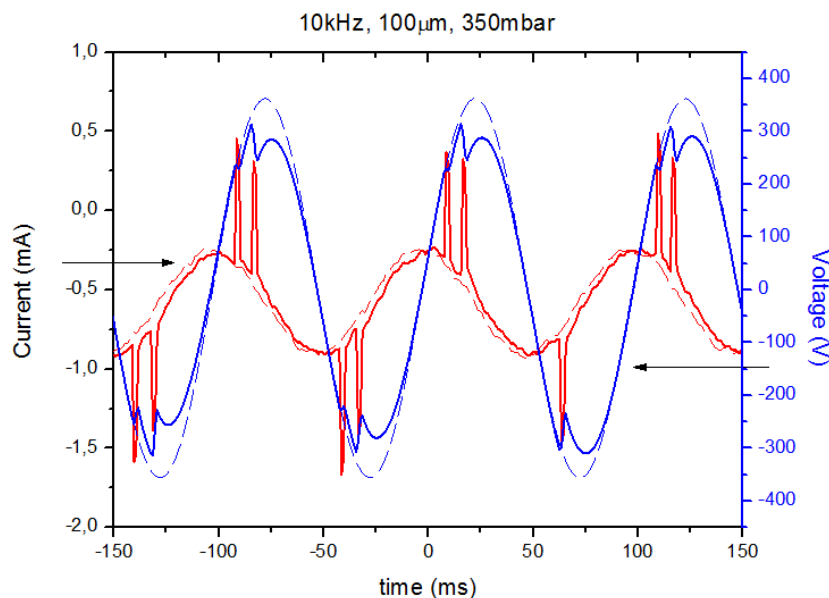


Figure 4: Current-voltage waveforms before (dash line) and after (solid line) the breakdown at frequency 10 kHz.

4. Conclusion

The experimental results have shown the differences in electrical properties of high pressure AC microdischarges in Hydrogen. At low frequencies (from 100Hz up to 10kHz) no significant effects on breakdown voltages were measured. The frequency is sufficiently low such that a large fraction of electrons and ions reach and are lost to the electrodes each half cycle before the polarities are reversed. When the discharge is ignited both waveforms exhibit minor distortion. This scenario is qualitatively similar to the dynamics in DC discharge. Every half period the current waveform has one or two peaks which represent the breakdown and that time the voltage between the electrodes is decreased due to lower resistance.

Acknowledgments

This work was supported by Slovak Research and Development Agency project APVV-0733-11.

5. References

- [1] Conrads H and Schmidt M 2000 Plasma generation and plasma sources *Plasma Sources Sci. Technol.* **9** 441–54.
- [2] Lieberman M A and Lichtenberg A J 1994 *Principles of Plasma Discharges and Materials Processing* (New York: Wiley)
- [3] Raizer Y P 1991 *Gas Discharge Physics* (Berlin: Springer)
- [4] L Schwaedler *et al* *J. Phys. D: Appl. Phys.* **45** (2012).
- [5] K. H. Becker, K. H. Schoenbach, and J. G. Eden, *J. Phys. D: Appl. Phys.* **39**, R55 (2006).
- [6] F. Iza, G. J. Kim, S. M. Lee, J. K. Lee, J. L. Walsh, Y. T. Zhang, and M. G. Kong, *Plasma Processes Polym.* **5**, 322 (2008).
- [7] A. Fridman, *Plasma Chemistry* (Cambridge Univ. Press, Cambridge, 2008).
- [8] W. Zhang, T. S. Fisher, and S. V. Garimella, *J. Appl. Phys.* **96**(11), 6066–6072 (2004).
- [9] V. A. Lisovskiy, S. D. Yakovin, and V. D. Yegorenkov, *J. Phys. D* **33**(21), 2722 (2000).
- [10] Y. P. Raizer, M. N. Shneider, and N. A. Yatsenko, *Radio-Frequency Capacitive Discharges* (CRC Press, Boca Raton, 1995).
- [11] V. Lisovskiy, J. P. Booth, K. Landry, D. Douai, V. Cassagne, and V. Yegorenkov, *EPL (Europhys. Lett.)* **80**(2), 25001 (2007).
- [12] J. L. Walsh, Y. T. Zhang, F. Iza, and M. G. Kong, *Appl. Phys. Lett.* **93**(22), 221505 (2008).
- [13] Semannai *et al.*, *Applied physics letters* **103**, 063102 (2013)

HIGH SPEED CAMERA IMAGING OF MINI GLIDARC DISCHARGE

Piotr Terebun¹, Michał Kwiatkowski¹, Piotr Krupski¹, Joanna Pawlat¹, Jarosław Diatczyk¹, Mario Janda², Karol Hensel², Zdenko Machala²,

¹*Institute of Electrical Engineering and Electrotechnologies,
Lublin University of Technology, Lublin, Poland,*

²*Division of Environmental Physics, Faculty of Mathematics, Physics and Informatics,
Comenius University, Bratislava, Slovakia
E-mail: askmik@hotmail.com*

The gliding arc discharge plasma reactors are known as a source of non-equilibrium plasma at atmospheric pressure. In the present study, the high speed camera has been used for imaging of discharge propagation and subsequent calculation of the velocity of discharge propagating generated in mini GlidArc reactor at different flow rate and composition of working gas mixture.

1. Introduction

The gliding arc (GlidArc) is a source of low temperature plasma, that is often effectively used for the process of disposal and treatment of different gaseous pollutants [1-5]. The basic gliding arc is an arc discharge generated between two diverging electrode, that is blown along the electrodes by very fast transverse gas flow. The gas nozzle is placed between the electrodes in their axis of symmetry. The arc initiates at the shortest gap between two electrodes and after that is elongated by the fast gas flow from its initial position [5-7]. As the arc is elongated, its current is at its maximum and the voltage at the minimum. (quasi-thermal regime).. The elongating arc demands more power to be sustained, until it reaches the maximum that the power supply can provide and then subsequently drops on both plasma and external resistance. This is the transition point for the regime of GlidArc operation [5, 6]. Due to continuous gas flow, the length of the arc continues to grow, but the power supplied by the source is insufficient to balance the convective energy losses to the surrounding gas and discharge disappears.

"Mini GlidArc" reactor that we used in the experiment has small discharge space, where initial distance between electrodes in the ignition point can be equal to one tenth of a millimetre . The reactor allows many possible adjustments and settings, e.g. continuous change of distance between the electrodes. The electrodes move axially and radially with respect to the axis of symmetry of the electrodes and the gas nozzle. The discharge mechanisms of "Mini GlidArc" are alike the traditional GlidArc. One of the key parameters determining the amount of generated active particles in the plasma, is the shape and size of the arc discharge.

Plasma reactors with gliding discharge can be operated with DC, AC and pulsed power supplies [4]. The "Mini GlidArc" reactor is supplied by high voltage power supply with no separate ignition system, which can deliver certain part of the energy in the single cycles of plasma. The reactor has the possibility to work in different conditions, e.g. in various gas mixtures containing nitrogen, oxygen and carbon dioxide. This work objective was to identify the factors affecting the length and propagation velocity of the discharge.

2. Experimental

Measurements were made in the setup shown in Fig. 1. AC high-voltage power supply was applied to supply the Mini GlidArc plasma reactor. The flow and composition of the gas mixture was adjusted by gas flow controllers. High speed camera Casio EX-F1 capable to shoot 1200 frames per second was used to capture the discharge between electrodes to be able to evaluate the discharge propagation and calculate its velocity. For accurate processing of ten consecutive images of the discharge were used and video editing and graphics processing programs were applied.

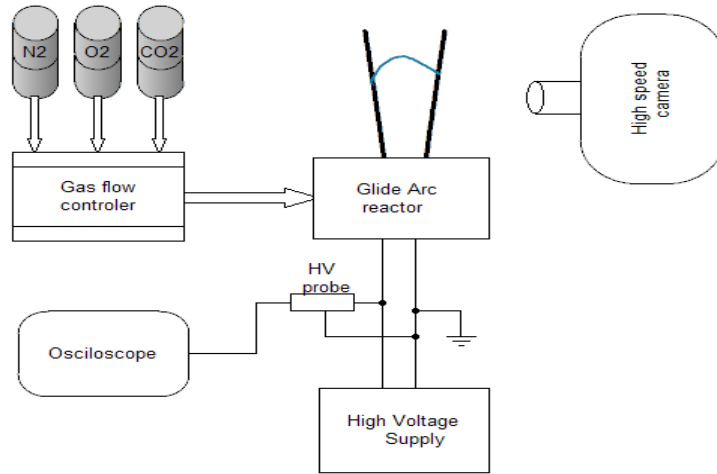


Fig. 1. Schematic diagram of the experimental setup.

The sequence of images in Fig. 2. shows individual steps of the discharge propagation between electrodes in the gas mixture of 30% of O₂ in N₂ (total gas flowrate 7 L/min). The duration of the discharge calculated on the basis of the results from the high speed camera was approximately 8.33 ms.

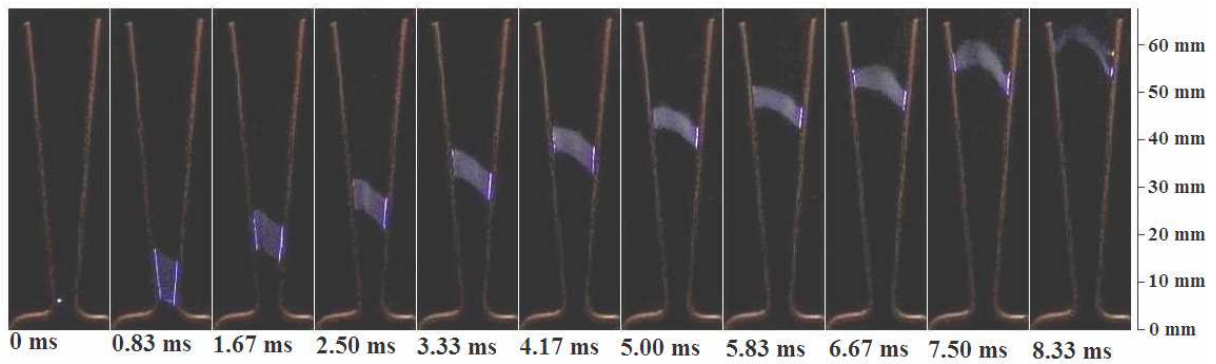


Fig. 2. Sequence of images of the gliding arc propagation taken by the high speed camera (30% of O₂ in N₂, 7 L/min, 1200 fps).

Measurements were made for nitrogen, oxygen, carbon dioxide and mixtures of these gases. Examples of images obtained for different mixtures are shown in fig. 3.

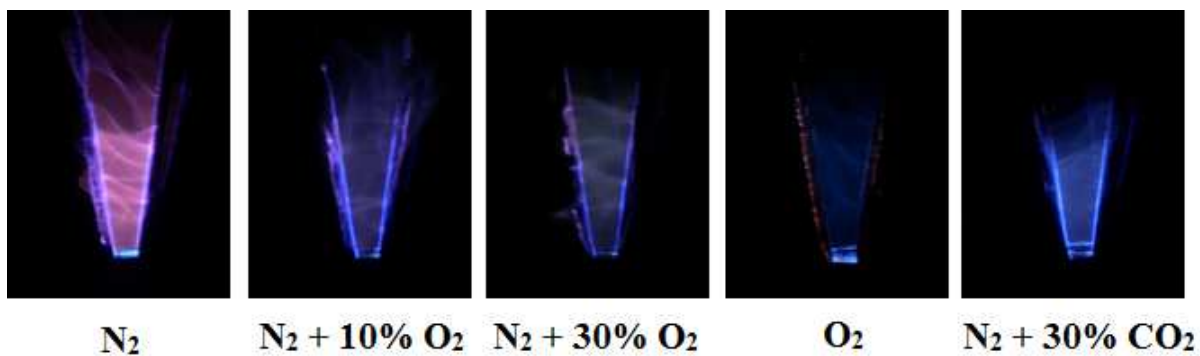


Fig. 3. Effect of gas mixture (exposure time 1/4 s).

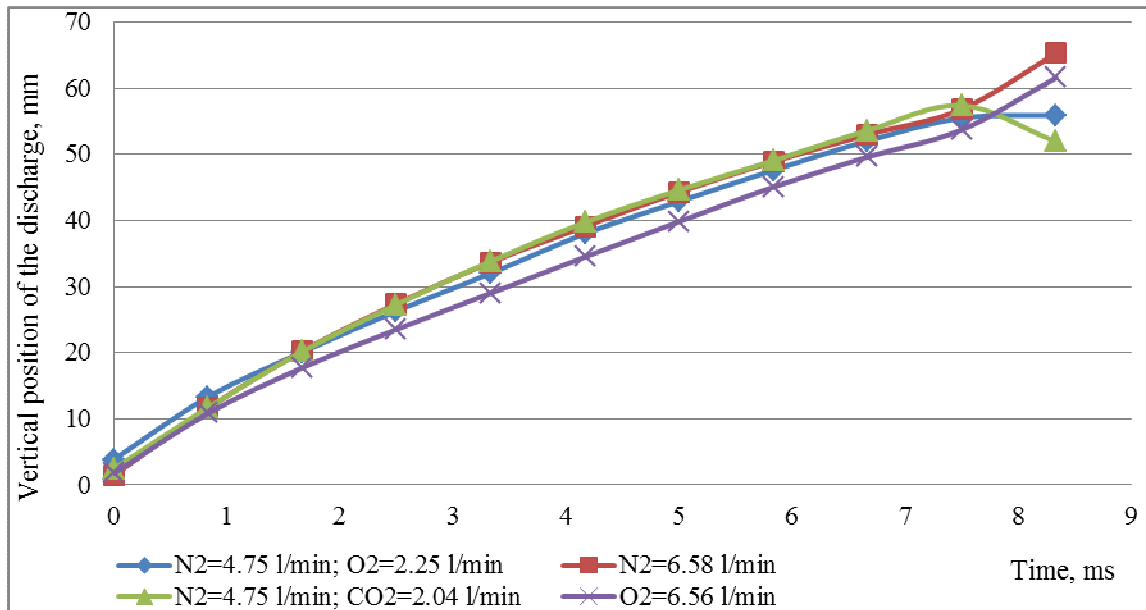


Fig. 4. Vertical position of the discharge propagation in different gas mixtures and at the constant flow rate.

Fig. 4. depicts the vertical position of the discharge front in different gas mixtures of nitrogen, oxygen and carbon dioxide and at constant total flow rate of approximately 6.60 l/min.. As can be seen on the figure, the composition of gas mixtures had no significant effect on the discharge propagation. At the last stages of the discharge the propagation slows down, which is correlated with the uneven fading of the discharge at the end of its life cycle.

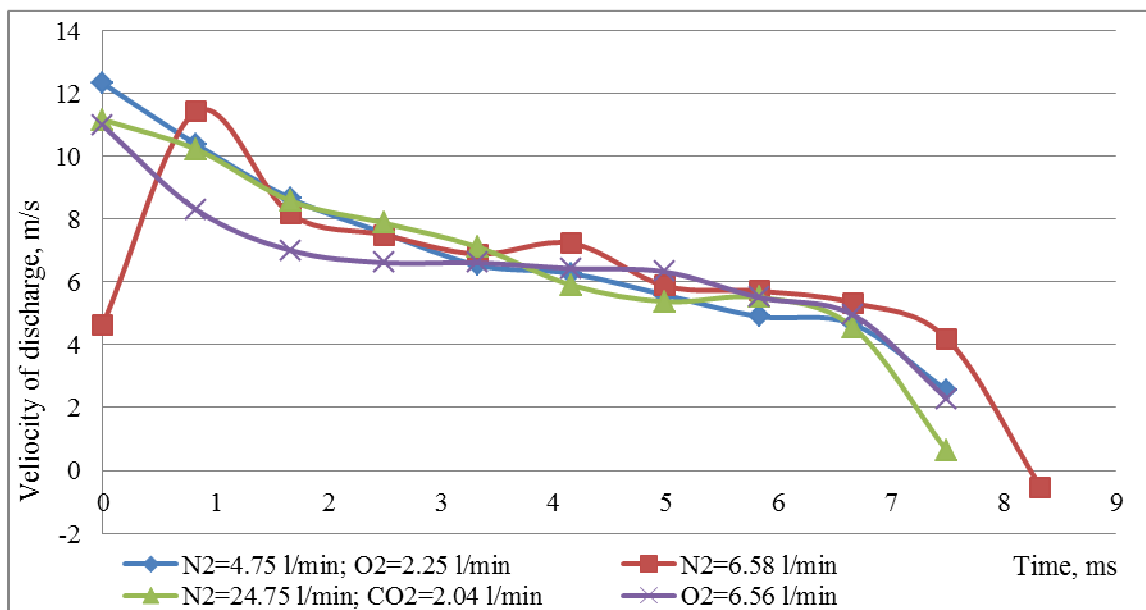


Fig. 5. Velocity of the discharge for constant gas flow rate and different gas mixtures.

The discharge propagation velocity along the electrodes is shown in Fig. 5. and is similar for any gas flow rate. The highest velocity of electric arc discharge can be observed at the beginning of the cycle, while with the slight growth of the arc volume, its velocity decreased. The end of the recession curve is correlated with its disappearance.

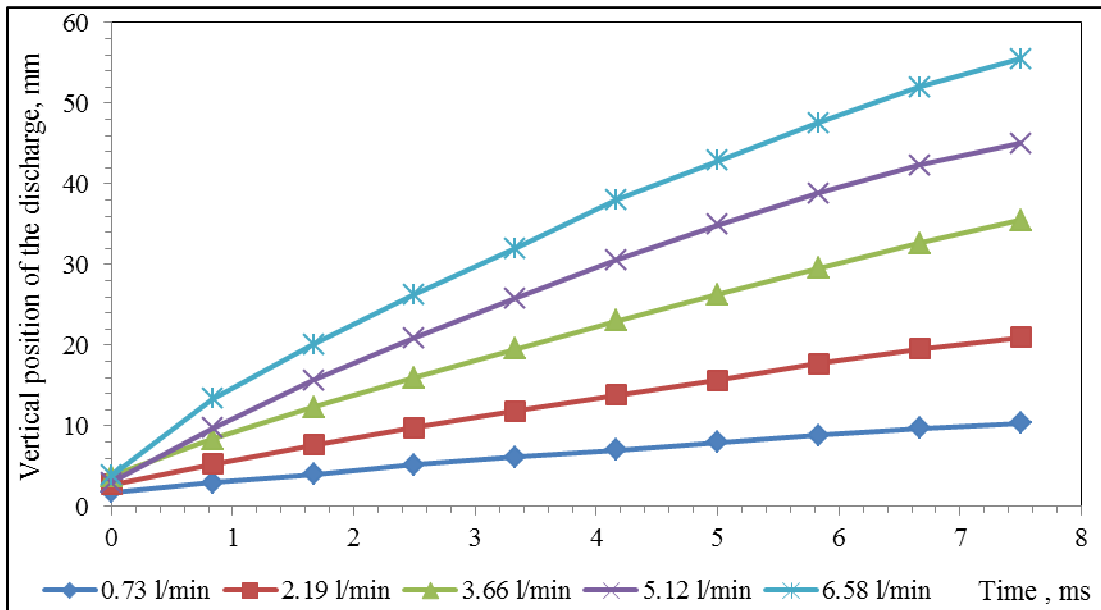


Fig. 6 Vertical position of the discharge propagation for different flow rates (N₂).

Figure 6 shows the results obtained for the different gas flow rate in nitrogen. Increase of the flow rate resulted in significant elongation of the arc, which could be explained by the strong influence of gas-dynamic forces on the shape of the discharge. This was particularly evident in the final stage of discharge, for example 67% flow rate increase (from 2.19 l/min to 3.66 l/min) allowed 68% increase in length. Uncertainty of the front propagation was calculated and is displayed as the standard deviation in Fig. 7. For most of the measurements, the uncertainty increased with time and length of discharge, due to the more complex shape of the arc during the final stages of its propagation.

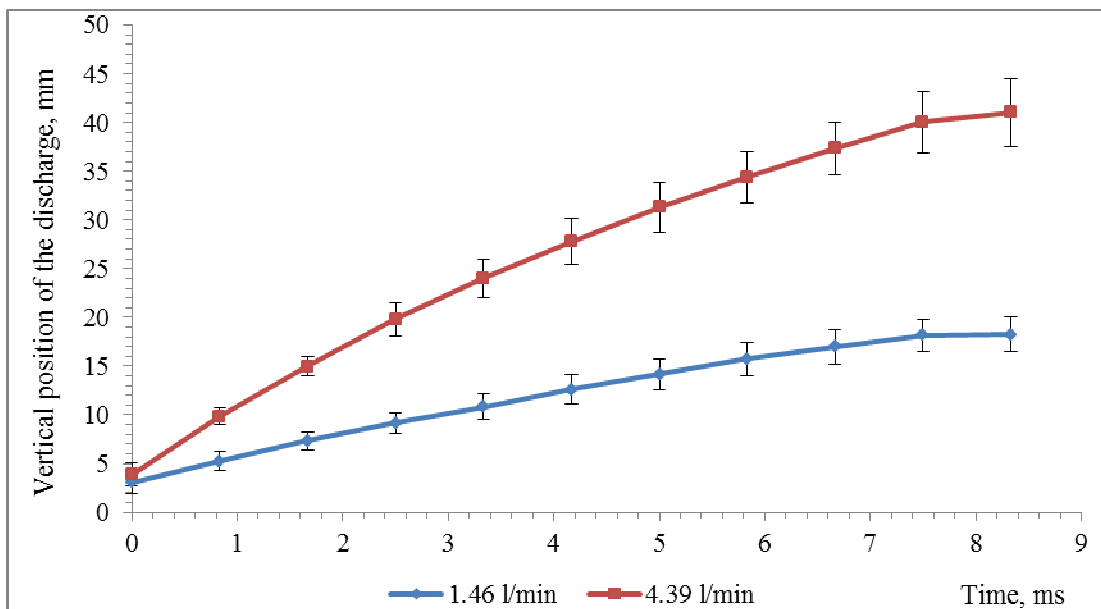


Fig.7. Uncertainty of measurement as the standard deviation for two flow rates (N₂).

Fig. 8. shows the change in velocity of the discharge during its life cycle. Increasing the flow rate also caused greater ranges of calculated velocity results for several series of discharges in oxygen.

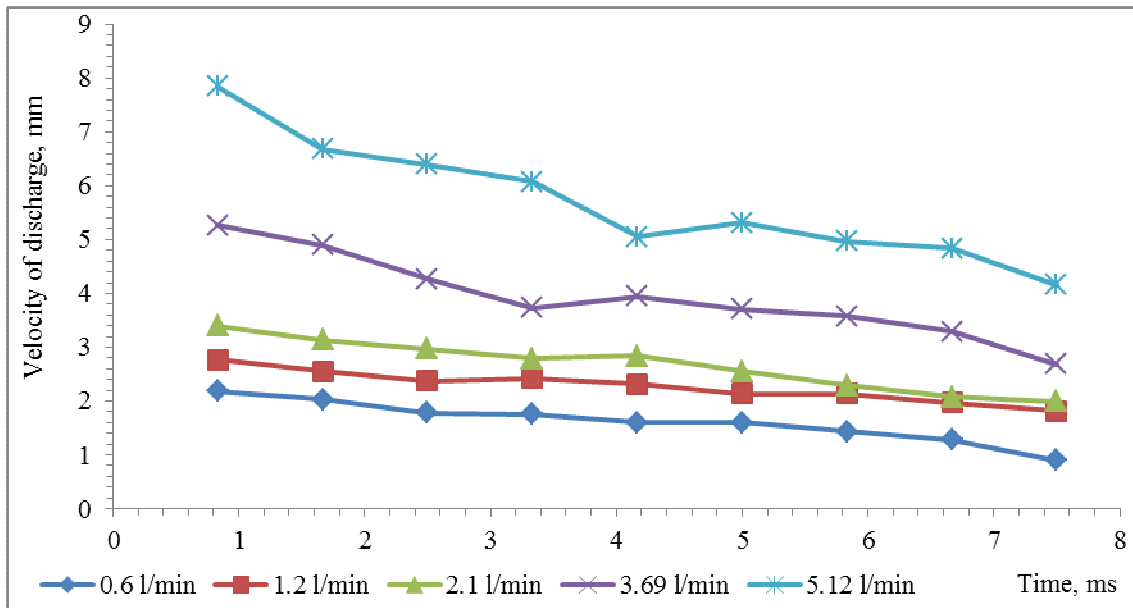


Fig. 8. Velocity of discharge for different flow rates (O₂).

Vertical velocity of the discharge was calculated from the average change in vertical propagation of the discharge in time. In general, velocity decreased in time. In some cases (for example: 3.7 l/min, 3.69 l/min), increase of the velocity was observed in the middle of discharge propagation. It may be the result of changes in the shape of the arc, which appeared to be more stretched in its central part.

For all mixtures and flow-rates, the lifetime of the discharge was the same. Thus, it depends mainly on the power parameters, such as frequency.

3. Summary

By using the high speed camera we characterized the gliding arc discharge in various gas mixtures and in the range of flow rates to measure its propagation velocity, height, and length. The obtained results show that the main factor affecting the length and velocity of the discharge is the gas flow rate. Different mixtures of gasses do not effect the height of the discharge and its life time depends mainly on the power parameters. The results may allow not only to determine the optimum gas flow rate for maximum performance, but also the operating point for the various required distances from end of the “Mini GlidArc” reactor.

4. Acknowledgement

This work was supported by Slovak Research and Development Agency SK-RO-0024-12 and APVV 0134-12 grants and by COST TD1208 Action.

5. References

- [1] Pawlat J, Diatczyk J, Stryczewska H 2011 *Przegląd Elektrotechniczny* **1** 245
- [2] Komarzyniec G, Janowski W, Stryczewska H, Pawlat J, Diatczyk J 2011 *Przegląd Elektrotechniczny* **7(87)** 32
- [3] Czernichowski, A. Czernichowski, P., 2010 *Environment Protection Engineering* **36(4)** 37
- [4] Stryczewska H, Jakubowski T, Kalisiak S, Giżewski T, Pawlat J 2013 *JAOTs* **6(1)** 52
- [5] Kalra C, Gutsol A, Fridman A 2005 *IEEE Transactions on Plasma Science* **33** 32
- [6] Fridman A and Kennedy L 2004 *Plasma Physics and Engineering*, Taylor & Francis
- [7] Kuznetsova I, Kalashnikov A, Gutsol A, Fridman A, Kennedy L 2002 *J. Applied Physics* **92** 4231

NON-RADIOACTIVE SOURCE OF ELECTRONS AT ATMOSPHERIC PRESSURE

Matúš Sámel¹, Michal Stano¹, Štefan Matejčík¹

¹Faculty of Mathematics, Physics and Informatics, Comenius University, Mlynská Dolina, 842 48 Bratislava

E-mail: msgraniar@gmail.com

Electron guns are reliable ion sources in Mass Spectrometry. For atmospheric pressure ionisation (API) ions source we are developing electron source with membrane interface to the atmosphere. Here we present our first device based on Si₃N₄ membrane 100 nm thick.

1. Introduction

Electron guns are devices used to generate electron beams. The electron guns are used in plenty of applications, such as ion source in mass spectrometry (MS), electron welding, electron microscopy and many others. The electron guns are operated in vacuum. At atmospheric pressure, electrons interact with the gas and undergo ionisation reactions and subsequent thermalisation. Most common source of the electrons at atmospheric pressure is a photocathode irradiated by UV light of suitable wavelength [1]. Recently, vacuum electron guns with nanomembrane vacuum-atmosphere interface (window) developed of 300 nm thickness, which allow transport of keV electrons from vacuum to atmosphere [2 - 4]. Such electron sources are suitable as replacement for radioactive ion sources based on β radiation and could be applied for API in MS, ion mobility spectrometry (IMS) or other analytical methods at atmospheric pressure (e.g. excitation fluorescence, electron swarm experiments...)[5].

Our plan is to develop similar non-radioactive Source of Electrons at Atmospheric Pressure (SEAP), which would allow transmission of electrons at lower energies as reported in previous studies [2 - 4]. We plan to apply three times thinner windows Si₃N₄ as in above cited works (100 nm thick), this would allow transmission of electrons to the atmosphere below 8 keV. Following chapters present the design and first results.

2. Experimental setup

The SEAP consist of two important parts i) vacuum located electron gun, ii) nanomembrane (window) as interface between vacuum and atmosphere. For beginning we just used very simple electro gun consisting of hairpin filament (company), cylindrical electrode and anode with sealed Si₃N₄ membrane of 100 nm thickness and 1 mm site (square shape). In the Figure 1 is the schematic view of the SEAP and also electric scheme for the measurements. In previous works [2 - 4] the researcher already used membranes from this material (Si₃N₄) thick 300 nm and area of window 1x1 mm² and achieved good results regarding operation of SEAP, however, electron transmission only at electron energies above 8 kV was efficient.

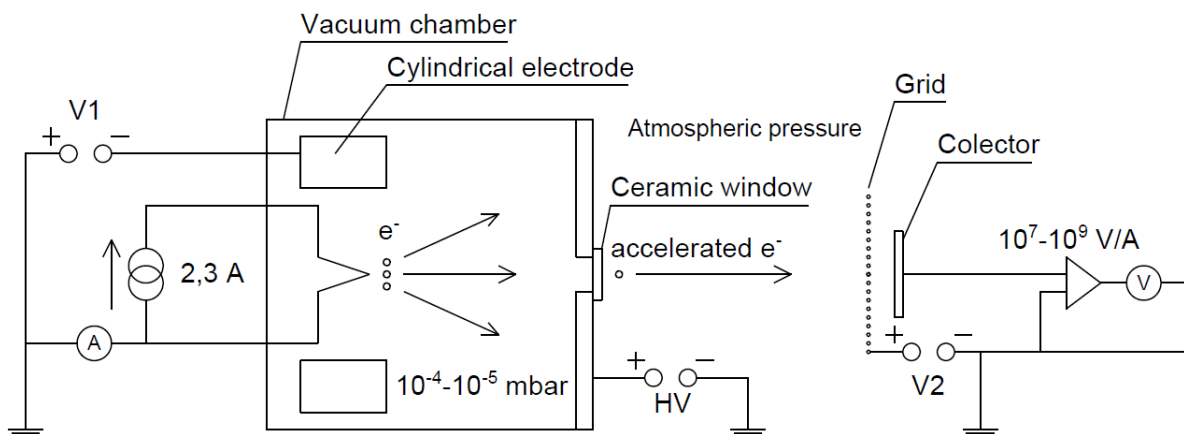


Fig. 1 Experimental setup of electron gun

The filament was heated by current of 2.3 A, what result in temperature of about 2600 K and thermal emission of free electrons with distribution of energy (maximum at 1 eV) [6]. These electrons are accelerated to anode connected to HV source (see, Fig. 3). In the middle of anode is drilled hole (diameter 1.5 mm) and from atmospheric site we have stuck the Si_3N_4 window. The Figure 2 left panel show the anode with window. Role of cylindrical electrode around the filament in Fig. 3 is to focus electron flux to membrane. Electrons with sufficient kinetic energy can penetrate through Si_3N_4 membrane to air at atmospheric pressure and ionize it. According to [1] penetration depth of 10 keV electrons in air is maximally 2 mm. The positive ions generated by SEAP are collected by a shielded ion collector. The measure ion current was in order of $10^{-7} - 10^{-12}$ A. The secondary electrons generated by ionization of air are attracted to the positive HV electrode.



Fig. 2 Left: Image of transparent 100 nm stick window, when filament is heated, Right: Image of vacuum part of electron gun.

3. Results

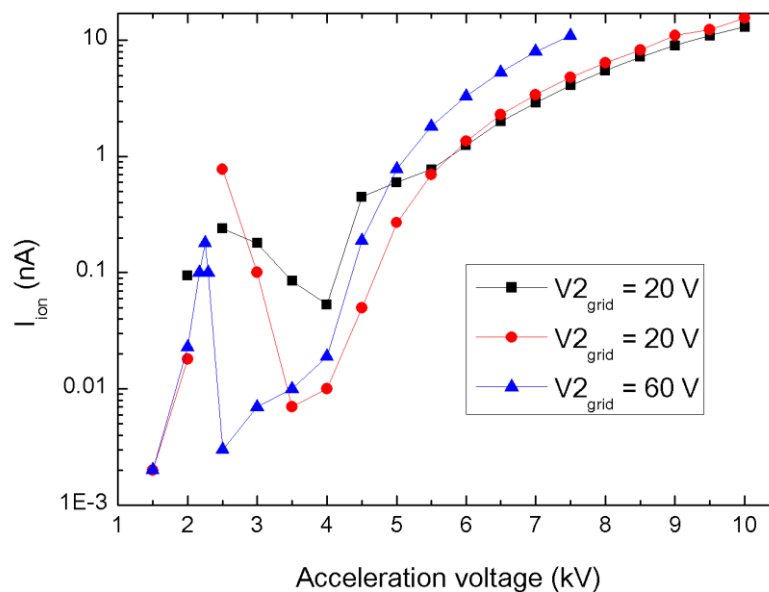


Fig. 3 Dependence of ion current in air and acceleration voltage at different grid potentia

In the Figure 3 we can see our very first measurements of the ion current generated by electron beam in air at atmospheric pressure as function of the acceleration voltage (AV) applied by HV source. The distance between anode with Si_3N_4 window and the ion collector was 6.5 cm during all three measurements (no special reason for this distance). We expected continuous increase of the ion current with increasing AV. In lower range of AV we observed a distinguished local maximum peaking between 2 – 2.5 kV. At this peak ion current reached values from 0.1 nA up to 1 nA. In the AV range 3.5 - 4 kV there was a minimum and at AV above 4 kV we have observed a gradual increase in ion current. At present time we do not have yet explanation for this phenomenon, but we will try to resolve it in our further studies.

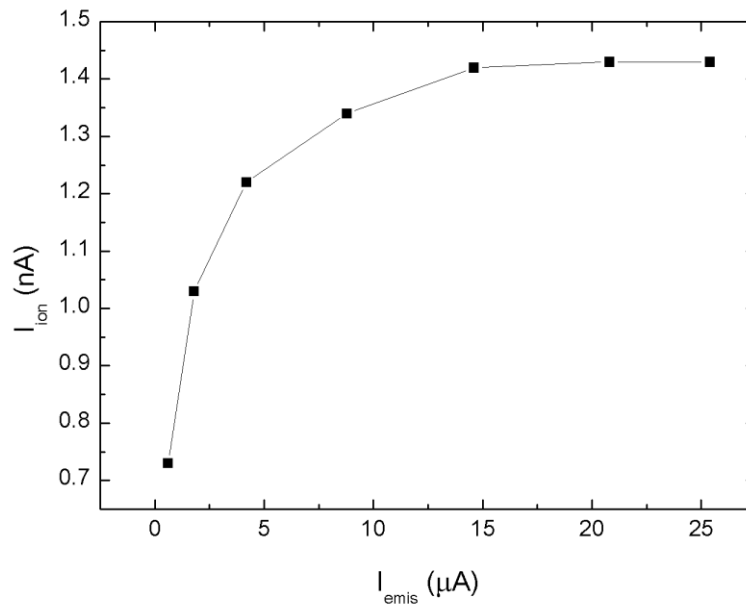


Fig. 4 Rise of Ion current with increase of emission current from filament

In the Figure 4 we present the dependence of the ion current in air on the electron current emitted from the tungsten filament. Above emission current of 15 μA , the ion current was saturated, but already at 5 μA , the ion current at collector achieved almost 60 % of the saturated value. We suppose this effect could be caused by the surface charges created on Si_3N_4 window, which repulses most of electrons approaching from the filament. Similar saturation effects were observed also in earlier studies. Data in the Figure 4 were measured at $AV = 6$ kV.

4. Conclusion

In this paper we present recently constructed SEAP source and very first results. We have succeeded to generate first electrons at atmospheric pressure and the ion currents generated by these electrons were in the order 1 - 10 nA. Which are acceptable values for an API source for IMS. We have observed electron transmission already at relatively low accelerating voltages 2 – 2.5 kV where the ion current exhibits a distinguished local maximum. The first result we consider promising and in future we plan to improve the SEAP in order to use it in different application in field of MS, IMS, electron drift and electron induced fluorescence.

5. References

- [1] de Urquijo-Carmona J, *J. Phys. D: Appl. Phys.*, (1983) **16**: 1603-1609.
- [2] Gunzer F, Ulrich A and Baether W, A novel non-radioactive electron source for ion mobility spectrometry, *Int. J. Ion Mobil. Spec.* (2010) **13**:9-16
- [3] Cochems P, Langejuergen J, Heptner A and Zimmermann S, Towards a miniaturized non-radioactive electron emitter with proximity focusing, *Int. J. Ion Mobil. Spec.* (2012) **15**:223-229
- [4] Cochems P, Runge M and Zimmermann S, A current controlled miniaturized non-radioactive electron emitter for atmospheric pressure chemical ionization based on thermionic emission, *Sensors and Actuators A206* (2014) 165– 170
- [5] Ulrich A, Heindl T, Krücken R, Morozov A, Skrobol C, Wieser J, Electron beam induced light emission, *Eur. Phys. J. Appl. Phys.* (2009) **47**: 22815 p1-p4
- [6] Hawkes P W and Kasper E, Principles of Electron Optics, Volume 2 Applied Geometrical Optics. ACADEMIC PRESS LIMITED, 1989. ISBN 0-12-333352-0

UPGRADE OF THE 5-CHANNEL NEUTRAL PARTICLE ANALYSER FOR THE COMPASS TOKAMAK

Michal Stano¹, Adam Seman¹, Štefan Matejčík¹, Jan Stöckel²

¹*Department of Experimental Physics, Comenius University, 842 48 Bratislava, Slovakia*

²*Institute of Plasma Physics AS CR, Tokamak Department, Za Slovankou 1782/3, 182 00 Prague 8, Czech Republic*

E-mail: stano@fmph.uniba.sk

A 5-channel neutral particle analyser has been refurbished for use on the Compass tokamak in Prague. This paper provides brief description of the diagnostic method, the analyser, and presents results of the calibration of the instrument. The calibration involves both simulation of ion trajectories using the Simion program and calibration measurements using an auxiliary ion source.

1. Introduction

Neutral particle analysis (NPA) is a well established plasma diagnostic method. It has been used since early tokamak experiments in 1960's. The method is based on measurement of kinetic energy of neutral atoms emitted from a high-temperature magnetically confined plasma. In the analyser, the neutral atoms are ionized by flying through a stripping cell and their energy is evaluated using an electrostatic analyser coupled with an array of detectors. The primary use of NPA is measurement of the ion temperature and ion energy distribution function. The NPA may also include magnetic field sector for mass separation of the analysed particles. In this case, it provides additional information on H-D or D-T isotope ratio and measures ion energy distribution for each species individually [1, 2].

The analyser used in this work was built by the Ioffe Physical-Technical Institute of the Russian Academy of Sciences in 1974 and was previously used on the CASTOR tokamak in the Institute of Plasma Physics, the Czech Academy of Sciences (IPP). Currently, IPP intends its use at the Compass tokamak [3]. To achieve this objective, the analyser needs to be refurbished and fitted with new control and data acquisition electronics. The analyser is being refurbished at the Comenius University. It has been equipped with channeltron detectors and first tests using an auxiliary ion source have been performed [4].

2. Simulation of ion trajectories

In order to simulate ion trajectories in the analyser, the geometry of all electrodes and the whole analyser was digitized from photographs of the respective parts of analyser using the LibreCAD program. The geometry was then imported into the Simion[®] program. This program uses finite difference method to calculate trajectories of charged particles in electric and magnetic field.

Potential on the deflection electrode was set to be the same as in the calibration measurements and potentials of guiding electrodes for each channel were optimised for the best ion transmission. Example of the simulation is shown in the Figure 1. The ions were flown from a single spot corresponding to position of the auxiliary ion source used in the calibration measurements. Initial energy of ions was varied while potentials on all electrodes were fixed. In this way, the energy range covered by each channel was evaluated for a given deflection voltage.

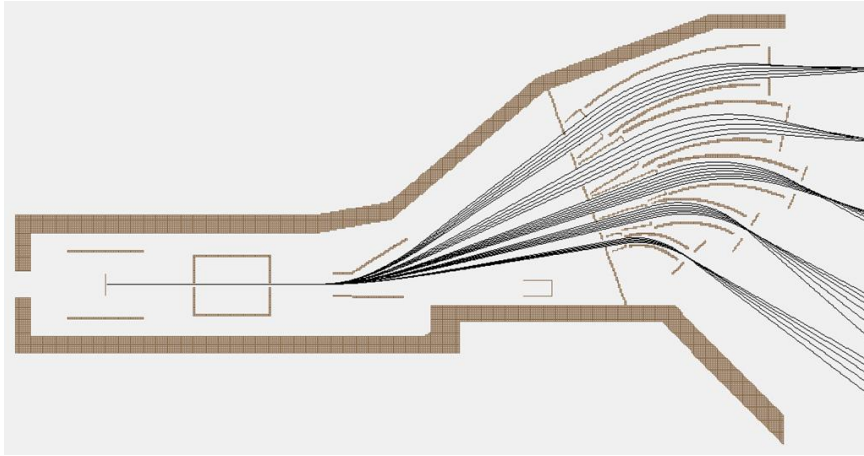


Fig. 1. Ion trajectories calculated for various ion energies using the Simion program.

3. Calibration of the analyser

Schematics of the setup used for the calibration is shown in Figure 2. The ion beam is generated by an auxiliary ion source using thermal evaporation of an alkali salt from a heated metal substrate. The ions were accelerated to desired kinetic energy by a positive potential applied to the substrate. The purpose of the calibration was to determine the energy range of each detection channel for a given voltage applied on the deflection electrode. This was achieved by measurement of ion count registered on a selected detection channel as a function of the accelerating voltage, while potentials on the deflection electrode as well as guiding electrodes were kept constant. The acceleration voltage was controlled by Multi channel scaler (MCS), Ortec. The MCS also registered ion count at given acceleration voltage. Ions were detected by type VEU-6 channeltrons, Gran, Russia. The signal was conditioned by the Model 113 preamplifier, Ortec, and shown on Agilent DSO5032A oscilloscope. The oscilloscope was used also as a discriminator, its TTL trigger output was coupled to MCS to count the ions registered at given ion energy. The measurement was done for all channels at the same deflection voltage. The calibration was performed in the energy range up to 800 eV. This range was limited by isolation of the floating heater power supply.

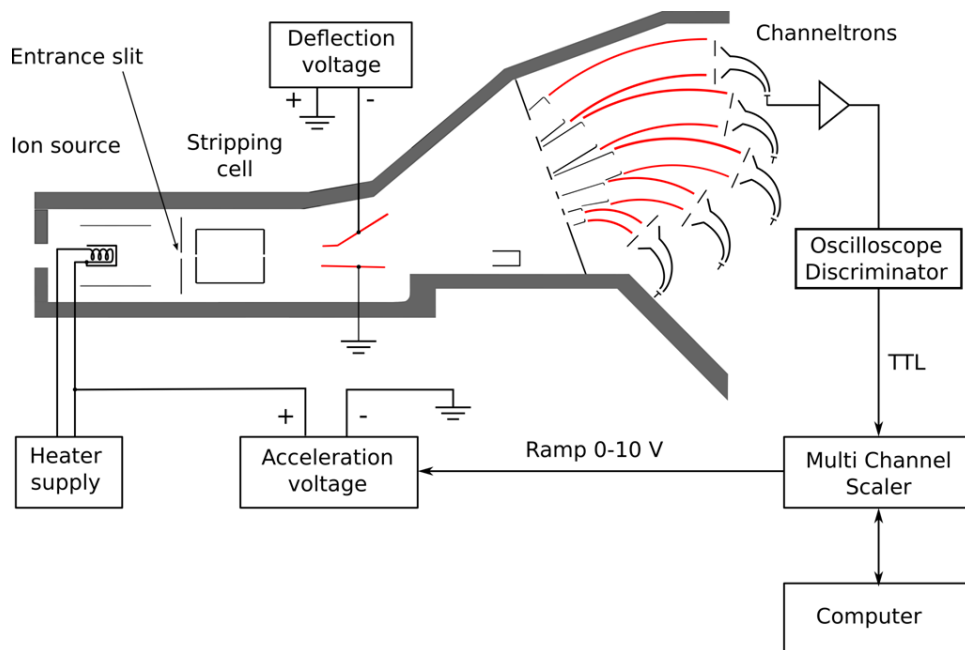


Fig. 2. Schematics of the setup used for calibration.

Two examples of calibration measurement are shown in Figure 3. Both measurements were done at deflection voltage of 71.3 V. Opening of the entrance slit was adjusted to 4 mm and 2 mm, respectively. Figure also shows energy range of the each channel resulting from simulation at the same deflection voltage.

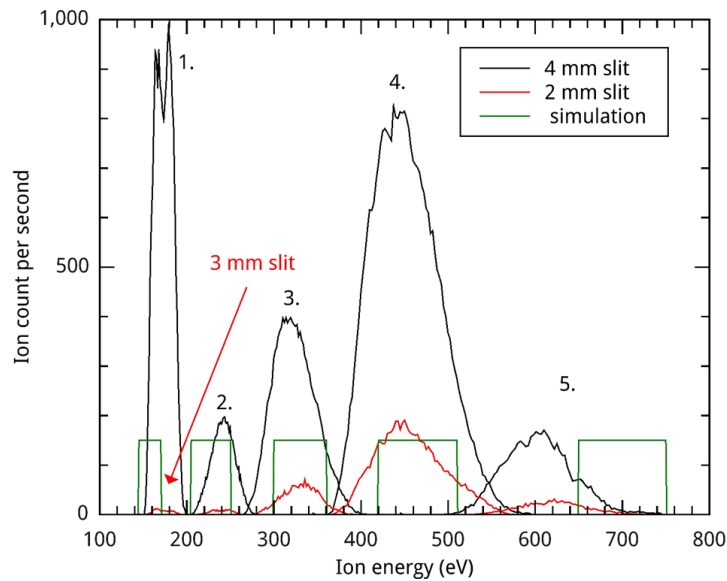


Fig. 3. Comparison of experimental energy spectrum with the numerical simulation.

Reasonable agreement between the simulation and measurement has been observed for the energy range of the first four detection channels while the 5th channel ions were registered at lower energies than predicted by the simulation. It is also seen that reduction of the entrance slit from 4 mm to 2 mm results in more than 50% signal loss for all channels. The signal reduction is the most significant at the first channel where no ion flux could be registered with 2 mm slit. Consequently, the slit had to be opened to at least 3 mm to register some ions. The unproportional loss of signal at reduced entrance slit may be caused by misalignment of the entrance slit with respect to the stripping cell.

Energy range of the each channel was studied as a function of deflection voltage, see Fig. 4.

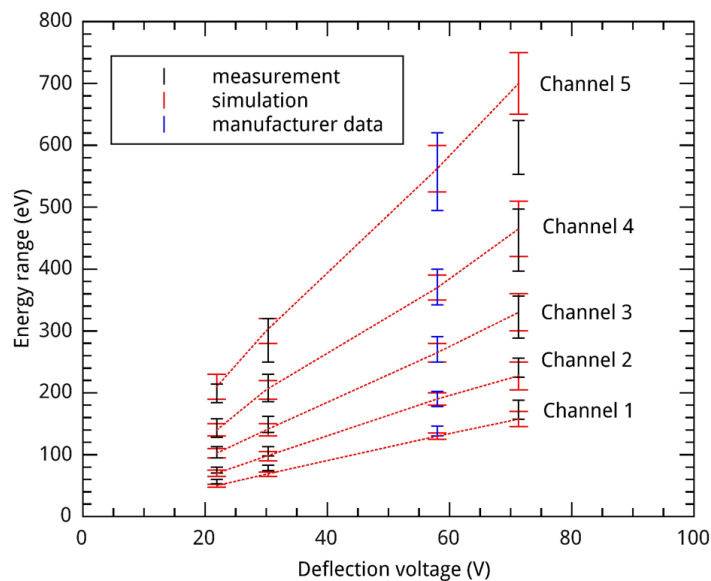


Fig. 4. Energy range of the each detection channel as a function of the deflection voltage.

The calculated results exhibit the expected linear dependence. Measured data follow the same trend except of the 5th channel at the highest deflection voltage. Data from the analyser documentation [5] are also shown.

Although all detection channels are operational, the results indicate that accuracy of both ion energy and ion intensity measurement needs to be improved prior to use of the analyser at the Compass tokamak.

This work was supported by the Slovak Research and Development Agency under Contract No. APVV-0733-11 and VEGA grant agency, project Nr. 1/0514/12.

4. References

- [1] J.Wesson and D.J.Campbell. Tokamaks. International Series of Monographs on Physics. OUP Oxford, (2011).
- [2] S.S. Medley, A.J.H. Donné, R. Kaita, A.I Kislyakov and M. P. Petrov, A.L. Roquemore, Rev. Sci. Instrum. **79**, 011101 (2008)
- [3] V. Weinzettl, R. Panek, M. Hron, J. Stockel, F. Zacek et al., Fusion Engineering and Design, **86**, (2011)
- [4] A. Seman, Bachelor thesis, Comenius University (2014)
- [5] V.N.Ageev, 5-channel neutral particle analyser, Ioffe Physical-Technical Institute of the Russian Academy of Sciences, St. Petersburg, Russia (1974)

PLASMA-ASSISTED ENCAPSULATION OF POLLEN FOR QUANTITATIVE ANALYSIS USING LASER INDUCED BREAKDOWN SPECTROSCOPY

Mária Suchoňová¹, Corinne Foissac², Michaela Horňáčková¹, Brigitte Mutel², Adriana Annušová¹, Pavel Veis¹ and Philippe Supiot²

¹*Department of Experimental Physics, Faculty of Mathematics, Physics and Informatics, Comenius University, Mlynská dolina F2, 84248 Bratislava, Slovak Republic,*

²*Institute of Electronics, Microelectronics and Nanotechnology (IEMN) UMR-CNRS 8520, Lille 1 University, 59650 Villeneuve d'Ascq, France*

E-mail: maria.suchonova@fmph.uniba.sk

To conduct qualitative and quantitative studies using LIBS technique, a method of encapsulation of pollen assisted by plasma was developed and achieved. The methodology required the deposition of a monolayer of pollen on a calibrated hydrophilic surface. This latter was achieved in several steps involving a polymerization RPECVD and a treatment step in the LRA. Moreover, optimal setups of measurements of pollen samples using the LIBS technique such as energy of laser per pulse, gate delay and gate width were studied and found. Subsequently, the selected setup parameters were tested for two pollen samples, liliun and hibiscus rosa-sinensis. On the basis of analysis of measured data it was shown that LIBS is a suitable method for pollen samples analysis.

1. Introduction

Today, the pollen is the subject of many studies, due to the allergenic effects but also to its participation in the transport of many pollutants.

This work aims to propose a study of the quantitative and qualitative analysis of pollen samples using the Laser Induced Breakdown Spectroscopy (LIBS) technique. Based on optical emission spectroscopy, this method allows the analysis of elementary composition of ablated samples. To perform analysis by LIBS on small sized samples like pollen grains, it is necessary to develop a method of pollen immobilization based on a process of surface modification by plasma to control and quantify the distribution of pollen. This methodology of encapsulation requires the deposition of a monolayer of pollen on a calibrated hydrophilic surface. This latter requires several steps involving the polymerization of the 1,1,3,3-tetramethyldisiloxane (TMDSO) by Remote Plasma Chemical Vapour Deposition (RPECVD) [1-4] and the treatment steps in the Lewis-Rayleigh-Afterglow (LRA) of nitrogen discharge, characterized by high nitrogen atoms concentration [5].

Several studies mentioned the use of LIBS for the analysis of plants. Most of them showed that LIBS coupled with supporting procedures such as principal components analysis (PCA), linear discriminant analysis and hierarchical cluster analysis is suitable for distinctive study between bacterial spores, molds and pollen or can classify several type of plants pollen [6-9]. Based on these studies and thanks to the advantages of LIBS, like the minor or no sample preparation, high speed of data acquisition and minimal damage to the sample, we assumed that the LIBS method is also useful in analysing samples of pollens.

The analysed pollen samples were prepared at the Institute of Electronics, Microelectronics and Nanotechnology of Lille and analysed by LIBS at the Department of experimental physics of Faculty of Mathematics, Physics and Informatics in Bratislava.

2. Experiments

The experimental set up of the RPECVD reactor for plasma polymerization is shown in Fig. 1(a). The nitrogen (grade 99.99%) flow (1.8 NL/min) was excited by a microwave discharge in a fused silica tube. By a continuous pumping (roots pump Pfeiffer), the reactive species flow from the discharge to the deposition chamber located 1 m from the discharge in the LRA. The main reactive species in this latter zone which is free of charged particles are nitrogen atoms in the ground electronic state N(⁴S) [5]. The TMDSO monomer (Sigma Aldrich, grade 97%) premixed with oxygen or nitrogen (grade ≥ 99.5%) was introduced in the LRA region through a coaxial injector. Flows of N₂, O₂ and

TMDSO were controlled at 550 Pa by means of MKS mass-flow controllers. The deposition step was always preceded by a pre-treatment in the LRA in order to clean the substrate and to desorb contaminants. The deposition step begins with the introduction of the monomer (premixed with oxygen or/and nitrogen) leading to a plasma polymerized organosilicon film (called pp-TMDSO). At last, the deposited film was treated in the LRA in order to modify its surface properties.

Pollen grains were deposited on polypropylene (PP) substrates prepared according method shown in section 3.1. (Goodfellow, $1.2 \times 2 \times 0.9 \text{ mm}^3$). Water contact angles (θ_w) were measured using a PGX+ goniometer. The analyses were performed by deposition of deionized water droplets ($3 \mu\text{L}$) on considered surface.

Fig. 1(b) shows the scheme of the experimental apparatus implemented for LIBS analysis. For the plasma creation a Q-switched Nd: YAG laser (Brilliant EaZy, Quantel) with a modul for generating second harmonic at 532 nm and maximum energy of 165 mJ per pulse was used. Laser pulse duration was 4 ns. Echelle spectrometer (Mechelle ME 5000, Andor Technology) with intensified CCD camera (iStar, Andor Technology) were used for detection of plasma emission. The spectral resolving power of the spectrometer is $\lambda / \Delta\lambda = 4000$ and the range of recorded wavelengths is 200 - 975 nm. Optical elements, such as mirrors, lenses (Thorlabs, BK7) and optical fibre (Ocean optics, quartz), were used for focusing laser pulse and collecting plasma emission.

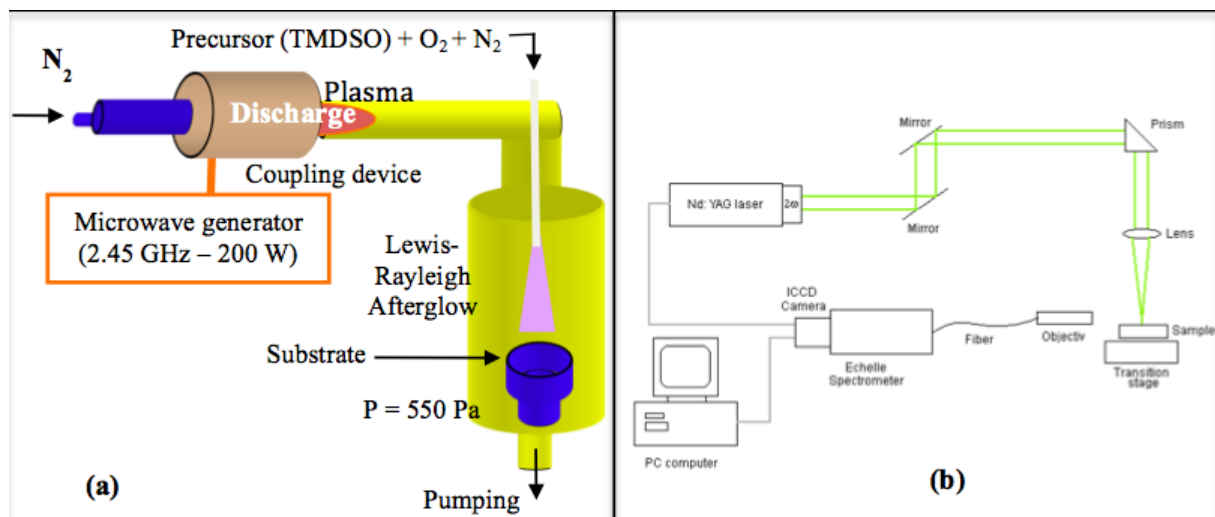


Fig. 1 Scheme of the RPECVD reactor (a) and LIBS (b) experimental set up.

3. Results and discussion

3.1. Sample preparation

The aim of the study being to perform a quantitative analysis of pollen, it is necessary to be able to prepare samples with various concentrations of pollen. To reach this aim, a calibrated wettable area ($\theta_w = 0^\circ$) was created on a superhydrophobic ppTMDSO surface ($\theta_w = 160^\circ$) deposited on PP samples. These surfaces with adjustable wettability were created by a treatment in the LRA. The pollen dispersed in an aqueous solution was then deposited on this surface in order to obtain a monolayer and encapsulated prior analysis.

The procedure of sample preparation before their LIBS analysis includes 6 steps schematically shown in Fig. 2:

- Step 1) Before its introduction in the plasma reactor, the PP substrate was sonicated with ether for 3 min in order to clean it. The θ_w value, initially about 85° , reaches 54° after this degreasing step.
- Step 2) The pre-treatment step in the LRA during 15 minutes allows to increase the wettability of the PP and leads to a θ_w value equal to 27° .
- Step 3) A super hydrophobic deposition film was obtained with N_2 , O_2 and TMDSO flows respectively equal to 20, 5 and 2.1 sccm. In these conditions, θ_w reaches 160° .

- Step 4) The calibrated wettable area is created using a mask with a hole ($\phi = 8 \text{ mm}$) placed on the superhydrophobic film. The masked sample is then treated in the LRA during 17 min. In these conditions, the calibrated area shows a θ_w value equal to 0° .
- Step 5) Pollen monolayers (see Fig. 3) are then performed. Liliun pollen is dispersed in water by means of a vortex and $9 \mu\text{L}$ are collected using a micropipette and deposited on the calibrated hydrophilic surface. Fig. 3(a) and 3(b) show that it is possible to obtain monolayers with different concentrations. These ones could then be determined using a counting chamber.
- Step 6) The last step before the LIBS analysis is to encapsulate the monolayer of pollen in order to allow the transport of samples and to limit contamination. So after water evaporation at room temperature, the pollen is covered with a film of pp-TMDSO obtained under standard conditions i.e. with flows of TMDSO and O_2 equal to 5 and 25 sccm, respectively [3].

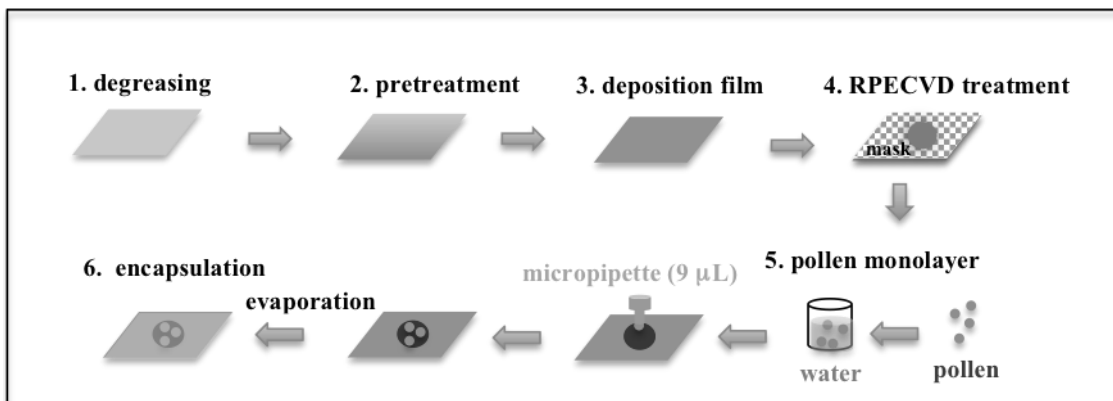


Fig. 2 Methodology of samples preparation

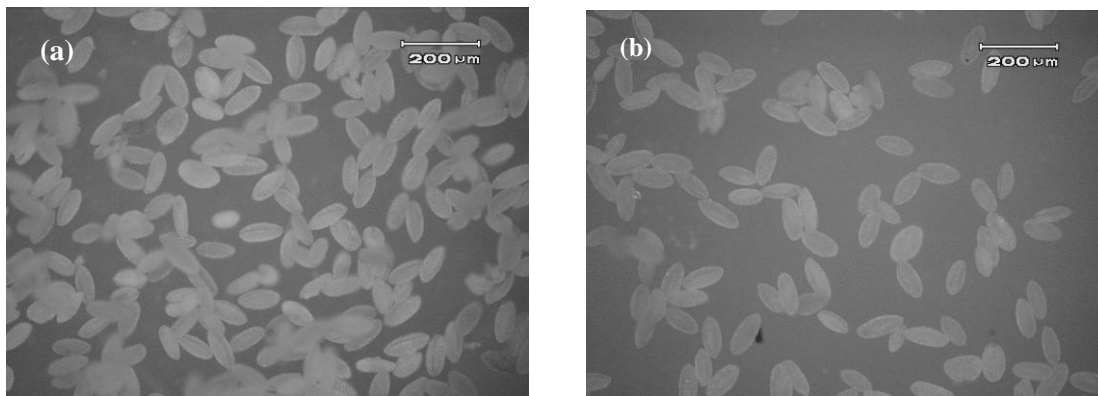


Fig. 3 Images of pollen monolayers obtained from optical microscopy.

3.2. LIBS analysis

In this work, we focused on determine optimal parameters of LIBS apparatus in order to analyse pollen samples, like the minimum laser power, optimal gate delay and gate width of the spectrometer window. For this purpose, a sample of the polymer surface without pollen, i.e. a PP substrate submitted to the steps 1, 2, 3, 4 and 6, was used. This "white" sample was used in order to avoid the destruction of samples with pollen, as we found out, that using the maximum power of Nd: YAG laser samples of pollen can be damaged.

At first, the optimal value of minimum laser energy per pulse was studied. The following measurements were realised at a constant value of the gate delay and width (both $1 \mu\text{s}$) and the laser power was changed. Energy of laser was changed by the setup of FLQS (Flash lamp Q-switched synchronization), FLQS = 170, 160, 150, 140, 130, 120, 110 μs . Seven different spectra with seven different values of laser energy per pulse, using a number of accumulation equal to 10, were recorded.

The optimal laser energy per pulse was at FLQS = 130 μs . It was the minimum energy at which it was possible to study emission spectra of the samples.

Thereafter, optimal gate delay and width values of the spectrometer window were looked for. In this case, the laser energy per pulse was set at FLQS = 130 μs while the gate delay (GD) and gate width (GW) were changed: GD = GW = 0,2; 0,5; 1; 2 and 5 μs . The optimal setup was chosen as GD = GW = 2 μs for obtaining the best signal to noise ratio.

After finding the appropriate parameters, we made test measurements in which two samples of pollen: liliium and hibiscus rosa- sinesis, were used. The samples contained of layer of Si with cyanoacrylate coating along with pollen. On the basis of previous findings the delay between the acquisition and plasma collection was set to 2 μs , using values of GW of 2 μs and FLQS of 130 μs . Each spectrum was recorded with an accumulation of 10 measurements. Elemental composition of the samples was determined from quantitative analysis. Pollen samples contained elements such as Ca, Mg, K, Na, Al, Si, N, O, C and H. Si was shown as the main component to the signal, because it formed the samples base. The presence of O and N elements is related to the fact, that the measurements were realized under ambient atmosphere. The C, N and O elements are also related to the presence of cyanoacrylate layer. The elements: Ca, Mg, K, Na and Al are components from the pollen itself.

For distinguish pollen samples a differential spectrum, which together with the original spectra of the individual samples is shown in figures 4, was used. Differences especially concerning the following elements: Mg, Ca and K were found. It shows that it is possible to differentiate individual pollen samples from each other by following these elements, a subject we will focus on in a future work. Moreover, we planed to perform quantitative analysis of pollen samples using the LIBS method as a continuation of this recent study. This task will present an original point of view on the problematic of quantification of pollen.

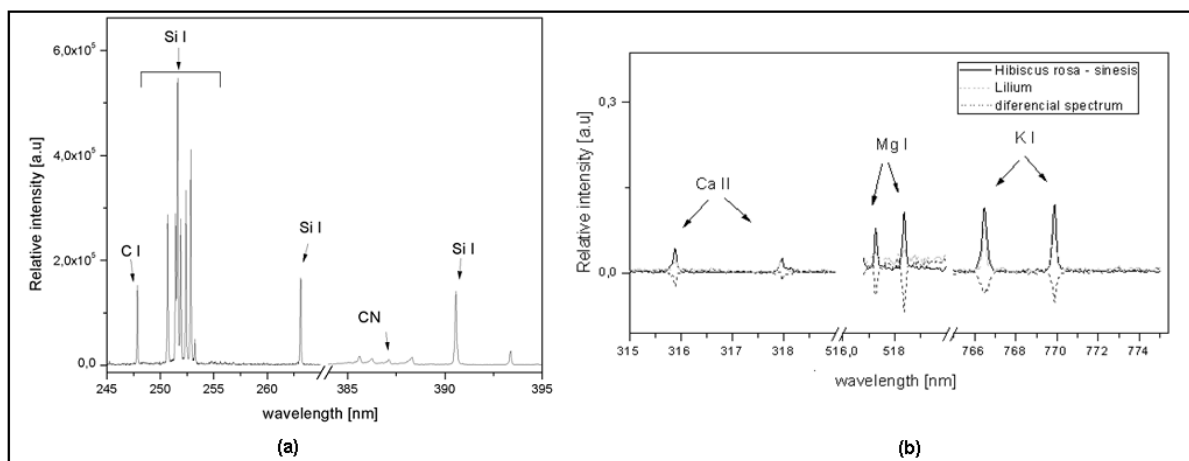


Fig. 4 Experimental spectra of the sample of polymer surface without pollen (a) and pollen samples and differential spectra (b).

4. Conclusion

In this study, a method of immobilization of pollen assisted by plasma to control and quantify the distribution of pollen in order to perform analysis by LIBS technique was developed and achieved. The methodology of encapsulation requires 6 steps: 1) the degreasing step of the PP substrate ; 2) the pre-treatment step in the LRA ; 3) the super hydrophobic film deposition obtained from polymerisation RPECVD ; 4) the calibrated wettable area creation step realised by the treatment of the masked sample in the LRA ; 5) the pollen monolayers deposition step and 6) the pollen encapsulation step with a pp-TMDSO film. For the LIBS analysis, optimal setups of experimental measurements of pollen samples such as energy of laser per pulse, gate delay and gate width were studied and found. For this purpose, a PP substrate submitted to the steps 1, 2, 3, 4 and 6 (i.e. a sample without pollen) was used. Indeed, the high power of laser can damaged the samples of pollen. Subsequently, the

selected setup parameters were tested for two pollen samples, liliun and hibiscus rosa-sinensis. On the basis of analysis of measured data it has been shown that LIBS is a suitable method for pollen samples analysis.

Acknowledgement: This work was supported by the French Ministries of Foreign Affairs (MAE) and of Higher Education and Research (MESR) under the project 31802YA (PHC Stefanik 2014), by the Slovak Research and Development Agency under the project number: SK-FR-2013-0035, by the Scientific Grant Agency of the Slovak Republic (VEGA) under the contract No. 1/0925/14 and by Comenius University under the project numbers: UK/491/2014, UK/503/2014, UK/587/2014.

5. References

- [1] Callebert F, Supiot P, Asfardjani K, Dessaux O, Goudmand P, Dhamelincourt P and Laureyns 1994 *J. of Appl. Polymer Science* **52** 1595
- [2] Supiot P, Vivien C, Granier A, Bousquet A, Mackova A, Escaich D, Clergereaux R, Raynaud P, Stryhal Z and Pavlik 2006 *Plasma Processes and Polymers* **3** 100
- [3] Rich S A, Vianner M, Vivien C, Godey S and Supiot P 2010 *Plasma Processes and Polymers* **7** 775
- [4] Ghali N, Vivien C, Mutel B and Rives A 2014 *Surface and Coatings Technology* **259** Part C 504
- [5] Mazouffre S, Foissac C, Supiot P, Vankan P, Engeln R, Schram D C and Sadeghi N 2001 *Plasma Sources Sci. Technol.* **10** 168
- [6] Samuels A C, DeLucia F C, McNesby K L and Miziolek A W 2003 *Applied Optics* **42** 6205
- [7] Boyain-Goitia A R, Beddows D C S, Griffiths B C and Telle H H 2003 *Applied Optics* **42** 6119
- [8] Merdes D W, Suhan J M, Keay J M, Hadka D M and Bradley W R 2007 *Spectroscopy* **22** (4) 28
- [9] Mularczyk-Oliwa M, Bombalska A, Kaliszewski M, Wlodarski M, Kopczynski K, Kwasny M, Szakowska M and Trafny E A 2012 *Spectrochimica Acta Part A: Molecular and Biomolecular Spectroscopy* **97** 246

LIPID MODIFICATIONS BY COLD ATMOSPHERIC PLASMA TREATMENTS AND THE INFLUENCE OF CHOLESTEROL

M. U. Hammer¹, S. Kupsch¹, E. Forbrig¹, H. Jablonowski¹, K. Masur¹, K.-D. Weltmann², A. Beerlink⁴, T. Gutschmann³, S. Reuter¹

¹Centre for Innovation Competence (ZIK) plasmatis at the INP Greifswald, Felix-Hausdorff-Str. 2, 17489 Greifswald, Germany

²Leibniz Institute for Plasma Science and Technology (INP Greifswald e.V.), Felix-Hausdorff-Straße 2, 17489, Greifswald, Germany

³Divisions of Biophysics, Leibniz Centre for Medicine and Biosciences, Research Centre Borstel, 23845 Borstel, Germany

⁴Deutsches Elektronen-Synchrotron (DESY), Notkestraße 85, 22607 Hamburg, Germany

E-mail: Malte.Hammer@INP-Greifswald.de

In plasma medicine, cells and bacteria are treated with cold atmospheric plasma that create reactive species both in the gas and in the liquid phase. A dogma of membrane biophysics is, that any externally applied substance has to interact or overcome the most outward interface of a cell to its environment -the membrane- before a cellular reaction takes place. Therefore the membrane is the first cellular target of reactive species during plasma treatment of eu- and prokaryotes. We used model systems composed out of lipids to investigate the effect of plasma treatments on cellular membranes. We studied the modification of important biophysical parameters of the membrane by plasma treatment. The observed effects on a membrane model representing eukaryotes were significantly reduced compared to the effects on a model representing prokaryotes. The findings help to understand the observed lower susceptibility of eukaryotes compared to prokaryotes against plasma treatment.

1. Membrane as first cellular target

A new and emerging field of applied plasma physics is the usage of cold atmospheric plasma (CAP) sources for the purpose of medical treatments. A plasma treatment leads to diverse effects on tissue and cells depending on the exact type of plasma source as well as operating parameters. Also indirect treatment, meaning plasma-treatment of liquids which are subsequently brought into contact with cells, results in cellular effects. Observed biological effects include growth modulation, induction of apoptosis or, especially at higher treatment times, necrosis; but the underlying molecular mechanisms are unclear.

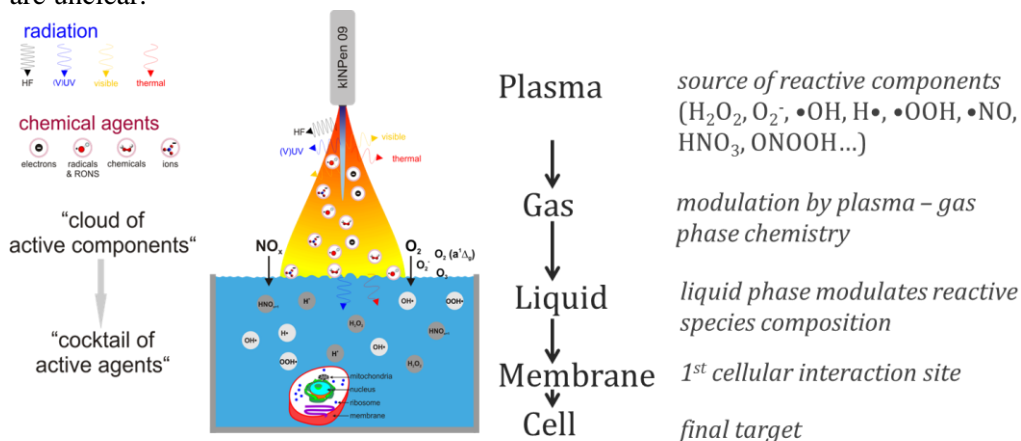


Figure 2: Schematical presentation of the pathway of reactive species from plasma to cell via gas and liquid phase. As it is the interface to the environment, the membrane is the first cellular interaction site.

The plasma sources create a “cloud” of highly reactive species in the gas phase due to interaction of ionized feed gas species with surrounding molecules. If liquids are treated, reactive species like OH radicals, superoxide anion radicals, hydrogenperoxide as well as nitrate/nitrite, indicating peroxyxynitrite production, are formed in or incorporated into the plasma-treated liquid. This “cocktail” of highly

reactive oxygen or nitrogen species (ROS, RONS) is capable of inducing biological effects including lipid peroxidation which leads to significant modifications of the biophysical properties of lipid bilayers (lipid whisker model [1]).

Based on a dogma of membrane biophysics, the first interaction site of any externally applied substances including ROS / RONS in plasma-treated liquids is the cellular membrane. Proteins and lipids are the constituents of cell membrane, the later responsible not only for the structural properties e.g. barrier function but also involved in signalling (“lipid signalling”) by raft/domain formation.

To get insight into the mechanisms of plasma-treatments on cells, we investigated the effects of plasma-treated (plasma source: kinpen (figure 2)) biological relevant liquids on liposomes and solid-supported bilayer.

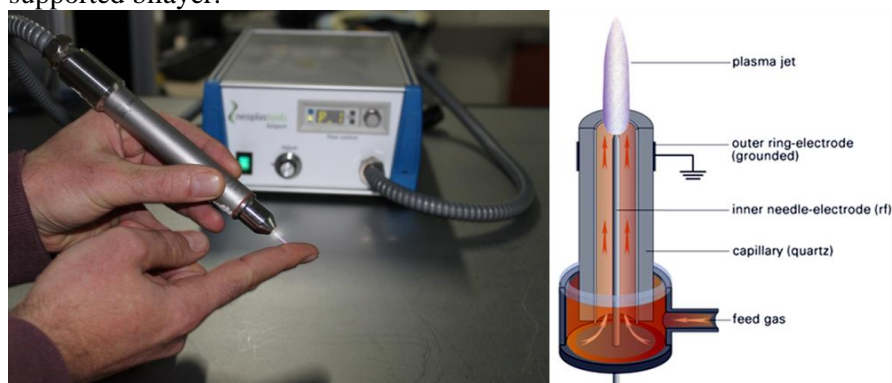


Fig. 2: Left: picture of kinpen with visible plasma effluent at the nozzle of the pen-type hand-held unit. The power supply is in the background, the gas supply unit is not shown. Right: a technical schema of the kinpen showing the electrode configuration.

By means of electron spin resonance spectroscopy, small angle x-ray and dynamic light scattering, x-ray reflectometry, patch-clamp, atomic force microscopy, and fluorophoric agents the influence of plasma-treatments on ROS/RONS generation, bilayer thickness, domain formation, liposome size and zeta-potential, and fluidity was investigated. Furthermore, we found that plasma-treated liquids can induce lesions in lipid bilayers as well as in HaCaT cells.

Based on our experimental findings and literature, a detailed molecular mechanism for the observed formation of transient lesion is proposed [2], which is based on the concepts of Hancock's self-promoted uptake [3], the umbrella model for lesion formation [4] and the lipid whisker model for oxidized membranes [1].

To investigate the observed phenomena, that bacteria shown a higher susceptibility against plasma treatment than eukaryotic cells, we investigated the effect of cholesterol -which is a constituent of eukaryotic membranes but not of prokaryotic organism- on plasma-induced modification of biophysical parameters of reconstitute model membranes. The results indicate clearly, that the influence of plasma-treatments on lipid membranes is dramatically reduced or modified if cholesterol is part of the membrane. This could explain the observed susceptibility differences of pro- and eukaryotes.

The authors acknowledge the funding by the BMBF (03Z2DN12) within the ZIK plasmatis at the INP Greifswald.

2. References

- [1] Greenberg M E, Li X-M, Gugiu B G, Gu X, Qin J, Salomon R G and Hazen S L 2008 The lipid whisker model of the structure of oxidized cell membranes *Journal of Biological Chemistry* **283** 2385-96
- [2] Hammer M U, Forbrig E, Kupsch S, Weltmann K-D and Reuter S 2013 Influence of Plasma Treatment on the Structure and Function of Lipids *Plasma Medicine* **3** 97-114
- [3] Hancock R E W 1984 Alterations in outer-membrane permeability *Annual Review of Microbiology* **38** 237-64
- [4] Shai Y 2002 Mode of action of membrane active antimicrobial peptides *Biopolymers* **66** 236-48

DC TRANSIENT SPARK DISCHARGE IN WATER: EFFECTS ON CELLS, DNA, PROTEINS AND ENZYMES

K. Hensel¹, K. Tarabová¹, K. Sano^{1,2}, B. Tarabová¹, M. Janda¹, Z. Machala¹,
R. Jijie³, C.T. Mihai³, L. Gorgan³, V. Pohoata³, I. Topala³

¹Comenius University, 84248 Bratislava, Slovakia

²Toyohashi University of Technology, 4418580 Toyohashi, Japan

³Alexandru Ioan Cuza University, 700508 Iasi, Romania

E-mail: hensel@fmph.uniba.sk

DC-driven transient spark (*TS*) discharge operated in air in contact with water (phosphate buffered solution (*PBS*) or deionized water) was used for the treatment of mammalian cells (*Vero line* normal cells, *HeLa line* cancerous cells), dsDNA, protein (*Bovine Serum Albumin*) and enzyme (*pepsin*). Two systems using different methods of water treatment were used: water electrospray and water electrode. Direct exposure of cells to the discharge and indirect exposure to discharge activated gas flow were compared, as well as the effects of *TS* discharge and pulsed plasma jet in helium used in parallel experiment. The cells were analyzed for viability and apoptosis. Viability of cells was evaluated by trypan/methylene blue staining, apoptosis by complementary analysis using Annexin V and Propidium iodide, while DNA, protein, and enzyme concentrations were evaluated by UV absorption and fluorescence spectroscopy.

1. Introduction

Cold atmospheric pressure plasmas generated by various electrical discharges have been successfully tested for various biological and biomedical applications over the past decade. Thanks to ionizations, dissociations, excitations, production of various chemically active species and reactions occurring at relatively low gas temperatures, the plasmas can efficiently kill bacteria, or even spores and biofilms that are generally very difficult to inactivate. Plasmas are very suitable for bio-decontamination, disinfection and sterilization of surfaces, medical instruments, water, air, food, and even living tissues. Despite many reported positive effects of the plasmas, their interaction with living cells and microorganisms remains still relatively not well understood.

2. Experimental

The objective of this work was to study the plasma interaction with living cells and selected biomolecules (DNA, protein, enzyme). The plasma was generated by DC-driven transient spark (*TS*) discharge in atmospheric pressure air [1] in contact with water – either phosphate buffered solution (*PBS*) or deionized water (*DI*). Elementary processes in the plasma were investigated and linked to the biophysical response of normal cells (*Vero line*, monkey kidney cells) and cancerous cells (*HeLa line*, human cervical cells) and effects on DNA, protein (*Bovine Serum Albumin*) and enzyme (*pepsin*). Direct plasma exposure was compared with an indirect exposure of the water to the plasma activated gas flow. The effects of *TS* discharge were compared with the results obtained with He pulsed plasma jet in parallel experiment.

Two systems of *TS* discharge using different methods of water treatment were used. The first system, *water electrode system (WE)*, with a point-to-plane discharge geometry consisted of high voltage needle electrode placed above the inclined grounded plane electrode (**Fig. 1a**). The water was run through a narrow channel in the plane electrode and circulated by a peristaltic pump with various flow rates (up to 30 mL/min). The second system, *water electrospray system (WS)*, also with point-to-plane geometry, consisted of high voltage hypodermic needle placed above the grounded mesh electrode with water delivered into the discharge zone via the hollow needle with a constant flow rate (0.5 mL/min), depicted in **Fig. 1b** and described in detail in [2]. Both systems were operated in atmospheric pressure air, with electrode distance 1 cm, frequency up to 4 kHz and the treatment time up to 20 min. Direct exposure of cells to the *TS* discharge systems was compared to indirect exposure to discharge activated gas flow using the setup depicted in **Fig. 1c**. The reference system of the *pulsed*

plasma jet was of a dielectric barrier discharge type generated in He with the constant gas flow rate, described in detail in [3].

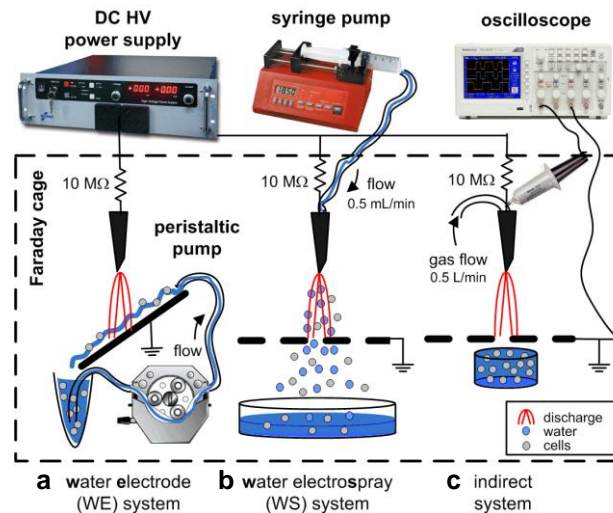


Fig. 1. Experimental setups of WE (a) and WS (b) systems for direct plasma exposure; and system for indirect exposure to the plasma activated gas flow (c).

The cells were analyzed for viability by trypan/methylene blue staining, and for apoptosis by complementary analysis using Annexin V and Propidium Iodide. The concentrations of DNA, protein, and enzyme were evaluated by UV absorption and fluorescence spectroscopy. The chemical analysis of treated water solutions was performed too and concentration of hydrogen peroxide, nitrites and nitrates, peroxy-nitrites, and dissolved ozone were measured, as well as acidity, conductivity and temperature of the solutions.

3. Results

This section presents the main results of direct and indirect plasma exposure of cells, DNA, protein and enzyme to *TS* discharge. **Fig. 2** shows the results of direct treatment of *TS* discharge on viability of HeLa cells. The initial concentration was approximately 500,000 cells/mL of *PBS*. Comparison of *WE* and *WS* systems (**Fig.2a**) shows similar lethal effect obtained in both systems. i.e. 51-56 % cytotoxicity. In general, cell viability decreased with increasing treatment time and discharge power. The maximal cytotoxicity of 93.5% was observed for 20 min treatment time and 4 kHz (**Fig.2b**).

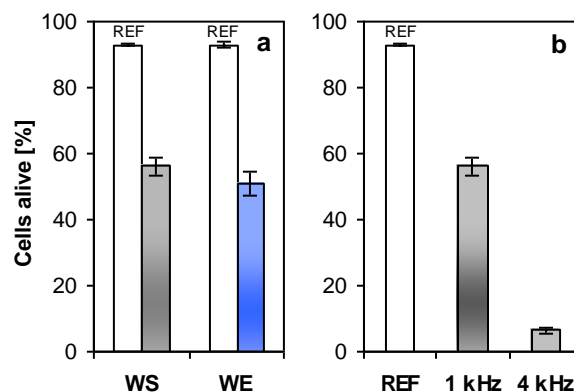


Fig. 2. Viability of HeLa line cells after direct exposure to *TS* discharge: **a)** comparison of *WS* and *WE* systems efficiency at 1 kHz after 10 min treatment, **b)** efficiency of *WS* system after 10 min at 1 Hz and 4 kHz.

Direct exposure of the cells to the discharge was compared with the indirect exposure of the cells to the discharge activated gas flow (30% O₂ in N₂, 0.5 L/min) delivered via syringe needle in point-to-plane geometry with mesh electrode placed 1-2 mm above the water surface. **Fig. 3** shows the viability of both Vero and HeLa cells after several minutes of indirect exposure. Stronger effect of plasma exposure was observed for HeLa (cancerous) cells than Vero (normal) cells. In general, lower cytotoxicity was observed for the indirect exposure compared with the direct exposure. In case of HeLa cells, 71% of cells were found still alive after 4 min of indirect exposure and 24 hours of incubation. The incubation is the time interval the cells were allowed to grow in an incubator after the plasma exposure to enter to the log phase, after which they were detached and re-suspended in *PBS*. Longer incubation time usually resulted in smaller overall cytotoxicity. Incubation time also affected the apoptotic behaviour of cells before their final death (**Fig. 4**).

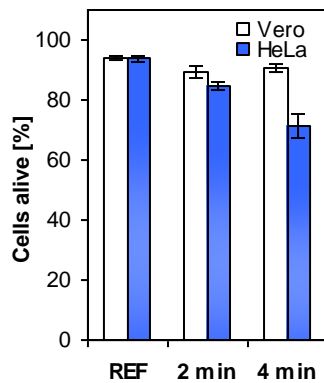


Fig. 3. Viability of Vero and HeLa line cells after 2 and 4 min of indirect *TS* plasma exposure [12.5 kV, 2 kHz].

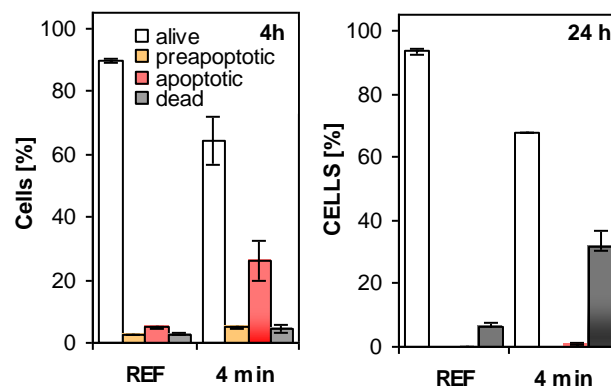


Fig. 4. Viability and apoptosis of HeLa line cells after 4 min of indirect treatment and 4h and 24 h of incubation [*TS*, 12.5 kV, 2 kHz].

The apoptosis was analysed by complementary tests using Annexin V and Propidium iodide. The results showed an increase of the number of apoptotic cells after 4 hours (26%), which were responsible for the increase of dead cells after 24 hours (32%). The effects of *TS* discharge and pulsed plasma jet were compared in parallel experiments. The jet was operated in helium (3 L/min) and used to treat HeLa and Vero cells for 4 min (applied voltage 4-8 kV, frequency 1-4 kHz). Maximum cytotoxicity of the plasma jet (29%, HeLa) was found comparable with indirect *TS* discharge exposure, but smaller compared to the direct exposure of *TS* discharge.

TS discharge was also used for the treatment of various biomolecules normally present inside the cells, including DNA, protein and enzyme. **Fig. 5a** shows the effect of *TS* discharge on the solution of DNA (9 ng/μL of DNA, 2 mL *DI*, flowrate 5mL/min) in *WE* system. The concentration of DNA

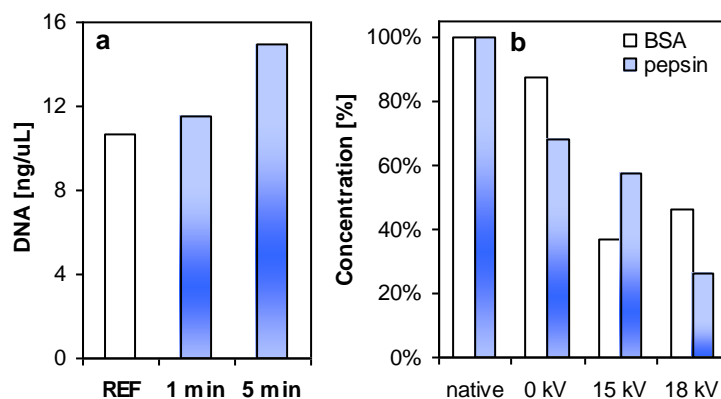


Fig. 5. Concentration of DNA in *WE* system (a) and protein (BSA) and enzyme (pepsin) in *WS* system after direct exposure by *TS* discharge (b).

analysed by UV spectrometry (260 nm) increased in time as a result of DNA fragmentation. Similar characteristics were also obtained for different initial concentrations of DNA and applied voltages. Likewise DNA, solutions of BSA and pepsin were exposed to *TS* discharge of different power and treatment time. Their concentration was monitored by UV (268 nm) and fluorescence (λ_{exc} 285 nm, λ_{em} 340 nm) spectrometry. **Fig. 5b** shows the decrease of their concentration (1mg/mL, 3 mL *DI*, 0.5 mL/min) as the function of the applied voltage in *WS* system. Similar tests performed in *WE* system showed even stronger effect.

4. Summary

DC transient spark discharge operated in air in contact with water was used for the treatment of cells, DNA, proteins and enzymes. Direct exposure of cells to the discharge in water electrode (*WE*) and water electro spray (*WS*) systems was compared with indirect exposure of cells to *TS* discharge activated gas flow and He pulsed plasma jet. *WE* and *WS* systems showed similar cytotoxicity that increased with treatment time and discharge power. The maximal cytotoxicity of 93.5% was observed for 20 min treatment time and 4 kHz. The results also demonstrated apoptotic behaviour of cells. Stronger effect of plasma exposure was observed for cancerous than normal cells; and for direct exposure than indirect exposure. The cytotoxicity of the plasma jet was found comparable with indirect *TS* discharge exposure, but smaller compared to the direct exposure of *TS* discharge. The treatment of DNA, protein and enzyme in *DI* solutions showed increase of DNA fragmentation and decrease of concentration of biomolecules with discharge treatment time and power. Thus, the results successfully demonstrated the potential of *TS discharge* as the efficient for bio-medical applications.

Acknowledgment

This work was supported by Slovak Research and Development Agency SK-RO-0024-12 and APVV 0134-12 grants, and Scientific Grant Agency VEGA 1/0998/12 grant .

References

- [1] Janda M., Machala Z., Niklová A., et al., 2012 Plasma Sources Sci. Technol. 21, 045006
- [2] Machala Z., Tarabová B., Hensel K., et al., 2013 Plasma Process. Polym. 10, 649
- [3] Topala I., Dumitrascu N., Dimitriu D.G., 2012 IEEE Trans. Plasma Sci. 40, 2811

IMPROVEMENT OF POLYMER SURFACE CYTOCOMPATIBILITY BY PLASMA TREATMENT AND SUBSEQUENT GRAFTING OF VICINAL COMPOUNDS

Zdeňka Kolská¹, Simona Lupínková¹, Karel Výborný², Nikola Kasálková Slepíčková², Alena Řezníčková², Michaela Nagyová², Václav Švorčík²

¹Faculty of Science, J. E. Purkyně University in Ústí nad Labem, České mládeže 8, 400 96 Ústí nad Labem, Czech Republic

²Department of Solid State Engineering, Institute of Chemical Technology, Technická 5, 16628 Prague, Czech Republic

E-mail: zdenka.kolska@ujep.cz

Vicinal compounds were grafted on different polymer foils previously treated (activated) in plasma discharge. Properties of the sample surfaces change significantly before and after plasma treatment and compounds grafting and they were studied using various methods to characterize changes in surface chemistry, polarity, wettability, etc. Representatives of unmodified and modified polymers were used for *in vitro* study of adhesion and proliferation of vascular smooth muscle cells.

1. Introduction

Polymers are well known and useful for their excellent bulk properties. They are frequently employed in industry, biotechnology, tissue engineering studies, medicine, etc. However, the inert nature of most polymer surfaces may limit their use. Surface chemistry, polarity, roughness and morphology strongly influence cell adhesion, proliferation and they are important for many potential applications of polymers in medicine and related fields [1].

Many modification techniques have been developed to improve surface properties of polymers. Grafting of plasma treated polymers with vicinal compounds is expected to provide new materials of excellent properties for potential usage in tissue engineering.

In this work some selected vicinal compounds were grafted on polymer foils previously activated by plasma. Surface properties changed significantly and were studied using various methods, by X-ray photoelectron spectroscopy, electrokinetic analysis, goniometry, atomic force microscopy. Representatives of unmodified and modified polymers were used for *in vitro* study of adhesion and proliferation of vascular smooth muscle cells. Plasma treatment and cysteamine grafting improved dramatically surface cytocompatibility [2].

2. Experimental

Materials

The following polymers in the form of foils supplied by Goodfellow Ltd., UK were used in this study: polyethyleneterephthalate (PET, 23 μm thick foils, density 1.30 g cm^{-3}), polytetrafluoroethylene (PTFE, 25 μm , 2.20 g cm^{-3}), polyvinyl fluoride (PVF, 50 μm , 1.37 g cm^{-3}), polyvinylidene fluoride (PVDF, 50 μm , 1.76 g cm^{-3}), polystyrene (PS, 30 μm , 1.05 g cm^{-3}), poly L-lactic acid (PLLA, 50 μm , 1.25 g cm^{-3}). The high density polyethylene (HDPE, 40 μm , 0.96 g cm^{-3}) and low density polyethylene (LDPE, 30 μm , 0.92 g cm^{-3}) were supplied by Granitol Ltd., CR. Tissue culture polystyrene (TCPS, TPP Switzerland) substrate was used as a control for cytocompatibility test of VSMCs. For grafting the following vicinal compounds were employed: (i) 2-aminoethanol ($\text{OH}-(\text{CH}_2)_2-\text{NH}_2$) and (ii) 2-aminoethanethiol (cysteamine, $\text{HS}-(\text{CH}_2)_2-\text{NH}_2$) by Sigma-Aldrich, Czech Republic.

Plasma treatment

The samples were firstly treated in DC Ar plasma in Balzers SCD 050 at room temperature (RT) under the following conditions: gas purity 99.997 %, flow rate 0.3 l s^{-1} , pressure 10 Pa, electrode distance 50 mm, its area 48 cm^2 , chamber volume approx. 1000 cm^3 , plasma volume 240 cm^3 , discharge power 8.3 W, treatment times were 120, 240 and 480 s.

Chemical grafting

Immediately after the plasma treatment the samples were inserted into water solution (2 wt. %) of cysteamine or 2-aminoethanol for 24 hours. Then the samples were rinsed by methanol and dried by inert nitrogen and then at Petry dishes for 48 hours.

Used analytical methods

Properties of all samples, pristine polymers, polymers treated by the plasma and polymers treated by the plasma and then grafted with vicinal compounds were characterized using different methods. Surface chemistry was characterized by X-ray photoelectron spectroscopy, chemistry and polarity by electrokinetic analysis and by goniometry, roughness and morphology by atomic force microscopy.

Electrokinetic analysis (determination of zeta potential) of all samples was accomplished on SurPASS Instrument (Anton Paar, Austria). Samples were studied inside the adjustable gap cell in contact with the electrolyte ($0.001 \text{ mol dm}^{-3}$ KCl) at RT. All samples were measured four times at constant pH (pH = 6.0) with a relative error of 10 %. For determination of the zeta potential the streaming current and streaming potential methods were used and the Helmholtz–Smoluchowski (HS) and Fairbrother–Mastins (FM) equations were applied to calculate zeta potential [3].

Surface concentrations of elements on sample surfaces were measured by X-ray photoelectron spectroscopy (XPS). Omicron Nanotechnology ESCAProbeP spectrometer was used to measure photoelectron spectra (typical error of 10 %). Exposed and analyzed area had dimension $2 \times 3 \text{ mm}^2$. X-ray source was monochromated at 1486.7 eV with step size 0.05 eV. The spectra were measured stepwise with a step in the binding energy of 0.05 eV at each of the six different sample positions with respect to the detector axis, at angle 0° (perpendicularly to sample). The spectra evaluations were carried out by CasaXPS program.

Surface wettability was determined by measurement of contact angle of samples. Surface contact angle of distilled water was determined by goniometry, i.e. the static (sessile) water drop was measured at RT at ten positions on two samples of each polymer using a Surface Energy Evolution System (SEES, Masaryk University, Czech Republic). The contact angles were evaluated using SEES code. Experimental error is 5 %.

Surface roughness and morphology of samples were examined by AFM method using VEECO CP II setup (tapping mode). Si probe RTESPA-CP with the spring constant $20\text{--}80 \text{ N m}^{-1}$ was used. It was proved by repeated measurements of the same region ($2 \times 2 \text{ }\mu\text{m}^2$ or $10 \times 10 \text{ }\mu\text{m}^2$ in area) that the surface morphology did not change after five consecutive scans.

Cell adhesion, proliferation

The adhesion and proliferation of vascular smooth muscle cells (VSMCs) on selected samples were studied by *in vitro* method described in detail earlier [2].

3. Results and discussion

Electrokinetic analysis provides information about surface chemistry and surface charge. Both of these are important for cell adhesion. Fig. 1 shows the results of zeta potential values for PTFE treated by plasma and grafted with vicinal compounds. It is evident the zeta potential depends on the polymer surface properties and it changes after the plasma treatment and also after vicinal compounds grafting. Plasma treatment results in a cleavage of original bonds (e.g. C-H, C-C, C-O), and creation of new reactive places on the polymer surface ("free" radicals, double bonds and new chemical groups, e.g. carbonyl, carboxyl and ester groups) [4]. Due to this plasma treatment leads to changes in the surface charge, chemistry and polarity and to change in zeta potential too. More pronounced results are obtained after vicinal compounds grafting. The most dramatic increase of zeta potential was obtained on PTFE plasma treated and grafted with cysteamine. It may be due to (i) different amount of grafted cysteamine and also (ii) the preferential bonds of cysteamine (via -SH or -NH₂ group) to surface [2,5]. Probably the cysteamine is bonded with the higher amount and even preferentially via -SH group with "free" -NH₂ group, which creates a positive charge on the surface in the presence of KCl water solution ($-\text{NH}_2 + \text{H}_2\text{O} \rightarrow -\text{NH}_3^+ + \text{OH}^-$) and as a result zeta potential increases to more positive (less negative) values.

The same results were obtained by other methods of characterization, by XPS, goniometry and AFM. All of them are presented in Tabs.1 and 2. XPS measurement confirmed the successful grafting both of vicinal compounds (presence of amino groups on surfaces). Also plasma treatment leads to surface chemistry change, the presence of oxygen groups increases.

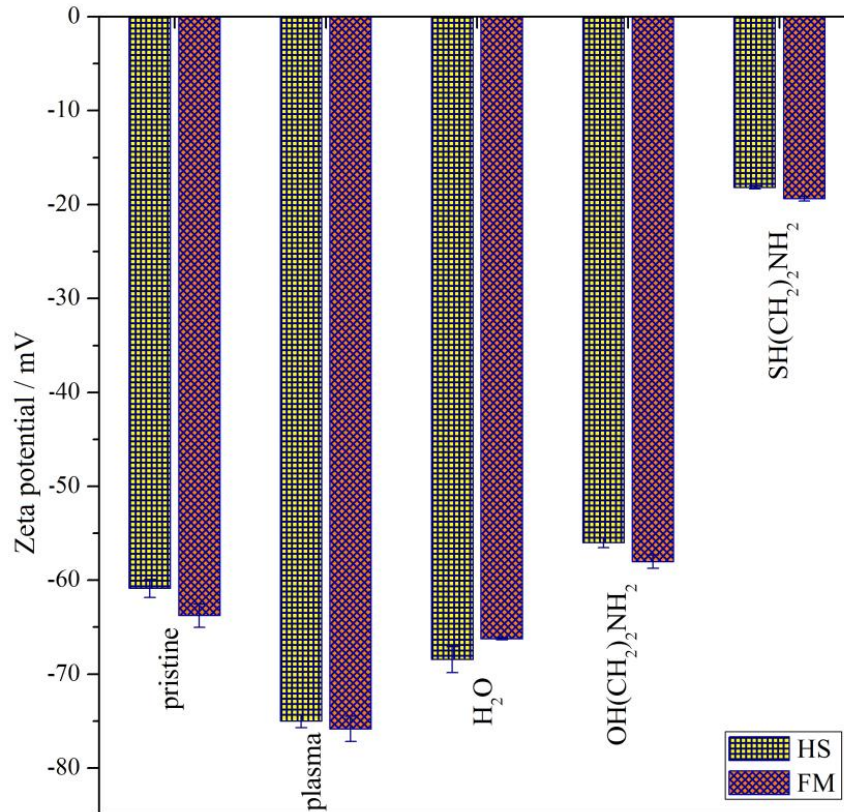


Fig. 1. Zeta potential of PTFE surfaces, unmodified (pristine), modified by plasma (plasma), etched by water (H_2O) and grafted with solutions of $OH(CH_2)_2NH_2$ and $SH(CH_2)_2NH_2$ [5].

Tab. 1. Atomic concentrations of C(1s), O(1s), F(1s), S(2p) and N(1s) measured by XPS method at angle 0° on (i) pristine polymers (pristine), (ii) polymers treated by plasma (plasma), (iii) polymers treated by plasma and etched by water (H_2O) and (iv) subsequently grafted by vicinal compounds $OH(CH_2)_2NH_2$ and $SH(CH_2)_2NH_2$ [5].

Sample	C(1s)	O(1s)	F(1s)	S(2p)	N(1s)
Pristine	30.4	-	69.6	-	-
Plasma	35.9	5.9	58.2	-	-
H_2O	36.8	6.0	57.2	-	-
$OH(CH_2)_2NH_2$	36.5	4.1	56.9	-	2.5
$SH(CH_2)_2NH_2$	41.3	7.1	44.7	3.1	3.8

Tab. 2. Contact angles of water droplets determined by goniometry and surface roughness obtained by AFM of (i) pristine polymers (pristine), (ii) polymers treated by plasma (plasma), firstly of the fresh sample (fresh) and also sample aged for 14 days (aged), (iii) polymers treated by plasma and etched by water (H_2O) and (iv) subsequently grafted by vicinal compounds $OH(CH_2)_2NH_2$ and $SH(CH_2)_2NH_2$ [5].

Sample	Contact angle θ [°]	Roughness R_a [nm]
Pristine	125.0 ± 2.6	13.8
Plasma (fresh)	65.5 ± 10.7	9.7
Plasma (aged)	92.3 ± 3.5	9.7
H_2O	79.4 ± 4.8	10.0
$OH(CH_2)_2NH_2$	86.4 ± 8.6	20.0
$SH(CH_2)_2NH_2$	90.3 ± 3.6	11.6

The cytocompatibility of prepared samples were tested using the vascular smooth muscle cells (VSMCs). Fig. 2 presents the photographs of adhered (1st day after seeding) and proliferated (6th day from cultivation) VSMCs on pristine selected polymers (left side) and with cysteamine grafted

polymers previously treated by plasma (right side). It is evident the cytocompatibility of grafted polymers are better in comparison with those on pristine polymers.

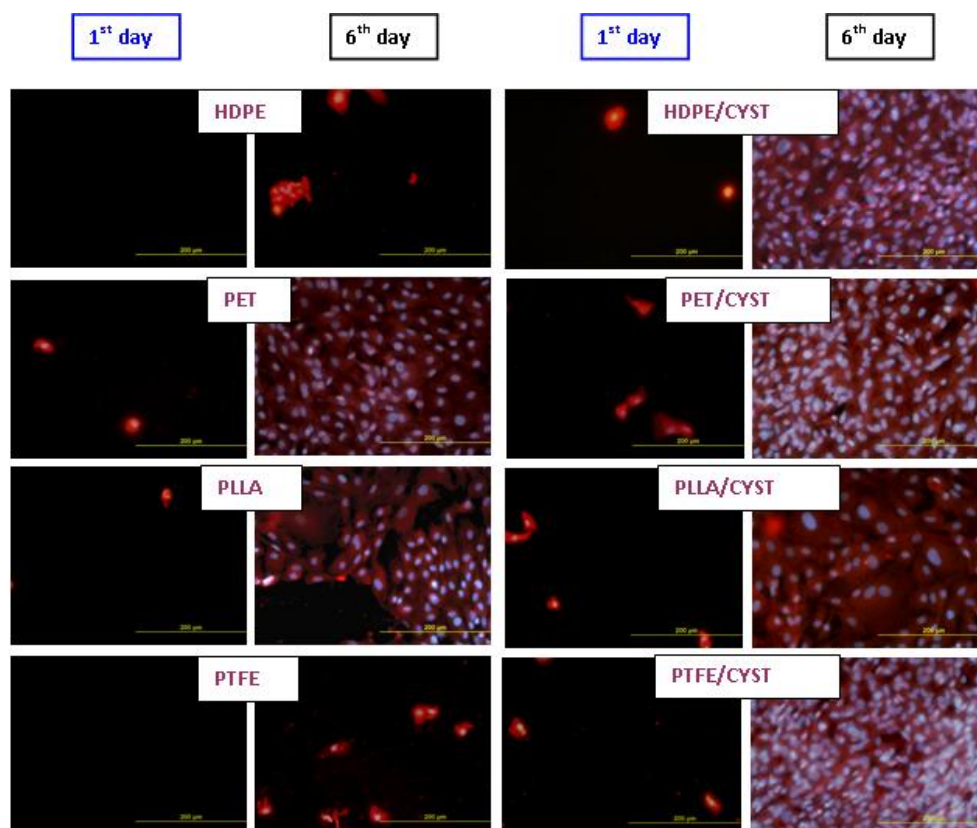


Fig. 2. Photographs of VSMCs adhered (1st day) and proliferated (6th day after cells seeding) on pristine and plasma treated for 120 s and subsequently grafted with cysteamine HDPE, PET, PLLA and PTFE [2].

4. Conclusions

Plasma treatment and vicinal compounds grafting lead to the dramatic changes in surface charge, chemistry and polarity and also roughness and morphology of the polymer foils under study. Plasma treatment and/or grafting of vicinal compounds improve the surface cytocompatibility. The modified polymers with enhanced biocompatibility may be of interest for applications in biomedicine and some other related fields.

Acknowledgement

This work was supported by the GACR project No. 13-06609S.

5. References

- [1] Reisinger B, Fahrner M, Frischauf I, Yakunin S, Svorcik V, Fiedorowicz H, Bartnik A, Romanin C, and Heitz J 2010 *Appl. Phys. A* **100** 511.
- [2] Kolska Z, Reznickova A, Nagyova M, Slepickova Kasalkova N, Sajdl P, Slepicka P and Svorcik V 2014 *Polym. Degrad. Stabil.* **101** 1.
- [3] Kolská Z, Řezníčková A and Švorčík V 2012 *e-Polymers* **83** 1.
- [4] Bačáková L, Filová E, Pařízek M, Ruml T and Švorčík V 2011 *Biotechnol. Adv.* **29** 739.
- [5] Lupinková S, Výborný K, Benkocká M, Slepícková Kasálková N, Švorčík V and Kolská Z 2014, *Chem. Listy*, in press.

SURFACE TREATMENT OF HIGH-IMPACT POLYSTYRENE USING RF-APPJ

Joanna Pawlat¹, Piotr Terebun¹, Michał Kwiatkowski¹, Piotr Krupski¹,
Jarosław Diatczyk¹, Tomoyuki Murakami²

¹*Institute of Electrical Engineering and Electrotechnologies,
Lublin University of Technology, Lublin, Poland*

²*Department of Energy Sciences, Interdisciplinary Graduate School of Science and Engineering,
Tokyo Institute of Technology, Tokyo, Japan*
E-mail: askmik@hotmail.com

RF-powered atmospheric pressure plasma jet was applied for changing surface properties of rubber-modified styrenic polymers on the example of high-impact polystyrene. We have utilized a zero dimensional chemical kinetic model to identify the dominant particle species generated by our device in experimental conditions. Influence of the plasma treatment on HIPS surface wettability was discussed.

1. Introduction

Surface properties of polymers can be partly adjusted using physical and chemical techniques such as ozone treatment, UV grafting, plasma treatment, flame treatment or chemical wet oxidation [1-4]. Plasma treatment enabling advanced oxidation processes gained special attention because of its simplicity and fastness [5,6]. Atmospheric pressure plasma jet (APPJ) can be a convenient tool for the decontamination and modification of treatment of polymer surface properties. The paper presents basic data concerning application of APPJ for high-impact polystyrene (HIPS) surface treatment. Global model is applied for determination of species generated in plasma zone [7-9].

2. Experimental set up and results

Proposed experimental set-up consisted of gas and liquid dosing sub-system, electrical discharge generating sub-system, control and data acquisition sub-system, and chemical and biological analyzing sub-system.

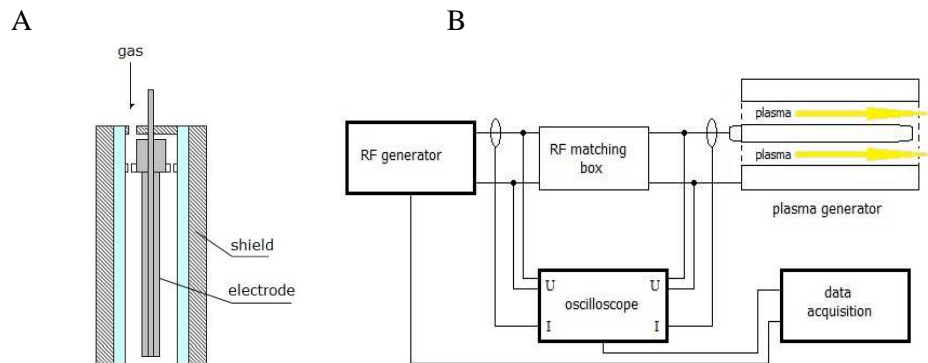


Fig. 1. Atmospheric pressure plasma jet (A) and its electrical supply (B).

The main part of the device, which is presented in Fig. 1A, was RF-powered changeable rod electrode of tungsten or acid-proof stainless steel. The electrode was powered by a regulated RF supply (AG 1021 RF generator, T&C Power Conversion) via impedance matching network (Fig. 1B). It was possible to power plasma reactor with frequencies from 10 kHz to 20MHz [10, 11].

Gas temperature was measured using uninsulated K-type thermocouple with electronic temperature compensation multimeter. AFM (NT-MDT Ntegra Spectra) was used for observation of the surface structure of the samples.

In order to understand the underlying operating principles of the present system and to optimize its performance in applications, it is important to know the chemical kinetics of the reactive multi-species plasma. As a first attempt, we have utilized a zero dimensional (0D) time-dependent chemical kinetic global model and simulation code to solve the governing rate equation for the time derivative of the species concentrations in the present study. Global (volume averaged) models are computationally efficient in identifying the overall relevant reaction channels, however they are limited, e.g. with respect to account for the spatial distribution, diffusion and convective transport of particles. The applied global plasma chemical kinetics model is identical in terms of reaction scheme and numerics to the model previously used to explore the detailed plasma chemistry in a core plasma region (plasma zone) of an exemplar micro-scale rf-driven APPJ [7-9]. Conditions for the model were as follows: (total) gas pressure: 0.1 MPa (atmospheric pressure); gas temperature: 72 °C; gas constitution: helium-oxygen-mixture (He 59.95% and O₂ 40.0%) with ambient humid air (N₂ (78.25%), O₂ (20.97%), CO₂ (0.03%), H₂O (0.75%)). The humid air fraction to the total He+O₂ mixture is 0.05% and the relative humidity of air is 50%. The extended reaction scheme comprises 1360 elementary reactions among 65 species.

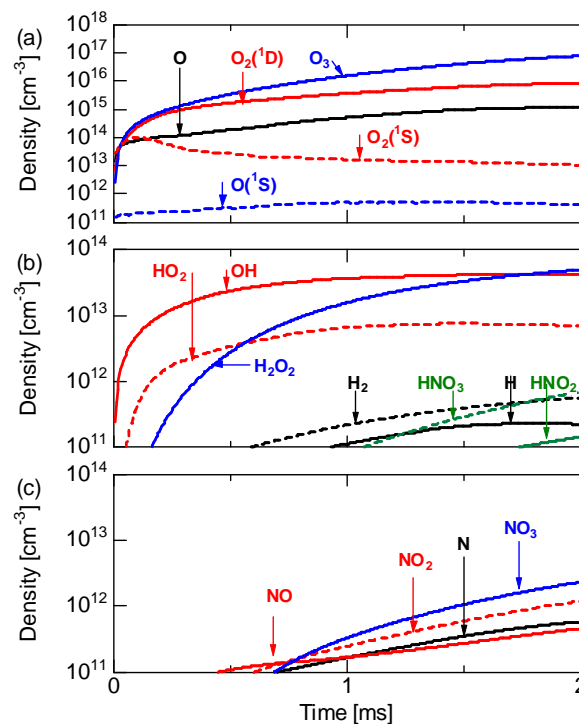


Fig. 2. Temporal evolution of major neutral reactive species in the core plasma region.

Fig. 2(A-C) shows the temporal evolution of pronounced reactive neutral species in the core plasma region. The global model revealed that the most pronounced neutral species are reactive oxygen species. The O₃ density gradually increases and reaches a value of $8 \times 10^{16} \text{ cm}^{-3}$ during 2 ms. The maximum O₂(¹D) density at the jet's nozzle is $9 \times 10^{15} \text{ cm}^{-3}$. The O-atom density reaches a value of $1 \times 10^{15} \text{ cm}^{-3}$ at the exit of the core region. The densities of atomic oxygen metastable O(¹S) and molecular oxygen metastable O₂(¹S) are smaller than the O-atom and O₂(¹D) densities by orders of magnitude at the exit of the core. The global model indicates that the reactive species, H, H_xO_y, NO_x and HNO_x resulting from the humid air impurity appear during residence time of 2 ms even at the small humid air fraction. Those reactive species will make significant contributions to the afterglow chemistry. The main ion species are molecular oxygen ions, i.e. O₄⁺, O₂⁻ and O₄⁻. The global model suggests that the dominant reactive species is O₃ in the present APPJ with the significant admixture of O₂ to the feed gas He.

Ozone was also main active compound detected experimentally, what is in a good accordance with the simulation results. Ozone concentration was measured in dependence on the gas type, gas flow rate, power and the type of electrode via continuous gas sampling from sealed container. Achieved ozone concentrations ranged 0.82g/m^3 (at 50 W and 40% O₂/60% He feed gas mixture). Ozone along with temperature and UV irradiation had a crucial influence on modification of HIPS surface, possible reaction steps are depicted in Fig. 3 [12, 13].

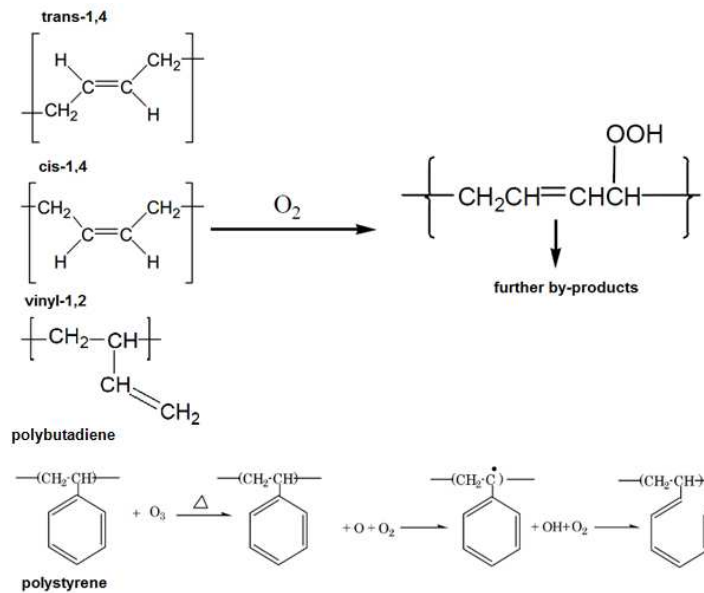


Fig. 3. Selected paths of oxidation of HIPS [12, 13].

APPJ enabled regulation of temperature of outlet gas and the lowest temperature limit was slightly below 40°C. Experimental results in dependence of the gas flow rate at P = 50 W, f=14.23 MHz with 60% He/40% O₂, are depicted in Fig. 4. Obtained results show obvious simple dependence of temperature decrease with increasing the distance from the reactor.

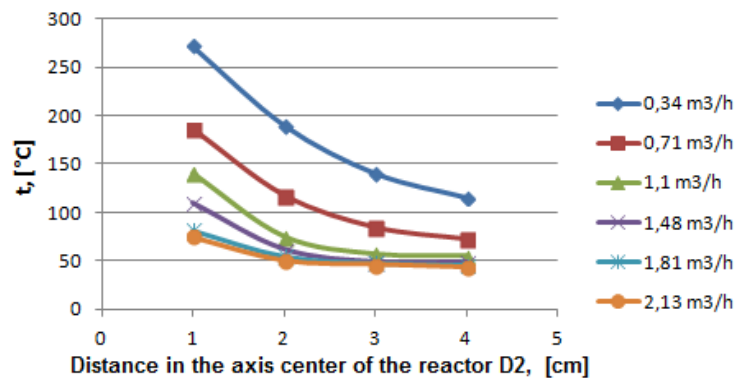


Fig. 4. Gas temperature measurement in APPJ.

APPJ was used for the treatment of HIPS surfaces. The measurements of static water contact angle for HIPS were performed for the operating voltage, frequency and power of 500 V, 14.355 MHz and 40W, respectively. Measurements were made for three mixtures of gases: helium with oxygen, argon with oxygen and helium with air. During the measurements, the reactor was directed perpendicularly to the surface of the sample.

Immediately after plasma treatment, one 10 μl water drop was injected into a treated surface for calculating the average contact angle from pictures made by CMOS camera.

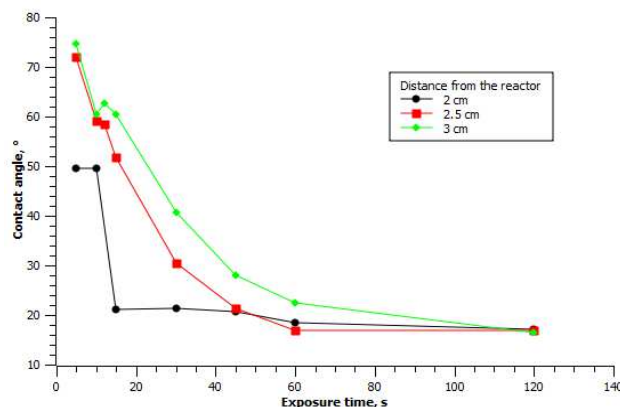


Fig. 5. The dependence between contact angle and treatment time for different distances from the end of reactor.

The results obtained at various distances from the end of reactor (Fig. 5) show significant influence of distance for treatment times less than one minute. For two minutes the angle was the same for all distances, which could allow more freely treatment objects with more complex surfaces. After one day, the contact angle started to return to its previous value, which is particularly evident at longer exposure times. This may indicate that the effect of plasma treatment in the material is not too deep, and the process is reversible.

3. Summary

According to performed global model simulations and experimental data ozone is the most important oxidant generated in plasma zone in helium/oxygen feed has mixture, which can react with the sample surface.

Obtained results allow to conclude an effective change in static water contact angle through the use of the radio frequency APPJ source. Significant changes in the angle could be seen for treatment time of 15 seconds, which may be important in reducing the cost of modifying low cost materials such as HIPS.

4. Acknowledgement

This work was supported by KORANET project and by COST TD1208 Action.

5. References

- [1] Hollaham J, Bell A, 1974 *Techniques and Application of Plasma Chemistry*, New York, Wiley
- [2] Ko Y, Kim Y, Park K, Le He, Lee W, Park H, Kim S, Lee G, Ahn D 2001 *Biomaterials* **22(15)** 2115
- [3] Favia P, Sardella E, Gristina R, d' Agostino R 2003 *Surf. and Coatings Technol.* **169–170** 707
- [4] Kropke S, Akishev Y, Hollander A 2001 *Surf. Coat. Technol.* **142-144** 512
- [5] Pawlat J, Diatczyk J, Stryczewska H 2011 *Przegląd Elektrotechniczny* **1** 245
- [6] Pawlat J 2013 *EPJAP* **61(2)** 2013 1
- [7] Murakami T, Niemi K, Gans T, O'Connell D, Graham W 2013 *Plasma Sources Sci. Technol.* **22** 015003.
- [8] Murakami T, Niemi K, Gans T, O'Connell D, Graham W 2013 *Plasma Sources Sci. Technol.* **22** 045010.
- [9] Murakami T, Niemi K, Gans T, O'Connell D, Graham W 2014 *Plasma Sources Sci. Technol.* **23** 025005.
- [10] Stryczewska H, Giżewski T, Pawlat J, Jakubowski T, Kalisiak S 2013 *JAOTs* **16(1)** 52
- [11] Pawlat J, Stryczewska H, Diatczyk J, Giżewski T, Samoń R 2013 *EPJAP* **61(2)** DOI:<http://dx.doi.org/10.1051/epjap/2012120428>.
- [12] Vilaplana F 2007 *Modelling the degradation processes in high-impact polystyrene during the first use and subsequent recycling* (KTH Chemical Science and Engineering, 2007) ISBN 978-91-7178-678-4.
- [13] Kobayashi T, Kurniawan W, Arisawa M 2009 *Polymer Surface Modification: Relevance to Adhesion*, Part 5 (Ed.K. L. Mittal, BRILL)139

GRAFTING OF PROTEINS ON PLASMA TREATED POLYMERS FOR TISSUE ENGINEERING

Václav Švorčík¹, Nikola Kasálková Slepíčková¹, Zdeňka Kolská², Štěpánka Kučková³, Petr Slepíčka¹

¹*Department of Solid State Engineering, Institute of Chemical Technology, 16628 Prague, Czech Republic*

²*Faculty of Science, J. E. Purkyně University in Ústí nad Labem, 400 96 Ústí nad Labem, Czech Republic*

³*Department of Biochemistry and Microbiology, Institute of Chemical Technology Prague, 166 28 Prague, Czech Republic*

E-mail: vaclav.svorcik@vscht.cz

In this work an influence of bovine serum albumin proteins grafting on the surface properties of plasma treated polyethylene and poly-L-lactic acid was studied. The interaction of the vascular smooth muscle cells with the modified polymer surface was determined. The surface properties were characterized by X-ray photoelectron spectroscopy, Atomic force microscopy, nano-LC-ESI-Q-TOF spectrometry, electrokinetic analysis and goniometry. It was proven, that proteins bond on the plasma treated high-density polyethylene and poly-L-lactic acid surfaces. Since the proteins are bonded to the substrate surface they can stimulate the cell adhesion and proliferation.

1. Introduction

Tissue engineering (TE) is a discipline which includes both creation of the new tissue, design and realization of the cells on substrates. Substrates play a key role in creation of cell environment. To guide the organization, growth and differentiation of cells in TE constructs, the biomaterial scaffold should be able to provide not only a physical support but also the chemical and biological clues needed in forming of functional tissue [1].

Polymeric materials have been widely studied as a substrates for tissue engineering due to their unique features such as mechanical properties, high availability, low cost and relatively easy design and production. But only few polymers provide the biocompatibility necessary for the cells *in vitro* and *in vivo* [1].

Polymer surfaces are often modified by thin layers of protein like collagen or fibronectin to improve their cytocompatibility [1]. Bioactive molecules influence also the growth factors and regulate the cells adhesion, migration and proliferation. Bovine serum albumin (BSA) is a globular protein that is used in numerous biochemical applications. BSA can be used like reference (model) protein which properties are compared with other proteins. BSA is also inclusive in the protein part of the various media used for operations with cells. BSA was chosen as a representative proteins present in cell culture as a supplement to increase the growth of cells and increase overall cell health.

In this work the influence of bovine serum albumin (BSA) protein grafting on the surface properties of the polyethylene (HDPE) and poly-L-lactide acid (PLLA) was studied. HDPE was chosen like the representative of the non-polar/non-biodegradable polymer. With its very simple structure containing only carbon and hydrogen atoms this polymer can serve as a model material. PLLA was chosen as a polar/biodegradable polymer, whose cell affinity is often compromised due to the hydrophobicity and low surface energy [1,2]. The surface properties were characterized by X-ray photoelectron spectroscopy, nano-LC-ESI-Q-TOF mass spectrometry, atomic force microscopy, electrokinetic analysis and goniometry. One of the motivations for this work is the idea that due to cell interaction with the substrate the proteins form interlayer between cell and the substrate surface [2].

2. Experimental

Material's and chemical modification

The experiments were performed on high-density polyethylene (HDPE) foil (thickness 40 μm , density 0.951 $\text{g}\cdot\text{cm}^{-3}$, Granitol a.s. CR) and biopolymer poly-L-lactic acid (PLLA) foil (50 μm , 1.25 $\text{g}\cdot\text{cm}^{-3}$, Goodfellow, Ltd.)

The surface modification of polymer substrates consisted of plasma treatment and subsequent grafting with proteins. The samples were modified by plasma discharge on Balzers SCD 050 device. The parameters of the deposition were: DC Ar plasma, gas purity 99.995 %, flow $0.3 \text{ l}\cdot\text{s}^{-1}$, pressure 8 Pa, power 3 W, electrode distance of 50 mm, time 300 s.

Immediately after treatment, the activated polymer surfaces were grafted by immersion into water solution of bovine serum albumin (BSA, concentration 2 wt. %, Sigma Aldrich) for 24 hours at room temperature (RT). The excess of non-bound molecules were removed by consequent immersion of the samples into distilled water for 24 hours. Samples were then dried at RT for 13 hours.

Used analytical methods

The surface wettability was determined by water contact angle (WCA) measurement immediately after modification and after 17 days using distilled water (drop of volume $8 \mu\text{l}$) at 20 different positions and Surface Energy Evaluation System..

The presence of the grafted proteins molecules on the modified surface was detected by nano-LC-ESI-Q-TOF mass spectrometry. Samples were inserted in Petri dish. $10 \mu\text{l}$ solutions ($2 \mu\text{l}$ trypsin, concentration of $20 \mu\text{g}\cdot\mu\text{l}^{-1}$ in $100 \mu\text{l}$ $50 \text{ mmol}\cdot\text{l}^{-1} \text{NH}_4\text{HCO}_3$) were applied on the sample surface. In the inside perimeter of Petri dishes, pieces of wet pulp were placed, in order to avoid drying of the solution on the surface of foils, and consequently the dish was closed. After 2 hours of the molecules cleavage new peptides were concentrated and desalted by reverse phase Zip Tip C18 at RT.

The presence of the carbon, oxygen and nitrogen atoms in modified surface layer was detected by X-ray photoelectron spectroscopy (XPS). The spectra of samples were measured with Omicron Nanotechnology ESCAProbeP spectrometer. This elemental analysis was performed 17 days after modification of the samples.

Study of the changes in surface morphology and roughness of samples were examined 17 day after modification by atomic force microscopy (AFM) using a VEECO CP II device ("tapping" mode, probe RTESPA-CP, spring constant $20\text{-}80 \text{ N}\cdot\text{m}^{-1}$). The surface roughness value (R_a) represents the arithmetic average of the deviation from the centre plane of the samples.

The electrokinetic analysis (zeta potential) of samples was examined using SurPASS Instrument, (adjustable gap cell, $0.001 \text{ mol}\cdot\text{dm}^{-3}$ water solution of KCl, pH = 6.3, RT). The values of the zeta potential were determined by two methods, a streaming current and a streaming potential and calculated by Helmholtz-Smoluchowski and Fairbrother-Mastins equations [3]. Each sample was measured four times with the experimental error of 5 %.

Biological test of adhesion and proliferation

For cell culture experiments, evaluation of cell number and morphology, three pristine and modified HDPE and PLLA samples were used for analysis by randomly chosen fields. The adhesion and proliferation of vascular smooth muscle cells (VSMCs) on selected samples were studied by *in vitro* method described in detail earlier [2].

3. Results and discussion

It was shown, that the presence of the grafted protein on the modified samples was proved using mass spectrometry. First five peptides (for HDPE) or four others (for PLLA) detected on the grafted HDPE and PLLA, resp. [2]. Protein that was identified by the largest number of peptides was BSA in both cases, as expected. Furthermore the work [2] inclusives other analyzed proteins which come from the cattle (cow, *Bos Taurus*) and sheep (*Ovis Aries*) that have been identified at least with nine peptides. The other founded proteins come from probably commercially supplied BSA (purity 96 %). Although the samples were grafted with BSA and therefore proteins from other species would not appear on the surface of samples, it is possible to explain their identification on the basis of similar amino acid sequences between even-toed ungulate (artiodactyls).

Surface morphology and roughness of samples were examined by AFM. From the scans shown in Fig. 1 it is evident that the treatment of foils leads to an increase of surface roughness and morphology change. This can be caused by a different ablation rate of crystalline and amorphous phase [4]. It is also evident that in the case of HDPE the plasma treatment caused the highlight of the lamellar structure, in the case of PLLA it resulted in creation of granular structure. The subsequent grafting by the BSA leads to different surface arrangements of both polymers. The lamellar structure of HDPE is maintained but it is noticeably lower and finer in comparison with plasma treated one and the surface

roughness considerable decreased. In the case of grafted PLLA, the granular morphology is maintained but the “tops” are sharper and narrower than only plasma treated one and surface roughness increased.

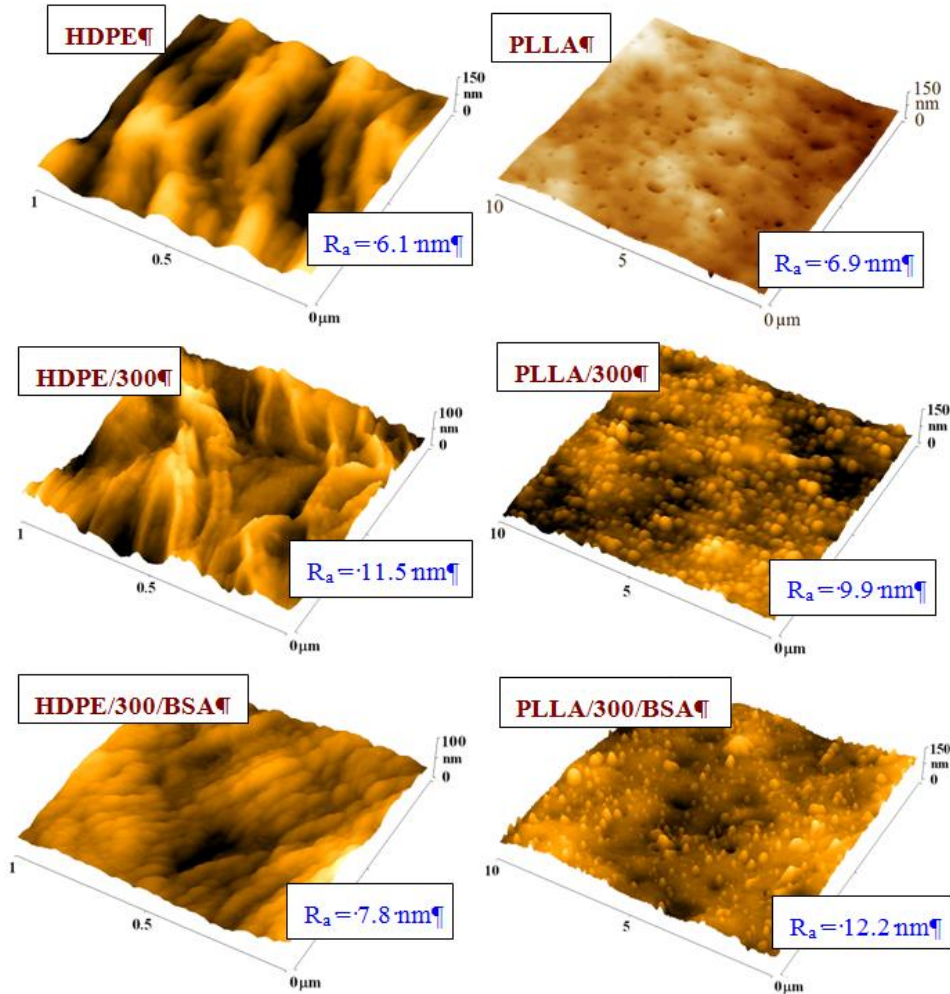


Fig. 1. AFM images and surface roughness R_a of the pristine (HDPE, PLLA), plasma treated (/300) and subsequently grafted (/BSA) samples of polymer foils. [2].

Numbers of the cultivated VSMCs on the pristine and BSA grafted HDPE and PLLA for 2, 4 and 6 days from seeding are shown in Fig. 2 [2]. On the 2nd day after seeding the number of the VSMCs was significantly lower on the pristine HDPE in comparison with HDPE grafted by BSA. From the 2nd day to the 4th day after seeding, the intense increase of the VSMCs on the grafted HDPE was detected. On the contrary the number of cells cultivated 4 days from seeding on the pristine HDPE was comparable with the 2nd day. Between the 4th and 6th day, the cell's proliferation on the grafted HDPE slowed down, probably due to reaching the cell's confluence. In the case of pristine HDPE, from the 4th to 6th day the VSMCs started to proliferate and after 6 days of cultivation they reached the number ca 22 000 cells cm^{-2} , which is considerably less than number of cells on grafted HDPE (ca 85 200 cells cm^{-2}). The cells cultivated on the grafted HDPE were better spread, spreading areas were larger in comparison to the pristine. After 6 days from cultivation, the cells cover homogeneously the surface of the grafted HDPE.

The explanation of biocompatibility improvement of surface after plasma modification and protein grafting is connected with surface chemistry change, especially with amino groups presented on the modified surface. It is known that the major proteins (especially proteins of fetal bovine serum) as well as cell membranes are negatively charged under physiological pH. The adhesion of cells with negatively charged membranes may be facilitated by electrostatic interactions and the better cell adhesion may be expected on positively charged surfaces [5]. The surface charge (of solid substrates

and of cells) significantly determines both cell-cell and cell-solid interactions. In low ionic strength environment, the adhesion is influenced mostly by electrostatic interactions between surfaces, where the surface chemistry, surface functional groups and surface charge play the important role, while with increasing ionic strength (increasing concentration of surrounding) grows the importance of non-polar (hydrophobic) interactions [6]. Also it was presented earlier for human umbilical vein endothelial cells or for human fibroblasts [7] that better protein adsorption occurs if the surface contains $-NH_2$ groups. Adsorbed proteins play a major role in the attachment of anchorage-dependent cells through their binding to integrins [7].

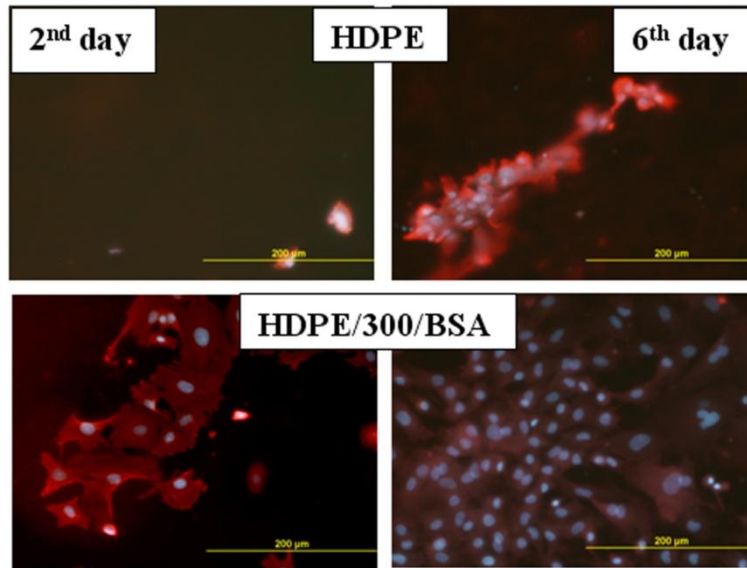


Fig. 2. Illustrative photographs of the VSMCs cultivated on the pristine and BSA grafted HDPE for 2 and 6 days [2].

4. Conclusions

It was proven, that during interaction of BSA protein with the plasma treated HDPE and PLLA it is grafted on their surfaces. Chemically bonded BSA protein was confirmed with XPS, mass spectrometry, AFM, electrokinetic analysis and goniometry. These results have the significant contribution to understanding of cell and substrate behaviour during the cell interaction with chemically active polymer in tissue engineering field. Due to plasma treatment and subsequent BSA grafting to polymer surface the cell adhesion and proliferation can be stimulated due to the presence of active functional groups on surface which improve the electrostatic interactions between substrates and cells.

Acknowledgement

This work was supported by the GACR project No. P108/12/G108.

5. References

- [1] Bačáková L, Filová E, Pařízek M, Ruml T and Švorčík V 2011 *Biotechnol. Adv.* **29** 739.
- [2] Slepíčková Kasálková N, Slepíčka P, Kolská Z, Hodačová P, Kučková Š and Švorčík V 2014 *Nanoscale Res. Lett.* **9/161** 1.
- [3] Kolská Z, Řezníčková A and Švorčík V 2012 *e-Polymers* **83** 1.
- [4] Švorčík V, Kolářová K, Slepíčka P, Macková A, Novotná M and Hnatowicz V 2006 *Polym. Degrad. Stab.* **91** 1219.
- [5] Kolska Z, Reznickova A, Nagyova M, Slepickova Kasalkova N, Sajdl P, Slepicka P and Svorcik V 2014 *Polym. Degrad. Stab.* **101** 1.
- [6] Sirmerova M, Prochazkova G, Siristova L, Kolska Z and Branyik T 2013 *J. Appl. Phycol.* **25** 1687.
- [7] Faucheux N, Schweiss R, Lutzow K, Werner C and Groth T 2004 *Biomaterials* **25** 2721.

USING DIRECT LIQUID SAMPLING FOR AMINO ACID MEASUREMENTS BY CORONA DISCHARGE ION MOBILITY SPECTROMTRY (CD-IMS)

Oľga Harmathová¹, Martin Sabo¹ and Štefan Matejčík¹

¹*Department of Experimental Physics, Faculty of Mathematics, Physics and Informatics, Comenius University, Mlynská dolina F2, 842 48 Bratislava, Slovakia*

oliharmathova@gmail.com

In this work the ability is presented of ion mobility spectrometry with corona discharge as an ionization source to analyse liquid samples. Using the direct liquid sampling technique for ion mobility spectrometry is be presented. This technique was applied for detection of amino acids, such as leucine, phenylalanine, serine and glycine. The measured positive ion mobility spectra of these amino acids are presented.

1. Introduction

Amino acids are the building blocks of proteins and they are essential for many life processes. Their most important tasks include optimal transport and storage of all nutrients. A majority of diseases can be traced back to metabolic disturbances linked with amino acids. These are the reasons why it is important to have an analytical instrument for qualitative and quantitative analysis of amino acids [1]. Ion Mobility Spectrometry (IMS) is an analytical technique based on the movement of ions of at gaseous sample in a homogeneous electric field and drift gases which is determined by the size, mass, charge and shape of the ions [2], [3]. A schematic of the prototype apparatus is shown in Figure 1. The instrument has an inlet through which gaseous compounds enter the ionization region - consisting of an ionization source and a reaction chamber. There are many types of ionization sources, one of them is the corona discharge (CD) [4]. After introduction of gaseous compounds these samples are ionized by the reactant ions. The product ions pass through a shutter grid which controls the passage of the ions into the drift tube. Inside the drift tube the ions are guided by the homogeneous electric field at atmospheric pressure [3].

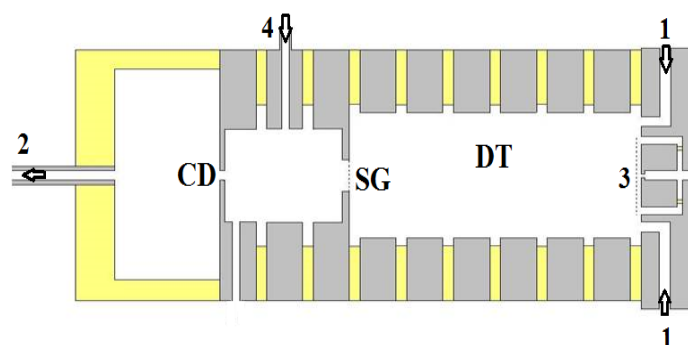


Fig. 1. Schematic view of the CD IMS instrument: 1 - drift gas inlet, 2 - gas outlet, 3 - ion collector, 4 - sample inlet, corona discharge (CD), shutter grid (SG), drift tube (DT).

The drift velocity is given by the formula $v_D = KE$, where K is the ion mobility and E is the intensity of the electric field. The ion mobility can be expressed also by the formula $K = l_D^2/t_D U$ - where l_D is the length of the drift tube, t_D is the drift time of the ions and U is the voltage. The ion mobility depends not only on the ion size, mass, charge and shape but also on the collision cross section of the drift gas

and, thus, on the type of the drift gas and density and temperature. Therefore, correction to the standard conditions (273°K, 1010 mbar) is made and the resulting value is reported as a reduced mobility K_0 given by formula [2], [3].

$$K_0 = 273Kp/1010T.$$

IMS is a simple, fast, and very sensitive technique for analysis of a wide range of compounds. Because of the above, IMS has found a wide use for detection of volatile and semivolatile chemical compounds such as explosives, narcotics and chemical warfare agents [2]. The implementation of electrospray ionization (ESI) to the IMS technique results in ability of this technique to analyse nonvolatile samples dissolved in a liquid sample [5], [6], [7], [8]. However, ESI usually requires methanol or another solution for sample analysis and these, solutions can bring about changes of the compounds as well as decrease the sensitivity of the instrument. In this work we will present a new technique suitable for direct liquid samples (DLS) analysis. This new technique allows direct liquid sampling into the ion mobility spectrometer without using methanol or other special solutions. This allows to analyse biological samples in their naturale conditions. In addition, DLS is a technique which allows regulation of the flow of the sample during the measurement.

2. Experiment

The CD-IMS apparatus used in this study was constructed in the laboratory at Comenius University, Faculty of Mathematics, Physics and Informatics. A corona discharge ionization source in point-to-plate geometry was used as an ionization source. The drift tube was held at a constant temperature of 45°C. Table 1 summarizes the operating conditions under which the IMS spectra were taken.

Tab. 1. Operation parameters of IMS instrument

IMS drift tube length	11.05 cm
electric voltage	6.43 kV
IMS operating temperature	318 K
drift gas flow rate	1 l/min
carrier gas flow rate	600 ml/min
material of drift gas	purified air
material of carrier gas	purified air
SG pulse width	5 μ s
IMS operating mode	positive

All amino acids used in this work were purchased from Sigma Aldrich and used without further purification. Water and methanol were used as solvents. The samples were prepared by weighing out known quantities of amino acids and then dissolving them in deionized water or in a solvent consisting of water and methanol. The sample concentrations were 1 mg/ml. Then they were diluted again for every individual experiment as required. The final sample concentrations are given separately for every individual spectrum.

3. Results and discussion

DLS-CD-IMS performance figures for amino acids in two different solutions

Initial investigations were designed to determine the effect of methanol used as a solution for electrospray ionization IMS measurements of amino acids upon their drift times and reduced mobilities. Two similar proteinogenic amino-acids Leucine (Leu) and Phenylalanine (Phe) - were analysed. Both are nonpolar, hydrophobic and essential amino acids. Both amino acids were

sequentially dissolved in two solutions. The first solvent consisted of 0.9 ml of methanol and 0.1 ml of deionized water and the second solvent was only deionized water. Positive mode CD-IMS spectra for Leucine (Leu) dissolved in both solutions are plotted together in Figure 2. The molar mass of Leucine is 131.17 g/mol. Sample concentrations are 0.5 mg/ml for both cases. Constant temperature 45°C was maintained inside the drift tube. The spectra were obtained by direct liquid sampling, which a new technology allowing regulation of the flow of the vapour sample injected into the ion mobility spectrometer. A flow of 100 $\mu\text{l}/\text{min}$ was used in both spectra.

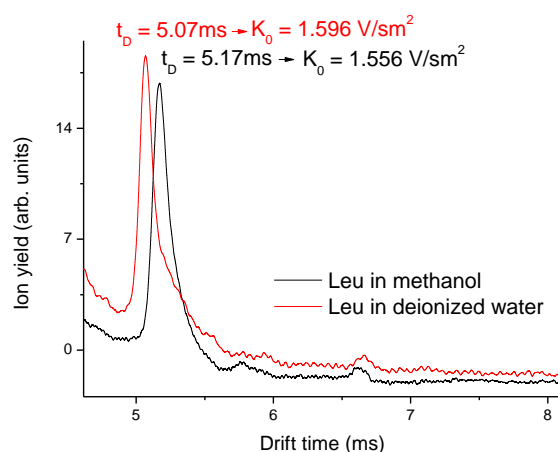


Fig. 2. Ion mobility spectrum obtained by direct liquid sampling CD-IMS analysis of Leucine in two different solutions in purified drift air.

The measured drift time of Leucine in methanol is $t_D = 5.17$ ms and the corresponding reduced mobility is $K_0 = 1.556$ V/sm^2 . The measured drift time of Leucine in deionized water is $t_D = 5.07$ ms and the corresponding reduced mobility is $K_0 = 1.596$ V/sm^2 . The difference between the two reduced mobility values is 0.04. The graphs in Fig. 2 show the effect of methanol shifting the drift time to higher values. Similar results are presented in Fig. 3 with Phenylalanine. These spectra plotted together in Fig. 3 are obtained by positive mode CD-IMS using direct liquid sampling with a flow of 60 $\mu\text{l}/\text{min}$ at constant temperature 45°C. The first spectrum belongs to Phenylalanine dissolved in deionized water and the second one to Phenylalanine dissolved in methanol. The molar mass of Phenylalanine is 165.17 g/mol. Sample concentrations are 0.1 mg/ml for both cases. The measured drift time of Phenylalanine in deionized water is $t_D = 5.36$ ms and the corresponding reduced mobility is $K_0 = 1.51$ V/sm^2 . In the case of Phenylalanine in methanol two peaks appeared in the spectrum: the first is on the position with drift time $t_D = 5.48$ ms and its corresponding reduced mobility is $K_0 = 1.48$ V/sm^2 and the second peak is on the position with drift time $t_D = 8.497$ ms and its corresponding reduced mobility is $K_0 = 0.95$ V/sm^2 . The second peak is probably a result of a clustering process. This second peak is visible only in the spectrum of Phenylalanine in methanol. A shift of the main peak to higher values of the drift time occurs again in the case of methanol. A difference of 0.03 was determined between the two reduced mobility values for the main peak.

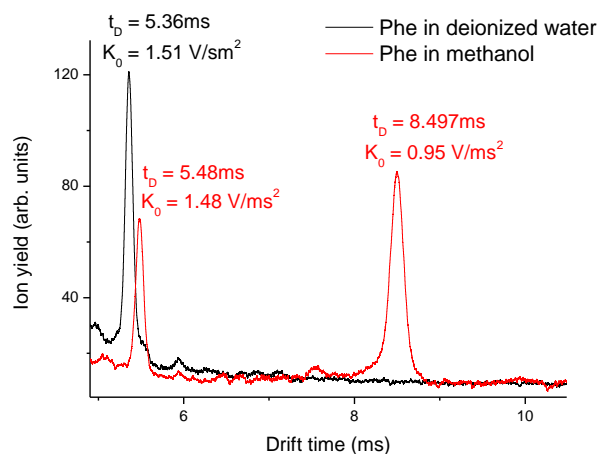


Fig. 3. Ion mobility spectrum obtained by direct liquid sampling CD-IMS analysis of Phenylalanine in two different solutions in purified drift air.

Application of direct liquid sampling CD-IMS to some polar amino acids

The above described results were measured on nonpolar hydrophobic essential amino acids. For completion of the investigation some polar amino acids were analysed. Glycine (Gly) and Serine (Ser) are polar nonessential proteinogenic amino acids. The molar mass of Glycine is 76 g/mol and the molar mass of Serine is 106 g/mol. Positive mode CD-IMS spectra for these two species are plotted together in Fig. 4. The spectra were obtained using direct liquid sampling with flow 60 $\mu\text{l}/\text{min}$ at constant temperature 45°C. Sample concentrations were 0.2 mg/ml.

Tab. 2. Molar mass (MW) and reduced mobilities of four amino acids obtained with N_2 and drift purified air. Matz and Hill (2001) used electrospray ionization, in our case direct liquid sampling was used.

amino acid	MW	K_0 (V/sm^2) in N_2 measured by ESI, Matz and Hill (2001)	K_0 (V/sm^2) in drift purified air measured by direct liquid sampling
Glycine	76	1.851	1.858
Serine	106	1.734	1.778
Leucine	132	1.526	1.596
Phenylalanine	166	1.448	1.51

The measured drift time of Glycine in deionized water is $t_D = 1.922$ ms and the corresponding reduced mobility is $K_0 = 1.86$ V/sm^2 . The measured drift time of Serine in deionized water is $t_D = 4.556$ ms and the corresponding reduced mobility is $K_0 = 1.78$ V/sm^2 . In Table 2, the reduced mobilities measured with deionized water as a solvent using direct liquid sampling in purified air are compared with reduced mobilities measured with ESI technique. The values are in very good agreement with the literature values. As seen in Table 2, the effect of methanol which is used in ESI-IMS is evident.

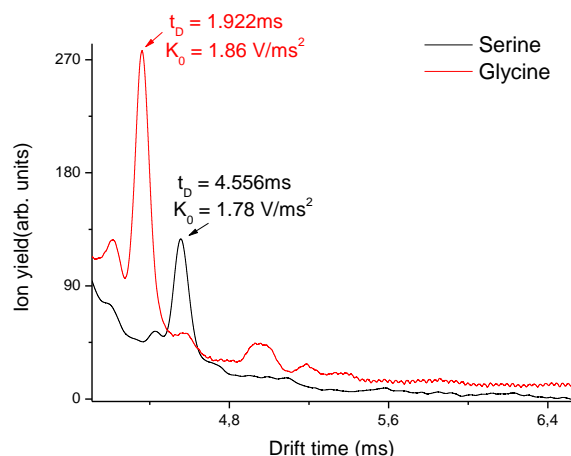


Fig. 4. Ion mobility spectrum obtained by direct liquid sampling CD-IMS analysis of Serine and Glycine dissolved in deionized water in drift purified air.

4. Conclusions

The drift times and reduced ion mobilities of two polar and two nonpolar amino acids were determined by corona discharge ion mobility spectrometry using direct liquid sampling. It has been demonstrated that this new technology of evaporated and injected liquid samples to an ion mobility spectrometer is sufficiently precise for analysis of amino acids. By virtue of this technique the effect of methanol onto amino acids spectra, which is observed in electrospray ionization, has been eliminated.

5. Acknowledgment

This work was supported by Slovak research and development agency project APVV-0259-12.

6. References

- [1] Bohrer B C and Merenbloom S I and Koeniger S L and Hilderbrand A E and Clemmer D E 2008 *Annu. Rev. Analytical Chemistry*. 1:10.1-10.35
- [2] Eiceman G A and Karpas Z 2005 *CRC Press: Boca Raton, FL* ISBN 0-8493-2247-2
- [3] Kanu A B and Hill J H Jr 2014 *LPI* WA 99164-4630
- [4] Shumate Ch B and Hill H H Jr. 1989 *Analytical Chemistry* 601-606
- [5] Beegle L W and Kanik I and Matz L and Hill H H Jr. 2001 *Analytical Chemistry* 3028-3034
- [6] Wittmer D and Chen Y H and Luckenbill B K and Hill J H Jr. 1994 *Analytical Chemistry* No.14, 2348-2355
- [7] Midey A J and Patel A and Moraff C and Krueger C A and Wu Ch 2013 *Talanta* 77-83
- [8] Thomas J J and Bothner B and Traina J and Benner W H and Siuzdak G 2004 *Spectroscopy* 31-36, IOS Press

POSSIBILITIES OF COUPLING ION MOBILITY SPECTROMETRY TO MINIATURIZED SEPARATION TECHNIQUES

Jasna Hradski¹, Martin Sabo², Štefan Matejčík², Marián Masár¹

¹*Department of Analytical Chemistry, Faculty of Natural Sciences, Comenius University in Bratislava, Mlynská dolina CH-2, 84215 Bratislava, Slovak Republic*

²*Department of Experimental Physics, Faculty of Mathematics, Physics and Informatics, Comenius University in Bratislava, Mlynská dolina F2, 84248 Bratislava, Slovak Republic*

E-mail: hradski@fns.uniba.sk

Ion mobility spectrometry (IMS) is an analytical technique used to characterize gaseous ions based on their mobility in a weak electric field. In this work introduction of the sample by electrospray and subsequent ionization by corona discharge (CD) is employed to analysis of the model samples of organic acids (malic, tartaric, lactic and citric) and the wine samples by IMS.

1. General aspects of IMS

IMS is an analytical technique based on the separation of ionized molecules with respect to their different mobilities in the gas phase. This technique is characterized by fast and reliable analysis of ionized analytes, as well as low cost, portability and relatively easy manipulation of IMS instrumentation [1]. It is for these reasons, that IMS has found application in the detection of explosives, chemical warfare agents, pharmaceuticals, food industry and analysis of biomolecules [2-4].

Molecules have to be ionized prior to the analysis by IMS in order to achieve separation and detection. Ionization is usually achieved by radioactive sources, e.g. ⁶³Ni. Nevertheless several ionization techniques have been employed to IMS as a suitable substitution for radioactive materials, such as photoionization, electrospray ionization, CD or matrix-assisted laser desorption/ionization [1].

CD offers relatively high signal intensity, the possibility of changing the reactant ions, simple instrumentation and applicability to a wide range of analytes, including liquids [5]. The advantages of ESI are the possibility of direct analysis of liquid samples, retaining the molecular information and in some cases formation of multiply charged ions [1].

2. Experimental

Instrumentation characteristics of CD-IMS used in this work are described in details elsewhere [6]. This instrument is composed of: (i) an ionization chamber, where the CD is located and ionization takes place; (ii) a shutter grid; (iii) a drift tube, where the separation of ions occurs; and (iv) a detection unit.

Several aspects of the CD ionization process have been studied, e.g. geometry of CD, distances of electrodes and gas flow directions. Point to ring geometry was employed for introducing the sample into the IMS. Analyzed liquid samples were introduced into IMS via the stainless steel capillary heated to 470 K. This capillary was placed in front of another capillary at which the potential of 3 kV was applied. Negative CD was employed as an ionization source, while air was used as a drift gas.

Model samples of organic acids (malic, lactic, tartaric and citric) were prepared from chemicals of p.a. purity. Wine samples studied were purchased at a local store.

3. Results and Discussion

Electrospray was used in order to introduce liquid sample to the capillary. Although electrospray is usually used for ionization of the sample, in our case it was used only for transformation of liquid sample to vapour and droplets. Ionization by CD was used for creation of charged particles. This type of sample introduction allows sample ionization in both positive and negative polarity. Main advantage of positive polarity is that the primary ions are quickly converted to stable ions $\text{H}_3\text{O}^+(\text{H}_2\text{O})_n$ or $\text{NO}^+(\text{H}_2\text{O})_n$ ions [7-9]. Compared to positive polarity, negative polarity is more complicated, due to

sensitivity of negative CD to many parameters, such as gas composition (air, synthetic air, and impurity level), gas flow, time period between ion formation and their detection (CD gap dimensions), pressure, temperature and discharge power related to concentration of neutral and radical species in CD gap [5]. Negative polarity was employed for studying of organic acids, due to the character of analytes.

Two operation modes of CD with different gas flow conditions were used for the generation of negative reactant ions: (1) reverse gas flow mode and (2) standard gas flow mode. In the first mode gas flow has the opposite direction to the direction of the ion movement in the CD gap. This mode is used for a removal of neutrals and radicals from the CD gap and for generation of “soft” reactant ions, e.g. O_2^- [6]. When operating in reverse gas flow mode the gas exit in the reaction region was closed, the gas exit located behind the CD gap was used and the drift gas flowed through reaction region. Under these conditions the IMS was operating in single flow regime. The standard gas flow mode is characterized by the same direction of gas flow and ion movement in the CD gap and is used for generation of reactant ions, e.g. NO_3^- , $N_2O_2^-$ and $NO_3^-(HNO_3)$. When operating in this mode the gas exit was located in the reaction region, therefore the IMS was operating in dual flow regime [5]. The selective formation of reactant ions can lead to higher sensitivity and selectivity in IMS.

Introduction of the sample by electrospray with CD ionization and IMS separation was used for direct analysis of wine samples. Studied analytes included organic acids primary found in wine (tartaric, malic and citric), as well as some other organic acids formed during winemaking or storage process, e.g. lactic acid. As shown in the CD-IMS spectrum, we were able to confirm the presence of various organic acids in wine samples, e.g. malic acid (Fig. 1).

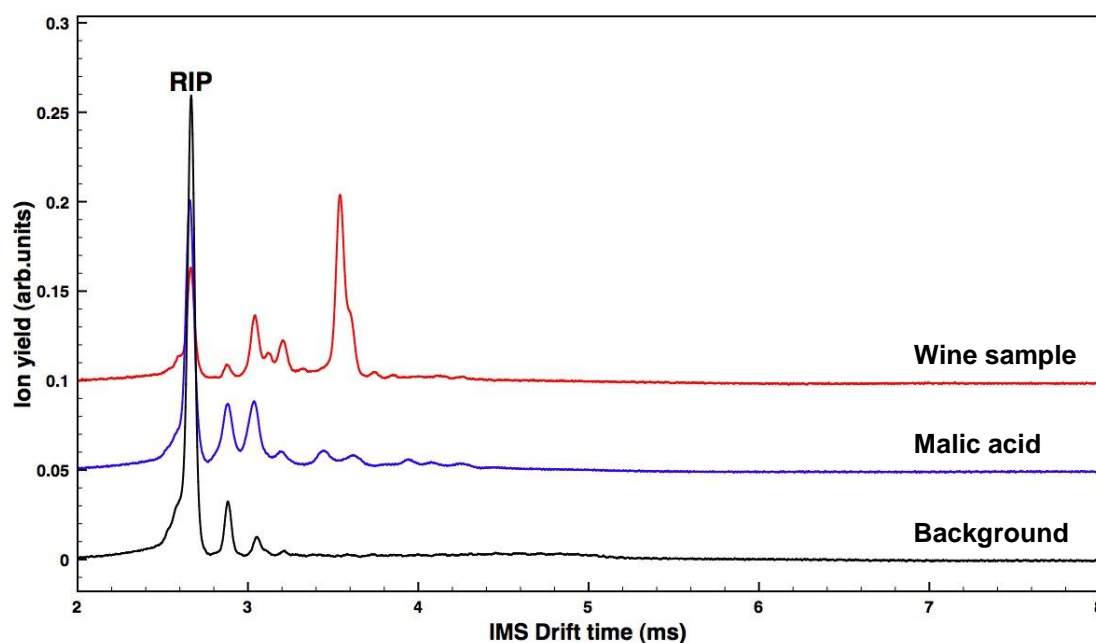


Fig. 1. CD-IMS spectrum of wine sample.

4. Conclusion

In this work the sample introduction by electrospray for fast analysis of liquids by IMS was presented. Ionization process by CD was optimized in order to achieve selective generation of reactant ions and applied to analysis of organic acids. This combination of sample introduction and ionization can be furthermore applied to other similar analytes and has the potential to be coupled with separation techniques, such as high performance liquid chromatography or capillary electrophoresis.

5. Acknowledgment

This work was supported by the Slovak Research and Development Agency (APVV-0259-12).

6. References

- [1] Eiceman, G.A., Karpas, Z. (2005) *Ion mobility spectrometry, 2nd ed.*, Taylor & Francis Group, Boca Raton.
- [2] Eiceman, G.A., Stone, J.A. (2004) *Anal Chem* **76** (12), 390A-397A.
- [3] Karpas, Z. (2013) *Food Res Int* **54** (1), 1146-1151.
- [4] Bohrer, B.C., Merenbloom, S.I., Koeniger, S.L., Hilderbrand, A.E., Clemmer, D.E. (2008) *Ann Rev Anal Chem* **1** (1), 293-327.
- [5] Sabo, M., Okuyama, Y., Kučera, M., Matejčík, Š. (2013) *Int J Mass Spectrom* **334**, 19-26.
- [6] Sabo, M., Matúška, J., Matejčík, Š. (2011) *Talanta* **85** (1), 400-405.
- [7] Shahin, M.M. (1966) *J Chem Phys* **45** (7), 2600-2605.
- [8] Shahin, M.M. (1969) In: Blaustein, B.D. (ed.) *Chemical Reactions in Electrical Discharges*, 48-58.
- [9] Pavlík, J., Skalný, J.D. (1997) *Rap Commun Mass Sp* **11** (16), 1757-1766.

THE RESEARCH OF EXPLOSIVE 2,4,6-TRINITROTOLUENE BY CORONA DISCHARGE-ION MOBILITY-MASS SPECTROMETRY

Zuzana Lichvanová^a, Martin Sabo^a, Bartosz Michalczuk^b and Štefan Matejčík^a

^a*Comenius University in Bratislava, Faculty of Mathematics, Physics and Informatics, Department of Experimental Physics, Mlynská dolina, F2 842 48, Bratislava, Slovakia, matejcik@fmph.uniba.sk*

^b*Siedlce University, Department of Chemistry, 3 Maja 54, 08110 Siedlce, Poland*
zuzana.lichvanova@fmph.uniba.sk

This research was focused on an interaction between reactant ions (RI) produced from corona discharge as an ionization source and molecules of well known explosive 2,4,6-Trinitrotoluen (TNT) by method ion mobility and mass spectrometry (IMS-MS). The IMS device has worked in standard gas flow mode with dominant RI N_2O_2^- , NO_3^- , $\text{NO}_3^- \cdot \text{HNO}_3$ and $\text{NO}_2^- \cdot \text{HNO}_3$ or $\text{NO}_3^- \cdot \text{HNO}_3$ only. The response of sample TNT on present RI resulted in generation of various interesting species. The major product represented proton abstracted anion (TNT-H). The rest of generated ions were ascribed to degradation of TNT by neutrals and radicals formed by the CD.

1. Introduction

Nowadays, the increasing worldwide terrorist threads have made it necessary to detect all variety of explosives such as TNT, RDX, PETN in order to secure protection for important places such as airports, embassies, governmental buildings, public or holy places, power stations, dams, etc. Currently a wide variety of methods are available for explosives detection, for instance IMS, ITMS (Ion Trap Mobility Spectrometry), chemiluminescence, mass spectrometry, UV, thermo-redox [1],[2] or Raman spectroscopy [3]. Each of these techniques has some specific limitations. The world-wide and the most commonly applied detectors are the IMS-based instruments. The IMS is an instrumental technique applied for chemical analysis, an object of many research works for almost 40 years and a method that has been systematically used in practice for 20 years. Different substances are distinguished on the basis of velocity of ions, which varies depending on compound and they are also moving in electric field in the gas. The velocity of compounds is proportional to the mobility coefficient which depends on the mass, shape and dimensions of ions [4].

The IMS devices are equipped with different kinds of ionization sources, for instance ^{63}Ni emitter, corona discharge, secondary electrospray ionization source [5]. The ^{63}Ni source is the most common used source because of its long-term stability and reliability in ion chemistry. However, there have been rising financial and operational reasons to discontinue use of these sources and implement nonradioactive source like corona discharge. This source is constructed in many various configurations (e.g. point-to-plane geometry). The advantages of this source include not only greater ion current, long-term stability but also easy maintenance [5].

In our work, corona discharge ion mobility-orthogonal accelerated time of flight (CD-IMS-oaTOF) was applied for detection of explosive TNT. The reactions of this compound with multiple RI as N_2O_2^- , NO_3^- , $\text{NO}_3^- \cdot \text{HNO}_3$, $\text{NO}_2^- \cdot \text{HNO}_3$ have been investigated in details. To reach a generation of all possible product ions two different power modes of CD in IMS have been set.

2. Experiment

The CD-IMS-oaTOF was described in our previous research [6]. The IMS operated at atmospheric pressure at temperature 353 K. The length of the drift tube was 8.25 cm and the typical intensity of the drift tube was 495 V/cm. The Bradbury-Nielsen type of shutter grid operated with pulse width 110 μs with frequency 50 Hz. The hybrid IMS-oaTOF device has been working in three analytical modes, in single IMS, in single TOF and in two-dimensional mode with both spectrometers working synchronically together. The IMS has been working in standard gas flow mode where gas outlet is

located in the reaction region of IMS and the gas flows through the CD in the same direction as is the movement of the ions in CD gap. The CD in geometry point to plate was applied as an ionization source in this study. The discharge power with 10 and 50 μA has been applied due to ability of CD to produce different variety of RI. If the CD was operating in low power mode (10 μA), the main RI generated from the ionization source were N_2O_2^- , NO_3^- , $\text{NO}_3^-.\text{HNO}_3$ and $\text{NO}_2^-.\text{HNO}_3$ [7] while the further increase of the discharge power up to 50 μA caused formation only RI $\text{NO}_3^-.\text{HNO}_3$ ions [7]. Zero air as a CD gas flow was set to 0.2 l/min, zero air as a IMS drift gas flow was set to 0.8 l/min and zero air as a gas flow of 50 ml/min transported the sample TNT into the reaction region of IMS.

3. Results and discussion

As it was mentioned before, in standard gas flow mode the neutrals and radicals are removed to the reaction region of IMS and influence the interaction between RI and molecules of sample. This interaction can end up in decomposition of investigated species.

3.1. RI of corona discharge N_2O_2^- , NO_3^- , $\text{NO}_3^-.\text{HNO}_3$ and $\text{NO}_2^-.\text{HNO}_3$

The RI N_2O_2^- , NO_3^- , $\text{NO}_3^-.\text{HNO}_3$ and $\text{NO}_2^-.\text{HNO}_3$ with reduced mobility $2.37 \text{ cm}^2.\text{V}^{-1}.\text{s}^{-1}$, $2.29 \text{ cm}^2.\text{V}^{-1}.\text{s}^{-1}$, $2.11 \text{ cm}^2.\text{V}^{-1}.\text{s}^{-1}$ and $2.02 \text{ cm}^2.\text{V}^{-1}.\text{s}^{-1}$ depicted in figure 1a produced from CD have been present when the CD operated under low discharge power 10 μA [7]. An addition of TNT with concentration 2ppb to the IMS caused formation of major peak with reduced mobility $1.54 \text{ cm}^2.\text{V}^{-1}.\text{s}^{-1}$. This peak was by mass spectrometric analysis assigned to proton abstracted anion (TNT-H^-) detected also in previous works [5][8]. We suppose that presence of neutrals and radicals caused interaction with TNT and there have been observed new species with reduced mobilities $1.54 \text{ cm}^2.\text{V}^{-1}.\text{s}^{-1}$, $1.39 \text{ cm}^2.\text{V}^{-1}.\text{s}^{-1}$, $1.32 \text{ cm}^2.\text{V}^{-1}.\text{s}^{-1}$, $1.2 \text{ cm}^2.\text{V}^{-1}.\text{s}^{-1}$, $1.12 \text{ cm}^2.\text{V}^{-1}.\text{s}^{-1}$ and $1.08 \text{ cm}^2.\text{V}^{-1}.\text{s}^{-1}$ seen in figure 1a for TNT concentration 2.3ppm. Related mass spectrometric scan shown in figure 1b indicates except for the dominant ions of $m/z=226$ Da also presence of ions with $m/z=197$ Da, 201 Da, 213 Da, 243 Da, 259 Da, 275 Da, 289 Da, 305 Da, 377 Da, 423 Da and 439 Da. Based on two dimensional IMS-MS analysis depicted in figure 1c the ions of $m/z=197$ Da, 201 Da, 213 Da, 226 Da and 243 Da, were ascribed to IMS peak of reduced mobility $1.54 \text{ cm}^2.\text{V}^{-1}.\text{s}^{-1}$, the ions of $m/z=259$ Da and 275 Da were attributed to IMS peak with reduced mobility $1.39 \text{ cm}^2.\text{V}^{-1}.\text{s}^{-1}$, the ions of $m/z=289$ Da and 305 Da were assigned to IMS peak with reduced mobility $1.32 \text{ cm}^2.\text{V}^{-1}.\text{s}^{-1}$, the ions of $m/z=377$ were ascribed to IMS peak with reduced mobility $1.2 \text{ cm}^2.\text{V}^{-1}.\text{s}^{-1}$, the ions of $m/z=423$ Da were attributed to IMS peak with reduced mobility $1.08 \text{ cm}^2.\text{V}^{-1}.\text{s}^{-1}$ and the ions of $m/z=439$ Da were assigned to IMS peak with reduced mobility $1.12 \text{ cm}^2.\text{V}^{-1}.\text{s}^{-1}$.

As mentioned before the dominant ions of $m/z=226$ Da were ascribed to proton abstracted anion (TNT-H^-), the ions of $m/z=197$ Da were attributed to (TNT-NO^-) [9], the ions of $m/z=243$ Da were assigned to oxygen adduct ions (TNT+O^-) [9] and presence of ions $m/z=213$ Da was ascribed to loss of NO group from [TNT+O^-] adduct. Based on our best knowledge, there are not any information about appearance of ions $m/z=201$ Da and we also do not offer any relevant explanation about composition of these species. The IMS peak with reduced mobility $1.39 \text{ cm}^2.\text{V}^{-1}.\text{s}^{-1}$ is composed of ions $m/z=259$ and 275 Da and ascribed to (TNT+O_2^-) and to (TNT+O_3^-) adduct ions, respectively. Based on the 2D analysis (fig 1c) the IMS peak of reduced mobility $1.32 \text{ cm}^2.\text{V}^{-1}.\text{s}^{-1}$ is composed of the ions of $m/z=289$ Da and 305 Da. The presence of both ions we ascribe as a direct consequence of the presence of neutrals and radicals in reaction region. The ions of $m/z=289$ Da were assigned to (TNT+NO_3^-) adduct ions while the species of $m/z=305$ Da were ascribed to (TNT+NO_4^-) adduct ions. It seems reasonable to attribute the peak with reduced mobility $1.2 \text{ cm}^2.\text{V}^{-1}.\text{s}^{-1}$ to the ions clusters (TNT-H^-).($\text{TNT-N}_2\text{O}_3$) where the ($\text{TNT-N}_2\text{O}_3$) is fragment product of TNT [10]. The radicals and neutrals should be responsible also for the loss of N_2O_3 group from TNT. The last visible peak with reduced mobility $1.12 \text{ cm}^2.\text{V}^{-1}.\text{s}^{-1}$ is composed of ions $m/z=439$ Da. We suggest that these species can be (TNT-H^-).(TNB) ions where the TNB are molecules of 1,3,5-trinitrobenzen formed from the decomposition of TNT by ozone. The last IMS peak with reduced mobility $1.08 \text{ cm}^2.\text{V}^{-1}.\text{s}^{-1}$ is composed of ions $m/z=423$ Da. We ascribe these ions to (TNT-H^-).(TNT-NO) clusters and loss of group NO was caused by radicals and neutrals.

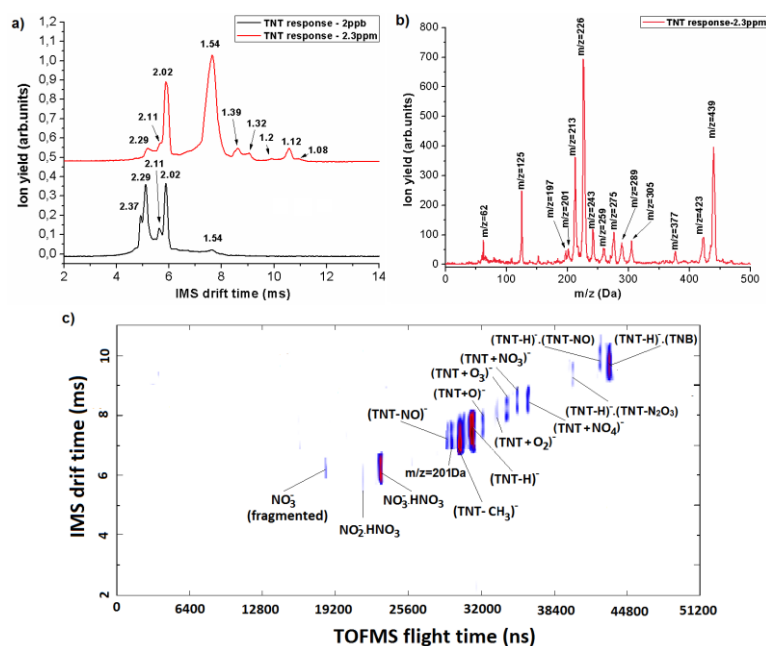


Fig.1 TNT response on RI N_2O_2^- , NO_3^- , $\text{NO}_3^- \cdot \text{HNO}_3$ and $\text{NO}_2^- \cdot \text{HNO}_3$ a) response for 2ppb and 2.3ppm b) related MS spectrum for TNT concentration 2.3ppm and c) two dimensional IMS-MS spectrum for 2.3ppm of TNT.

3.2. RI of corona discharge $\text{NO}_3^- \cdot (\text{HNO}_3)$

The reactant ions $\text{NO}_3^- \cdot (\text{HNO}_3)$ have appeared in corona discharge operated in standard gas flow mode when the power of CD was increased up to the 50 μA . The reduced mobility of these ions is $2.02 \text{ cm}^2 \cdot \text{V}^{-1} \cdot \text{s}^{-1}$ as it can be seen in figure 2a. The related mass spectrum approves the presence of ions $m/z=125 \text{ Da}$ and $m/z=62 \text{ Da}$ which were attributed to the ions $\text{NO}_3^- \cdot (\text{HNO}_3)$ and ions NO_3^- as a product of fragmentation $\text{NO}_3^- \cdot (\text{HNO}_3)$ clusters.

The small concentration of TNT (2ppb) resulted in formation of dominant peak with reduced mobility $1.54 \text{ cm}^2 \cdot \text{V}^{-1} \cdot \text{s}^{-1}$ and $m/z=226 \text{ Da}$. These ions are proton abstracted anions $(\text{TNT-H})^-$ and it confirms previous results reached with lower power of CD. The created peak in IMS with reduced mobility $2.29 \text{ cm}^2 \cdot \text{V}^{-1} \cdot \text{s}^{-1}$ and related $m/z=62 \text{ Da}$ was attributed to the ions NO_3^- which were formed by the loss of NO_2 group from TNT molecule and in next step formed. The further increase of TNT concentration resulted in formation of peaks with reduced mobilities $1.59 \text{ cm}^2 \cdot \text{V}^{-1} \cdot \text{s}^{-1}$, $1.54 \text{ cm}^2 \cdot \text{V}^{-1} \cdot \text{s}^{-1}$, $1.39 \text{ cm}^2 \cdot \text{V}^{-1} \cdot \text{s}^{-1}$, $1.32 \text{ cm}^2 \cdot \text{V}^{-1} \cdot \text{s}^{-1}$ and $1.11 \text{ cm}^2 \cdot \text{V}^{-1} \cdot \text{s}^{-1}$ as we can see from figure 2a. The mass spectrometric scan shown on figure 2b indicates except for the dominant ions of $m/z=226 \text{ Da}$ also the presence of ions with $m/z=211 \text{ Da}$, 243 Da , 259 Da , 275 Da , 289 Da , 305 Da and 437 Da . By the two dimensional IMS-MS analysis shown on figure 2c were the ions of $m/z=211 \text{ Da}$ assigned to IMS peak with reduced mobility $1.59 \text{ cm}^2 \cdot \text{V}^{-1} \cdot \text{s}^{-1}$, the dominant IMS peak of reduced mobility $1.54 \text{ cm}^2 \cdot \text{V}^{-1} \cdot \text{s}^{-1}$ is composed of ions with $m/z=226 \text{ Da}$ and 243 Da , the ions of $m/z=259 \text{ Da}$ and 275 Da belong to IMS peak with reduced mobility $1.39 \text{ cm}^2 \cdot \text{V}^{-1} \cdot \text{s}^{-1}$, the IMS peak with reduced mobility $1.32 \text{ cm}^2 \cdot \text{V}^{-1} \cdot \text{s}^{-1}$ is composed of species with $m/z=289 \text{ Da}$ and 305 Da and the last IMS peak with reduced mobility $1.11 \text{ cm}^2 \cdot \text{V}^{-1} \cdot \text{s}^{-1}$ is composed of ions with $m/z=437 \text{ Da}$.

Ions with $m/z=211 \text{ Da}$ were assigned to $(\text{TNT-O})^-$ adduct ions and we suppose that degradation of TNT to these ions occurs similarly as in Fenton process [11]. The IMS peak with reduced mobility $1.54 \text{ cm}^2 \cdot \text{V}^{-1} \cdot \text{s}^{-1}$ is composed of ions with $m/z=226 \text{ Da}$ and 243 Da which were ascribed to $(\text{TNT-H})^-$ and $(\text{TNT+O})^-$ anions. Another peak with reduced mobility $1.39 \text{ cm}^2 \cdot \text{V}^{-1} \cdot \text{s}^{-1}$ is composed of ions with $m/z=259 \text{ Da}$ and 275 Da and these ions were previously identified as $(\text{TNT+O}_2)^-$ and $(\text{TNT+O}_3)^-$ anions. The IMS with reduced mobility $1.32 \text{ cm}^2 \cdot \text{V}^{-1} \cdot \text{s}^{-1}$ is composed of ions with $m/z=289 \text{ Da}$ and 305 Da and ascribed to $(\text{TNT+NO}_3)^-$ and $(\text{TNT+NO}_4)^-$ anions. The last appeared peak with reduced mobility $1.11 \text{ cm}^2 \cdot \text{V}^{-1} \cdot \text{s}^{-1}$ and $m/z=437 \text{ Da}$ has not been previously mentioned and it seems to be reasonable to assign it to species $(\text{TNT-H})^- \cdot (\text{TNT-O})^-$ clusters.

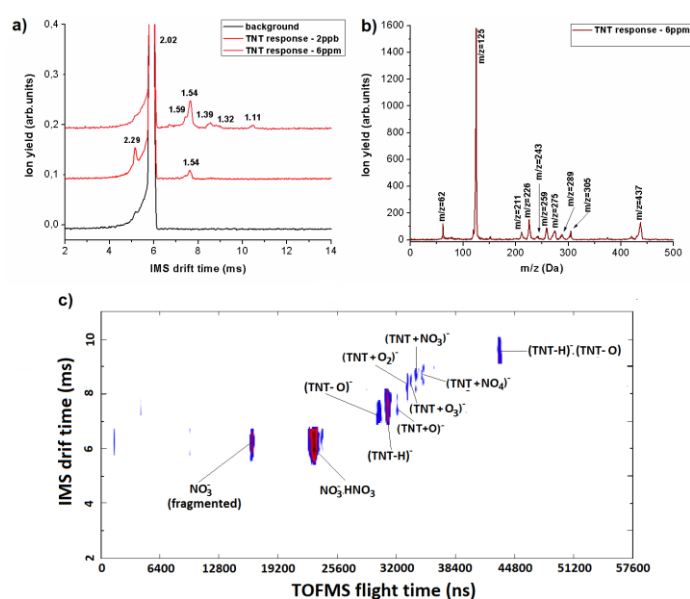


Fig.2 TNT response on RI $\text{NO}_3^- \cdot \text{HNO}_3$ a) response for 0,2ppb and 6ppm b) related MS spectrum for TNT concentration 6ppm and c) two dimensional IMS-MS spectrum for 6ppm of TNT

4. Conclusion

Our research was focused on the response of TNT on multiple RI generated by CD in IMS-MS instrument. In standard gas flow mode the operation of CD was divided into two sections based on CD power. If the CD operated in low discharge power with 10 μA , the dominant RI observed were N_2O_2^- , NO_3^- , $\text{NO}_3^- \cdot \text{HNO}_3$ and $\text{NO}_2^- \cdot \text{HNO}_3$ ions. The response of these RI on TNT molecules resulted in generation of many species, where the major observed products were proton abstracted anions (TNT-H^-). The generation of other product ions was ascribed to degradation of TNT by the neutrals and radicals produced from CD. If the CD worked under high discharge power with 50 μA , the only RI ions generated from the discharge were $\text{NO}_3^- \cdot \text{HNO}_3$ clusters. The response of $\text{NO}_3^- \cdot \text{HNO}_3$ ions on TNT resulted also in formation of (TNT-H^-) ions as dominant species. Similarly as in case of CD operated under low discharge, the response on TNT molecules was accompanied by the formation of many other interesting species. However, the nature of these species was significantly different and it was explained by the higher generation of radical and neutrals generated from CD operated under high discharge power.

5. Acknowledge

The research was supported by Slovak Research and Development Agency Projects APVV-0259-12.

6. Refereces

- [1] Thiesan L Hannum D Murray D W Parmeter J E 2005 *Survey of Commercially Available Explosives Detection Technologies and Equipment* 2004 Document No.: 208861 National Institute of Justice U.S. Department of Justice.
- [2] Rhykerd Ch L Hannum D W Murray D W Parmeter J E 1999 *Guide for the Selection of Commercial Explosives Detection Systems for Law Enforcement Application*, National Institute of Justice, U.S. Department of Justice NIJ Guide 100-99.
- [3] Weyermann C Mimoune Y Anglada F Massonnet G Esseiva P Buzzini P 2011 *Applications of a transportable Raman spectrometer for the in situ detection of controlled substances at border controls* Forensic Sci. Int. **209** 21–28.
- [4] Eiceman G A Karpas Z 2005 *Ion mobility spectrometry 2nd ed* CRC Press/Taylor Francis Boca Raton.

- [5] Crawford C L Hill H H 2013 *Comparison of reactant and analyte ions for ^{63}Ni , corona discharge and secondary electrospray ionization sources with ion-mobility-mass spectrometry* *Talanta* **107** 225-232.
- [6] Sabo M Malásková M Matejčík Š 2014 *Ion mobility spectrometry-mass spectrometry studies of ion processes in air at atmospheric pressure and their application to thermal desorption of 2,4,6-trinitrotoluen* *Plasma Sources Sci. Technol.* **23** 015025.
- [7] Sabo M Okuyama Y Kučera M Matejčík Š 2013 *Transport and stability of negative ions generated by negative corona discharge in air studied using ion mobility-*oa*TOF* *International Journal of Mass Spectrometry* **334** 19-26.
- [8] Lee J Park S Cho S G Goh E M Lee S Koh S S Kim J 2014 *Analysis of explosives using corona discharge ionization combined with ion mobility spectrometry-mass spectrometry* *Talanta* **120** 64-70.
- [9] Laakia J Pederson C S Adamov A Viidanoja J Sysoev A Kotiaho 2009 *Sterically hindered phenols in negative ion mobility spectrometry-mass spectrometry* *RCM* **23** 3069-3076.
- [10] Sulzer P Rondinob F Ptasinskaa S Illenberger E Mark T D Schier P 2008 *Probing trinitrotoluene (TNT) by low-energy electrons* *electron IJMS* **272** 149-153.
- [11] Rodrigues M B Silva F T Paiva T B C 2009 *J Hazard Mater* **168** 1065-1069.

LASER DESORPTION OF EXPLOSIVES USING ION MOBILITY SPECTROMETRY

Michaela Malásková¹, Martin Sabo¹, Štefan Matejčík¹

¹*Department of Experimental Physics, Comenius University, Mlynská dolina F2, 842 48 Bratislava, Slovakia*

E-mail: michaela.malaskova@gmail.com

In this work we will present laser desorption technique for surface explosives detection by ion mobility spectrometry (IMS) equipped with corona discharge (CD) ionization source. Three Laser Diode Modules (LDM) with wavelengths 445 nm, 532 nm and 665 nm were used in our experiment, desorbing sample directly from the surface without any pre-treatment. The reached limits of detection (LOD) were 86 pg for 2,4,6 trinitrotoluene (TNT), 305 pg for cyclotrimethylene-trinitramine (RDX) and 1,22 ng for pentaerythritoltetranitrate (PETN). These LOD were achieved directly, but after including limiting factors of laser desorption, theoretical LOD were 500 fg for TNT, 1,3 pg for RDX and 5,2 pg for PETN.

1. Introduction

In our society threats from groups with radical attitude increase every day. Therefore it is very important to develop a quick and easy method to trace explosives and dangerous weapons. IMS is commonly used technology to detect explosives due to its high sensibility, quick response and relatively low price. The most used ionization source in the world is radioactive ⁶³Ni [1], which is often unavailable on markets. In our laboratory CD in point to plane geometry is used. CD is doped with carbon tetrachloride, which leads to react ions Cl⁻, increasing sensibility of IMS [2]. Another factor important in detection of explosives is the sampling technique. In our previous work we used thermal desorption and achieved LOD for TNT 350 pg. Laser desorption was first used by Huang et al. [3], who achieved LOD 300 pg for TNT using pulsed laser. In our work cheaper LDM with various wavelengths for estimated LOD will be used for three used explosives TNT, RDX and PETN. Later we will discuss the desorption mechanism, limitations of this technique and we will determine theoretical LOD.

2. Experiment

The IMS used in our experiment (Fig 1.a) was build from 12 stainless ring electrodes isolated by Teflon rings. As a ion source CD in point to plate geometry was used. The gas outlet was located behind the CD in order to remove neutrals. Atmospheric air purified by molecular sieve traps with typical flow 1,2 l/min was used as a drift gas. Bradbury-Nielsen type of SG with opening time 60 μs was located at the third electrode. The length of drift tube was 12,1 cm and electric field intensity was 462,8 V/cm. IMS was heated to 386 K to minimize memory effect. The sample gas flow was 0,9 l/min through stainless capillary, which was heated to 356 K for the same reason as the IMS. The operation parameters of IMS instrument are summarized in Table 1.

Atmospheric pressure chemical ionization mass spectrometer (APCI-MS), which was modified from IMS-oaTOFMS [4] was used to estimate limits of detection. CD used in APCI-MS was designed in the same geometry as in IMS in order to obtain comparable results. Drift gas flow and sample gas flow was similar as in the IMS experiment.

Three LDM with wavelengths 445 nm, 532 nm and 665 nm were used in our experiment. The power of the LDM was 500 mW for 445 nm and 300 mW for 532 and 635 nm. Each LDM desorbed sample directly from the explored surface (stainless needle) from the same distance.

Explosives obtained from Slovak Department of Defense were weighed out and in case of TNT diluted in methanol and in the cases of RDX and PETN first in acetone, then in methanol to reach required concentration. This solution was sampled by 1 μl syringe, the volume of which was released on the needle tip. After evaporation of the solvent the needle tip was inserted in front of the capillary and explored for tracks of explosives.

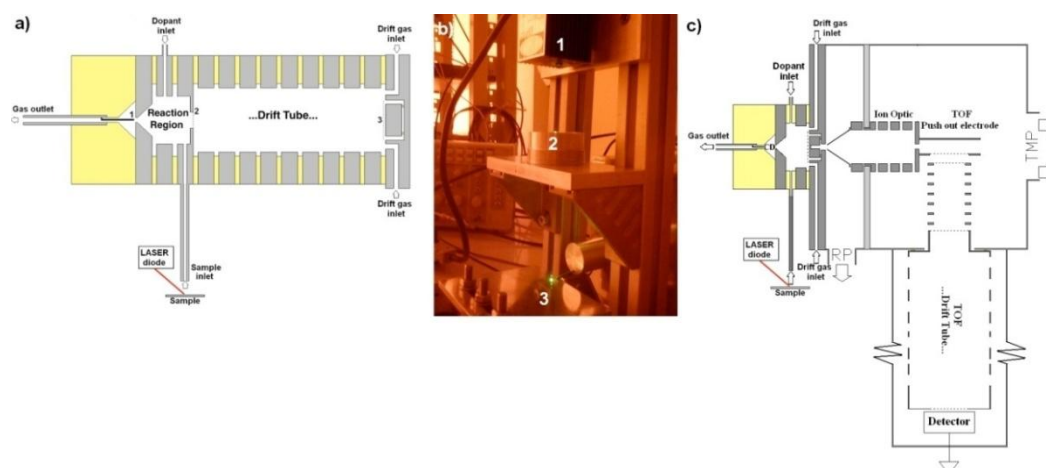


Fig. 1. a) The schematic view of CD-IMS instrument, b) photograph of the LD unit (1-LDM, 2-focusing lens, 3-investigated surface), c) schematic view of APCDI-MS instrument.

Drift tube length	12.1 cm	Drift tube pressure	≈455 mbar
Electric field intensity	462.8 V/cm	Used resolution	≈30
SG pulse	60 μs	CD current	20 μA
Drift gas flow	1.1 L/min	445nm LASER diode	500 mW
Sample gas flow	0.9 L/min	532nm LASER diode	300 mW
Drift tube temperature	386 K	635nm LASER diode	300 mW

Tab. 1. Operation parameters of IMS instrument.

3. Results and discussion

In IMS spectrum (Fig 2.a) we can see reactant ion peak (RIP) with drift time 2,76 ms and reduced ion mobility of $2,96 \text{ cm}^2 \cdot \text{V}^{-1} \cdot \text{s}^{-1}$. The corresponding mass spectrum (Fig 2.b) shows that this peak is composed of $\text{Cl}^-(\text{H}_2\text{O})_n$ ($n \leq 8$) clusters. In IMS spectrum of a mixture of all three explosives (Fig 2.a) we are able to identify TNT as $(\text{TNT-H})^-$ ion with drift time 5,07 ms and reduced mobility of $1.61 \text{ cm}^2 \cdot \text{V}^{-1} \cdot \text{s}^{-1}$ with $m/z = 226$. The response for RDX leads to the formation of peak $\text{Cl}^- \cdot \text{RDX}$ with drift time 5.3 ms, reduced mobility of $1.54 \text{ cm}^2 \cdot \text{V}^{-1} \cdot \text{s}^{-1}$ and $m/z = 257$. Response for PETN leads to the formation of $\text{Cl}^- \cdot \text{PETN}$ with drift time 6.39 ms, reduced mobility $1.27 \text{ cm}^2 \cdot \text{V}^{-1} \cdot \text{s}^{-1}$ and $m/z = 351$. We are able to identify peaks with reduced mobility of $2,45 \text{ cm}^2 \cdot \text{V}^{-1} \cdot \text{s}^{-1}$ and $2,02 \text{ cm}^2 \cdot \text{V}^{-1} \cdot \text{s}^{-1}$, which we assign to $\text{Cl}^- \cdot (\text{NO})_2$ and $\text{Cl}^- \cdot (\text{NO})_3$ clusters [2].

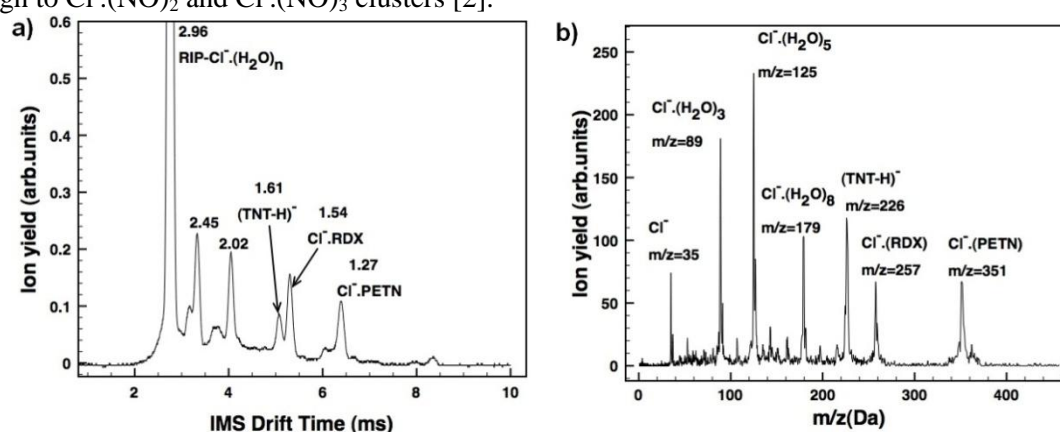


Fig. 2. a) IMS and b) MS spectrum of investigated explosives.

Reached LOD for each explosive and LDM can be seen in table 2. The highest sensitivities for TNT and RDX were achieved with green LDM, while for PETN with red LDM. Blue LDM with higher power showed the lowest sensitivity. IMS spectra of LOD are in figure 3. In other works using laser desorption [5] it was concluded that heating of the surface is the main effect in laser desorption. We assume that the absorption of laser light also plays an important role, because we did not reach the lowest sensitivity with one LDM. With this observation we can support desorption of special substance by choosing LDM with proper wavelength. This can result in additional selectivity to IMS.

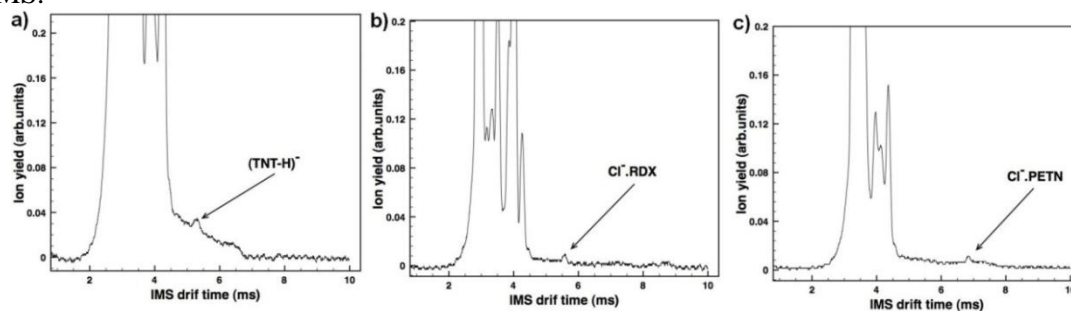


Fig. 3. Measured sensitivities for a) TNT, b) RDX, c) PETN.

Tab. 2. Reached LOD for explosives.

	445 nm (500mW)	532nm (300mW)	635nm (300mW)
TNT	600 pg	86 pg	520 pg
RDX	6500 pg	305 pg	1315 pg
PETN	5000 pg	1400 pg	1220 pg

After measuring the time of desorption we find out that relevant parts of the samples of TNT (Fig 4.a) and RDX (Fig. 4.b) evaporate in 8 s, while the desorption time for PETN (Fig 4.c) is 6 s. After considering that duty cycle of IMS is 0,272 s we can calculate theoretical LOD as 3 pg for TNT, 14 pg for RDX and 42 pg for PETN. Another important factor is the area of desorption (Fig. 4.d), which is 5 times smaller than the area of the needle tip. If we are able to desorb whole area, we can reached new theoretical LOD as 0.6 pg for TNT, 2.8 pg for RDX and 8.4 pg for PETN.

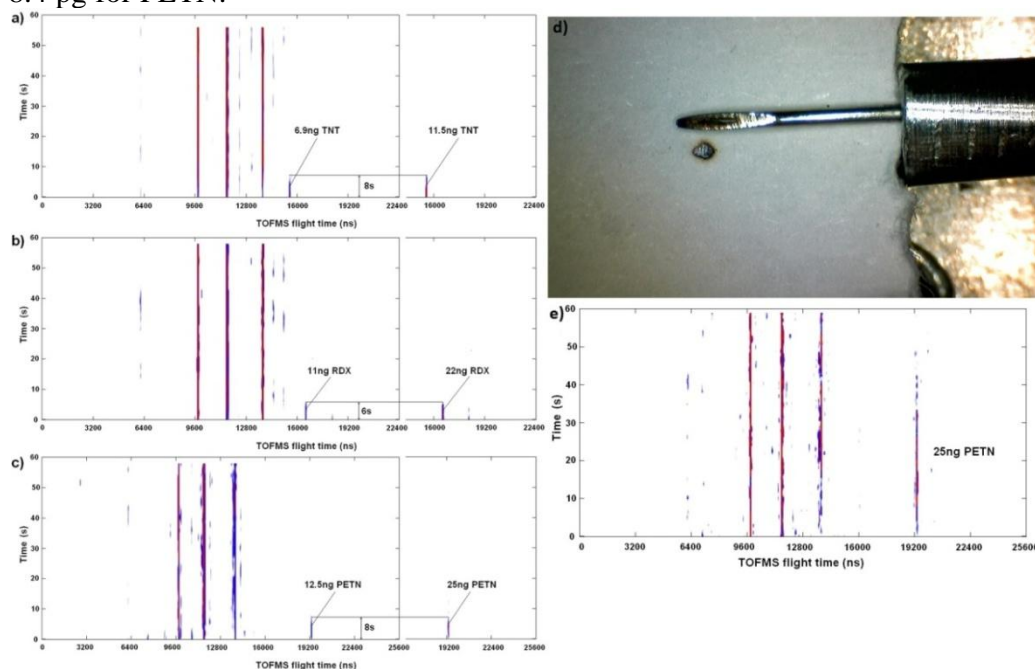


Fig. 4. The desorption profiles measured by APCI-MS of a) TNT, b) RDX, c) PETN, d) comparison of the area desorbed by LDM with needle tip, e) desorption profile of 25 ng of PETN reached when the needle tip was continually moving under the focal point of LDM.

4. Conclusion

The CD-IMS instrument supported with laser desorption was presented in this work. For TNT and RDX LOD were reached using green laser and for PETN with red laser. Directly reached LOD were 86 pg for TNT, 305 pg for RDX and 1,22 ng for PETN. After including limiting factors of laser desorption as desorption time and area of desorption we can establish theoretical LOD as 0,6 pg for TNT, 2,8 pg for RDX and 8,4 pg for PETN.

5. Acknowledgement

This work was supported by Slovak research and development agency project APVV-0259-12.

6. References

- [1] G.A. Eiceman, Z. Karpas, *Ion Mobility Spectrometry 2nd ed.*, CRC press, **2005**
- [2] M. Sabo, M. Malásková, Š. Matejčík, *PSST*, **2014**, 25,015025
- [3] S.H. Huang, L. Kolaitis, D.M. Lubman, *Applied Spectroscopy*, **1987**, 41, 1371
- [4] M. Sabo, Š. Matejčík, *Anal. Chem.*, **2012**, 84, 5327
- [5] S.Ehlert, A. Walte, R. Zimmermann, *Anal. Chem.*, **2013**, 85, 11047

DETECTION OF 2,4,6-TRINITROTOLUENE USING CORONA DISCHARGE-ION MOBILITY SPECTROMETRY WITH AN ORTHOGONAL ACCELERATED TIME OF FLIGHT

Bartosz Michalczuk¹, Martin Sabo², Zuzana Lichvanova², Wiesława Barszczewska¹

¹Siedlce University, Faculty of Natural Sciences, Department of Chemistry,
3 Maja 54, 08-110 Siedlce, Poland

²Comenius University in Bratislava, Faculty of Mathematics, Physics and Informatics,
Department of Experimental Physics, Mlynska dolina F2 842 48, Bratislava, Slovakia
E-mail: bartosz.michalczuk@uph.edu.pl

Corona discharge-ion mobility spectrometry with an orthogonal accelerated time of flight (CD-IMS-oaTOFMS) apparatus has been used as a potential method for detection of 2,4,6-Trinitrotoluene (TNT). The ion mobility spectrometer with corona discharge as a ionization source responded in two modes in standard and reverse mode. In the reverse mode trinitrotoluene responded with two peaks. (TNT-H⁺) ($m/z=226$) with reduced mobility equal to $1,55 \text{ cm}^2\text{V}^{-1}\text{s}^{-1}$ and TNT⁻ ($m/z=227$) and reduced mobility of $1,50 \text{ cm}^2\text{V}^{-1}\text{s}^{-1}$.

1. Introduction and experimental

Detection of all kinds of explosives in a days when terrorism is omnipresent and is a real threat became extremely important. It is crucial to ensure the safety in places like airports, public utility buildings, embassies, places of worship, etc. 2,4,6-trinitrotoluene commonly known as a TNT is a yellow-coloured solid which is used in chemical synthesis, but TNT is best known as a explosive material. The explosive yield of TNT is considered to be the standard measure of strength of bombs and other explosives. Despite TNT was used during The World War I it is still widely used by the military all over the world.

In recent years many methods of detecting explosives has been reported e.g. X-ray screening[1], neutron and γ -ray spectroscopy[2], LC-MS[3], SPME-HPLC[4]. Due to the low detection limit IMS has proved to be an ideal method for the detection of trace level of explosives. Other advantages which make IMS appropriate for detecting explosives are: fast response (order of milliseconds), simple design and portability.

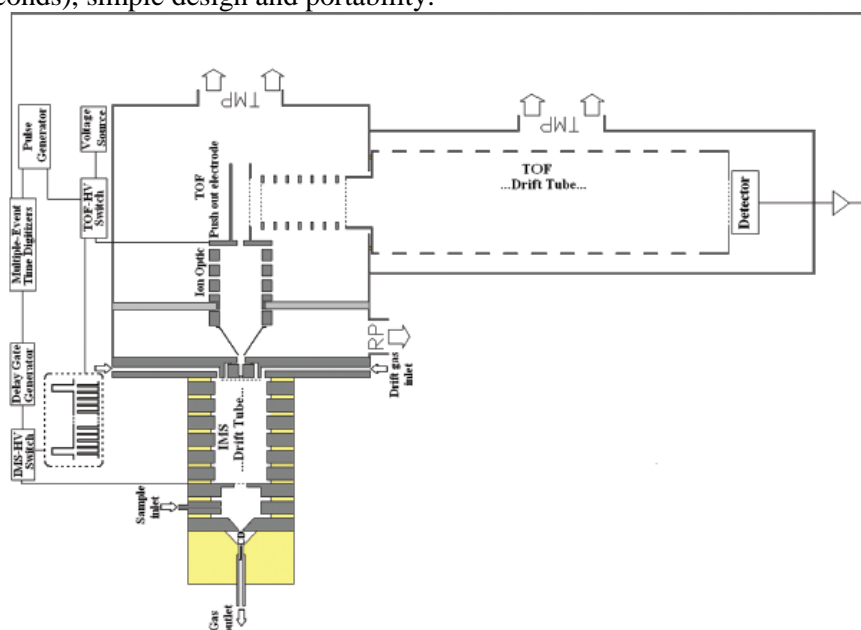


Figure 1. Schematic of the IMS-oaTOFMS apparatus.

The IMS-oaTOFMS instrument used in this study is shown in figure 1 and was fully described in [5,6]. The experiment was carried out at atmospheric pressure in negative polarity with drift field equal to 543 V/cm. Apparatus was operated in two modes. Standard mode when drift gas flow rate was set at 1,2 L/min, sample gas flow rate at 0,1 L/min and corona discharge gas flow at 0,1 L/min. The gas outlet was located in the reaction region. Reverse mode with following parameters: drift gas flow rate- 1,2 L/min, sample gas flow rate- 0,1 L/min, gas outlet was positioned behind the CD gap.

2. Results

Reverse mode

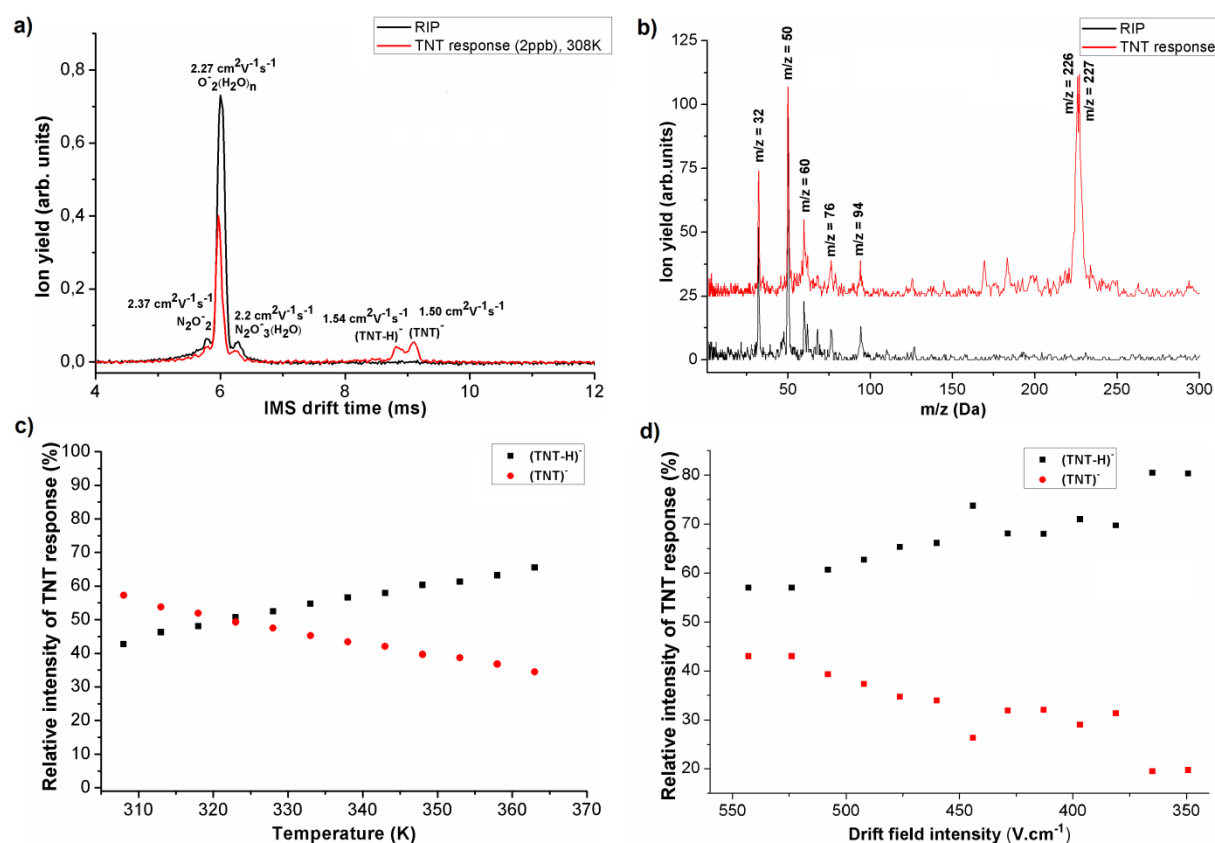


Figure 2. The TNT response in reverse gas flow mode. a) IMS spectrum at 308 K b) corresponding MS spectrum c) relative intensity of $(\text{TNT})^-$ and $(\text{TNT-H})^-$ depending on IMS drift tube temperature d) relative intensity of $(\text{TNT})^-$ and $(\text{TNT-H})^-$ as a function of IMS drift field.

There are three peaks in the IMS spectrum (figure 2a) which correspond to reactant ion peaks (RIP) created in CD. First peak with reduced mobility $2,37 \text{ cm}^2 \text{ V}^{-1} \text{ s}^{-1}$ corresponds to N_2O_2^- ($m/z=60$). Mass spectrum (figure 2b) shows four additional reactant ions peaks ($m/z=32, 50, 76,$ and 94) this fact reflects another peaks in IMS spectrum with reduced mobilities of $2,27 \text{ cm}^2 \text{ V}^{-1} \text{ s}^{-1}$ and $2,2 \text{ cm}^2 \text{ V}^{-1} \text{ s}^{-1}$ which can be assigned to several molecules O_2^- , $\text{O}_2^-(\text{H}_2\text{O})$, N_2O_3^- , $\text{N}_2\text{O}_3^-(\text{H}_2\text{O})$. Sample of 2,4,6-trinitrotoluene responded with two peaks with reduced mobilities of $1,54 \text{ cm}^2 \text{ V}^{-1} \text{ s}^{-1}$ and $1,50 \text{ cm}^2 \text{ V}^{-1} \text{ s}^{-1}$. Mass spectrum of TNT as it has been proved [7] is characterized by two peaks, $m/z=226$ and $m/z=227$ which correspond to $(\text{TNT-H})^-$ and $(\text{TNT})^-$ respectively.

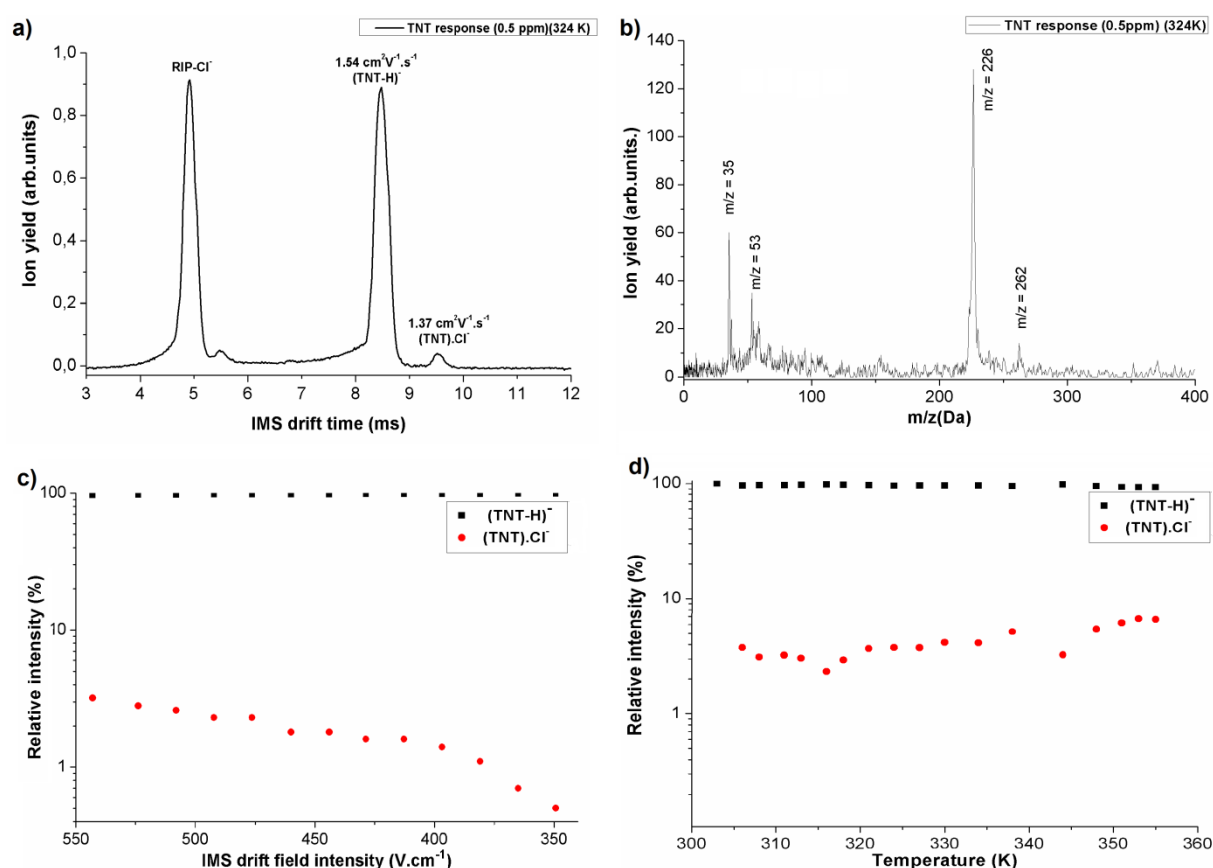
Reverse mode with CCl_4 as a dopant

Figure 3. The TNT response in reverse gas flow mode with CCl_2 as a dopant a) IMS spectrum at 324 K b) related MS spectrum to IMS spectrum, c) relative intensity of $(\text{TNT-H})^-$ and $\text{TNT}\cdot\text{Cl}^-$ ions depending on IMS drift field intensity d) relative intensity of $(\text{TNT-H})^-$ and $\text{TNT}\cdot\text{Cl}^-$ as a function of IMS drift field temperature.

As we can see from figure 3, there are two characteristic peaks in the IMS spectrum (figure 3a) which correspond to $(\text{TNT-H})^-$ and $\text{TNT}\cdot\text{Cl}^-$ with reduced mobilities of $1,54 \text{ cm}^2\text{V}^{-1}\text{s}^{-1}$ and $1,37 \text{ cm}^2\text{V}^{-1}\text{s}^{-1}$ respectively. Mass spectrum (figure 2b) apart from typical for TNT ion with $m/z=226$ ($(\text{TNT-H})^-$) shows also peak with $m/z=262$ which corresponds to $\text{TNT}\cdot\text{Cl}^-$.

3. References

- [1] Y. Yang, Y. Li, H. Wang, T. Li, B. Wu, Explosives detection using photoneutrons produced by X-rays, Nucl. Instrum. Methods A 579 (2007) 400–403,
- [2] M. Farahmand, A.J. Boston, A.N. Grint, P.J. Nolan, M.J. Joyce, R.O. Mackin, B.D. Mellow, M. Aspinall, A.J. Peyton, R. Van Silfhout, Detection of explosive substances by tomographic inspection using neutron and gamma-ray spectroscopy, Nucl. Instrum. Methods B 261 (2007) 396–400,
- [3] E. Holmgren, H. Carlsson, P. Goedeke, C. Crescenzi, Determination and characterization of organic explosives using porous graphitic carbon and liquid chromatography–atmospheric pressure

- chemical ionization mass spectrometry, *J. Chromatogr. A* 1099 (2005) 127–135. [5] M. Gaft, L. Nagli, UV gated Raman spectroscopy,
- [4] G.V. Kaur, A.K. Kumar, P.K. Malik, K. Rai, SPME-HPLC: a new approach to the analysis of explosives, *J. Hazard. Mater.* 147 (3) (2007) 691–697,
- [5] M.Sabo, Š.Matejčík, *Anal. Chem.*, 84 (2012) 5327,
- [6] M.Sabo, Y.Okuyama, M.Kucera, Š.Matejčík, *IJMS*, 334 (2013) 19,
- [7] J. Laakia, C. S. Pedersen, A. Adamov, J. Viidanoja, A. Sysoev, T. Kotiaho, *Rapid Commun. Mass Spectrom.*, 23 (2009) 3069-3076,

USING ION MOBILITY SPECTROMETRY FOR DIRECT DETECTION OF 2,4,6-TRICHLOROANIZOL FROM CORK STOPPER

Martin Sabo, Michela Malásková and Štefan Matejčík

Department of Experimental Physics, Faculty of Mathematics, Physics and Informatics, Comenius University, Mlynska dolina F2, 842 48 Bratislava, Slovakia

Martin.Sabo@gmail.com

In this work we demonstrate the detection of 2,4,6-Trichloroanisole (TCA) from cork stopper without any pre-separation or pre-concentration. The TCA was identified by its peak with reduced ion mobility of $1.66 \text{ cm}^2 \cdot \text{V}^{-1} \cdot \text{s}^{-1}$.

1. Introduction

The wine industry and consumers themselves deem that wine aroma is an important attribute of product quality. The presence of halo-anisoles is an enological problem in wine industry because of their low sensory threshold. TCA, particularly the 2,4,6-TCA isomer, is considered as main substance responsible for unpleasant odour of wine also known as “cork taint”, mentioned in some researches [1,2]. This musty, mouldy odour of tainted wine originating from the cork material is directly detected by consumers of wine and is defined as similar to wet cardboard, mushrooms, earthy smell, etc [1].

Detection problem of this semi-volatile compound is associated with low concentration at which this analyte is present in wine or cork. Hence, in many methods it is substantial for detection of 2,4,6-TCA to retrieve suitable pre-concentration, pre-separation and sensitive analytical device for measuring signal intensity. Several analytical methods have been proposed for the proper concentration determination of the compounds responsible for tainted wine flavour [1,3,4]. Considering the physic-chemical properties of semi-volatile compound 2,4,6-TCA, a novel gas chromatography-mass spectrometry (GC-MS) method, focused on this compound residues in white and red wine was reported by S.H. Patil [3]. The efficiency of 2,4,6-TCA analysis was affected by few factors, including extraction solvent type chosen (toluene in this case) and particularly its volume. The detection limit of this compound reached value of $0.0083 \text{ ng} \cdot \text{mL}^{-1}$. This technique offers distinct advantages, but it still does not dispose of such sensitivity as ion mobility spectrometry. Ion mobility spectrometry (IMS) is an analytical technique that characterizes molecules by their gas phase mobility and is frequently used for detection of various kinds of explosives, drugs and narcotics. IMS provides fast and high sensitive response to presence of not only explosives, but also toxic chemicals. In addition, ion mobility spectrometers are comparatively inexpensive and provide spectra in milliseconds range. These advantages make IMS device suitable for investigation of volatiles compounds in different fields [5]. Several studies have been focused on detection of presence of 2,4,6-TCA in wine with IMS [1,4].

In this work we will demonstrate the detection of TCA directly from the cork stoppers in analytical time 5s.

2. Experiment

The IMS instrument developed at Department of Experimental Physics in collaboration with MaSaTECH and modified for TCA detection from the cork stoppers was used in this experiment. The 2,4,6-Trichloroanisole as a reference compound was obtained from Sigma Aldrich. The cork stoppers were obtained from Orlando Teodoro - Universidade Nova de Lisboa. The cork stoppers were in three different concentration: 1. Corks stoppers with TCA concentration 19ppt (determine via the GC-MS), 2. Cork stoppers with TCA detected by the smell and 3. Cork stoppers with unknown concentration.

3. Results and discussion

The IMS spectrum without any sample is show on figure 1. From this spectrum we can see the dominant reactant ion peak (RIP).

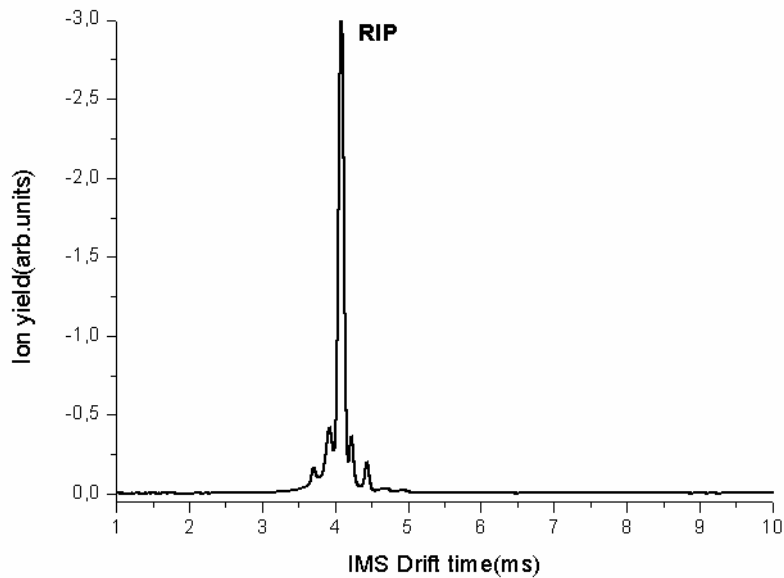


Fig. 1. The IMS spectrum without any sample.

The IMS response of pure TCA (Sigma Aldrich) is shown in Figure 2. From this figure we can see that the response of IMS instrument results in formation several peaks.

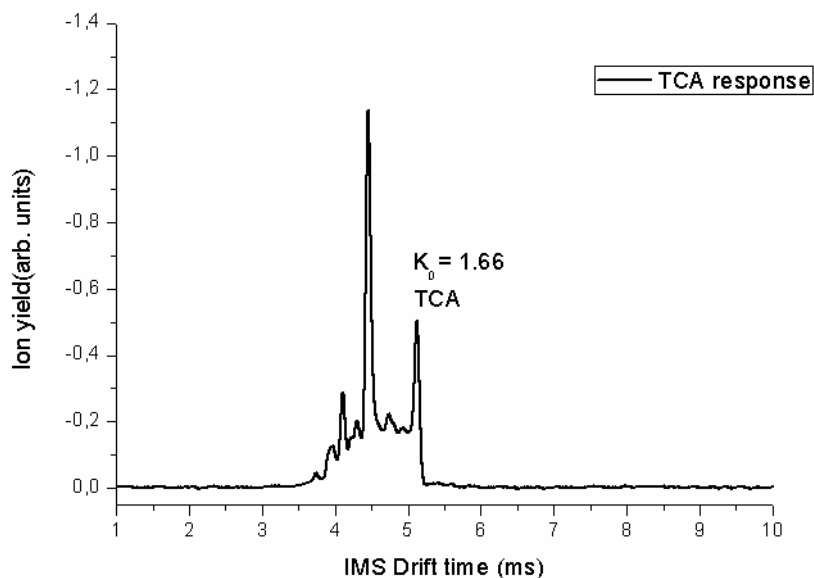


Fig.2. IMS response on TCA.

The slowest peak with reduced mobility $1.66 \text{ cm}^2 \cdot \text{V}^{-1} \cdot \text{s}^{-1}$ was evaluated as a TCA peak. This value of reduced mobility is in very good agreement with values reported in previous work [1]. The analysis of the cork stoppers with TCA concentration 19ppt determined by GC-MS technique results in immediate detection of TCA is presented in the Figure 3.

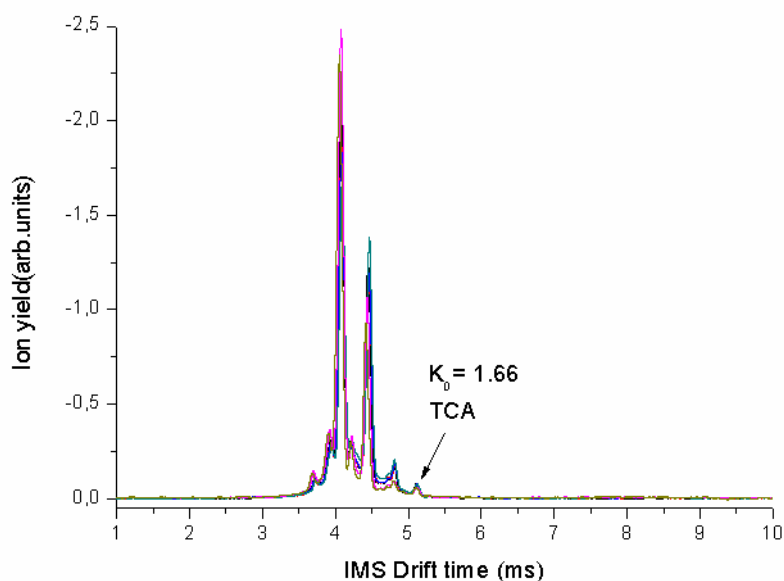


Fig.3. The IMS response on the cork stopper with TCA concentration 19ppt.

It has to be pointed out that analytical time required for TCA detection from the cork stoppers was less than 5 seconds with memory effect less than 4 seconds. The detection of TCA from cork stoppers with unknown TCA concentration will be also demonstrated at conference.

4. Conclusion

In this work we have demonstrated that the IMS instrument has ability to detect TCA from cork directly without any pre-treatment of the material. The analytical time required for analysis of cork stoppers was less than 5 second. These first results are very promising and allow a hope for future applications in industry.

5. Acknowledgement

This work was supported by Slovak research and development agency project APVV-0259-12.

6. References

- [1] Z. Karpas, A.V.Guaman, D. Calvo,A.Pardo,S.Marco, Talanta, 93 (2012) 200
- [2]H.R.Buser, C. Zanier,H.Tanner, J.Agric. Food Chem., 30 (1982) 359
- [3]S.H.Patil, K.Banerjee, S.C.Utture, A.R.Fontana,J.C.Altamirano, D.P.Oulkar, S.S.Wagh, S.Dasgupta,S.B. Patil, M.R. Jadhav, B.R. Ugare, P.G. Adsule, M.B. Deshmukh, Food Chem, 124 (2011) 1734
- [4]I.M.Sillero, S.Cardenas,M.Valcarcel, J.Chrom.A, 1265 (2012) 149
- [5]G.A.Eiceman, Z.Karpas, Ion mobility spectrometry 2nd ed., 2005, CRC Press